N° d'ordre H279

Université des Sciences et Technologies de Lille

Travaux présentés par

Frédéric PAROL

En vue de l'obtention de

L'HABILITATION A DIRIGER DES RECHERCHES
EN SCIENCES PHYSIQUES

CONTRIBUTION A L'ETUDE DES NUAGES ETENDUS A PARTIR D'OBSERVATIONS RADIOMETRIQUES

Soutenue le 17 novembre 2000

Devant le jury composé de:

E. RASCHKE	Professeur, GKSS, Geesthacht	Rapporteur
R. KANDEL	Directeur de recherche, CNRS	Rapporteur
B. WIELICKI	Senior Research Scientist, NASA	Rapporteur
Y. FOUQUART	Professeur, Université de Lille	Directeur de Recherche
J.L. BRENGUIER	Ingénieur de la Météo, CNRM	Examinateur
J.C. BURIEZ	Professeur, Université de Lille	Examinateur
M. DESBOIS	Directeur de recherche, CNRS	Examinateur
P. JONAS	Professeur, Université de Manchester	Examinateur
J.J. MORCRETTE	Chargé de Recherche, CNRS	Examinateur

U.F.R. de Physique Fondamentale

Laboratoire d'Optique Atmosphérique

"Les nuages ?..., c'est nos rêves qui s'envolent !"

Shani, 5 ans

A Isabelle,
Evalyn, Pierrick et Shani

RESUME

Dans le contexte d'un changement du climat global du à l'augmentation des gaz à effet de serre, la rétroaction des nuages varie considérablement d'un modèle de prévision du climat à l'autre. Sur le plan radiatif, les limitations les plus évidentes de l'actuelle représentation des nuages dans les modèles sont, sans doute, le formalisme usuel de nuage "plan-parallèle homogène" et la méconnaissance de la microphysique dans les nuages de glace. L'étude de ces limitations est au cœur du travail que nous avons effectué et notre approche a été largement basée sur l'utilisation de mesures satellitales et aéroportées.

Une première partie de notre travail a été consacrée à la détermination de propriétés radiatives (température, émissivité) et microphysiques des nuages de glace à partir de mesures effectuées dans la fenêtre atmosphérique située entre 8 et 14µm. Notre démarche initialement basée sur la seule utilisation de l'instrument spatial AVHRR s'est rapidement enrichie dans le contexte des campagnes internationales ICE et EUCREX par une utilisation conjointe de cet instrument et d'autres équipements de terrain (radiomètre infrarouge thermique, auréolemètre).

En parallèle, nous avons étudié l'effet de l'hétérogénéité des nuages d'eau liquide (i) sur le bilan radiatif terrestre et (ii) sur la dérivation des propriétés optiques et radiatives des nuages à partir de la télédétection aux courtes longueurs d'onde. L'avènement de l'instrument aéroporté POLDER au laboratoire nous a offert l'opportunité de pouvoir effectuer des mesures dans le contexte de plusieurs expériences internationales (SOFIA/ASTEX en 92, EUCREX en 94, ACE2 en 97). Elles nous ont permis d'illustrer les limitations de la modélisation actuelle des nuages mais aussi de proposer des techniques d'évaluation de l'hypothèse dite "plan-parallèle" et de son utilisation dans l'inversion des mesures radiométriques.

Nous avons été rapidement impliqués dans la préparation du projet spatial POLDER/ADEOS et nos recherches ont été fortement orientées vers le développement des algorithmes opérationnels d'extraction des produits géophysiques (nébulosité, pression, épaisseur optique, albédo, ...), la validation de ces produits et leur utilisation scientifique.

ABSTRACT

In the context of global climate change caused by increasing emissions of greenhouse gases, cloud feedback strongly vary from a climate general circulation model to another. The reason for such a variation is the primitive state of cloud modelling in climate models. From the radiation point of view, the main limitations remain the usual "plan-parallel layer" hypothesis and the lack of accurate knowledge of ice cloud microphysics. The present study points out these two aspects and our approach has been mainly based on the use of spaceborne and airborne radiation measurements.

The first part of this work is devoted to the determination of radiative and microphysical properties of ice clouds using measurements in the thermal infrared window (8-14μm). Our initial approach based on the only use of AVHRR satellite data was made more comprehensive in the context of international field experiments as ICE and EUCREX where satellite data were combined with those acquired by ground-based instruments (thermal infrared radiometer, aureolemeter).

Concurrently, we investigated the effects of liquid water cloud heterogeneity both (i) on the Earth radiation budget and (ii) on the derivation of optical and radiative cloud properties from remote sensing at short wavelengths. The new airborne POLDER instrument arrived opportunely for doing original measurements in the context of several international field campaigns (SOFIA/ASTEX in 92, EUCREX in 94, ACE2 in 97). Indeed, POLDER data analysis allowed to illustrate some limitations in current cloud modelling and to propose a methodology for evaluating the "plane-parallel cloud" assumption when used for radiometric data inversion.

Finally, we were involved in the spatial POLDER/ADEOS project very soon as well as in the development of operational algorithms for cloud property retrievals (cloudiness, cloud optical thickness, cloud albedo, cloud pressure, ...). Furthermore, our research of interests included the validation of these cloud properties and their scientific use.

SOMMAIRE

AVIS AU LECTEUR

Les publications citées en **gras** dans les différentes parties rédigées en français, sont celles qui sont signées ou co-signées par l'auteur et qui forment les différents chapitres de ce document de synthèse ou que l'on retrouve dans les annexes en fin de document. Les autres publications, citées en *italique*, sont référencées à la fin du document.

INTRODUCTION

Le Climat est ce qui rend la Terre habitable. Et le climat est en perpétuel changement...comme une conséquence à la fois des processus naturels et de l'activité humaine. Même les faibles modifications du climat de la Terre doivent être suivies avec un grand intérêt, car elles peuvent affecter le confort de l'humanité, son bien-être, voire même sa survie. Quelques années successives avec un taux de pluie en dessous de la moyenne, un hiver inhabituellement froid ou un changement dans les émissions dues au brûlage des pâturages, peuvent influer sur la qualité de vie des hommes, des animaux ou des plantes dans les régions concernées.

Durant le siècle à venir, la Terre sera confrontée au risque potentiel de changements environnementaux rapides. L'amplitude, la distribution régionale et temporelle du changement global auront un impact important sur notre société, mais encore aujourd'hui il nous est impossible de fournir des réponses précises aux questions qui sont soulevées à propos des effets probables de ce changement climatique. Ceci est du pour une large part à notre connaissance insuffisante des processus interdépendants qui affectent le climat régional ou global. Parmi les problèmes qui ont reçu une attention croissante ces dernières années il faut citer celui qui a motivé les recherches qui sont présentées dans ce document de synthèse, c'est à dire les changements dans les effets radiatifs des nuages dus au réchauffement global et à l'augmentation des aérosols anthropogéniques (i.e. liés aux activités humaines). En effet ce sont principalement les échanges d'énergie radiative qui constituent le moteur climatique et plus que n'importe quel autre composant du système climatique, les nuages affectent le flux d'énergie à l'intérieur de l'atmosphère et à la surface terrestre. Les nuages réfléchissent vers l'espace une partie du rayonnement solaire alors indisponible pour la surface, mais cet effet est très variable allant du fort pouvoir réfléchissant des nuages d'orage, qui permettent à si peu de lumière d'atteindre la surface que l'on a l'impression que le Soleil s'est couché prématurément, aux couleurs subtiles et douces de la lumière du Soleil transmise à travers un Cirrus fin. L'influence des nuages s'étend à la partie infrarouge thermique du spectre électromagnétique, où ils contribuent de façon importante à l'effet de serre naturel. En plus de leurs effets sur le rayonnement, les nuages jouent un rôle clé dans le cycle de l'eau de la Terre. La chaleur latente, qui est l'énergie nécessaire à l'évaporation de l'eau à la surface terrestre, est redistribuée dans l'atmosphère quand la vapeur d'eau se condense de nouveau pour former les nuages. C'est un des mécanismes qui permet à la surface de transférer vers l'Espace le surplus d'énergie qu'elle reçoit du Soleil (voir Fig.1). Dans ce contexte, les systèmes nuageux les plus importants sont évidement ceux qui présentent une large extension spatiale et une longue durée de vie en plus d'une prédominance clairement définie pour l'un ou l'autre des deux effets antagonistes sur le rayonnement solaire (augmentation de l'albédo) et le rayonnement infrarouge (augmentation de l'effet de serre), c'est à dire les nuages de couche limite et les cirrus. Ces deux types de nuages sont au centre du travail qui est présenté dans ce document.

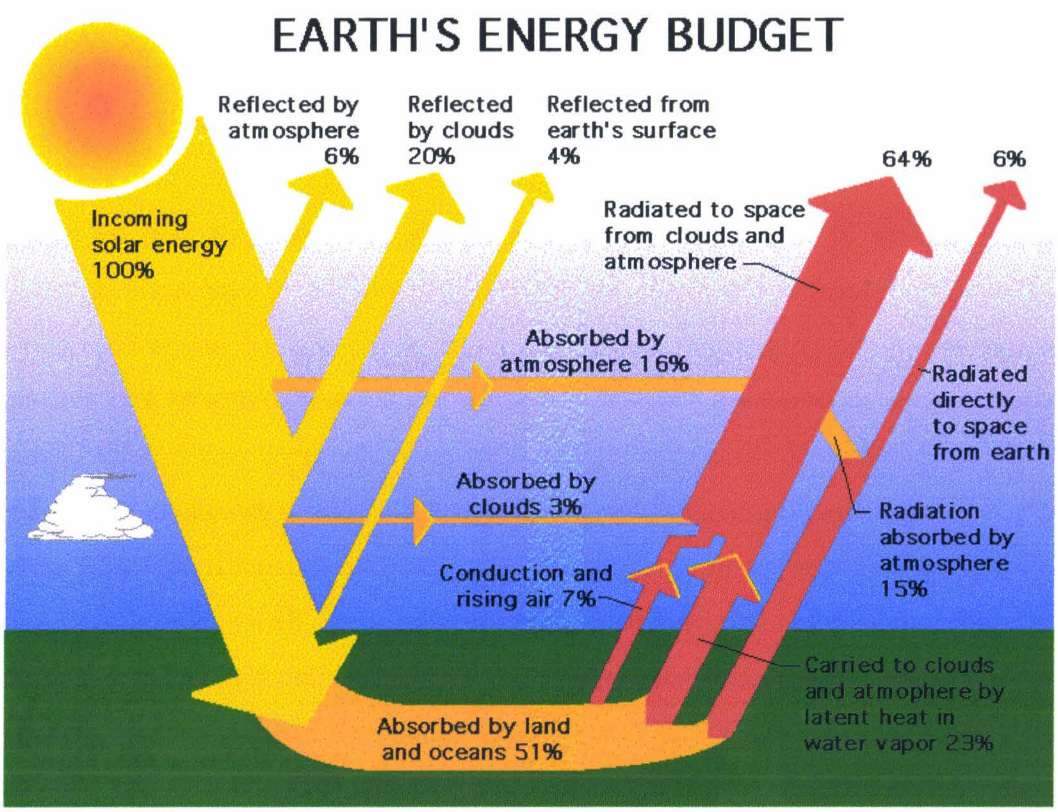

Fig.1. Schéma du bilan énergétique de la Terre
(site Web de la NASA: http://asd-www.larc.nasa.gov/erbe/)

Bien qu'il soit évident que les nuages doivent être pris en compte dans les études du Climat, ils sont difficiles à décrire mathématiquement dans les modèles de simulations du Climat (GCM). Une grande variété de propriétés de nuages peuvent potentiellement avoir leur rôle à jouer: la forme, la taille, la localisation horizontale et verticale, la durée de vie, la distribution en taille et en forme des particules nuageuses, et bien d'autres encore. La manière dont les nuages absorbent, diffusent et émettent le rayonnement est influencée par chacune de ces propriétés.

Dans le contexte d'un changement du Climat global du à une augmentation des gaz à effet de serre et des aérosols anthropogéniques, la rétroaction des nuages varie, encore aujourd'hui, considérablement d'un modèle climatique à l'autre. Par exemple, lorsque l'on fait l'hypothèse d'un doublement instantané de la concentration préindustrielle en dioxyde de carbone (CO_2), cela engendre une réduction du rayonnement infrarouge thermique émis par notre système climatique d'environ 4 Wm^{-2} (*Houghton et al*, 1990, 1994). En supposant que ce changement climatique n'induit qu'un nouvel équilibre de la température moyenne de surface de la Terre, celle ci devrait augmenter d'environ 1°C pour maintenir l'équilibre radiatif du système, si tous les autres facteurs (nuages, vapeur d'eau et aérosols) étaient maintenus constants. Quoiqu'il en soit la réponse d'un modèle de simulation du Climat à un tel forçage radiatif est extrêmement variable. Les effets des nuages sur le climat sont si compliqués que les modèles climatiques donnent des réponses contradictoires quant à leur impact sur le climat. D'après *Cess et al.* (1990, 1996) qui ont comparé le comportement de plusieurs GCM, lorsqu'il n'y a pas de nuages dans les modèles, la variation de la température globale moyenne est peu dépendante du modèle. Au contraire, la rétroaction des nuages diffère considérablement d'un modèle à l'autre, et par conséquent la température globale moyenne peu varier de 1.5°C à environ 4.5°C lorsque les nuages sont introduits dans les modèles climatiques. En fait, l'incertitude qui persiste à l'heure actuelle dans le traitement des interactions nuages-rayonnement dans les modèles climatiques est plus large que l'ensemble des conséquences radiatives attendues par un doublement du CO_2. Ceci est du en grande partie au fait que les nuages présentent des hétérogénéités à différentes échelles spatiales qui ne sont pas prises en compte à l'heure actuelle dans les modèles climatiques. Sur le plan radiatif, les limitations les plus évidentes de l'actuelle représentation des nuages dans les modèles sont, sans doute, l'hypothèse de sphéricité pour les particules nuageuses quelque soit le type de nuage, et le formalisme usuel de nuage "plan-parallèle homogène infini". L'étude de ces limitations est au cœur du travail qui est présenté dans ce document de synthèse.

Ce qui est exposé ci-dessus démontre clairement le besoin d'une représentation réaliste des nuages et de leur influence sur le bilan radiatif terrestre. Pour ce faire les satellites en orbite autour de la Terre semblent vraiment bien adaptés puisqu'ils nous permettent de faire des mesures globales du rayonnement au sommet de l'atmosphère. De plus, pour vérifier les paramétrisations de nuages introduites dans les GCM, nous avons besoin d'informations sur les propriétés des nuages à l'échelle globale. Les satellites ne peuvent pas fournir toutes les réponses, mais des mesures de rayonnement depuis l'espace jouent un grand rôle et nous aident à comprendre comment le rayonnement dépend des propriétés des nuages. Quoiqu'il en soit, les observations *in situ* restent essentielles, à la fois pour étudier des processus physiques à des échelles spatiales et temporelles fines, mais aussi pour valider les propriétés de nuages dérivées depuis satellites, pour mettre au point les techniques de dérivation de ces propriétés, ou tout simplement pour compléter les mesures satellitales.

Le travail présenté dans cette thèse s'inscrit tout à fait dans ce schéma. Il constitue mon activité de recherche effectuée depuis le début des années 1990 au Laboratoire d'Optique Atmosphérique sous la direction du professeur Yves Fouquart.

La première partie de ce document est consacrée à la détermination de propriétés radiatives (température, émissivité) et microphysiques des Cirrus à partir de mesures effectuées essentiellement dans l'infrarouge thermique, plus précisément dans la fenêtre atmosphérique située entre 8 et 14μm. Notre démarche initialement basée sur la seule utilisation de l'instrument spatial AVHRR s'est rapidement enrichie dans le contexte de la campagne internationale ICE par une utilisation conjointe de cet instrument et d'autres équipements de terrain (radiomètre infrarouge thermique, auréolemètre).

La seconde partie de ce document rassemble les études que nous avons menées ces dernières années sur l'effet de la distribution spatiale de l'eau dans les nuages à la fois sur le bilan radiatif terrestre et sur la dérivation des propriétés optiques et radiatives des nuages à partir de la télédétection passive aux courtes longueurs d'onde. Notre intérêt pour ce thème de recherche a débuté par l'influence des hétérogénéités des nuages sur les flux radiatifs au sommet et à la base de l'atmosphère. Avec l'avènement de l'instrument POLDER au laboratoire, il nous est apparu évident qu'il fallait valider (ou plutôt invalider) l'hypothèse du modèle de nuage plan-parallèle homogène directement par l'observation du diagramme de rayonnement solaire réfléchi par des nuages et non plus simplement par des simulations numériques dans lesquelles sont souvent introduits des modèles de nuages qui peuvent paraître tout aussi irréalistes que le modèle plan-parallèle. Nous avons eu l'opportunité de pouvoir effectuer des mesures aéroportées avec POLDER dans le contexte de plusieurs expériences internationales (SOFIA/ASTEX, EUCREX'94, ACE2) auxquelles j'ai personnellement participé en tant que responsable scientifique des mesures POLDER au dessus des nuages. Elles nous ont permis d'illustrer les limitations de la modélisation actuelle des nuages mais aussi de proposer des techniques d'évaluation de l'hypothèse plan-parallèle et de son utilisation dans l'inversion des mesures radiométriques visible.

Parallèlement à cette analyse des données aéroportées acquises par POLDER, nous avons été rapidement impliqués dans la préparation du projet POLDER spatial et nos recherches ont donc été fortement orientées par l'utilisation future de ces données. Le premier point a été le développement des algorithmes d'extraction des produits géophysiques (nébulosité, pression, épaisseur optique, albédo, ...) à partir des données de luminances acquises par POLDER. Un effort important a ensuite porté sur la préparation d'un plan de validation de ces produits géophysiques et le développement de l'utilisation scientifique de ces produits. Je me suis très rapidement impliqué dans le projet POLDER spatial puisque je suis Principal Investigateur d'une proposition de recherche sur les nuages et je participe à l'IPSWT (International POLDER Science Working Team) depuis 1994. Cet aspect de mes recherches est présenté dans la troisième partie de cette thèse.

Chapitre 1

Détermination de Propriétés Radiatives et Microphysiques des Cirrus à partir de Mesures dans l'Infrarouge Thermique

Introduction

Les Cirrus sont bien connus pour exercer une forte influence sur le bilan radiatif terrestre et sur la répartition du forçage radiatif entre l'atmosphère et la surface, ainsi qu'au sein même de l'atmosphère. A ce titre, les Cirrus sont une composante significative du système climatique global. Ces nuages sont souvent non-opaques (ou semi-transparents) et, par conséquent, sont des modulateurs relativement inefficaces du rayonnement solaire en comparaison à d'autres types de nuages tels que les stratus. Quoiqu'il en soit les Cirrus se trouvent dans la partie la plus élevée de la troposphère où les températures sont froides, surtout par contraste avec la surface, et ils exercent ainsi une influence forte sur l'échange de rayonnement infrarouge thermique entre la surface et l'espace. La compréhension du système climatique global requiert donc une connaissance précise de la couverture nuageuse de Cirrus incluant sa distribution spatiale ainsi que ses propriétés optiques et radiatives. La télédétection des Cirrus depuis satellites s'efforce de remplir ce besoin. Néanmoins, le caractère souvent semi-transparent et hautement variable des Cirrus les rend uniques et difficiles à détecter depuis l'Espace.

Aux Etats-Unis comme en Europe, plusieurs projets ont vu le jour après 1985 dans le but d'améliorer nos capacités de détection des Cirrus, ainsi que notre compréhension des processus physiques mis en jeu dans la formation, la maintenance et la dissipation de ces nuages (et des Stratus). Au delà, la finalité de ces projets était, bien entendu, d'améliorer la représentation des Cirrus utilisée dans les modèles du système climatique global (voir par exemple *Cox et al*, 1987). Ainsi furent initiés les projets FIRE en 1985 aux Etats-Unis et ICE et son successeur EUCREX à la fin des années 80 et au début des années 90 en Europe. Chacun de ces programmes a mis en place une série d'expériences sur le terrain focalisées sur les Cirrus et en particulier sur la télédétection de leurs propriétés depuis l'espace (voir par exemple *Starr*, 1987; *Raschke et al*, 90; *Raschke et al*, 98). Ces campagnes de mesures impliquaient des observations *in situ* en coordination étroite avec l'état de l'art des mesures de télédétection aéroportées et depuis la surface, ainsi que des observations satellitales. C'est dans ce contexte que nous avons entrepris en 1988 l'étude des propriétés des Cirrus depuis l'espace à partir de l'imagerie infrarouge thermique.

Une première étude a été menée à partir de la différence de températures radiatives observée dans les deux canaux infrarouges thermiques (centrés sur 10.5 et 11.5 μm) du radiomètre AVHRR embarqué sur les satellites héliosynchrones de la NOAA. Nous avons montré que cette différence était très sensible à la composition microphysique des cirrus semi-transparents. Les modèles de particules nuageuses diffusantes considérées étaient soit des sphères d'eau liquide ou de glace, soit des cylindres de glace. Nous avons ainsi montré que ces derniers, quoique a priori plus réalistes, ne permettaient pas d'expliquer les différences importantes de températures radiatives observées (**Parol et al, 1991**).

Le travail théorique développé par Gérard Brogniez au laboratoire a ensuite permis de calculer les propriétés optiques de cristaux de glace plus réalistes, de forme hexagonale. Nous avons pu alors simuler les propriétés radiatives de nuages de glace composés de tels cristaux, en particulier dans les canaux thermiques de AVHRR.

Nous avons étudié plus particulièrement l'image AVHRR acquise le 18 octobre 1989 au cours de la campagne intensive de ICE. L'analyse des données a montré que (1) les mesures d'émissivité des Cirrus semi-transparents observés depuis satellite – typiquement de l'ordre de 0.1 – étaient en très bon accord avec les mesures effectuées au sol à l'aide d'un radiomètre infrarouge ; (2) les différences de températures observées dans les deux canaux thermiques étaient compatibles avec les différences de températures radiatives simulées à partir du modèle de cristaux de glace hexagonaux dérivé de mesures d'auréolemètre effectuées depuis la surface ; (3) des particules sphériques de même volume donneraient un signal en différence de température trop faible ; (4) les différences de températures observées ont mis en évidence une taille de cristaux de glace nettement plus petite dans les traînées d'avion que dans les Cirrus naturels (**Brogniez et al, 1995**).

Afin de généraliser ce type de modèle microphysique, il était nécessaire de passer à l'analyse de nombreuses observations de Cirrus depuis l'espace. Ce fut l'objet de la thèse de Vincent Giraud, que j'ai co-encadrée en collaboration avec Jean-Claude Buriez, et qui avait pour but d'appréhender l'évolution temporelle des propriétés microphysiques et radiatives des Cirrus. Notre étude s'est ainsi étendue à l'ensemble des images AVHRR qui couvraient la zone de l'expérience ICE durant la période comprise entre le 10 et le 20 octobre 1989. Le déplacement des Cirrus au cours du temps a été obtenu grâce à l'utilisation conjointe des images METEOSAT acquises toutes les demi-heures durant la même période. Pour une reconnaissance automatique du type de nuages présents sur les images AVHRR, nous avons adapté la méthode de classification dite des "nuées dynamiques", développée et utilisée au Laboratoire de Météorologie Dynamique pour la classification des images METEOSAT (Sèze and Desbois, 1987).

Des études approfondies sur l'interprétation des températures de brillance observées à partir des deux canaux thermiques de AVHRR ont permis de développer une procédure automatique d'analyse conduisant à l'estimation globale des propriétés microphysiques et de la température physique des Cirrus. Une analyse statistique, appliquée à l'ensemble des données AVHRR, a montré qu'il y avait une dépendance de la microphysique des nuages froids avec leur température de sommet. Nous avons ainsi mis en évidence un changement important de la dimension équivalente moyenne des hydrométéores pour des températures de nuages voisines de 235K. Pour des températures de nuages inférieures à 235K, seules des particules de rayons effectifs équivalents supérieurs à 10µm ont été observées, tandis que pour des nuages plus chauds des particules beaucoup plus petites ont pu être mises en évidence (**Giraud et al, 1997**)

Reprinted from JOURNAL OF APPLIED METEOROLOGY, Vol. 30, No. 7, July 1991
American Meteorological Society

Information Content of AVHRR Channels 4 and 5 with Respect to the Effective Radius of Cirrus Cloud Particles

F. PAROL, J. C. BURIEZ, G. BROGNIEZ AND Y. FOUQUART

Laboratoire d'Optique Atmosphérique, Université des Sciences et Techniques de Lille, Villeneuve d'Ascq, France

(Manuscript received 27 June 1990, in final form 9 November 1990)

ABSTRACT

This paper investigates the important difference in the relationship between brightness temperatures between the 11-μm and the 12-μm AVHRR data and the microphysical properties of the semitransparent cirrus clouds. In the nonscattering approximation, the emittance for channels 4 and 5 are related through the absorption coefficient ratio that is the key parameter giving access to the size of cloud particles. The observed mean value of this parameter corresponds to effective radius of 18 μm for polydisperse spheres and 12 μm for polydisperse infinitely long ice cylinders. Taking the multiple scattering into account, the brightness temperature difference enhances much more for cylinders than for spheres owing to the fact that the forward peak of scattering is less large for cylinders. To obtain the size of cloud particles, the method developed in the nonscattering case is still applicable if one makes use of the effective emittance that implicitly includes the effects of scattering. Thus, an effective absorption coefficient ratio is defined and we derive a direct relationship between this ratio and the optical properties of the cloud particles. The mean value of the effective absorption coefficient ratio corresponds to ice spheres of effective radius of 26 μm or a bit less in the case of water spheres (supercooled droplets), but no agreement can be obtained for fully randomly oriented cylinders.

1. Introduction

Cloud and radiation interactions have long been considered to constitute one of the key problems in climate research (Houghton and Morel 1983). This question has become even more crucial, these last years, as several sensitivity studies [see, for example, Schlessinger and Mitchell (1986) or Cess et al. (1989)] have shown that the response of numerical climate models was extremely dependent on the various hypotheses and parameterizations used to simulate this process.

This large sensitivity results from the opposite, but potentially very large influences that clouds have on the shortwave (the so-called "albedo effect") and longwave radiation. The predominance of either of these two effects depends on many conditions, but it is quite clear that clouds of large spatial and temporal extension are the most important to consider and that low-level stratiform clouds have the maximum potential albedo effect, whereas high-level clouds and particularly cirrus clouds have the largest greenhouse effect.

The International Satellite Cloud Climatology Project (ISCCP: Schiffer and Rossow 1983) and the associated regional experiments [FIRE: Cox et al. (1987), and ICE: Raschke and Rockwitz (1988)] have been designed to improve the modeling of clouds and radiation interactions. A major achievement of the ISCCP was the building of a consistent dataset of cloud covers and cloud properties at the planetary scale. However, even if satellite observations appear particularly appropriate for observing upper-level clouds which, then, are unmasked, cirrus clouds still constitute a challenging problem in cloud research. Indeed, they are often tenuous so that their detection from satellite is really difficult.

Therefore, particular attention has been given, these last years, on testing cloud detection algorithms in the case of cirrus clouds or on developing specific algorithms. Reynolds and Vonder Haar (1977) used ground-based observations to calibrate a relationship between visible albedo and infrared emissivities to correct for the cirrus semitransparency. Szejwach (1982) determined cirrus cloud-top temperature from Meteosat water vapor and infrared window channels; his technique was then integrated in the automatic cloud clustering method of Desbois et al. (1982). This method is based on three-dimensional histograms of the three Meteosat channels (visible, infrared window, and water vapor).

Satellite-derived cirrus climatologies were presented by Woodbury and McCormick (1983, 1986), Barton (1983), and Prabhakara et al. (1988). The first authors derived the cirrus cloud cover from their analysis of the Statospheric Aerosol and Gas Experiment (SAGE). Using a limb-viewing absorption technique, their

Corresponding author address: F. Parol, Laboratoire D'Optique Atmospherique, Universite des Sciences et Techniques de Lille Flandres Artois, Batiment P5, 59655 Villeneuve d'Ascq Cedex, France.

method is very sensitive to cirrus clouds that are seen with a very small elevation angle, which maximizes their opacity. Therefore, it is not surprising that the frequency of occurrence of cirrus found by Woodburry and McCormick is systematically much larger than that found by Barton, who used the data collected by the nadir looking Selective Chopper Radiometer onboard of Nimbus 5. Barton's method made use of dual-wavelength observations of reflectances near 2.7 μm. Prabhakara et al. used a bispectral technique based on Nimbus 4 Infrared Interferometer Spectrometer (IRIS). Their method is based on the significant differences that exist between the spectral extinctions at 10.8 and 12.6 μm.

The physical basis of the methods suggested by Inoue (1985) and Wu (1987) was quite similar. They showed that cirrus cloud-top temperature and infrared effective emissivity could be derived from two window channels centered at 11 and 12 μm. According to these authors, 1) the difference in brightness temperatures of the two channels is always more important for thin cirrus clouds than for thick clouds or clear-sky areas and 2) this difference is very sensitive to the clouds' radiative and microphysical properties.

Inoue (1985) used a simple model of a purely absorbing cloud. In this model, the key parameter is the "absorption coefficient ratio" β, which relates the cirrus emissivities at 11 and 12 μm and depends on the cloud microphysical properties. Experimentally, Inoue found that on average $\beta = 1.08$. In this paper, scattering is accounted for and the dependence of β on the particle size is investigated for two ideal shapes of particles: spheres and infinitely long cylinders. Our method of analysis closely follows that of Inoue. The physical basis of his method is thus first recalled in section 3 for the case of purely absorbing clouds; the more realistic case of scattering spheres and cylinders is considered next. In section 4, we shown that Inoue's method of analysis still applies for scattering particles provided that β be replaced by an "effective absorption coefficient ratio." To make it for the readers who are not familiar with Inoue's method, we find it convenient to consider in section 2, a practical case on which the method is applied.

2. Observations

Eight cirrus cloud cases have previously been analyzed by Inoue (1985) to determine a simple relationship between the emissivities in channels 4 and 5 of the Advanced Very High Resolution Radiometer (AVHRR). In this section, we use a practical example to support our theoretical analysis.

We consider a 1000 km $\times$ 1000 km satellite picture taken by the AVHRR instrument on board of NOAA 9. The picture is centered on the west Atlantic Ocean (40°N, 20°W) and was collected on 30 January 1985 at 1500 UTC. Figure 1a is a channel 1 (0.58–0.68 μm) reflectance image and Fig. 1b presents channel 4 (10.5–11.3 μm) brightness temperature T_4, whereas Fig. 1c shows the brightness temperature difference (BTD) between channel 4 and channel 5 (11.5–12.5 μm). For each pixel, the AVHRR digital counts are given a grey level from black (0 count) to white (255 counts).

A large high-level cloud system covers nearly half of the northwestern (upper left) part of the image. This system contains thick high clouds, which appear white on both Figs. 1a and 1b, and more tenuous clouds that have a rather small reflectance but appear white on both Figs. 1b and 1c. Other cirrus streaks may also be detected on the southeastern (lower right) part of the pictures; despite the fact that they are situated above low-level clouds, they are very easily identified on the BTD picture. Figure 1 clearly confirms that the BTD method allows the identification of semitransparent cirrus clouds, at least over midlatitude oceanic areas.

Figure 2 presents the brightness temperature difference $T_4 - T_5$ plotted as a function of T_4 for a small area (200 km $\times$ 60 km) marked on Fig. 1. In spite of the very large dispersion, the histogram has the characteristic shape of an arch. For the thickest part of the cirrus ($T_4 \approx 220$ K), the BTD is close to zero, whereas for the pixels with semitransparent cirrus, T_4 ranges between ~230 K and ~270 K, and the BTD is always positive; the maximum is a little bit greater than 6 K for $T_4 \approx 250$ K. For the cloud-free pixels ($T_4 \approx 280$ K), the BTD is small but positive, corresponding to the different water-vapor spectral absorptions in the lower troposphere.

The present illustration is restricted to the marked area for clarity: 1) the zone under study must be small enough to keep reasonable spatial homogeneity, 2) it must contain both clear pixels and fully overcast pixels of infrared emissivity close to unity, 3) the clear pixels must be gathered enough for the hypothesis of either totally clear or totally cloudy pixels to be realistic. Histograms similar to those of Fig. 2 can also be drawn for other areas of the satellite picture. However, they generally have a much less significant cold cluster. This is particularly the case when one considers the cirrus streaks of the southeastern part of the image. In this case, the cold cluster is not well marked with only a few pixels around 240 K; a deep analysis of the BTDs for those semitransparent clouds is thus ambiguous since the actual temperature is not well known. Moreover, the signal is also affected by some low clouds that can be seen on Fig. 1a. It will be seen, in section 3a, that our selected zone can be considered as typical of the cirrus clouds analyzed by Inoue. A more comprehensive study of high-level clouds would, no doubt, be useful, but it would not improve the understanding of our method of analysis.

3. Analysis

Wu (1987) has shown that the BTD is highly sensitive to the size distribution of cloud particles. In this

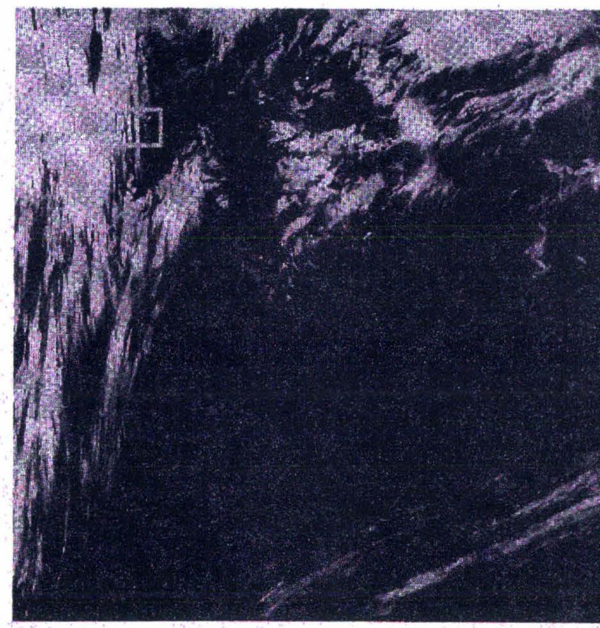

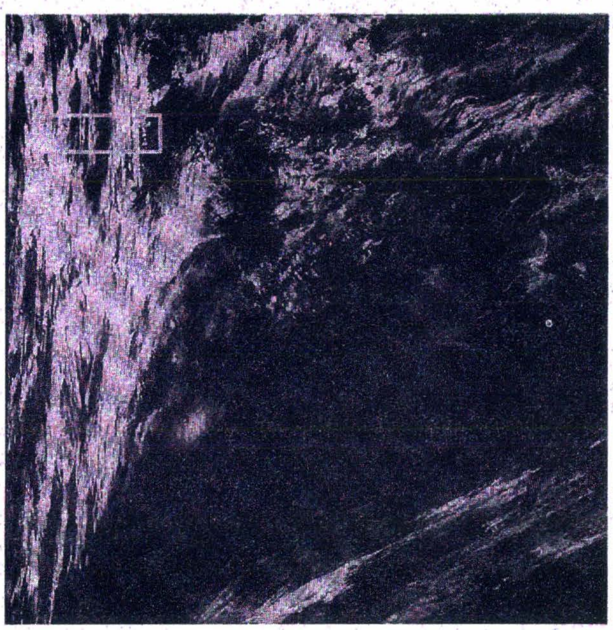

FIG. 1. Image constructed from visible (channel 1) reflectivity, (a), infrared (channel 4) brightness temperature, (b) and brightness temperature difference between channel 4 and channel 5, (c) for 1000 km × 1000 km region of the Atlantic Ocean centered at (40°N, 20°W) on 30 January 1985 at 1500 UTC. The AVHRR digital count values are given a grey level from black to 0 count to white at 255 counts. The grey scales represent a change in reflectivity from 0 to 0.8 (a), in brightness temperature from 290 to 210 K (b), and in brightness temperature difference from 0 to 5 K (c). Thick high clouds appear as light shade against a dark ocean background in visible and infrared images. Semitransparent cirrus clouds appear as light shades while thick clouds appear as black ones against the relatively dark cloud-free background in (c). The small area outlined in white is the area used for the bidimensional plot shown on Fig. 2.

section, we further investigate the relationship between the BTD and the cloud optical properties and microphysics. For this analysis, the atmosphere is assumed to be horizontally homogeneous and the radiative influence of the clear atmosphere situated above the cloud base is neglected. As a consequence, the outgoing radiance I_i^{clear} at the top of the atmosphere under clear-sky conditions is equal to the upward incoming radiance at cloud base. This is a reasonable approximation since AVHRR channels 4 and 5 are situated in the infrared window region where most radiation is coming from the lower atmosphere and since we are only considering high clouds.

In these conditions, the upward radiance from cloud top in the satellite direction is

$$I_i(\theta) = (1 - N)I_i^{\text{clear}}(\theta) + N\bigg[\int_0^{\pi/2} t_i(\theta, \theta')I_i^{\text{clear}}(\theta') \times \sin\theta' d\theta' + \int_0^{\pi/2} r_i(\theta, \theta')I_i^{\downarrow}(\theta') \sin\theta' d\theta' + \epsilon_i(\theta)B_i(T^{\text{cloud}})\bigg]. \quad (1)$$

In this expression, θ is the satellite viewing angle, i is the channel number, N the fractional cloud cover, $t_i(\theta,$

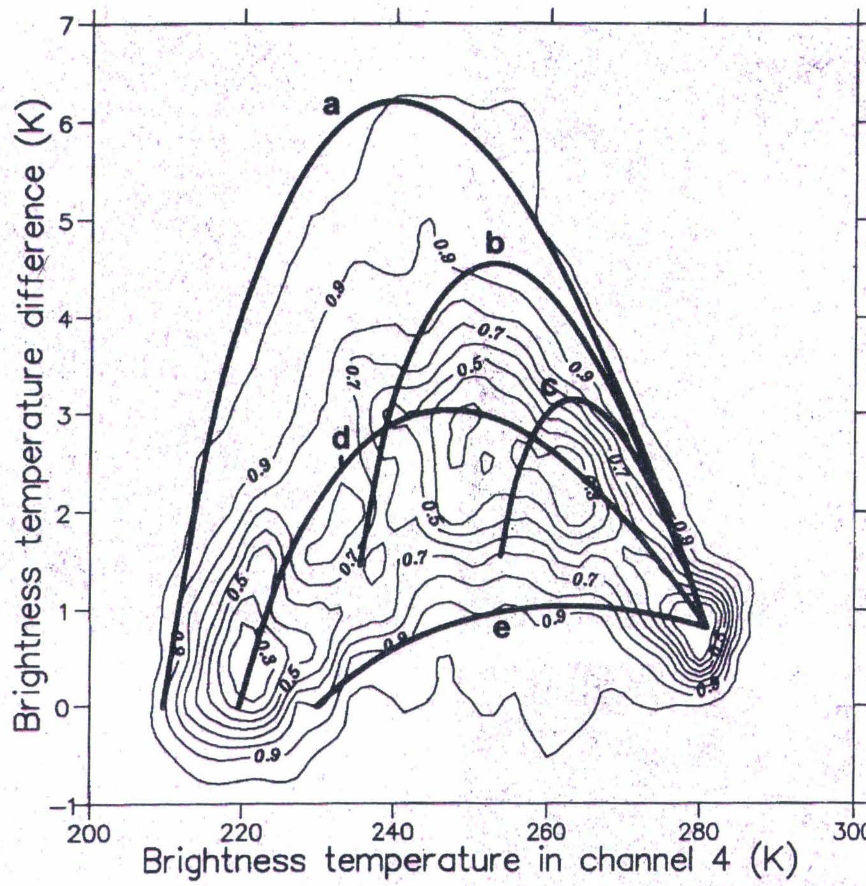

FIG. 2. Comparison between observed (isolines) and theoretical (thick lines) brightness temperature differences $T_4 - T_5$ for the small outlined area in Fig. 1. For example, 70% of the pixels are situated within the isolines 0.7. The thick lines correspond to several combinations of the cloud top temperature $T^{\rm cloud}$, the cloud cover N, and the absorption coefficient ratio β: (a) $T^{\rm cloud}$ = 210 K, N = 1.00, β = 1.18; (b) $T^{\rm cloud}$ = 210 K, N = 0.75, β = 1.18; (c) $T^{\rm cloud}$ = 210 K, N = 0.50, β = 1.18; (d) $T^{\rm cloud}$ = 220 K, N = 1.00, β = 1.08; (e) $T^{\rm cloud}$ = 230 K, N = 1.00, β = 1.00. The cloud-free brightness temperatures is fixed to 281.0 and 280.2 K in channels 4 and 5, respectively.

θ') the cloud transmission function in the satellite direction for radiation incident at cloud base in direction θ', $r_i(\theta, \theta')$ the cloud-top reflection function, $I_i^{\downarrow}(\theta')$ the downward radiance at cloud top, $\epsilon_i(\theta)$ the cloud emittance in the satellite direction, $B_i(T)$ the Planck function, and $T^{\rm cloud}$ the cloud temperature assuming that the cloud layer is isothermal. To the extent that temperature changes with depth, $T^{\rm cloud}$ represents the cloud emitting temperature that is a weighted mean of the temperature of the penetrable portion of the cloud. For optically thin clouds, even if they are isothermal, there can be considerable differences between $T^{\rm cloud}$ and the brightness temperature T_i, which is the equivalent blackbody temperature defined by

$$B_i(T_i) = I_i. \qquad (2)$$

To simplify, we assumed isotropic incoming radiance at cloud base; the validity of this approximation will be discussed in section 4. The cirrus directional transmittance in the satellite direction is thus defined by

$$\bar{t}_i(\theta) = \int_0^{\pi/2} t_i(\theta, \theta') \sin\theta' d\theta'. \qquad (3)$$

In a first step, let us assume also isotropic downward radiance at cloud top. The cirrus directional reflectance $\bar{r}_i(\theta)$ can thus be defined in a similar way. Reflectance and transmittance are related to the emittance through the Kirchoff's law

$$\epsilon_i(\theta) = 1 - \bar{t}_i(\theta) - \bar{r}_i(\theta). \qquad (4)$$

In establishing Eq. (1), we likened the upward radiance at cloud top with the outgoing one at the top of the atmosphere; that is, we neglected the upper atmospheric emission. Consistently the downward radiance in Eq. (1) should be neglected. Therefore, Eq. (1) becomes

$$I_i(\theta) = \{1 - N[\epsilon_i(\theta) + \bar{r}_i(\theta)]\}I_i^{\text{clear}} + N\epsilon_i(\theta)B_i(T^{\text{cloud}}). \quad (5)$$

a. Nonscattering approximation

In longwave radiative transfer in water clouds, the usual approximation is to neglect scattering and consider cloud droplets as purely absorbing particles. This is mainly justified because of the very strong molecular absorption out of the infrared window (8–14 μm) that limits the impact of liquid water on the radiation field to that spectral range where the scattering efficiency of particles with dimensions typical of nonprecipitating clouds is much smaller than in the visible. Another important but often neglected reason lies in the fact that the distribution of the sources of radiation is obviously much more isotropic than in the shortwave, thus, reducing the role of scattering. For cirrus, scattering may play a more important role due to both the larger difference between the surface and cloud temperatures and the smaller asymmetry factor of crystals leading to larger reflectivities (Stephens 1980a). However, in his analysis of the BTDs, Inoue (1985) did not consider the influence of multiple scatterings, and Wu (1987) only considered the influence of scatterings by spherical particles. In this section, as a first step of a more complete analysis, we disregard the influence of scatterings.

In the absence of scattering, the cirrus reflectance is zero. Thus, the upward radiance at the top of the atmosphere is simply

$$I_i^{ns}(\theta) = [1 - N\epsilon_i^{ns}(\theta)]I_i^{\text{clear}} + N\epsilon_i^{ns}(\theta)B_i(T^{\text{cloud}}) \quad (6)$$

where the superscript ns is a reminder of the nonscattering approximation.

As a first approximation, one can consider that the absorption coefficient σ_{α_i} of liquid water and ice are constant over the spectral bandpass of each AVHRR channel. The cloud emittance can thus be written as

$$\epsilon_i^{ns}(\theta) = 1 - \exp\left(-\frac{\sigma_{\alpha_i}Z}{\cos\theta}\right) \quad (7)$$

where Z is the cloud thickness.

From Eq. (7), the emittance for channels 4 and 5 are related by

$$\epsilon_5^{ns}(\theta) = 1 - [1 - \epsilon_4^{ns}(\theta)]^{\beta} \quad (8)$$

where $\beta = \sigma_{\alpha_5}/\sigma_{\alpha_4}$ is the absorption coefficient ratio, as defined by Inoue (1985). According to Eqs. (6) and (8), the relationship between the brightness temperature difference $T_4 - T_5$ and T_4 depends on the cloud temperature T^{cloud}, the fractional cloud cover N, the absorption coefficient ratio β, and the upward radiance at the cloud base. In the present analysis, the last quantity is approximated by the clear-sky radiance I_i^{clear}.

If the sea surface temperature may be assumed to be uniform, I_i^{clear} can be estimated from the cloud-free areas in the neighboring of the cirrus cloud. This is more difficult in the case of multilayered clouds. However, if the underlying layer is homogeneous, Eq. (6) may be used, all the same, provided that I_i^{clear} is now defined as the cirrus-free radiance. In the present case, I_i^{clear} is determined for each channel as the averaged radiance of the cloud-free pixels of the selected area. The cloud-free brightness temperature T_4 is 281 K and the corresponding BTD is $T_4 - T_5 = 0.8$ K. On the other hand, T^{cloud} cannot be directly derived from the radiances escaping from semitransparent cirrus cloud. We get access to it only if the cirrus has an optically thick part, assuming that the emitting temperature of the semitransparent part is approximately the same as that of the optically thick. Strictly speaking, this is certainly not true because since cirrus can be some kilometers thick, their emitting temperature can vary very substantially according to their opacity; these variations may still be large even for thick cirrus clouds as a result of variations in the vertical profile of ice content and size distribution. Without any additional information, however, this remains the most reasonable approximation.

From a study of eight cirrus cases, Inoue (1985) suggested that for overcast pixels $\beta \approx 1.08$. Using $N = 1$, $\beta = 1.08$, and $T^{\text{cloud}} = 210$ K, we calculated T_4 and the BTD for varying cirrus emissivities. We then obtained a theoretical curve (curve d on Fig. 2) which is nearly the mean curve of the histogram.

The largest BTDs, however, do not fit this particular set of parameters and with $\beta = 1.08$ they would lead to $T^{\text{cloud}} \approx 180$ K, which is probably too cold. Curve a presents another possible set of parameters ($N = 1$, $T^{\text{cloud}} = 220$ K, $\beta = 1.18$), which agrees with the largest BTD. Curve e ($N = 1$, $T^{\text{cloud}} = 230$ K, $\beta = 1.00$) represents another extreme choice with agreement for small BTDs. Other possibilities also exist and are as likely as those drawn on Fig. 2; it is important to note that for partial cloud covers, β must be higher to explain large BTDs (see curve b and c).

If there were perfect coincidence between an AVHRR picture or a subset of it and a high spatial resolution image such as Landsat, the fractional cloud cover at the AVHRR pixel level could be determined unambiguously. In our case, coincident Landsat images were not available; we thus used the analysis of the characteristics of the cirrus clouds observed from 12 Landsat scenes by Kuo et al. (1988). These authors found a large number of cloud cells of diameter 0.1–1.5 km. They showed that these cells have significantly different structural characteristics than larger cloud cells. This suggests that different microphysical processes may be active at these different spatial scales.

Nevertheless, except for the case of contrails, the cells of size smaller than an AVHRR pixel have a relatively small importance in terms of cloud cover. Therefore, in the following, we assume that the cloud cover is either 1 or 0 at the scale of an AVHRR pixel, keeping in mind that some pixels may have a different fractional cloud cover. For these pixels, (i) the actual value of β may differ from that derived from larger cloud cells and (ii) the apparent value based upon the assumption that $N = 1$, is smaller than the actual one.

b. Sensitivity of the BTD to microphysics

In the nonscattering approximation, $\beta = 1.08$ seems a good mean value although there must be a large variability. The absorption coefficient ratio depends strongly on the cloud microphysics (phase, shape, size distribution). The sensitivity of the BTD to the particle-size distribution has been studied by Wu (1987), but no attempt has been conducted so far to derive usable microphysical information from the BTD. In the following sections, β is interpreted in terms of effective radius of cloud particles.

Although there are growing evidences of the presence of supercooled water droplets in cirrus (Heymsfield et al. 1988), they are generally formed of crystals of various shapes (Weickmann 1945, 1947; Heymsfield 1975, 1977); see also the review by Liou 1986). In this paper, we only consider the two simplest shapes: spheres and infinitely long cylinders. Figure 3 illustrates the geometry of the problem in the case of cylinders. Three cases are considered: uniform orientation UOC(θ, γ), random orientation in the horizontal plane 2D − ROC(θ), and full random orientation in space 3D − ROC. In the nonscattering case, θ on Fig. 3 is the zenith angle of the satellite direction, $\theta = 0°$ corresponds to the subtrack, and $\theta = 60°$ to a satellite viewing angle of roughly 50°, for the NOAA polar orbiters.

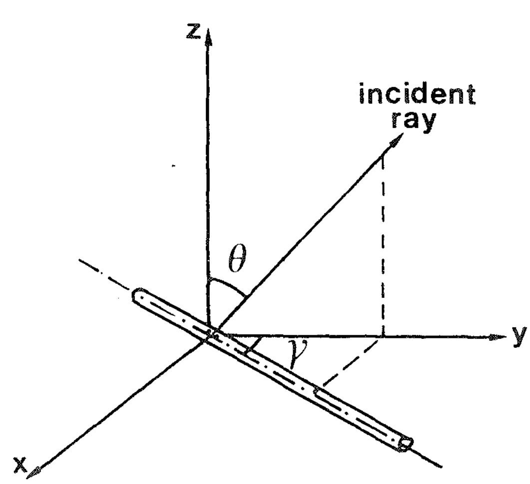

FIG. 3. Geometry of the orientation of a cylinder with respect to the incident ray.

TABLE 1. Real and imaginary parts of the complex index of refraction of water and ice.

AVHRR channel	υ (cm^{-1})	λ (μm)	Water n_r	Water n_i	Ice n_r	Ice n_i
4	929.02	10.76	1.1674	0.0835	1.0905	0.1710
5	844.80	11.84	1.1315	0.1840	1.2457	0.4023

For both spheres and cylinders, the particle-size distribution is assumed to be a *gamma* function (Deirmendjian 1969):

$$n(r) = N_0 r^6 \exp(-6r/r_0), \qquad (9)$$

where $n(r)$ is the number of particles per volume unit with radii between r and $r + dr$, and r_0 is the mode radius. For this distribution, the mean radius is $7r_0/6$ and the effective radius,

$$r_{\rm eff} = \int_0^\infty r^3 n(r)dr \Big/ \int_0^\infty r^2 n(r)dr \qquad (10)$$

is $3r_0/2$. This size distribution has been used by Arking and Childs (1985) to retrieve ice- and water-cloud parameters from multispectral satellite images. The relationship between the absorption coefficient and the effective radius is expected to be nearly independent on the size distribution [see Stephens et al. (1990); their Fig. 3]. In our simulations, $r_{\rm eff}$ varies from 3 to 100 μm.

The absorption coefficient σ_α, the scattering coefficient σ_s, and the scattering phase function have been calculated for AVHRR channels 4 and 5. They were computed, for water and ice spheres, from Mie theory and, for the cylinders, according to Van de Hulst (1957). The spectrally averaged real and imaginary parts of the refractive index of water (Downing and Williams 1976) and ice (Warren 1984) are listed in Table 1 for NOAA 9 AVHRR channels 4 and 5.

In the nonscattering approximation, Eqs. (6)–(8) apply and $\beta = \sigma_{\alpha_5}/\sigma_{\alpha_4}$ is the key parameter giving access to the size of particles. Figure 4 presents the variations of β as a function of the effective radius $r_{\rm eff}$ for polydispersions of spheres and cylinders. All curves present the same hyperbolic shape, the curves representative of ice and water spheres are very close to each other and β is always smaller for cylinders than for spheres. The difference between the curves representative of cylinders and spheres increases with θ. This was confirmed by additional calculations performed for larger θ and not shown here. According to Fig. 4, $\beta = 1.08$ corresponds to spheres of effective radius $r_{\rm eff} \approx 18$ μm or to cylinders with $r_{\rm eff} \approx 9$–15 μm.

c. Influence of multiple scatterings

The influence of scattering is small either when the single-scattering albedo $\omega_i = \sigma_{s_i}/(\sigma_{s_i} + \sigma_{\alpha_i})$ is small,

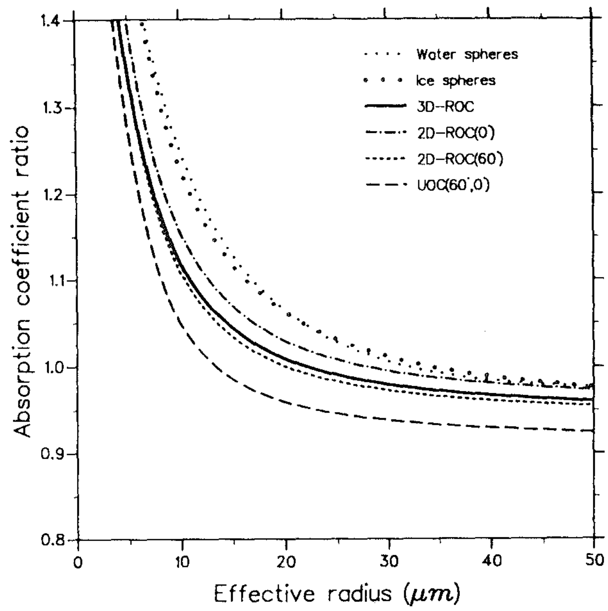

FIG. 4. The absorption coefficient ratio β versus the effective radius of spheres and long cylinders. The ice cylinders are uniformly oriented [(UOC(θ, γ)] and randomly oriented in the horizontal plane [2D – ROC(θ)] or in space (3D – ROC). Note that 2D – ROC (θ = 0) is equivalent to UOC (θ = 0, γ) and UOC (θ, γ = 0).

close to zero or, since scattering in the forward peak does not redistributes the radiation, when the scattering phase function $P_i(\theta)$ is reduced to the forward scattering peak; i.e., when the asymmetry factor

$$g_i = \frac{1}{2}\int_{-1}^{+1} P_i(\theta)\cos(\theta)d(\cos\theta) \qquad (11)$$

is close to 1.

Figures 5 and 6 present the variations with r_{eff} of the single-scattering albedo and the asymmetry factor, respectively. For ice spheres and cylinders, both ω_4 and ω_5 increase with r_{eff}, and ω_5 is always larger than ω_4. For liquid droplets, on the contrary, ω_5 is always smaller than ω_4, and ω_4 presents a slight maximum for $r_{\text{eff}} \approx 15$ μm. For all cases, ω_i is close to its asymptotic value for $r_{\text{eff}} > 20$ μm.

The asymmetry factor is always the largest for channel 4; there is, however, quite a significant difference between spheres and cylinders. Liou (1976) described in detail this property of the cylinder phase function which, compared to that of spheres, gives a large probability of scattering in the region $\theta \approx 20°–160°$ at the expense of forward and backward scattering. The asymmetry factor of randomly oriented cylinders is thus systematically smaller than that of spheres.

Despite recent evidences of the presence of small supercooled water droplets, observations concluded that cirrus is mostly made of relatively large ice crystals (Liou 1986). In these conditions, the single-scattering albedo of cirrus particles is close to 0.5 and the influence of scattering must be larger for cylinders than for spheres that have a much larger forward peak of scattering.

d. Calculation of brightness temperatures in scattering conditions

The upward radiances at the top of the atmosphere have been calculated for both spheres as well as the 3D – ROC for which there is no privileged orientation that makes the calculations much simpler. The scattering problem was solved using the spherical harmonics method (Devaux 1977). To simplify the calcula-

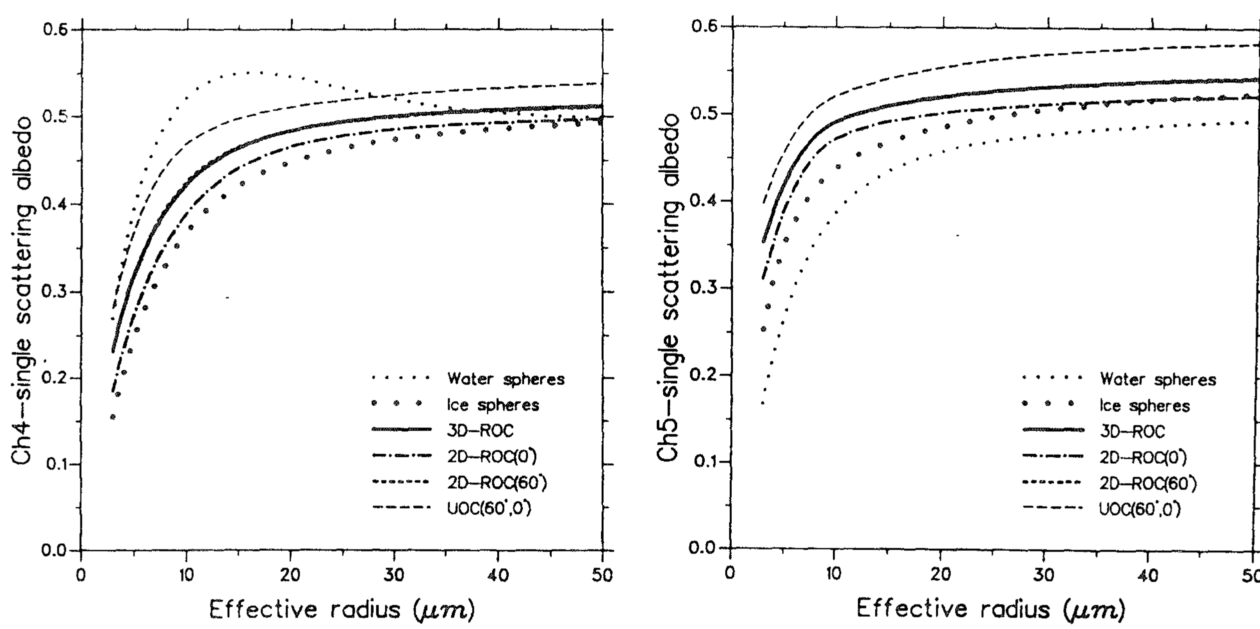

FIG. 5. Single-scattering albedoes ω_4 and ω_5 as functions of the effective radius of spheres and long ice cylinders.

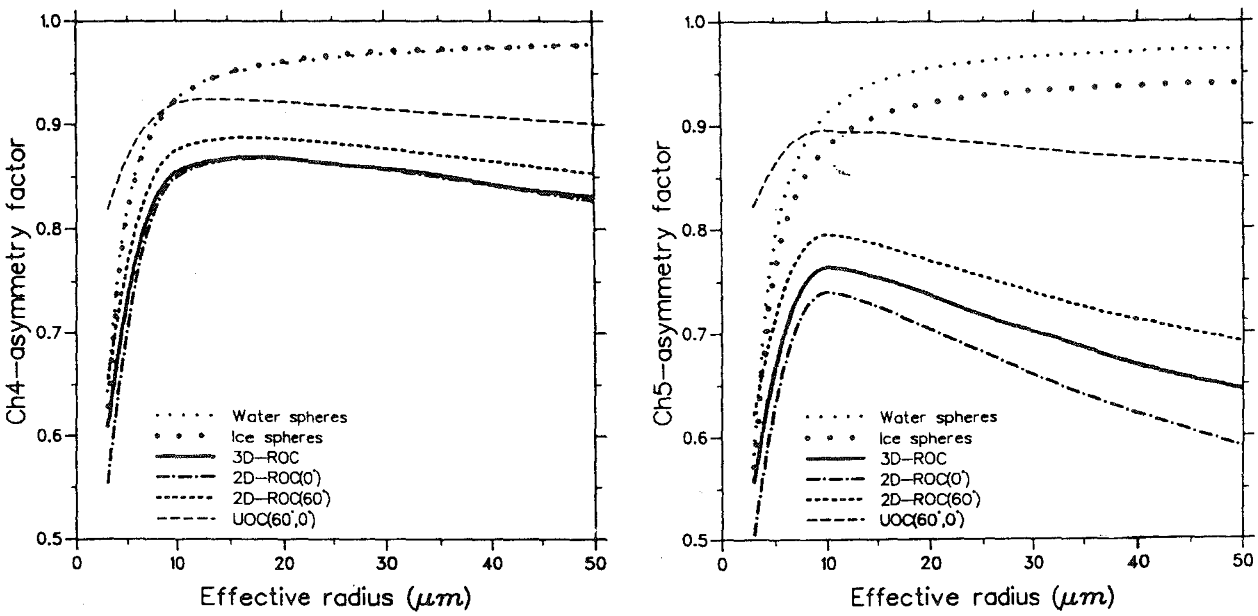

FIG. 6. Asymmetry factors g_4 and g_5 as functions of the effective radius of spheres and long ice cylinders.

tions, here we assumed isotropic upward radiance at cloud base.

Further specifications are $T^{\text{cloud}} = 220$ K, $T_4^{\text{clear}} = 281$ K, and $T_5^{\text{clear}} = 280.2$ K where T_i^{clear} is the brightness temperature for the upward radiation at cloud base I_i^{clear}.

Let us consider the case of complete overcast pixels ($N = 1$). If scattering is accounted for, the upward radiance escaping from cloud top in the satellite direction is given by Eq. (5), which can be rewritten as

$$I_i(\theta) = [1 - \bar{r}_i(\theta)]B_i(T^{\text{cloud}}) + \bar{t}_i(\theta)[I_i^{\text{clear}} - B_i(T^{\text{cloud}})], \quad (12)$$

while in the nonscattering approximation, for $N = 1$, Eq. (6) gives

$$I_i^{ns}(\theta) = B_i(T^{\text{cloud}}) + t_i^{ns}(\theta)[I_i^{\text{clear}} - B_i(T^{\text{cloud}})]. \quad (13)$$

The differences between the radiances calculated with and without scattering may be important, as Fig. 7 shows. For small viewing angles, the multiple scatterings enhance the path length and $\bar{t}_i(\theta) < t_i^{ns}(\theta)$. Consequently, $I_i(\theta) < I_i^{ns}(\theta)$ so that the difference $\delta T_i = T_i - T_i^{ns}$ between the brightness temperatures calculated with and without scattering is always negative. For large viewing angles, the multiple scatterings may, on the contrary, reduce the pathlength so that δT_i may become positive (Parol et al. 1988). Nevertheless, δT_i is generally negative. For thick clouds, the cloud transmittances are zero in both cases and δT_i is always negative, whatever the viewing angle, since $\bar{r}_i(\theta)$ is necessarily positive.

Another important feature of Fig. 7 is that $|\delta T_5|$ is always larger than $|\delta T_4|$. That must be attributed to the difference in the asymmetry of the phase function:scattering is more anisotropic in channel 4 (see

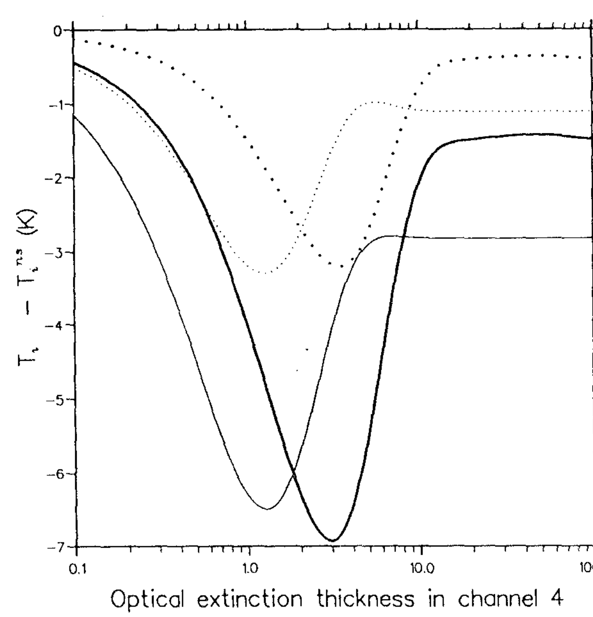

FIG. 7. Difference between the brightness temperatures T_i (accounting for the scattering) and T_i^{ns} (when scattering is neglected) as a function of the cloud optical extinction thickness in channel 4 for the two zenith angle values: $\theta = 0$ (thin curves) and $\theta = 60°$ (thick curves). The effective radius of the long ice cylinders, randomly oriented in space (3D − ROC), is $r_{\text{eff}} = 33$ μm. The full lines correspond to $T_5 - T_5^{ns}$ and the dotted lines to $T_4 - T_4^{ns}$.

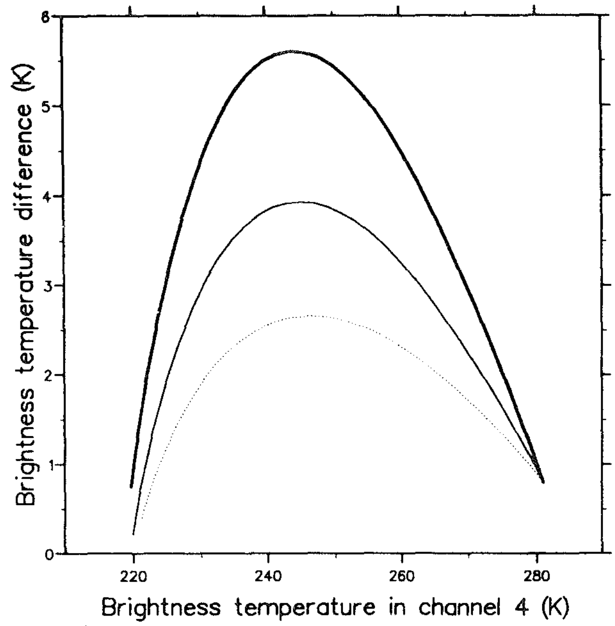

FIG. 8. Brightness temperature difference $T_4 - T_5$ versus the brightness temperature T_4, for a zenith angle $\theta = 30°$, for 3D − ROC of effective radius $r_{\rm eff} = 12$ μm (thick line), and for ice spheres of effective radius $r_{\rm eff} = 18$ μm (thin line), both corresponding to the same absorption coefficient ratio $\beta = 1.08$. The dotted line refers to neglecting the scattering effect.

Fig. 6); it, thus, redistributes radiation less efficiently than in channel 5. Indeed, since the asymmetry factor is larger for spheres, the scattering effect should be even smaller. This is confirmed on Fig. 8 where the BTDs are reported for both ice spheres and 3D − ROC. On this figure, both spheres and cylinders present the same BTDs in the nonscattering approximation. Clearly, the enhancement of the BTD due to scattering is much larger for cylinders.

4. Effective absorption coefficient ratio

We consider that a simple method based on the nonscattering approximation, as used by Inoue (1985), and presented in section 3a, is adapted the most easily to satellite data analysis. It is still applicable in scattering conditions if one makes use of the effective emittances $\epsilon_i^{\rm eff}$ (Cox 1976) defined from

$$I_i = (1 - \epsilon_i^{\rm eff}) I_i^{\rm clear} + \epsilon_i^{\rm eff} B_i(T_{\rm eff}^{\rm cloud}), \quad (14)$$

which implicitly includes the effects of scattering. Primarily, the concept of the effective emittance was applied to in situ measurement of upward (or downward) infrared irradiances, so that the equivalent cloud emitting temperature $T_{\rm eff}^{\rm cloud}$ was fixed to be equal to the cloud top (or bottom) temperature. In this satellite application, the determination of the cloud-top temperature is not easy; the apparent cloud temperature corresponding to thick clouds is always slightly smaller than the cloud top temperature since, because of the reflectance term, $I_i < B_i(T^{\rm cloud})$ when $\bar{\tau}_i \to 0$. Note also that, since the cloud reflectances are different in channels 4 and 5, the BTD differ slightly from zero even for thick clouds.

Practically, $T_{\rm eff}^{\rm cloud}$ is found at the intersection of the curve $T_4 - T_5 \doteq f(T_4)$ at the T_4 axis (see Inoue 1985 or Derrien et al. 1988). An effective absorption coefficient ratio is thus defined as

$$\beta_{\rm eff} = \ln\left[\frac{I_5 - B_5(T_{\rm eff}^{\rm cloud})}{I_5^{\rm clear} - B_5(T_{\rm eff}^{\rm cloud})}\right] \Bigg/ \ln\left[\frac{I_4 - B_4(T_{\rm eff}^{\rm cloud})}{I_4^{\rm clear} - B_4(T_{\rm eff}^{\rm cloud})}\right]. \quad (15)$$

Actually, the cloud layer reflectance and emittance in Eq. (5) are angularly dependent; therefore, even for isotropic incoming radiance at the cloud boundaries, the BTD is dependent on the viewing angle. Consequently, $\beta_{\rm eff}$, which establishes a correspondence between the actual cloud and a purely absorbing one is also dependent on θ. Figure 9 gives an example of this angular dependence for 3D randomly oriented cylinders of effective radius $r_{\rm eff} = 33$ μm. In this example, the actual BTDs were calculated using the spherical harmonics method and the $\beta_{\rm eff}$ were calculated by adjusting the actual BTDs with equivalent nonscattering ones through a least-square fit for variable cloud thick-

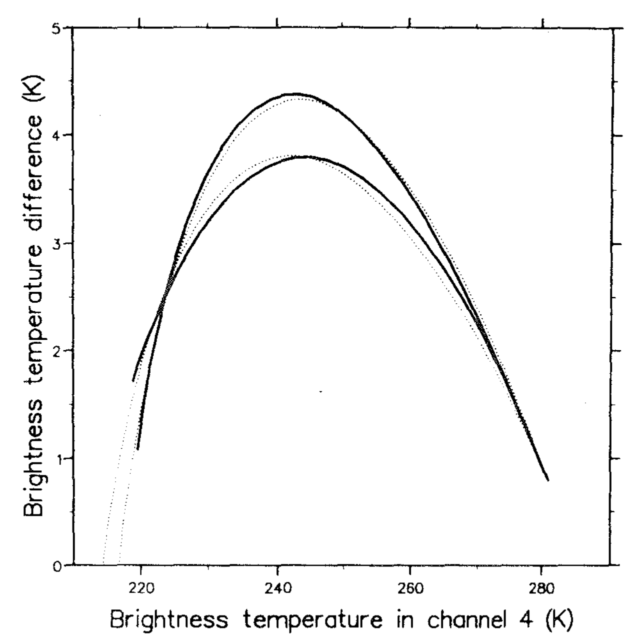

FIG. 9. Brightness temperature difference $T_4 - T_5$ versus the brightness temperature T_4, for 3D − ROC of effective radius $r_{\rm eff} = 33$ μm. The full lines refer to actual BTDs for $\theta = 0$ (upper curve) and for $\theta = 60°$ (lower curve). The dotted lines refer to approximate BTDs: $\beta_{\rm eff} = 1.146$ (upper curve adjusted for $\theta = 0$), and $\beta_{\rm eff} = 1.116$ (lower curve adjusted for $\theta = 60°$). Note that $\beta_{\rm eff}$ differs very significantly from $\beta = 0.975$.

nesses. In this case, $\beta_{eff} = 1.146$ for $\theta = 0°$ and $\beta_{eff} = 1.116$ for $\theta = 60°$; the relative variation is thus only 3% and is generally less than 1% for spheres.

To estimate the impact of the simplifying assumption of isotropic radiation, we performed a series of calculations with the Lowtran 7 computer code (Kneizys et al. 1988). We considered the United States standard atmosphere, the tropical and subartic winter atmospheres, and calculated the angular dependency of the upward radiances at the cloud level for three different sea surface temperatures: the surface air temperature and two temperature jumps: +10 K and −10 K. The largest anisotropy is for the tropical atmosphere and a surface temperature jump of +10 K; in this case, the upward radiance decreases by about 9% when θ varies from 0° to 60°. Without surface discontinuities, the decrease is only 1% for the tropical atmosphere and less than 1% for the very dry subarctic winter atmosphere. In the worst case, the influence on β_{eff} is typically 1% for $\theta = 60°$, 0.3% for $\theta = 30°$, and nearly zero for $\theta = 0°$.

Even if we account for the errors induced by the simplifying assumption of isotropic incoming radiation, the variation of β_{eff} with θ is small. Therefore, in the following, we neglect this angular dependence and all calculations are performed for an average viewing angle $\theta = 30°$.

Figure 10 shows the variation of β_{eff} with r_{eff} for both 3D − ROC and spheres. Comparing Fig. 10 with Fig. 4 exemplifies the role of multiple scatterings: for purely absorbing clouds, the average of Inoue (1985)'s observations ($\beta \approx 1.08$, see also Fig. 2) corresponds to spheres with $r_{eff} \approx 18$ μm for both water and ice;

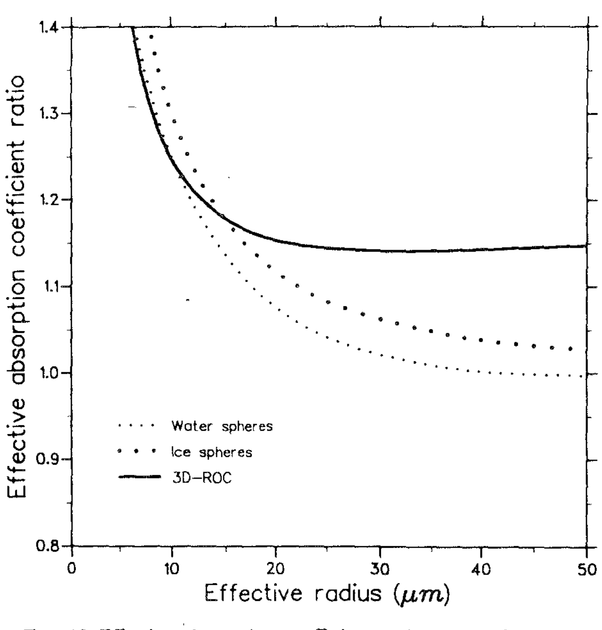

FIG. 10. Effective absorption coefficient ratio β_{eff} as a function of the effective radius of spheres and randomly oriented long ice cylinders.

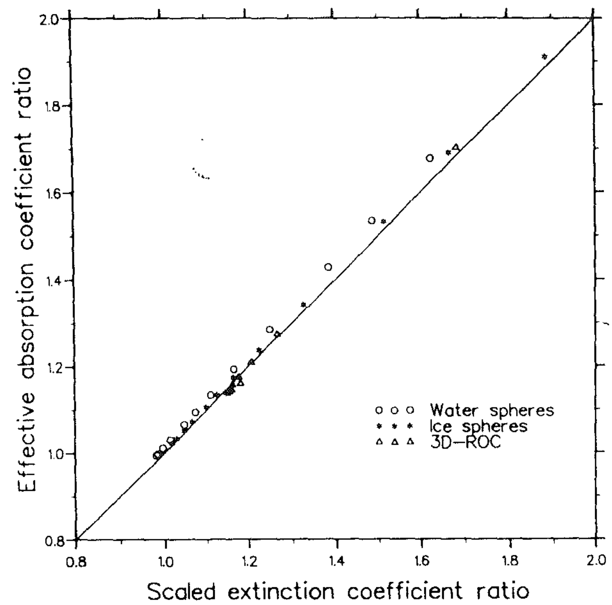

FIG. 11. Effective absorption coefficient ratio β_{eff} as a function of the scaled extinction coefficient ratio $[(1 - \omega_5 g_5)\sigma_{e_5}]/[(1 - \omega_4 g_4)\sigma_{e_4}]$ for spheres and randomly oriented long ice cylinders of effective radius varying from 3 to 100 μm.

when scattering is accounted for, it corresponds to $r_{eff} \approx 20$ μm for water spheres and 26 μm for ice spheres. As expected from section 3c, the influence of multiple scatterings is small for water spheres and slightly larger for ice spheres, which have a significantly larger single-scattering albedo than water spheres around 20 μm. The largest influence, however, is for 3D − ROC, whose asymmetry factor is much smaller than that of spheres; in the case, the calculations cannot conciliate the observations whatever r_{eff}.

Since β_{eff} is a key parameter for the practical analysis of satellite observations of the BTDs, it would be of interest to derive a direct relationship between β_{eff} and the optical properties of the cloud particles. Drawing inspiration from Van de Hulst (1980) similarity principles, we found that β_{eff} is well represented by a ratio of scaled extinction coefficients

$$\beta_{eff} \approx \frac{(1 - \omega_5 g_5)\sigma_{e_5}}{(1 - \omega_4 g_4)\sigma_{e_4}} \equiv \frac{(1 - \omega_5 g_5)(1 - \omega_4)}{(1 - \omega_4 g_4)(1 - \omega_5)}\beta. \quad (16)$$

The effective absorption coefficient ratio β_{eff} differs significantly from the absorption ratio β (compare Fig. 4 to Fig. 10). Oppositely, the agreement between β_{eff} and the right-hand side of Eq. (16) is excellent both for water and ice spheres and for 3D randomly oriented cylinders (see Fig. 11).

Actually, the smallest crystals are very sensitive to very small-scale turbulence movements; their orientation in space may thus be completely random. However, as indicated by the various halos that cirrus experience, this fully random orientation is very unlikely for all sizes and shapes of particles. Indeed, for the largest crystals, the Archimede's pressure has a much larger influence and the crystals have preferential orientations with regard to the vertical. The most likely distribution is, thus, random or even uniform distribution in the horizontal plane. However, in this case, the resolution of the radiative transfer equation is considerably more complicated (Liou 1980; Stephens 1980b; Asano 1983).

In view of the very good correlation between β_{eff} and the scaled extinction coefficient ratio that appears on the right-hand side of Eq. (16), it is very tempting to establish a relationship between it and the single-scattering parameters. Figure 12 compares the variation of the scaled extinction coefficient with r_{eff} for different orientations and viewing conditions. According to this figure, cylinders would agree with observations only for a limited set of observing conditions in the particular case of uniformly oriented cylinders. We have no proof that the fairly good agreement of Fig. 11 still holds for 2D randomly oriented cylinders and uniformly oriented cylinders. The comparison of variations of single-scattering albedoes and asymmetry factors for different orientations of cylinders on Figs. 5 and 6 suggests that this approximation is still applicable, at least for 2D random cylinders. However, more accurate calculations are needed to fully demonstrate this indication.

5. Discussion and conclusion

In contradiction with the affirmation of Prabhakara et al. (1988), the BTD is significantly dependent on

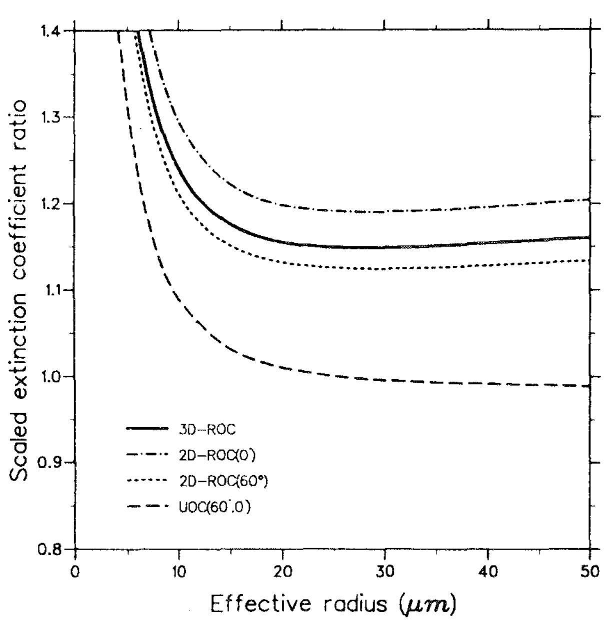

FIG. 12. Scaled extinction coefficient ratio $[(1 - \omega_5 g_5)\sigma_{e_5}]/[(1 - \omega_4 g_4)\sigma_{e_4}]$ as a function of the effective radius r_{eff} of long ice cylinders.

the shape of the particles. On the other hand, the phase has little influence, so that the presence of supercooled particles influence the radiation field through their shapes, since they are spherical, and consequently may have a scattering phase function very different from the ice crystal.

Our observations of the effective absorption coefficient ratio ($\beta_{\text{eff}} \approx 1.08$ for $\theta = 60°$) are in good agreement with Inoue (1985) who found the same averaged value for a larger dataset (8 images) and various satellite viewing angles. For overcast pixels, such a value might correspond to ice spheres of effective radius $r_{\text{eff}} \approx 26$ μm or a bit less in the case of supercooled particles (see Fig. 10), but no agreement can be obtained for fully random-oriented cylinders. The very good correlation obtained in section 4 between β_{eff} and the scaled extinction coefficient ratio suggests that agreement for 2D or even 1D uniformly oriented cylinders is unlikely, except for particular conditions of observations.

In any case, observed cirrus crystals differ significantly from cylinders and a reasonable hypothesis is that they have shapes that can be considered as intermediate between spheres and cylinders. In this case, $\beta_{\text{eff}} = 1.08$ would correspond to an equivalent radius strictly larger than 20 μm (see Fig. 10), but much larger values would be possible.

At the scale of one AVHRR pixel, the overcast hypothesis is also debatable, particularly for semitransparent cirrus clouds. For partial cloud covers, β_{eff} would thus be larger than 1.08 (see Fig. 2), but would certainly remain smaller than 1.18. This larger value agrees with spheres as cylinders with $r_{\text{eff}} \approx 15$ μm.

The large variability of the observed values of β_{eff} (roughly from 1.0 to 1.18 for the case of Fig. 2, with the assumption $N = 1$) could be explained by an increase of the particle size with temperature. Such a variation has been reported for cirrus clouds by Platt (1984) and Platt et al. (1989). According to this hypothesis, the large BTDs would correspond more to the coldest part of the cloud system (curve a on Fig. 2) and the smallest BTDs to the warmest parts (curve e on Fig. 2).

The BTD method is certainly very efficient to identify semitransparent clouds; however, our study shows that it is not sufficient to determine the shape and/or size of the cloud particles. It is, nevertheless, possible to put some limits on the range of possibilities, since, for example, large spheres ($r_{\text{eff}} > 50$ μm) cannot explain the observed BTDs. More research is needed to evaluate the influence of multiple scattering for more realistic particles; this also means that additional observations are necessary to determine the statistical distribution of sizes and shapes of ice crystals for a wide range of conditions. The preliminary results of FIRE (Starr 1987) and ICE (Raschke and Rockwitz 1988) constitute a first basis for this approach, but additional ground-based observations such as aureola measurements might also be of great help in determining the equivalent scattering phase functions of cirrus.

Acknowledgments. This work has been supported by the Direction des Recherches, Etudes et Techniques under Contract 87-181 and was part of the International Cirrus Experiment supported by European Economic Community.

REFERENCES

Arking, A., and J. D. Childs, 1985: Retrieval of cloud cover parameters from multispectral satellite images. *J. Climate Appl. Meteor.*, **24**, 322–333.

Asano, A., 1983: Light scattering by horizontally oriented spheroidal particles. *Appl. Opt.*, **22**, 1390–1396.

Barton, I. J., 1983: Upper-level cloud climatology from an orbiting satellite. *J. Atmos. Sci.*, **40**, 435–447.

Cess, R. D., G. L. Potter, J. P. Blanchet, G. J. Ghan, J. T. Kiehl, H. Le Treut, Z. X. Li, X. Z. Liang, J. F. B. Mitchell, J. J. Morcrette, D. A. Randall, M. R. Riches, E. Roeckner, U. Schlese, A. Slingo, K. E. Taylor, W. M. Washington, R. T. Wetherald and I. Yagai, 1989: Interpretation of cloud climate feedback as produced by 14 atmospheric general circulation models. *Science*, **245**, 513–516.

Cox, S. K., 1976: Observations of cloud infrared effective emissivity. *J. Atmos. Sci.*, **33**, 287–289.

——, D. S. McDougal, D. A. Randall and R. A. Schiffer, 1987: FIRE—The First ISCCP Regional Experiment. *Bull. Amer. Meteor. Soc.*, **68**, 114–118.

Deirmendjian, D., 1969: *Electromagnetic Scattering on Spherical Polydispersions.* Elsevier, 290 pp.

Derrien, M., L. Lavanant and H. Legleau, 1988: Retrieval of the top temperature of semitransparent clouds with AVHRR. *Proc. of the IRS '88*, Lille, France, International Association of Meteorology and Atmospheric Physics, 199–202.

Desbois, M., G. Seze and G. Szejwach, 1982: Automatic classification of clouds on METEOSAT imagery: Application to high-level clouds. *J. Appl. Meteor.*, **21**, 401–412.

Devaux, C., 1977: Contribution à l'étude de la couverture nuageuse de Vénus par l'analyse des mesures photométriques et des profils de flux solaires transmis. Ph.D. thesis, Université des Sciences et Techniques de Lille, 134 pp.

Downing, H. D., and D. Williams, 1975: Optical constants of water in the infrared. *J. Geophys. Res.*, **80**, 1656–1661.

Heymsfield, A. J., 1975: Cirrus uncinnus generating cells and the evolution of cirriform clouds. Part I: Aircraft measurements of the growth of the ice phase. *J. Atmos. Sci.*, **32**, 798–808.

——, 1977: Precipitation development in stratiform ice clouds: A microphysical and dynamical study. *J. Atmos. Sci.*, **34**, 367–381.

——, N. C. Knight and K. Sassen, 1988: Hydrometeor development in cold clouds in FIRE. *FIRE Science Team Workshop*, Vail, Colorado, 402 pp.

Houghton, H. T., 1984: *The Global Climate.* Cambridge University Press, 233 pp.

Inoue, T., 1985: On the temperature and effective emissivity determination of semitransparent cirrus clouds by bispectral measurements in the 10 μm window region. *J. Meteorol. Soc. Jpn.*, **63**, 88–98.

Kneyzys, F. X., E. P. Shettle, L. W. Abreu, J. H. Chetwynd, G. P. Anderson, W. O. Gallery, J. E. A. Selby and S. A. Clough, 1988: Users guide to LOWTRAN 7. AFGL-TR-88-0177, Air Force Geophysics Laboratory, Hanscom AFB, MA, 146 pp.

Kuo, K. S., R. M. Welch and S. K. Sengupta, 1988: Structural and textural characteristics of cirrus clouds observed using high spatial resolution Landsat imagery. *J. Appl. Meteor.*, **27**, 1242–1260.

Liou, K. N., 1976: On the absorption, reflection, and transmission of solar radiation in cloudy atmospheres. *J. Atmos. Sci.*, **33**, 798–805.

——, 1980: *An Introduction to Atmospheric Radiation.* Academic Press, 404 pp.

——, 1986: Influence of cirrus clouds on weather and climate processes: A global perspective. *Mon. Wea. Rev.*, **6**, 1167–1199.

Parol, F., J. C. Buriez, G. Brogniez and Y. Fouquart, 1988: On the determination of properties of semitransparent cirrus clouds using channels 4 and 5 of the Advanced Very High Resolution Radiometer. *Proc. of the IRS '88*, Lille, France, International Association of Meteorology and Atmospheric Physics, 203–206.

Platt, C. M. R., 1984: Extinction in clouds. *Proc. of the IRS '84*, Perugia, Italy, International Association of Meteorology and Atmospheric Physics, 163–166.

——, J. D. Spinhirne and W. D. Hart, 1989: Optical and microphysical properties of a cold cirrus cloud: Evidence for regions of small ice particles. *J. Geophys. Res.*, **94**, 11 151–11 164.

Prabhakara, C., R. S. Fraser, G. Dalu, M. L. C. Wu, R. J. Curran and T. Styles, 1988: Thin cirrus clouds: Seasonal distribution over oceans deduced from Nimbus-4 Iris. *J. Appl. Meteor.*, **27**, 379–399.

Raschke, E., and K.-D. Rockwitz, 1988: The international cirrus experiment: Some preliminary results from the first field phase. *Proc. of the IRS '88*, Lille, France, International Association of Meteorology and Atmospheric Physics, 6–9.

Reynolds, D. W., and T. H. Vonder Haar, 1977: A bispectral method for cloud parameter determination. *Mon. Wea. Rev.*, **105**, 446–457.

Schiffer, R. A., and W. B. Rossow, 1983: The International Satellite Cloud Climatology Project (ISCCP): The first project of the world climate research program. *Bull. Amer. Meteor. Soc.*, **64**, 779–784.

Schlesinger, M. E., and J. F. B. Mitchell, 1987: Climate model simulations of the equilibrium climatic response to increased carbon dioxide. *Rev. Geophys.*, **25**, 760–798.

Starr, D. O'C., 1987: A cirrus-cloud experiment: intensive field observations planned for FIRE. *Bull. Amer. Meteor. Soc.*, **68**, 119–124.

Stephens, G. L., 1980a: Radiative properties of cirrus clouds in the infrared region. *J. Atmos. Sci.*, **37**, 435–445.

——, 1980b: Radiative transfer on a linear lattice: Application to anisotropic ice crystal clouds. *J. Atmos. Sci.*, **37**, 2095–2104.

——, S. C. Tsay, P. W. Stackhouse, Jr. and P. J. Flatau, 1990: The relevance of the microphysical and radiative properties of cirrus clouds to climate and climatic feedback. *J. Atmos. Sci.*, **47**, 1742–1753.

Szejwach, G., 1982: Determination of semitransparent cirrus cloud temperature from infrared radiances: Application to METEOSAT. *J. Appl. Meteor.*, **21**, 384–393.

Van de Hulst, H. C., 1957: *Light Scattering by Small Particles.* Wiley, 470 pp.

——, 1980: *Multiple Light Scattering, Tables, Formulas, and Applications.* Vol. 2. Academic Press, 739 pp.

Warren, S. G., 1984: Optical constants of ice from the ultraviolet to the microwave. *Appl. Opt.*, **23**, 1206–1225.

Weickmann, H. K., 1945: Formen und bildung atmosphärisher eiskristalle. *Beitr. Phys. Atmos.*, **28**, 12–52.

——, 1947: Die eisphase in der atmosphäre. Library Trans. 273, Royal Aircraft Establishment, 96 pp.

Woodbury, G. E., and M. P. McCormick, 1983: Global distributions of cirrus clouds determinated from SAGE data. *Geophys. Res. Letters*, **10**, 1180–1183.

——, and ——, 1986: Zonal and geographical distributions of cirrus clouds determinated from SAGE data. *J. Geophys. Res.*, **91**, 2775–2785.

Wu, M. C., 1987: A method for remote sensing the emissivity, fractional cloud cover, and cloud top temperature of high-level, thin clouds. *J. Climate Appl. Meteor.*, **26**, 225–233.

Reprinted from MONTHLY WEATHER REVIEW, Vol. 123, No. 4, April 1995
American Meteorological Society

Determination of Effective Emittance and a Radiatively Equivalent Microphysical Model of Cirrus from Ground-Based and Satellite Observations during the International Cirrus Experiment: The 18 October 1989 Case Study

G. BROGNIEZ, J. C. BURIEZ, V. GIRAUD, F. PAROL, AND C. VANBAUCE

Laboratoire d'Optique Atmosphérique, Université des Sciences et Technologies de Lille, Villeneuve d'Ascq, France

(Manuscript received 3 January 1994, in final form 6 July 1994)

ABSTRACT

Ground-based observations and satellite data have been compared for the 18 October 1989 case study of the International Cirrus Experiment (ICE) field campaign. They correspond to thin cirrus clouds with infrared emittances in the range 0–0.3. Good correspondence was obtained when comparing the time variability of the effective downward beam emittance of the cirrus clouds observed at Nordholz (53.8°N, 8.3°E) to the spatial variability of the effective upward beam emittance derived from *NOAA-11* Advanced Very High Resolution Radiometer (AVHRR) data acquired at 1225 UTC. A simple model of cirrus cloud particles was found to satisfy both the ground-based observations of the angular dependence of the scattered solar radiation at 0.85 μm and the satellite observations of the brightness temperatures in channel 4 (11 μm) and channel 5 (12 μm) of *NOAA-11* AVHRR. The best fit was obtained for fully randomly oriented hexagonal ice plates with a thickness of 10–20 μm and a diameter of 200–500 μm. Although actual cloud ice crystals are probably not all hexagonal plates, our simple model of randomly oriented ice plates allows us to appropriately simulate the optical properties of the observed cirrus in which particles surely present a large variety of shapes. The equivalent radius of the retrieved ice plates (i.e., the radius of spheres of the same volume) is 50–80 μm. However, ice spheres do not simulate the halo of cirrus clouds observed from the aureolemeter measurements. Moreover, assuming spherical particles to explain brightness temperature measurements in AVHRR channels 4 and 5 leads to an effective radius of 27 μm, which is noticeably smaller than the one obtained with the hypothesis of hexagonal plates.

On the other hand, analysis of AVHRR data also highlights the important difference between natural thin cirrus and jet contrail microphysics. Contrails are revealed to be composed of smaller equivalent spherical particles with an effective radius of about 4.5 μm.

1. Introduction

Cirrus clouds are generally known to have a very significant impact on the climate. This idea is supported by two main arguments. (i) Cirrus are extended both in space and time; according to Warren et al. (1986, 1988) the average cirrus cloud cover is 12.6% over ocean areas and 23.4% over land. (ii) The greenhouse effect of cirrus is maximum because of their large temperature contrast with the surface. This effect is usually not counterbalanced by their influence on the shortwave albedo since cirrus are frequently optically thin.

However, whether or not cirrus have an overall warming effect depends strongly on cirrus characteristics, particularly on their microphysics (Stephens et al. 1990). Nevertheless, several simulations of climate change with interactive clouds predict a positive cloud feedback, partly because of an increase of high-level cloudiness at middle and high latitudes (Hansen et al. 1984; Wetherald and Manabe 1988; see also Cess et al. 1990) and due largely to the enhanced liquid water content of high clouds (Roeckner et al. 1987; Roeckner 1988).

To be able to understand the role of cirrus on the present climate, one thus has to investigate systematically their optical characteristics. If one wants to account realistically for their feedback in possible climate changes, one thus has to fully understand their conditions of formation, maintenance, and dissipation.

Several important experiments have been conducted to investigate cirrus dynamical and physical properties [First ISCCP (International Satellite Cloud Climatology Project) Regional Experiment (FIRE) (Starr 1987); International Cirrus Experiment (ICE) (Raschke and Rockwitz 1988)]. These experiments were the product of considerable cooperative efforts, and they led to a harvest of extremely important results. Yet they are no more than snapshots in an extremely variable medium.

In addition to the natural variability of cirrus, they are very difficult to observe in situ simply because of their high altitude. Thus it is quite clear that in order to

Corresponding author address: Dr. Gérard Brogniez, Laboratoire d'Optique Atmosphérique, CNRS URA 713, Université des Sciences et Technologies de Lille, Bâtiment P5, 59655 Villeneuve d'Ascq, Cedex, France.

support an inevitably small number of intensive field experiments, we will have to rely heavily on remote observations from the ground and from satellites. The problem is whether remote observations of the radiation field emerging from cirrus clouds are sufficient by themselves to determine the most important physical characteristics of the cirrus.

The first remote observations of cirrus were restricted to the determination of their emittance (Allen 1971; Platt 1971). Since then, simultaneous visible and infrared observations of cirrus have been compared to different models of cloud particles (Platt 1973; Platt et al. 1980; Platt et al. 1987; Spinhirne and Hart 1990; Wielicki et al. 1990). Investigations of the microphysical characteristics of cirrus have also been performed using the brightness temperature difference between two thermal window channels (Wu 1987; Prabhakara et al. 1988; Parol et al. 1991) and using the angular dependence of the solar radiation scattered by a thin cirrus (Platt and Dilley 1984). In this paper, we use ground-based observations of the angular dependence of the scattered solar radiation to derive an equivalent microphysical model of a thin cirrus cloud that was observed during the ICE'89 intensive field experiment. We show that predictions using this model agree with satellite observations of the brightness temperatures. Even if the good agreement between the two remote sensing techniques is limited to only one case study, we believe that such an experimental approach can be extremely useful to develop a systematic investigation of the physical characteristics of cirrus and of their dynamical evolution. However, in situ field experiments remain essential to validate such remote sensing methods by using well-documented cloud cases.

Section 2 presents the data used in the paper. Comparison of infrared emittances derived from ground-based and satellite observations are presented in section 3. Finally, in section 4, cirrus microphysical properties derived from ground-based measurements are compared to those derived from satellite observations.

2. Data

a. Ground-based measurements

The measurements were acquired at Nordholz (53.8°N, 8.3°E) on 18 October 1989 during ICE'89 (18 September–20 October 1989) (Raschke et al. 1990). The instruments in use were an aureolemeter, an infrared radiometer, and a lidar. Both the radiometer and the lidar were pointing toward the zenith, while the aureolemeter measured the forward-scattered light near the sun.

During the measurement period (1130–1400 UTC) of the lidar at 1.06 μm, the cirrus cloud was approximately located between 8.5 km (cloud base) and 9.5 km (cloud top) of altitude, that is, a midcloud height of 9 km (Elouragini 1991; Ansmann et al. 1993).

The Barnes PRT-5 infrared radiometer measured the downward radiance in the 8–14-μm atmospheric window. The instrumental noise was 0.2 W m^{-2} sr^{-1}, and the infrared radiances were recorded each 5 s. The angular field of view of the radiometer was 2°, and the instantaneous field of view (IFOV) was therefore 300 m at an altitude of 9 km. The time variation of the measured infrared radiance is reported in Fig. 1. Early in the morning, the radiometer response appears flat because there were no clouds. Nevertheless, the humidity was already large enough to enable the formation of two contrails that were visually observed at 1030 and 1110 UTC. After 1120 UTC, cirrus clouds caused the signal to vary. The relatively stable part of the recording around 1230–1300 UTC is consistent with a visual inspection of the sky. The cirrus layer appeared rather homogeneous during this period.

The aureolemeter measures the downward solar radiance at 0.85 μm along the almucantar of the sun. Such aureole measurements have already been used in order to derive aerosol size distributions (see for instance Green et al. 1971; Ward et al. 1973; Twitty et al. 1976; Santer and Herman 1983). The aureolemeter used in this experiment scans in the azimuth with a radial velocity of 4° min^{-1} between 0° and 60° from the sun direction (see Fig. 2). The viewing zenith angle is equal to the solar one at the beginning of the data acquisition (θ_s = 66°) and then remains constant. The angular field of view of 0.8° corresponds to an IFOV of about 300 m × 700 m at an altitude of 9 km. The recording of the radiance acquired every second around 1300 UTC is reported in Fig. 3. The first maximum corresponds to the direct viewing in the sun direction. The second maximum corresponds to the well-known 22° halo that characterizes the presence of hexagonal ice crystals in the cirrus cloud.

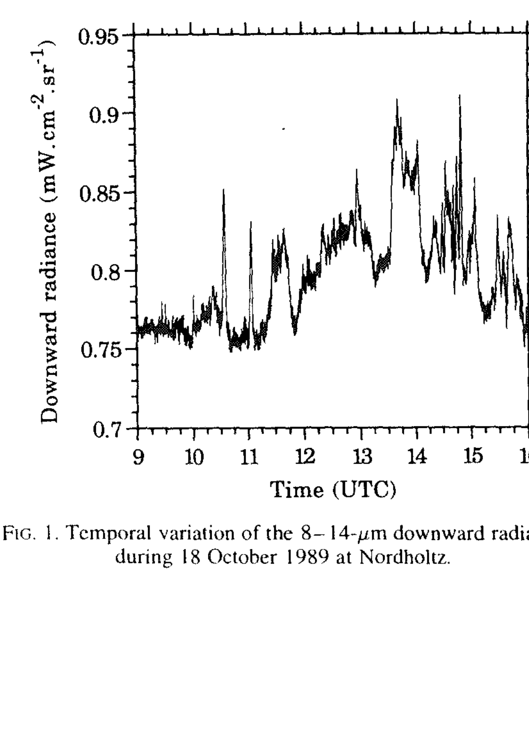

FIG. 1. Temporal variation of the 8–14-μm downward radiance during 18 October 1989 at Nordholtz.

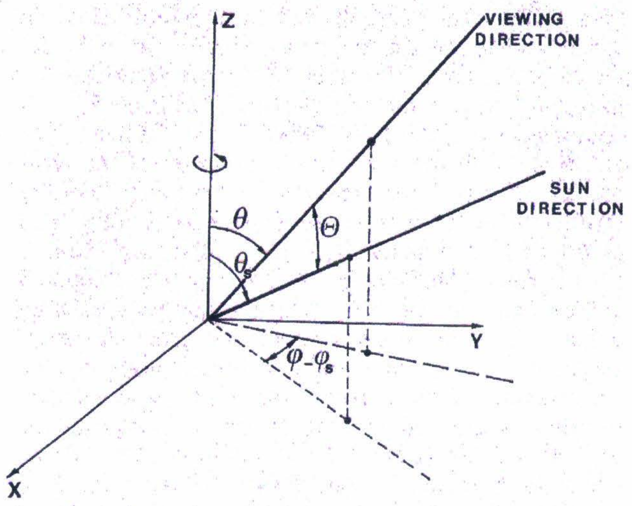

FIG. 2. Geometry of the aureolemeter measurements. All the parameters are defined in the text.

Platt and Dilley (1984) have already performed measurements of the scattering phase function of cirrus particles. They used a lidar receiver looking at the zenith to measure the radiation scattered by semitransparent cirrus clouds at $\lambda = 0.694$ μm for various solar elevations. The solar scattered radiation appeared as a background offset signal on the lidar echo. Nevertheless, the temporal dispersion of the measurements (several clouds are involved during several days) led to a possible variability of the observed scattering phase functions. By contrast, the aureolemeter working during ICE'89 enables an almost instantaneous (about 15 min) derivation of the forward part of the scattering phase function of an extended semitransparent cirrus layer.

b. Satellite data

A 600 km × 600 km subregion of the *NOAA-11* AVHRR (Advanced Very High Resolution Radiometer) scene was used in this analysis. The region was centered at (52°N, 8°E). The corresponding channel 2 (0.83 μm) image is shown in Fig. 4. The *NOAA-11* overpass was at 1225 UTC 18 October 1989. The cross indicates the location of Nordholz, where the ground instruments were based. The infrared emittances are derived along the straight line *AB* (see section 3b). The white rectangle indicates the area used for the satellite retrieval of microphysical properties (see section 4c). The area is about 200 km long by 50 km wide, and the viewing zenith angles were within 10° of nadir. Thick clouds appear bright against a dark ocean background (upper-right part of the image), and very thin cirrus clouds are visible in the upper left part of the image. Note that it is not possible to visually discriminate the thin cirrus present in the area of interest from the background signal due to land.

3. Comparisons between satellite and ground-based observations of infrared effective beam emittances

The main goal of this paper is to compare cirrus microphysical properties derived from ground-based measurements to those derived from satellite observations. Direct comparisons are difficult. Ground-based measurements cover a long time period but are limited to a single geographical area. On the other hand, satellite data cover a large area but only at a single overpass time. The properties of cirrus clouds are known to be spatially variable. It is therefore important that both types of measurements correspond to the same cirrus or, at least, to the same type of cirrus clouds.

In order to ensure such similarity, we first compare the downward ($\epsilon^{\downarrow}$) and upward ($\epsilon^{\uparrow}$) infrared effective beam emittances derived from ground-based and satellite observations, respectively.

Rigorously, the comparison can only be made for one geographic scene (Nordholz) at one overpass time (1225 UTC). Nevertheless, a semiquantitative comparison may be attempted on a larger dataset, knowing the velocity of the wind at the cirrus altitude. We assume the cloud drift velocity to be equal to the wind velocity at the mean cloud height and to be constant over the study period. The Sylt radiosonde ascent at 1200 UTC indicates, for the height of 9 km, a wind speed of 18 m s^{-1} and a wind direction (265°) close to the orientation of the lines on the AVHRR picture. This radiosounding was close in time (±3 h) and space (100 km eastward from Nordholz) to all the measurements used in this study, and thus we assume that this radiosonde profile is representative of the synoptic weather situation around Nordholz.

Cirrus clouds are known to be long-lived. Therefore, if no changes other than a global motion by 18 m s^{-1}

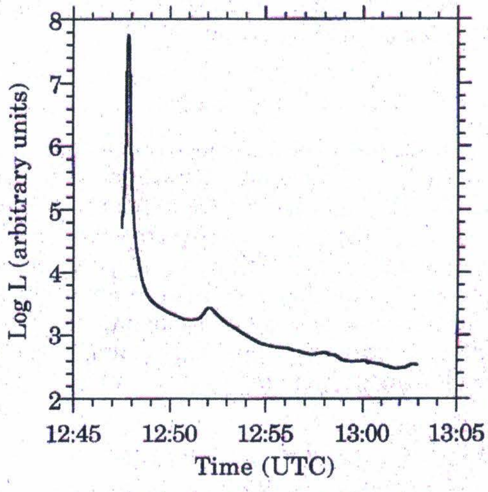

FIG. 3. Recording of the 0.85-μm downward radiance measured by the aureolemeter on 18 October 1989 at Nordholtz.

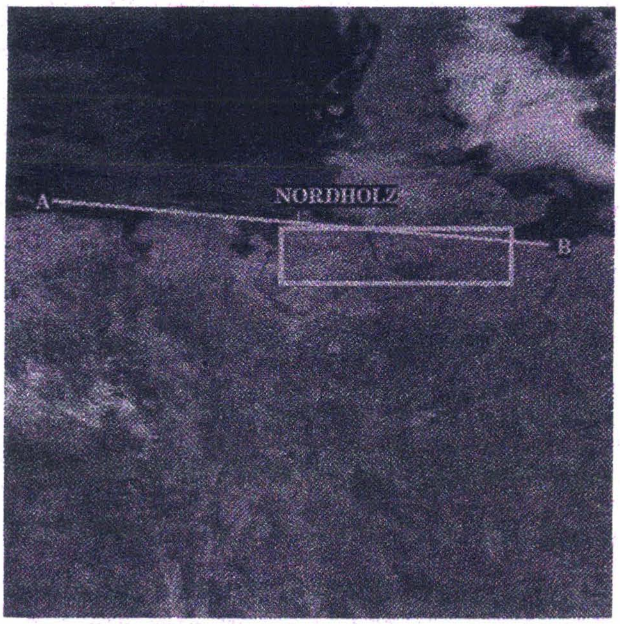

FIG. 4. Image constructed from the near-infrared (AVHRR channel 2, 0.83 μm) reflectance data for 600 km × 600 km region centered at 52°N, 8°E at 1225 UTC 18 October 1989. The gray scale represents a change in reflectance from 0 (black) to 0.2 and more (white). The cross indicates the location of Nordholz where the ground instruments were based. The rectangular area outlined in white is the area of interest used for the satellite retrieval of microphysical properties (see section 4c). The upward emittances of cirrus are calculated along the line *AB*.

occurred, the cirrus clouds over Nordholz from 0925 to 1525 UTC would be seen at 1225 UTC along the satellite cross-track from −200 km to +200 km southeast of Nordholz. Of course, this assumption is rather crude. Nevertheless, one can expect that the observed time variability of effective beam emittance may be comparable to its associated spatial variability (Platt 1975).

The "effective" beam emittances derived from observations are defined by (Allen 1971)

$$\epsilon^{\uparrow\downarrow} = \frac{\mathbf{L}^{\uparrow\downarrow} - \mathbf{L}_0^{\uparrow\downarrow}}{\mathbf{L}_1^{\uparrow\downarrow} - \mathbf{L}_0^{\uparrow\downarrow}}, \qquad (1)$$

where $\mathbf{L}^{\downarrow}$ is the downward radiance measured at ground level, and $\mathbf{L}^{\uparrow}$ is the upward radiance measured at the satellite. Here $\mathbf{L}_0^{\uparrow\downarrow}$ and $\mathbf{L}_1^{\uparrow\downarrow}$ are the radiances that would be measured if the cirrus emittance were zero (i.e., clear sky) or unity (i.e., blackbody), respectively. Generally, these effective beam emittances are slightly different from the true absorption beam emittances of the cirrus cloud because they implicitly contain the effects of infrared scattering and reflection (Platt and Stephens 1980).

a. Effective downward beam emittance

The effective downward beam emittances have been calculated from the zenith measurements of $\mathbf{L}^{\downarrow}$ by the PRT-5. The clear-sky radiance $\mathbf{L}_0^{\downarrow}$ was determined from the radiometer measurements when no clouds were detected by the lidar. The radiance $\mathbf{L}_1^{\downarrow}$ was derived in the following way. First, the clear-sky radiance $\mathbf{L}_0^{\downarrow}$ was computed using the LOWTRAN 7 code (Kneyzys et al. 1988) with the spectral transmission of the radiometer filter as input. The temperature and humidity profiles were taken from the Sylt radiosounding, and ozone data were taken from the midlatitude summer ozone profile (McClatchey et al. 1971). The computed value of $\mathbf{L}_0^{\downarrow}$ was found to be larger than the measured value by 10% because of errors in the radiometer measurement, the sounding, and the computational model. To account for these errors, the water vapor density profile was adjusted until the computed $\mathbf{L}_0^{\downarrow}$ equaled the measured value. Second, $\mathbf{L}_1^{\downarrow}$ was computed by adding a blackbody at the midcloud level of 9 km derived from the lidar measurements; the midcloud temperature derived from radiosounding was then 231 K.

Figure 5a shows temporal variations of the effective downward beam emittance. The two distinct peaks near 1100 UTC correspond to contrails that were visually observed in the clear sky. The highly variable cirrus clouds present after 1120 UTC had a mean effective emittance on the order of 0.1. The radiometric noise induces fluctuations in the calculated emittance on the order of 0.02. The major uncertainty in the derivation of the effective downward beam emittance is related to the cirrus cloud temperature. The cloud-base and cloud-top heights obtained from the lidar returns were compared with the Sylt radiosounding to provide esti-

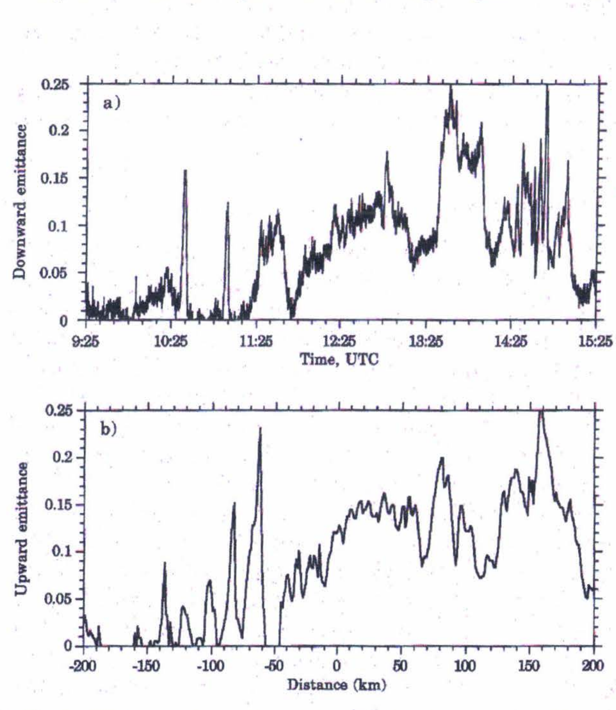

FIG. 5. (a) Temporal variation of the effective downward emittance derived from ground-based measurements. (b) Spatial variation of the effective upward emittance derived from satellite imagery.

mates of cloud-base and cloud-top temperatures. The cloud geometrical thickness of 1 km thus corresponded to a temperature variability of ±4 K around the cirrus midcloud temperature. An uncertainty of ±4 K induces a relative uncertainty in effective emittance of ±25%, which is typically an absolute uncertainty of ±0.03. By comparison, errors due to the use of a nonscattering cloud approximation (i.e., the use of effective infrared beam emittance instead of absorption infrared beam emittance) are clearly less important [less than a few percent in the case of cirrus cloud at 11 μm following Platt (1973, 1975)].

b. Effective upward beam emittance

We now derive the effective upward beam emittance of the cirrus clouds that passed over Nordholz from the AVHRR data acquired at 1225 UTC. Assuming no change in the cirrus cloud formation other than a global motion, the satellite data can be compared to the ground-based measurements by simply accounting for the cirrus drift velocity along the straight line AB reported in Fig. 4. The distance *AB* of 400 km (from −200 km to +200 km from Nordholz) corresponds to clouds passing over Nordholz from 3 h before until 3 h after the satellite overpass.

The values of effective upward beam emittance have been calculated using Eq. (1) from the AVHRR channel 4 (10.5–11.3 μm) data. Sea and land surfaces have been distinguished using the AVHRR channel 2 reflectance data. For each surface type, the clear-sky radiance $L_0^\uparrow$ has been determined from the peak temperature in the channel 4 histogram. The radiance $L_0^\uparrow$ is then the blackbody radiances at temperatures of 284 and 287 K for sea and land surfaces, respectively.

Figure 5b shows local variations of the effective upward emittance along the straight line *AB*. The values vary from 0 to 0.25. The major uncertainty in the derivation of the effective upward emittance mainly depends on the surface temperature uncertainty. A variation of ±1 K in the land (or sea) surface temperature induces an absolute uncertainty in effective emittance of ±0.03.

c. Comparison

The cirrus cloud effective beam emittance was determined both from ground-based and satellite-based measurements above the Nordholtz site at 1225 UTC. At this moment and for this location, $\epsilon^\downarrow$ (0.11 ± 0.03) and $\epsilon^\uparrow$ (0.12 ± 0.03) were found to be very close to each other.

Moreover, the correspondence between the two datasets of independently derived cloud emittance reported in Fig. 5 is quite good. Both sets of infrared emittances vary in a range between 0 and 0.25. Even if physical changes in the cloud structure may have occurred during the course of the experiment, the main features of the cirrus cloud "variability" appear to have been preserved in spite of the difference in spatial resolution (300 m and 1.1 km, respectively). Such a good comparison between cirrus cloud emittances derived from both NOAA satellite AVHRR and ground-based measurements was already obtained by Stone et al. (1990). This was not the case in a previous comparison from ground-based radiometer and *Nimbus-4* satellite THIR data because of the low THIR resolution (15–20 km) (Platt 1975).

The good correspondence between the two types of measurements suggests a comparison between measurements from ground-based aureolemeter (300 m × 700 m of resolution) and from NOAA AVHRR (1.1 km of resolution). This comparison is presented in the following section.

4. Radiatively equivalent microphysical properties

This section is devoted to the remote sensing of microphysical properties of cirrus clouds from both ground-based measurements and thermal infrared satellite data. The solar downward radiance measured by the aureolemeter and the brightness temperatures derived from satellite data are sensitive to the cloud microphysics via the optical properties of the cloud particles. The first part of this section briefly presents the theoretical microphysical models used in this paper and the associated computational methods used to derive optical properties of cloud particles. Then aureolemeter and AVHRR measurements are compared with theoretical model results to retrieve a radiatively equivalent microphysical model for the observed cirrus cloud.

a. Computed optical properties of ice crystals

Cirrus clouds are generally composed of crystals of various shapes (Heymsfield 1975, 1977). To assess the sensitivity of the results shown hereafter to the shape of cloud particles, we considered two ideal shapes of ice particles: spherical and hexagonal crystals.

The size distribution of the spheres was assumed to be a modified gamma function (Deirmendjian 1969). This function was chosen to smooth out the fluctuations that are characteristic of the scattering by a single particle. Such a smoothing is not necessary for randomly oriented hexagonal crystals in either a plane or in space (Liou and Hansen 1971).

The shape, size, and orientation of the cloud particles, along with the real and imaginary parts of the refractive index, are inputs that are required for the scattering computations. The real (n_r) and imaginary (n_i) parts of the refractive index of ice, spectrally averaged over the wavelength ranges used in this study, are listed in Table 1 (Warren 1984). Note that at the central wavelength of the aureolemeter (0.85 μm) n_i is so small that the single-scattering albedo of the ice particles is very close to 1.

TABLE 1. Spectrally averaged real (n_r) and imaginary (n_i) parts of the refractive index of ice (Warren 1984) for the wavelength ranges used in this study.

Wavelength (μm)	n_r	n_i
0.85	1.304	1.8×10^{-5}
10.8	1.090	0.177
11.9	1.265	0.410

Using these characteristics of the particles, the cloud optical parameters (the scattering phase function, the single-scattering albedo, and the extinction coefficient) can be derived using Mie theory for polydisperse spheres and using a ray-tracing technique for hexagonal ice crystals (Jacobowitz 1971). Relative to the direction of the unpolarized incident wave, for all the possible orientations of an ice crystal, the polarized fields are calculated by means of the Snell and Fresnel laws until the emergence. In addition, from the Babinet principle, we calculated the angular distribution of the energy of the diffracted wave in the Fraunhofer limit by an aperture that was the projection of the hexagonal crystal on the plane normal to the incident wave (Cai and Liou 1982; Brogniez 1988).

b. Application to the ground-based measurements

This subsection is devoted to the treatment of data acquired by the aureolemeter in order to derive information about equivalent microphysical composition of the semitransparent cirrus cloud observed 18 October 1989. As mentioned in section 2, the aureolemeter measures the downward radiance at a constant viewing zenith angle that remains always very close to the solar one during the acquisition record.

At a given wavelength in the shortwave solar range, the global radiance transmitted through a homogeneous cloudy atmosphere $\mathbf{L}(\mu_s, \mu, \varphi_s, \varphi)$ is the sum of the directly transmitted radiance and of the diffuse radiance

$$\mathbf{L}(\mu_s, \mu, \varphi_s, \varphi) = \Delta(\mu_s - \mu)\Delta(\varphi_s - \varphi)\mathbf{E} \times \exp\left[\frac{-(\delta + \delta^*)}{\mu_s}\right] + \mathbf{L_d}, \quad (2)$$

where $\Delta(x)$ stands for the Dirac function, μ_s and μ are the cosine of the solar zenith angle and the cosine of the viewing zenith angle, respectively, φ_s and φ are the solar and viewing azimuth angles, respectively. The constant $\mathbf{E}$ is the solar irradiance on a plane perpendicular to the solar beam, convoluted by the spectral bandpass of the filter, which, in the case of the aureolemeter, is centered at 0.85 μm. Finally, δ and δ^* are the cloudy and the cloud-free atmospheric extinction optical depths, respectively.

The diffuse radiance $\mathbf{L_d}$ is a complex expression that depends on the following parameters:

$$\mathbf{L_d}[\mathbf{E}, \mu_s, \mu, \varphi_s, \varphi, P(\Theta), \omega, \delta, P^*(\Theta), \omega^*, \delta^*, \rho_s], \quad (3)$$

where P and ω (P^* and ω^*) are the scattering phase function and single-scattering albedo of the cloud layer (clear atmosphere), Θ is the scattering angle defined as the angle between the incident and the scattered beam, and ρ_s is the surface reflectance.

According to Eq. (2), almucantar scanning with the aureolemeter theoretically allows separation of the directly transmitted part of the global radiance from the diffuse one. Nevertheless, when viewing the sun, the aureolemeter with its finite field of view measures not only the directly transmitted radiance but also a scattered radiance that is all the more important because the atmospheric particles yield extremely strong forward scattering. However, as shown hereafter, the true optical depth can be retrieved using a correction method presented by Shiobara and Asano (1992). On the other hand, when doing measurements away from the sun, only the diffuse radiance have to be considered. So the sensitivity of the diffuse radiance [see Eq. (3)] to the cloud optical parameters, and finally to the cloud microphysical model, can be evaluated.

However, if one wants to derive information about cloud microphysics by measuring the diffuse radiance $\mathbf{L_d}$, one has to determine all the other parameters that affect $\mathbf{L_d}$ for a given illumination–observation condition. In particular, as $\mathbf{L_d}$ depends on clear-sky optical properties, the determination of the cirrus characteristics have to be done in two steps: (i) clear-sky aureolemeter measurements, and (ii) homogeneous cirrus cloud measurements.

1) CLEAR ATMOSPHERE AND SURFACE PROPERTIES

AVHRR channel 2 data have been analyzed to derive the surface reflectance ρ_s. The central wavelength of this channel is nearly 0.83 μm, which is very close to that of the aureolemeter. The surface reflectance was thus fixed to 0.2.

Under clear sky conditions, the global radiance depends on molecular and aerosol properties. Nevertheless, the contribution of the Rayleigh scattering to the entire signal is easy to take into account, and moreover it is very low at 0.85 μm. Thus, the optical properties of the clear atmosphere can be inferred when the aerosol characteristics are known.

The aerosol particle size distribution was derived from the clear-sky diffuse radiance measurements using a method developed by Santer and Herman (1983). The retrieved size distribution is characterized by an effective radius (Hansen and Hovenier 1974) $r_{\text{eff}} = 0.41$ μm and an associated effective variance $v_{\text{eff}} = 2.8$. The spectrally averaged refractive index at 0.85 μm is assumed to be 1.33.

In order to determine the true clear-sky optical depth δ^*, we have measured the directly transmitted radiance.

First, the value of the solar irradiance **E** was inferred by applying the Bouguer–Langley method to direct sun viewing measurements for three days corresponding to very clear sky conditions (21 September, 3 and 5 October).

Following Shiobara and Asano (1992), due to the scattering into the field of view of the aureolemeter, the apparent optical thickness measured by the instrument is given by $(1 - \omega^* f^*)\delta^*$, where f^* is the ratio of the light scattered within the solid angle $\Delta\Omega$ (of half-angle $\alpha = 0.4°$) to the entire scattered light,

$$f^* = \int_0^{\alpha} P(\Theta)\sin\Theta d\Theta. \quad (4)$$

Under clear sky conditions, the light scattered by molecules and aerosols over the field of view of the aureolemeter is very small compared to the directly transmitted light: less than 0.2% of the photons scattered by the observed aerosol fall within the angular field of view. The transmission is thus $\exp(-\delta^*/\cos\theta_s)$. The optical depth derived from direct measurements near 1030 UTC was $\delta^* = 0.104$.

2) MEASUREMENTS UNDER CLOUDY CONDITIONS

Under cloudy conditions, the light scattered by cirrus particles near the forward direction is no more negligible compared to the directly transmitted light. Indeed, the scattering diagram of large particles presents a very sharp diffraction peak near $\Theta = 0°$. Moreover, in the case of polyhedral particles, there is Dirac delta function transmission through parallel planes at $\Theta = 0°$ (Takano and Liou 1989). Thus, the cloud optical depth directly derived from radiances is generally underestimated, and the actual cloud optical depth δ is extremely dependent on the particle size and shape.

The apparent total optical depth $[(1 - \omega f)\delta + \delta^*]$ measured near 1300 UTC was 0.209. Assuming there was no change in the atmosphere below the cirrus layer since the clear-sky measurements at 1030 UTC, the apparent cloud optical depth was 0.105. As mentioned above, to determine the true cloud optical thickness δ, the value of the parameter f is required, that is, the scattering phase function has to be known. Some computed examples of cloud phase functions are presented in the next subsection.

3) CLOUD SCATTERING PHASE FUNCTION $P(\Theta)$

To illustrate the differences between spheres and hexagonal ice crystals, several phase functions have been calculated at $\lambda = 0.85$ μm. The computed phase functions for scattering angles between 0° and 60° are reported in Fig. 6 for randomly oriented hexagonal crystals with various aspect ratios $L/2R$, where L is the length and $2R$ is the diameter of the particle. Columns with $L/2R = 1000$ μm/47 μm present a larger peak at the 22° halo region than plates of the same volume with

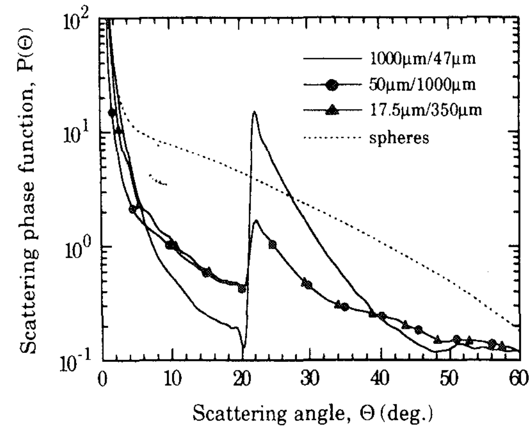

FIG. 6. Scattering phase functions computed at 0.85 μm for randomly oriented hexagonal ice crystals and spheres.

$L/2R = 17.5$ μm/350 μm. For comparison, the scattering phase function for spheres with an effective radius $R_v = 70$ μm, which corresponds to the same particle volume, is also reported. The case of larger plates with $L/2R = 50$ μm/1000 μm amplifies the influence of diffraction near the 0° scattering angle. The two phase functions corresponding to the plates with the same aspect ratio are nearly equal for scattering angles greater than 20°.

Assuming that the cirrus cloud is composed of hexagonal plates with dimensions $L/2R = 17.5$ μm/350 μm, we find $f = 0.8$, that is, 80% of the photons once scattered are within the solid angle $\Delta\Omega$. If the above-mentioned ice particle model is correct, then the actual cloud optical depth was 0.53. However, the determination of the actual cloud optical depth is thus extremely dependent on the particle size and shape.

4) RESULTS

Transmitted radiances **L** were calculated using the method of successive orders of scattering (Lenoble 1985). For a precise simulation, 384-point Gaussian quadrature was used.

The computed radiances were compared to the measurements. The radiances derived from the aureolemeter measurements were obtained by dividing the measured fluxes by the solid angle $\Delta\Omega$. Moreover, since the measured values of **L** and of the solar irradiance **E** are in arbitrary units, here the values of **L/E** are compared with the computed ones.

On the other hand, the comparison of measured and computed **L/E** values assumes no variability of the cirrus layer during the measurement of the radiance. An azimuthal shift of the aureolemeter of 60° gives a horizontal displacement of 22 km at the 9-km altitude (the midcloud altitude). In fact, due to the simultaneous cloud motion in the wind direction, the displacement caused by repointing is expected to be reduced to about

6 km. We thus assume that the measurements have not been affected significantly by the heterogeneity of the cirrus cloud.

The comparisons between measurements and computations are reported in Fig. 7 for various particle volumes and in Fig. 8 for various aspect ratios. Comparisons for clear-sky radiances $\mathbf{L}^*$ are also reported. The clear-sky measurements of diffuse radiance were recorded around 1030 UTC, while cloudy-sky measurements of L were recorded around 1300 UTC. Therefore, correction for solar angle variations had to be taken into account. The apparent disagreement between the observed and the calculated values of $\mathbf{L}^*$ beyond $\Theta = 40°$ is related to the very small clear-sky radiance values.

Using a trial and error method, the best agreement for the cloudy-sky radiances was found for plates with an aspect ratio $L/2R \approx 0.05$ and an equivalent spherical radius $R_v \approx 100$ μm. Keeping in mind the uncertainties due to the spatial variability of the cirrus cloud, one can expect that the values of $L/2R$ and R_v are determined within a factor of 2. These dimensions are in good agreement with Ono's measurements (1969) in natural clouds, which show a size distribution of plates with a peak in the 200–400-μm-diameter region.

Obviously, even for the cirrus observed the 18 October 1989, actual ice crystals are not all plates of these dimensions. Moreover, according to Platt (1978), such plate crystals in the atmosphere should fall with their long axe aligned in the horizontal, that is, it should not be randomly oriented in space. However, our model with these dimensions must be considered as an effective model (i.e., a synthetic model) that produces the same effects on the radiation field as the real particle size distribution. As the hexagonal columns ($L/2R > 1$) give too large halo, a mixture of hexagonal columns and spheres would also restore the measurements, but in this case the number of parameters to be determined (the dimensions of the hexagonal crystals, the radius of the spheres, and the abundance ratio of these two types of particles) would be too large for the available informations. In the following, we attempt to see if our simplified model also satisfies satellite observations of the brightness temperatures.

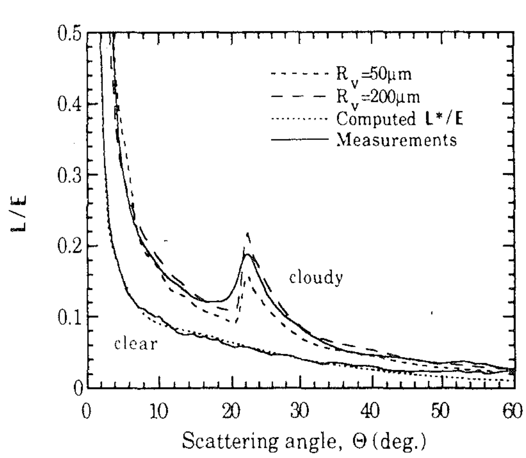

FIG. 7. Comparison between experimental (full lines) and calculated (dashed lines) downward radiances at 0.85 μm. The cloudy-sky radiance L and the clear-sky radiance $\mathbf{L}^*$ are displayed from top to bottom. The calculated radiances are for randomly oriented ice plates with $L/2R = 0.05$ and $R_v = 50$ and 200 μm.

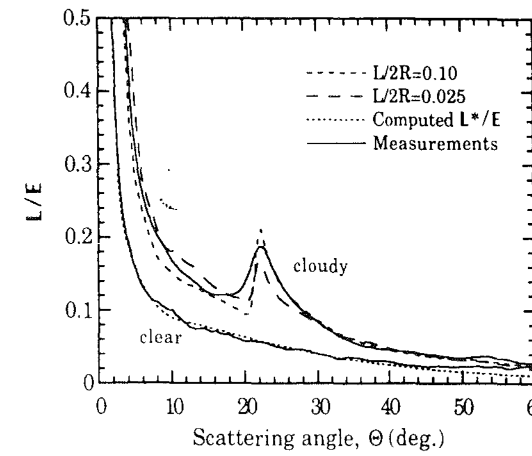

FIG. 8. The same as for Fig. 7 but with $R_v = 100$ μm and $L/2R = 0.025$ and 0.10.

c. Application to satellite data

Up until now, few studies have attempted to derive cloud microphysical properties from satellite data. Arking and Childs (1985) used the 3.7-μm AVHRR channel to extract what they call a "microphysical model parameter," which is an index representing the properties of cloud particles (size and phase, shape being assumed to be spherical).

Wu (1987) has shown that the method developed by Inoue (1985, 1987) to detect semitransparent cirrus clouds is highly sensitive to the cloud particles size distribution. This method is based on the significant brightness temperature differences (BTD) that exist between channels 4 and 5 of the AVHRR radiometer for pixels covered by thin cirrus clouds. Recently, Parol et al. (1991) showed that, although the BTD method is not sufficient for estimating the shape and/or size of ice particles, it makes it possible to put some limits on their variability. For instance, they showed that neither large ice nor water spheres ($R_v > 50$ μm) nor fully randomly oriented cylinders could explain their observations.

This section further investigates the contribution of the BTD method to the determination of the microphysical properties of the cirrus observed on 18 October 1989.

Figure 9 shows the image constructed from brightness temperature differences between channel 4 (10.5–

FIG. 9. Satellite image constructed from brightness temperature difference between channels 4 and 5 of *NOAA-11* AVHRR for the same region as in Fig. 4. The gray scale represents a change in brightness temperature difference from 0 (black) to 3 K (white).

11.3 μm) and channel 5 (11.5–12.5 μm) for the same 600 km × 600 km region as in Fig. 4. The AVHRR digital counts are shown with an 8-bit gray level corresponding to brightness temperature differences from 0 to 3 K. Semitransparent cirrus clouds appear as light objects, while thick clouds appear black (upper-right part of the image) against the relatively dark cloud-free background. Indeed, many cirrus streaks can be detected over the North Sea (upper left part of the image) that are not identifiable in the channel 2 reflectance image. Moreover, despite the fact that they are situated over land, which often shows large spatial heterogeneity of surface temperature, other semitransparent cirrus are also easily identified in the southern part of the BTD picture. Figure 9 shows that the BTD method is able to identify very thin cirrus (infrared emissivities are smaller than 0.3 for this region) and that it remains a very efficient method for detecting semitransparent cirrus clouds over land.

Figure 10 presents the observed (isolines) brightness temperature differences, plotted as a function of the brightness temperature in channel 4, T_4, for the small region (200 km × 50 km) outlined in Fig. 4 and Fig. 9. This area was chosen to be consistent with the aureolemeter measurements that were in the sun direction. In addition, this zone is small enough to maintain reasonable spatial homogeneity of the brightness surface temperatures. Finally, jet contrails were present in this area, and their properties will be compared to those of natural cirrus.

For the cloud-free pixels ($T_4 \approx 287$ K), the BTD is small, close to 0.8 K, corresponding to the difference in water vapor absorptions between the two spectral intervals in the lower troposphere. Because the cirrus infrared emissivities are very small, the histogram does not have the usual arch shape; the "cold foot" corresponding to pixels totally covered by thick cirrus [$\epsilon_4 \approx \epsilon_5 \approx 1$, $T_4 \approx T_5 \approx T^{\text{cloud}} = 231$ K (see section 3a)] is not present. Moreover, the magnitude of the BTD is not very large (~2–3.5 K) for the pixels covered by semitransparent cirrus. However, this 2D histogram shows two distinct branches. The first branch presents a large variation of the BTD for a small range of brightness temperature ($T_4 \sim 283$–287 K). The second branch shows variations of the BTD very similar to those obtained in previous studies (Inoue 1985; Parol et al. 1991) and can thus be considered as typical of cirrus clouds.

According to Parol et al. (1991), these variations depend on the cloud temperature T^{cloud}, the clear-sky radiative temperatures T_4^{clear} and T_5^{clear}, the pixel cloud fraction N, and the cloud microphysical properties. As a first approximation, we assume $N = 1$, keeping in mind that if $N < 1$, the retrieved effective dimension of cloud particles would be smaller. Using $T^{\text{cloud}} = 231$ K, $T_4^{\text{clear}} = 287.2$ K, and $T_5^{\text{clear}} = 286.4$ K, theoretical temperatures T_4 and T_5 have been calculated for varying cloud emissivities, taking multiple scattering into

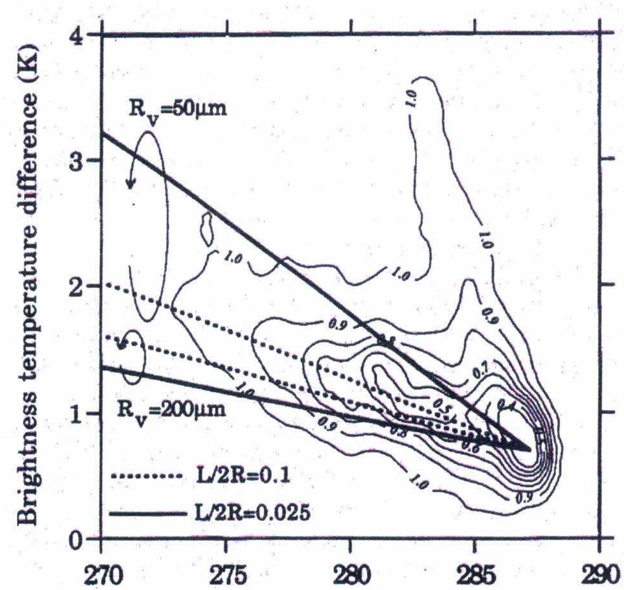

FIG. 10. Comparison between observed (isolines) and theoretical (nearly straight lines) brightness temperature differences between channels 4 and 5 of *NOAA-11* AVHRR for the area outlined in Fig. 9. For example, 70% of the pixels are situated within the isolines 0.7. The nearly straight lines correspond to randomly oriented hexagonal ice plates with various aspect ratios $L/2R$ and equivalent volume radius R_v.

account according to the method developed by Parol et al. (1991).

On the basis of the results presented in section 4b, we consider various hexagonal ice crystals with dimensions around $L/2R = 0.05$ and $R_v = 100$ μm. Figure 10 shows the BTD curves obtained with various aspect ratios $L/2R$ and various equivalent spherical radius R_v. For a given aspect ratio, the magnitude of the BTD decreases as the particle volume increases. For a given volume, the magnitude of the BTD is found to first decrease and then increase when the aspect ratio increases. When the aspect ratio varies from 0.025 to 0.1, the magnitude of the BTD decreases for $R_v = 50$ μm, is rather stationary for $R_v = 100$ μm (not shown here), and increases for $R_v = 200$ μm.

As shown in Fig. 10, for $L/2R = 0.1$ and $R_v = 50$ μm the variation of the BTD with T_4 is very similar to the main branch of the histogram of the observations; that is, it goes through the clusters with maximum pixel density. Good agreement is also obtained when $L/2R$ is decreased to 0.025 while increasing R_v to 80 μm. Thus, the hexagonal ice crystal model with dimensions $L/2R$ from 12.5 μm/500 μm to 20 μm/200 μm correctly simulates both solar (0.85 μm) measurements from ground-based observations (as described in section 4b) as well as satellite measurements in the infrared window (10–12 μm).

For comparison purposes, we also consider ice spheres since this is the simplest and most often used cloud particle shape. As shown in Fig. 11, it is possible to retrieve the observed BTD assuming that the thin cirrus clouds are composed of spherical particles with an effective radius close to 27 μm, which is two to three times smaller than the value obtained with the assumption of hexagonal crystals. This confirms that the BTD signal significantly depends on the shape of the cloud particles. In any case, as discussed in section 4b, spherical particles are not in agreement with the aureolemeter measurements in the solar range.

The global 2D histogram on Fig. 11 also shows another set of points that presents a great variation of BTD (from 0.8 K to about 3.5 K) for a small range of brightness temperature (283–287 K). The corresponding satellite pixels have been clearly identified as following nearly straight line segments that characterize jet contrails (right part of the outlined area in Fig. 9). Such a BTD signal can be reproduced assuming ice spheres with $R_v = 4.5$ μm. No attempt was made using hexagonal ice particles because the ray-tracing method cannot be applied when the particle dimensions are too small relative to the wavelength (Liou and Hansen 1971). However, the primary interest of this comparison is to highlight the important differences between the microphysical properties of natural thin cirrus and jet contrails. During our study, several comparisons performed on the global AVHRR image (not shown here) have revealed such a discrepancy between cirrus clouds and contrails microphysical properties. Note

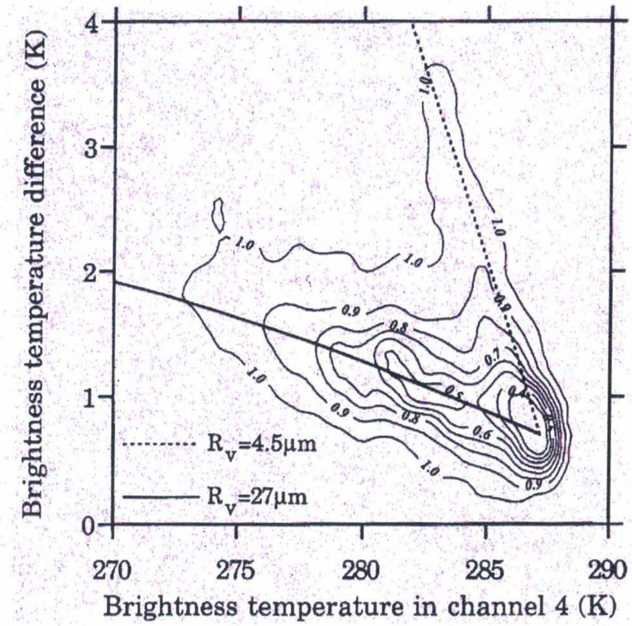

FIG. 11. The same as Fig. 10 but for ice spheres with radius R_v.

that images constructed from the brightness temperature difference between the two AVHRR thermal channels allow jet contrail identification (Lee 1989) and may allow their automated detection (Engelstad et al. 1992). A lot of white streaks that could be contrails appear in Fig. 9. In favorable atmospheric conditions, these contrails can add significantly to high-level cloudiness (Kuhn 1970; Seaver and Lee 1989). However, the possible effect of this additional cloudiness on the climate is still under discussion (Detwiler 1986; Carleton and Lamb 1986).

5. Conclusions

Ground-based observations and satellite data have been compared for the 18 October 1989 ICE cirrus case study. The measured infrared effective emittances were in the range 0–0.3. Good agreement was obtained when comparing the time variability of the downward emittance of the cirrus clouds observed at Nordholz (53.8°N, 8.3°E) and the spatial variability of the upward emittance derived from *NOAA-11* AVHRR data at 1225 UTC.

An equivalent microphysical model of cirrus clouds was found to satisfy both the ground-based observations of the angular dependence of the scattered solar radiation and the satellite observations of the brightness temperatures in channels 4 and 5 of *NOAA-11* AVHRR. The model consists of randomly oriented ice plates with $L \sim 10$–20 μm and $2R \sim 200$–500 μm. The optical properties of these plates are reported in Table 2.

Obviously, actual ice crystals in the observed cirrus cloud are not all plates of these dimensions. The di-

TABLE 2. Optical properties of our model ice crystals ($L/2R$ = 12.5 μm/500 μm to 20 μm/200 μm) for the wavelength ranges used in this study.

Wavelength (μm)	Asymmetry factor	Single-scattering albedo
0.85	0.967–0.935	1.000
10.8	0.926–0.914	0.554–0.547
11.9	0.840–0.819	0.567–0.565

mensions of our model must be considered as radiatively effective ones.

Ice spheres do not simulate the observed halo, whereas hexagonal columns ($L/2R > 1$) give too large halo. Consequently, a mixture of hexagonal columns and spheres would also restore the aureole measurements, but the information content of the observations is unsufficient to determine the parameters needed to describe the model.

During this study, hexagonal ice crystals were also assumed to be randomly oriented *in the horizontal plane.* An angle of tilted orientation of $\pm 10°$ relative to the horizontal plane has been considered. These models do not agree with the aureolemeter measurements. Such models were not reported in this paper since the goal was to find a possible model for both solar range and telluric radiations but not to consider the whole of possible models. The fact that a model with crystals randomly oriented *in space* is convenient might be explained by the large variety of shapes of cirrus particles that would be better simulated by a full random orientation of identical crystals.

The phase function of the hexagonal ice plates is highly anisotropic and presents a very sharp peak near 0°. Due to the large percentage of single-scattered photons within the field of view of the aureolemeter, the cloud optical depth derived from the attenuation of the direct solar radiation significantly differs from the actual one. This is an important consideration when cirrus optical depth measurements are compared to independent measurements of ice water content.

Assuming spherical particles to explain brightness temperature measurements in AVHRR channels 4 and 5 leads to a particle size about three times smaller than the one obtained with the hypothesis of hexagonal plates. This may explain the often observed discrepancy between satellite and in situ observations (see, for instance, Ackerman et al. 1990).

Our model of full randomly oriented ice plates might be appropriate only for the cirrus clouds that were observed near Nordholtz during 18 October 1989. Analysis of many other cirrus observations are needed. Recommendations for future cirrus experiments include aureolemeter measurements. An improved aureolemeter is under development at the LOA for this purpose.

Acknowledgments. This work was part of the International Cirrus Experiment (ICE), followed by the European Cloud and Radiation Experiment (EUCREX), which are both supported by the European Economic Community. The authors gratefully acknowledge the assistance of Dr. B. Bonnel and Dr. C. Devaux in the analysis of aureolemeter data, and Dr. P. Flamant with lidar data processing.

REFERENCES

Ackerman, S. A., W. L. Smith, J. D. Spinhirne, and H. E. Revercomb, 1990: The 27–28 October 1986 FIRE IFO cirrus case study: Spectral properties of cirrus clouds in the 8–12 μm window. *Mon. Wea. Rev.*, **118,** 2377–2388.

Allen, J. R., 1971: Measurements of cloud emissivity in the 8–13 μm waveband. *J. Appl. Meteor.*, **10,** 260–265.

Ansmann, A., J. Bösenberg, G. Brogniez, S. Elouragini, P. H. Flamant, K. Klapheck, H. Linn, L. Menenger, W. Michaelis, M. Riebesell, C. Senff, P.-Y. Thro, U. Wandinger, and C. Weitkamp, 1993: Lidar network observations of cirrus morphological and scattering properties during the International Cirrus Experiment 1989: The 18 October 1989 case study and statistical analysis. *J. Appl. Meteor.*, **32,** 1608–1622.

Arking, A., and J. D. Childs, 1985: Retrieval of cloud cover parameters from multispectral satellite images. *J. Climate Appl. Meteor.*, **24,** 322–333.

Brogniez, G., 1988: Light scattering by finite hexagonal crystals arbitrarily oriented in space. *Proc. of the IRS'88,* Lille, France, International Association of Meteorology and Atmospheric Physics, 64–67.

Cai, Q., and K. N. Liou, 1982: Polarized light scattering by hexagonal ice crystals: Theory. *Appl. Opt.*, **21,** 3569–3580.

Carleton, A. M., and P. J. Lamb, 1986: Jet contrails and cirrus clouds: A feasability study employing high resolution satellite imagery. *Bull. Amer. Meteor. Soc.*, **67,** 301–309.

Cess, R. D., and Coauthors, 1990: Intercomparison and interpretation of climate feedback processes in 19 atmospheric general circulation models. *J. Geophys. Res.*, **95,** 16 601–16 615.

Deirmendjian, D., 1969: *Electromagnetic Scattering on Spherical Polydispersions.* Elsevier, 290 pp.

Detwiler, A., 1986: Comments on "Jet contrails and cirrus clouds: A feasability study employing high resolution satellite imagery." *Bull. Amer. Meteor. Soc.*, **67,** 1150–1151.

Elouragini, S., 1991: Etude des propriétés optiques et géométriques des cirrus par télédétection optique active (lidar) et passive (radiométrie). Ph.D. thesis, Université Paris, 6, 280 pp.

Engelstad, M., S. K. Sengupta, T. Lee, and R. M. Welch, 1992: Automated detection of jet contrails using the AVHRR split window. *Int. J. Rem. Sens.*, **13,** 1391–1412.

Green, A. E. S., A. Deepack, and B. J. Lipofsky, 1971: Interpretation of the sun's aureole based on atmospheric aerosol models. *Appl. Opt.*, **10,** 1263–1279.

Hansen, J. E., and J. W. Hovenier, 1974: Interpretation of the polarization of Venus. *J. Atmos. Sci.*, **28,** 137–160.

——, A. Lacis, D. Rind, G. Russel, P. Stone, I. Fung, R. Ruedy, and J. Lerner, 1984: Climate sensitivity: Analysis of feedback mechanisms. *Climate Processes and Climate Sensitivity.* J. E. Hansen and T. Takahashi, Eds., Geophys. Monogr. Ser., **29,** M. Ewing Vol. 5, Amer. Geophys. Union, 130–163.

Heymsfield, A. J., 1975: Cirrus uncinnus generating cells and the evolution of cirriform clouds. Part I: Aircraft measurements of the growth of the ice phase. *J. Atmos. Sci.*, **32,** 798–808.

——, 1977: Precipitation development in stratiform ice clouds: A microphysical and dynamical study. *J. Atmos. Sci.*, **34,** 367–381.

Inoue, T., 1985: On the temperature and effective emissivity determination of semi-transparent cirrus clouds by bispectral measurements in the 10 μm window region. *J. Meteor. Soc. Japan*, **63**, 88–98.

——, 1987: A cloud type classification with NOAA-7 split-window measurements. *J. Geophys. Res.*, **92**, 3991–4000.

Jacobowitz, H., 1971: A method for computing the transfer of solar radiation throught clouds of hexagonal ice crystals. *J. Quant. Spectrosc. Radiat. Transf.*, **11**, 691–695.

Kneyzys, F. X., E. P. Shettle, L. W. Abreu, J. H. Chetwynd, G. P. Anderson, W. O. Gallery, J. E. A. Selby, and S. A. Clough, 1988: Users guide to LOWTRAN 7. AFGL-TR-88-0177, Air Force Geophysics Laboratory, Hanscom AFB, MA, 146 pp.

Kuhn, P. M., 1970: Airborne observation of contrail effects on the thermal radiation budget. *J. Atmos. Sci.*, **27**, 937–942.

Lenoble, J., 1985: *Radiative Transfer in Scattering and Absorbing Atmospheres: Standard Computational Procedures*. A. Deepak, 300 pp.

Lee, T. F., 1989: Jet contrail identification using the AVHRR split window. *J. Appl. Meteor.*, **28**, 993–995.

Liou, K. N., and J. E. Hansen, 1971: Intensity and polarization for single scattering by polydisperse spheres: A comparison of ray optics and Mie theory. *J. Atmos. Sci.*, **28**, 995–1004.

McClatchey, R. A., R. W. Fenn, J. E. A. Selby, F. E. Volz, and J. S. Garing, 1971: Optical properties of the atmosphere. *AFCRL 71-0279*, Air Force Cambridge Research Laboratories, Envir. Res. Papers, Bedford, MA, 85 pp.

Ono, A., 1969: The shape and riming properties of ice crystals in natural clouds. *J. Atmos. Sci.*, **26**, 138–147.

Parol, F., J. C. Buriez, G. Brogniez, and Y. Fouquart, 1991: Information content of AVHRR channels 4 and 5 with respect to the effective radius of cirrus cloud particles. *J. Appl. Meteor.*, **30**, 973–984.

Platt, C. M. R., 1971: A narrow-beam radiometer for atmospheric radiation studies. *J. Appl. Meteor.*, **10**, 1307–1313.

——, 1973: Lidar and radiometric observations of cirrus clouds. *J. Atmos. Sci.*, **30**, 1191–1204.

——, 1975: Infrared emissivity cirrus—Simultaneous satellite, lidar and radiometric observations. *Quart. J. Roy. Meteor. Soc.*, **101**, 119–126.

——, 1978: Lidar backscatter from horizontal ice crystal plates. *J. Appl. Meteor.*, **17**, 482–488.

——, and G. L. Stephens, 1980: The interpretation of remotely sensed high cloud emittances. *J. Atmos. Sci.*, **37**, 2314–2322.

——, and A. C. Dilley, 1984: Determination of the cirrus particle single-scattering phase function from lidar and solar radiometric data. *Appl. Opt.*, **23**, 380–386.

——, D. W. Reynolds, and N. L. Abshire, 1980: Satellite and lidar observations of the albedo, emittance, and optical depth of cirrus compared to model calculations. *Mon. Wea. Rev.*, **108**, 195–204.

——, J. C. Scott, and A. C. Dilley, 1987: Remote sounding of high clouds. Part VI: Optical properties of midlatitude and tropical cirrus. *J. Atmos. Sci.*, **44**, 729–747.

Prabhakara, C., R. S. Fraser, G. Dalu, M. L. C. Wu, R. J. Curran, and T. Styles, 1988: Thin cirrus clouds: Seasonal distribution over oceans deduced from Nimbus-4 Iris. *J. Appl. Meteor.*, **27**, 379–399.

Raschke, E., and K.-D. Rockwitz, 1988: The International Cirrus Experiment: Some preliminary results from the first field phase. *Proc. of the IRS '88*, Lille, France, Int. Asso. Meteor. Atmos. Phys., 6–9.

——, J. Schmetz, J. Heintzenberg, R. Kandel, and R. W. Saunders, 1990: The International Cirrus Experiment (ICE)—A joint european effort. *ESA Journal*, **14**, 193–199.

Roeckner, E., 1988: Cloud–radiation feedbacks in a climate model. *Atmos. Res.*, **21**, 293–303.

——, V. Schlese, J. Biercamp, and P. Loewe, 1987: Cloud optical depth feedback and climate modeling. *Nature*, **329**, 138–140.

Santer, R., and M. Herman, 1983: Particle size distributions from forward scattering light using Chahine inversion scheme. *Appl. Opt.*, **22**, 2294–2301.

Seaver, W. L., and J. E. Lee, 1987: A statistical examination of sky cover changes in the contiguous United States. *J. Climate Appl. Meteor.*, **26**, 88–95.

Shiobara, M., and S. Asano, 1992: Estimation of cirrus optical thickness from sunphotometer measurements. *Int. WCRP Symp., Extented Abstract, Cloud and Ocean in Climate*. Nagoya, Japan, Japanese National Committee for WCRP & Nagoya University, 8.16–8.19.

Spinhirne, J. D., and W. D. Hart, 1990: Cirrus structure and radiative parameters from airborne lidar and spectral radiometer observations: The 28 October 1986 FIRE study. *Mon. Wea. Rev.*, **118**, 2329–2343.

Starr, D. O'C., 1987: A cirrus-cloud experiment: Intensive field observations planned for FIRE. *Bull. Amer. Meteor. Soc.*, **68**, 119–124.

Stephens, G. L., S. C. Tsay, P. W. Stackhouse Jr., and P. J. Flatau, 1990: The relevance of the microphysical and radiative properties of cirrus clouds to climate and climatic feedback. *J. Atmos. Sci.*, **47**, 1742–1753.

Stone, R. S., G. L. Stephens, C. M. R. Platt, and S. Banks, 1990: The remote sensing of thin cirrus cloud using satellites, lidar, and radiative transfer theory. *J. Appl. Meteor.*, **29**, 353–366.

Takano, Y., and K. N. Liou, 1989: Solar radiative transfer in cirrus clouds. Part I: Single scattering and optical properties of hexagonal ice crystals. *J. Atmos. Sci.*, **46**, 3–19.

Twitty, J. T., R. J. Parent, J. A. Weinman, and E. L. Eloranta, 1976: Aerosol size distributions: Remote determination from airborne measurements of the solar aureole. *Appl. Opt.*, **15**, 980–989.

Ward, G., K. M. Cushing, R. D. McPeters, and A. E. S. Green, 1973: Atmospheric aerosol index of refraction and size–altitude distribution from bistatic laser scattering and solar aureole measurements. *Appl. Opt.*, **12**, 2585–2592.

Warren, S. G., 1984: Optical constants of ice from the ultraviolet to the microwave. *Appl. Opt.*, **23**, 1206–1225.

——, C. J. Hahn, J. London, R. M. Chervin, and R. L. Jenne, 1986: Global distribution of total cloud cover and cloud type amounts over land. NCAR Tech. Note, TN-273 + STR, Boulder, CO.

——, ——, ——, ——, and ——, 1988: Global distribution of total cloud cover and cloud type amounts over the ocean. NCAR Tech. Note, TN-317 + STR, Boulder, CO.

Wetherald, R. T., and S. Manabe, 1988: Cloud feedback processes in a general circulation model. *J. Atmos. Sci.*, **45**, 1397–1415.

Wielicki, B. A., J. T. Suttles, A. J. Heymsfield, R. M. Welch, J. D. Spinhirne, M.-L. C. Wu, D. O'C. Starr, L. Parker, and R. F. Arduini, 1990: The 27–28 October 1986 FIRE IFO cirrus case study: Comparison of radiative transfer theory with observations by satellite and aircraft. *Mon. Wea. Rev.*, **118**, 2356–2376.

Wu, M. C., 1987: A method for remote sensing the emissivity, fractional cloud cover, and cloud-top temperature of high-level, thin clouds. *J. Climate Appl. Meteor.*, **26**, 225–233.

Printed in the United States of America
Reprinted from JOURNAL OF APPLIED METEOROLOGY
Vol. 36, No. 6, June 1997

Large-Scale Analysis of Cirrus Clouds from AVHRR Data: Assessment of Both a Microphysical Index and the Cloud-Top Temperature

V. GIRAUD, J. C. BURIEZ, Y. FOUQUART, AND F. PAROL

Laboratoire d'Optique Atmosphérique, Université des Sciences et Technologies de Lille, Villeneuve d'Ascq, France

G. SEZE

Laboratoire de Météorologie Dynamique, Ecole Normale Supérieure, Paris, France

(Manuscript received 4 March 1996, in final form 27 November 1996)

ABSTRACT

An algorithm that allows an automatic analysis of cirrus properties from Advanced Very High Resolution Radiometer (AVHRR) observations is presented. Further investigations of the information content and physical meaning of the brightness temperature differences (BTD) between channels 4 (11 μm) and 5 (12 μm) of the radiometer have led to the development of an automatic procedure to provide global estimates both of the cirrus cloud temperature and of the ratio of the equivalent absorption coefficients in the two channels, accounting for scattering effects. The ratio is useful since its variations are related to differences in microphysical properties. Assuming that cirrus clouds are composed of ice spheres, the effective diameter of the particle size distribution can be deduced from this microphysical index.

The automatic procedure includes first, a cloud classification and a selection of the pixels corresponding to the envelope of the BTD diagram observed at a scale of typically 100 × 100 pixels. The classification, which uses dynamic cluster analysis, takes into account spectral and spatial properties of the AVHRR pixels. The selection is made through a series of tests, which also guarantees that the BTD diagram contains the necessary information, such as the presence of both cirrus-free pixels and pixels totally covered by opaque cirrus in the same area. Finally, the cloud temperature and the equivalent absorption coefficient ratio are found by fitting the envelope of the BTD diagram with a theoretical curve. Note that the method leads to the retrieval of the maximum value of the equivalent absorption coefficient ratio in the scene under consideration. This, in turn, corresponds to the minimum value of the effective diameter of the size distribution of equivalent Mie particles.

The automatic analysis has been applied to a series of 21 AVHRR images acquired during the International Cirrus Experiment (ICE'89). Although the dataset is obviously much too limited to draw any conclusion at the global scale, it is large enough to permit derivation of cirrus properties that are statistically representative of the cirrus systems contained therein. The authors found that on average, the maximum equivalent absorption coefficient ratio increases with the cloud-top temperature with a jump between 235 and 240 K. More precisely, for cloud temperatures warmer than 235 K, the retrieved equivalent absorption coefficient ratio sometimes corresponds to very small equivalent spheres (diameter smaller than 20 μm). This is never observed for lower cloud temperatures. This change in cirrus microphysical properties points out that ice crystal habits may vary from one temperature regime to another. It may be attributed to a modification of the size and/or shape of the particles.

1. Introduction

Numerous studies of climate change have stressed the importance of cloud feedback (Ramanathan 1987; Ramanathan et al. 1989; Mitchell et al. 1989, etc.). Clouds modify both solar and terrestrial radiation by absorption, scattering, and emission. The intensity of those processes depends on amount, thickness, altitude, shape, and microphysical properties of the clouds. According to their characteristics, clouds can provide either positive or negative feedback to a climate system. Among the different cloud types, the cirrus cloud is characterized by particularly large spatial dimensions, long lifetime, and low emission temperatures. Therefore, more than other cloud types, the cirrus clouds can alter the energy available at the earth's surface by reflecting the incoming solar radiation and by modifying the quantity of outgoing longwave radiation.

To be able to understand the role of cirrus clouds on radiative processes and then to develop accurate general circulation model (GCM) parameterizations of the cirrus radiation interactions, one has to analyze frequent, consistent, and global-scale observations to systematically investigate their radiative and microphysical properties (Stephens et al. 1990). Naturally, satellites are perceived as the primary data sources for large-scale observations.

Corresponding author address: Dr. V. Giraud, Laboratoire d'Optique Atmosphérique, Université des Sciences et Technologies de Lille, 59655 Villeneuve d'Ascq, France.
E-mail: giraud@loa.univ-lille1.fr

However, cirrus clouds are very often semitransparent; some are undetectable from the visible channels of satellite radiometers and are difficult to distinguish from lower (and warmer) clouds on thermal infrared images. During the last 15 years, intensive research on cirrus cloud characterization from multispectral satellite imagery has been done. Numerous methodologies have been proposed using infrared channels (e.g., Szejwach 1982; Inoue 1985; Wu 1987; Prabhakara et al. 1988; Parol et al. 1991; Prata and Barton 1993). They are commonly based on the significant wavelength dependence of the cirrus cloud absorption in the infrared window (10–12 μm).

Inoue (1985) developed a bispectral technique based on the NOAA Advanced Very High Resolution Radiometer (AVHRR). He used a simple model to establish a link between the cloud emittance and the brightness temperature difference (BTD) observed between the two window channels centered on 11 and 12 μm. In this model, the key parameter is the absorption coefficient ratio β, which relates to the cirrus cloud emittances at 11 and 12 μm. This parameter is highly sensitive to the microphysical characteristics of the cloud as shown by Wu (1987) and Parol et al. (1991). Since this study, similar methods have been operated by many researchers to retrieve the microphysical properties, the emittance, the temperature, or the fractional cloud cover of cirrus clouds from AVHRR data (see, e.g., Lin and Coakley 1993; Baum et al. 1994; Brogniez et al. 1995). However, until now, this method has been applied only on very restrictive conditions and limited to only a few case studies. For example, Lin and Coakley (1993) analyzed six regions covered by very well defined single-level cirrus clouds; Baum et al. (1994) investigated multilayered cloud systems and analyzed three small regions.

The aim of the present work is to adapt the method based on cirrus BTD observations to provide estimates on a global scale of both the microphysical index and the cirrus cloud temperature. The physical basis of the method is first recalled in section 2, along with an example of cirrus BTD observations from AVHRR imagery. The procedure used to automatically analyze areas of typically 100 $\times$ 100 AVHRR pixels that contain cirrus clouds is described in section 3. As an application of this procedure, a dataset of 21 AVHRR images acquired over Europe and the North Atlantic Ocean from 10 to 20 October 1989 is analyzed. Statistics of cloud properties (cloud-top temperature and microphysical index) for the cirrus clouds observed for this region and period are reported in section 4 and discussed in section 5.

2. Theory

Inoue (1987) proposed a cloud-type classification based on applying a threshold technique to the two-dimensional diagram whose axes are the BTD and the brightness temperature at 11 μm. Inoue exploited his previous work (Inoue 1985), where he had experimentally determined from eight cirrus cloud cases a relation between the emittances at 11 and 12 μm. Among others, Parol et al. (1991) investigated the relations between BTD and cirrus cloud properties more deeply. In this analysis, the cirrus cloud is assumed to be a horizontally homogeneous layer overlying a homogeneous surface (sea, land, or lower-level cloud). The influence of the clear atmosphere situated above the cirrus cloud is neglected. In these conditions, the upwelling radiance at the top of the atmosphere in the satellite viewing direction may be expressed as

$$I_i(\theta) = \{1 - N[\epsilon_i(\theta) + r_i(\theta)]\} I_{s,i} + N\epsilon_i(\theta) I_{c,i}, \quad (1)$$

where $i = 4, 5$ is the channel number, θ is the satellite viewing angle, N is the fraction of the field of view covered by the cirrus cloud, $\epsilon_i(\theta)$ is the cirrus cloud emittance in the satellite direction, $r_i(\theta)$ is the cirrus cloud directional reflectance, $I_{s,i}$ is the radiance associated with the cirrus-free portion of the field of view, and $I_{c,i}$ is the radiance that would be observed for the portion covered by the cirrus cloud if it radiated like a blackbody.

The scattering effect can be important for ice clouds in the thermal infrared window (Platt et al. 1987). However, a simple method based on the nonscattering approximation is still applicable if one makes use of the effective emittances $\epsilon_i^e(\theta)$ defined by Cox (1971)

$$I_i(\theta) = \{1 - N\epsilon_i^e(\theta)\} I_{s,i} + N\epsilon_i^e(\theta)I_{c,i}^e, \quad (2)$$

which implicitly includes the scattering effect. Because of the reflectance term, the effective emittance is greater than the true emittance. Thus, the radiance $I_{c,i}^e$ corresponding to thick cirrus clouds is slightly smaller than $I_{c,i}$.

As in Inoue (1985), the emittances for channels 4 and 5 are assumed to be related by

$$\epsilon_5^e(\theta) = 1 - [1 - \epsilon_4^e(\theta)]^{\beta^e}, \quad (3)$$

but, here, β^e is not the ratio of the absorption coefficients in the two channels. It is obtained by fitting the actual BTD, which is affected by multiple scattering with an equivalent nonscattering BTD. This equivalent absorption coefficient ratio is nearly independent in the viewing direction; it is a microphysical parameter that is related directly to the effective diameter of the particle size distribution if the particles are assumed to be spherical (Parol et al. 1991).

In practice, the main problem with deriving cirrus cloud properties from AVHRR data does not arise from the scattering effect, but instead from the heterogeneity of the observed scenes. Indeed, the determination of the microphysical parameter β^e of semitransparent cirrus clouds, using Eqs. (2) and (3), presents several limitations. First, knowledge of the cirrus-free radiances $I_{s,4}$ and $I_{s,5}$, and of the thick cirrus cloud ones $I_{c,4}^e$ and $I_{c,5}^e$, is required. Usually, this is obtained from the radiances observed in the vicinity of the semitransparent cirrus

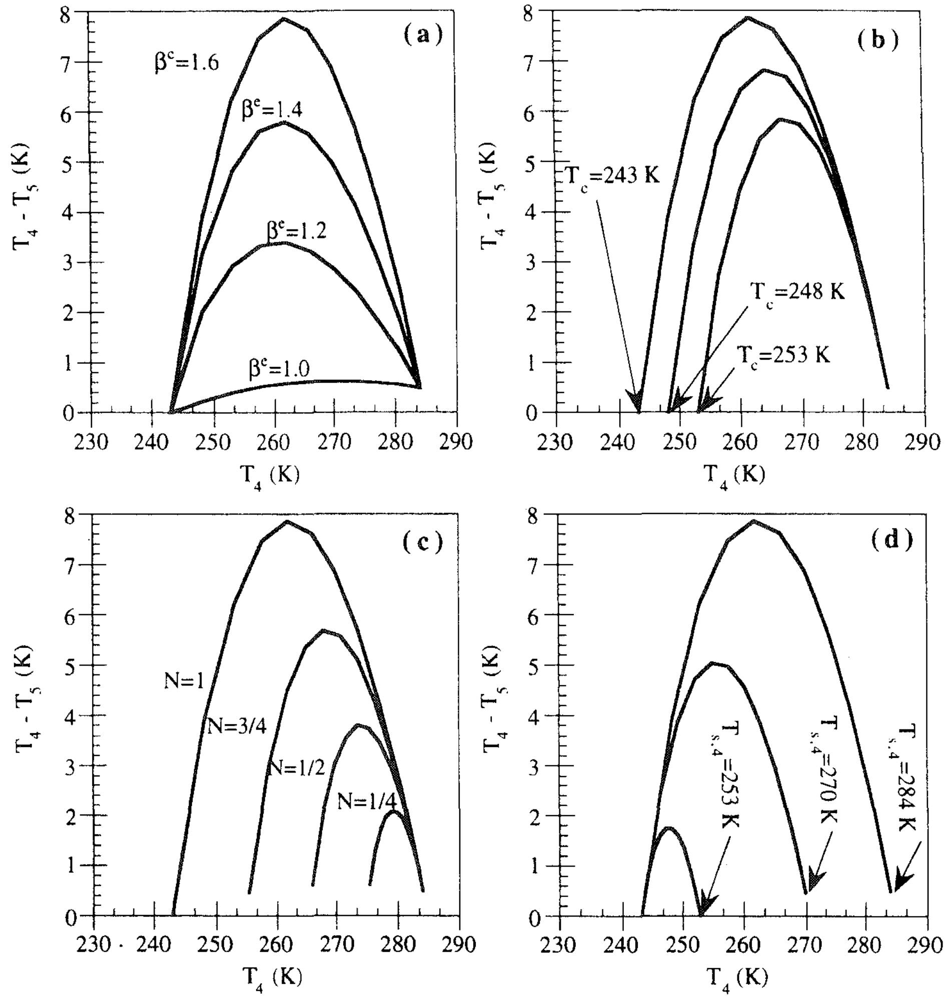

FIG. 1. Brightness temperature difference curves for (a) a range of equivalent absorption coefficient ratio, β^e ($T_{s,4} = T_{s,5} + 1 = 284$ K, $T^e_{c,4} = T^e_{c,5} = 243$ K, $N = 1$); (b) a range of effective cloud top temperature, T^e_c ($T_{s,4} = T_{s,5} + 1 = 284$ K, $\beta^e = 1.6$, $N = 1$); (c) a range of cloud amount, N ($T_{s,4} = T_{s,5} + 1 = 284$ K, $T^e_{c,4} = T^e_{c,5} = 243$ K, $\beta^e = 1.6$): and (d) a range of cirrus cloud free conditions, T^e_s ($T^e_{c,4} = T^e_{c,5} = 243$ K, $\beta^e = 1.6$, $N = 1$).

clouds by assuming that the surface temperature is uniform and that all the cirrus clouds over the scene emit at the same temperature. In other words, it is necessary for the cirrus clouds to be located in a single, well-defined layer over a uniform, well-defined surface. Finally, either the fractional cloud cover N at the pixel-scale ($\sim$1 km^2) is assumed to be equal to unity as in Parol et al. (1991) or the cloud microphysical properties are assumed to be constant over an area of about 2500 km^2 as in Lin and Coakley (1993). In both cases, the assumption is crude since local variations of fractional cloud cover and of cirrus microphysics are very likely.

These ambiguities are illustrated in Figs. 1 and 2. For convenience, we use the brightness temperature, which is the equivalent blackbody temperature defined by the Planck function, $B(T)$,

$$B_i(T_i) = I_i. \tag{4}$$

Figures 1a, 1b, 1c, and 1d show theoretical curves of the BTD versus the brightness temperature in channel 4. They are calculated following Eqs. (2)–(4) for several values of (a) the equivalent absorption coefficient ratio β^e, (b) the cirrus cloud temperature, (c) the pixel-scale cloud cover, and (d) the atmospheric conditions under the cirrus cloud layer. Figure 2a is an example of an actual diagram corresponding to the observations performed over a small region of 100 × 100 AVHRR pixels. Figure 2b is the compilation of all the diagrams shown in Fig. 1 such that the envelope of these diagrams includes nearly all the observations of Fig. 2a. Figures 2a and 2b show clearly that the hypothesis that the total condensed water path is the only quantity to vary from pixel to pixel is invalid in this region. Indeed, for a given T_4 the observed BTDs are greatly dispersed. Diagrams observed in different regions show similar dis-

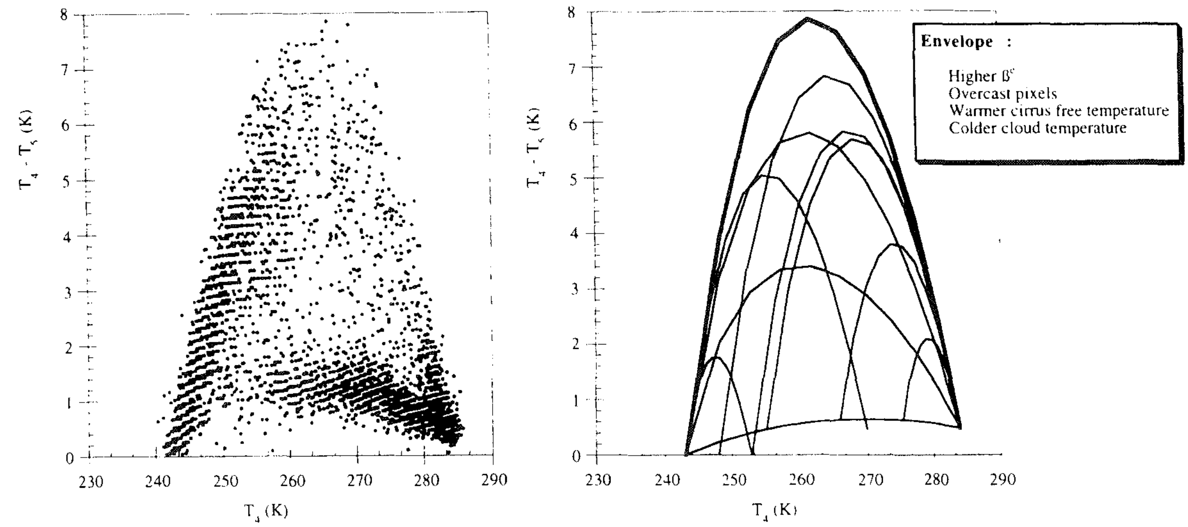

FIG. 2. (a) Example of a scatter diagram of observed brightness temperature difference for 100 × 100 pixel area. (b) BTD curves for all the conditions described in Figs. 1a–d. The envelope of the system of $T_4 - T_5$ versus T_4 curves has been adjusted to the above-presented observations and corresponds to $\beta^e = 1.6$, $T_c = 243$ K, $T_{s,4} = 284$ K, and $N = 1$.

persion. In other words, a given (T_4, T_5) dataset may correspond to a variety of conditions. Therefore, as noted by Lin and Coakley (1993), the retrieval of the microphysical index contains a large amount of uncertainty. However, Figs. 1 and 2b show that the BTD increases with (i) the equivalent absorption coefficient ratio, (ii) the contrast between the cirrus-free and the opaque cirrus brightness temperatures, and (iii) the fractional cloud cover. Accordingly, the envelope of the diagram in Fig. 2a corresponds to pixels totally covered by the coldest cirrus with largest equivalent absorption coefficient ratio.

3. Description of the method of analysis

Our method is directed toward determining the largest equivalent absorption coefficient ratio $(\beta^e)^{max}$, which characterizes the coldest part of the cirrus cloud system. Since we are interested in a large-scale analysis of cirrus clouds, our retrieval method has been automated. In a preliminary processing, the dynamic cluster analysis method (Desbois et al. 1982) is applied to the AVHRR images under study. The pixels covered by cirrus clouds are thus identified. Then, at the scale of typically 100 × 100 pixels, a series of tests is performed to check the conditions needed for the derivation of $(\beta^e)^{max}$, that is, to check if the envelope of the diagram may be described by the theory. When possible, this microphysical parameter and the associated cirrus cloud-top temperature are calculated.

a. Preliminary analysis

The first step of the analysis is the identification of the cirrus pixels containing cirrus clouds. As shown by Inoue (1987), the BTD is a good parameter to screen clouds such as low or midlevel water clouds (which have small BTDs) from cirrus clouds (which have larger BTDs). However, if cirrus clouds can be characterized by a small value of β^e (i.e., close to unity), their associated BTDs are small, as shown in Fig. 1a. As a result, such cirrus clouds cannot be identified by a simple BTD threshold. Moreover, important BTDs are sometimes observed for pixels partially covered by low or midlevel water clouds (i.e., cloud edges or small cumulus). A simple BTD threshold cannot separate these pixels from cirrus cloudy pixels. Therefore, a classification based on BTD thresholds, which could bias our statistical analysis, is not accurate enough for this study. The cloud-type classification method selected for this study is based on the dynamic cluster analysis method (DCAM). For this method, each AVHRR pixel is characterized by an infrared radiance (mean of channel 4 and 5 radiances), a visible radiance (channel 1), and the infrared and visible local standard deviations calculated from the 3 × 3 radiances centered on the pixel. This classification method was first developed by Desbois et al. (1982) for Meteosat data analysis. Using DCAM, AVHRR pixels are labeled as clear or cloudy. More precisely, information about cloud level, thickness, and/or pixel amount is obtained using DCAM. Careful comparisons between DCAM and Inoue's (1987) method have shown that the DCAM (i) better separates partially and completely cloudy pixels, (ii) is as efficient as the BTD method in detecting semitransparent cirrus cloud when high values of BTD occur, and (iii) is more efficient when small values of BTD are observed. In particular, partly cloud-filled pixels, which could present high BTD values are clearly identified by DCAM.

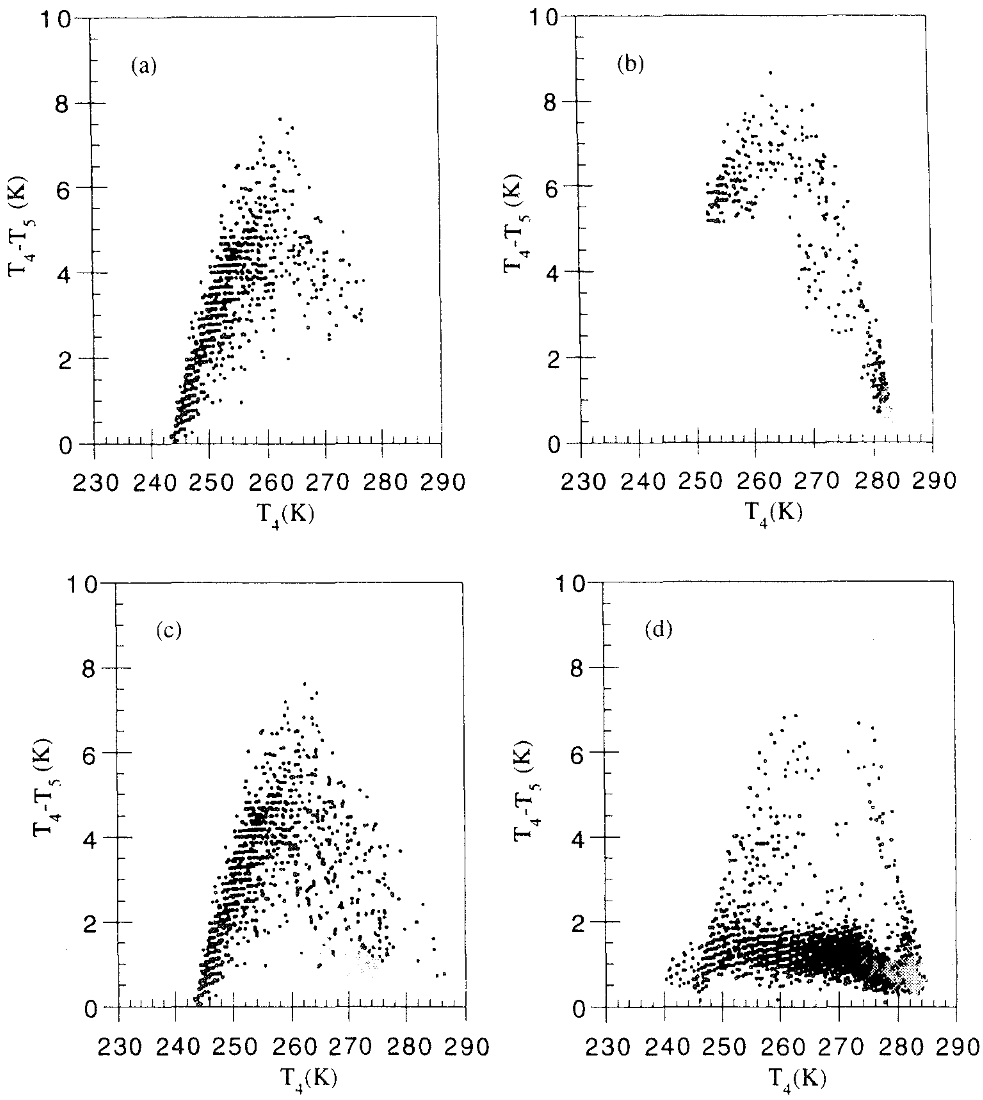

FIG. 3. Examples of scatter diagrams for 100 × 100 AVHRR pixel areas extracted from several images under study. Cirrus cloudy pixels are represented in small black circles, free cirrus pixels (i.e., clear pixels and pixels covered by low- or middle-level clouds) are in gray.

b. Series of sequential tests

A series of tests verify that all the information needed for the determination of $(\beta^e)^{max}$ is present and consistent in an $n \times n$ pixel area of the AVHRR image. Typically, $n = 100$ but 50 and 200 are also considered. Many diagrams showing more or less complex cirrus cloud signatures have been studied carefully to build and validate the test procedure. These tests are described below following the order in which they are applied to each pixel area. Figure 3 shows examples of typical observed experimental diagrams and illustrates the relevance of several tests.

1) TEST FOR THE PRESENCE OF CIRRUS PIXELS

The number of pixels labeled as high-level clouds by the DCAM algorithm must be more than 5% of the total number $n \times n$. Otherwise, the cirrus cloud signature is not documented enough to be correctly derived.

2) TEST FOR THE PRESENCE OF CIRRUS-FREE PIXELS

To determine the microphysical parameter, the brightness temperatures $T_{s,4}$ and $T_{s,5}$ associated with the cirrus-free conditions must be known. Figure 3a shows an incomplete arch where the atmospheric cirrus-free temperature cannot be determined unambiguously. The procedure is therefore aborted for this scene. In our method, the cirrus-free conditions are assumed to be defined only if at least 100 pixels of the area under study are classified as cirrus-free (i.e., labeled neither as high-level clouds nor as cloud edges by the DCAM algorithm). The brightness temperatures $T_{s,4}$ and $T_{s,5}$ are then calculated by averaging the highest 5% of the temperatures of these cirrus-free pixels.

3) TEST FOR THE PRESENCE OF OPAQUE CIRRUS PIXELS

The effective temperatures associated with opaque cirrus clouds, $T_{c,4}$ and $T_{c,5}$, are also essential. Among the pixels labeled as cirrus clouds, the 5% associated with both the lowest temperatures in channel 4 and the lowest BTDs are selected. The effective temperatures $T_{c,4}$ and $T_{c,5}$ are calculated by averaging the brightness temperatures of these pixels. To verify that they correspond to an opaque part of the cirrus clouds, an additional test is performed.

The BTD of thick cirrus clouds may differ from zero because of cirrus cloud reflectivity. This quantity, however, is expected to be weak compared to the BTD of semitransparent cirrus clouds. Therefore, the pixel area is rejected if $T_{c,4} - T_{c,5}$ is larger than one-fifth of the maximum of $T_4 - T_5$ observed in the scene. To consolidate this test, the temperature $T_{c,4}$ is compared to the temperature T_4 observed for the maximum BTD. If the difference between these two temperatures is lower than 5 K, the cirrus cloud signature is assumed to be truncated and the retrieval is canceled. Indeed, the highest values of BTD are observed at temperatures close to $(T_{s,4} + T_{c,4})/2$ (see Fig. 1). Figure 3b illustrates the utility of these tests. The cirrus cloud signature is not entirely defined in this diagram. The value of the cloud-top temperature is undefined.

4) COHERENCE TESTS

The brightness temperatures of the pixels labeled as high-level clouds have to be colder than the cirrus-free brightness temperatures, $T_{s,4}$ and $T_{s,5}$. Otherwise, the latter do not correspond to the upwelling radiances at the base of the cirrus clouds and the pixel area is rejected. In Fig. 3c, the cirrus-free temperature is observed only for pixels labeled as midlevel clouds, following the DCAM algorithm. However, some pixels containing cirrus clouds are warmer than the observed cirrus-free pixels. In fact, in this area, some pixels are covered by thin cirrus clouds with no cloud below and there are no clear pixels. Therefore, "the warm foot" of the envelope is not well defined and this area has to be rejected from the analysis.

c. Solution procedure and final test

Once the above criteria are satisfied, we identify the pixels of the envelope. To do so, we follow the methodology proposed by Lin and Coakley (1993). The cloudy pixels are distributed into 20 equal classes of brightness temperature at 11 μm, uniformly distributed between the cirrus-free and the coldest cirrus temperatures. Then, for each class, the 5% of the pixels representing the highest BTDs are selected. Finally, the retrieval procedure can be carried out.

Two calculations are employed to minimize the differences between the radiances of the previously selected pixels and the theoretical values computed using Eqs. (2) and (3). In the first method, $(\beta^e)^{max}$ is the only unknown. The temperatures of the cirrus-free pixels, $T_{s,4}$ and $T_{s,5}$, and the effective cloud-top temperatures, $T_{c,4}$ and $T_{c,5}$, are set to the values calculated in the sequential test procedure (see 3b). In the second approach, $T_{s,4}$, $T_{c,4}$ and $(\beta^e)^{max}$ are unknown and the cirrus-free and the cloud-top BTDs are those set previously. The comparison of the results of the two procedures allows a further consistency test. This last test requires the differences between the two values of $(\beta^e)^{max}$ to be smaller than 0.1 and the differences between the temperatures retrieved by the two methods to be smaller than 5 K. Figure 3d shows a typical case for which this final test is not satisfied: the coldest pixels that correspond to a cirrus cloud temperature close to 240 K do not correspond to the higher values of β^e, which were observed in the area. In this example, the retrieved parameters [cloud-top temperature and $(\beta^e)^{max}$] differ from one calculation to the other. Therefore, the results are not reliable and this case is rejected.

In the following sections, the retrieved parameters used for the statistical study are those that satisfy the final test. Only the values of $(\beta^e)^{max}$ and $T_{c,4}$ derived from the calculation that does not make use of a priori effective cloud-top temperatures and cirrus-free pixel temperatures are presented.

In summary, the four scatter diagrams presented in Fig. 3 do not fulfill the criteria of our automated algorithm and fail to provide the cirrus cloud characteristics, $(\beta^e)^{max}$ and $T_{c,4}$. The scatter diagram shown in Fig. 2a is an example of a pixel area in which cirrus properties can be retrieved. The retrieved parameters are $T_{c,4}$ = 243 K and $(\beta^e)^{max}$ = 1.6.

4. Results

The proposed retrieval method was applied to 21 AVHRR images acquired during daytime overpasses of the *NOAA-11* satellite over midlatitude regions from 10 to 20 October 1989. The data were obtained during the International Cirrus Experiment (Raschke et al. 1990). The region under study is over Europe and the North Atlantic Ocean (as shown in Fig. 4). Note that the specific analysis presented here is only an illustration of the application of the retrieval method. We do not assert that the cirrus properties found in this particular case can be extended at planetary scale due to the restrictive region and period studied. Nevertheless, the present data are large enough to derive cirrus cloud properties that are statistically significant for the region and the period analyzed.

The DCAM was applied to the 21 images and the results were partitioned into eleven output classes. Clear

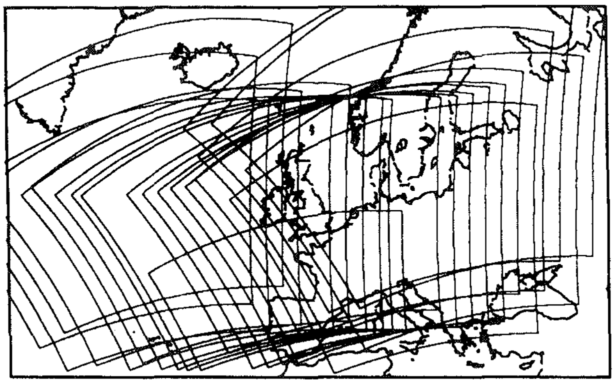

FIG. 4. Outlines of the 21 AVHRR *NOAA-11* images used in this study. They have been acquired between 10 and 20 October 1989 during the International Cirrus Experiment.

pixels have been distributed into two classes: "sea surface or homogeneous land" and "land." Two classes correspond to broken clouds and have been separated depending on whether they are thick or thin. Four classes correspond to high-level clouds and range from very thin to very thick clouds. Low- and midlevel clouds comprise two classes. Finally, one class corresponds to thin high-level clouds above thick lower clouds.

This classification is very detailed. For our study, we need only to separate pixels containing cirrus clouds from clear pixels and pixels containing lower-level and broken clouds. Therefore, a simplified classification restricted to four classes has been used. Figure 5 shows an example of this simplified image classification. A single class corresponds to high-level clouds (very thin to very thick cloud are considered, including multilayer clouds); the other three classes correspond, respectively, to low- or midlevel clouds, broken clouds, and clear sky.

In Fig. 5, snow surfaces (e.g., see the Alps) were classified as broken clouds. This is, of course, a limitation of the classification. Nevertheless, this problem is not important for our study. Indeed, pixels identified as covered by broken clouds are not considered in the treatment.

The BTD analysis has been applied to elementary areas defined such as the centers of two successive areas are separated with 33 pixels on the 21 AVHRR images. It results in 77 691 elementary areas. Three area sizes have been considered: 50 × 50, 100 × 100, and 200 × 200 pixels centered on the central pixel of an elementary area. Pixels containing cirrus clouds have been observed, respectively, for 60%, 74%, and 85% of the areas. In most of these cases, the retrieval was aborted due to an incomplete cirrus cloud signature. The al-

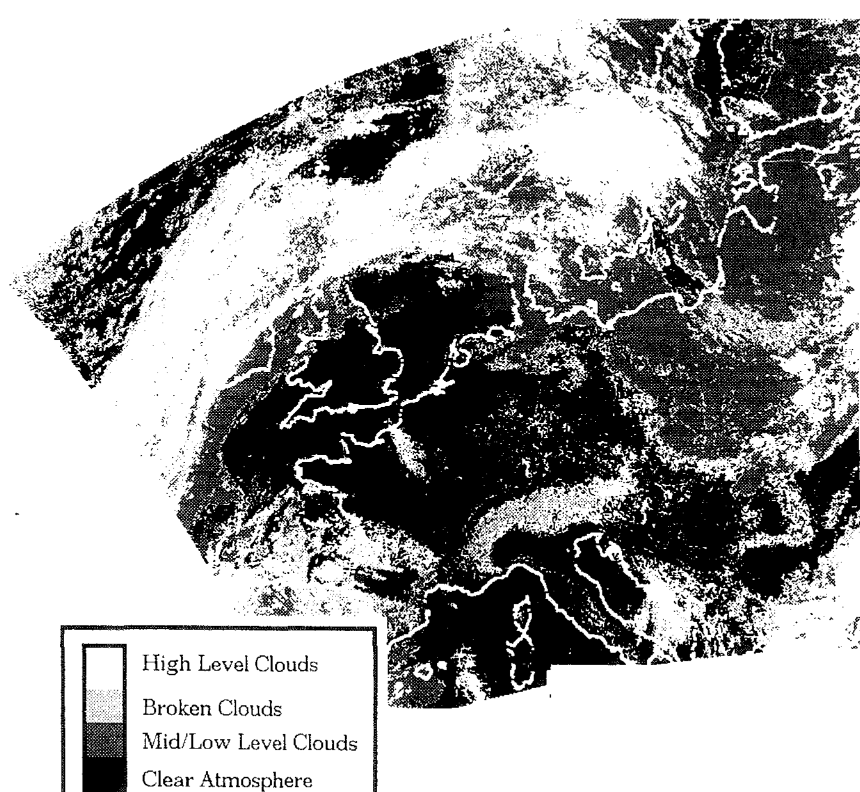

FIG. 5. Example of AVHRR image classified by the dynamic cluster analysis method. This image has been acquired at 1230 UTC 17 October 1989.

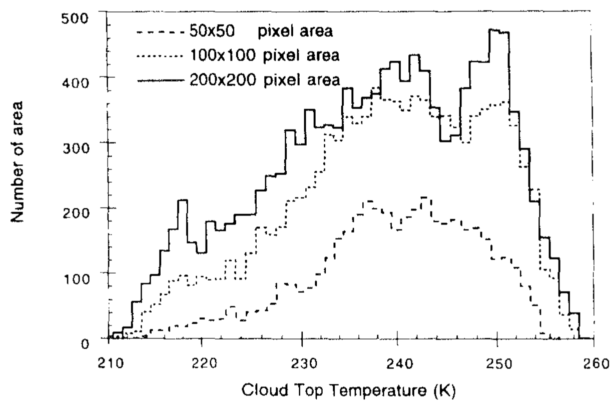

FIG. 6. Histogram of derived cloud-top temperature, for the three considered sizes of areas. The 21 AVHRR images under study are cumulated.

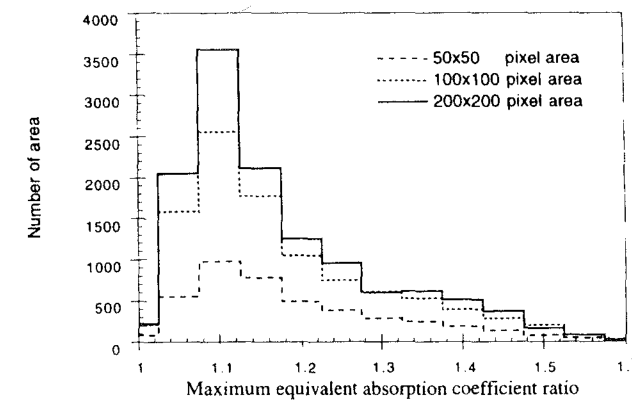

FIG. 7. Same as Fig. 6 but for derived maximum equivalent absorption coefficient ratio, $(\beta^e)^{max}$.

gorithm resulted in the determination of cirrus cloud properties, respectively, for 4348 (5.6% of the scenes), 10 119 (13%), and 12 546 (16%) areas of 50 × 50, 100 × 100, and 200 × 200 pixels, respectively. Opaque cirrus pixels and cirrus-free pixels were not frequently observed in the same area, especially for the smaller areas studied (i.e., 50 × 50 pixels). A complete signature was more often observed for larger areas. However, in order to investigate possible effects of the size of the area used for the calculations, the results obtained for the three area sizes are presented and discussed below.

The histogram of the retrieved cloud-top temperatures $T_{c,4}$ is shown in Fig. 6 for the three area sizes. These temperatures are very spread out and range between 210 and 260 K with a large occurrence of temperatures between 230 and 250 K. The mean values of $(\beta^e)^{max}$ are 1.22, 1.21, and 1.20 for 50 × 50, 100 × 100, and 200 × 200 pixel areas, respectively. The histogram of the derived $(\beta^e)^{max}$ in Fig. 7 shows that very high values, greater than 1.5, are sometimes observed; nevertheless the most frequent values range between 1.05 and 1.2 for the three sizes of observed areas.

With a similar method, Inoue (1985) found $\beta^e = 1.08$. His study was restricted to eight cirrus cases. Parol et al. (1991) found that, for their particular case study, β^e ranged between 1.0 and 1.18. The results of the present study apply to a much larger dataset. It is important to note here that our method leads to values of $(\beta^e)^{max}$ (maximum of β^e), which quite logically are larger than the mean values of β^e obtained by these authors. However, the primary importance of the present method is that variations of $(\beta^e)^{max}$ can be linked almost uniquely to differences in the microphysical properties since it derives from the envelope of BTD curves (see Figs. 1 and 2).

Figure 8 presents the retrieved $(\beta^e)^{max}$ plotted as a function of the retrieved cloud-top temperature, $T_{c,4}$. Each isoline represents the density of the observations. For example, 50% of the retrievals are situated inside the isoline 0.5. Two cloud temperature regions are well separated. In the first region, the cloud temperature is colder than 235 K and only small values of $(\beta^e)^{max}$, lower than 1.3, are retrieved. In the second region, for cloud temperatures varying between 235 and 250 K, higher values of $(\beta^e)^{max}$ (up to 1.4) are observed. This means that, among all the scenes that were analyzed, and irrespective of their size, values of $(\beta^e)^{max}$ up to 1.3 have never been observed for cloud-top temperatures lower than 235 K, whereas for warmer clouds $(\beta^e)^{max}$ values up to 1.4 were sometimes observed. Of course, in-cloud vertical variations of $(\beta^e)^{max}$ are not accessible from satellite measurements and the derived value characterizes the whole cloud. Consequently, in the coldest cirrus clouds, some levels may have $(\beta^e)^{max}$ greater than 1.3. However, as a whole, in our study they are characterized by $(\beta^e)^{max}$ lower than 1.3 whereas larger values occur only for warmer cirrus clouds. Figure 9 illustrates the variation of the average and standard deviation of the retrieved $(\beta^e)^{max}$ with respect to derived effective cloud-top temperature $T_{c,4}$. The averaged value of $(\beta^e)^{max}$ is close to 1.12 with standard deviations between 0.01 and 0.04 for cloud-top temperatures colder than 235 K. For cloud-top temperatures ranging from 240 to 255 K, the mean value of $(\beta^e)^{max}$ is larger (around 1.3) and the standard deviations are about 0.08. Figures 8 and 9 show that the size of the observed areas does not significantly influence the retrieved parameters. Although the coldest cloud-top temperatures are more frequent when considering the largest observed areas, the abrupt change of $(\beta^e)^{max}$ with temperature is similar for the three area sizes studied.

Mie calculations, assuming spherical particles, have been performed to calculate β^e for various particle size distributions; the right-hand ordinates on Figs. 8 and 9 show the results from these calculations. They allow interpretation of the results of our analysis in effective diameter, which is related to the ratio of the volume to cross sectional area of the entire size distribution if the particles are assumed to be spherical. Thus, the D^e values reported on Figs. 8 and 9 correspond to the maximum values of β^e, which can be encountered in the area

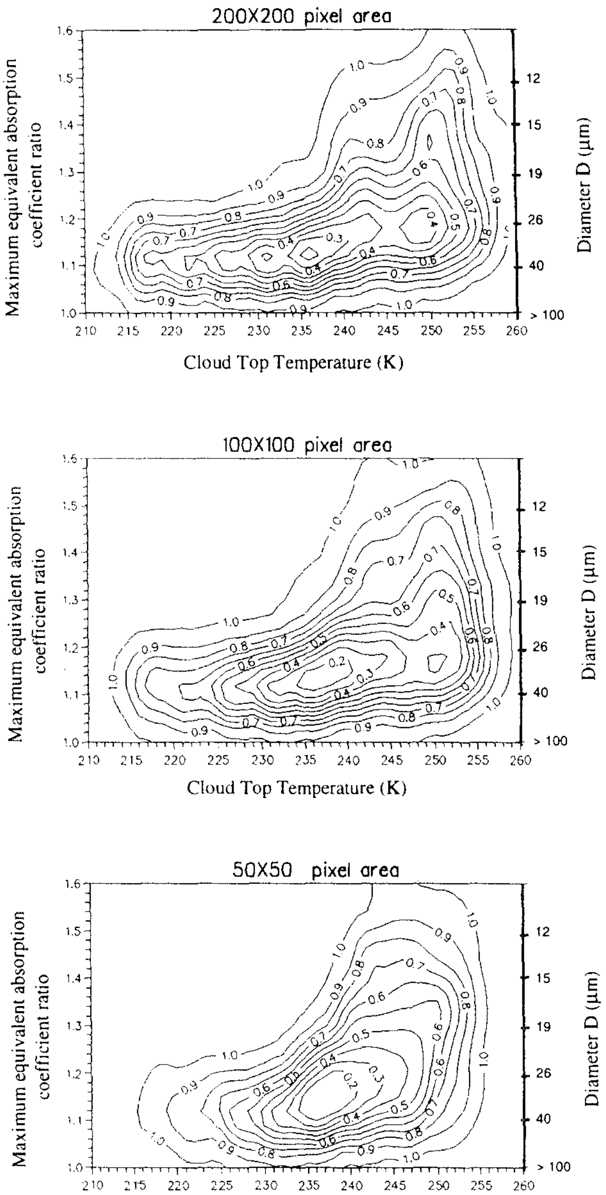

FIG. 8. Two-dimensional diagrams of the frequency of retrieved cirrus cloud parameter: $(\beta^e)^{max}$ versus $T_{c,4}$, for the three sizes of observed area: 200 × 200, 100 × 100, and 50 × 50 pixels. Each isoline represents the density of the observations.

under investigation. Very small equivalent Mie particles ($D^e < 20$ μm) are associated with the warmest cirrus clouds ($T_{c,4} > 235$ K). This equivalent particle size is never found for lower cloud temperatures. This result agrees with that of Lin and Coakley (1993) (see Table 1), who analyzed six well-defined single-level cirrus cloud cases from AVHRR 1-km local area coverage data as well as from 4-km global area coverage data obtained for *NOAA-9* overpasses over Wisconsin and over the Atlantic Ocean off the African coast. Their analyzed subregions were boxed areas of 60–120 km on a side. Their retrieved hydrometeor diameter, which is assumed not to vary over a given area practically corresponds to our diameter D^e. They are in agreement with our statistics; the smaller particles are found for the warmer cirrus cloud temperatures (see Table 1).

5. Discussion

Surprisingly, the observed increase of $(\beta^e)^{max}$ with cloud temperature suggests that the smallest ice particles ($D^e < 20$ μm) are observed at temperatures larger than 235 K. Inside a cirrus cloud, particle size is expected to increase with temperature. Such a behavior is reported, among others, by Heymsfield and Platt (1984) and more recently by Francis et al. (1994) from two ICE'89 flights. However, our present results refer to temperature variations from cloud to cloud, not inside a particular cloud.

An important question is the meaning of the diameter D^e of equivalent Mie particles. By using the anomalous diffraction theory, the absorption cross section of randomly oriented particles can be expressed as (Bryant and Latimer 1969; Mitchell and Arnott 1994)

$$\sigma_{abs} = S\left[1 - \exp\left(-\frac{4\pi n_i V}{\lambda S}\right)\right], \tag{5}$$

where S is the average projected area of the particle, that is one-fourth of the total surface area, V is the volume, n_i is the imagery part of the refractive index, and λ is the wavelength. Therefore, if scattering effects were negligible, β^e would be reduced to the ratio of the absorption coefficients in channels 4 and 5

$$\beta = \frac{1 - \exp\left(-\dfrac{4\pi n_5 V}{\lambda_5 S}\right)}{1 - \exp\left(-\dfrac{4\pi n_4 V}{\lambda_4 S}\right)}, \tag{6}$$

which is a function of the V/S ratio. Parol et al. (1991) have shown that multiple scattering has a significant influence on BTD so that β^e differs from β. However, one can expect that β^e is chiefly related to the V/S ratio and the equivalent diameter D^e is thus rather close to (3/2) V/S. Consequently, the equivalent diameter derived from BTD roughly corresponds to

$$D^e \approx D_{V/S} \le D_V \le D_S, \tag{7}$$

where $D_{V/S}$, D_V, and D_S are the diameter of a sphere having the same V/S ratio, the same volume, and the same projected area, respectively. The equality in (7) is found only for spherical particles. For particles with aspect ratio very different from unity, $D_{V/S}$ is highly weaker than D_V.

In the particular case of hexagonal columns (or plates) it results from geometrical considerations (e.g., Sun and Shine 1994) that

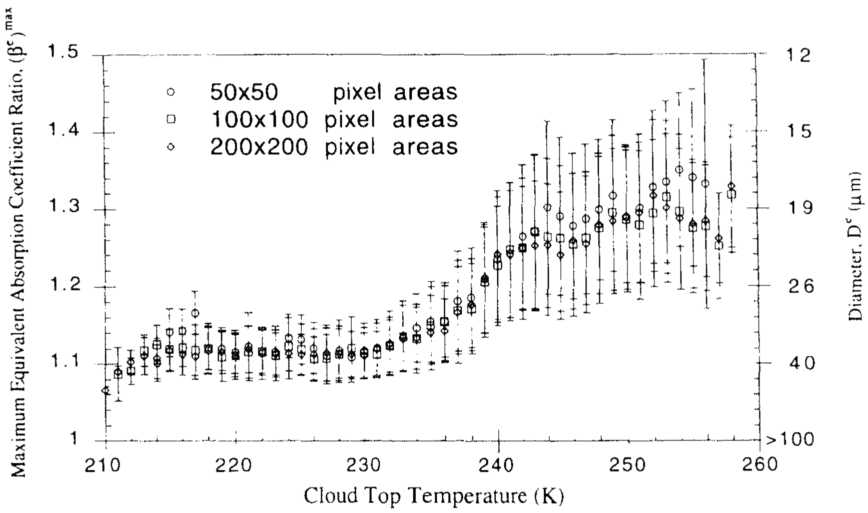

FIG. 9. Retrieved maximum equivalent absorption coefficient ratio $(\beta^e)^{max}$ plotted as a function of the retrieved cloud-top temperature, for the three sizes of observed area: 200 × 200, 100 × 100, and 50 × 50 pixels. Each point is an average of $(\beta^e)^{max}$ for a retrieved cloud-top temperature between $T_{c,4}$ and $T_{c,4}$ + 1 K. Vertical bars correspond to the standard deviations.

$$D_{V/S} = \frac{D_V^3}{D_S^2} = WL\left(\frac{W}{3} + \frac{4L}{3\sqrt{3}}\right)^{-1}, \tag{8}$$

where W and L are, respectively, the width and the length of the crystal. That explains why Brogniez et al. (1995) found as a best fit to their BTD observations a hexagonal ice plate model with dimensions L/W between 12.5 µm/500 µm and 20 µm/200 µm (that is, $D_V \sim$ 100–160 µm but $D_{V/S} \sim$ 35–50 µm), while a spherical model leads to a diameter $D^e \sim$ 50 µm. From (8), it clearly appears that $D_{V/S}$ is bounded both by $3L$ and by $1.3W$. Consequently, $D_{V/S}$—and thus D^e—is chiefly related to the minimum dimension of the crystal while ice crystals are generally described against their maximum dimension. Therefore, the observed low values of D^e might correspond to ice crystals having a weak length and/or a weak width. However, the smallest ice particles ($D^e \sim$ 10–20 µm) are expected to be nearly isometric (Heymsfield et al. 1990). The presence of supercooled particles is likely. That would not affect our result since BTDs are very similar for water and ice spheres (Parol et al. 1991).

The BTD-derived microphysical properties are not easily comparable to airborne microphysical measurements. The most often used instruments are the PMS 1D and 2D, and the PMS forward-scattering spectrometer probe (FSSP) (Knollenberg 1976). The PMS 1D and 2D do not sense crystals smaller than 25–100 µm and the first size class is affected by response time to optical array probes (Platt et al. 1989). FSSP is not reliable for the measurement of ice particles with a complex shape and is poorly efficient for the sizing of small ice particles as well as liquid water drops in the presence of big ice crystals (Gardiner and Hallett 1985). Such classic in situ measurements cannot accurately determine the small-particle end of the complete size spectrum. Against this, Noone et al. (1993) employed for the first time the counterflow virtual impactor (CVI, Ogren et al. 1985) in cirrus clouds during ICE'89. They analyzed five cirrus flights. One of the flights was done in prefrontal cirrus uncinus and floccus, the other flights were inside cirrostratus clouds. The CVI measures the condensed water content and the cloud element concentration. Noone et al. (1993) deduced from their measurements a frequency distribution of the time-averaged diameter of mean mass or equivalently of mean volume, that corresponds to our D_V defined above. In cirrostratus clouds, they found quite similar observations for the four flights; the temperatures were in the range of 221–245 K and the average diameter of mean mass of the cloud elements (D_V) ranged from 37 to 54 µm. In cirrus uncinus and floccus flight, the temperatures were warmer (245–258 K) and smaller D_V were obtained. They found a substantial number of parts of clouds where D_V was between 20 and 30 µm. These observations are compatible with our observed decrease of the minimum value of D^e with increase of cloud temperature.

Moreover, the abrupt change in microphysical properties observed around 235–240 K has already been

TABLE 1. Cloud-top temperature and effective diameter retrieved by Lin and Coakley (1993) for their six selected regions.

Region	$T_{c,4}$ (K)	D^e (µm)
B. Fig. 16	215.4	29
B. Fig. 13	236.0	23
B. Fig. 6	236.5	27
A. Fig. 6	238.5	10
A. Fig. 13	245.7	6
A. Fig. 16	254.8	8

asserted by several authors. Using a 0.693-μm lidar Platt and Diley (1981) observed 22 cirrus cloud systems. They found an abrupt change in backscatter to extinction ratio between 228 and 233 K, which was attributed to a change in crystal habit, cloud particle phase, and/or ice particle size spectra. In the same way, in cloud chamber experiments DeMott and Rogers (1990) demonstrated a sharp increase in ice nucleation rates between 234 and 239 K due to homogeneous freezing of haze droplets.

6. Conclusions

In this paper, we have presented an algorithm that allows the automatic analysis of cirrus microphysical properties from AVHRR observations. The method is based on the well-known BTD analysis technique. The first step of the method is a cloud classification based on a dynamic cluster analysis independent of the BTD. The BTD analysis itself is restricted to the envelope of the usual bidimensional diagram. It has been established that the corresponding pixels were totally covered by cirrus clouds that present both the coldest cloud-top temperature and the largest equivalent absorption coefficient ratio of the selected areas. The final retrieval is performed only if the signature of the diagram is complete, that is, if the emittance of the cirrus clouds varies from 0 to approximately 1. The parameter derived from this analysis is the maximum equivalent absorption coefficient ratio $(\beta^e)^{max}$, which can be related to the effective diameter of the size distribution of equivalent Mie particles. For nonspherical particles $(\beta^e)^{max}$ is chiefly related to the minimum dimension of the crystal.

As an example, 21 *NOAA-11*/AVHRR images of ICE'89 Intensive Field Experiment have been analyzed. For this case, our analysis showed that the microphysical properties of the observed cirrus depend on the cloud-top temperature. Indeed, an abrupt change in the average values of $(\beta^e)^{max}$ was found for cloud temperature on the order of 235 K. This result may be attributed to a modification of the size and/or shape of the particles and points out that microphysical process may differ from one temperature regime to another. An abrupt change of cirrus microphysical properties around 235–240 K has already been asserted by several authors from lidar analyses (Platt and Diley 1981) and cloud chamber experiments (DeMott and Rogers 1990). These findings suggest that relatively high ice crystal production rates often occur between 235 and 240 K through homogeneous nucleation of haze and cloud droplets.

Our method of analysis should allow a more global analysis to confirm or deny this result for cirrus clouds observed at different periods and locations.

Acknowledgments. This work was part of the International Cirrus Experiment (ICE), which was followed by the European Cloud and Radiation Experiment (EUCREX). Both were supported by the European Economic Community. The authors gratefully acknowledge the assistance of J. L. Raffaelli in the development of the cluster analysis applied to the cloud classification of AVHRR data. They are also very grateful to R. Parada for his helpful comments on the manuscript.

REFERENCES

Baum, A. B., R. F. Arduini, B. A. Wielicki, P. Minnis, and S. C. Tsay, 1994: Multilevel cloud retrieval using multispectral HIRS and AVHRR data: Nighttime oceanic analysis. *J. Geophys. Res.*, **99**, 5499–5514.

Brogniez, G., J. C. Buriez, V. Giraud, F. Parol, and C. Vanbauce, 1995: Determination of effective emittance and radiatively equivalent microphysical model of cirrus from ground-based and satellite observations during the International Cirrus Experiment: The 18 October 1989 case study. *Mon. Wea. Rev.*, **123**, 1025–1036.

Bryant, E. D., and P. Latimer, 1969: Optical efficiencies of large particles of arbitrary shape and orientation. *J. Colloid Interface Sci.*, **30**, 291–304.

Cox, S. K., 1971: Cirrus clouds and the climate. *J. Atmos. Sci.*, **28**, 1513–1515.

DeMott, P. J., and D. C. Rogers, 1990: Freezing nucleation rates of dilute solution droplets measured between −30°C and −40°C in laboratory simulations of natural clouds. *J. Atmos. Sci.*, **47**, 1056–1064.

Desbois, M., G. Seze, and G. Szejwach 1982: Automatic classification of clouds on METEOSAT imagery: Application to high-level clouds. *J. Appl. Meteor.*, **21**, 401–412.

Francis, P. N., A. Jones, R. W. Saunders, K. P. Shine, A. Slingo, and Z. Sun, 1994: An observational and theoretical study of the radiative properties of cirrus: Some results from ICE'89. *Quart. J. Roy. Meteor. Soc.*, **120**, 809–848.

Gardiner, B. A., and J. Hallett, 1985: Degradation of in-cloud forward scattering spectrometer probe measurements in the presence of ice particles. *J. Atmos. Oceanic Technol.*, **2**, 171–180.

Heymsfield, A. J., and C. M. R. Platt, 1984: A parameterization of the particle size spectrum of ice clouds in terms of the ambient temperature and the ice water content. *J. Atmos. Sci.*, **41**, 846–855.

——, K. M. Miller, and J. D. Spinhirne, 1990: The 27–28 October 1986 FIRE IFO cirrus case study: Cloud microstructure. *Mon. Wea. Rev.*, **118**, 2313–2328.

Inoue, T., 1985: On the temperature and effective emissivity determination of semi-transparent cirrus clouds by bi-spectral measurements in the 10 μm window region. *J. Meteor. Soc. Japan*, **63**, 88–98.

——, 1987: A cloud type classification with NOAA7 split-window measurements. *J. Geophys. Res.*, **92**, 3991–4000.

Knollenberg, R. G., 1976: Three new instruments for cloud physics measurements: The 2-D spectrometer, the forward scattering spectrometer probe, and the active scattering aerosol spectrometer. Preprints, *Int. Conf. on Cloud Physics*, Boulder, CO, Amer. Meteor. Soc., 554–561.

Lin, X., and J. Coakley Jr., 1993: Retrieval of properties for semitransparent clouds from multispectral infrared imagery data. *J. Geophys. Res.*, **98**, 18 501–18 514.

Mitchell, D. L., and W. P. Arnott, 1994: A model predicting the evolution of ice particle size spectra and radiative properties of cirrus clouds. Part II: Dependence of absorption and extinction on ice crystal morphology. *J. Atmos. Sci.*, **51**, 817–832.

Mitchell, J. N. F., C. A. Senior, and W. J. Ingram, 1989: CO_2 and climate: A missing feedback? *Nature*, **341**, 132–134.

Noone, K. B., K. J. Noone, J. Heintzenberg, J. Ström, and J. A. Ogren, 1993: In situ observations of cirrus cloud microphysical properties using the counterflow virtual impactor. *J. Atmos. Oceanic Technol.*, **10**, 294–303.

Ogren, J. A., J. Heintzenberg, and R. J. Charlson, 1985: In-situ sampling of clouds with a droplet to aerosol converter. *Geophys. Res. Lett.*, **12,** 121–124.

Parol, F., J. C. Buriez, G. Brogniez, and Y. Fouquart, 1991: Information content of AVHRR channel 4 and 5 with respect to the effective radius of cirrus cloud particles. *J. Appl. Meteor.*, **30,** 973–984.

Platt, C. M. R., and A. C. Dilley, 1981: Remote sensing of high clouds: Part IV: Observed temperature variations in cirrus optical properties. *J. Atmos. Sci.*, **38,** 1069–1082.

——, J. C. Scott, and A. C. Dilley, 1987: Remote sensing of high clouds: Part VI: Optical properties of mid-latitude and tropical cirrus. *J. Atmos. Sci.*, **44,** 729–747.

——, J. D. Spinhirne, and W. D. Hart, 1989: Optical and microphysical properties of a cold cirrus cloud: Evidence for regions of small particles. *J. Geophys. Res.*, **94,** 11 151–11 164.

Prabhakara, C., R. S. Fraser, G. Dalu, M. C. Wu, and R. J. Curran, 1988: Thin cirrus clouds: Seasonal distribution over oceans deduced from Nimbus-4 IRIS. *J. Appl. Meteor.*, **27,** 379–398.

Prata, A. J., and I. J. Barton, 1993: A multichannel, multiangle method for the determination of infrared optical depth of semitransparent high cloud from an orbiting satellite. Part I: Formulation and simulation. *J. Appl. Meteor.*, **32,** 1623–1637.

Ramanathan, V., 1987: The role of the earth radiation budget studies in climate and general circulation research. *J. Geophys. Res.*, **92,** 4075–4095.

——, R. D. Cess, E. F. Harrison, P. Minnis, B. R. Barkstrom, E. Ahmad, and D. Hartmann, 1989: Cloud-radiative forcing and climate: Results from the Earth Radiation Budget Experiment. *Science,* **243,** 57–63.

Raschke, E., J. Schmetz, J. Heintzenberg, R. Kandel, and R. Saunders, 1990: The International Cirrus Experiment (ICE)—A joint European effort. *ESA Journal,* **14,** 193–199.

Stephens, G. L., S. Tsay, P. W. Stackhouse Jr., and P. J. Flatau, 1990: The relevance of the microphysical and radiative properties of cirrus clouds to climate and climatique feedback. *J. Atmos. Sci.*, **47,** 1742–1753.

Sun, Z., and K. P. Shine, 1994: Studies of the radiative properties of ice and mixed-phase clouds. *Quart. J. Roy. Meteor. Soc.*, **120,** 117–137.

Szejwach, G., 1982: Determination of semitransparent cirrus cloud temperature from infrared radiances: Application to METEOSAT. *J. Appl. Meteor.*, **21,** 384–393.

Wu, M. C., 1987: A method for remote sensing the emissivity, fractional cloud cover, and cloud top temperature of high-level, thin clouds. *J. Climate Appl. Meteor.*, **26,** 225–233.

Chapitre 2

Validité du Modèle de Nuage Plan-Parallèle Usuel

Introduction

De nombreuses études (*Welch et Wielicki*, 1984, *Kobayashi*, 1988, *Cahalan et al*, 1994, *Loeb et al*, 1998, etc....) ont mis en évidence l'influence potentielle de la forme des nuages et de la distribution spatiale de l'eau nuageuse sur les propriétés radiatives des systèmes nuageux. Cependant les modèles climatiques reposent sur l'hypothèse de nuages horizontalement homogènes et infinis (plans parallèles). De même, l'analyse des observations satellitales (cf. les programmes ISCCP ou POLDER dans le chapitre 3 de cette thèse) repose, sauf cas d'études, sur la même hypothèse. On sait aujourd'hui que l'hypothèse plan-parallèle peut être une faiblesse majeure dans l'estimation de l'effet des nuages sur le bilan radiatif terrestre. L'hétérogénéité des nuages constitue donc une source importante d'erreurs dans la simulation de l'évolution du climat comme dans l'interprétation quantitative des observations satellitales. L'évolution récente des modèles climatiques vers une formulation pronostique de l'eau condensée a donné à ce thème une importance croissante.

Notre intérêt pour ce thème de recherche a débuté par l'influence des hétérogénéités des nuages sur les flux radiatifs au sommet et à la base de l'atmosphère. Plus particulièrement, nous avons quantifié, à partir d'un cas concret, la différence entre les flux aux courtes et grandes longueurs d'onde calculés en faisant l'hypothèse de nuages "plans parallèles" et les flux radiatifs modélisés en tenant compte de l'hétérogénéité d'un champ de nuages convectifs observé durant l'expérience ICE sur une image Landsat (**Parol et al., 1994**). Notre démarche visait à quantifier les influences respectives de la répartition horizontale de l'eau liquide et de la forme des nuages sur la détermination du bilan radiatif terrestre. Pour cela nous avons été amenés à envisager différents modèles de nuages de complexité croissante, allant du nuage plan-parallèle homogène (tel que dans les modèles climatiques) jusqu'à une distribution de nuages de forme hémi-ellipsoïdale, en passant par le modèle de nuage plan-parallèle inhomogène, dont l'esprit est très proche de ce l'on connaît aujourd'hui sous le nom de "l'Approximation des Pixels Indépendants" (IPA en anglais; voir par exemple *Cahalan et al*, 1994). Cette étude a montré que la forme même des nuages semblait avoir un impact moins crucial sur le bilan radiatif que l'effet de distribution horizontale des nuages, tout au moins pour le type de nuages observés.

Dès lors, notre champ d'investigation s'est élargi à l'ensemble du champ de rayonnement ; et nous nous sommes intéressés à l'influence des hétérogénéités des nuages sur les luminances aux courtes longueurs d'onde et non plus seulement sur les flux. Nous avons bénéficié du tout nouveau développement au laboratoire de l'instrument aéroporté POLDER qui offre des possibilités d'observation importantes, quoique limitées au domaine du rayonnement solaire réfléchi: distribution angulaire, dépendance spectrale, mesure de polarisation. POLDER offrant la possibilité d'observer une scène sous différents angles de vue il est donc apparu évident qu'il fallait valider (ou plutôt invalider) l'hypothèse du modèle de nuage plan-parallèle directement par l'observation du diagramme de rayonnement solaire réfléchi par des nuages naturels et non plus simplement par des simulations numériques dans lesquelles sont introduits des modèles de nuages tout aussi irréalistes (c'est à dire loin de la réalité) que le modèle plan-parallèle. Les objectifs affichés de notre implication au projet POLDER ont ainsi concerné (i) l'étude de la distribution angulaire du rayonnement réfléchi et l'amélioration des fonctions directionnelles nécessaires à la restitution du bilan radiatif à partir d'observations spatiales et (ii) l'étude des propriétés optiques des nuages par inversion de la distribution angulaire et spectrale du rayonnement solaire réfléchi.

La version aéroporté de POLDER est apparue comme un outil précieux pour les études de cas. C'est dans cette perspective que s'est située notre participation à l'expérience SOFIA/ASTEX aux Açores en Juin 1992 (**Weill et al, 1995 ; Annexe A**). L'exploitation des données acquises durant cette campagne a fait l'objet d'une partie du travail de thèse de Jacques Descloitres, que j'ai co-encadrée avec Jean-Claude Buriez. Pour la première fois, des mesures de réflectances bidirectionnelles à 865nm effectuées au dessus de bancs de stratocumulus relativement homogènes ont permis de valider l'approximation "plan-parallèle" généralement usitée pour traiter l'effet des nuages sur le rayonnement dans les modèles de prévision du temps météorologique ou du climat, ou pour dériver les propriétés des nuages à partir de mesures satellitales comme dans ISCCP (**Descloitres et al., 1994**).

Ce travail s'est poursuivi avec l'exploitation des données acquises par les versions aéroportées de POLDER durant EUCREX'94 et il s'est élargi au cas des cirrus épais et homogènes. Deux études ont été entreprises dans le contexte de la campagne EUCREX'94:

- la première était de valider (ou d'invalider) l'hypothèse plan-parallèle pour les deux types de nuages à partir des mesures multidirectionnelles de POLDER,
- la deuxième était d'utiliser cette hypothèse sur les nuages pour lesquels elle était justifiée afin de dériver leur épaisseur optique. Dans ce cas, les épaisseurs optiques ont été comparées, lorsque c'était possible, à des mesures de contenu en eau et de dimension de particules nuageuses

effectuées par le Fast FSSP de Jean-Louis Brenguier (CNRM/Météo-France, Toulouse), cet instrument étant installé à bord du Merlin de Météo-France durant EUCREX'94.

Des résultats prometteurs ont été obtenus pour la première partie de l'étude. Nous avons montré que POLDER permet de construire des signatures bidirectionnelles qui sont caractéristiques des types de nuages. Lorsque l'on compare la signature bidirectionnelle observée à celle d'un plan-parallèle théorique, il apparaît que la différence entre l'observation et le modèle est un bon indicateur pour savoir si oui ou non le nuage peut-être considéré comme un plan-parallèle. Dans le cas des Stratocumulus il est apparu raisonnable de conclure que les nuages observés agissaient en moyenne comme un nuage plan-parallèle composé de gouttes de 10µm de rayon (dimension utilisée dans les projets ISCCP et POLDER spatial, voir chapitre 3). En ce qui concerne les Cirrus, la signature angulaire observée s'est révélée être en désaccord total avec celle du nuage plan-parallèle formé de gouttes de10µm. Cela n'est pas surprenant et souligne le fait que des cristaux de glace n'agissent pas vis à vis du rayonnement comme des gouttelettes d'eau. Cela est cependant important et une étude plus approfondie a été menée durant laquelle des cristaux de glace ont été introduits dans le modèle. Nous avons alors obtenu un bien meilleur accord entre les signatures angulaires de cirrus observées et les signatures modélisées (**Descloitres et al, 1998**). Cette étude à mis l'accent également sur le fait qu'il s'avère nécessaire d'effectuer depuis l'espace une discrimination [nuage d'eau liquide/nuage de glace] avant d'appliquer un modèle pour retrouver l'épaisseur optique des nuages à partir de mesures de luminances solaires réfléchies. C'est aussi l'un des objectifs du projet POLDER que de déterminer la phase des nuages (voir chapitre 3).

Le deuxième point de notre étude a été abordé dans un premier temps dans le cas d'un vol au dessus des Stratocumulus durant EUCREX'94. Les épaisseurs optiques dérivées des mesures POLDER ont été comparées aux mesures microphysiques effectuées in-situ par le Fast-FFSP de la Météo. Malgré l'hétérogénéité du nuage observé et la forte variation de l'épaisseur optique, les mesures des deux instruments nous ont permis de restituer une valeur moyenne d'épaisseur optique comparable (environ 10) et les mêmes valeurs extrêmes (valeurs de 2 à 21). De plus, la tendance générale de l'évolution horizontale de l'épaisseur optique a été retrouvée par les deux instruments ; Nous avons pu montrer qu'elle était en très bon accord avec l'évolution du sommet de nuage observé par le lidar LEANDRE. (*Descloitres et al*, 1996; **Pawlowska et al, 2000 ; Annexe B**).

Ce second point a de nouveau été abordé avec la version aéroportée de POLDER lors de la campagne ACE2 qui a eu lieu durant l'été 1997 aux îles Canaries. Les premières exploitations des mesures POLDER acquises durant ACE2 ont été le travail de stage de DEA de François Thieuleux, que j'ai encadré en 1998.
Une attention particulière a été accordée aux données acquises par POLDER les 26 juin et 9 juillet 1997. Les stratocumulus échantillonnés lors de ces deux vols se sont développés dans des masses d'air d'origine très différentes. Le 26 juin correspondait à un air marin pur alors que le 9 juillet était un jour pollué. Les épaisseurs optiques de nuages dérivées de POLDER aéroporté variaient typiquement de 1 à 5 pour le 26 juin et étaient 2 à 3 fois plus importantes le 9 juillet. Ces valeurs étaient en bon accord avec les valeurs dérivées des mesures microphysiques effectuées par Météo-France à bord du Merlin IV. (*Brenguier et al*, 2000).
Par ailleurs, notre étude a permis de montrer que la capacité multidirectionnelle de POLDER peut être également très utile pour sélectionner le modèle microphysique (en terme de rayon effectif des gouttes) utilisé pour dériver l'épaisseur optique et/ou l'albédo des nuages d'eau liquide à partir de mesures de luminances dans le domaine visible. Nous avons pu montrer que le rayon effectif moyen des gouttes était d'environ 12 µm le 26 juin (en air marin pur) alors qu'il était de l'ordre de 6 à 10 µm le 9 juillet (en air pollué) (**Parol et al, 2000**). Ce résultat est apparu comme une confirmation de l'effet indirect des aérosols. Il était totalement cohérent avec l'augmentation significative de la concentration en gouttelettes mesurée in situ dans le cas pollué en comparaison au cas pur (**Brenguier et al, 2000, Annexe C**)

Le 26 juin 97, les épaisseurs optiques et albédos des nuages d'eau liquide dérivés de la version spatiale de POLDER ont également été comparées à celles qui ont été obtenues avec la version aéroportée. Cependant ces valeurs, en général faibles, ont des variabilités spatiales et angulaires élevées ce qui signifie une forte hétérogénéité spatiale de la macrophysique et/ou de la microphysique des nuages. Nous avons montré que les variations angulaires observées ne sont pas directement liées aux variations spatiales telles qu'elles sont mesurées par POLDER à une échelle d'environ 60x60 km^2. En effet, le comportement de ces deux paramètres en fonction du taux de couverture nuageuse est totalement différent. Ceci indique que l'écart entre la variabilité angulaire des réflectances observées et celle des réflectances calculées avec le modèle standard de nuage plan-parallèle 10 µm ne doit pas être considéré comme un indicateur fiable de la distribution tridimensionnelle de l'épaisseur optique des nuages (**Parol et al, 2000**).

Ann. Geophysicae 12, 240–253 (1994) © EGS – Springer-Verlag 1994

Annales Geophysicae

The impact of cloud inhomogeneities on the Earth radiation budget: the 14 October 1989 I.C.E. convective cloud case study

F. Parol, J. C. Buriez, D. Crétel, Y. Fouquart

Laboratoire d'Optique Atmosphérique, Université des Sciences et Technologies de Lille, F-59655 Villeneuve d'Ascq Cedex, France

Received 27 July 1993/Revised: 29 November 1993/Accepted: 30 November 1993

Abstract. Through their multiple interactions with radiation, clouds have an important impact on the climate. Nonetheless, the simulation of clouds in climate models is still coarse. The present evolution of modeling tends to a more realistic representation of the liquid water content; thus the problem of its subgrid scale distribution is crucial. For a convective cloud field observed during ICE 89, Landsat TM data (resolution: 30m) have been analyzed in order to quantify the respective influences of both the horizontal distribution of liquid water content and cloud shape on the Earth radiation budget. The cloud field was found to be rather well-represented by a stochastic distribution of hemi-ellipsoidal clouds whose horizontal aspect ratio is close to 2 and whose vertical aspect ratio decreases as the cloud cell area increases. For that particular cloud field, neglecting the influence of the could shape leads to an over-estimate of the outgoing longwave flux; in the shortwave, it leads to an over-estimate of the reflected flux for high solar elevations but strongly depends on cloud cell orientations for low elevations. On the other hand, neglecting the influence of cloud size distribution leads to systematic over-estimate of their impact on the shortwave radiation whereas the effect is close to zero in the thermal range. The overall effect of the heterogeneities is estimated to be of the order of 10 W m^{-2} for the conditions of that Landsat picture (solar zenith angle 65°, cloud cover 70%); it might reach 40 W m^{-2} for an overhead sun and overcast cloud conditions.

1 Introduction

Considering the large impact of clouds on both albedos and outgoing infrared fluxes, it is not surprising that climate models exhibit a large sensitivity to cloud and radiation interactions (Schlessinger and Mitchell, 1986; Cess *et al.*, 1990; IPCC, 1990). In spite of this sensitivity, the treatment of cloud and radiation interactions in climate models is still very crude. Only recently have attempts been made to include the condensed water content among the model variables (Sundqvist, 1984; le Treut, 1985; Roeckner and Schlese, 1985). Preliminary results of this approach are encouraging (le Treut and Li, 1991) and the trend in the climate community is such that one can reasonably expect that, in the near future, most models will explicitly calculate the total content of condensed water in every grid mesh.

However, in the real world, the influence of clouds on radiation not only depends on total liquid water or ice content; it also depends on cloud microphysical properties such as the particle shape, size distribution, and on cloud morphology and spatial distribution. As shown recently by Stephens and Greenwald (1991), cloud morphology is likely to have a larger impact on the Earth radiation budget than cloud microphysics. Thus, it is very important to quantify and parameterize the influence of cloud inhomogeneities on the radiation field.

In the last few years, various studies have dealt with radiative properties of heterogeneous cloud covers. Most of them investigated the effects of cloud geometrical shape using either Monte Carlo methods (e.g., McKee and Cox, 1974; Wendling, 1977; Kite, 1987) or analytical methods (e.g., Harshvardhan and Weinman, 1982; Duvel and Kandel, 1984). For practical reasons, those theoretical studies were essentially limited to simplified cloud geometrical shapes (cubes, spheres, cylinders, etc.). In the case of cloud field assemblies, Monte Carlo simulations were restricted to regular arrays of simply shaped clouds. However, the effect of brokenness was found to be potentially important and, if not accounted for, could lead to significant biases in calculated radiation budgets and satellite-derived cloud radiative properties, both in the shortwave (Welch and Wielicki, 1984; Coakley and Kobayashi, 1989) and in the longwave (Ellingson, 1982; Harshvardhan and Weinman, 1982; Duvel and Kandel, 1984).

Correspondence to: F. Parol

More experimental approaches are being developed, based on satellite observations, to quantify the main characteristics of the morphology of real cloud fields (Welch *et al.*, 1988; Kuo *et al.*, 1988). The idea of the present analysis is to use a similar approach to estimate the impact of observed spatial inhomogeneities on the radiation budget. As a preliminary step, this is done for a particular convective cloud field. Obviously, the results of a single analysis cannot be generalized to draw any conclusion at the global scale, but our feeling is that this paper may be a first stage to a more systematic analysis. The study is performed in two steps. First, a high spatial resolution satellite image is used to characterize the cloud cover in terms of cloud shape and cloud size distribution and a model of finite shaped clouds is built which satisfies the observations. Next, this model is then used to calculate the radiation fluxes at the top of the atmosphere and estimate the impact of the observed cloud inhomogeneities by comparing with the radiation fluxes produced by an usual plane-parallel cloud model. *The influence of the cloud shape and of the horizontal variations of cloud thickness are estimated separately in order to assess their relative importance.*

The satellite data used for the study are presented in Section 2. We used a Landsat-TM image whose size is close to that of a mesh of General Circulation Models (about $185 \times 185\,\mathrm{km}^2$) but with a spatial resolution (30 m in the visible or near-infrared bands, and 120 m in the thermal band) which allows us to study the small-scale cloud structures which might affect the large-scale radiation field. The structural analysis of the satellite-observed cloud cover is presented in Section 3. In Section 4, the cloud optical properties are adjusted to the observations. The impact of the cloud inhomogeneities on the radiation fluxes at the top of the atmosphere is estimated in Section 5.

2 Data

In the context of the intensive field campaign of the International Cirrus Experiment (ICE IFO: 18 September – 20 October 1989) described by Raschke *et al.* (1990), a series of satellite images have been analyzed. In this paper, we concentrate on a Landsat image acquired on October 14, 1989. The experimental ICE domain roughly covered the south east part of the North Sea. The time of the Landsat overpass is about 1000 UTC and the scene is centered on (54.4°N, 6.3°E), so that the solar zenith angle is about 65°. The nominal wavelength ranges and maximum bidirectional reflectances of the Landsat-TM visible and near-infrared bands at the time of the overpass are shown in Table 1.

The large-scale cloud pattern is visible on the NOAA 11 Advanced Very High Resolution Radiometer (AVHRR) image shown in Fig. 1 (channel 2:0.7–1.1 μm). The NOAA 11 overpass (1300 UTC) is not coincident with the Landsat overpass, but the AVHRR image is only used here to give a general overview of the synoptic situation. Many convection streets lie roughly along the wind direction. Cloud cell dimensions vary from a few kilometers to tens of kilometers but this variation is relatively slow and, on a scale equivalent to a few streets, the cell distribution can be considered as nearly uniform. A description of the mechanisms that cause such cloud streets and cells is reported in Scorer (1989). The solid rectangle indicates the approximate region of the Landsat scene. The region is covered by a field of convective cells with typical size of about 20 km.

At the Landsat TM scale (30 m in the visible, 120 m in the thermal infrared), the intercellular "clear" regions are actually filled with a large number of small cumulus clouds whose dimensions are much smaller than the AVHRR resolution. Moreover, in solar band 4 (Fig. 2a), the high solar zenith angle highlights a considerable spatial structure not resolved by AVHRR. These structures also appear in the Landsat band 6 (Fig. 2b), which is a thermal band that reveals important cloud-top temperature variations.

Table 1. Nominal wavelength ranges and maximum reflectances for Landsat-5 TM bands with a solar zenith angle of 65°

Band	Wavelenght (μm)	R_{max}
1	0.45–0.52	0.61
2	0.52–0.60	1.30
3	0.63–0.69	1.17
4	0.76–0.90	1.63
5	1.55–1.75	1.07
6	10.4–12.5	–
7	2.08–2.35	1.68

Fig. 1. Image constructed from the AVHRR channel 2 (0.7–1.1 μm) for 1000 km × 1000 km region centered at (56°N, 7°E) on 14 October 1989 at 1300 UTC. Clouds appear as light shade against a darker background. The *solid rectangle* indicates the approximate region of clouds seen by Landsat 3 h earlier

Many "cloudy" pixels exhibit bidirectional reflectances much larger than 1, and bands 1, 3 and 5 are saturated. In bands 2, 4 and 7 the measurable maximum bidirectional reflectance is higher than 1.3 and the percentage of saturated pixels is quite small. The following structural analysis uses TM bands 4 and 6. The near-infrared band 4 is chosen to avoid Rayleigh scattering – the effect of which could be significant at shorter wavelengths – whereas its spectral interval (0.76–0.09 μm) is much more representative of the shortwave domain than that of band 7 (2.08–2.35 μm).

Solar bidirectional reflectance and infrared brightness temperature histograms are shown in Fig. 3a and Fig. 3b respectively. The histogram of the solar band shows a clear-sky peak at 0.03, which corresponds to the sea surface. Beyond 0.10, the histogram decreases regularly to the value at saturation. The slight rise at the end of the histogram (about 0.3% of the pixels) simply corresponds to the radiometric limit of the TM radiometer. If the cloud cover consisted of uniform white sheets with some mean bidirectional reflectance over a black background, then the histogram should have shown a peak around that bidirectional reflectance corresponding to the overcast pixels. Obviously, in this particular case, this model is inappropriate. According to previous studies (see Welch and Wielicki, 1986, for fog; Wielicki and Welch, 1986, for

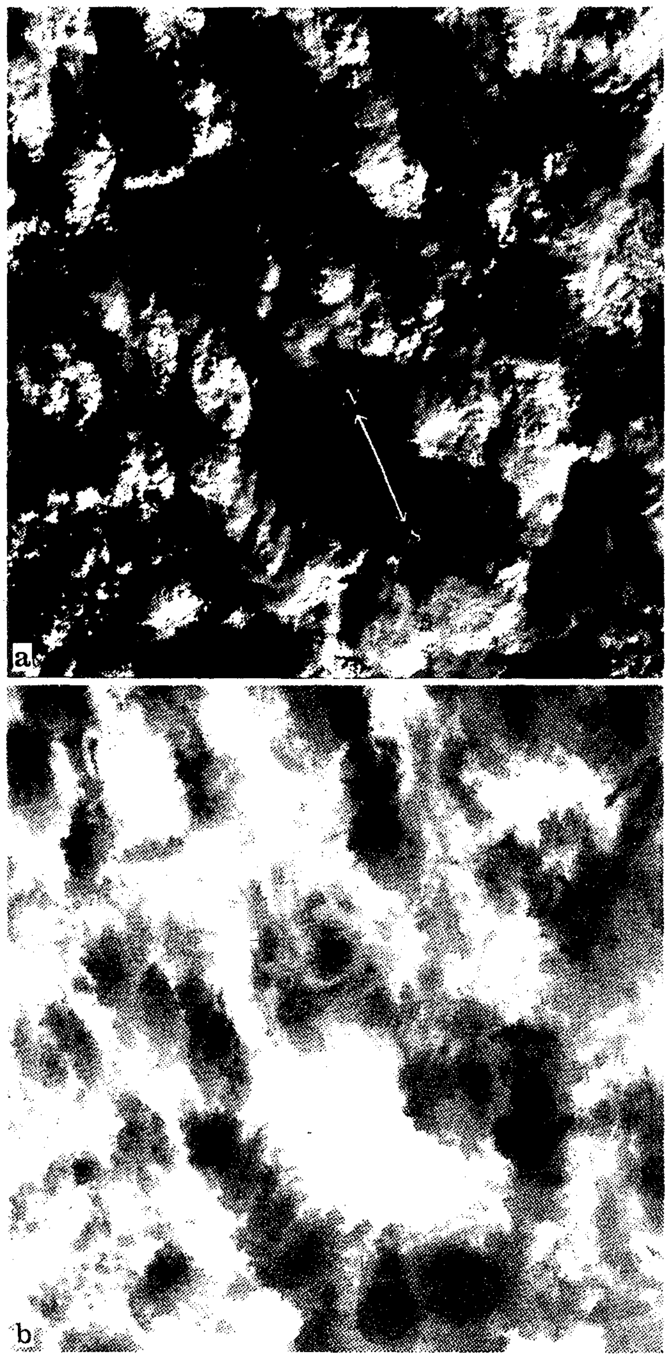

Fig. 2. a Image constructed from Landsat-5 TM channel 4 (0.76–0.90 μm) for ($\simeq$ 180 km)^2 region of the North Sea centered at (54.4°N, 6.3°E) on 14 October 1989 at 1000 UTC. The grey scale represents a change in reflectance from 0 to 1.6. Clouds appear as light shade against a dark ocean background in this image. b Image constructed from Landsat TM channel 6 (10.4–12.5 μm) brightness temperature for the same region. The grey scale represents a change in brightness temperature from 290 to 220 K. Clouds appear as dark shade against a clear ocean background in this infrared image

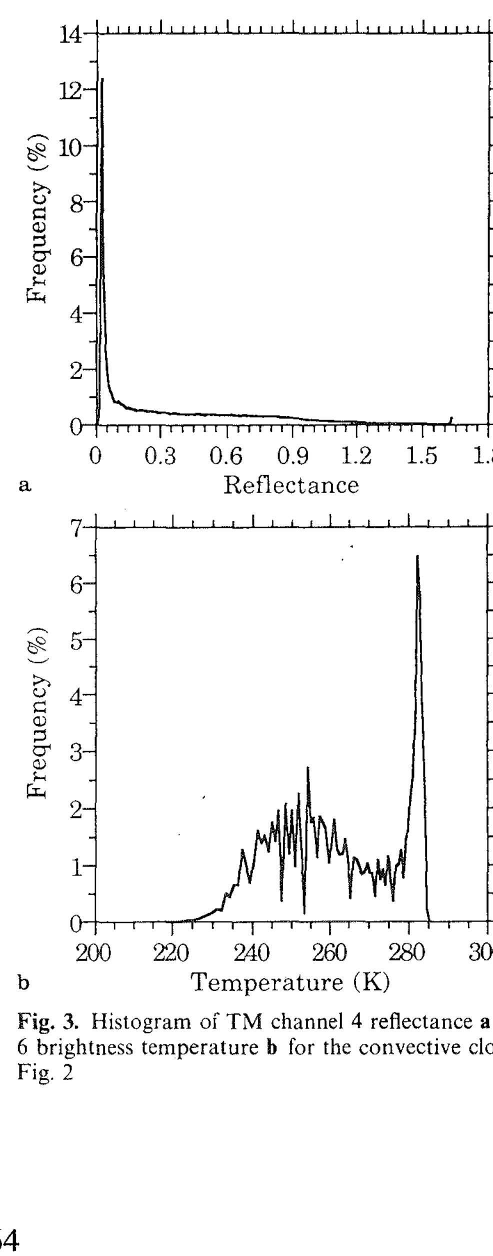

Fig. 3. Histogram of TM channel 4 reflectance a and TM channel 6 brightness temperature b for the convective cloud field shown in Fig. 2

cumulus; Kuo *et al.*, 1988, for cirrus and Welch *et al.*, 1988, for stratocumulus), the bidirectional reflectance is highly variable within individual cloud cells and its variations near cloud edges are not sharp but rather smooth. At the Landsat TM scale, the remarkably uniform distribution of the cloud bidirectional reflectances of the present scene indicates that the observed convective cloud field would be more accurately modeled by a smoothly varying distribution of bidirectional reflectances. This characteristic is important because of the nonlinear relationship between cloud radiative properties and liquid water content.

In Fig. 3b, the IR histogram shows a high clear-sky temperature peak near 282 K and a broad "cloudy" peak with a maximum near 255 K. The very large dispersion of brightness temperatures (220 K–280 K) corresponds either to variations of more than 8 km for the cloud-top altitude, assuming 6.5°C/km, or to many pixels with partial cloud cover, or both.

Various observed characteristics are due to the influence of cloud finiteness. First, a significant number of pixels exhibit bidirectional reflectances larger than the saturated value – assuming plane-parallel clouds for the satellite and solar zenith angles that correspond to the present Landsat data (0.8 according to Stuhlmann *et al.*, 1985). Second, a maximum is generally found at the south of the cloud cell top (compare Fig. 2a and 2b) whereas at the north of the cloud top the bidirectional reflectances are often very low. This reveals the presence of shadow effects, which are due to cloud shape. Third, for both channels, Fig. 4 shows a cross-section in the solar azimuthal plane over a representative cloud cell. Assuming that the infrared emissivity of "cloudy" pixels is 1 with exceptions for cloud edge pixels, brightness temperature variations are linked to variations of cloud-top altitude.

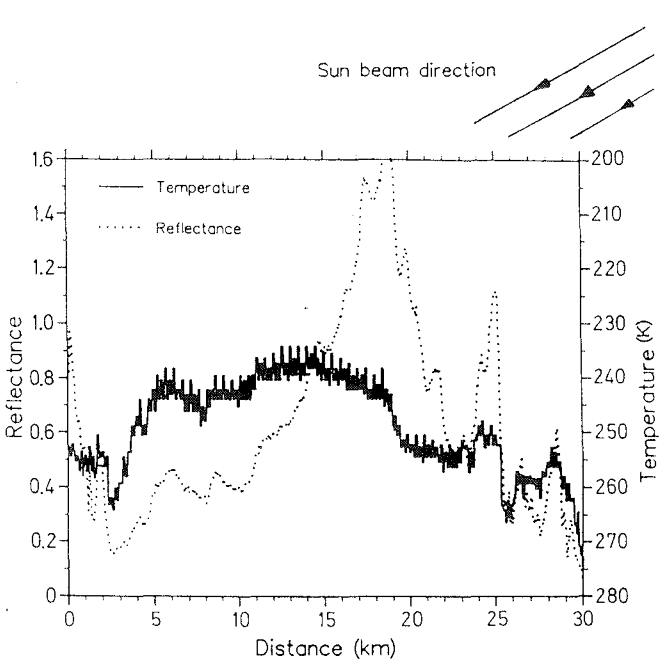

Fig. 4. An example of cross-section in the solar azimuthal plane of channel-4 reflectance and channel-6 brightness temperature over a representative cloud cell in Fig. 2

Therefore, the temperature curve gives a good idea of the cloud-top topology along this particular cross-section. Figure 4 clearly shows that the coldest parts of the image do not correspond to the brightest ones. The maximum bidirectional reflectance is shifted from the minimum of temperature towards the sun beam direction.

3 Structural analysis using Landsat-TM data

The analysis of the structural characteristics of the observed scene includes four steps: (i) pixels are classified as "cloudy" or "clear", (ii) connected clusters of pixels are recognized as individual cloud cells, (iii) for each single cloud cell, structural properties are determined (area, effective cloud diameter, horizontal aspect ratio and orientation, defined in more details below), (iv) the cloud field is described statistically by grouping cloud cells into a finite number of classes according to their effective diameter.

Following Wielicki and Welch (1986), the clear/cloud threshold applied to channel 4 was set to 0.03 above the background bidirectional reflectance R_b. This background reflectance was chosen as the first peak of the solar histogram of Fig. 3a. All pixels with a bidirectional reflectance greater than the threshold were flagged as totally cloud filled, all other pixels were assumed totally clear. For the present case, the first peak in the reflectance histogram corresponds to a clear-sky bidirectional reflectance of 0.025. The threshold $R_b + 0.03$ thus corresponds to a cloud amount of 71%. The cloud/no cloud threshold in the thermal band was derived from the cumulative distribution of brightness temperature and was chosen such that the total cloud cover is the same as in the solar channel. It was found to be 278.7 K.

Given the above thresholds, cloudy pixels may be connected into individual cloud cells. This is done separately for both solar and infrared channels. When a cloudy pixel has one or more adjacent clear pixels, it is flagged as a cloud edge pixel. Then both cloud edge and cloud interior pixels are grouped into individual cloud cells. When cloudy pixels are gathered into cloud cells, cloud field characteristics are derived following Wielicki and Welch (1986). These characteristics are cloud cell area, cloud perimeter, long and short axis moment, cloud horizontal aspect ratio and orientation angle, cloud mean bidirectional reflectance and mean temperature.

The statistical description of the cloud field is obtained by grouping individual cloud cells into cloud size classes according to their effective diameter. The effective cloud diameter is defined as that of a circular cell of the same area. Because the number of cloud cells tends to decrease with increasing cloud size, the width of the classes increases by a factor 1.5 with mean diameter (see Welch *et al.*, 1988; Kuo *et al.*, 1988). To prevent biases due to radiometric noise, cloud cells smaller than 4 pixels in size are not counted.

3.1 Fractional cloud cover and cloud size distribution

The distributions of fractional cloud cover are defined as the cloud cover per 1 km cloud diameter interval. Let $n(D)$

be the cloud size distribution or the cloud cell number density, i.e., the number of cloud cells per 1 km^2 surface area per 1 km cloud diameter interval. The fractional cloud cover of cells with diameter between D and $D + dD$ is

$$dN(D) = n(D)\frac{\pi D^2}{4}dD. \quad (1)$$

The total cloud cover is thus

$$N = \int_{D_{min}}^{D_{max}} n(D)\frac{\pi D^2}{4}dD, \quad (2)$$

where D_{min} and D_{max} are the smallest and largest observed cloud cell diameters respectively.

In Fig. 5, the cloud fraction distributions are plotted for two thresholds levels for each spectral band. These two levels are labeled "100%" and "10%". For each spectral band, the "100%" threshold level corresponds to the clear-sky/cloud threshold determined above (0.055 in the solar band, 278.7 K in the thermal band). In Cahalan and Joseph (1989), this level is labeled cloud "base" level. The "10%" threshold level is chosen so that the cloud fraction above it is equal to 10% of the total cloudiness. In Cahalan and Joseph (1989) this level is defined as the cloud "top" level.

The "100%" cloud fraction distributions are very similar for the two bands. They show an important decrease when the cloud diameter varies from 500 m to 7 km. The cloud sizes above 7 km are either empty or include only one cloud cell. Note that the last two classes represent a large percentage of the total cloud amount (about 90%). However, they are not really significant since the cells that compose these classes are actually made of several connected middle-sized cloud cells. Indeed, the cloud classification algorithm is not able to separate large cells at the "100%" level. A visual analysis of both solar and thermal images (see Fig. 2) clearly highlights the presence of

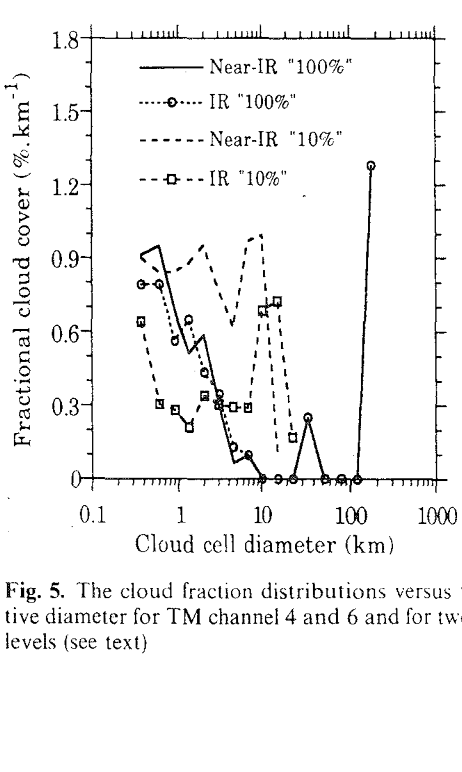

Fig. 5. The cloud fraction distributions versus the cloud cell effective diameter for TM channel 4 and 6 and for two selected threshold levels (see text)

convective cloud cells with effective diameters between 20 and 30 km.

At the "10%" level, the distributions of fractional cloud cover are very different. The middle-size classes are filled whereas the largest classes are empty. In addition, the distributions differ from channel to channel. These differences are not surprising since in the solar range "cloud tops" are selected according to maximum brightness which is more directly dependent on liquid water path or particular orientation than in the thermal, where the selection is mostly done according to altitude.

Even though the distribution of fractional cloud cover (dN/dD) seems to be the chief parameter to characterize cloud cell distributions, many studies have focused on cloud size distributions $n(D)$. By visual analysis of aircraft photographs of fair-weather cumulus cloud fields, Planck (1969) and Hozumi et al. (1982) showed that $n(D)$ decreases exponentially with increasing diameter. This feature was confirmed by Wielicki and Welch (1986) who found the same behavior using high spatial resolution satellite data. However, for different synoptic situations and cloud types, many experimental studies showed that the cloud size distributions were rather better represented by single or bimodal power laws of the cell diameter (Welch and Wielicki, 1986; Welch et al., 1988: Kuo et al., 1988; Cahalan and Joseph, 1989). However, since in the present case the size distribution is very unevenly distributed, it seems more reasonable to search for simpler analytical forms. A single power law of the form

$$n(D) = n_0 D^{-\alpha} \quad (3)$$

is considered. This implies that this particular convective cloud pattern satisfies the scaling invariance principle (Falconer, 1985). The parameters to be determined are thus the number of cloud cells with a diameter of 1 km, n_0, the slope of the distribution, α, and the minimum and maximum cloud cell diameters, D_{min} and D_{max}.

Cloud cells smaller than 4 pixels in size are not considered in the analysis. Because the spatial resolution is that of the IR channel (120 m), D_{min} must be smaller or equal to 270 m (the diameter of the circle of the same surface area). In fact, this value is not crucial, since $D_{min} \ll D_{max}$. In the following, we set $D_{min} = 0$. Thus, three quantities remain to be determined: n_0, α and D_{max}. Note that they are related to the total cloud cover N, since, from Eqs. 2 and 3

$$N = n_0 \frac{\pi}{4}\frac{D_{max}^{3-\alpha}}{(3-\alpha)}. \quad (4)$$

Welch et al. (1988) and Kuo et al. (1988) studied the influence of cloud cell thresholds on several structural parameters including the cloud size distribution. For well separated cloud cells, they found that the slopes of the size distributions were nearly insensitive to the threshold. In the present case, although individual cells can be identified visually, they are connected and the automatic algorithm cannot separate them without altering their dimensions. Thus, as shown in Table 2, α varies with threshold. When one goes from the "100%" to the "10%" threshold level, α first decreases rapidly and then seems to converge.

Table 2. Variations of α for increasing thresholds

Threshold	Fraction of total cloud cover	Band 4	Band 6
1	100	2.94	2.76
2	75	2.49	2.12
3	50	2.12	2.02
4	25	2.12	1.83
5	10	2.00	1.97

Table 3. Variations of α versus the number of cloud size classes

Number of classes	Band 4	Band 6
8	2.94	2.76
7	2.95	2.65
6	2.51	2.40
5	2.37	2.34
4	2.49	2.24
3	2.33	2.39
2	1.91	2.00

When the contrast increases, the cloud cells tend to individualize. Therefore, it seems reasonable to think that the size distributions are much less biased by cloud cell determined at the lowest threshold levels; α should thus be close to 2.

Another approach assumes that the derivation of the cloud cell density $n(D)$ is more accurate for small D. Table 3 shows the variation of α with the number of classes used in the regression. In this table the number of classes at the "100%" level is reduced at each step by excluding the largest one. In both spectral bands, α decreases with the number of classes. The "limits" of α are close to 2 and quite close to the values that have been determined at the "10%" threshold level.

The most reasonable estimate of the slope of the cloud size distribution is thus $\alpha \simeq 2$ with an uncertainty of about 10%. Since the very large cells which fill the last classes are indeed made of a number of smaller cells that are connected, the number of cells in the small classes increases after separation. Thus, n_0 is at least equal to the value obtained from the automatic classification, that is at the "100%" threshold level. In that case $n_0 \geq 1.2610^{-2}\ \mathrm{km}^{-3}$ in channel 4 and $n_0 \geq 1.0110^{-2}\ \mathrm{km}^{-3}$ in channel 6. With these values and $\alpha = 2$, from Eq. 4 $D_{max} \leq 78$ km for channel 4 and $D_{max} \leq 90$ km for channel 6.

Finally, the mean dimension of the cloud cells that composed the greatest part of the cloud amount is visually estimated to be about 25 km. In that case and for $\alpha = 2$, D_{max} should be closer to 50 km, in agreement with a visual inspection of the Landsat pictures. In the following we use this estimate of D_{max}. Then with Eq. 4, $n_0 \simeq 1.8\ 10^{-2}\ \mathrm{km}^{-3}$.

Note that this cloud size distribution gives roughly 15 cloud cells with diameter larger than 20 km. That appears to be in good agreement with a visual inspection of Figs. 2a and 2b.

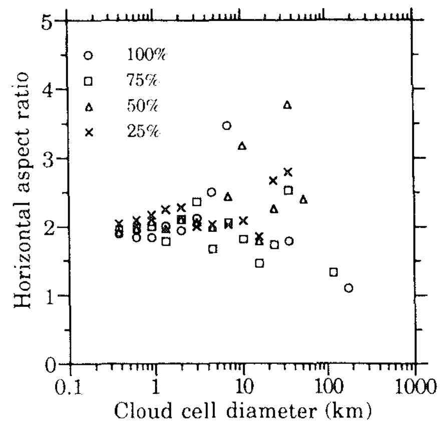

Fig. 6. The cloud cell horizontal aspect ratio versus the cloud cell effective diameter for TM channel 4 and for selected threshold levels

3.2 Horizontal aspect ratio and cloud cell orientation

The radiation field also depends on individual cloud characteristics such as horizontal and vertical aspect ratios and oreintation.

The horizontal aspect ratio is defined as the length-to-width ratio, A/B, of elongated cloud cells. For cubic, spherically or cylindrically-shaped cloud, $A/B = 1$, whereas A/B is the long axis-to-short axis ratio for clouds with ellipsoidally-shaped bases.

Figure 6 shows the variation of the cell horizontal aspect ratio A/B with effective diameter for different threshold levels. Only the results for channel 4 are presented, since the results for band 6 are very similar. Whatever the threshold, $A/B \simeq 2$ for effective diameters ranging from 350 m to about 5 km. That means that cloud cells are in average twice as long as wide. For cloud cells larger than 5 km, the important fluctuations of the horizontal aspect ratio are due more to the almost empty cloud size classes than to actual variations of apparent cross section of cloud with altitude.

The cloud cell orientation is first related to the dynamical fields. It is an important parameter to develop in a physical model of the cloud cover, since it can have a very large effect on the three-dimensional radiation field. Bidirectional effects seen on Fig. 4 are certainly due to cloud shapes but also to cloud cell orientation with respect to the solar beam direction. Here, cloud cell orientation is characterized by the effective azimuth angle $\psi_e = |\psi - \gamma|$ where both the cell azimuth angle ψ and the solar beam azimuth angle γ are defined relative to an arbitrary axis.

The effective azimuth angle ψ_e has been computed for each cloud cell and averaged for each cloud size class. The results show that, except for small cloud cells which seem to be randomly oriented whatever the threshold, ψ_e varies generally between 0° and 20°, as clearly seen on Fig. 2, even if some cloud cells present slightly different azimuth angles. Obviously, these values are only valid for that particular convective situation and should not be generalized.

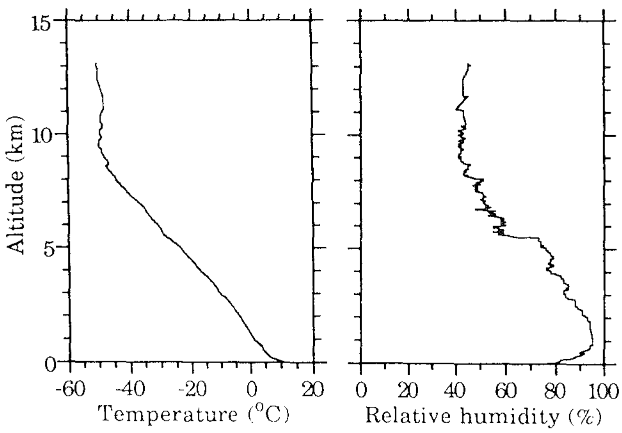

Fig. 7. Temperature and relative humidity profiles of the Helgoland (54.1°N, 7.5°E) radiosounding made at 1020 UTC

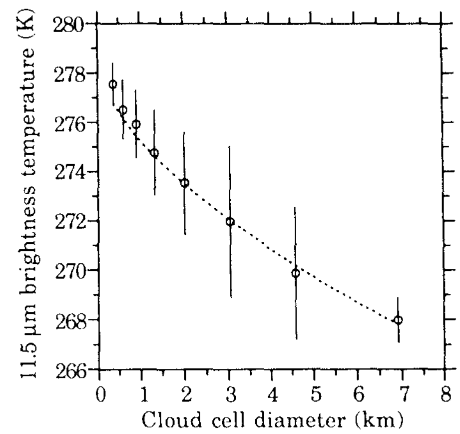

Fig. 8. The variations of the mean radiative temperature of the clouds versus the cell effective diameter. The *dotted line* refers to approximate relation in Eq. 15. The *open circles* and the *vertical bars* refers to the mean value and to the standard deviation of each class respectively

3.3 Vertical aspect ratio

To complete the characterization of the cloud field structure, we need to relate the mean geometrical thickness of the cloud cells to their horizontal dimension. This is done in this section using the thermal infrared image in conjunction with a radiosounding performed nearby in Helgoland (54.1°N, 7.5°E) at 1020 UTC as part of the ICE intensive field operation period.

According to this sounding (Fig. 7), the altitude of the tropopause is close to 8.5 km and above 1.5 km the temperature decreases nearly linearly with altitude according to

$$T = T_0 + \left(\frac{\partial T}{\partial Z}\right) Z, \tag{5}$$

with $T_0 = 283.4$ K and $(\frac{\partial T}{\partial Z}) = -6.82\,\mathrm{km}^{-1}$.

With the hypothesis that the cloud base temperatures differ only slightly from the threshold temperature and neglecting the influence of the atmosphere above the cloud, the cloud-base altitude, Z_{base}, is found to be around 700 m. This is consistent with the value estimated from the humidity profile obtained at Helgoland (600 m) and with those given by the ground observers at the various meteorological stations (800–1000 m).

Figure 8 presents the variation of the cloud cell mean radiative temperature with effective diameter. Clearly, the temperature decreases when the cloud size increases. If all cloud bases are assumed to be at the same altitude, which seems legitimate in the case of a convective cloud field, then the geometrical thickness of the cloud cells increases with their horizontal dimension.

To realistically simulate the decrease of cloud-top altitude of individual cells shown in Fig. 2b, a hemi-ellipsoidally shaped cloud is chosen. This shape has already been used by Kite (1987). Moreover, considering that the horizontal cloud aspect ratio is approximately 2 (see Section 3.2), the cloud base is assumed to be an ellipse. This cloud shape also agrees with the decrease of the bidirectional reflectances from cloud center to cloud edge noted in Section 2.

Assuming that the cloud cells are hemi-ellipsoids, we search for a fit of the form

$$\bar{H} = \nu D^{\beta}, \tag{6}$$

where $\bar{H}$ is the mean thickness of a cell of effective diameter D. ν and β are two constants that are determined so that the scene-averaged and the maximum cloud thickness of the distribution coincide with observations.

The scene averaged cloud thickness is

$$\langle H \rangle = \int_{D_{min}}^{D_{max}} \bar{H}(D)\,dN(D) \Big/ \int_{D_{min}}^{D_{max}} dN(D), \tag{7}$$

where $\bar{X}$ represents the mean value of the variable X for an individual cell and $\langle X \rangle$ is the value averaged over all the cells of the scene. Using Eqs. 1, 3 and 6, Eq. 7 becomes

$$\langle H \rangle = \frac{\nu(3-\alpha)}{\beta + 3 - \alpha} D^{\beta}_{max}. \tag{8}$$

Assuming that the mean radiative temperature corresponds to the actual temperature, the scene-averaged cloud temperature is

$$\langle T \rangle = T_0 + (Z_{base} + \langle H \rangle)\left(\frac{\partial T}{\partial Z}\right). \tag{9}$$

With the numerical values determined in Section 3.1 and the averaged cloud temperature calculated from Fig. 2b ($\langle T \rangle = 256.3$ K), we obtain

$$\nu \frac{50^{\beta}}{\beta + 1} \simeq 3.28\,(\mathrm{km}). \tag{10}$$

A second relation makes use of the maximum cloud-top altitude. For hemi-ellipsoidal cloud, the cloud-top altitude is related to the mean thickness by

$$Z_{top} = Z_{base} + \frac{3}{2}\bar{H}, \tag{11}$$

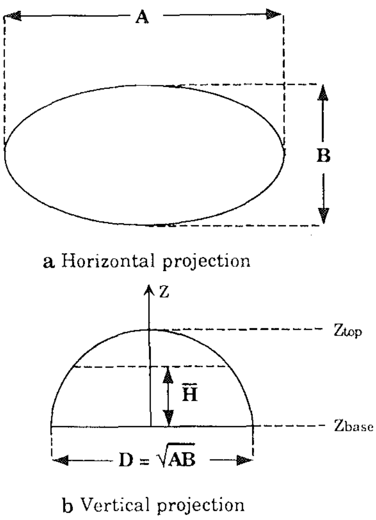

Fig. 9. The cloud geometry used in this study

so that, from Eq. 6, the maximum cloud top altitude is

$$Z_{top}^{max} = Z_{base} + \frac{3}{2} \nu D_{max}^{\beta} \tag{12}$$

The radiosounding indicates that the tropopause was near 8.5 km with a temperature of 225 K. Such temperatures are observed locally in the thermal image. Assuming that the maximum cloud-top altitude is 8.5 km, Eq. 12 gives

$$\nu(50)^{\beta} = \frac{2}{3}(8.5 - 0.7) = 5.2\,(\mathrm{km}). \tag{13}$$

Equations 10 and 13 give $\beta \simeq 0.6$ and $\nu \simeq 0.5$. Therefore, the mean height to effective diameter ratio is

$$\frac{\bar{H}}{D} = \frac{0.5}{D^{0.4}}, \tag{14}$$

where D is in km.

For diameters varying between 270 m and 3 km, $\bar{H}/D$ decreases from 0.9 to 0.3, in good agreement with Plank (1969) and Hozumi *et al.* (1982). For cells with diameter larger than 3 km, $\bar{H}/D$ is relatively small and it is minimum, $\simeq 0.1$, when $D = D_{max}$. Figure 9 shows the hemi-ellipsoidal cloud pattern that is here defined.

From Eqs. 5 and 14, the mean temperature of a cloud cell is related to its effective diameter by

$$\bar{T} = 278.7 - 3.41\,D^{0.6}, \tag{15}$$

with D in km.

The corresponding curve is shown in Fig. 8. The fit is more than satisfactory (the root mean square error is 0.2 K), except for the smallest clouds for which the radiative temperature may significantly differ from their physical temperature.

4 Specification of cloud optical properties

The cloud optical properties depend on the drop size distribution (DSD). The DSD used $n(r) \propto r^2 \exp(-0.328\frac{r}{r_0})$, corresponds to *cumulus-cumulus congestus* clouds as defined by Fenn *et al.*, (1985). For this distribution, the mean radius is equal to 9.2 μm and the effective radius is $r_e = 15.2$ μm.

This DSD is very similar to that deduced from the measurements made with the Knollenberg "FSSP probe" on board the MERLIN aircraft near the Landsat scene during the ICE experiment. The measured effective radii were typically 12 to 15 μm (Gayet *et al.*, 1991) with very large local variations due to the presence of ice crystals. Note that in the present context it is not necessary that the DSD of the model clouds be the real one. The observations are used to check that the chosen standard DSD is reasonable.

The normalized absorption and scattering coefficients of the particles, as well as the phase function $p(\theta)$, were calculated from Mie theory using the values reported by Hale and Querry (1973) for the complex refractive index of water. For Landsat channel 4, $m = 1.329 - 0.182\,10^{-6}\,i$ and the single scattering albedo $\tilde{\omega}$ and the asymmetry factor g are respectively 0.999938 and 0.863. The extinction coefficient at 0.83 μm was derived from the satellite observations using the following procedure.

We made the simplifying hypothesis that the optical properties are independent of height. In these conditions, optical thickness and cloud size are linked by (see Eq. 6)

$$\bar{\delta} = \nu \sigma D^{\beta}. \tag{16}$$

The extinction coefficient σ was chosen so that the bidirectional reflectance of a distribution of clouds that satisfies Eqs. 3 and 6 agrees with the observed bidirectional reflectance averaged over the cloudy portion of the scene ($\langle R(0.83\,\mu\mathrm{m})\rangle = 0.51$).

To calculate the bidirectional reflectances we used the spherical harmonics method (Devaux, 1977). The best agreement was obtained for $\sigma = 7\,\mathrm{km}^{-1}$. Thus, the optical thickness of a cloud with an effective diameter of 1 km is $\bar{\delta} = 3.5$. The optical thickness of the largest cloud ($D = 50$ km) is $\bar{\delta} = 37$.

The liquid water content is approximately 0.07 g m^{-3}. This value is small but it agrees with the few liquid water content measurements (typically 0.1 g m^{-3}) performed with the Johnson–William probe, which was flown on the MERLIN aircraft in the area of the Landsat scene (Gayet *et al.*, 1991). In addition, the liquid water paths were measured with a microwave radiometer on board the RV Poseidon ship located at 55.5°N and 3.5°E. The results, typically of the order of 0.2 kg m^{-2} (Hargens *et al.*, 1991) are in agreement with the mean value calculated for the Landsat scene (0.23 kg m^{-2} for the cloudy part and 0.16 kg m^{-2} for the whole scene).

5 Modeling of the radiative impact of cloud inhomogeneities

The structure of a highly inhomogeneous convective cloud field has been modeled in Section 3. We now try to quantify the influence of this heterogeneity on the radiative field at the scale of the Landsat picture, with dimensions comparable to those of a numerical model. To do this, we compare the outgoing shortwave (SW) and longwave (LW) radiative fluxes calculated for the statistical distribution and cloud shapes derived in Section 3 to the fluxes calculated using a plane parallel cloud field hypothesis.

Difference may arise from two reasons: (i) cloud size distribution, that is, variations of optical thickness from cloud to cloud compared to constant optical thickness and (ii) cloud shape influence (hemi-ellipsoidal compared to plane-parallel). To better distinguish between these two effects, we proceed in two steps. In the first step, we compare the radiation fluxes produced by a plane-parallel cloud layer to those produced by a field of plane-parallel clouds of variable optical thickness. In the second step, we compare a plane-parallel cloud layer to a field of identical hemi-ellipsoidal clouds.

5.1 Description of cloud models

Flux computations were performed for several schematic models:

1. The Homogeneous Plane-parallel model (HP) is an approximation using a linear weighting of the plane-parallel flux. This is the usual assumption in climate models.
2. In the Inhomogeneous Plane-parallel model (IP) each cloud cell is equivalent to a uniform plane-parallel portion of layer whose mean optical thickness is linked to the horizontal dimension of the cell and varies from cloud to cloud. This model is designed to estimate the influence of the horizontal distribution of liquid water in the scene.
3. For Homogeneous hemi-Ellipsoid model (HE), the clouds are identical hemi-ellipsoids, with geometrical thickness $\bar{H} = \langle H \rangle$ and equivalent diameter (see Eq. 6) $D = D_e = (\langle H \rangle / \nu)^{1/\beta}$. They are randomly distributed on the plane of the lower boundary. When compared to HP, this model should help in evaluating the influence of cloud shape.

In order to estimate the influence of cloud inhomogeneities, we compare the scene-averaged outgoing radiative fluxes for various total cloud covers N. The cloud size distribution is that determined in Section 3; $n_0 = 0.018\,\mathrm{km}^{-3}$ and $\alpha = 2$ are kept constant and D_{max} varies linearly with N according to Eq. 4. From Eqs. 4 and 7, the mean thickness of the cloudy part of the scene varies with N as

$$\langle H \rangle = \frac{\nu(3-\alpha)}{\beta+3-\alpha}\left(\frac{4N(3-\alpha)}{n_0 \pi}\right)^{\beta/(3-\alpha)}, \tag{17}$$

which simplifies to $\langle H \rangle \simeq 4N^{0.6}$ (km). For the HE model, the equivalent diameter D_e is thus related to N through Eqs. 6 and 17. The result is that $D_e \simeq 32N$ (km).

The calculations of the radiative fluxes also require the specification of a number of thermodynamical and geophysical parameters. They have been chosen to match as well as possible the actual parameters associated with the Landsat scene. The temperature and humidity profiles were taken from the Helgoland radiosounding (see Fig. 7). The total aerosol optical thickness was taken from observations performed in Nordholz (53.5°N, 8.4°E) as part of the ICE observations. The aerosol optical properties correspond to those of maritime aerosols (WCP 55, 1983). The Midlatitude Summer ozone profile (McClatchey *et al.*, 1971) was used. The surface albedo was set to 0.065 in the SW and to zero in the LW, which is reasonable for a field of clouds above the sea, excluding the conditions of specular reflectance.

5.2 Methods of calculation of the radiative fluxes

5.2.1 Shortwave radiation

The basis of the computation of the radiative fluxes is Fouquart and Bonnel's parameterized code (1980). For the HP model the outgoing SW flux is simply weighted by the cloud cover N as in climate models,

$$F_{HP}(N) = (1-N)F_0 + NF_1, \tag{18}$$

where F_0 is the clear sky flux and F_1 the overcast flux for a plane-parallel cloud of thickness $\langle H \rangle$ linked to N through Eq. 17. For the inhomogeneous plane-parallel case (IP), the fluxes are calculated as a function of cell thickness, $\bar{H}(D)$, weighted by the corresponding cloud covers and averaged over the whole scene.

For the hemi-ellipsoidal clouds (HE) the Monte Carlo method is extremely cumbersome for broad band flux calculations. We therefore used the approximation of equivalent cloud cover. First we used the Monte Carlo method (Crétel *et al.*, 1988) to calculate the monochromatic directional reflectance (or albedo), $\alpha_{HE}(\theta_0, N)$, at 0.83 µm for a field of hemi-ellipsoidal clouds of total cloud cover N illuminated at solar zenith angle θ_0, neglecting the influence of the rest of the atmosphere as well as that of the surface. Second, we derive the effective cloud cover N_{HE} as

$$\alpha_{HE}(\theta_0, N) = N_{HE}\,\alpha_{HP}(\theta_0, 1), \tag{19}$$

where $\alpha_{HP}(\theta_0, 1)$ is the albedo of the plane-parallel cloud of thickness $\langle H \rangle$. Finally, we simulate the outgoing shortwave fluxes for the case of the finite clouds of cloud cover N with the plane-parallel ones for effective cloud cover N_{HE},

$$F_{HE}(N) = F_{HP}(N_{HE}) = (1-N_{HE})F_0 + N_{HE}F_1. \tag{20}$$

To compute the monochromatic albedo $\alpha_{HE}(\theta_0, N)$, we consider that the differences between the albedo of an isolated cloud and that of the cloud field are due to the effects of enhanced illuminated area (E_f) and cloud-cloud interaction (I_a) (Welch and Wielicki, 1984; Kobayashi, 1988). Thus the cloud field albedo is given by

$$\alpha_{HE}(\theta_0, N) = \alpha_{isol}(\theta_0)N\,E_f(\theta_0, N)I_a(\theta_0, N), \tag{21}$$

where $\alpha_{isol}(\theta_0)$ is the albedo calculated from the Monte Carlo method for the isolated cloud.

When multiplied by the cloud cover, the enhancement factor represents the probability, $P(\theta_0, N)$, that a solar ray interacts with a cloud in the direction θ_0. Following

Busygin *et al.*, (1973), we assume that the cumulus cloud bases are distributed according to a Poisson distribution. In these conditions, we have

$$NE_f(\theta_0, N) = P(\theta_0, N) = 1 - (1 - N)^{S(\theta_0)/S(0)}, \quad (22)$$

where $S(\theta_0)$ is the cloud area projected onto the horizontal plane along the direction θ_0. For a hemi-ellipsoidal cloud oriented with respect to the solar beam direction such as $\psi_c = 0$, the area ratio is

$$\frac{S(\theta_0)}{S(0)} = \frac{1}{2}\left(1 + \sqrt{1 + 9\frac{B}{A}\left(\frac{\bar{H}}{D}\tan\theta_0\right)^2}\right), \quad (23)$$

where the horizontal aspect ratio $A/B = 2$ (see Section 3.2) and the vertical aspect ratio is given by Eq. 14.

For the cloud-cloud interaction, $(I_a(\theta_0, N))$, we used the parameterization proposed by Kobayashi (1988) which assumes a linear relationship between I_a and N,

$$I_a(\theta_0, N) = 1 + N\left(\frac{\alpha_{HP}(\theta_0, 1)}{\alpha_{isol}(\theta_0)} - 1\right), \quad (24)$$

so that $\alpha_{HE}(\theta_0, N)$ converges to $\alpha_{HP}(\theta_0, 1)$ as N approaches 1. The same procedure that gives good results for round clouds such as hemispheres and capped cylinders (Kobayashi, 1988) is expected to give satisfactory results for the HE model.

5.2.2 Longwave radiation

In the longwave, we assumed that all clouds emit as black bodies. This simplification should have had a small influence since, neglecting the effect of scattering, the fractional coverage corresponding to cloud cell emissivities smaller than 0.99 ($D < 0.8$ km) was found to be less than 0.01.

For the plane-parallel models, the outgoing LW fluxes were computed with Morcrette's (1984) high-spectral resolution model. To estimate the influence of the cloud shape, we followed Ellingson's (1982) approach. To further simplify, we assumed that the cloud cell bases are circular. This seems reasonable since, for constant cloud area, the outgoing LW fluxes primarily depends on the vertical distribution of the emitting sources. Indeed, Harshvardhan and Weinman (1982) on one hand and Ellingson (1982) on the other obtained very similar relationships between effective and real cloud cover even though the latter considered a Poisson distribution of cylindrical clouds while for the former, the clouds were cubic and regularly distributed. This indicates that the influence of the shape of cloud bases is likely to be small. In the HE model, the cloud cells are thus identical hemi-ellipsoids with circular bases, distributed according to a Poisson distribution. In addition, the variation of temperature inside individual clouds is neglected; each cloud cell is thus isothermal at temperature $T(\bar{Z})$.

Let $P(\theta, N)$ be the probability that a line of sight corresponding to a zenith angle θ encounters a cloud. The upward and downward fluxes can then be written as:

$$F_{HE}(N) = 2\pi \int_0^{\pi/2} P(\theta, N) I_1(\theta)\cos\theta\sin\theta d\theta + 2\pi \int_0^{\pi/2} (1 - P(\theta, N)) I_0(\theta)\cos\theta\sin\theta d\theta, \quad (25)$$

where $I_0(\theta)$ and $I_1(\theta)$ are the upward and downward radiances coming respectively from clear and cloudy parts of the scene (Niylisk, 1972). Assuming that I_0 and I_1 are isotropic, Eq. 25 becomes

$$F_{HE}(N) = F_0 + 2(F_1 - F_0)\int_0^{\pi/2} P(\theta, N)\cos\theta\sin\theta d\theta, \quad (26)$$

where F_0 and F_1 represent the fluxes in clear and overcast conditions respectively and are calculated with the plane-parallel approximation. The effective cloud cover is thus

$$N_{HE} = 2\int_0^{\pi/2} P(\theta)\cos\theta\sin\theta d\theta, \quad (27)$$

where $P(\theta, N)$ is determined as in Eqs. 22 and 23 with $A/B = 1$.

5.3 Results

5.3.1 Influence of the size distribution of the clouds

We first estimate the influence of the horizontal variability of the cloud thickness on plane parallel clouds. We thus compare the radiative fluxes produced by a homogeneous plane-parallel cloud (HP) to those corresponding to a distribution of plane-parallel clouds of variable optical thickness (IP).

Figure 10 presents the differences between the SW fluxes, F_{IP}, obtained using the IP model, and those calculated for a unique plane-parallel cloud (F_{HP}). They are shown for three solar zenith angles (0°, 45° and 65°). For the particular cloud cover and illumination conditions of the Landsat picture ($N = 0.71$ and $\theta_0 = 65°$), the difference between the models, $F_{IP} - F_{HP}$, is approximately $-10\,\mathrm{Wm}^{-2}$. The relative difference is thus -3.5%. Assuming that the cloud conditions do not vary with the solar zenith angle, the flux difference increases for small solar zenith angles and is of the order of $-25\,\mathrm{Wm}^{-2}$ (-4.2%) for $\theta_0 = 0$. The deviation also increases with cloud cover and is nearly $-40\,\mathrm{Wm}^{-2}$ (-6.7%) for overcast conditions and $\theta_0 = 0$. Note that, in the overcast case,

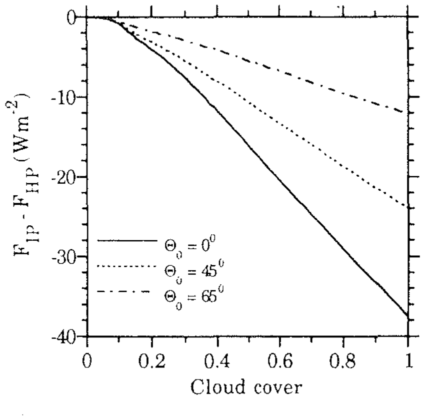

Fig. 10. Difference between the outgoing plane-parallel shortwave flux obtained by averaging on the various cloud cells and the plane-parallel flux corresponding to the mean optical depth, as a function of cloud amount for different solar zenith angles

the optical thickness of the individual cells varies between 1.5 and 45 for the IP model and is $\langle\delta\rangle = 28$ for the HP model.

For the inhomogeneous plane-parallel case, as in the case of shaped clouds, we can define an effective cloud cover. Here, N_{IP} is defined as that fraction of a plane parallel cloud which would provide the same radiation budget as the inhomogeneous cloud field, for the same mean optical thickness $\langle\delta\rangle$. Remember that $\langle\delta\rangle = \sigma\langle H\rangle$ varies with N (see Eq. 17).

Figure 11 shows the differences between effective and actual cloud covers. N_{IP} is always smaller than N and $|N_{IP} - N|$ increases with decreasing θ_0 and increases almost linearly with N.

The influence of the size distribution is not as important in the longwave. Because of the quasi-linear variation of temperature with altitude, the outgoing longwave flux depends almost linearly on cloud top altitude. Therefore, since the scene-averaged cloud top altitudes are the same for both homogeneous and inhomogeneous models, it is not surprising that the scene averaged longwave fluxes are almost independent of the spatial inhomogeneities. For example, for the cloud cover corresponding to the observations ($N = 0.71$), the longwave fluxes calculated with the HP and IP models are respectively 218.1 and 218.4 Wm^{-2}.

5.3.2 *Influence of the cloud shape*

Figures 12a and 12b show the differences, calculated at 0.83 µm, between the effective cloud cover for homogeneous ellipsoidal clouds and the actual cloud cover.

For solar angle $\theta_0 = 0$, the albedo of the broken cloud field is smaller than its plane-parallel counterpart because of the escape of photons through the sides of the finite clouds. This is only partly compensated by the cloud-cloud interactions. When θ_0 increases, the cloud surface intercepting the solar energy is enhanced in the finite cloud case. As reported by Kobayashi (1988), either effect (loss of photons or area enhancement) may prevail according to the cloud field geometry. Here, the illuminated area enhancement is moderate when the long axis of the hemi-ellipsoidal clouds is in the incident plane ($\psi_e = 0$) but noticeably larger when $\psi_e = 90°$. Such differences explain, for a large part, the different features of $N_{HE} - N$ curves shown in Figs. 12a and 12b.

Figures 13a and 13b present the differences, derived from the effective cloud covers, between the top of the atmosphere SW fluxes simulated for identical hemi-ellipsoidal clouds (F_{HE}) and calculated for a plane-parallel cloud (F_{HP}). When $\psi_e = 0°$, the flux differences are always smaller than 10 Wm^{-2}. For the conditions of the Landsat picture, they are only 0.5 Wm^{-2}. They would be 14 Wm^{-2} for the same conditions but $\psi_e = 90°$.

In the longwave domain, the effective cloud cover N_{HE} is always larger than N, but the differences $N_{HE} - N$ remain relatively small. Figure 14 shows these differences compared to those obtained in the case of cylinders. Such cylinders have been considered by Ellingson (1982) so that Fig. 14 may be compared to his Fig. 13a but for a vertical aspect ratio which decreases when N increases (see Section 3.3). For example, $\bar{H}/D_e$ decreases from 0.31 to 0.14 and D_e increases from 3.2 km to 23 km when N varies from 10% to 71%. Because of their rounded shape, hemi-ellipsoids deviate less from "plane-parallel" than cylinders. Note that this "rounding" effect vanishes as $\bar{H}/D_e$ increases; the differences between hemi-ellipsoids and cylinders would not be so significant for $\bar{H}/D_e$ greater than 1. This remark is important insofar as, for the clouds observed from Landsat, $\bar{H}/D_e$ is always relatively small.

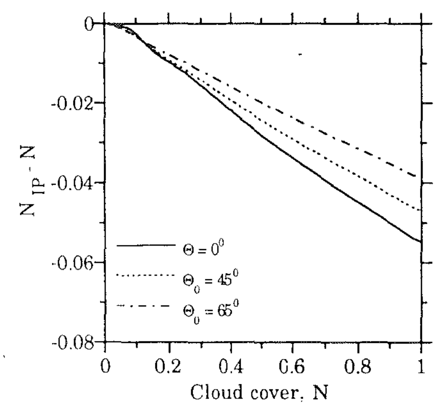

Fig. 11. Difference between the shortwave effective cloud cover of an inhomogeneous plane-parallel cloud field and the actual cloud cover. Different curves pertain to different solar zenith angles as denoted in the figure

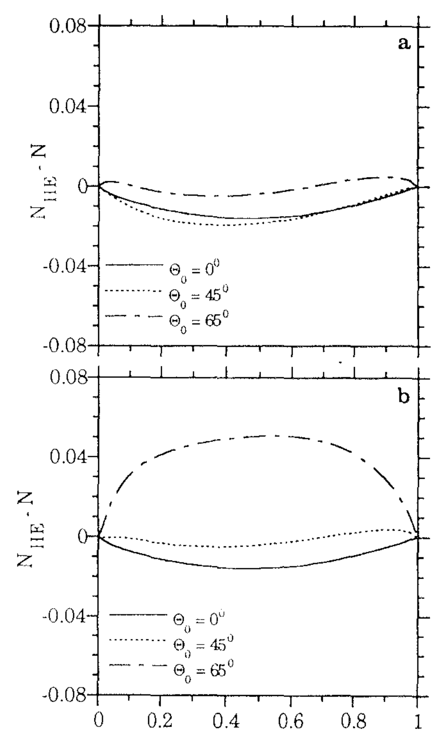

Fig. 12. Difference between the shortwave effective cloud cover of a homogeneous hemi-ellipsoidal cloud field and the actual cloud cover. The long axis of the hemi-ellipsoidal clouds is either in **a** the incident plane or **b** normal to the incident plane

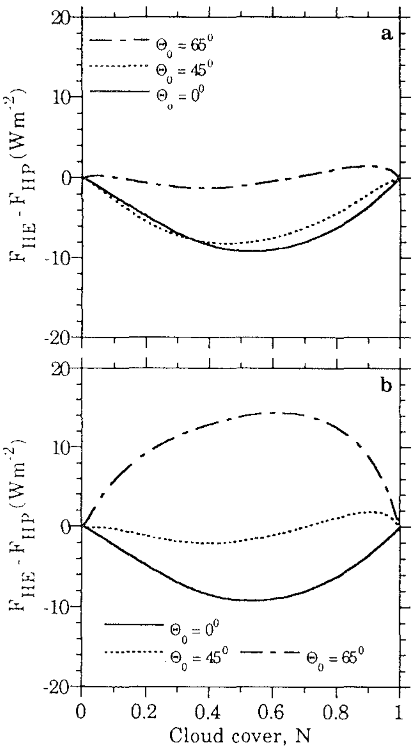

Fig. 13. Difference between the homogeneous hemi-ellipsoidal cloud field and the homogeneous plane-parallel shortwave fluxes at the top of the atmosphere, as a function of cloud amount for different solar zenith angles. Cases **a** and **b** refer to different cloud orientations as in Fig. 12

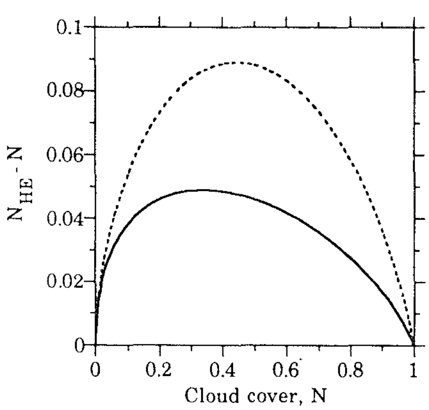

Fig. 14. Difference between the infrared effective cloud cover and the actual cloud cover for the homogeneous hemi-ellipsoidal cloud field (*full line*). The *dashed line* refers to cylinders

The differences between the outgoing LW fluxes calculated for the homogeneous field of hemi-ellipsoidal clouds (HE) and the plane-parallel case (HP) are shown in Fig. 15. The largest difference is about $-1.8\,\mathrm{Wm}^{-2}$: roughly -0.8%. Since the influence of the cloud size distribution was found to be less than 0.2%, the impact of cloud heterogeneities remain, in the present case, smaller than 1% in the longwave domain.

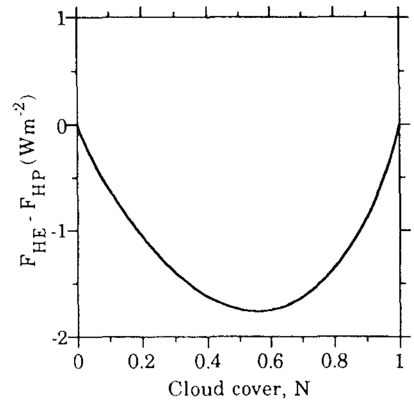

Fig. 15. Difference between the outgoing longwave flux calculated for the homogeneous field of hemi-ellipsoidal clouds and for the plane-parallel case, as a function of the actual cloud cover

6 Conclusion

From model calculations based on a satellite observation of a particular convective cloud field, the influence of cloud horizontal inhomogeneities on the radiation budget at the scale of a Landsat scene ($185 \times 185\,\mathrm{km}^2$) have been estimated. This estimate was based on a comparison between top of the atmosphere outgoing radiative fluxes produced by a plane-parallel cloud layer of varying optical thickness and partial cloud cover and those produced by a distribution of cloud cells of various shapes and dimensions. As deduced from the satellite observation, the thickness of the individual cells was dependent on their horizontal size. The simulations performed in this study indicate that for given cloud cover and scene-averaged liquid water content, the outgoing shortwave fluxes reflected by the inhomogeneous cloud fields are systematically smaller than those reflected by the homogeneous ones. This results from the horizontal variability of the individual cell thicknesses and is also a consequence of the non-linearity of the reflectance of the scattering layers with respect to their optical thickness. This effect is almost proportional to the cloud cover and depends on the solar illumination. It is of the order of $10\,\mathrm{Wm}^{-2}$ for the particular conditions corresponding to the Landsat picture ($\theta_0 = 65°$ and cloud cover $N = 0.71$); it would reach $40\,\mathrm{Wm}^{-2}$ in the extreme case of total cloud cover under normal incidence. It can be accounted for with a homogeneous plane-parallel layer providing that an "effective" partial cloud cover N_{IP} be substituted for the actual one N. Since the saturation effects tend to reduce the fluxes reflected from horizontally inhomogeneous cloud layers, N_{IP} must be *smaller* than N. In the LW, on the contrary, the effect of the cloud size distribution is negligible.

As shown by many authors (see Fouquart *et al.*, 1990), the effect of neglecting the cloud shape is to increase the outgoing radiative flux for most cases in the shortwave and for all cases in the longwave. The result is an effective cloud cover N_{HE} generally *smaller* than N in the SW, and *larger* than N in the LW. However, even in the SW, N_{HE} can be larger than N for high solar zenith angles and particular cloud orientations. For the hemi-ellipsoidal clouds whose vertical and horizontal aspect ratios correspond to the Landsat scene under study, the effect of cloud finiteness may exceed 10 Wm^{-2} in the shortwave but is always less than 2 Wm^{-2} in the longwave. However, when daily averaged, some counterbalancing is expected concerning the cloud shape influence in the solar range, unlike the influence of the cloud cell distribution.

If one considers the overall effect of the inhomogeneities, the flux reflected by an inhomogeneous field of hemi-ellipsoidal clouds is weaker than the plane-parallel flux whatever the cloud cover for weak and moderate solar zenith angles, and regardless of the solar zenith angle for very large cloud cover. In other conditions, it may be weaker or larger, greatly depending on the orientation of the cloud cells with regard to the sun beam direction. If many solar zenith angles and cloud cell orientations are considered, the effect of cloud cells distribution is expected to be the main influence of the heterogeneities.

These conclusions apply to a particular convective situation; they are not general, but, compared to the purely theoretical simultations usually performed, the present study may be a first contribution to a better understanding of the influence of actual cloud inhomogeneities. Indeed, although they are useful in evaluating the potential influence of various structural characteristics, theoretical cloud models do not allow us to distinguish which effects are the most important in the real world. This can be done only with the support of observations. The present approach must be considered as a preliminary attempt and the results of this study are only indicative. However, that the effect of spatial variations of cloud thickness appears to be more important in this particular case than the effect of cloud shape is interesting. It supports simple parameterizations such as the "inherent plane-parallel approximation" as proposed by Kobayashi (1991). Obviously, many other similar studies are needed before realistic parameterizations become suitable for climate studies.

Acknowledgements. We are grateful to J.-F. Gayet for providing microphysical data from the MERLIN aircraft. We would also like to thank U. Hargens for providing microwave data from the RV Poseidon ship. We thank Dr. K. Shine and Dr. E. Raschke for their very helpful comments and suggestions. This work has been supported by the Direction des Recherches, Etudes et Techniques under contract 87-181 and was part of the International Cirrus Experiment supported by European Economic Community. Topical Editor, H. le Treut thanks Dr. E. Raschke and an anonymous referee for their help in refereeing this paper.

References

Busygin, V. P., N. A. Yevstratov, and E. M. Feigelson, Optical properties of cumulus and radiant fluxes for cumulus cloud cover, *Izv. Atmos. Ocean Phys.*, **9,** 1142–1151, 1973.

Cahalan ,R. F., and J. H. Joseph, Fractal statistics of cloud fields, *Mon. Weather. Rev.*, **117,** 261–272, 1989.

Cess, R. D., G. L. Potter, J. P. Blanchet, G. J. Boer, A. D. Del Genio, M. Deque, V. Dymnikov, V. Galin, W. L. Gates, S. J. Ghan, J. T. Kiehl, A. A. Lacis, H. le Treut, Z. X. Li, X. Z. Liang, B. J. McAvaney, V. P. Meleshko, J. F. B. Mitchel, J. J. Morcrette, D. A. Randall, L. Rikus, E. Roeckner, J. F. Royer, U. Schlese, D. A. Sheinin, A. Slingo, A. P. Sokolov, K. E. Taylor, W. M. Washington, R. T. Wetherald, I. Yagai, and M. H. Zhang, Intercomparison and interpretation of climate feedback processes in 19 atmospheric general circulation models, *J. Geophys. Res.*, **95,** 16601–16616, 1990.

Coakley, J. A., and T. Kobayashi, Broken cloud biases in albedo and surface isolation derived from satellite imagery data, *J. Climate*, **2,** 721–730, 1989.

Crétel, D., M. Herman, and D. Tanré, Fluxes and directional effects for broken clouds, *Proc. of the IRS'88,* Lille, France, International Association of Meteorology and Atmospheric Physics, 95–98, 1988.

Devaux, C., Contribution à l'étude de la couverture nuageuse de Vénus par l'analyse des mesures photométriques et des profils de flux solaires transmis, *Ph. D. thesis,* University of Sciences and Technologies of Lille, France, 1977.

Duvel, J. P., and R. S. Kandel, Anisotropy of longwave radiation emergent from a broken cloud field and its effect on satellite estimates of flux, *J. Climate Appl. Meteor.*, **23,** 1411–1420, 1984.

Ellingson, R. G., On the effects of cumulus dimensions on longwave irradiance and heating rate calculations, *J. Atmos. Sci.*, **39,** 886–896, 1982.

Falconer, K. J., *The Geometry of Fractal Sets,* Cambridge University Press, 1985.

Fenn, R. W., S. A. Clough, W. O. Gallery, R. E. Good, F. X. Kneizys, J. D. Mill, L. S. Rothman, E. P. Shettle, and F. E. Volz, in Handbook of Geophysics and the Space Environment, Ed., A. S. Jursa, AFGL, 1985.

Fouquart, Y., and B. Bonnel, Computations of solar heating of the Earth's atmosphere: A new parametrization, *Contrib. Atmos. Phys.*, **53,** 35–62, 1980.

Fouquart, Y., J. C. Buriez, M. Herman, and R. S. Kandel, The influence of clouds on radiations: A climate modeling perspective, *Rev. Geophys.*, **28,** 145–166, 1990.

Gayet, J. F., G. Febvre, P. Wendling, P. Moerl, and G. Brogniez, Microphysical and optical properties of cirrus clouds obtained from airborne measurements, *Report of the third ICE Workshop.* Available from Laboratoire d'Optique Atmosphérique, University of Sciences and Technologies of Lille, Villeneuve d'Ascq, France, 1991.

Hale, G., and M. Querry, Optical constants of water in the 200 nm to 200 μm wavelength region, *Appl. Opt.*, **12,** 555–563, 1973.

Hargens, U., C. Simmer, E. Ruprecht, and M. Schrader, Microwave remote sensing of cloud liquid water during ICE'89, *Report of the third ICE Workshop.* Available from Laboratoire d'Optique Atmosphérique, University of Sciences and Technologies of Lille, Villeneuve d'Ascq, France, 1991.

Harshvardhan, and J. A. Weinman, Infrared radiative transfer through a regular array of cuboïdal clouds, *J. Atmos. Sci.*, **39,** 431–439, 1982.

Hozumi K., T. Harimaya, and C. Magono, The size distribution of cumulus clouds as a function of cloud amount, *J. Meteorol. Soc. Jap.*, **60,** 691–699, 1982.

Intergovernmental Panel on Climate Change, report to IPCC from Working Group 1, third draft, 2 May 1990, prepared by the IPCC Group at the Meteorological Office, Bracknell, UK, 1990.

Kite, A., The albedo of broken cloud fields, *Q. J. R. Meteorol. Soc.*, **113,** 517–531, 1987.

Kobayashi, T., Parameterization of reflectivity for broken cloud fields, *J. Atmos. Sci.*, **45,** 3034–3045, 1988.

Kobayashi, T., Reflected solar flux for horizontally inhomogeneous atmospheres, *J. Atmos. Sci.*, **48,** 2436–2447, 1991.

Kuo, K. S., R. M. Welch, and S. K. Sengupta, Structural and textural characteristics of cirrus clouds observed using high spatial resolution Landsat imagery, *J. Appl. Meteorol.*, **27,** 1242–1260, 1988.

le Treut, H., 'Cloud prediction experiments with the LMD GCM', *Report of the ECMWF Workshop on Cloud Cover Parameterization in Numerical Models,* 65–86, ECMWF Publications, Reading, England, 1985.

le Treut H., and Z. X. Li, Sensitivity of an atmospheric general circulation model to prescribed SST changes: feedback effects assciated with the simulation of cloud optical properties, *Clim. Dyn.*, **5,** 175–187, 1991.

McClatchey, R. A., R. W. Fenn, J. E. A. Selby, F. E. Volz, and J. S. Garing, Optical properties of the atmosphere, *AFCRL 71-0279,* Air Force Cambridge Research Laboratories, Envir. Res. Papers, Bedford, Mass., 85, 1971.

McKee, T. B., and S. K. Cox, Scattering of visible radiation by finite clouds, *J. Atmos. Sci.*, **31,** 1885–1892, 1974.

Morcrette, J. J., Sur la parametrisation du rayonnement dans les modèles de la circulation générale atmosphérique, *Ph. D. thesis*, University of Sciences and Technologies of Lille, France, 1984.

Niylisk, Kh. Yu., Cloud Characteristics in problems of radiation energitics in the earth's atmosphere. *Izv. Acad. Sci. USSR, Atmos. Oceanic Phys.*, **8,** 270–281, 1972.

Planck, V., The size distribution of cumulus clouds in representative Florida populations, *J. Appl. Meteorol.*, **8,** 46–67, 1969.

Raschke, E., J. Schmetz, J. Heintzenberg, R. Kandel, and R. Saunders, The International Cirrus Experiment (ICE) - A Joint European Effort, *ESA Journal*, **14,** 193–199, 1990.

Roeckner, E., and U. Schlese, 'January simulation of clouds with a prognostic cloud cover scheme', *Report of the ECMWF Workshop on Cloud Cover Parameterization in Numerical Models*, 87–108, ECMWF Publications, Reading, England, 1985.

Schlesinger, M.E., and J. F. B. Mitchell, Model projections of equilibrium climatic response to increased CO_2 concentration, in *Projecting the Climatic Effects of Increasing Carbon Dioxide*, Ed. M. C. McCracken and F. M. Luther, U. S. Department of Energy, Washington, D. C., 1986.

Scorer, R., *Cloud Investigation by Satellite*, Ellis Horwood, Chichester, 1986.

Stephens, G. L., and T. J. Greenwald, The Earth's radiation budget and its relation to atmospheric hydrology. 2. Observations of cloud effects, *J. Geophys. Res.*, **96,** 15325–15340, 1991.

Stuhlmann R., P. Minnis, and G. L. Smith, Cloud bidirectional reflectance functions: a comparison of experimental and theoretical results, *Appl. Opt.*, **24,** 396–401, 1985.

Sundqvist, H., Inclusion of cloud liquid water as a prognostic variable. *Report of the ECMWF Workshop on Cloud Cover Parameterization in Numerical Models*, 249–262, ECMWF Publications, Reading, England, 1984.

Welch, R. M., and B. A. Wielicki, Stratocumulus cloud field reflected fluxes: The effect of cloud shape, *J. Atmos. Sci.*, **41,** 3085–3103, 1984.

Welch, R. M., and B. A. Wielicki, The stratocumulus nature of fog. *J. Climate Appl. Meteor.*, **25,** 101–111, 1986.

Welch, R. M., K. S. Kuo, B. A. Wielicki, S. K. Sengupta, and L. Parker, Marine stratocumulus cloud fields off the coast of Southern California observed using Landsat imagery. Part I: Structural characteristics, *J. Applied Meteorol.*, **27,** 341–362, 1988.

Wendling, R., Albedo and reflected radiance of horizontally inhomogeneous clouds, *J. Atmos. Sci.*, **34,** 642–650, 1977.

Wielicki, B. A., and R. M. Welch, Cumulus cloud properties derived using Landsat satellite data, *J. Climate Appl. Meteor.*, **25,** 261–276, 1986.

World Climate Research Program WCP-55, Report of WMO (CAS)/Radiation commission of IAMAP meeting of experts on aerosols and their climatic effects (Williamsburg, Virginia, USA), 1983

Ann. Geophysicae 13, 108–110 (1995) © EGS – Springer-Verlag 1995

Annales Geophysicae

Letter to the Editor

On the validity of the plane-parallel approximation for cloud reflectances as measured from POLDER during ASTEX

J. Descloitres, F. Parol, J. C. Buriez

Laboratoire d'Optique Atmosphérique, Université des Sciences et Technologies de Lille, Villeneuve d'Ascq, France

Received: 1 August 1994/Accepted: 24 October 1994

Abstract. The POLDER instrument provides multidirectional radiance measurements in the visible and near-infrared range and thus allows to measure the anisotropy of the reflected solar radiation. As a result POLDER allows to investigate the validity of the usual plane-parallel approximation for cloud reflectances. The airborne instrument was flown over stratocumulus clouds in the Azores region during June 1992. The bidirectional reflectances of overcast scenes have been analyzed. These scenes are not similar to homogeneous plane-parallel layers but their bidirectional reflectances compare favorably with those of heterogeneous plane-parallel layers within 2 - 3 %.

1 Introduction

Clouds are commonly treated as homogeneous plane-parallel layers in the modeling of their effects on climate in general circulation models and in the derivation of cloud properties from satellite radiances as in ISCCP (International Cloud Climatology Project ; Rossow and Schiffer, 1991). This plane-parallel assumption is known to be a major weakness in the estimate of the effect of clouds on radiation (e.g., see the review by Fouquart *et al.*, 1990). However, only few comparisons have been made between observations of cloud bidirectional reflectances and calculations based on radiative transfer theory. For example, such comparisons were made by Davis and Cox (1982) from airborne multidetector measurements and by Stuhlmann *et al.* (1985) from Nimbus 7 and GOES data.

POLDER (POLarization and Directionality of the Earth's Reflectances) is a new instrument devoted to the global observation of the polarization and directionality of the solar radiation reflected by the Earth surface-atmosphere system (Deschamps *et al.*, 1994). It provides quasi-simultaneous multidirectional radiance measurements of a given target, and thus gives a new opportunity to measure the anisotropy of the reflected solar radiation. In this context, POLDER seems to be quite suitable for investigating the impact of the usual plane-parallel approximation on cloud bidirectional reflectances. POLDER has been selected to fly on board the Japanese ADEOS payload scheduled for launch in 1996. This paper reports on cloud bidirectional reflectances measured by the airborne simulator during the ASTEX-SOFIA campaign (Weill *et al.*, 1994).

2 Data

POLDER was flown aboard the French ARAT aircraft over stratocumulus clouds in the Azores region during June 1992. The airborne instrument includes a wide field-of-view lens, a rotating wheel carrying 9 spectral and polarizing filters and a CCD array of 384 x 288 detectors. In order to reduce both the data flow and the radiometric noise, the resolution is degraded to 10 x 10 pixels. The angular coverage extends over ± 51° in the along-track direction and ± 42° in the cross-track direction. Angular deviations due to the pitch and roll of the aircraft are taken into account. The radiometer measures the radiances in 5 channels from 0.44 µm to 0.91 µm. The multi-polarization capability of POLDER has already been analyzed (Goloub *et al.*, 1994). Here, we focus on its multi-angle viewing capability and make use of the bidirectional reflectance measurements at 0.86 µm without polarization.

The flight on 12 June 1992 has been selected because it includes two legs, more than 150 km long, above a solid stratocumulus cloud deck. The cloud top altitude is 1 km. The two legs provide respectively 185 and 175 images of about 9 km x 7 km. The aircraft altitude is 4.5 km. Its displacement between two successive acquisitions of POLDER data is close to 0.9 km. The solar zenith angle varies from 37° to 33° along the first leg and from 29° to 27° along the second leg. The mean reflectance value is 0.58. Although the whole scene appears rather homogeneous from a visual inspection, the values of bidirectional reflectance vary from 0.20 to 0.90 along a leg; they typically vary within ± 0.15 over a single image.

3 Comparison between observed and modeled reflectances

The observed cloud bidirectional reflectances are compared to computations of bidirectional reflectances performed using the discrete ordinate method (Stamnes *et al.*, 1988). The ocean surface is modeled following Cox and Munk (1956). The effect of standard aerosols (World Climate Programme, 1986) and molecules is included. The cloud is assumed to be a plane-parallel layer composed of spherical water drops with an effective radius of 10 μm (Hansen and Travis, 1974) as in the ISCCP algorithm.

Because the POLDER instrument samples a large part but not the whole of the viewing angles, we define a pseudo-albedo as

$$\alpha(\mu_0) = \iint_\Omega R(\mu_0, \mu, \phi)\mu d\mu d\phi \Big/ \iint_\Omega \mu d\mu d\phi \;, \quad (1)$$

where the integration is over the solid angle Ω limited by the instrument field-of-view. R represents the bidirectional reflectance, μ_0 is the cosine of the solar zenith angle, μ is the cosine of the viewing zenith angle and ϕ is the relative azimuth angle, which is measured with respect to the principal plane, such that the azimuthal coordinate of the sun is at $\phi = 0°$.

Comparison image by image

Typical patterns of the observed and modeled reflectances, $R(\mu_0,\mu,\phi)$ and $R_{pp}(\mu_0,\mu,\phi)$ respectively, are reported on Fig. 1 (compare a to b and c to d). For each image, the cloud optical thickness is adjusted so that the plane-parallel pseudo-albedo is equal to the observed one, i.e.

$$\alpha_{pp}(\mu_0) = \alpha(\mu_0) \,. \quad (2)$$

The backscatter maximum and the cloudbow are well recognizable on the modeled reflectances but hardly distinguishable on the observed ones. The global difference between the plane-parallel approximation and the measurements can be characterized by the relative weighted root mean square difference defined as

$$S = \frac{1}{\alpha(\mu_0)} \left(\frac{\iint_\Omega \left[R_{pp}(\mu_0, \mu, \phi) - R(\mu_0, \mu, \phi)\right]^2 \mu d\mu d\phi}{\iint_\Omega \mu d\mu d\phi} \right)^{\frac{1}{2}} . \quad (3)$$

The histogram of the 360 values of S is reported on Fig. 2. This r.m.s. difference is typically 10 % ; it is always greater than 4 % and may increase up to 18 %. Note that more heterogeneous scenes observed during other flights exhibit much larger values of S.

A part of this r.m.s. difference may be related to (i) our algorithm and (ii) the limits of the POLDER instrument. Practically, the radiative transfer code is run off-line to calculate reflectances as a function of viewing/illumination geometry and cloud optical thickness. It results a table from which the reflectances are interpolated for the particular conditions. Nevertheless, the r.m.s. error introduced by these interpolations remains less than 0.2 %. The influence of the fixed drop size distribution has been estimated from theoretical simulations with an effective radius of 6 μm instead of 10 μm ; it results a r.m.s. error of 1.0 %.

The POLDER calibration was performed in laboratory. The estimated accuracy in absolute reflectance is about 5 % and the pixel-to-pixel intercalibration accuracy is 0.5 %. Simulations show that a global error of 5 % for the whole of the reflectances induces only a value of S of 0.4 %. Summing quadratically the uncertainties due to both the algorithm and the instrument gives a total r.m.s. error of 1.2 %. Therefore, the r.m.s. difference S expected from POLDER data in the "perfect" plane-parallel case is clearly less than 4 %.

Not surprising, the 9 km x 7 km images of stratocumulus clouds are not similar to images of homogeneous plane-parallel cloud layers.

Comparison to averaged images

In fact, variations in bidirectional reflectance observed in a single POLDER image are related to both the anisotropy of the reflected radiation from the site and the fact that each detector of the CCD matrix sees a different geographic target. In order to remove the last effect, two different approaches are considered. First, a series of successive images along a flight leg is averaged. The bidirectional

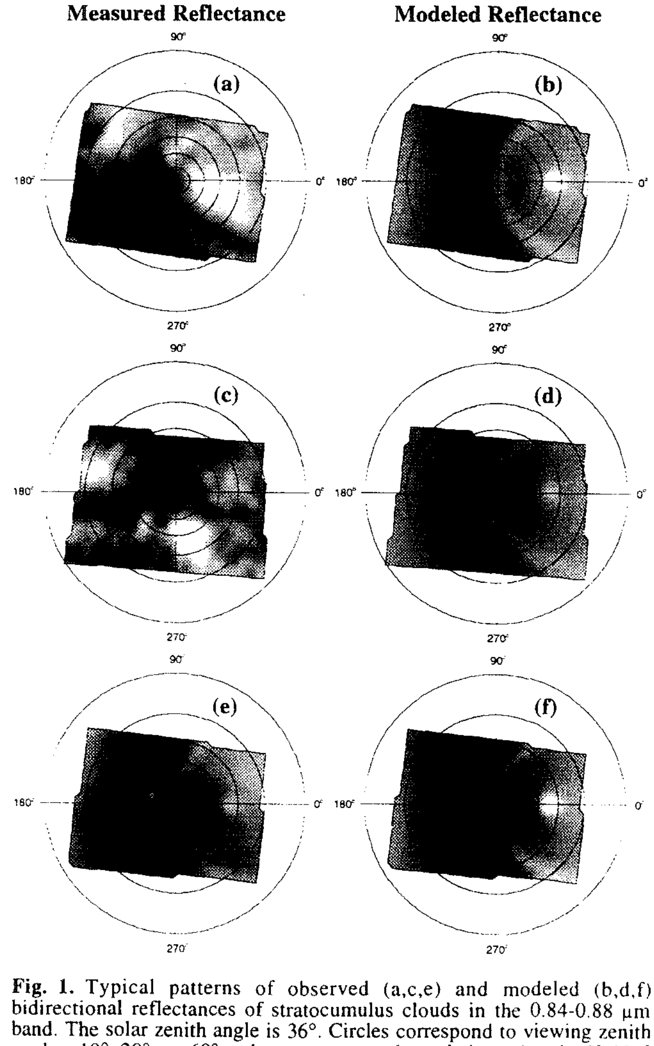

Fig. 1. Typical patterns of observed (a,c,e) and modeled (b,d,f) bidirectional reflectances of stratocumulus clouds in the 0.84-0.88 μm band. The solar zenith angle is 36°. Circles correspond to viewing zenith angles 10°, 20°, ..., 60° and axes correspond to relative azimuths 0°-180° and 90°-270°. The reflectance grey scale varies from 0.62 to 0.74 for (a,b), from 0.46 to 0.64 for (c,d), and from 0.55 to 0.65 for (e,f). Each of the sets (a,b) and (c,d) corresponds to a single image (image number 552 and 613 respectively), while the set (e,f) corresponds to an average of 100 images (image number 531 to 630). The r.m.s. difference between the measurements and the plane-parallel approximation is 6.3 % for (a,b), 13.5 % for (c,d) and 2.2 % for (e,f).
Note that the outline is not so rectangular as the CCD array because of the resolution degraded to 10 x 10 pixels and the geometric correction related to the aircraft attitude.

reflectance of the scene is now defined as

$$R(\mu_0,\mu,\phi)=\frac{1}{N}\sum_{i=1}^{N}R_i(\mu_0,\mu,\phi)\ , \qquad (4)$$

where N is the number of images, $R_i(\mu_0,\mu,\phi)$ is the bidirectional refectance value on the image i for a given viewing geometry.

We made 34 averages of 100 consecutive POLDER images by using a sliding average method along each leg, each time shifting the beginning of the sequence of 5 images. A typical pattern is reported on Fig. 1 (compare c to f). Now, the backscatter maximum and the cloudbow clearly appear on the averaged observations. The histogram of the new differences S obtained from Eqs. (4) and (1)-(3) is reported on Fig. 2. This r.m.s. difference ranges from 1.3 % to 3.2 %. The lower value is thus very close to the expected r.m.s. error related to the algorithm and the instrument.

Comparison target by target

Thus, a stratocumulus cloud deck appears not similar to a *homogeneous* plane-parallel layer but acts *on an average* as a plane-parallel layer. Therefore, in a second approach, we consider a horizontally inhomogeneous cloud as composed of parts of plane-parallel layers. Since POLDER observes any geographical target with 9 viewing angles, the 9 bidirectional reflectances of every target are compared to a plane-parallel model. To do that, the POLDER pixels are related to the corresponding geographic coordinates at the cloud top level. The deviation from the plane-parallel approximation is now characterized for every target by the relative r.m.s. difference of reflectances defined by

$$S'=\left(\frac{1}{9}\sum_{j=1}^{9}\left[R_{pp}(\mu_0,j)-R(\mu_0,j)\right]^2\right)^{\frac{1}{2}}\Bigg/\left(\frac{1}{9}\sum_{j=1}^{9}R(\mu_0,j)\right), \qquad (5)$$

where the index j refers to the viewing direction.

This r.m.s. difference is typically 2 % (see Fig. 2). It is quite good despite the difficulty to locate the POLDER pixels onto a geographic grid.

4 Conclusion

Although selected for its rather homogeneous aspect, the observed stratocumulus deck is not similar to a *homogeneous* plane-parallel cloud layer over areas of 9 x 7 km^2. Nevertheless, it acts *on an average* as a plane-parallel layer and compares favorably with a set of *various* plane-parallel layers. That can be considered as a validation of the ISCCP approach for such a cloud type.

The r.m.s. difference between the observed and the modeled reflectances is typically 2-3 %, both from an average of a hundred images and from a target-by-target comparison. In the present state of art, this difference is quite comparable to the uncertainty of an instantaneous measurement of the bidirectional reflectance at the top of the Earth's atmosphere. Barkstrom *et al.*(1990) report an accuracy of 2-3 % for instantaneous observations of shortwave radiance from ERBE (Earth Radiation Budget Experiment) instruments. A calibration accuracy of 2-3 % is also expected for the satellite version of POLDER.

For the averaged bidirectional reflectances, the lower deviation from the plane parallel approximation is 1.3 %. It is very close to the expected r.m.s. error related to the algorithm and the instrument.

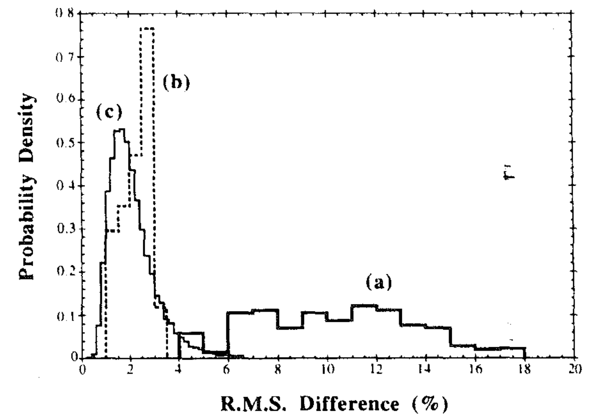

Fig. 2. Histogram of the relative r.m.s. difference between the observed reflectances and the plane parallel approximation.
(a) comparison image by image (360 images)
(b) comparison to averaged images (34 averages)
(c) comparison target by target (35000 targets).

Those results lead us to be confident in the multi-angle viewing capability of POLDER to help verifying the validity of radiative transfer modeling over a large range of conditions in an early future.

Acknowledgements. This work has been supported by the European Economic Community and the Centre National d'Etudes Spatiales. The authors are very grateful to F. Lemire for processing the POLDER data.

References

Barkstrom, B.R., E.F. Harrison and R.B.Lee, Earth Radiation Budget Experiment. Preliminary seasonal results, *EOS*, **71**, 297-305, 1990.

Cox, C., and W. Munk, Slopes of the sea surface deduced from photographs of sun glitter, *Bull. Scripps Int. Oceanogr. Univer. Califor.*, **6**, 401-488, 1956.

Davis, J.M., and S.K. Cox, Reflected solar radiances from regional scale scenes, *J. Appl. Meteor.*, **21**, 1698-1712, 1982.

Deschamps, P.Y., F.M. Breon, M. Leroy, A. Podaire, A. Bricaud, J.C. Buriez and G. Seze, The POLDER mission: Instrument characteristics and scientific objectives, *IEEE Trans. Geosci. Rem. Sens*, **32**, *598-615*, 1994.

Fouquart, Y., J.C. Buriez, M. Herman, and R.S. Kandel, The influence of clouds on radiation : A climate modeling perspective, *Rev. Geophys.*, **28**, 145-166, 1990.

Goloub, P., J.L. Deuzé, M. Herman and Y. Fouquart, Analysis of the POLDER polarization measurements performed over cloud covers, *IEEE Trans. Geosci. Rem. Sens.*, **32**, 78-88, 1994.

Hansen, J.E., and L.D. Travis, Light scattering in planetary atmospheres, *Space Sci. Rev.*, **16**, 527-610, 1974.

Rossow, W.B, and R.A. Schiffer, ISCCP cloud data products, *Bull. Amer. Meteor. Soc.*, **6**, 2394- 2418, 1991.

Stamnes, K., S.C. Tsay, W. Wiscombe and K. Jayaweera, Numerically stable algorithm for discrete-ordinate-method radiative transfer in multiple scattering and emitting layered media, *Appl. Opt.*, **12**, 2502-2509, 1988.

Stuhlmann, R., P. Minnis, and L. Smith, Cloud bidirectional reflectance functions: a comparison of experimental and theoretical results, *Appl. Opt.*, **24**, 396-401, 1985.

Weill, A., F. Baudin, H. Dupuis, L. Eymard, J.P. Frangi, E. Gerard, P. Durand, B. Benech, J. Dessens, A. Druilhet, A. Rechou, P. Flamant, S. Elouragini, R. Valentin, G. Seze, J. Pelon, C. Flamant, J.L. Brenguier, S. Planton, J. Rolland, A. Brisson, P. Le Borgne, A. Marsouin, T. Moreau, K. Katsaros, R. Monis, P. Queffeulou, J. Tournadre, P.K. Taylor, E. Kent, R. Pascal, P. Schibler, F. Parol, J. Descloitres, J.Y. Balois, M. Andre and M. Charpentier, SOFIA 1992 experiment during ASTEX. *The Atmosphere Ocean-System* , in press, 1994.

World Climate Programme, A preliminary cloudless standard atmosphere for radiation computation, *Rep. WCP-112*, 53 pp., Radiation Commission, Boulder, Co, 1986.

JOURNAL OF GEOPHYSICAL RESEARCH, VOL. 103, NO. D10, PAGES 11,411–11,418, MAY 27, 1998

POLDER observations of cloud bidirectional reflectances compared to a plane-parallel model using the International Satellite Cloud Climatology Project cloud phase functions

J. Descloitres,[1] J. C. Buriez, F. Parol, and Y. Fouquart

Laboratoire d'Optique Atmosphérique, Université des Sciences et Technologies de Lille, Villeneuve d'Ascq, France

Abstract. This study investigates the validity of the plane-parallel cloud model and in addition the suitability of water droplet and ice polycrystal phase functions for stratocumulus and cirrus clouds, respectively. To do that, we take advantage of the multidirectional viewing capability of the Polarization and Directionality of the Earth's Reflectances (POLDER) instrument which allows us to characterize the anisotropy of the reflected radiation field. We focus on the analysis of airborne-POLDER data acquired over stratocumulus and cirrus clouds during two selected flights (on April 17 and April 18, 1994) of the European Cloud and Radiation Experiment (EUCREX'94) campaign. The bidirectional reflectances measured in the 0.86 μm channel are compared to plane-parallel cloud simulations computed with the microphysical models used by the International Satellite Cloud Climatology Project (ISCCP). Although clouds are not homogeneous plane-parallel layers, the extended cloud layers under study appear to act, on average, as a homogeneous plane-parallel layer. The standard water droplet model (with an effective radius of 10 μm) used in the ISCCP analysis seems to be suitable for stratocumulus clouds. The relative root-mean-square difference between the observed bidirectional reflectances and the model is only 2%. For cirrus clouds, the water droplet cloud model is definitely inadequate since the rms difference rises to 9%; when the ice polycrystal model chosen for the reanalysis of ISCCP data is used instead, the rms difference is reduced to 3%.

1. Introduction

Because of their multiple interactions with radiation in the Earth's surface-atmosphere system, clouds play an important role in the Earth radiation budget and consequently have a strong impact on the climate. In order to improve the estimate of their influence on the evolution of the climate, recent general circulation models predict the cloud condensed water content and then derive radiative properties of clouds [e.g., *Cess et al.*, 1996]. However, a small variation in cloud characteristics could have a large influence on the evolution of the climate [*Senior and Mitchell,* 1993]. Consequently, there is a clear need of long-term observations of the Earth radiation balance and cloud properties. In this way, the International Satellite Cloud Climatology Project (ISCCP) has been designed to establish a climatology of cloud properties at the global scale [*Rossow and Schiffer*, 1991].

One of the most significant cloud parameters used to determine the cloud-radiation interactions is the cloud optical thickness, which is directly related to the cloud particle size distribution and the condensed water path. Programs like ISCCP try to retrieve the cloud optical thickness from satellite measurements of visible radiances. In practice, all radiometers so far are based on the same principle of a single detector plus a scanning mechanism which allows us to observe a target from only one single direction per overpass. However, the radiation outgoing from any target depends on the angle of observation. To compensate for the lack of observation of this angular dependence, one has to provide additional information. In ISCCP, this is done by assuming that the clouds are plane-parallel layers with a prescribed cloud particle size distribution; under these conditions, the radiative transfer theory predicts the angular dependence of the reflected radiation. If the model is wrong, the relationship between the radiance observed in the satellite direction and the optical thickness is inadequate and the retrieval fails. The magnitude of the corresponding error depends on the cloud type as well as on the conditions of observation and illumination.

The angular dependence of the reflected solar radiation can be characterized by the cloud bidirectional reflectance

$$\rho_\nu(\mu_0,\mu,\varphi) = \frac{\pi L_\nu(\mu_0,\mu,\varphi)}{\mu_0 E_{0\nu}}, \tag{1}$$

where μ_0 is the cosine of the solar zenith angle, μ is the cosine of the viewing zenith angle, φ is the relative azimuth angle measured with respect to the solar plane, $L_\nu(\mu_0,\mu,\varphi)$ is the upward radiance at wavenumber ν in the viewing direction (μ,φ), and $\mu_0 E_{0\nu}$ is the incident solar flux.

Only few direct observations of cloud bidirectional reflectance have been compared to radiation fields calculated using the plane-parallel cloud model. *Davis and Cox* [1982] constructed empirical cloud models from airborne multidetector

[1]Now at Department of Geography, University of Maryland, College Park.

Paper number 98JD00592.
0148-0227/98/98JD-00592$09.00

measurements. They compared their altostratus cloud model to plane-parallel simulations. They obtained a rather good agreement in the solar plane except in the backward direction. *Stuhlmann et al.* [1985] also constructed empirical cloud models but from Nimbus 7 Earth Radiation Budget (ERB) and Geostationary Operational Environmental Satellite (GOES) data. Their comparison between theoretical and empirical models showed a rather good agreement, about 10% for solar zenith angles lower than 70°. *Descloitres et al.* [1995] used the Polarization and Directionality of the Earth's Reflectances (POLDER) airborne simulator during the Atlantic Stratocumulus Transition Experiment (ASTEX). They found that the bidirectional reflectances of a solid stratocumulus cloud deck compare favorably (within 2-3%) with those of plane-parallel layers composed of liquid water drops. *Spinhirne et al.* [1996] used the Tilt Scan CCD Camera (TSCC) radiometer during the First ISCCP Regional Experiment (FIRE II) to measure the bidirectional reflectance of cirrus clouds in the solar plane. They compared their observations to plane-parallel cloud model calculations based on various cloud phase function models. The measured angular reflectance pattern was flatter than predicted by the models. The agreement of measurements with the liquid water model was very poor. A better agreement was obtained for a phase function derived by *Takano and Liou* [1989] for cirrostratus ice crystal columns, but in some cases a simple Henyey-Greenstein phase function gave better comparison, although the authors did not conclude that this phase function was generally appropriate or superior to the ice column model. The aim of this study is to contribute to such comparisons, using POLDER airborne simulator data acquired over extended stratocumulus and cirrus clouds during the European Cloud and Radiation Experiment (EUCREX'94) [*Raschke et al.*, 1998], which is the continuation of the International Cirrus Experiment (ICE) [*Raschke et al.*, 1990]. Indeed, the multidirectional viewing capability of the POLDER instrument allows us to observe a part of the bidirectional reflectance distribution function (BRDF) of any scene. It is thus possible to investigate the validity of the plane-parallel cloud model and in addition the suitability of water droplet and ice polycrystal phase functions for stratocumulus and cirrus clouds, respectively. More particularly, the two phase functions routinely used in the ISCCP scheme [*Rossow et al.*, 1996] will be considered.

The POLDER data used in this study are described in section 2. A method for constructing BRDFs representative of the observed cloud types is presented in section 3. Then, in section 4, observations are compared to simulations based on the cloud microphysics used in the ISCCP scheme. Conclusions are given in section 5.

2. Data

POLDER is an instrument designed and built by the Laboratoire d'Optique Atmosphérique (LOA) and the Centre National d'Etudes Spatiales, France (CNES). It is devoted to the global observation of polarization and directionality of the solar radiation reflected by the Earth's surface-atmosphere system. The instrument was launched in August 1996 aboard the Japanese Advanced Earth Observing Satellite (ADEOS) platform. One of the scientific objectives of the satellite mission concerns the cloud characteristics: BRDF, optical thickness, pressure, and phase. Here we limit our study to the cloud bidirectional reflectance measured in the 0.86 μm channel of the airborne POLDER simulator and the cloud optical thickness retrieved from those measurements.

Figure 1. Schematic representation of the observational mode of POLDER. As the aircraft moves between successive acquisitions of POLDER, a given target appears on several locations on the charge-coupled device array detector under different viewing angles. Two observations (at time t_1 and t_2) of a target are represented; θ_1 and θ_2 are the corresponding viewing zenith angles.

During the EUCREX campaign in April 1994, POLDER was flown over stratocumulus and cirrus clouds aboard the German Falcon of the Deutsche Forschungsanstalt für Luft und Raumfahrt (DLR). The western part of Brittany, over the Atlantic Ocean, had been chosen for the aircraft missions. This paper focuses on two flights performed on the afternoon of April 17, 1994, and on the morning of April 18, 1994, corresponding to visually extended thick cirrus and stratocumulus cloud layers, respectively.

On April 17, the meteorological analysis indicated a high-pressure system located over the North Atlantic Ocean, Ireland, and England. A low was centered on southern France, spreading from Spain to northern Italy. One day before (April 16), this low was located northeast of Europe. It was connected to another cyclonic depression centered north of Iceland and Sweden, making the jet stream stronger and leading cold polar air over northern Europe. That resulted in the formation of a wide cirrus cloud deck throughout the experimental area on April 17. The cloud top was located between 9 km and 10 km, say, at a temperature of 220 K. The cloud base was around 6 km at a temperature of about 250 K. Microphysical measurements lead to an effective radius of equivalent spherical particles around 24 μm [*Sauvage et al.*, 1998]. The hereafter reported data have been acquired at flight altitude of 10,700 m.

On April 18, air from the northeast entered the experimental area between a ridge of high pressure centered east of Ireland and a low located over central Europe; this resulted in wide stratocumulus fields throughout the English Channel, over western France, and in the Bay of Biscay. The cloud depth was only 200 m, but the stratocumulus was optically thick. The cloud top height was varying from 800 m to 1100 m. The aircraft flight altitude was 3050 m.

The POLDER instrument is composed of a charge-coupled device (CCD) array detector, a rotating wheel which carries spectral and polarizing filters, and a wide field of view lens (see *Deschamps et al.* [1994] for further details). The instrument field of view of the airborne simulator extends up to ± 52° in the along-track direction and ± 42° in the cross-track direction. Angular deviations due to the pitch and roll of the aircraft are taken into account. The CCD array is composed of 288 x 242 pixels. Considering the typical aircraft-cloud relative altitude, it corresponds to a scene of 9 km x 7 km for low-level clouds and 2.2 km x 1.8 km for high-level clouds; the respective spatial resolution of the instrument is 25 m and 8 m. However, the resolution is degraded to 10 x 10 pixels in order to reduce both the data flow and the measurement noise. Therefore the typical size of a cloud target is 250 m for low-level clouds and 80 m for high-level clouds. The aircraft displacement between two successive acquisitions of POLDER is around 1 km.

An original feature of POLDER is its ability to provide multidirectional reflectance measurements of any scene. As illustrated in Figure 1, a given target is seen under several viewing directions. The number of directions depends on the aircraft speed and the aircraft-cloud relative altitude. Typically, it was 9 directions for low-level clouds and 2 for high-level clouds during EUCREX'94. Figure 2 presents an example of POLDER images acquired over a stratocumulus cloud deck. The same geographical target appears several times on this set of images but at different locations on the CCD array; that means this target is observed under different viewing angles. For instance, in Figure 2, the same hole is clearly seen on the images number 85 and 90 (dark part of the images). However, directional effects like the backscatter spot appear at the same location (at bottom right) on all images.

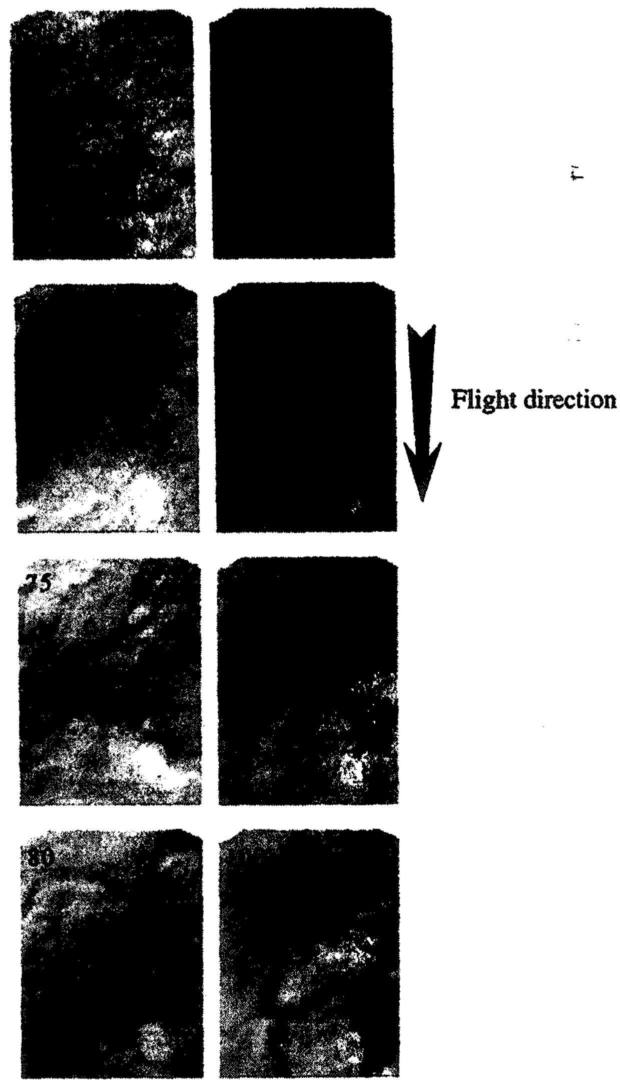

Figure 2. Example of POLDER images acquired during the European Cloud and Radiation Experiment (EUCREX'94) (mission 206, April 18, 1994, images 65-100) over a stratocumulus cloud deck off the coast of Brittany, France. Every fifth image of the sequence is reported. The gray shading corresponds to reflectance values varying from 0 to 1.0.

3. Methodology

In order to analyze the anisotropy of the radiation reflected by the observed clouds, a first possible approach is based on the fact that any geographical target is observed under several (typically 9 for low-level clouds) viewing angles. The POLDER pixels can be related to geographical coordinates at the cloud level, and then a given target can be located on successive images. For each target, the set of measured values of bidirectional reflectance can be compared to the plane-parallel model at the corresponding viewing angles.

Another approach consists in analyzing the bidirectional reflectance over the whole field of view of POLDER. Indeed, if a cloudy scene observed by POLDER were perfectly homogeneous, a single image could be considered as a cloud BRDF pattern limited to the solid angle Ω corresponding to the instrument field of view. In fact, each detector of the CCD array sees a different part of the cloud. It results that variations in bidirectional reflectance are due both to the anisotropy of the radiation reflected by the scene and to the horizontal variations in optical thickness from one cloud target to another within the instrument field of view. In order to remove the last effect and to characterize the anisotropy itself, the simplest approach consists in averaging a sequence of successive images. The BRDF pattern of the average image is then considered as the BRDF pattern of one equivalent target representative of the scene.

Descloitres et al. [1995] applied both approaches to POLDER data acquired during ASTEX above a stratocumulus cloud deck. Not surprisingly, the results obtained from averaged images and from the target-by-target method were quite similar; in both cases, the rms difference between the observed and the modeled reflectances was about 2-3%. Indeed, averaging whole images along a flight leg is equivalent to constructing one BRDF pattern from the measured bidirectional reflectances of all the targets of the leg.

The target-by-target method presents some limitations. When the cloud top height varies a lot along a flight leg, the altitude of a target becomes uncertain, and thus it is difficult to locate targets on successive images. Moreover, the number of viewing angles for each target decreases drastically as the cloud top height draws near to the aircraft level; it is reduced to 2 directions for high-level clouds observed from the Falcon. Therefore we chose the simple average method, in order to present both a stratocumulus case and a cirrus case with the same method.

For the average BRDF calculation, we define the average bidirectional reflectance of a series of images as

$$\langle\rho\rangle_N(\mu_0,\mu,\varphi) = \frac{1}{N}\sum_{i=1}^{N}\rho_i(\mu_0,\mu,\varphi), \quad (2)$$

where N is the number of averaged images and $\rho_i(\mu_0,\mu,\varphi)$ is the bidirectional reflectance value of the image i. We also define the average pseudoalbedo $\bar{\alpha}_N(\mu_0)$ of the series of images,

$$\bar{\alpha}_N(\mu_0) = \frac{\iint_\Omega \langle\rho\rangle_N(\mu_0,\mu,\varphi)\,\mu\,d\mu\,d\varphi}{\iint_\Omega \mu\,d\mu\,d\varphi}, \quad (3)$$

where the integration is over the solid angle Ω limited by the instrument field of view.

The average BRDF pattern obtained with (2) can actually be considered as representative of one scene if each detector of the CCD array sees a similar distribution of targets. In other words, the scene can be very inhomogeneous, but each pixel must see the same variability. In a first step, when averaging successive images, we assume their number N becomes sufficiently large when the averaged BRDF becomes stationary, that is, the difference between $\langle\rho\rangle_{N-1}$ and $\langle\rho\rangle_N$ tends toward zero. Therefore we define a variability rate as

$$\zeta(N,N-1) = \frac{1}{\bar{\alpha}_N(\mu_0)} \times \left(\frac{\iint_\Omega [\langle\rho\rangle_N(\mu_0,\mu,\varphi) - \langle\rho\rangle_{N-1}(\mu_0,\mu,\varphi)]^2\,\mu\,d\mu\,d\varphi}{\iint_\Omega \mu\,d\mu\,d\varphi}\right)^{\frac{1}{2}}. \quad (4)$$

The variability rate decreases more or less quickly as N increases, according to the repetitivity of cloud inhomogeneities along the flight leg. From the inspection of various observations, a threshold of 0.5% was chosen for $\zeta(N,N-1)$. This threshold is reached after averaging a few tens of images typically (see Figure 3). However, the analysis of many POLDER observations shows that this criterion is sometimes insufficient to obtain a BRDF pattern representative of one scene. Indeed, the average BRDF can remain asymmetric in relation to the principal plane when a singular target with an exceedingly high or low reflectance is seen under a limited range of viewing directions. In that case, the distribution of observed targets differs from one viewing angle to another over the whole field of view. Thus we define an azimuthal asymmetry rate by

$$\xi(N) = \frac{1}{2\,\bar{\alpha}_N(\mu_0)} \times \left(\frac{\iint_\Omega [\langle\rho\rangle_N(\mu_0,\mu,\varphi) - \langle\rho\rangle_N(\mu_0,\mu,-\varphi)]^2\,\mu\,d\mu\,d\varphi}{\iint_\Omega \mu\,d\mu\,d\varphi}\right)^{\frac{1}{2}}, \quad (5)$$

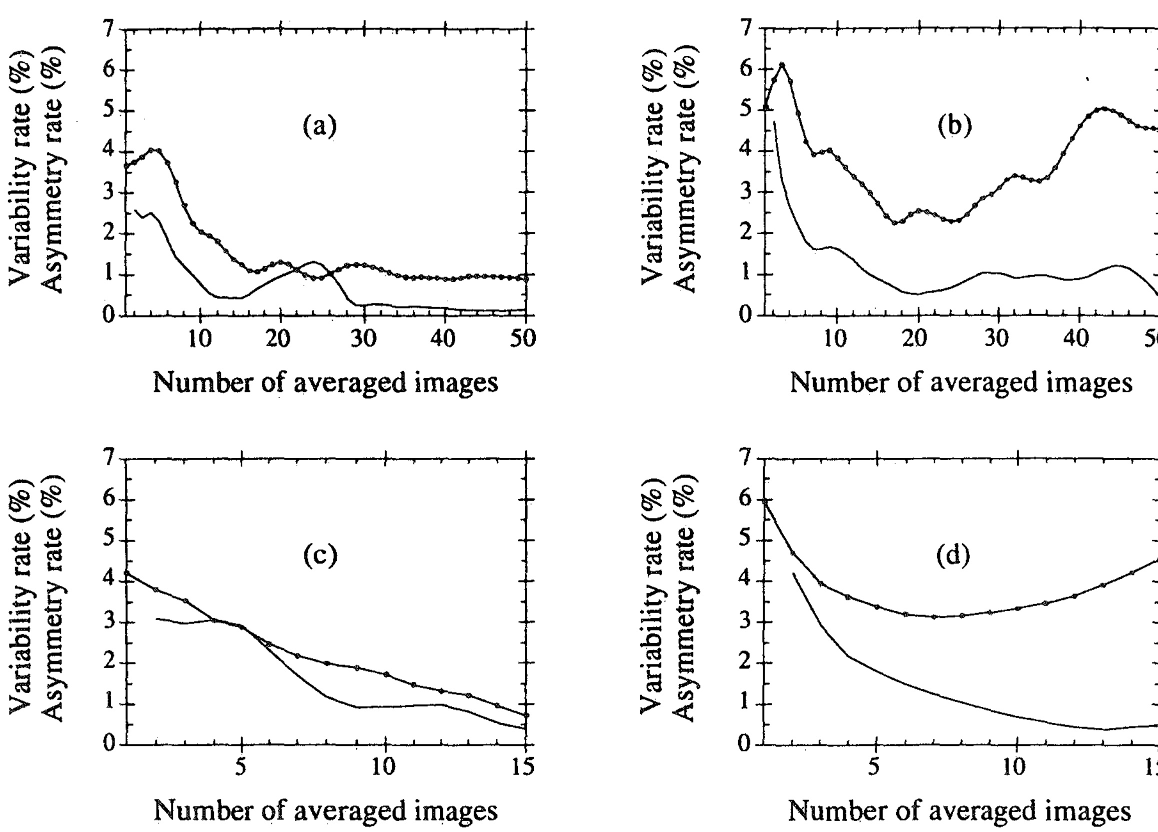

Figure 3. Variability (solid curve) and asymmetry (dotted curve) rates as a function of the number of averaged images for different cloud types observed from POLDER. Sequences corresponding to a stratocumulus cloud (EUCREX, mission 206, April 18, 1994) are shown: (a) images 65-114 and (b) images 116-165. Also sequences corresponding to a cirrus cloud (EUCREX, mission 205, April 17, 1994) are shown: (c) images 723-737 and (d) images 689-703.

which tends toward zero when the mean BRDF becomes symmetric in relation to the principal plane. For two scenes with similar variability rates, different asymmetry rates can be observed (compare Figures 3a to 3b and Figures 3c to 3d).

Practically, N is chosen such as $\zeta(N,N-1)$ is lower than 0.5% and $\xi(N)$ is lower than 1% (sequences shown in Figures 3a and 3c can be retained, whereas sequences in Figures 3b and 3d are rejected). Under these conditions, the anisotropy of the radiation reflected by an inhomogeneous scene is well characterized since the noise related to differences between the distribution of observed targets from one viewing direction to another is expected to be reduced to about 1%. Note that, because of the asymmetry rate criterion, scenes where the structure of cloud inhomogeneities depends on a particular direction (e.g., cloud streets) are excluded from this study.

4. Results

The cloud BRDF patterns measured from POLDER have been compared to computations of bidirectional reflectance based on the plane-parallel approximation. These calculations have been performed by using the discrete ordinate method [*Stamnes et al.*, 1988]. The ocean surface is modeled following *Cox and Munk* [1956]. The effect of standard aerosols [*World Climate Programme*, 1986] and molecules is taken into account. The clouds are assumed to be homogeneous plane-parallel layers composed of the same particles as in the new ISCCP cloud analysis procedure [*Rossow et al.*, 1996]. The microphysical model for liquid water clouds is a gamma distribution of spherical liquid water drops with an effective radius of 10 µm and an effective variance of 0.15 [*Hansen and Travis*, 1974]. In the first ISCCP analysis [*Rossow and Schiffer*, 1991], that model was used for all cloud types. Now, an ice crystal model with a random fractal crystal shape [*Macke*, 1996] is used for high-level clouds; it corresponds to a −2 power law size distribution with an effective radius of 30 µm and an effective variance of 0.10 [*Mishchenko et al.*, 1996]. The respective phase function of the two microphysical models is plotted in Figure 4.

For a sequence of POLDER images, the mean observed reflectance $\langle\rho\rangle_N(\mu_0,\mu,\varphi)$ over N images can be compared to the

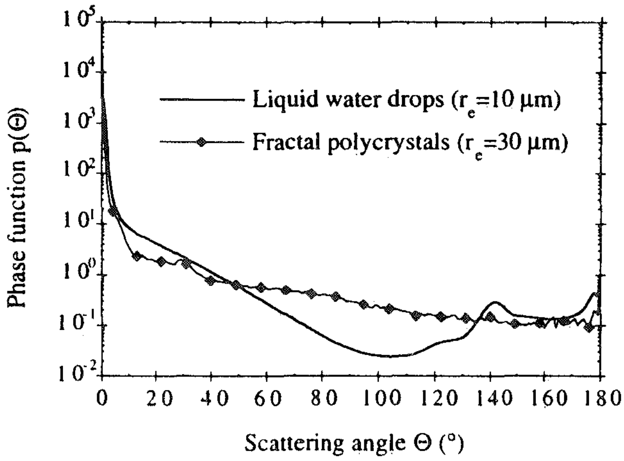

Figure 4. Phase function for a size distribution of liquid water drops (effective radius r_e is 10 µm) and a size distribution of fractal polycrystals (effective radius r_e is 30 µm).

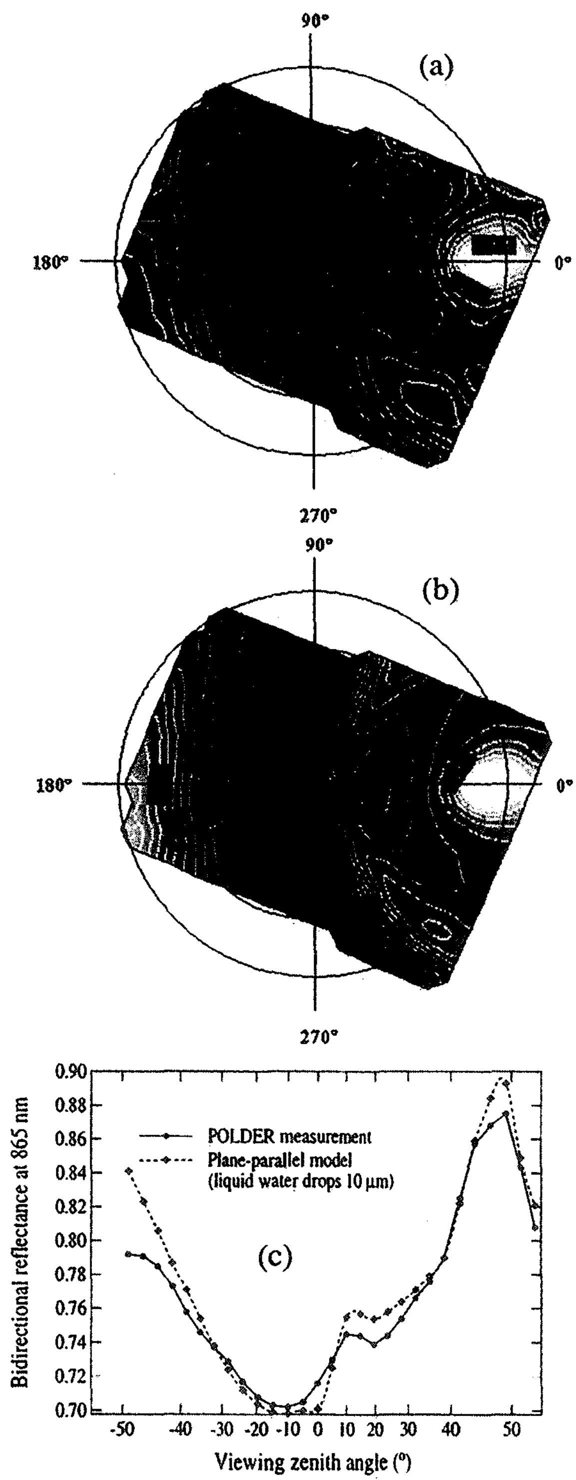

Figure 5. Comparison between (a) the bidirectional reflectance distribution function (BRDF) at 0.86 µm of a stratocumulus cloud observed by POLDER (EUCREX, mission 206, April 18, 1994, images 65-100) and (b) the one of the nearest plane-parallel layer, computed using the International Satellite Cloud Climatology Project (ISCCP) model (spherical drops with r_e equal to 10 µm). The rms difference is σ_{pp} = 1.9%. The concentric circles correspond to viewing zenith angles 10°, 20°, ..., 50° (from inside to outside). Azimuth 0° corresponds to the backscatter direction. (c) The cross section in the principal plane. The positive viewing zenith angles are toward the Sun, and the negative angles are toward the antisolar location. The solar zenith angle is equal to 47°.

modeled reflectance $\rho_{PP}(\mu_0,\mu,\varphi)$ of the nearest plane-parallel model, of which the cloud optical thickness is adjusted so that the plane-parallel pseudoalbedo defined by (3) is equal to the observed one, that is,

$$\tilde{\alpha}_{PP}(\mu_0) = \tilde{\alpha}_N(\mu_0). \tag{6}$$

The discrepancy between the POLDER measurements and the plane-parallel model is characterized by the relative weighted root-mean-square difference $\sigma_{PP}(N)$ defined as

$$\sigma_{PP}(N) = \frac{1}{\tilde{\alpha}_N(\mu_0)} \times \left(\frac{\iint_{\Omega} \left[\langle\rho\rangle_N(\mu_0,\mu,\varphi) - \rho_{PP}(\mu_0,\mu,\varphi) \right]^2 \mu \, d\mu \, d\varphi}{\iint_{\Omega} \mu \, d\mu \, d\varphi} \right)^{\frac{1}{2}}. \tag{7}$$

When considering low-level clouds, some previous results have already shown that the model for liquid water clouds is roughly suitable for stratocumulus clouds observed by POLDER [*Descloitres et al.*, 1995]. Because of horizontal inhomogeneities, they are not homogeneous plane-parallel layers over one single POLDER image, with $\sigma_{PP}(N=1) \sim 10\%$, but they act on average as a homogeneous plane-parallel layer for a sequence of images, with $\sigma_{PP}(N{\sim}50) \sim 2\%$. As illustrated in Figure 5, the results obtained from POLDER measurements of the EUCREX campaign are quite similar to those of the ASTEX campaign, as presented by *Descloitres et al.* [1995]. Particularly, the backscatter peak and the cloudbow are clearly visible on the mean observed BRDF pattern, whereas they are hardly distinguishable on single images (see Figure 2).

With regard to cirrus clouds, scattering by ice crystals is known to be very different from spheres and very sensitive to crystal shapes [e.g., *Takano and Liou*, 1989]. Therefore, as shown in Figure 6, the use of one microphysical model for all clouds in an interpretation of satellite data, as in the first ISCCP algorithm, is a source of strong uncertainties for the retrieved characteristics of ice crystal clouds. For that reason, the fractal polycrystals of *Macke* [1996], which are expected to be representative of irregularly shaped and randomly oriented ice particles, were introduced into the new ISCCP algorithm to model scattering properties of cirrus clouds. As illustrated in Figure 6, a good agreement between that model and the first observations of POLDER over cirrus clouds is observed ($\sigma_{PP}(N{\sim}15) \sim 3\%$), whereas the model for liquid water clouds is definitely inadequate ($\sigma_{PP}(N{\sim}15) \sim 9\%$). In particular, the relative difference between modeled and observed reflectances in the backscatter direction is 4% with the polycrystal model, but it reaches 20% with the droplet model.

When we have one single viewing direction, the optical thickness must be retrieved from that single radiance measurement, as in ISCCP, for example; clearly some error can be expected from the dependence of the retrieval on the available viewing direction. To illustrate the additional information given by the multidirectional capability of POLDER, Figure 6 also compares the cloud optical thickness retrieved from one single direction to the one obtained when using all available viewing directions. The dependence of the retrieved optical thickness on the viewing angle is notably reduced with the ice polycrystal model as compared to the water droplet model.

5. Conclusion

The airborne measurements of POLDER clearly illustrate the importance of multidirectional observations to estimate errors when cloud properties are retrieved by using the plane-parallel assumption. Although clouds are not homogeneous plane-parallel layers, the extended cloud layers observed by the airborne version of POLDER during the EUCREX campaign appear to act on average as a homogeneous plane-parallel layer.

As given by *Descloitres et al.* [1995], the standard water droplet model (with an effective radius of 10 µm) used in the ISCCP analysis seems to be suitable for stratocumulus clouds. The relative root-mean-square difference between the observed bidirectional reflectances and the model is only 2%. This rms difference is hardly reduced when the effective radius is changed to obtain a better fit.

With regard to ice crystal clouds, the POLDER observations underline the need of a phase discrimination in the analysis of satellite data. Furthermore, we found an encouraging agreement between our first measurements over cirrus clouds and the polycrystal model used in the new ISCCP algorithm. For ice crystal clouds, the water droplet model is definitely inadequate since the relative root-mean-square difference between modeled and observed bidirectional reflectances rises to 9%. When the polycrystal model is used instead, the difference is reduced to 3%. However, we cannot conclude that the polycrystal model is generally appropriate for all the cirrus clouds.

The suitability of the plane-parallel cloud model does not imply that the retrieved cloud optical thickness is accurate. *Cahalan et al.* [1994] have considered a fractal cloud model which simulates the horizontal variability observed in marine stratocumulus clouds. They found that the cloud albedo is approximated properly by a plane-parallel model having an optical thickness typically 30% smaller than the actual mean optical thickness. Therefore the cloud optical thickness derived from a plane-parallel model has to be considered as an "effective" optical thickness. The suitability of the plane-parallel model to our measurements over stratocumulus clouds suggests that the net horizontal photon transport can be ignored at the observed scale (250 m). In other words, the independent pixel approximation is valid for that resolution, since the mean reflectance of a distribution of cloud targets is very close to the plane-parallel model. Thus the break in the scaling properties of stratocumulus cloud scenes, which appears generally around 200-400 m [*Davis et al.*, 1997], would be below 250 m in the present case study.

Our analysis was restricted to extended thick clouds. Features similar to those here reported were obtained from the other flights made over extended thick stratocumulus clouds during ASTEX and EUCREX experiments. However, the cirrus case analyzed in this paper is a rare case of extended thick high-level cloud observed by the POLDER airborne simulator. Therefore the conclusions about the plane-parallel model concern neither the broken stratocumulus clouds nor the whole of high-level clouds. The spaceborne version of POLDER should allow us to perform similar comparisons between observed and modeled bidirectional reflectances at extended scale, using a target-by-target method. Operational algorithms have been developed in this way [*Buriez et al.*, 1997]. So we hope it will be possible to quantify the validity of the plane-parallel approximation at the global scale.

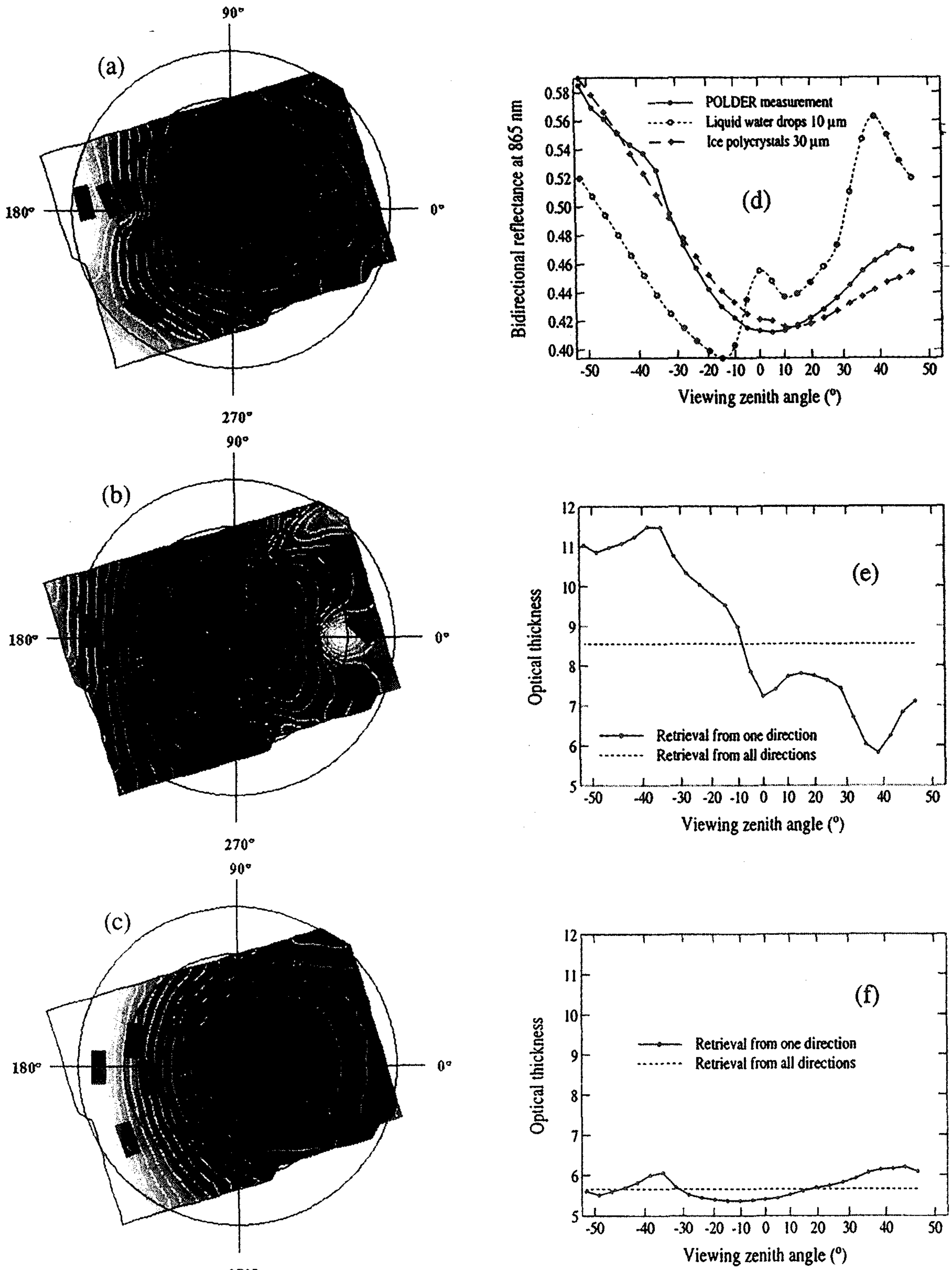

Figure 6. Comparison between (a) the bidirectional reflectance distribution function (BRDF) at 0.86 µm of a cirrus cloud observed by POLDER (EUCREX, mission 205, April 17, 1994, images 725-737) and the one of the nearest plane-parallel layer, computed using the ISCCP model for (b) liquid water clouds and (c) ice crystal clouds (fractal polycrystals with r_e equal to 30 µm). The rms difference σ_{PP} is 8.3% for liquid water clouds and 2.8% for ice crystal clouds. (d) The cross section in the principal plane. The optical thickness which would be retrieved using one single radiance measurement, compared to the one retrieved using the whole field of view, is shown, corresponding (e) to the water droplet phase function and (f) to the ice crystal phase function. The positive viewing zenith angles are toward the Sun, and the negative angles are toward the antisolar location. The solar zenith angle is equal to 38°.

Acknowledgments. This work was supported by the European Economic Community (EEC) and the Centre National d'Etudes Spatiales (CNES). The authors are grateful to F. Lemire for his help in processing the POLDER data. They thank A. Macke and M. Mishchenko for providing useful information about the polycrystal phase function. Pr. E. Raschke is acknowledged for his leading activity in EUCREX.

References

Buriez, J. C., C. Vanbauce, F. Parol, P. Goloub, M. Herman, B. Bonnel, Y. Fouquart, P. Couvert, and G. Seze, Cloud detection and derivation of cloud properties from POLDER, *Int. J. Remote Sens.*, *18*, 2785-2813, 1997.

Cahalan, R. F., W. Ridgway, W. J. Wiscombe, S. Gollmer, and Harshvardhan, Independent pixel and Monte Carlo estimates of stratocumulus albedo, *J. Atmos. Sci.*, *51*, 3776-3790, 1994.

Cess, R. D., et al., Cloud feedback in atmospheric general circulation models: An update, *J. Geophys. Res.*, *101*, 12,791-12,794, 1996.

Cox, C., and W. Munk, Slopes of the sea surface deduced from photographs of Sun glitter, *Bull. Scripps Int. Oceanogr.*, *6*, 401-488, 1956.

Davis, J. M., and S. K. Cox, Reflected solar radiances from regional scale scenes, *J. Appl. Meteorol.*, *21*, 1698-1712, 1982.

Davis, A., A. Marshak, R. Cahalan, and W. Wiscombe, The Landsat scale break in stratocumulus as a three-dimensional radiative transfer effect: Implications for cloud remote sensing, *J. Atmos. Sci.*, *54*, 241-260, 1997.

Deschamps, P. Y., F. M. Bréon, M. Leroy, A. Podaire, A. Bricaud, J. C. Buriez, and G. Sèze, The POLDER mission: Instrument characteristics and scientific objectives, *IEEE Trans. Geosci. Remote Sens.*, *32*, 598-615, 1994.

Descloitres, J., F. Parol, and J. C. Buriez, On the validity of the plane-parallel approximation for cloud reflectances as measured from POLDER during ASTEX, *Ann. Geophys.*, *13*, 108-110, 1995.

Hansen, J. E., and L. D. Travis, Light scattering in planetary atmospheres, *Space Sci. Rev.*, *16*, 527-610, 1974.

Macke, A., Single scattering properties of atmospheric ice crystals, *J. Atmos. Sci.*, *53*, 2813-2825, 1996.

Mishchenko, M. I., W. B. Rossow, A. Macke, and A. A. Lacis, Sensitivity of cirrus cloud albedo, bidirectional reflectance and optical thickness retrieval accuracy to ice particle shape, *J. Geophys. Res.*, *101*, 16,973-16,985, 1996.

Raschke, E., J. Schmetz, J. Heintzenberg, R. Kandel, and R. Saunders, The International Cirrus Experiment (ICE) - A joint European effort, *Eur. Space Agency J.*, *14*, 193-199, 1990.

Raschke, E., P. Flamant, Y. Fouquart, P. Hignett, H. Isaka, P. Jonas, and H. Sundqvist, Cloud-radiation studies during the European Cloud and Radiation Experiment (EUCREX), *Surv. Geophys.*, in press, 1998.

Rossow, W. B., and R. A. Schiffer, ISCCP cloud data products, *Bull. Am. Meteorol. Soc.*, *72*, 2-20, 1991.

Rossow, W. B., A. W. Walker, D. E. Beuschel, and M. D. Roiter, International Satellite Cloud Climatology Project (ISCCP): Documentation of new cloud data sets, *WMO/TD 737*, 115 pp., World Meteorol. Organ., Geneva, 1996.

Sauvage, L., H. Chepfer, V. Trouillet, P. H. Flamant, G. Brogniez, J. Pelon, and F. Albers, Remote sensing of Cirrus radiative parameters during EUCREX'94: Case study of 17 April 1994, 1, Observations, *Mon. Weather. Rev.*, in press, 1998.

Senior, C. A., and J. F. B. Mitchell, Carbon dioxide and climate: The impact of cloud parameterization, *J. Clim.*, *6*, 393-418, 1993.

Spinhirne, J. D., W. D. Hart, and D. L. Hlavka, Cirrus infrared parameters and shortwave reflectance relations from observations, *J. Atmos. Sci.*, *53*, 1438-1458, 1996.

Stamnes, K., S. C. Tsay, W. Wiscombe, and K. Jayaweera, Numerically stable algorithm for discrete-ordinate method radiative transfer in multiple scattering and emitting layered media, *Appl. Opt.*, *27*, 2502-2509, 1988.

Stuhlmann, R., P. Minnis, and G. L. Smith, Cloud bidirectional reflectance functions: A comparison of experimental and theoretical results, *Appl. Opt.*, *24*, 396-401, 1985.

Takano, Y., and K. N. Liou, Solar radiative transfer in cirrus clouds, I, Single scattering and optical properties of hexagonal ice crystals, *J. Atmos. Sci.*, *46*, 3-19, 1989.

World Climate Programme, A preliminary cloudless standard atmosphere for radiation computation, *Rep. WCP-112*, 53 pp., Radiat. Comm., Boulder, Colo., 1986.

J. C. Buriez, Y. Fouquart, and F. Parol, Laboratoire d'Optique Atmosphérique, Université des Sciences et Technologies de Lille, 59655 Villeneuve d'Ascq, France. (e-mail: Jean-Claude.Buriez@univ-lille1.fr; Yves.Fouquart@univ-lille1.fr; Frederic.Parol@univ-lille1.fr.)

J. Descloitres, NASA Goddard Space Flight Center, Code 922, Greenbelt, MD 20771. (e-mail: jack@ltpmail.gsfc.nasa.gov)

(Received March 31, 1997; revised February 12, 1998;
accepted February 17, 1998.)

Tellus (2000), 52B, 888–908
Printed in UK. All rights reserved

TELLUS
ISSN 0280–6509

Cloud optical thickness and albedo retrievals from bidirectional reflectance measurements of POLDER instruments during ACE-2

By FRÉDÉRIC PAROL*, JACQUES DESCLOITRES‡ and YVES FOUQUART, *Laboratoire d'Optique Atmosphérique, Université des Sciences et Technologies de Lille, Villeneuve d'Ascq, France*

(Manuscript received 2 February 1999; in final form 8 October 1999)

ABSTRACT

The POLDER instrument is devoted to global observations of the solar radiation reflected by the Earth–atmosphere system. The airborne version of the instrument was operated during the ACE-2 experiment, more particularly as a component of the CLOUDYCOLUMN project of ACE-2 that was conducted in summer 1997 over the subtropical northeastern Atlantic ocean. CLOUDYCOLUMN is a coordinated project specifically dedicated to the study of the indirect effect of aerosols. In this context, the airborne POLDER was assigned to remote measurements of the cloud optical and radiative properties, namely the cloud optical thickness and the cloud albedo. This paper presents the retrievals of those 2 cloud parameters for 2 golden days of the campaign 26 June and 9 July 1997. Coincident spaceborne ADEOS-POLDER data from 2 orbits over the ACE-2 area on 26 June are also analyzed. 26 June corresponds to a pure air marine case and 9 July is a polluted air case. The multidirectional viewing capability of airborne POLDER is here demonstrated to be very useful to estimate the effective radius of cloud droplet that characterizes the observed stratocumulus clouds. A 12 μm cloud droplet size distribution appears to be a suitable cloud droplet model in the pure marine cloud case study. For the polluted case the mean retrieved effective droplet radius is of the order of 6–10 μm. This only preliminary result can be interpreted as a confirmation of the indirect effect of aerosols. It is consistent with the significant increase in droplet concentration measured in polluted marine clouds compared to clean marine ones. Further investigations and comparisons to in-situ microphysical measurements are now needed.

1. Introduction

One of the major uncertainties in the determination of the climate sensitivity to human perturbations is the lack of understanding of the feedbacks associated with cloudiness changes and the difficulty for GCMs to correctly take into account cloud–radiation–climate interactions (Cess et al., 1990, 1996; Senior and Mitchell, 1993). The magnitude of the radiative cloud forcing is significant (see for instance Harrison et al., 1990) and a slight variation of cloud characteristics could have a strong influence on the evolution of the climate. Consequently, GCMs need a realistic representation of cloud properties and their effects on radiation budget at global and regional scale. Global observations are essential to achieve this objective.

Of course, the most comprehensive way to obtain global cloud observations is by means of spaceborne measurements. Nevertheless, airborne

* Corresponding author address: Laboratoire d'Optique Atmosphérique, Université des Sciences et Technologies de Lille, UFR de Physique, Bât. P5, 59655 Villeneuve d'Ascq Cedex, France.
e-mail: frederic.parol@univ-lille1.fr
‡ Present affiliation: University of Maryland, Department of Geography, College Park, USA.

experiments and ground-based measurements remain essential to support the interpretation of satellite observations. Satellites can directly observe the spatial and temporal variabilities of clouds (Rossow and Schiffer, 1991) and also their effects on Earth's radiation budget at the top of the atmosphere (Ramanathan et al., 1989; Harrison et al., 1990). POLDER (POLarization and Directionality of the Earth's Reflectances) is a component of a series of new sensors that may provide key information to improve our knowledge of clouds, radiation and climate interactions (Buriez et al., 1997; Parol et al., 1999). The next generation of satellite instruments such as CERES (Cloud and the Earth's Radiant Energy System) (Wielicki and Barkstrom, 1991), MODIS (Moderate Resolution Imaging Spectrometer) (King et al., 1992), MISR (Multi-angle Imaging SpectroRadiometer) (Diner et al., 1998), POLDER will play a crucial rôle in helping to better understand clouds and their influence on the Earth's radiation balance.

One of the most significant cloud parameters used to determine the cloud–radiation interactions is the cloud optical thickness, which is directly related to the cloud droplet size distribution and the condensed water path (Fouquart et al., 1990). Projects as ISCCP (International Cloud Clymatology Project, Rossow and Schiffer, 1991) try to retrieve the cloud optical thickness from satellite measurements of visible radiance. They make the crude assumption of plane-parallel cloud layers with a prescribed cloud droplet size distribution. Thus the interpretation of satellite observations is based on both macrophysical and microphysical hypotheses. Numerous studies have derived the cloud optical thickness from remote sensing measurements using the plane-parallel approximation, but only few direct observations of cloud bidirectional reflectance have been compared to radiation fields calculated using the plane-parallel model (Davis and Cox, 1982; Stuhlmann et al., 1985; Baldwin and Coakley, 1991; Descloitres et al., 1995; Spinhirne et al., 1996; Descloitres et al., 1998).

This paper contains preliminary results related to such comparisons within the framework of the CLOUDYCOLUMN component (Brenguier et al., 2000) of the North Atlantic Regional Aerosol Characterisation Experiment (ACE-2). ACE-2 was the third experiment coordinated by the International Global Atmospheric Chemistry Project (IGAC) that addresses atmospheric aerosol properties relevant to radiative forcing and climate. ACE-2 was conducted from 15 June to 31 July 1997 over the sub-tropical north-eastern Atlantic Ocean, with the base of operations in the Canary Islands (Raes et al., 2000; Verver et al., 2000). The present study has been conducted using data from both the spaceborne version of POLDER and the airborne simulator of the instrument. The multidirectional viewing capability of the POLDER instrument allows to observe a part of the Bidirectional Reflectance Distribution Function (BRDF) of any cloud scene. The BRDF is the angular distribution of radiances upcoming from the cloud layer. A direct integration of the BRDF over the hemispherical solid angle 2π provides the true cloud albedo. However POLDER can instantaneously measure reflectances only in a limited number of view directions (up to ~ 14) while albedo calculation requires reflectances from all angles. An alternate method is applied that derives cloud optical thickness from measured bidirectional reflectance using the plane-parallel approximation. The plane-parallel model is then used again to derive the cloud albedo from that retrieved optical thickness. However the multidirectional measurement capability of POLDER offers a new perspective to this procedure. POLDER also enables to test the validity of the hypotheses (on cloud macrophysics and microphysics) used to determine the cloud optical thickness. This paper illustrates this new perspective. A feasibility study is presented that shows that the multiangular capability of the airborne POLDER can be useful to infer an approximate value of the cloud water drop size.

Both POLDER instruments and respective data are described in Section 2. The method for analyzing the angular dispersion of POLDER data is presented in Section 3. Sections 4 and 5 present the cloud properties, cloud amount, optical thickness, and albedo, derived from airborne POLDER data and coincident spaceborne ADEOS-POLDER data respectively. The original contribution of POLDER with respect to these products is emphasized. Airborne POLDER data acquired over the ACE-2 region on 2 golden days of the campaign 26 June and 9 July 1997, and coincident spaceborne POLDER data from 2 ADEOS orbits over the Atlantic Ocean and Europe on 26 June

1997 are analyzed. Results are summarized and discussed in Section 6.

2. The POLDER instrument and data

POLDER is a multispectral visible radiometer/polarimeter devoted to observations of polarization and directionality of solar radiation reflected by the Earth's surface–atmosphere system. The instrument concept is simple and very similar to a camera. POLDER is composed of a 2-dimensional charge-coupled device (CCD) detector array, a rotating wheel carrying spectral and polarizing filters, and a wide field of view telecentric optics (see Deschamps et al., 1994, for further details).

2.1. The satellite data

The spaceborne version of POLDER is a CNES (the French Space Agency) instrument which flew aboard the Japanese ADEOS (ADvanced Earth Observing Satellite) polar orbiting platform between August 1996 and June 1997, including the first couple of weeks of the ACE-2 experiment. ADEOS is on a sun-synchronous orbit at an altitude of 797 km. The along-track and cross-track fields of view of POLDER extend up to $\pm 42°$ and $\pm 52°$ respectively. Thanks to POLDER's large swath width ($\sim$2200 km), each point on the Earth is observed almost every day, and 4 days out of 5 near the equator. The CCD sensor array is composed of 242×274 pixels. The ground size of a POLDER pixel aboard ADEOS is (6×7) km^2 at nadir. As the ADEOS satellite passes over a scene, up to 14 successive measurements are made in 8 narrow spectral bands ranging from 0.44 µm to 0.91 µm. The POLDER level-1 products routinely processed by CNES consist of calibrated radiances and Stokes parameters projected on a reference equal-area global grid at 6.2 km resolution. There are no onboard calibration sources and the POLDER in-flight radiometric calibration is based on terrestrial targets (Hagolle et al., 1999).

One of the scientific objectives of the satellite mission relates to the Earth radiation budget and cloud characteristics (hereafter noted as "ERB & clouds"): BRDF, cloud fraction, optical thickness, pressure, and phase (Buriez et al., 1997; Vanbauce et al., 1998; Parol et al., 1999). The level-2 and 3 "ERB & clouds" products provide cloud properties averaged over $\sim 56 \times 56$ km^2 "super-pixel" regions ($\sim 9 \times 9$ pixels). The spatial resolution of the super-pixel ($0.5° \times 0.5°$ at the equator) is convenient for comparisons to ISCCP products and to ERB instruments as ScaRaB (Scanner for the Earth Radiation Budget) (Kandel et al., 1994) and CERES (Wielicki and Barkstrom, 1991).

One example of 0.865 µm level-1 radiance acquired by ADEOS-POLDER during the ACE-2 period is shown in Fig. 1. It is a composite image of 0.865 µm reflectance measured along 2 successive ADEOS orbits on 26 June 1997. The image is made using the 8th observation for each pixel, which is practically close to the minimum view angle (POLDER observes a given target under up to 14 view angles). The 8th observation corresponds to view angles ranging from $\sim 5°$ near the swath center to $\sim 65°$ near the edges. The experimental ACE-2 domain approximately covers the image. In this figure clouds appear as bright pixels against a darker ocean background. In spite of the coarse spatial resolution of POLDER (6.2 km), the image clearly shows high variations of cloud structure ranging from scattered cumulus clouds to solid stratocumulus cloud layers.

2.2. The airborne data

During the ACE-2 campaign in Tenerife in June–July 1997, the airborne simulator of POLDER was operated aboard the German Dornier aircraft of the DLR (Deutsche Forschungsanstalt für Luft und Raumfahrt) and was flown over stratocumulus clouds. The field of view of the airborne instrument extends up to $\pm 52°$ in the along-track direction and $\pm 42°$ in the cross-track direction. Its CCD array is composed of 288×242 pixels. Considering the typical aircraft-cloud relative altitude, the field of view of the instrument corresponds to a scene of ~ 4 km $\times$ 3 km (approximately the size of one ADEOS-POLDER pixel). The spatial resolution of the airborne data is ~ 15 m, but it is degraded to 10×10 pixels, in order to reduce both the data flow and the measurement noise. The aircraft motion between 2 successive acquisitions of POLDER is approximately 500 m. Angular deviations due to the pitch and roll of the aircraft are taken into account. The radiometer measures radi-

Fig. 1. ADEOS-POLDER composite image constructed from top of atmosphere reflectance at 0.865 μm for a ~2500 km × 2500 km area of the Atlantic Ocean centered on (28°N, 16°W) corresponding to the ACE-2 region on 26 June 1997 at 11:15 UTC (east orbit) and 12:50 UTC (west orbit). The top right of the image is Spain. Western Africa appears on the east orbit down to latitude ~20°N. The grey scale indicates the minimum and maximum values of observed bidirectional reflectance. The black dots near the inside boarders of these paths are missing data.

ances in 5 channels from 0.44 μm to 0.91 μm. The POLDER calibration is performed in laboratory. The estimated accuracy in absolute reflectance is 5% and the pixel-to-pixel intercalibration accuracy is 0.5%.

Similarly to the satellite version, the airborne POLDER can provide multidirectional reflectance measurements of any scene. A given target is seen under several view directions. The number of directions depends on the aircraft speed and the relative altitude of the aircraft with respect to the cloud top. Typically, it was 15 for stratocumulus clouds observed during ACE-2. Consequently, the same geographical target appears several times on a set of images but at different locations on the CCD matrix (i.e., as many view angles). Fig. 2 illustrates this property of the instrument. It is easy to follow a given target (for instance, a hole in the cloud deck) on a series of successive images. In a cloud scene observed in a single high resolution POLDER image (which is in fact a BRDF limited to the solid angle corresponding to the instrument field of view), variations in bidirectional reflectances are due to both the anisotropy of the radiation coming from the scene and the horizontal variations in optical thickness from a cloud section to another within the instrument field of view (Descloitres et al., 1995). Nevertheless, as seen in Fig. 2, some parts of the observed cloud system are spatially uniform enough to make the

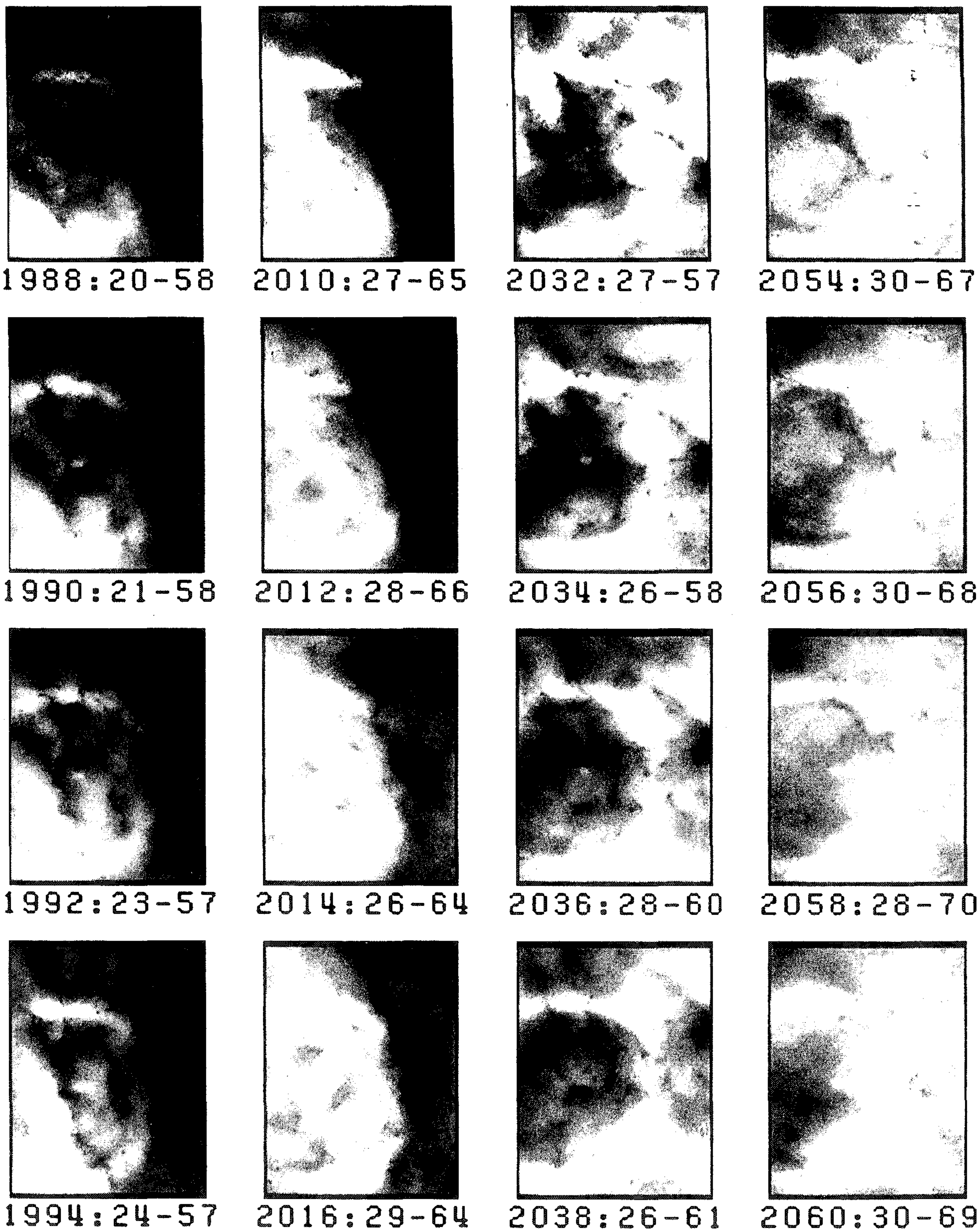

Fig. 2. Series of single 0.865 μm reflectance images acquired by the airborne POLDER on 26 June 1997 approximately 1.5 km above stratocumulus clouds. The image number followed by the bidirectional reflectance range (in percent) corresponding to the grey scale are indicated at the bottom of each image. The grey scale in each panel is stretched from black to white to maximize contrast.

anisotropy effects preponderant: the backscatter peak and the cloudbow (~140° scattering angle) clearly appear on a lot of single images. Note that the cloudbow is a typical feature of clouds composed of liquid water drops.

3. Methodology

Measurements from both the spaceborne version of POLDER and the airborne simulator are used to estimate the angular dependency of cloud optical thickness and albedo retrieved under the plane-parallel approximation. A conventional procedure is applied to estimate the albedo for cloudy scenes. The upward radiance is used to determine the optical thickness, assuming the cloud scene homogeneous. The plane-parallel model is then used to derive the cloud albedo corresponding to the retrieved optical thickness.

In this procedure, the size distribution of cloud water droplets is prescribed and the cloud is assumed to be vertically uniform with respect to that distribution. In these conditions the optical thickness is the only cloud variable. Here, the horizontal dimensions of a cloud scene are $(\sim 150\ \mathrm{m})^2$ and $(6.2\ \mathrm{km})^2$ for the airborne and spaceborne POLDER, respectively. Since cloud scenes are assumed homogeneous (constant geometrical thickness) cloud optical thickness variations are proportional to variations in liquid water content.

3.1. The airborne POLDER

Following the methodology developed by Descloitres et al. (1995, 1996), cloud optical thickness and cloud albedo are estimated from the POLDER reflectance measurements at 0.865 μm, using the so-called "Independent Pixel Approximation" (Cahalan et al., 1994). For each cloud target $(\sim 150\ \mathrm{m})^2$, the bidirectional reflectance set (i.e., ~15 observations) is compared to the plane-parallel model, using the discrete ordinate method (Stamnes et al., 1988). The mean optical thickness of a cloud target is adjusted so that the mean reflectance over the ~15 different view angles equals the plane-parallel one (Descloitres et al., 1995). The corresponding plane-parallel albedo is then derived from the mean retrieved optical thickness. In the plane-parallel model the surface ocean is modeled following Cox and Munk (1956). A prescribed droplet size distribution is used to model clouds.

Descloitres et al. (1995) applied such an approach to airborne POLDER data acquired during the ASTEX campaign above a stratocumulus cloud deck. They showed that, because of horizontal inhomogeneities, the clouds are not homogeneous plane-parallel layers over one single POLDER image, with a rms difference between the observed and the modeled reflectances of approximately 10%. Nevertheless, the clouds compare favorably with a set of various independent plane-parallel layers. In that case the rms difference between observations and calculations is within 2–3%. Descloitres et al. (1998) conclude that the Independent Pixel Approximation is valid for such a spatial resolution since the mean reflectance of a distribution of cloud targets is very close to the plane-parallel model.

Assuming the Independent Pixel Approximation, optical thickness and aldebo can be derived for each cloud target and for each view direction. The angular dispersion of the ~15 retrievals is due to the departure of the POLDER observations from the bidirectional reflectances calculated using the cloud model selected for the inversion. In this paper the angular dispersions are characterized for every target by the relative angular standard deviation defined as the angular standard deviation normalized to the mean value of the cloud property under consideration.

3.2. The spaceborne POLDER

The cloud optical thickness is estimated from the ADEOS-POLDER radiance measurements, using the Independent Pixel Approximation (Buriez et al., 1997). For each cloudy pixel $(6.2\ \mathrm{km})^2$, the bidirectional reflectance is compared to the plane-parallel model, using the discrete ordinate method (Stamnes et al., 1988). For each view angle, the cloud optical thickness is adjusted to make the plane-parallel bidirectional reflectance equal the reflectance observed in this direction. So the cloud optical thickness is determined for each view direction and each pixel. Moreover, in order to make easier the comparison to ISCCP climatology (Rossow and Schiffer, 1991), the cloud optical depth is calculated using the ISCCP liquid water cloud droplet model in the operational processing

(Parol et al., 1999). It is a gamma distribution with an effective radius $r_e = 10$ μm and an effective variance of 0.15 (Hansen and Travis, 1974). The optical thickness is derived at 3 wavelengths (0.443 μm, 0.670 μm, and 0.865 μm) but finally only the value at 0.670 μm is distributed in the level-2 "ERB & clouds" products. The values at 0.443 μm and 0.865 μm are used as indicators of the reliability of the 0.670 μm optical thickness. For each channel (0.443 μm, 0.670 μm, and 0.865 μm) and for each view angle the narrow-band cloud albedo is derived from the retrieved optical thickness. The shortwave broadband albedo is determined for each view angle and estimated from the 3 narrow-band albedoes as explained by Buriez et al. (1997). These "directional" cloud properties are finally averaged at the super-pixel scale, i.e., on a 9×9 pixels area. As for the airborne POLDER retrievals, the angular dispersion is characterized for every super-pixel by the relative angular standard deviation of these ~ 14 values. Moreover the sub-super-pixel information is used to determine the relative spatial standard deviations for each viewing direction. In Section 5 the relative spatial standard deviation of the optical depth is computed for the 6th observation that corresponds to near-nadir viewing conditions for the central part of the orbit path.

In the operational retrieval the relation between the top-of-the-atmosphere reflectance and the cloud optical thickness is dependent on the surface reflectivity. For land pixels, the surface reflectance is obtained from surface parameters previously retrieved from POLDER observations in cloud-free conditions by the POLDER "Land surfaces" processing line (Leroy et al., 1997). For ocean pixels, the surface reflectance is calculated using Cox and Munk's (1956) model.

The plane-parallel approach used in the level-2 "ERB & clouds" operational processing can lead to substantial errors when used to infer cloud optical thickness from actual satellite measurements (Loeb and Coakley, 1998). It may be also a major weakness in the assessment of the effects of clouds on radiation (Parol et al., 1994; Brogniez et al., 1992). Numerous theoretical studies have shown that 3-dimensional and plane-parallel clouds reflect radiation differently (Bréon, 1992; Kobayashi, 1993; Loeb et al., 1997). However, it is hardly possible to derive global cloud properties from space and take into account the effect of cloud morphology on radiation, because of the complexity of the cloud structures and their variability from one cloud type to another. All retrieved "ERB & clouds" parameters are based on simple algorithms in order to be produced operationally. For instance, the cloud optical thickness is derived using the Independent Pixel Approximation. This does not take full advantage of the POLDER capability to observe the radiation field anisotropy. Nevertheless, the cloud parameters derived from POLDER at global scale are a first step to check the validity of the commonly used plane-parallel model. That is examined in Section 5.

4. Airborne POLDER derived cloud properties

During the ACE-2 CLOUDYCOLUMN closure experiment, the German Dornier was devoted to remote sensing above low-level clouds, providing observations at better resolution than satellite images. Coincident in-situ measurements were performed by the French Merlin IV aircraft from Météo-France. This is an opportunity to establish the relationship between microphysics measurements and horizontal variations of cloud properties captured by the POLDER and OVID (Barsch and Bakan, 1993) instruments aboard the Dornier (Brenguier et al., 2000). The aim of this section is to present some examples and analyses of the cloud optical thickness and spectral cloud albedo derived from POLDER reflectances at 0.865 μm for 26 June and 9 July 1997. These 2 days have been selected as golden days of the ACE-2 CLOUDYCOLUMN field project.

4.1. The 26 June 1997 case study

During the ACE-2 mission 02 on 26 June 1997, the Dornier was flown over extended low-level clouds, while quasi-simultaneous in-situ microphysics measurements were performed aboard the Merlin (Brenguier et al., 2000). The stratocumulus was sampled along 30-km legs. The visible and near-infrared channels (as at 0.865 μm) are primarily sensitive to the cloud optical thickness (see for instance Table 2 in Han et al., 1994). The retrieval of cloud optical thickness is thus almost not dependent on the drop size distribution. A gamma size distribution with an effective radius $r_e = 12$ μm and an effective variance of 0.15 is assumed (Hansen and Travis, 1974) to retrieve the optical thickness and derive the corresponding plane-parallel albedo.

The cloud optical thickness and cloud albedo maps of the ~ 30 km $\times$ 3 km scenes, observed from the Dornier along one leg, are reported in Fig. 3. This leg corresponds to the southeast part of the square pattern performed on 26 June. It was sampled from 14:27 to 14:32 UTC. The color scale (from black to red) represents a range of optical thickness from 0 to 4.5 or range of albedo from 0 to approximately 0.28. As expected for this flight mission, the cloud optical thickness values are low, ranging from 4.5 at the East point (point E) to less than 1.0 at the South point (point S) of the leg. As expected for optically thin clouds, the albedo varies almost linearly against the optical depth (see for instance Stephens, 1978; Arking and Childs, 1985). The retrieved albedo decreases from 0.28 at E to approximately 0.05 at S (see Fig. 3b).

In order to check the sensitivity of cloud optical thickness and albedo retrievals to cloud microphysics, the retrieval was also performed using a cloud droplet effective radius of 6 μm. As expected, the retrieved values are only slightly lower and their spatial distribution (not presented here) is obviously very similar to Fig. 3. Indeed, computations show that the relationship between bidirectional reflectance, cloud optical thickness and albedo are almost not dependent on the droplet size (see Section 8).

More interestingly, as already explained in Section 3, the multidirectional capability of POLDER allows to quantify the angular dispersion of the cloud property retrievals. An example of relative angular standard deviation of cloud optical thickness is reported in Fig. 4 for an effective radius of 12 μm and 6 μm.

On the maps in Fig. 4, a greater relative angular standard deviation indicates a less adequate cloud model. As shown in Fig. 4a, when inverting the POLDER reflectances assuming a 12 μm effective radius, a large part of the leg presents relatively low values of relative angular standard deviations, i.e., less than 5–6%. On the contrary, in Fig. 4b the map shows a wide central band with very high values. As noted in Subsection 2.2 and shown in Fig. 2, this part of the POLDER images is sometimes observed in view conditions that correspond to strong anisotropic features like the backscatter maximum and the cloudbow ($\sim 140°$ scattering angle).

Fig. 5 compares observed and calculated variations of the cloud bidirectional reflectance against the view angle in the principal plane. The relative azimuth angle ϕ is measured with respect to the principal plane, so that the azimuthal coordinate of the sun (backscatter direction) is $\phi = 0°$. For all plots in the principal plane presented in this paper, positive zenith angles correspond to relative azimuth $\phi = 0°$, while negative correspond to $\phi = 180°$. The plane-parallel simulations reported in Fig. 5 are made for 2 different sizes of cloud droplets, namely 6 μm and 12 μm. The observed bidirectional reflectance curve corresponds to the average of 100 consecutive images along the leg under investigation. As given by Descloitres et al. (1995), this procedure removes the noise due to cloud heterogeneity across the POLDER CCD array. The observed peak located around view zenith angle $-20°$ corresponds to the cloudbow (scattering angle $\sim 140°$) and the second one more intense observed at view zenith angle 20° in our case is the backscattered radiation (scattering angle 180°). As illustrated in this figure, the angular distribution of the simulated bidirectional reflectance is highly sensitive to the cloud microphysics in the observable domain of scattering angles. In the cloud optical thickness retrieval from POLDER measurements, the optical thickness of the plane-parallel model is adjusted to make the modeled reflectance match the average observed reflectance (0.182 for the present case). However, the angular distribution of the plane-parallel bidirectional reflectance may still be very different from the observed one. The smoothness of the angular distribution depends on the cloud droplet size. The smaller the droplet size, the broader the peaks. In addition, the relative amplitude of the 2 peaks is also highly sensitive to the droplet size. The relative angular standard deviation of the retrieved cloud optical thickness (and of the retrieved cloud albedo) can significantly increase if the selected cloud droplet model is inadequate (Fig. 4).

In Fig. 6, 2 cloud droplet models were used to retrieve the cloud optical thickness from reflectance measurements in the solar plane. This angular optical thickness is compared to the one retrieved using the whole field-of-view of the instrument (2.56 for $r_e = 6$ μm and 2.97 for $r_e =$

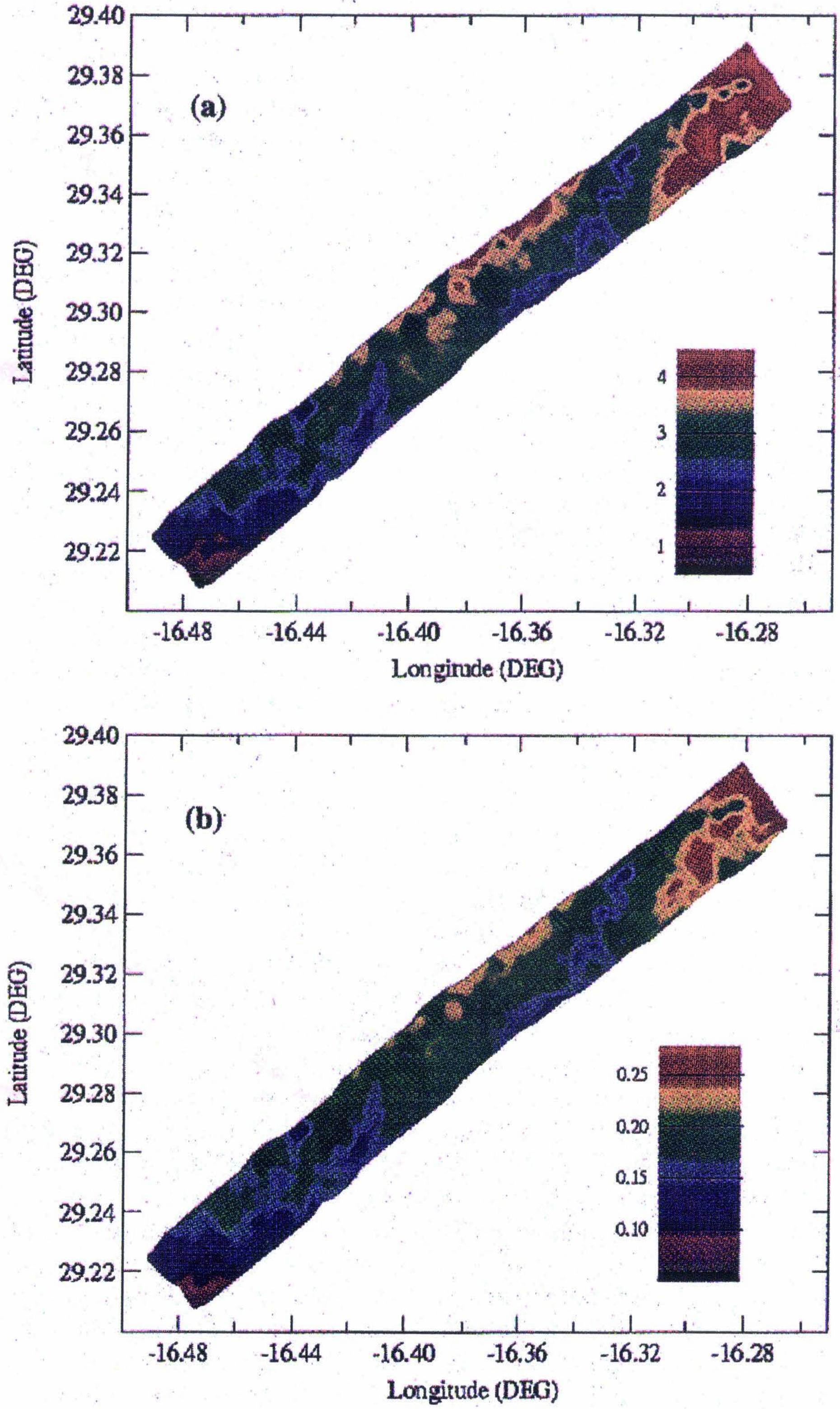

Fig. 3. (a) Cloud optical thickness and (b) cloud albedo maps established from airborne POLDER measurements acquired on 26 June 1997 between 14:27 and 14:32 UTC. The effective radius of droplet size distribution is 12 μm.

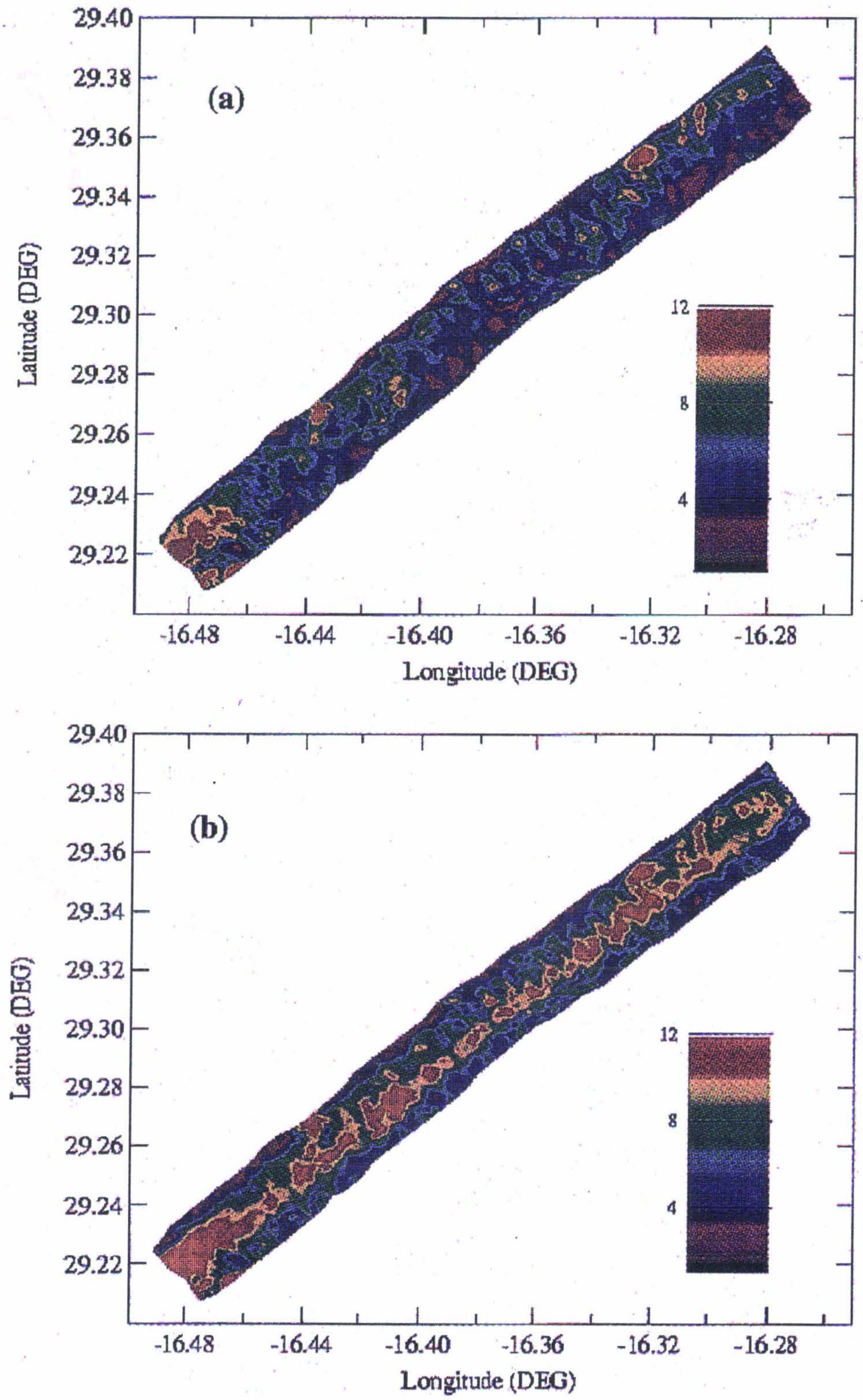

Fig. 4. Relative angular standard deviation (in %) of cloud optical thickness maps established from airborne POLDER measurements acquired on 26 June 1997 between 14:27 and 14:32 UTC. The effective radius of droplet size distribution is (a) 12 μm and (b) 6 μm.

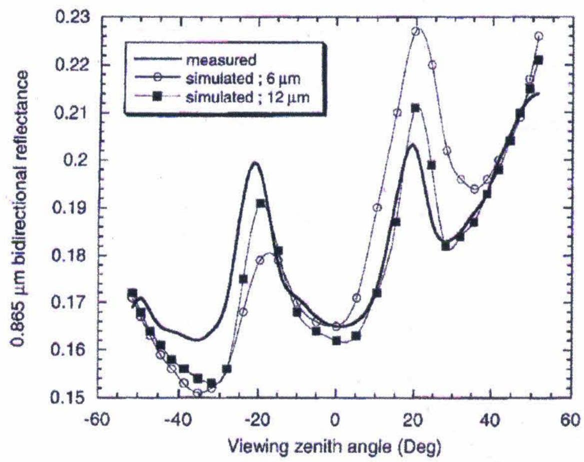

Fig. 5. Comparison between the measured cloud bidirectional reflectance (in the solar plane) and theoretical ones obtained using droplet effective radius of 6 μm or 12 μm. The simulations correspond to the 26 June 1997 case study. The surface albedo is fixed to 0.05. The mean retrieved cloud optical depth is equal to 2.56 and 2.97, for $r_e = 6$ μm and $r_e = 12$ μm, respectively.

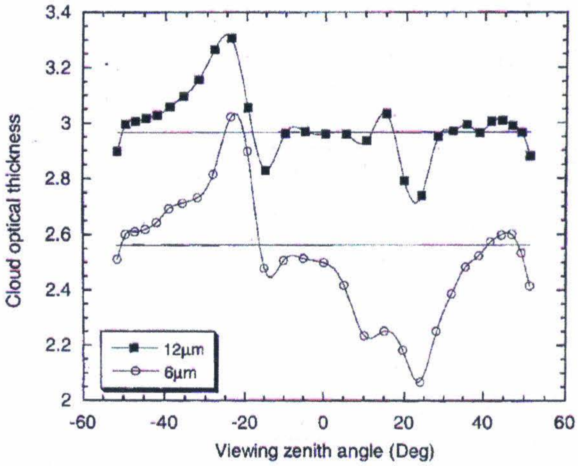

Fig. 6. Cross-sections along the principal plane of the retrieved cloud optical thickness using 2 droplet effective radius of 6 μm or 12 μm. The simulations correspond to the 26 June 1997 case study. The surface albedo is fixed to 0.05. The mean cloud optical depths retrieved using the whole field-of-view of POLDER (solid lines) are equal to 2.56 and 2.97, for $r_e = 6$ μm and $r_e = 12$ μm, respectively.

12 μm). This clearly illustrates the error that is made when the cloud optical thickness is retrieved from one single view angle. According to Fig. 5, the cloud optical thickness is notably underestimated in the backscatter direction and overestimated in the cloudbow region. The angular variability of the optical thickness is lower for $r_e = 12$ μm than for $r_e = 6$ μm. The 12 μm cloud droplet size distribution is a more suitable cloud model in this case study.

4.2. *The 9 July 1997 case study*

During the ACE-2 mission 06 on 9 July 1997, the Dornier was flown over extended stratocumulus clouds thicker than during mission 02. The cloud deck was sampled along 50-km legs. In this section we analyze a leg corresponding to the Northwest part of the square pattern performed on 9 July 1997 (Brenguier et al., 2000). It was sampled between 14:39 and 14:48 UTC. The procedure presented in the previous section was applied to this case. The best agreement between observed and simulated bidirectional reflectance is obtained for droplet size distributions with an effective radius ranging from 6 μm to 10 μm. As shown in Fig. 7, these 2 models minimize the angular variability of the retrieved cloud optical thickness. As noted previously and displayed in this figure, the mean retrieved cloud optical thickness is almost not dependent on the model drop size since the mean values are 7.02 and 7.68 for $r_e = 6$ μm and $r_e = 10$ μm, respectively.

The cloud optical thickness and cloud albedo

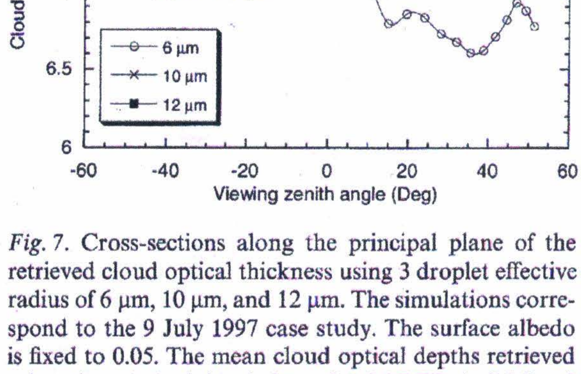

Fig. 7. Cross-sections along the principal plane of the retrieved cloud optical thickness using 3 droplet effective radius of 6 μm, 10 μm, and 12 μm. The simulations correspond to the 9 July 1997 case study. The surface albedo is fixed to 0.05. The mean cloud optical depths retrieved using the whole field-of-view of POLDER (solid lines) are equal to 7.02, 7.68, and 8.01, for $r_e = 6$ μm, $r_e = 10$ μm, and $r_e = 12$ μm, respectively.

maps of the ~ 50 km $\times$ 3 km scenes are derived from POLDER reflectance, assuming $r_e = 10$ µm, and are reported in Fig. 8. The color scale (from black to red) represents a range of optical thickness from 0 to 18.0 or a range of albedo from 0 to approximately 0.75. The optical thickness and albedo values are definitely greater than the values derived on 26 June 1997. The spatial distribution of cloud properties also appears much more heterogeneous than in the previous case.

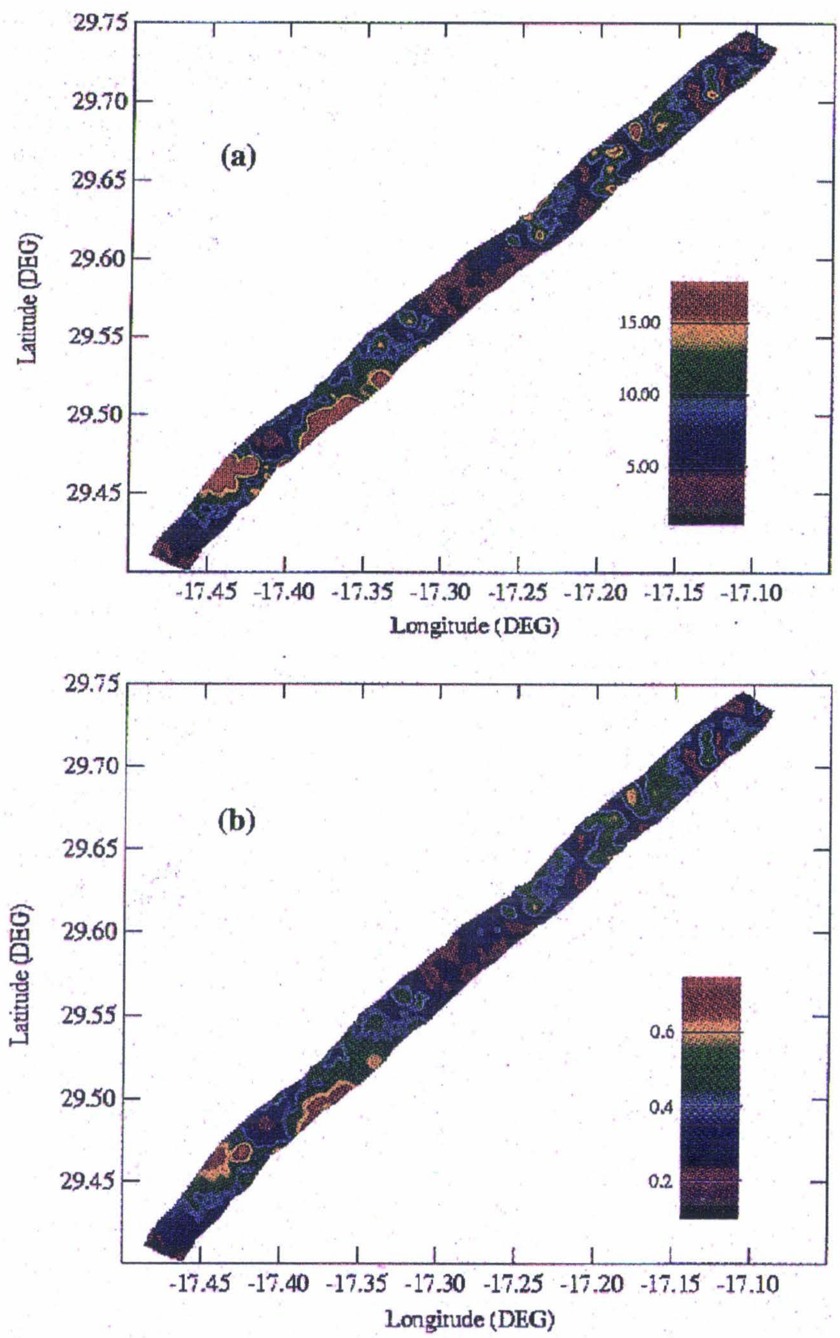

Fig. 8. (a) Cloud optical thickness and (b) cloud albedo maps established from airborne POLDER measurements acquired on 9 July 1997 between 14:39 and 14:48 UTC. The effective radius of droplet size distribution is 10 µm.

The overall relative angular standard deviation (not reported here) of the retrieved parameters is low (less than 5–6%) for most of the leg. Low values of relative angular standard deviations are mostly found where the cloud optical depth and albedo are moderate. The deviation is more significant where the cloud is more heterogeneous with sharp variations of optical thickness. In those particular cases the cloud deck locally departs from the plane-parallel approximation, regardless of the droplet size.

4.3. Discussion

The angular dispersion of cloud optical thickness derived from multidirectional measurements of cloud radiances with POLDER on board the Dornier are used to estimate the effective radius of droplets. Each cloud target $(\sim 150\,\mathrm{m})^2$ is assumed homogeneous and vertically uniform with respect to the droplet size distribution. This procedure is based on the Independent Pixel Approximation and was validated by Descloitres et al. (1995, 1998). This enables to model the cloud heterogeneity at spatial scales of a few hundred meters (Figs. 3, 8).

An important issue is the assumption of vertical homogeneity. Stratocumulus clouds have significant vertical heterogeneity and many authors have shown that liquid water content and effective radius increase with altitude from cloud base to cloud top (Slingo et al., 1982; Stephens and Platt, 1987). More recently Brenguier et al. (1999) have shown the adiabatic stratified plane-parallel model is more realistic than the vertically uniform plane-parallel model to parameterize the stratocumulus cloud optical thickness in global climate models (GCM). Brenguier et al. (2000) validate the adiabatic stratified plane-parallel model from in situ and remote sensing measurements collected during the ACE-2 CLOUDYCOLUMN field campaign. This result is important for the simulation of cloud effects in GCMs that include cloud geometrical thickness as a diagnostic parameter. Nonetheless, these results do not make our procedure questionable. Simulations by Nakajima and King (1990) suggest that the derived vertically uniform optical thickness differs from the true optical thickness by no more than 3% for typical vertically inhomogeneous conditions. Calculations performed by Brenguier et al. (1999) confirm this result. Moreover, Pawlowska et al. (1999) show that the vertically uniform optical thickness derived from POLDER compares well with the microphysical measurements. This optical thickness is used to validate the parameterization based on the adiabatic vertical profile of the microphysics proposed by Brenguier et al. (1999).

The other issue is the derivation of droplet effective radius from remote sensing data. Several authors have investigated methods based on multi-wavelength shortwave measurements to simultaneously retrieve the cloud optical thickness and the effective radius (Nakajima and King, 1990; Nakajima et al., 1991; Han et al., 1994; Brenguier et al., 1999). Sensitivity studies on the effect of vertical heterogeneity on the retrieval of effective radius suggest that this radius is typically 80–100% of the radius at cloud top (Nakajima and King, 1990; Brenguier et al., 1999). The present feasibility study is mainly based on the angular dependence of the reflected radiance (position and intensity of the cloudbow and backscatter peak; see Fig. 4). These features are mainly driven by single scattering (Hansen and Travis, 1974). Consequently the proposed approach is a retrieval of the upper few units of cloud optical thickness located at the cloud top.

The present results show that a 12 μm effective radius is a suitable cloud droplet size model in the pure marine case study (26 June) while an effective radius of 6 μm to 10 μm is more suitable to the polluted case (9 July). Assuming no variations of cloud morphological aspect, a verification of the indirect effect of aerosols (the so-called Twomey effect) may be reduced to a verification of the decrease of droplets size via an increase of anthropogenic aerosol concentration. In that sense, these preliminary results can be interpreted as a confirmation of the indirect effect of aerosols. They are consistent with the extended analysis presented by Brenguier et al. (2000; see their Fig. 5) who show a first experimental evidence of the indirect effect at the scale of a cloud system.

5. ADEOS-POLDER daily retrievals: the 26 June 1997 case study

This section presents the ADEOS-POLDER data acquired on 26 June 1997 along 2 ADEOS orbits over the Atlantic Ocean and Europe. The main results (cloud amount, cloud optical thickness and shortwave broadband albedo) of the "ERB & clouds" operational algorithm are discussed in details for a ~ 2500 km $\times$ 2500 km area corresponding to the ACE-2 region (Fig. 1). The original contribution of POLDER regarding these properties is emphasized.

In the operational "ERB & clouds" processing, the cloud detection algorithm is a threshold method applying several sequential tests for the presence of clouds. Parol et al. (1999) argue about the adjustments of the different tests and favorably compare the POLDER cloud detection algorithm to the Dynamic Clustering Method applied to Meteosat data (Sèze and Desbois, 1987). The tests are applied to each individual pixel (6.2 km) and for every view direction. The cloud cover is determined direction by direction and, and the cloudiness is then averaged (Buriez et al., 1997).

Fig. 9 shows the cloud cover, the cloud optical thickness and the shortwave broadband albedo (see Subsection 3.2) for the ACE-2 region of interest. The cloud cover presented in Fig. 9a is obtained by spatial and angular averaging for each POLDER super-pixel ($\sim 9 \times 9$ pixels). Similarly, the cloud optical thickness shown in Fig. 9b corresponds to a spatial and angular average on the cloudy pixels within the super-pixel. All large cloud structures associated with the main climate processes are easily identified and their location is consistent with what we would expect for this time of year: for instance the inter-tropical convergence zone (ITCZ) along the 10°N parallel and the large clear-sky area over the desert of Sahara. The spatial distribution of cloud cover is mainly linked to the meteorological synoptic situation at this date. In particular, a cyclone persisted over Western Europe at the end of June (Verver et al., 2000). High cloudiness is observed off the coast of Spain over the Atlantic Ocean.

The spatial distribution of cloud optical thickness and shortwave albedo is consistent with the observed structures of cloud cover and their expected regional reflective characteristics. There are some high values all along the ITCZ with some very bright cloud cells. High values also appear in mid-latitude depression areas (off Spain).

More extended than airborne POLDER observations, the ADEOS-POLDER images show that low broken stratocumulus clouds covered the ACE-2 area on 26 June 1997. The cloud cover and cloud optical thickness maps (Fig. 9a,b) confirm this synoptic situation. These cloud properties are highly variable in space. The proportion of partly cloudy pixels that can correspond to cumulus, scattered stratocumulus or cloud edges is important. Note that "partly cloudy" has not the same meaning for POLDER as for a usual radiometer. In the case of the POLDER cloud detection algorithm, some pixels can be labeled as cloudy for some directions and clear for others (Buriez et al., 1997; Parol et al., 1999). Over the ACE-2 region, the derived values of cloud optical depth and shortwave albedo are quite low. The cloud optical depth ranges from 1.0 to approximately 8.0 and the shortwave albedo is less than ~ 0.25 (see Fig. 9c). Because of 2 very different spatial scales ($(56\ \mathrm{km})^2$ in this case and $(\sim 150\ \mathrm{m})^2$ for the airborne POLDER) an exact comparison between these values and those obtained from the airborne data is not realistic. However, these values are consistent with low optical depths and spectral albedoes presented in Subsection 4.1.

These low values are associated to high values of spatial and angular dispersion of cloud optical depth. This is emphasized on Figs. 9d,e that respectively present the relative spatial and angular standard deviations of the optical thickness. As explained in Subsection 3.2, the cloud is assumed to be a plane-parallel layer composed of droplets with an effective radius of 10 μm in the level-2 "ERB & clouds" operational scheme (Buriez et al., 1997). Consequently, the relative angular standard deviations increase if this approximation is inadequate (Fig. 9e). Note that, in Figs. 9d,e, the color scale upper limits are very different. Generally, the spatial deviation is twice higher than the angular deviation.

A first reason for a high relative angular standard deviation is that the measured angular distribution can be very different from the plane-parallel cloud model depending on the cloud brokeness, because of cloud shape and mutual shadowing effects (Bréon, 1992; Loeb et al., 1997; Loeb and Coakley, 1998). Another reason is that the microphysical model is not suitable (Section 4). For instance, it is well known that cirrus cloud properties are very sensitive to ice crystal shape and orientation (Mishchenko et al., 1996). However, the study of ice clouds is far beyond the scope of ACE-2. So the rest of the analysis focuses on the derivation of liquid water cloud properties only.

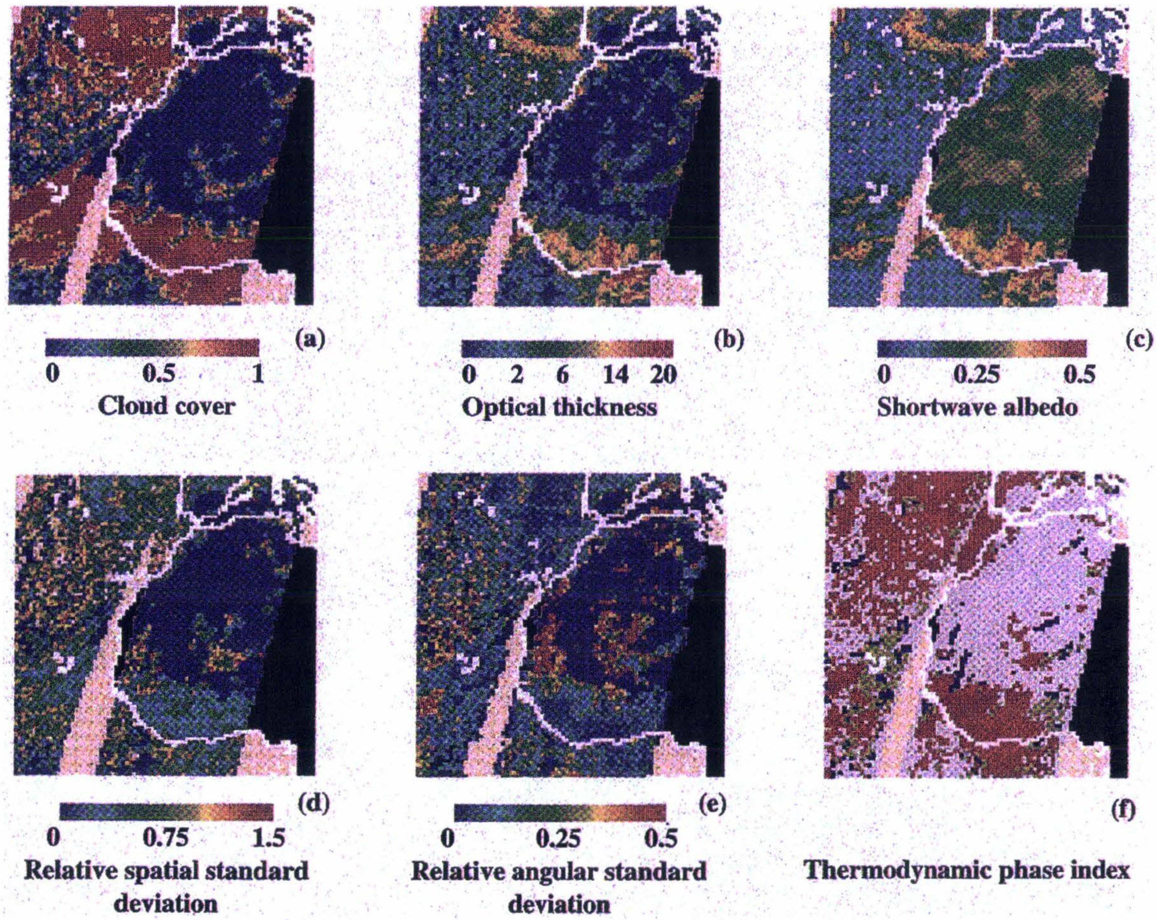

Fig. 9. Image constructed from POLDER level-2 (a) cloud cover, (b) cloud optical thickness and (c) shortwave albedo derived for 26 June 1997 over the ACE-2 region. (d) and (e) are respectively constructed from relative spatial standard deviation and relative angular standard deviation of cloud optical thickness. (f) is the thermodynamic phase index (red is for liquid droplets, dark blue for ice crystals, green for mixed phase, and grey for "clear" and "not computed" (Parol et al., 1999).

A thermodynamic phase index (Fig. 9f) derived from polarization measurements at 0.865 μm is used to identify the POLDER pixels composed of liquid water clouds (further details can be found in Parol et al., 1999). Fig. 10 presents the variability rates as a function of the cloud optical thickness only for these cloud pixels labeled "droplets". In order to assess the effect of brokeness on these curves, overcast situations are separated from the other ones. For the purpose of this analysis, a POLDER super-pixel is considered as overcast if the cloud fraction is greater than 0.95. Practically, overcast super-pixels are mainly located along the ITCZ and the southern part of the cyclone centered over Western Europe (Fig. 9a). The 2 sets of curves associated to the 2 cloud fraction cases are not significantly different. However, the magnitude of the standard deviations observed in overcast conditions is lower and the optical thickness is larger.

Figs. 10a,c confirm that large values of cloud optical thickness give moderate values of relative spatial standard deviation, while these get more scattered as the cloud optical depth gets small. In the case of broken cloudiness, small spatial standard deviation is always related to small optical thickness (Fig. 10a).

The relative angular standard deviation behaves differently (Figs. 10b,d). Low angular standard deviation is observed for all values of cloud optical

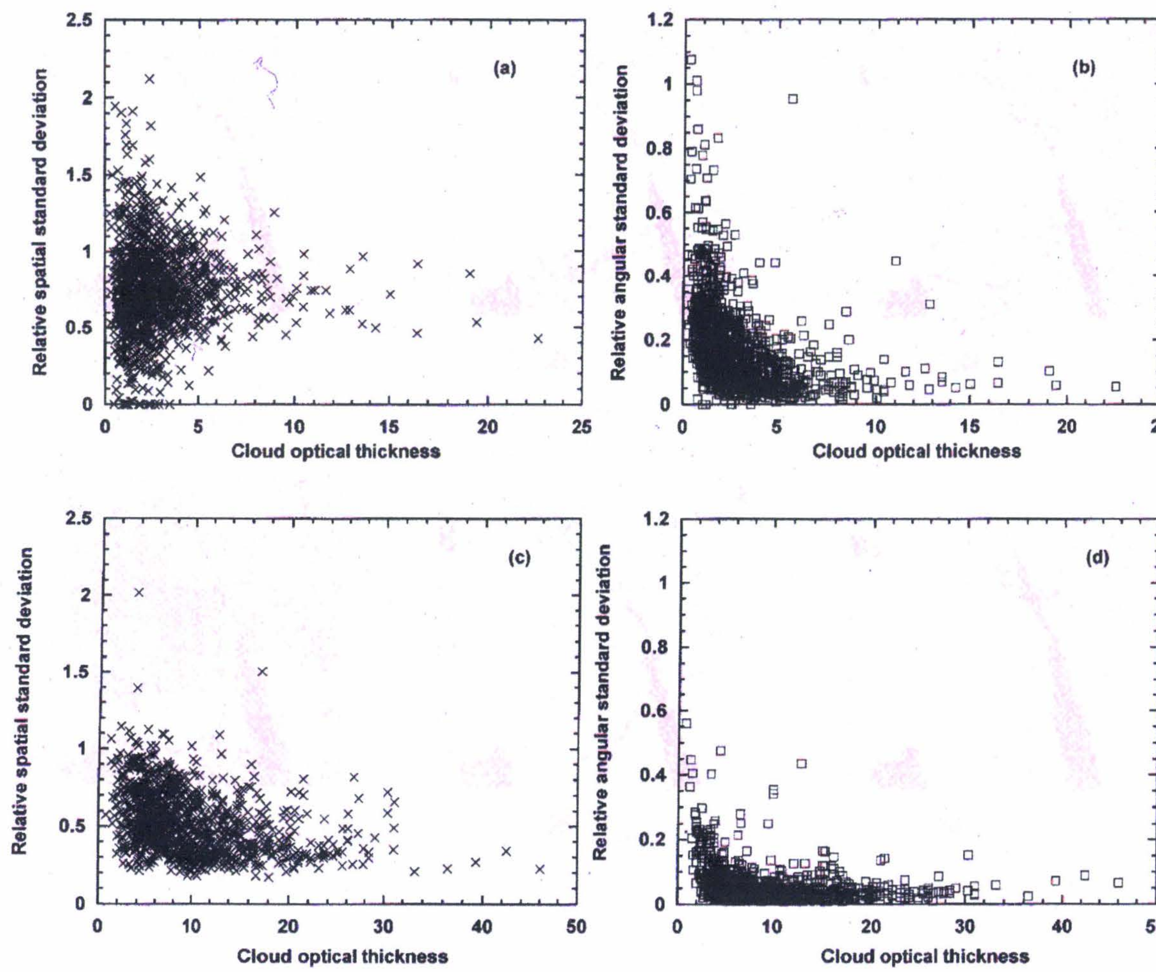

Fig. 10. (a) Relative spatial standard deviation and (b) relative angular standard deviation of cloud optical thickness versus the optical thickness for super-pixels labeled "droplets" in Fig. 9f; (a) and (b) are non-overcast super-pixels and (c) and (d) are overcast super-pixels.

thickness. Fig.10 shows that the angular dispersion is not necessarily correlated to the spatial variability, i.e., to the cloud heterogeneity.

Furthermore, the 2 relative standard deviations have been plotted as a function of the cloud cover for the cloudy pixels labeled "droplets" (Fig. 11). The variations of the 2 parameters against the cloud fractional cover are definitely different. The overall behavior of the spatial deviation can be described by an arch whereas the angular deviation varies almost linearly. Not surprisingly, the relative spatial standard deviation of cloud optical thickness is maximum for a cloud amount close to 0.5. For overcast situations the spatial standard deviation is still high and of the same order of magnitude as for broken cloudiness conditions. On the contrary, the relative angular deviation decreases with cloud fractional cover. For small cloud amounts, the high value of the relative angular standard deviation is indicative of the departure of these pixels from the 10 μm plane-parallel cloud model. This highlights the prime interest of POLDER multi-angular capability. Different cloud models could be investigated in order to minimize the retrieved angular dispersion. Further research is clearly needed. For overcast conditions the relative angular standard deviation tends to nearly zero. Although these overcast super-pixels (composed of $\sim 9 \times 9$ pixels) are not close to homogeneous clouds, they act on average as a plane-parallel model with $r_e = 10$ μm. This extends to larger spatial scales some previous

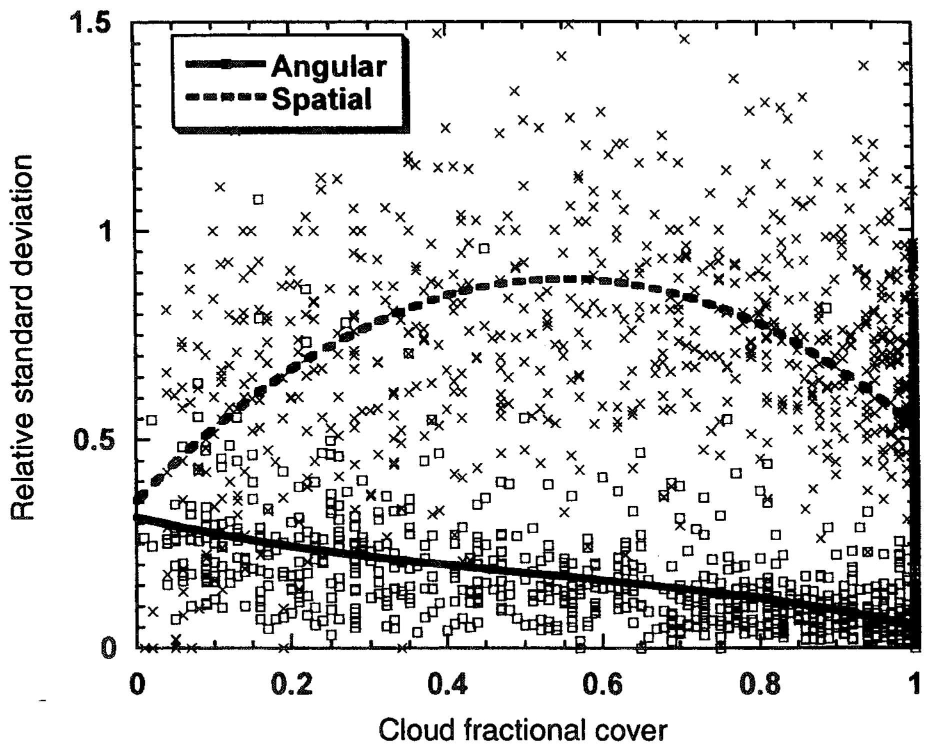

Fig. 11. Relative spatial and angular standard deviations of cloud optical thickness versus the cloud fractional cover for super-pixels labeled "droplets" in Fig. 9f. The lines are the mean curves.

results obtained using the airborne POLDER instrument (Descloitres et al., 1995, 1998). However, the suitability of the plane-parallel cloud model does not imply that the retrieved cloud optical thickness is accurate. For instance, for marine stratocumulus clouds, Cahalan (1994) found that the cloud albedo could be approximated properly by a plane-parallel model having an optical depth 30% smaller than the actual mean optical depth. In the present study, the derived cloud optical depth has to be considered as an "effective" optical depth.

6. Conclusion

Unlike the usual scanning radiometers, the POLDER instrument provides 10 or more quasi-simultaneous reflectance measurements of any cloud scene. It is always possible to adjust a multi-parameter cloud model (i.e., microphysical and macrophysical parameters) to match one single bidirectional observation of a given cloud scene. On the contrary, constraining such a model to adequately match a set of bidirectional observations is much more demanding. The multidirectionality of POLDER measurements is then a useful constraint for the selection of cloud parameters. POLDER allows to determine the cloud optical thickness under some hypotheses, and also enables to test the validity of these hypotheses. As mentioned in the introduction, numerous studies have derived the cloud optical thickness from space using the plane-parallel approximation and a prescribed cloud droplet size. However, up to now only few direct observations of cloud bidirectional reflectance have been compared to theoretical radiation fields calculated using the plane-parallel model (see for instance Stuhlmann et al., 1985; Descloitres et al., 1998).

This paper presented results related to such comparisons within the framework of the ACE-2 Experiment. Cloud optical thickness and cloud albedo retrieved from bidirectional reflectances measured by ADEOS-POLDER and its airborne simulator were presented. First, particular attention was given to airborne POLDER data acquired on 2 golden days of the campaign 26 June and 9 July 1997. Stratocumulus clouds sampled during these 2 days had developed in air masses of different origins (Brenguier et al., 2000). 26 June corresponded to a pure marine case and July 9 was the last day of a marine to polluted air transition. For the experimental characterization of the aerosol indirect effect, thin stratocumulus clouds had been selected in priority during ACE-2, because thin clouds are more sensitive to a change in droplet concentration. As expected for the 26 June flight mission, the cloud optical thickness values are very low, ranging typically between 1 and 5 for the leg under investigation in this paper. However, the optical thickness values retrieved on 9 July are approximately 2–3× larger.

Even though the cloud optical thickness and cloud albedo retrievals are shown to be almost not dependent on cloud droplet size in visible range channels, the multidirectional capability of POLDER is demonstrated to be very useful to select the cloud microphysical model (in terms of effective radius of droplets). The relative angular standard deviation of the retrieved parameters increases if the cloud microphysical model is inadequate. The relative angular standard deviations are more sensitive to the microphysical model as POLDER observed cloud scenes in view conditions that correspond to strong anisotropic features as the backscatter maximum and the cloudbow ($\sim 140°$ scattering angle). Taking advantage of this opportunity, we found that a 12 μm cloud droplet size distribution was a suitable cloud model in the pure marine cloud case study (26 June). For the polluted case (9 July), the mean retrieved effective radius of droplets is of the order of 6–10 μm. This result can be interpreted as a confirmation of the indirect effect of aerosols. It is consistent with the significant increase in droplet concentration measured in polluted marine clouds compared to pure marine clouds (Brenguier et al., 2000). Further investigations and comparisons to in-situ microphysical measurements are needed.

The last section of this paper presented the recently validated and processed satellite POLDER data acquired along 2 ADEOS orbits on 26 June. The ACE-2 polluted cases (during the first couple of weeks of July) were not documented by ADEOS-POLDER that ended acquisition on 29 June after an unexpected failure of the platform solar panel. The main results (cloud amount, cloud optical thickness and shortwave albedo) of the "ERB & clouds" operational algorithm were discussed for the ACE-2 region and the original contribution of POLDER regarding these properties was emphasized.

The cloud optical thickness and cloud albedo values are very low and are thus consistent with airborne POLDER retrievals. However, these low values are associated to high values of spatial and angular variability of cloud optical thickness that means to high spatial cloud macrophysical or microphysical inhomogeneity. In the "ERB & clouds" algorithm, a cloud water droplet model with a prescribed effective radius of 10 μm is used to operationally derive cloud optical thickness from ADEOS-POLDER data. Consequently, when inverting the POLDER reflectances, the optical thickness is the only cloud property that is allowed to vary. Once again, the multiangular capability of POLDER allows testing the standard cloud droplet model. Excluding the ice cloud cases for which the 10 μm droplet model seems definitely inadequate (Descloitres et al., 1998; Parol et al., 1999), it appears that the angular standard deviations are not straighforwardly related to the spatial standard deviations as measured by POLDER at $\sim 56 \times 56\,\mathrm{km}^2$ scale. Indeed, the variations of these 2 parameters against the cloud cover are definitely different. This indicates that the departure of the observations from the bidirectional reflectance variations of the cloud model selected for the inversion is not a tracer of the 3D optical thickness distribution.

7. Acknowledgements

The authors are very grateful to Françoise Hennequart for her help in processing raw data of the airborne POLDER. They also gratefully acknowledge 2 anonymous referees for their very helpful comments and suggestions. This study was supported by the European Community under grant ENV4-CT95-0117, CNES, Région Nord-Pas De Calais, and Préfecture du Nord through EFRO. Some results in this paper were obtained using CNES's POLDER onboard NASDA's ADEOS.

8. Appendix A

Basic formula for cloud optical thickness retrieval: droplet size effect

For a given drop size distribution $n(r)$, where $n(r)$ is the density of droplets with radius r per unit of volume, cloud optical thickness is given by:

$$\tau(\lambda)=\int_0^H\int_0^\infty Q_{ext}(x)\pi r^2 n(r)\,dr\,dh, \tag{8.1}$$

where $x=2\pi r/\lambda$ is the size parameter, and H is the cloud layer geometrical thickness. The efficiency factor for extinction $Q_{ext}(2\pi r/\lambda)$ is determined from Mie theory (Van de Hulst, 1957). $Q_{ext}(2\pi r/\lambda)$ is a function of r, wavelength λ, and refractive index, m (Hansen and Travis, 1974). The variation of $Q_{ext}(2\pi r/\lambda)$ with size parameter x is small particularly for large x and asymptote to a value of approximately 2. This is relevant for spherical droplets of radius r large compared to the wavelengths.

If the effective radius of droplet size distribution is introduced (Hansen and Travis, 1974) as:

$$r_e=\frac{\int_0^\infty \pi r^3 n(r)\,dr}{\int_0^\infty \pi r^2 n(r)\,dr}, \tag{8.2}$$

and the expression of the liquid water content, w ($g\,m^{-3}$), as

$$w=\int_0^\infty \frac{4}{3}\pi r^3\rho_w n(r)\,dr, \tag{8.3}$$

eq. (8.1) becomes:

$$\tau(\lambda)=\frac{3\bar{Q}_{ext}}{4\rho_w}\int_0^H \frac{w}{r_e}\,dh, \tag{8.4}$$

where ρ_w is the liquid water density ($\rho_w=10^3\,kg\,m^{-3}$) and $\bar{Q}_{ext}$ is the average of Q_{ext} over the droplet size distribution.

The liquid water path LWP ($g\,m^{-2}$) is formally defined as:

$$\mathrm{LWP}=\int_0^H w\,dh. \tag{8.5}$$

Assuming that the cloud is vertically uniform with respect to drop-size distribution, the cloud optical thickness is linked to liquid water path and effective radius by:

$$\tau(\lambda)=\frac{3\bar{Q}_{ext}}{4\rho_w r_e}\mathrm{LWP}. \tag{8.6}$$

For droplets of radius r large compared to the wavelength eq. (8.6) reduces to:

$$\tau(\lambda)\approx\tau=\frac{3}{2}\frac{\mathrm{LWP}}{r_e}, \tag{8.7}$$

where LWP is in ($g\,m^{-2}$) and r_e is in micrometers (Fouquart et al., 1990).

Two cloud layers have approximately the same reflection properties if they have the same values for scaled optical thickness and scaled single-scattering albedo (Van de Hulst, 1980). The similarity equation

$$\tau(1-\tilde{\omega}_0 g)=\tau'(1-\tilde{\omega}_0' g') \tag{8.8}$$

allows us to get τ' from τ and r (the asymmetry factor g and the single-scattering albedo $\tilde{\omega}_0$ are functions of droplet radius and wavelength; they are calculated using Mie theory and optical constants of liquid water).

The effect of drop size on cloud optical thickness retrieval from a single angular measurement of 0.865 μm POLDER reflectance can be estimated from this equation. Table 1 presents the relative difference $(\tau'-\tau)/\tau$ normalized to the cloud optical thickness retrieved assuming the 10 μm effective radius. In the same way, $(\tau'-\tau)/\tau$ represents the relative error caused by 10 μm effective radius assumption used in the spaceborne POLDER operational analysis. Table 1 also lists the values of Q_{ext}, $\tilde{\omega}_0$, and g for the different cloud droplet effective radii used in this study.

In this paper cloud optical thickness is derived from measured reflected radiance assuming the plane-parallel approximation and then it is applied to the plane-parallel model to infer the cloud albedo. From the similarity principles (Van de Hulst, 1980), the so-estimated plane-parallel albedo is not strongly dependent on drop size distribution so long as the same distribution is used in the 2 steps of the analysis.

Table 1. *Effect of drop size on cloud optical thickness retrieval from a single POLDER bidirectional reflectance measurement at 0.865 μm*

r_e (μm)	Q_{ext}	$\tilde{\omega}_0$	g	$(\tau'-\tau)/\tau$
6	2.2	0.999970	0.83804	−0.109
10	2.1	0.999953	0.8557	0
12	2.1	0.999943	0.85831	0.018

The values of Q_{ext}, $\tilde{\omega}_0$, and g for the different cloud droplet effective radii used in this study are also listed.

REFERENCES

Arking, A. and Childs, J. D. 1985. Retrieval of cloud cover parameters from multispectral satellite images. *J. Climate Appl. Meteor.* **24**, 322–333.

Baldwin, D. G. and Coakley Jr., J. A. 1991. Consistency of Earth Radiation Budget Experiment bidirectional models and the observed anisotropy of reflected sunlight. *J. Geophys. Res.* **96**, 5195–5207.

Barsch, B. and Bakan, S. 1993. First experiences with the new array spectrometer OVID. In: *ARKTIS 1993 field phase report. Ber. ZMK* (ed. Bruemmer, B), Ser. A, **11**, 147–156.

Bréon, F.-M. 1992. Reflectance of broken cloud fields: simulation and parameterization. *J. Atmos. Sci.* **49**, 1221–1232.

Brenguier, J.L., Chuang, P. Y., Fouquart, Y., Johnson, D. W., Parol, F., Pawlowska, H., Pelon, J., Schüller, L., Schröder, F. and Snider, J. 2000. An overview of the ACE-2 CLOUDYCOLUMN closure experiment. *Tellus* **52B**, 815–827.

Brenguier, J. L., Pawlowska, H., Schüller, L., Preusker, R., Fischer, J. and Fouquart, Y. 1999. Radiative properties of boundary layer clouds: optical thickness and effective radius versus geometrical thickness and droplet concentration. *J. Atmos. Sci.*, in press.

Brogniez, G., Parol, F., Buriez, J. C. and Fouquart, Y. 1992. Bidirectional reflectances of Cirrus clouds modelized from observations during the international cirrus experiment 89. In: Current Problems in Atmospheric Radiation, *Proc. of the IRS'92*, Tallin, Estonia, 3–8 August 1992, eds: S. Keevallik and O. Karner, 133–136.

Buriez, J. C., Vanbauce, C., Parol, F., Goloub, P., Herman, M., Bonnel, B., Fouquart, Y., Couvert, P. and Sèze, G. 1997. Cloud detection and derivation of cloud properties from POLDER. *Int. J. Remote Sensing* **13**, 2785–2813.

Cahalan, R. F. 1994. Bounded cascade clouds: albedo and effective thickness. *Nonlin. Proc. Geophys.* **1**, 156–167.

Cahalan, R. F., Ridgway, W., Wiscombe, W. J., Gollmer, S. and Harshvardhan. 1994. Independent pixel and Monte Carlo estimates of stratocumulus albedo. *J. Atmos. Sci.* **51**, 3776–3790.

Cess, R. D. et al. 1990. Intercomparison and interpretation of climate feedback processes in 19 atmospheric general circulation models. *J. Geophys. Res.* **95**, 16,601–16,610.

Cess, R. D. et al. 1996. Cloud feedback in atmospheric general circulation models: an update. *J. Geophys. Res.* **101**, 12,791–12,794.

Charlson, R. J., Schwartz, S. E., Hales, J. M., Cess, R. D., Coackley Jr., J. A., Hansen, J. E. and Hofmann, D. J. 1992. Climate forcing by anthropogenic aerosols. *Science* **255**, 423–430.

Cox, C. and Munk, W. 1956. Slopes of the sea surface deduced from photographs of the sun glitter. *Bull. of the Scripps Institute of Oceanography* **6**, 401–488.

Davis, J. M. and Cox, S. K. 1982. Reflected solar radiances from regional scale scenes. *J. Appl. Meteor.* **21**, 1698–1712.

Deschamps, P. Y., Bréon, F. M., Leroy, M., Podaire, A., Bricaud, A., Buriez, J. C. and Sèze, G. 1994. The POLDER mission: instrument characteristics and scientific objectives. *IEEE Trans. Geosci. Remote Sensing* **32**, 598–615.

Descloitres, J., Parol, F. and Buriez, J. C. 1995. On the validity of the plane-parallel approximation for cloud reflectances as measured from POLDER during ASTEX. *Ann. Geophysicae* **13**, 108–110.

Descloitres, J., Pawlowska, H., Pelon, J., Brenguier, J. L., Parol, F., Buriez, J. C. and Flamant, P. 1996. Experimental retrieval of cloud optical thickness during EUCREX: comparison of three approaches. *Proc. of the 12th International Conference on Clouds and precipitation.* Zurich, Switzerland. Page Bros. (Norwich), pp. 394–397.

Descloitres, J., Buriez, J. C., Parol, F. and Fouquart, Y. 1998. POLDER observations of cloud bidirectional reflectances compared to a plane-parallel model using the ISCCP cloud phase functions. *J. Geophys. Res.* **103**, 11,411–11,418.

Diner, D. J., Beckert, J. C., Reilly, T. H., Bruegge, C. J., Conel, J. E., Kahn, R., Martonchik, J. V., Ackerman, T. P., Davies, R., Gerstl, S. A. W., Gordon, H. R., Muller, J.-P., Myneni, R., Sellers, R. J., Pinty, B. and Verstraete, M. M. 1998. Multiangle Imaging Spectro-Radiometer (MISR) description and experiment overview. *IEEE Trans. Geosci. Rem. Sens.* **36**, 1072–1087.

Fouquart, Y., Buriez, J. C., Herman, M. and Kandel, R. S. 1990. The influence of clouds on radiation: a climate-modelling perspective. *Rev. of Geophys.* **28**, 145–166.

Hagolle, O., Goloub, P., Deschamps, P.-Y., Cosnefroy, H., Briottet, X., Bailleul, T., Nicolas, J.-M., Parol, F., Lafrance, B. and Herman, M. 1999. Results of POLDER in-flight calibration. *IEEE Trans. Geosci. Remote Sensing* **37**, 1550–1567.

Han, Q., Rossow, W. B. and Lacis, A. A. 1994. Near-global survey of effective droplet radii in liquid water clouds using ISCCP data. *J. Climate* **7**, 465–497.

Hansen, J. E. 1971. Multiple scattering of polarized light in planetary atmospheres. Part II: sunlight reflected by terrestrial water clouds. *J. Atmos. Sci.* **28**, 1400–1426.

Hansen, J. E. and Travis, L. D. 1974. Light scattering in planetary atmospheres. *Space Sci. Rev.* **16**, 527–610.

Harrison, E. F., Minnis, P., Barkstrom, B. R., Ramanathan, V., Cess, R. D. and Gibson, G. G. 1990. Seasonal variations of cloud radiative forcing derived from the Earth Radiation Budget Experiment. *J. Geophys. Res.* **95**, 18,687–18,703.

Houghton, J. T., Jenkins, G. J. and Ephraums, J. J. (eds.). 1990. *Climate change: the IPCC scientific assessment.* World Meteorological Organization/United Nations Environment Programme, Cambridge University Press, 364 pp.

Kandel, R. S., Monge, J. L., Viollier, M., Pakhomov, L. A., Adasko, V. I., Reitenbach, R. G., Raschke, E. and Stuhlmann, R. 1994. The ScaRaB project: Earth radiation budget observations from the Meteor satellites, World Space Congress (Washington)-COSPAR symp. A.2-S. *Adv. Space Research* **14**(1), 47–54.

King, M. D., Kaufman, Y. J., Menzel, W. P. and Tanré, D. 1992. Remote sensing of cloud, aerosol, and water vapor properties from the moderate resolution imaging spectrometer (MODIS). *IEEE Trans. Geosci. Rem. Sens.* **30**, 2–27.

Kobayashi, T. 1993. Effects due to cloud geometry on biases in the aldebo derived from radiance measurements. *J. Climate* **6**, 120–128.

Leroy, M., Deuze, J. L., Breon, F. M., Hautecoeur, O., Herman, M., Buriez, J. C., Tanre, D., Bouffies, S., Chazette, P. and Roujean, J. L. 1997. Retrieval of atmospheric properties and surface bidirectional reflectances over the land from POLDER/ADEOS. *J. Geophys. Res.* **102**, 17,023–17,037.

Loeb, N. G., Varnai, T. and Davies, R. 1997. The effect of cloud inhomogeneities on the solar zenith angle dependence of nadir reflectance. *J. Geophys. Res.* **102**, 9387–9395.

Loeb, N. G. and Coakley Jr., J. A. 1998. Inference of marine stratus cloud optical depths from satellite measurements: does 1D theory apply? *J. Climate* **11**, 215–233.

Mishchenko, M. I., Rossow, W. B., Macke, A. and Lacis, A. A. 1996. Sensitivity of cirrus cloud albedo, bidirectional reflectance and optical thickness retrieval accuracy to ice particle shape. *J. Geophys. Res.* **101**, 16,973–16,985.

Nakajima, T. and King, M. D. 1990. Determination of the optical thickness and effective particle radius of clouds from reflected solar radiation measurements. Part I: theory. *J. Atmos. Sci.* **47**, 1878–1893.

Nakajima, T., King, M. D., Spinhirne, J. D. and Radke, L. F. 1991. Determination of the optical thickness and effective particle radius of clouds from reflected solar radiation measurements. Part II: marine stratocumulus observations. *J. Atmos. Sci.* **48**, 728–750.

Parol, F., Buriez, J. C., Crétel, D. and Fouquart, Y. 1994. The impact of cloud inhomogeneities on the Earth radiation budget: The 14 October 1989 ICE convective cloud case study. *Ann. Geophysicae* **12**, 240–253.

Parol, F., Buriez, J. C., Vanbauce, C., Couvert, P., Sèze, G., Goloub, P. and Cheinet, S. 1999. First results of the POLDER "Earth Radiation Budget and Clouds" operational algorithm, *IEEE Trans. Geosci. Rem. Sens.* **37**, 1597–1612.

Pawlowska, H., Brenguier, J. L., Fouquart, Y., Armbruster, W., Descloitres, J., Fischer, J., Flamant, C., Fouilloux, A., Gayet, J. F., Ghosh, S., Jonas, P., Parol, F., Pelon, J. and Schüller, L. 1999. Microphysical and radiative properties of stratocumulus clouds. The EUCREX mission 206 case study. *Atmos. Res.*, in press.

Raes, F., Bates, T., McGovern, F. and Van Liedekerke, M. 2000. The second Aerosol Chatacterization Experiment (ACE-2): general context and main results. *Tellus* **52B**, 111–126.

Ramanathan, V., Cess, R. D., Harrison, E. F., Minnis, P., Barkstrom, B. R., Ahmad, E. and Hartmann, D. 1989. Cloud radiative forcing and climate: results from the earth radiation budget experiment. *Science* **243**, 57–63.

Rossow, W. B. and Schiffer, R. A. 1991. ISCCP cloud data products. *Bull. Amer. Meteor. Soc.* **72**, 2–20.

Senior, C. A. and Mitchell, J. F. B. 1993. Carbon dioxide and climate. The impact of cloud parameterisation. *J. Climate* **6**, 393–418.

Slingo, A., Nicholls, S. and Schmetz, J. 1982. Aircraft observations of marine stratocumulus during JASIN. *Quart. J. Roy. Meteor. Soc.* **108**, 833–856.

Spinhirne, J. D., Hart, W. D. and Hlavka, D. L. 1996. Cirrus infrared parameters and short-wave reflectance relations from observations. *J. Atmos. Sci.* **53**, 1438–1458.

Stamnes, K., Tsay, S. C., Wiscombe, W. and Jayaweera, W. 1988. Numerically stable algorithm for discrete-ordinate-method radiative transfer in multiple scattering and emitting layered media. *Appl. Opt.* **27**, 2502–2509.

Stephens, G. L. 1978. Radiation profiles in extended water clouds. II: parameterization schemes. *J. Atmos. Sci.* **35**, 2123–2132.

Stephens, G. L. and Platt, C. R. M. 1987. Aircraft observations of the radiative and microphysical properties of stratocumulus and cumulus cloud fields. *J. Climate Appl. Meteor.* **26**, 1243–1269.

Stuhlmann, R., Minnis, P. and Smith, G. L. 1985. Cloud bidirectional reflectance functions: a comparison of experimental and theoretical results. *Appl. Opt.* **24**, 396–401.

Vanbauce, C., Buriez, J. C., Parol, F., Bonnel, B., Sèze, G. and Couvert, P. 1998. Apparent pressure derived from ADEOS-POLDER observations in the oxygen A-band over ocean. *Geophys. Res. Lett.* **25**, 3159–3162.

Van de Hulst, H. C. 1957. *Light scattering by small particles.* John Wiley and Sons, New York, 470 pp.

Van de Hulst, H. C. 1980. *Multiple light scattering, tables, formulas, and applications*, vol. 1. Academic Press, 739 pp.

Verver, G., Raes, F., Vogelezang, D. and Johnson, D. 2000. The second Aerosol Characterization Experiment (ACE-2): meteorological and chemical context. *Tellus* **52B**, 126–140.

Wielicki, B. A. and Barkstrom, B. R. 1991. Cloud and the earth's radiant energy system (CERES): an earth observing system experiment. *Second Symp. on Global change studies.* New Orleans, LA, Amer. Meteor. Soc., pp. 11–16.

Chapitre 3

La Contribution de POLDER pour l'Etude des Nuages

Introduction

Ces dernières années et lors des prochaines à venir, une série de satellites en orbite autour de la Terre a emporté ou emportera plusieurs nouveaux instruments originaux, évolués, particulièrement bien étalonnés, conçus pour fournir des observations globales des océans, de la surface terrestre et de l'atmosphère. Parmi eux, POLDER est un instrument récent dédié à l'observation globale de la polarisation et de la directionalité du rayonnement solaire réfléchi par le système Terre-atmosphère (*Deschamps et al*, 1994). Le concept instrumental imaginé au Laboratoire d'Optique Atmosphérique fin des années 80 a été accepté par l'agence spatiale japonaise, la NASDA, au début des années 90. L'instrument spatial a été développé par le CNES et a volé sur la plate-forme japonaise ADEOS de Septembre1996 à fin Juin 1997.

Depuis la décision de lancement de la version spatiale de POLDER, je participe très activement à la définition et à la validation des algorithmes de traitement de données de la filière "Earth Radiation Budget, Water Vapor and Clouds" (ERB&Clouds) implantée au CNES **(Buriez et al, 1997)**. Je suis plus précisément responsable des algorithmes opérationnels de correction de l'absorption gazeuse et de la détermination de la pression des nuages à partir de l'absorption différentielle par l'oxygène. Sur ce thème, l'analyse des mesures aéroportées de POLDER acquises durant EUCREX'94 nous a permis rapidement de mettre en place un algorithme de dérivation de la pression des nuages et de comparer les résultats à ceux fournis par d'autres moyens de mesures **(Parol et al, 1994**; **Parol et al, 1996)**. Ce travail a également fait l'objet du stage de DEA que Thomas Pancak a effectué sous ma direction en 1995. Le travail entrepris sur l'utilisation des deux canaux spectraux de POLDER situés dans la bande A d'absorption par l'oxygène m'a amené également a développer une méthode d'étalonnage inter-bande de ces canaux. Ce travail a fait partie d'un ensemble d'approches originales d'étalonnage des canaux POLDER par des méthodes indirectes utilisant des cibles naturelles (déserts, réflexion spéculaire sur la mer, nuages, ...) **(Hagolle et al, 1999 ; Annexe D)**

Mon investissement dans le projet POLDER m'a conduit à être, depuis 1994, Principal Investigateur d'une proposition de recherche sur la validation et l'utilisation scientifiques des produits géophysiques de la filière ERB&Clouds et à participer à ce titre à l'IPSWT (International POLDER Scientific Working Team). Un effort important de validation des paramètres géophysiques obtenus a été effectué en collaboration avec d'autres laboratoires français, le LSCE et le LMD. Ce travail a été reconnu lors de la revue scientifique de validation des produits POLDER le 2 juillet 1998. Les premiers résultats de nos études ont été plus que satisfaisants (**Vanbauce et al, 1998**; **Parol et al, 1999**; *Parol*, 1999). Notre proposition de recherche s'est appuyée également sur des études plus spécifiques destinées à développer de nouveaux produits géophysiques pour la seconde version de POLDER qui sera mise en orbite fin 2001 à bord de la station ADEOS-2 (*Doutriaux-Boucher et al*, 1999; *Loeb et al*, 1999). Dans ce cadre, ma récente collaboration avec Norman J. Loeb (NASA LaRC), qui fait partie de l'équipe scientifique de l'instrument américain CERES, a donné lieu à des résultats originaux et prometteurs sur la conversion des luminances en flux aux courtes longueurs d'onde (**Loeb et al, 2000**). Les produits géophysiques dérivés de POLDER ont permis d'examiner comment les propriétés des nuages déterminées à partir de mesures satellitale pouvaient être utilisées pour définir des modèles angulaires empiriques. Cette étude a montré l'intérêt d'une approche basée sur des classes d'intervalles "en pourcentage" d'épaisseur optique.

C'est dans ce contexte de validation des produits géophysiques POLDER que Nicolas Got, stagiaire en DEA en 1998, a également effectué sous ma direction, les premières comparaison entre POLDER et l'instrument multispectral japonais OCTS (aussi à bord de la plate-forme ADEOS).

Cloud altimetry and water phase retrieval from POLDER instrument during EUCREX'94.

Frédéric Parol , Philippe Goloub, Maurice Herman and Jean-Claude Buriez

Laboratoire d'Optique Atmosphérique
Université des Sciences et Technologies de Lille
59655 Villeneuve d'Ascq, France

ABSTRACT

POLDER (POLarization and Directionality of the Earth's Reflectances) is a new instrument devoted to the global observation of the polarization and directionality of solar radiation reflected by the Earth surface-atmosphere system. The instrument concept has been accepted on the Japanese ADEOS platform scheduled to be launched early 1996. The original capabilities of POLDER, compared to previous current radiometers are, 1) its polarized reflectance measurements in the visible and near-infrared range of the solar spectrum, 2) its capability to measure a surface target reflectance from about 10 directions during a single pass.

A method for cloud phase retrieving from POLDER measurements is tested. Indeed, liquid water clouds could be discriminated from ice clouds provided they exhibit distinct polarization signatures. In the rainbow region (scattering angles of about 140°), water droplets strongly polarize incident sunlight while ice crystals probably do not. This feature is examined on data acquired by the airborne POLDER instrument over cirrus and stratocumulus clouds during the EUCREX'94 (EUropean Clouds and Radiation EXperiment, April 1994) experiment.

Moreover, over clouds, the polarized component of the reflectance at the wavelength of 443nm and scattering angle of 90-100° is sensitive to molecular optical thickness between the cloud top and the satellite altitude and, therefore, may be used for cloud altimetry. On the other hand, a method for cloud top pressure retrieval from POLDER measurements based on a differential absorption technique is presented. It makes use of the ratio of two radiances measured in the absorption A band of the oxygen (at 763nm). The two different methods are compared on data acquired during EUCREX'94. Considering the main limitations of the instrument and the methods, the two mean retrieved cloud-top pressures are found to be in good agreement and are close to the expected true one.

1. INTRODUCTION

Through their multiple interactions with radiation, clouds have an important impact on the Earth-atmosphere radiation balance and consequently on the climate. Clouds cover about 60% of the Earth and several sensitivity studies[1-2] have shown that the response of numerical climate models was extremely dependent on the various hypotheses and parameterizations used to simulate cloud-radiation interactions. This large sensitivity results from the opposite, but potentially very important influences that clouds have on the solar radiation scattered back into space (the so-called "albedo effect") and the terrestrial radiation emitted from the Earth'surface into space. In order to estimate the influence of clouds on radiation budget, many cloud properties are required as optical thickness, cloud-top height (cloud-top pressure), cloud microphysics (phase, shape and size of particles), etc. The International Satellite Cloud Climatology Project

(ISCCP)[3] and the associated regional experiments (FIRE[4], ICE[5], etc...) have been designed to improve the modelling of clouds and radiations interactions.

This paper is a part of the recent intensive field campaign of the EUropean Cloud and Radiation EXperiment (EUCREX) that took place over Brittany in April 1994. This campaign was remote sensing oriented and was dedicated to the development and validation of algorithms to derive quantitative informations on cloud structure and cloud microphysics from multispectral satellite observations. In particular, the new instrument POLDER was operated and tested prior to its spatialization. The concept of the instrument is presented in section 2. In section 3, the ability of POLDER to provide bidimensional images in polarized light is used to retrieve cloud water phase. Finally, the possibility of cloud altitude retrieval from two different techniques using POLDER is investigated in section 4.

2.THE POLDER INSTRUMENT

The POLDER instrument is a radiometer designed to measure the directionality and polarization of the sunlight scattered by the ground-atmosphere system[6]. The instrument concept consists in imaging bidimensional pictures of the site on a CCD (Charge Coupled Device) detector matrix, through a wide field of view (maximum of 114°) telecentric optics. A given ground target thus may be observed with different viewing angles in consecutive pictures acquired while the sensor overflies the experimental site. The spectral analysis of the radiance is provided by a filter wheel. In some spectral bands, 3 filters are equiped with analysors rotated by 60° and the polarization is deduced from combination of the 3 images. POLDER has been selected to fly on the Japanese ADEOS (ADvanced Earth Observing System) payload which is scheduled to be launched early 1996.

This paper reports on observed angular and spectral polarized signatures acquired by one airborne version of POLDER during EUCREX'94. POLDER was aboard the German Falcon aircraft of the DLR (Deutsche Luft and Raumfart) which was mainly dedicated to cirrus observations. The airborne instrument includes a CCD array of 288 x 242 detectors. In order to reduce both the data flow and the radiometric noise, the spatial resolution is degraded to 5 x 5 pixels. Angular deviations due to the pitch and roll of the aircraft are taken into account. The airborne version of POLDER used in this paper supported 2 polarized filters with spectral bands centered on 443nm and 865nm and 3 unpolarized filters with spectral bands centered on 763 nm, 765 nm and 910 nm.

3. CLOUDS POLARIZATION FEATURES

The interest of polarized measurements for cloud studies has been outlined long ago[7]. Firstly, polarization measurements from space should be able to provide cloud altimetry by the way of molecular scattering. For this purpose, measurements have to be performed at short wavelengths (say, $\lambda<500$ nm) and for observation geometries corresponding to scattering angles near $\Theta=90^{\circ}$. In these conditions, molecules are very efficient for scattering polarized light. Then, by considering that the ground and most of the aerosols are screened by the cloud and by neglecting or correcting the cloud contribution, the amount of polarized light should yield the optical thickness of the atmosphere above the cloud, i.e. the cloud top pressure or altitude. Preliminary results, using the airborne version of POLDER, have been obtained during CLEOPATRA campaign.[8]

On the other hand, the angular polarization signature of clouds, as measured at near infrared wavelengths, could help for discriminating between liquid and solid phases of cloud particles. Liquid cloud droplets should be evidenced by the characteristic polarization feature of the rainbow, exhibited by spherical particles for scattering angles near 140°. Conversely, theoretical studies of scattering by various crystalline particles (prisms, hexagonal crystals) all show that the rainbow characteristic disappears as soon as the particles depart from spherical geometry[9-10-11]. The lack of this characteristic feature in cloud polarization signature, therefore, should be indicative of the presence of ice crystals. More generally, cirrus clouds could exhibit their own characteristic signature. As shown by Masuda and Takashima[12] the degrees of linear polarization calculated for randomly oriented hexagonal ice crystals are very similar for column and plate shaped crystals, as are quite similar to the degrees of linear polarization calculated by Mishchenko and Travis[13] for randomly oriented prolate and oblate spheroids. This point, however, has to be ascertained from observations because the actual ice crystal geometries are probably very variable.

Here are reported observations acquired over water clouds, ice clouds and in clear sky conditions by the airborne version of POLDER during EUCREX'94 on April 17 (flight 205) and on April 18 (flight 206) 1994. Two versions of POLDER were used during this campaign: the first on the French ARAT aircraft and the second on the German Falcon aircraft which was mainly dedicated to cirrus observations. Observed angular and spectral polarized signatures of the second POLDER are now presented.

3.1. Liquid water cloud

During the flight 206, stratocumulus cloud fields were overflown by the Falcon at a flight level of about 6 km. Several hundred of cloudy images were acquired. Here, we focus on one image and observed polarized signatures are reported on Fig. 1.

We look at the polarized reflectance rather than at the polarization rate - defined as the ratio between polarized reflectance and total reflectance - because the polarized reflectance is known to be formed in the upper cloud layer[14] and to be few sensitive to the cloud optical thickness and to the underlying ground.

The 865 nm band is more convenient for observing the cloud intrinsic polarization signature since molecular scattering is negligible. Near 140° highly polarized reflectances corresponding to primary rainbow of spherical particles confirm the liquid thermodynamic phase. The other characteristic observation is that the polarization tends to vanish for scattering angle near 90-100°.

In the 443 nm spectral band, the angular evolution of the polarized reflectance also presents a maximum near 140° . But in the range of 90-100° the polarized reflectance is clearly larger than at 865 nm because of the great efficiency of the scattering by molecules above the cloud. This property will be used for cloud altimetry.

3.2. Ice cloud

Figure 2 shows observations of a cirrus cloud system. These observations were carried out by POLDER during flight 205: about one hundred of images were acquired at the altitude of 10.7 km, just above the cirrus layer. We report typical cirrus polarized signatures versus scattering angle for the two POLDER polarized channels . These were obtained from a single image.

Clearly the angular polarization signature of ice clouds is greatly different from that of water clouds. There is no cloudbow at 140° for cirrus clouds. Unfortunately, the observations performed by the POLDER instrument do not allow to reach the region of the 22° halo, which is a typical feature of non-spherical ice particles. On the other hand, one observes some weak spectral difference in the polarized signature. This could be due to the molecular contribution not completely screened by the thin cirrus layer. The effect of molecules remaining above the cirrus cloud should be very weak since POLDER flight level (10.7 km) was just above the cirrus layer. Other sets of observations over cirrus have shown some variablity of the mean apparent reflectance of the cirrus. The mean apparent reflectances over cirrus may range from 0.1-0.4 at 865 nm. This is the reason why it is useful to know the order of magnitude of reflectance and polarized reflectance in clear sky condition to be sure that no confusion would be possible.

3.3. Clear Sky case

The observations, here reported, concern the typical clear sky feature of polarized reflectance, over ocean (Fig. 3). Clear sky means only molecular and aerosol contribution. In the 865 nm band, the polarized reflectance observed near 140° is very weak and could be similar to the cirrus one if the aerosol optical thickness is high enough. But the reflectance of the cirrus must be greater than the clear sky one.

3.4. Feasibility of cloud phase detection using polarization

About one hundred POLDER images have been processed and a simple study of the correlation between polarized reflectance and reflectance (only for scattering angles close to 140 degrees) has been done in the 865 nm band. The results are plotted on Fig.4.

Clearly, Fig. 4 allows to distinguish two sets of points, i.e. two clusters . The first one, which corresponds to high reflectance values as well as to high polarized reflectances, is typical of rather thick liquid water clouds. The second one, which presents very weak polarized reflectance values and variable reflectances, corresponds to ice clouds, that means to clouds composed of polycristalline particles. Finally, the clear sky measurements over sea always present both weak reflectance and weak polarized reflectance (see Figs. 5, 6 and table 1).

	Clear Sky	Cirrus	Stratocumulus
Mean ρ_p(at 140°)	0.003	0.006	0.045
Mean ρ (at 140°)	0.02	[0.15-0.4]	0.75
Zaircraft(km)	6	10.7	6
Zcloud(km)	/	9-10	1

Table 1 : Mean values of polarized reflectance and reflectance at 865 nm for scattering angle near 140 degrees, observed during flights 205 and 206 of EUCREX'94

4. CLOUD ALTIMETRY

Together with cloud optical thickness which regulates the influence of clouds on the terrestrial albedo, one of the most important cloud properties with respect to global climate changes is cloud height - or cloud pressure. For instance, Ohring and Adler[15] found that an increase of 1 km in cloud height would result in a 1.2 K increase in surface temperature.

Several techniques for deriving cloud-top height from satellite observations have already been approached among them: (i) the well-known brightness temperature technique, (ii) the CO_2-slicing technique introduced by Smith and Platt[16], (iii) the analysis of stereoscopic images, and (iv) the analysis of reflected sunlight at wavelengths within the A band of absorption of O_2 (760-770 nm) introduced by Yamamoto and Wark.[17]

Using measurements acquired by the POLDER instrument aboard the Falcon during EUCREX'94, two methods for retrieving cloud pressure are evaluated. The first one is based on the analysis of polarized reflected sunlight at 443 nm. The second one is based on a differential absorption technique and makes use of the ratio of two radiances measured in the A band of the absorption of the Oxygen.

4.1. Use of polarization of molecular scattering :

In this approach, we consider that the polarized light measured at 443 nm around Θ=90° corresponds only to light scattered by the molecular layer, since cloud contribution is negligible in this direction. Let $\Delta\delta_m(\lambda)$ be the optical thickness of the molecular layer; because $\Delta\delta_m(\lambda)$ is small,single scattering approximation of the polarized reflectance, $\rho_m{}^P$, is valid and therefore

$$\rho_m^p = \frac{3\Delta\delta_m}{16\cos\theta_s\cos\theta v}\left(1-\cos^2\Theta\right) \quad (1).$$

During flight 206 over stratocumulus cloud field the Falcon flew at the altitude of 6 km, (image 710, hereafter case (a)), the derived estimate of $\Delta\delta_m$ is 0.077. With POLDER at a flight level of 3 km over an other stratocumulus cloud field (image 345, hereafter case (b)), the estimated $\Delta\delta_m$ is about 0.038.

Then we derive the cloud-top pressure, p_c, using the following formula

$$\Delta p_c = p_c - p_a = p_0 \frac{\Delta\delta_m}{\delta_m} \quad (2),$$

where δ_m is the total molecular optical thickness (δ_m=0.22 at λ=443 nm), p_a is the aircraft pressure level and p_0 is the surface pressure.

4.2. Differential absorption method :

Using atmospheric absorption in the oxygen A band (765 nm, 13070 cm^{-1}) to infer cloud pressure has been suggested by several authors[17-18]. Since then, some theoretical efforts[19-20] and aircraft measurements[21] have been carried out.

All these studies have shown that the oxygen A band is potentially efficient for determining the cloud-top pressure. During EUCREX'94 field campaign, the filter wheel of POLDER supported two filters with spectral bands centered on 763nm with 10nm wide (the narrow band) and on 765nm with 40nm wide (the wide band). The reflected radiance at 763nm is attenuated by absorption by O_2 and the 765nm radiance is attenuated by O_2 and H_2O (seeFig. 7). Moreover, both radiances are attenuated by H_2O and O_3 continuum.

The above-mentioned studies have also shown that the major difficulty is to resolve the "photon penetration" problem and the effect of ground reflectance. Indeed, because of multiple scattering and molecular absorption inside and outside the cloud, the reflection of solar radiation is modified in comparison with a perfect reflecting cloud layer. Moreover, if clouds are not optically thick, the effect of ground reflection has to be taken into account. Therefore, to infer true cloud-top pressure it is essential to accurately estimate these two physical processes.

However, in this paper, all scattering effects are neglected and the following modelization assumes the atmosphere as being a pure absorbing medium. The retrieved pressure level is thus the pressure of the apparent reflecting layer. For optically thick cloud, this apparent pressure should be very close to the true cloud-top pressure. Nevertheless, for thin cloud case, both ground reflectance and "photon penetration" effects may no more be neglected and the infered apparent pressure should be between the true cloud-top pressure and the pressure of the underlying surface. First a simple model is presented that allows to derive apparent pressure from POLDER measurements. Then, this model is tested on and applied to data acquired during EUCREX flight 206 over thick stratocumulus clouds.

4.2.1. Modelization

Let's assume a perfect reflecting layer with inherent reflectance at 765 nm, R^*, located at a pressure level, P, in the atmosphere. The reflected radiances measured in the narrow band and the wide band of POLDER are written respectively as

$$R_N = R^* \,.\, T_{O_2} \,.\, \dot{T}_{H_2O} \,.\, \dot{T}_{O_3} \qquad (3.a)$$

$$R_W = A \,.\, R_N + (1 - A) \,.\, R^* \,.\, \ddot{T}_{H_2O} \,.\, \ddot{T}_{O_3} \qquad (3.b)$$

where the constant A may be considered as the part of the wide spectral band attenuated by the oxygen absorption. T_{O_2} is the spectrally averaged oxygen transmitance, T'_{H2O} and T''_{H2O} correspond to transmitances of both water vapor lines and continuum, and finally T'_{O3} and T''_{O3} stand for spectrally averaged transmittances of the ozone continuum.

The spectrally averaged transmittance of the oxygen is derived from Eq. (3.a) and (3.b), as

$$T_{O_2} = \frac{(1 - A).\left(\frac{R_N}{R_W}\right)}{1 - A.\left(\frac{R_N}{R_W}\right)} . \left(\frac{\ddot{T}_{H_2O}}{\dot{T}_{H_2O}}\right) . \left(\frac{\ddot{T}_{O_3}}{\dot{T}_{O_3}}\right) \qquad (4).$$

All the spectrally averaged transmittances have been computed using the line by line model STRANSAC[22] and the spectroscopic data bank GEISA[23]. The computations have been performed using the standard atmospheric profiles[24] and varying both solar illumination and viewing conditions as well as aircraft altitudes. The derived constant A is about 0.3.

In the case of our airborne POLDER measurements, the simulations show that the transmittance ratio $(T''_{O3})/(T'_{O3})$ is very close to 1.

The transmittance ratio $(T''_{H2O})/(T'_{H2O})$ is greater than 0.97 and is parameterized as a function of the ratio of the two POLDER radiances measured at 910 nm and 865 nm. Since the 910 nm spectral band is located in a water vapor absorption band, the ratio of these two radiances is sensible to the water vapor content between the cloud-top and the instrument. However the $(T''_{H2O})/(T'_{H2O})$ ratio is often close to 1 and is just a minor corrective term.

The approximate T_{O2} values derived from Eq. (4) have been compared to the exact computed ones. The maximum error and the r.m.s. error are of the order of $2.5\ 10^{-4}$ and $1.2\ 10^{-4}$ respectively. Finally, depending on the viewing zenith angle, the apparent pressure is derived from the computed T_{O2} value as shown on Fig. 8. Our modelization induces a maximum error on the retrieved apparent pressure smaller than 2 hPa.

4.2.2. Calibration of the apparent pressure

In a first step of the analysis, the apparent pressure is calibrated on the true sea surface pressure. To do that, several POLDER images acquired in clear sky condition over sea during flight 206 are processed. The reflectance ratio $(R_N)/(R_W)$ is tuned so that the apparent pressure derived for the sunglint part of the images (high reflectance values) is equal to the true surface pressure (1013 hPa) as displayed on Fig. 9. In the case of POLDER data acquired during EUCREX'94, the reflectance ratio has been tuned by 1.12. This adjusting coefficient may be mainly explained by a probable deviation of the interband calibration during the in-situ experiments.

4.3. Comparison between the two methods:

The apparent cloud-top pressures deduced from molecular optical thickness are compared to those derived from differential absorption technique. This comparison is performed for two POLDER images (above-mentioned as case (a) and (b) respectively).

In cloud case (a) the cloud-top pressure derived from polarization measurements is about 830 ± 70 hPa when the apparent cloud-top pressure derived from differential absorption method is 920 ± 20 hPa (see Fig. 10). The two methods have been applied to another POLDER image acquired over the same stratocumulus cloud field but at a flight altitude of 3000m (case (b)). The retrieved apparent cloud-top pressures are 880 ± 80 hPa and 875 ± 25 hPa from the molecular scattering method and the oxygen absorption method respectively.

From thermodynamical measurements performed by the aircraft, the expected cloud-top pressure of the stratocumulus is around 900 hPa. Taking into account the main limitations of the two methods, i.e. instrumental limitations (calibration, radiometric noise) as well as physical limitations (the multiple scattering effects are neglected, ...), the two retrieved apparent cloud-top pressures are not too much different and on the other hand seem in good agreement with the expected true one.

5. CONCLUSIONS

In the context of the EUCREX'94 campaign, an airborne version of the new POLDER instrument has been used to investigate the angular polarization signature of cloudy atmospheres. The analysis of polarized light reflected by typical stratocumulus and cirrus clouds outlines that the characteristic rainbow of spherical particles appears as a good indicator of the presence of liquid water phase. POLDER seems well adapted to discriminate between ice clouds and liquid water clouds.

The difference in the polarized reflectance at 443 nm and 865 nm above clouds that corresponds to the residual molecular scattering is used to estimate the cloud top pressure of one stratocumulus. Another technique based on the oxygen absorption in the A band is developed and tested on the same cloud. The two mean retrieved cloud-top pressures are very close each other and are in good agreement with the true cloud-top pressure.

6. ACKNOWLEDGMENTS

The authors wish to thank Professor J.-L. Deuzé for his fruitful discussions. They are also very grateful to J.-Y. Balois and C. Verwaerde who conducted the campaign, and to F. Lemire who processed the POLDER data. This work has been supported by the European Economic Community and the Centre National d'Etudes Spatiales.

7. REFERENCES

1. M. E. Schlessinger and J. F. B. Mitchell, "MOdel projections of equilibrium climatic response to increased CO2 concentration", Projecting the Climatic Effects of Increasing Carbon Dioxide, edited by M. C. McCracken and F. M. Luther, U.S. Department of Energy, Washington D. C., 1986.

2. R. D. Cess, G. L. Potter, J. P. Blanchet, G. J. Boer, A. D. Del Genio, M. Deque, V. Dymnikov,

V. Galin, W. L. Gates, S. J. Ghan, J. T. Kiehl, A. A. Lacis, H. Le Treut, Z. X. Li, Z. Liang, B. J. McAvaney, V. P. Meleshko, J. F. B. Mitchel, J. J. Morcrette, D. A. Randall, L. Rikus, E. Roeckner, J. F. Royer, U. Schlese, D. A. Sheinin, A. Slingo, A. P. Sokolov, K. E. Taylor, W. M. Washington, R. T. Wetherald, I. Yagai and M. H. Zhang, "Intercomparison and interpretation of climate feedback processes in 19 atmospheric general circulation models", *J. Geophys. Res.*, 95, 16601-16616,1990.

3. R.A. Schiffer and W. B. Rossow, "The International Satellite Cloud Climatology Project (ISCCP): The fisrt project of the world climate research program", *Bull. Amer. Meteor. Soc.*, 64, 779-784, 1993.

4. S. K. Cox, D. S. McDougal, D. A. Randall and R. A. Schiffer, "FIRE- The First ISCCP Regional Experiment", *Bull. Amer. Meteor. Soc.*, 68, 114-118, 1987.

5. E. Raschke and K.-D. Rockwitz, "The International Cirrus Experiment: Some preliminary results from the first field phase, Proc. of the IRS'88, edited by J. Lenoble and J.-F. Geleyn, 6-9, A. Deepack publishing, Lille, France, 1988.

6. P.-Y. Deschamps, M. Herman, A. Podaire, M. Leroy, M. Laporte and P. Vermande, "A spatial instrument for the observation of polarization and directionality of Earth reflectances: POLDER", Proc. IGARSS'90, Washington D.C., 1990.

7. D. L. Coffeen and J.E.Hansen, "Airborne infrared polarimetry", Proc. of the eighth international symposium of remote sensing of environment, 1972.

8. P. Goloub, J.-L. Deuzé, M. Herman and Y. Fouquart, "Analysis of the POLDER Polarization Measurements Performed Over Cloud Covers", *IEEE Transactions on Geoscience and Remote Sensing*, 32, 78-88, 1994.

9. Q. Cai and K.-N. Liou, "Polarized light scattering by hexagonal ice cristals: theory". *Appl. Opt.*, 21, 3569-3580, 1982.

10. J. De Haan, "Effects of aerosols on the brightness and polarization of cloudless planetary atmospheres", M.S. Thesis, Free University of Amsterdam, Holland, The Netherlands, 1987.

11. G. Brogniez, "Contribution à l'étude des propriétés optiques et radiatives des cirrus", Thèse d'Etat, Université des Sciences et Technologies de Lille, 1992.

12. K. Masuda and T. Takashima, "Feasability study of derivation of cirrus information using polarimetric measurements from satellite", *Remote Sens. Environ.*, 39, 45-59, 1992.

13. M. J. Mishchenko and L. D.Travis, "Light scattering by polydisperse, rotationally symmetric nonspherical particles: linear polarization", *J. Quant. Spcetrosc. Radiat. Transfer*, 51, 759-788, 1994.

14. J. E. Hansen and L. D. Travis, "Light scattering in planetary atmospheres", *Space Sci. Rev.*, 16, 527-610, 1974.

15. G. Ohring and S. Adler, "Some experiments with a zonally averaged climate model", *J. Atmos. Sci.*, 35, 186-205, 1978.

16. W. L. Smith and C.M.R. Platt, "Comparison of satellite-deduced cloud heights with indications from radiosonde and ground-based laser measurements", *J. Appl. Meteor.*, 17, 1796-1802, 1979.

17. G. Yamamoto and D. Q. Wark, Discussion of the letter by R.A. Hanel: "Determination of cloud altitude from a satellite", *J. Geophy. Res.*, 66, 3596, 1961.

18. R. M. Chapman, "Cloud distributions and altitude profiles from satellite", *Planet. Space Sci.*, 9, 70-71, 1962.

19. J. Fisher and H. Grassl, "Detection of cloud-top height from backscattered radiances within the Oxygen A band. Part 1: Theoretical study", *J. Appl. Meteor.*, 30, 1245-1259, 1991.

20. D. M. O'Brien and R. M. Mitchell, "Error estimates for retrieval of cloud-top pressure using absorption in the A band of Oxygen", *J. Appl. Meteor.*, 31, 1179-1192, 1992.

21. J. Fisher, W. Cordes, A. Schmitz-Peiffer, W. Renger and P. Mörl, "Detection of cloud-top height from backscattered radiances within the Oxygen A band. Part 2: Measurements", *J. Appl. Meteor.*, 30, 1260-1267, 1991.

22. N. A. Scott, " A direct method of computation of the transmission function of an

inhomogeneous gaseous medium. I: description of the method", *J. Quant. Spectrosc. Radiat. Transfer*, 14, 691-704, 1974.

23. N. Husson, B. Bonnet, N. A. Scott and A. Chédin, " The "GEISA" Data Bank 1991 Version", *Internal Note L.M.D. No 163,* Available from Laboratoire de Météorologie Dynamique, École Polytechnique, Palaiseau, France, 1991.

24. R. A. Mc Clatchey, R. W. Fenn, J. E. A. Selby, F. E. Voltz and J. S. Garing, " Optical properties of the atmosphere", *Rep. AFCRL-72-0497,* 110pp., Hanscom Air Force Base, Bedford, Mass., 1972.

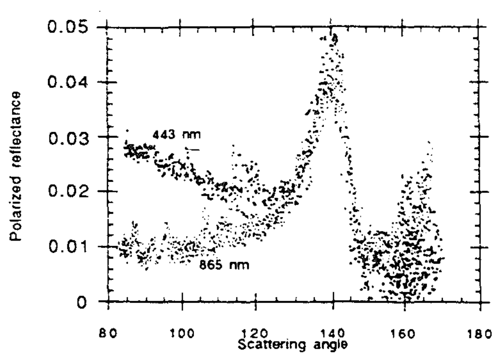

Figure 1 : Polarized reflectance of a stratocumulus , in the 443 and 865 bands, only for the viewing directions within the solar incident plane, as a function of the scattering angle

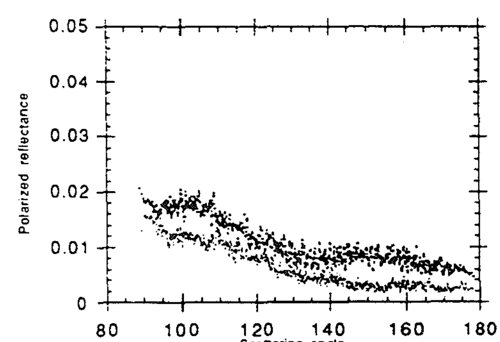

Figure 2 : Polarized reflectance of a cirrus in the 443 and 865 bands, only for the viewing directions within the solar incident plane, as a function of the scattering angle

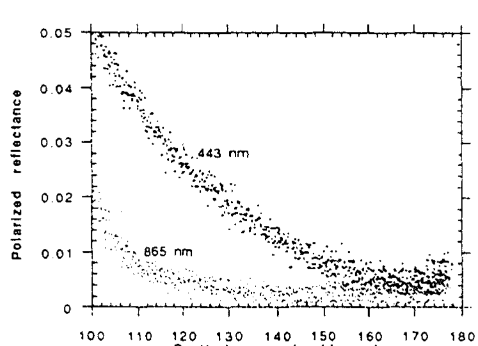

Figure 3: Clear sky typical polarization signatures.

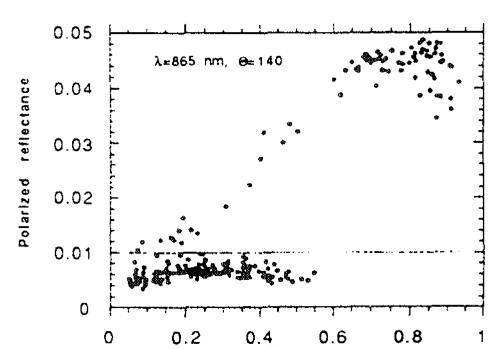

Figure 4: Polarized reflectance versus reflectance at 865 nm for scattering angle equals 140°

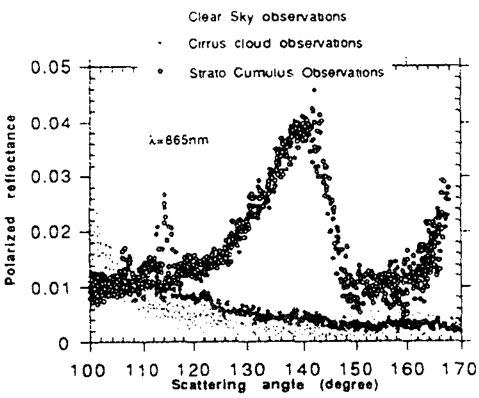

Figure 5 : Typical polarization features (liquid water cloud, ice cloud, clear atmosphere)

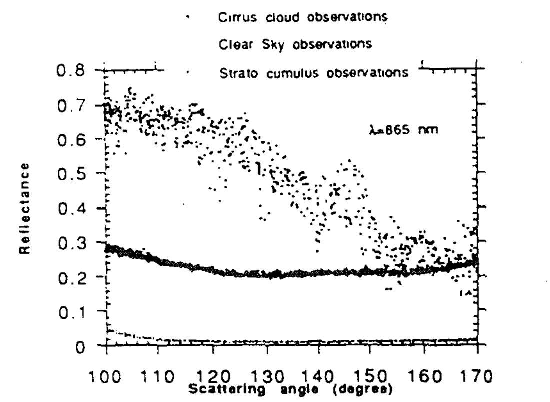

Figure 6: Typical angular signatures of mean reflectance for liquid water clouds, ice cloud and clear atmosphere.

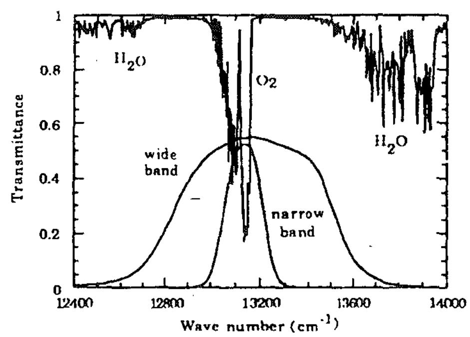

Figure 7: the A-band of Oxygen and the water vapor transmission spectra of the atmosphere at 5 cm^{-1} spectral resolution. The transmission is computed along a vertical path from space to surface using the Midlatitude Summer atmospheric profile (Mc Clatchey, 1972).

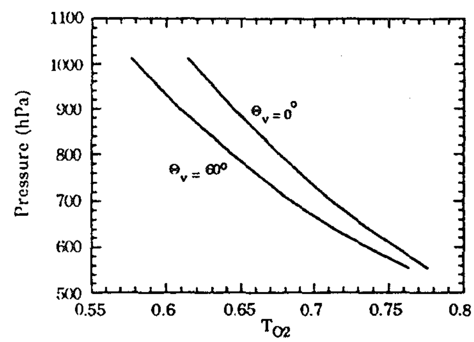

Fig ure 8 : Variations of the apparent pressure as a function of the spectrally averaged transmission of the oxygen for extreme values of the POLDER viewing zenith angle. The TO2 values correspond to EUCREX'94 flight 206 conditions (aircraft altitude 6000m, solar zenith angle 39.5°).

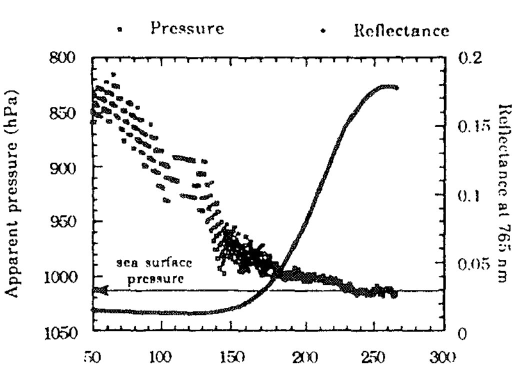

Figure 9: An example of cross-section of 765nm reflectance and retrieved apparent pressure over the sun glitter region observed on a representative image acquired by POLDER during flight 206.

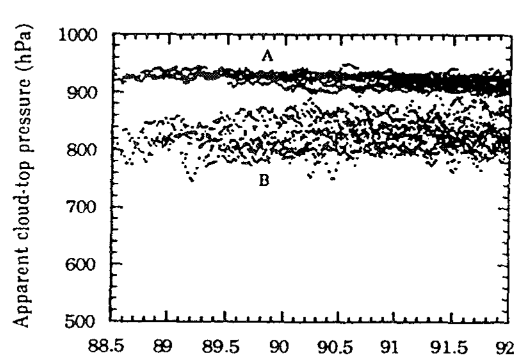

Figure 10: Retrieved apparent cloud-top pressure of a stratocumulus cloud from differential absorption method (A) or from polarization of molecular scattering (B). The expected cloud-top pressure is about 900 hPa.

COMPARISON BETWEEN FOUR INDEPENDENT METHODS OF CLOUD PRESSURE DERIVATION USING POLDER AND LIDAR MEASUREMENTS DURING EUCREX'94

F. Parol, P. Goloub and J. Descloitres
Laboratoire d'Optique Atmosphérique, Université des Sciences et Technologies de Lille
Villeneuve d'Ascq, 59650, France

J. Pelon
Service d'Aéronomie, Université P. et M. Curie
Paris, 75005, France

P. Flamant
Laboratoire de Météorologie Dynamique, Ecole Polytechnique
Palaiseau, 91128, France

ABSTRACT

Together with the cloud optical thickness, one of the most important cloud properties with respect to global climate change is the cloud pressure. Here, two methods developed for deriving cloud pressure from the spaceborne version of the POLDER instrument are here applied to data acquired by the two airborne simulators of POLDER operated during EUCREX'94. The so-derived cloud pressures are compared to those determined by using a stereoscopic imagery method based on the multiangular capability of POLDER, and on the other hand to cloud heights given by the LEANDRE lidar.

1. INTRODUCTION

These last years, several sensitivity studies have shown that the response of numerical climate models was strongly dependent on the various hypotheses and parameterizations used to simulate the cloud-radiation interactions (see for instance Cess et al., 1996). Consequently there was essential to build a consistent dataset of cloud covers and cloud properties at the planetary scale. The International Satellite Cloud Climatology Project (ISCCP: Schiffer and Rossow, 1983) has been a major component of this project.

Among the numerous cloud properties required for a better understanding of the role of clouds on radiation and climate, cloud altitude - or cloud pressure - is one of the most important because it highly regulates the effect of clouds on longwave radiation. For instance, Ohring and Adler (1978) found that an increase of 1km in cloud height would result in a 1.2K increase in surface temperature. Several techniques for deriving cloud altitude from satellite have already been investigated, among them the lidar, the well-known brightness temperature method, the CO2-slicing technique introduced by Smith and Platt (1979) or the analysis of backscattered radiances at wavelengths within the O_2 A-band introduced by Yamamoto and Wark (1961).

Cloud pressure is one of the cloud characteristics that will be retrieved from POLDER (POLarization and Directionality of the Earth's Reflectances) aboard the japanese ADEOS platform (Buriez et al., 1996). In this paper the two methods developed for cloud pressure derivation are applied to data acquired by the two airborne simulators of POLDER operated during EUCREX'94. The first method makes use of two POLDER radiances measured in the O_2 A-band. The second one is based on the analysis of polarized reflected sunlight at 443nm. The so-derived cloud pressures are compared to those determined by using a stereoscopic imagery technique based on the multiangular capability of POLDER, and on the other hand to cloud heights given by the LEANDRE lidar.

2. INSTRUMENTS AND DATA

During the EUCREX'94 campaign in Brittany (France), the two airborne remote sensing instruments, POLDER and LEANDRE, were flown over low-level clouds. In particular, on 18 April 1994, a stratocumulus cloud deck has been sampled along a 110km leg, between point M (48°25'N, 4°47'W) and point A (49°18'N, 5°34'W). Despite the significant variability that appears in the structure of the stratocumulus, the observed continuous gradient of cloud altitude (see section 4) at the 100km scale provides a unique data set for a comparison of the various estimations of cloud pressure.

The POLDER instrument is a radiometer designed to the global observation of polarization and directionality of the sunlight reflected by the Earth surface-atmosphere system (Deschamps et al., 1994). It is composed of a CCD detector matrix, a rotating wheel which carries spectral and polarizing filters, and a wide field of view telecentric optics. The original features of POLDER, when compared to previous current radiometers are its polarized reflectance measurements in the visible and near-infrared part of the solar spectrum, and its capability

IRS '96: Current Problems in Atmospheric Radiation
Smith and Stamnes (Eds.) ISBN 0-937194-39-5

to provide quasi-simultaneous multidirectional observations of any scene.

During EUCREX'94, two airborne versions of POLDER were flown simultaneously. For both of them, the field of view extends up to ±52° in the along-track direction and to ±42° in the cross-track direction. The first POLDER instrument was flown aboard the German Falcon aircraft of the DLR (Deutsche forschungsanstalt für Luft and Raumfahrt) and the second one was installed with LEANDRE aboard the French Fokker-27 ARAT (Avion de Recherche Atmosphérique et de Télédétection). The altitude of the Falcon and the ARAT was 3km and 4.5km respectively. The respective dimensions of the CCD array of POLDER were 288 x 242 and 384 x 288 detectors. In order to reduce both the data flow and the radiometric noise, the spatial resolution of the raw data is degraded to 5 x 5 pixels, that means to ~ 100m x 100m. In this paper, we make use of two polarized filters with spectral bands centered on 443nm and 865nm and three unpolarized filters with spectral bands centered on 763nm, 765nm and 910nm respectively.

The airborne backscatter lidar LEANDRE has flown aboard the ARAT to document the vertical structure of the marine boundary layer and clouds at the mesoscale. The two working Nd-YAG laser wavelengths are in visible and near-infrared at 532nm and 1064nm respectively. The backscattered signal is sampled with a vertical resolution of 15m. Further details on the system characteristics can be found in Pelon et al. (1990). The results presented here have been obtained with the lidar looking downward or upward and by using the polarized visible wavelength channel only. In this channel the signal is sampled on a shot to shot basis, corresponding to a 10m horizontal resolution. Then, to increase signal to noise ratio, 10 shots averages are performed. Taking into account the transceiver characteristics and the flight altitude, the lidar footprint at the stratocumulus level, averaged over 10 shots, is around 100m along-track and 20m cross-track, and so it is very similar to the spatial resolution of POLDER. Reaching the stratocumulus layer, the backscattering increases very sharply allowing to define precisely the cloud-top or the cloud-base altitudes.

3. METHODOLOGY

3.1 Differential absorption method

The use of atmospheric absorption in the O_2 A-band to infer cloud pressure has been suggested or investigated by several authors (see for instance Yamamoto and Wark, 1961 ; Fisher et al., 1991 ; O'Brien and Mitchell, 1992). The simple model used in this study has already been presented in Parol et al. (1994). It assumes the atmosphere as a pure absorbing medium. The retrieved pressure level is thus the pressure of the apparent reflecting layer.

During EUCREX'94 field campaign, the filter wheel of the POLDER simulator aboard the Falcon supported two filters with spectral bands centered on 763nm with 10nm wide (the narrow band) and on 765nm with 40nm wide (the wide band). Whereas the narrow band is strongly attenuated by the absorption by O_2, the wide band is only partially attenuated. The spectrally averaged oxygen transmittance T_{O2} is derived from the reflected radiances, R_N and R_W, measured in the narrow band and the wide band respectively. Weak absorption by H_2O and O_3 is taken into account. The H_2O - correction is made by using the POLDER water vapor channel at 910nm. The O_3 - absorption is computed by using the Midlatitude Summer atmospheric profile (McClatchey et al., 1972). Finally, depending on the viewing zenith angle, the apparent pressure is derived from the computed T_{O2}. Any additional detail about the accuracy of the model and the calibration procedure can be found in Parol et al. (1994).

3.2 Use of molecular polarization

The interest of polarization measurements for cloud study has been pointed out long ago (Coffeen and Hansen 1972). Cloud pressure can be retrieved by using polarized light measurements at short wavelengths (<500nm) because clouds are known to weakly polarize the reflected solar radiation near the neutral point, at scattering angle 90°-100° (see Fig.1). On the other hand, in these conditions molecules are very efficient for scattering polarized sunlight. Thus, considering that the underlying surface and most of aerosols are screened by the cloud and taking into account the cloud contribution, the amount of polarized reflected sunlight yields the molecular optical depth situated above the cloud, i.e. the cloud pressure (Goloub et al., 1994).

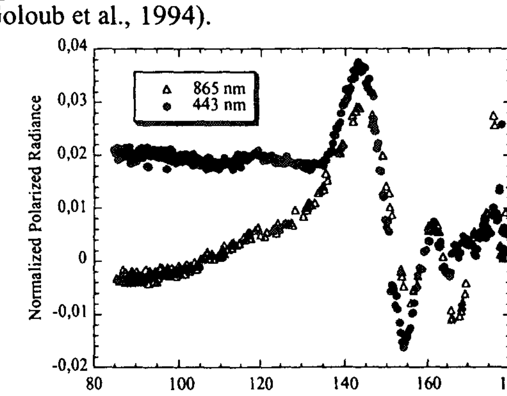

Fig.1: Normalized polarized radiance measured by POLDER at 443nm and 865nm for a typical part of the stratocumulus deck. The presented radiance values correspond only to the viewing directions within the solar incident plane. Clearly appears the neutral point of cloud polarization (near 100° at 865nm) as well as the cloudbow signature (around 140°).

For correcting the cloud contribution the basic idea is to use the polarization signal in the near infrared band of POLDER (865nm), where the molecular contribution is negligible, in order to infer the cloud microphysical properties and then to predict the position of the neutral point at 443nm. Numerical simulations using the General Spherical Harmonics in Polarization (GSHP) radiative transfer code (Gracia and Siewert, 1986) have been compared to data. The best fit for 865nm polarized reflectances was obtained using effective radius and effective variance for the droplet size distribution of 5µm and 0.1 respectively, in good agreement with microphysical measurements (Descloitres et al., 1996). Using that cloud particle size distribution the GSHP code indicates that the cloud contribution at 443nm is negligible for scattering angle 90°. According to these results and assuming that the single scattering approximation is valid, the cloud pressure, Pc, can be derived from the 443nm normalized polarized radiance Lp as

$$Lp = \frac{3\delta_R}{16\cos(\theta_v)} \cdot \frac{Pc - Pa}{Po} \qquad (1)$$

where θ_v is the viewing zenith angle, δ_R is the total molecular optical thickness (δ_R =0.23 at 443nm), Pa and Po are flight level and surface pressures respectively.

3.3 Stereoscopic imagery

The analysis of stereoscopic images for inferring target altitudes or relief maps is a well-known method which has already been applied successfully with SPOT (Satellite Probatoire d'Observation de la Terre) images and with simultaneous images from two geostationary satellites (Hasler et al., 1991). The CCD matrix of POLDER allows to observe any target (cloud in our case) on several successive images with different viewing angles, and thus to derive the relative altitude of the observed scene, h, with respect to the aircraft. The accuracy of cloud-top height determination is of the order of the pixel size.

4. RESULTS

For more convenience the so-retrieved cloud pressures are converted into cloud altitudes by using the atmospheric profile sampled by the Falcon standard instruments. Moreover, for differential absorption and molecular polarization methods, the degraded spatial resolution of POLDER images (5 x 5 pixels) makes the retrieved altitude of an elementary scene systematically lower than the altitude of the top of the cloud as determined by the lidar. In order to make comparable the different retrieving methods only the brighter POLDER pixels (864nm reflectance > 0.25) have been selected.

Of the techniques here investigated, lidar is the most precise with an accuracy of ~20m. As shown in Fig.2, the altitude of the stratocumulus cloud top as derived from LEANDRE is seen to decrease from 1100 m close to the coast (point M) down to 800 m near the edge of the stratocumulus deck close to point A. In the same time the cloud base height decreases from 900 m to 600 m, thus keeping the cloud depth nearly constant when going from point M to point A where the cloud deck is breaking. As seen on Fig.2.a, a quite good agreement is found between cloud heights derived from stereoscopic imagery and lidar, since the continuous variation of cloud altitude is observed on the two sets of data. The method based on molecular polarization gives cloud altitude close to cloud base at the beginning of the leg but highly variable at the end of the leg when the cloud structure is very inhomogeneous. Note that the molecular polarization method provides cloud pressure only for scattering angles near 90° that do not correspond to nadir viewing. Figure 2.b presents the cloud altitudes as they are derived from the different techniques applied to POLDER aboard the Falcon. It is remarkable that both differential absorption and stereoscopy methods reproduce a similar continuous gradient of cloud altitude at 100km scale. Once more the molecular polarization method

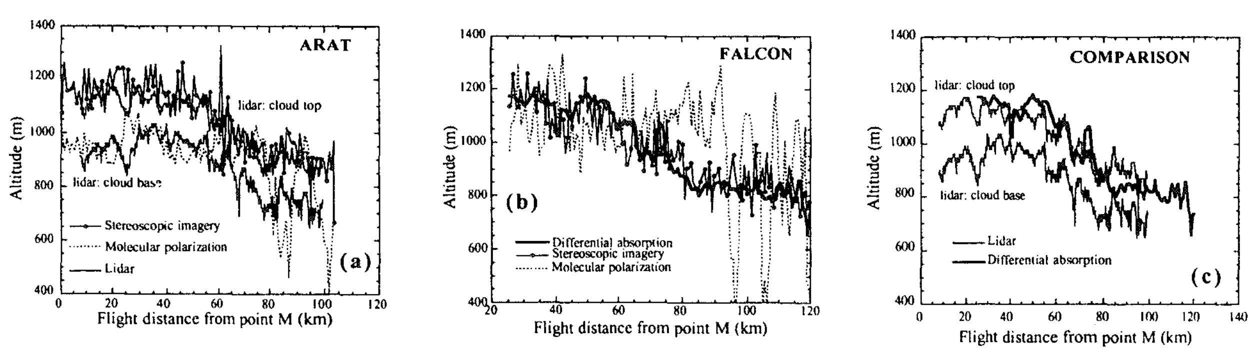

Fig.2: Cloud altitudes derived from the different methods applied to POLDER measurements along the leg from M to A. The LEANDRE lidar aboard the ARAT provided cloud top and cloud base heights during the same leg. Using POLDER/ARAT a good correlation is found between cloud heights derived from stereoscopy and lidar (a). Similarly, using POLDER/FALCON a quite good agreement is found between steroscopy and differential absorption method (b). For more convenience, (c) shows direct comparison between lidar and differential absorption method.

provides cloud altitudes highly noisy around a mean value that appears nearly constant (~1100m) before sharply decreasing when approaching point A. More in details, Fig. 2.c shows the comparison between cloud altitude derived from differential absorption method using POLDER aboard the Falcon and the cloud top and base heights determined by LEANDRE. Despite both the uncertainty on the location of the two aircrafts and the slight time lag between the respective measurements the agreement is more than satisfactory. This gives us some confidence in the differential absorption method that will be operationaly applied to spaceborne POLDER data very soon.

5. CONCLUSION

Three methods are presented that derive cloud altitude using the POLDER radiometers aboard the ARAT and Falcon aircrafts during the EUCREX'94 campaign. The results are compared to cloud top and cloud base heights provided by the LEANDRE lidar aboard the ARAT. The general trend of the cloud top altitude as a function of the flight distance is retrieved by all the methods. The agreement between cloud altitudes derived from both differential absorption by oxygen and stereoscopic imagery and cloud-top height determined by the lidar is quite satisfactory. On the other hand, the cloud altitude derived from molecular polarization method is much more noisy, even if it clearly appears a link between the derived cloud altitude and the cloud structure. That obviously underlines the need of further investigation to address a more specific analysis of polarization measurements.

ACKNOWLEDGMENTS

This work was supported by the European Economic Community (EEC) and the Centre National d'Etudes Spatiales (CNES). The authors thank F. Lemire for his help in processing the POLDER data. They are also very grateful to all persons who participated in POLDER campaigns.

REFERENCES

Buriez, J.C., C. Vanbauce, F. Parol, P. Goloub, M. Herman, B. Bonnel, Y. Fouquart, P. Couvert, and G. Seze, 1996: Cloud detection and derivation of cloud properties from POLDER. Submitted to *Int. J. Remote Sensing*.

Cess, R.D., et al., 1996: Cloud feedback in atmospheric general circulation models: An update. *J. Geophys. Res.*, **101**, 12791-12794.

Coffeen, D.L., and J.E. Hansen, 1972: Airborne infrared polarimetry. *Proc. 8th Internat. Symp. Remote Sensing Environment*.

Deschamps, P.Y., F.M. Bréon, M. Leroy, A Podaire, A. Bricaud, J.C. Buriez, and G. Sèze, 1994: The POLDER mission: instrument characteristics and scientific objectives. *IEEE Trans. Geosci. Remote Sensing*, **32**, 598-615.

Descloitres, J., H. Pawlowska, J. Pelon, J.L. Brenguier, F. Parol, J.C. Buriez, and P. Flamant, 1996: Experimental retrieval of cloud optical thickness during EUCREX: Comparison of three approaches. *Proc. of the ICCP'96*.

Fisher, J., W. Cordes, A. Schmitz-Peiffer, W. Renger, and P. Mörl, 1991: Detection of cloud-top height from backscattered radiances within the oxygen A band, Part 2: Measurements. *J. Appl. Meteor.*, **30**, 1260-1267.

Garcia, R.D.M., and C.E. Siewert, 1986: A generalized spherical harmonics solution for radiative transfer models that include polarization effects. *J. Quant. Spec. Rad. Transfer*, **36**, 401-423.

Goloub, P., J.L. Deuzé, M. Herman, and Y. Fouquart, 1994: Analysis of the POLDER polarization measurements performed over cloud covers. *IEEE Trans. Geosci. Remote Sensing*, **32**, 78-88.

Hasler, A.F., J. Strong, R.H. Woodward, and H. Pierce, 1991: Automatic analysis of stereoscopic image pairs for determination of cloud top height and structure. *J Appl. Meteor.*, **30**, 257-281.

McClatchey R. A., R. W. Fenn, J. E. A. Selby, F. E. Voltz, and J. S. Garing, 1972: Optical properties of the atmosphere. *Rep. AFCRL-72-0497*, 110pp., Hanscom Air Force Base, Bedford, Mass.

O'Brien, D.M., and R.M. Mitchell, 1992: Error estimates for retrieval of cloud-top pressure using absorption in the A band of Oxygen. *J. Appl. Meteor.*, **31**, 1179-1192.

Ohring, G, and S. Adler, 1978: Some experiments with a zonally averaged climate model. *J. Atmos. Sci.*, **35**, 186-205.

Parol, F., P. Goloub, M. Herman, and J.C. Buriez, 1994: Cloud altimetry and water phase retrieval from POLDER instrument during EUCREX'94. In *Atmospheric Sensing and Modelling*, R.P. Santer, Editor, *Proc. SPIE 2311*, 171-180.

Pelon, J., P.H. Flamant, and M. Meissonnier, 1990: The French airborne backscatter lidar LEANDRE I: Conception and operation. V.E. Zuev ed., 15th ILRC, Institute of Atmospheric Optics pub., Tomsk, USSR, p. 36.

Schiffer, R.A., and W.B. Rossow, 1983: The International Satellite Cloud Climatology Project (ISCCP): The fisrt project of the world climate research program. *Bull. Amer. Meteor. Soc.*, **64**, 779-784.

Smith, W.L., and C.R.M. Platt, 1979: Comparison of satellite-deduced cloud heights with indications from radiosonde and ground-based laser measurements. *J. Appl. Meteor.*, **17**, 1796-1802.

Yamamoto, G., and D.Q. Wark, 1961: Discussion of the letter by R.A. Hanel: "Determination of cloud altitude from a satellite", *J. Geophy. Res.*, **66**, 3596.

INT. J. REMOTE SENSING, 1997, VOL. 18, NO. 13, 2785–2813

Cloud detection and derivation of cloud properties from POLDER

J. C. BURIEZ, C. VANBAUCE, F. PAROL, P. GOLOUB,
M. HERMAN, B. BONNEL, Y. FOUQUART
Laboratoire d'Optique Atmosphérique,
Université des Sciences et Technologies de Lille, 59655 Villeneuve d'Ascq,
France

P. COUVERT
Laboratoire de Modélisation du Climat et de l'Environnement,
Centre d'Etudes de Saclay, 91191 Gif-sur-Yvette, France

and G. SÈZE
Laboratoire de Météorologie Dynamique, Ecole Normale Supérieure,
75231 Paris, France

(*Received 25 July 1996; in final form 25 November 1996*)

Abstract. POLDER (POLarization and Directionality of the Earth's Reflectances) is a new instrument devoted to the global observation of the polarization and directionality of solar radiation reflected by the Earth surface–atmosphere system. This radiometer has been on board the Japanese ADEOS platform since August 1996. This paper describes the main algorithms of the POLDER 'Earth radiation budget (ERB) & clouds' processing line used to derive products on a routine basis in the early phase of the mission. In addition to the bidirectional reflectance and polarization distribution functions, the main products will be the cloud optical thickness, pressure (from two different methods) and thermodynamic phase. Airborne POLDER observations support the present algorithms for the cloud detection and the derivation of cloud properties.

1. Introduction

In the near future, the Earth will be confronted with the potential risk of rapid environmental changes mainly generated by human activity. The magnitude, regional and temporal distribution of global change should have an important impact on society, but today, it is not possible to provide answers to questions about these probable effects, mainly due to a misreading of the interdependent processes that affect regional as well as global climate. Among the problems that have received increased attention in recent years are the changes in cloud radiative effects due to greenhouse warming and increase in anthropogenic aerosols.

The most comprehensive way to predict climate change due to an increase of greenhouse gases and aerosols is by means of general circulation models (GCMs). However, current models project sea-surface temperature increases due to given climate forces that differ by a factor of two or three (Cess *et al.* 1990). Such differences can be obtained from an individual GCM by changes only in the cloud parameterization (Senior and Mitchell 1993). This clearly shows the need of realistic representation of clouds in GCMs. Global observations of cloud properties and global measurements of the effect of clouds on radiation are essential to achieve this

0143–1161/97 $12.00

objective, even if field experiments and surface measurements remain essential to support the satellite measurements at the global scale.

Before the end of the century, a series of satellites will carry several advanced, well-calibrated, instruments designed to provide Earth observations (Wielicki *et al.* 1995). Among them, POLDER (POLarization and Directionality of the Earth's Reflectances) has been launched on the Japanese Advanced Earth Observing Satellite (ADEOS). Due to its multi-spectral, multi-directional and multi-polarization capabilities, this new radiometer will give useful information on the clouds and on their influence on radiation in the short-wave (SW) range.

A first issue concerns the modelling of cloud radiative properties. Clouds are often treated as homogeneous plane-parallel layers composed of spherical particles in the modelling of their effects on climate in GCMs as well as in the derivation of cloud properties from satellite radiances. This approach may be a major weakness in the assessment of the effects of clouds on radiation. For instance, Parol *et al.* (1994 a) and Brogniez *et al.* (1992) report errors in SW cloud forcing estimates that might be as large as $40\,\mathrm{Wm}^{-2}$ when the morphology of convective clouds or the particle shape in cirrus clouds is neglected. However, at present it is hardly possible to infer the actual global effect of cloud morphology, i.e., three-dimensional cloud structures, on radiation because from the usual scanner radiometers a given geographical target is observed from an unique direction during a satellite overpass. That means that it is always possible to find a cloud model that satisfies the *unique* radiance observation. POLDER will provide $\sim$*14* quasi-simultaneous radiance measurements of any cloud scene, allowing different cloud models to be checked and to verify if *one* of them fulfills the complete set of observations. Such comparisons have already been carried out from airborne POLDER observations (Descloitres *et al.* 1994, 1995).

The matter of the spherical particle hypothesis is related mainly to the treatment of interactions between cirrus clouds and radiation. To date, there is little information on cloud microphysics at the global scale, except for the effective radius of water droplets in low-level clouds (Han *et al.* 1994). The original features of the POLDER sensor offer some information on cloud phase and even potentially on the size/shape of cloud particles. Indeed, data acquired using the airborne version of POLDER have shown that the Bidirectional Polarization Distribution Function (BPDF) is a useful tool for detecting the presence of liquid particles (Goloub *et al.* 1994).

Another point of interest for improving our understanding of climate changes concerns the Earth Radiation Budget (ERB) measurements. The most advanced procedure to derive the SW flux from the radiance measured in a given direction from ERB scanners has been developed for the ERBE experiment. Estimates of instantaneous reflected fluxes at the pixel scale are obtained by applying the bidirectional models derived from a limited set of Nimbus 7/ERB scanner measurements (61 days) (Suttles *et al.* 1988). However, the uncertainty related to the use of these bidirectional models drastically limits the accuracy of the estimated fluxes in the short-wave range. Indeed, from ERBS/NOAA-9 intercomparisons, uncertainties of $\pm 15\,\mathrm{Wm}^{-2}$ are expected in the short-wave, on instantaneous observations of $(2{\cdot}5°)^2$ regions, i.e., 7–8 per cent for a typical reflected flux of $200\,\mathrm{Wm}^{-2}$, in comparison to only 2–3 per cent for radiance measurements (Barkstrom *et al.* 1990). In the same way, comparisons between the Nimbus-7-derived radiation field anisotropy and the ERBS-observed anisotropy indicate an instantaneous r.m.s. error ranging between 4 and 15 per cent due to the use of incorrect bidirectional models (Baldwin and Coakley 1991).

POLDER provides quasi-simultaneous multi-directional radiance measurements (~ 14 viewing angles) of any scene, which means that it observes a part of the Bidirectional Reflectance Distribution Function (BRDF) of the scene. Thus, POLDER could improve the SW flux derivation from ERB scanner measurements, both on a statistical basis, by permitting the construction of new bidirectional models for various surfaces, cloud types and cloud amounts, and, even more interestingly, on an instantaneous basis providing that in the future POLDER and an ERB scanner are aboard the same platform.

As outlined by Wielicki *et al.* (1995), POLDER is part of a series of new sensors that may provide key information for improving our knowledge of clouds, radiation and climate interactions. As a component of the POLDER project, the aim of this paper is to present the algorithms that will be operationally used to derive 'ERB & clouds' products (such as cloud cover, cloud pressure) from ADEOS/POLDER data. These products will be distributed by CNES (Centre National d'Etudes Spatiales, France) from the end of 1997. An overview of the algorithms and products is reported in § 2. Following the methodology applied in the ISCCP scheme (International Satellite Cloud Climatology Project, Rossow and Schiffer 1991) the cloud analysis based on POLDER measurements is separated into the cloud detection phase and the cloud properties derivation phase. The main algorithms for the cloud detection and the determination of cloud properties, that are supported by airborne POLDER observations, are presented in § 3 and 4, respectively.

2. POLDER 'ERB and clouds' processing line

The POLDER instrument on ADEOS is extensively described by Deschamps *et al.* (1994). It consists of a charged coupled device (CCD) matrix detector, a rotating filter wheel carrying the polarizers and filters, and a wide field-of-view (FOV) telecentric optics. The CCD array is composed of 242 by 274 independent sensitive areas. It corresponds to along-track and cross-track FOVs of $\pm 43°$ and $\pm 51°$ respectively, and to a diagonal FOV of $\pm 57°$. As the heliosynchronous ADEOS satellite is orbiting at 796 km altitude, the POLDER cross-track swath is about 2200 km and the pixel foot-print is about 6 km by 7 km at nadir. The equatorial crossing time is 10:30. As the satellite passes over a target, ~ 14 different images are acquired in each spectral band whose characteristics are reported in table 1.

The POLDER level 1 product will include calibrated reflectances and Stokes parameters projected on a reference Earth equal-area grid at 6·2 km resolution. The level 2 and 3 processings will be split in three lines according to the three thematic interests of POLDER, namely: 'ERB, water vapour and clouds', 'Ocean colour and aerosols over the ocean', 'Land surfaces and aerosols over land'.

The development of the 'ERB & clouds' processing line has two aims: (1) to derive cloud parameters such as cloud optical thickness, cloud pressure and cloud phase and the atmospheric water vapour content; (2) to provide the necessary data to construct BRDFs (and BPDFs) according to user's own criteria which may be selected afterwards (for instance, cloud cover, cloud pressure, meteorological conditions, etc.). As outlined in the previous section, this second item is important in view of the high remaining uncertainty when inverting radiances to fluxes, which is simply due to the use of limited and sometimes incorrect bidirectional models.

All the retrieved 'ERB & clouds' parameters are based on simple algorithms in order to be produced on a routine basis after a reasonably short validation period. For instance, cloud optical thickness is derived by using a radiative transfer model

Table 1. Characteristics of the spectral bands of the POLDER instrument. There are three channels for each polarized band. The channels with low dynamic range of reflectance are not used in the ERB & clouds processing line. Only the bands indicated by an asterix were present in the airborne POLDER instrument during the EUREX'94 campaign.

Central Wavelength (nm)	Band width (nm)	Polarization	Dynamic range
443	20	No	0–0·22
443 (*)	20	Yes	0–1·10
490	20	No	0–0·17
565	20	No	0–0·11
670	20	Yes	0–1·10
763 (*)	10	No	0–1·10
765 (*)	40	No	0–1·10
865 (*)	40	Yes	0–1·10
910 (*)	20	No	0–1·10

based on the plane-parallel approximation. This, however, does not take full advantage of the POLDER capability to observe the radiation field anisotropy, thus more complex algorithms should be developed in the future. Nevertheless, the present product should already permit the validity of the usual plane-parallel model to be checked on a global basis.

As mentioned above POLDER offers special capabilities but has limited data sampling because of the Sun-synchronous orbit of ADEOS. Another limitation, which is a constraint mainly for the 'ERB and clouds' line, is due to the geographical relocalization of the POLDER pixels which does not take into account the cloud altitude. By considering the 14 view angles for each pixel this induces an horizontal shift in the registration that varies from $\sim \pm 0{\cdot}1$ pixel for stratus up to $\sim \pm 2$ pixels for cirrus. Because of this shift, a pixel may present different properties according to the direction of the satellite observation. Consequently, calculations are independently made for every pixel and for every direction, then, in order to minimize the horizontal shift effect, the results are averaged over a super-pixel composed typically of 9 by 9 geographical pixels. This presents the advantage of a reduced data flow. However, in order to preserve some information about spatial heterogeneity, standard deviations are calculated. Precisely, a super-pixel corresponds to a 0·5° by 0·5° area at the equator which will make POLDER products easily comparable to ISCCP ones whose scale is 2·5° by 2·5° (Rossow and Schiffer 1991). The resolution of a super-pixel also appears to be adequate for BRDF studies because it is about $(50\,\mathrm{km})^2$ and close to the spatial resolution of typical ERB scanners. It should be noted that although one of the objectives of the POLDER mission is to construct new bidirectional models, only BRDFs corresponding to scene types defined in the context of ERBE (Suttles *et al.* 1988) are routinely produced. Our choice has been to leave the selection open for additional criteria according to which new classifications of the BRDFs will have to be made. The POLDER 'ERB & clouds' line thus provides the data necessary to construct these new BRDFs (and BPDFs) according to user's own criteria.

The 'ERB & clouds' level 2 and 3 products are detailed in tables 2 and 3 respectively. The chart of POLDER 'ERB & clouds' processing is reported in figure 1.

Table 2. POLDER level 2 ERB & clouds product provided for each orbit at the super-pixel scale.

Parameter	Description
General information	• Number of elementary pixels N_{pixels} • Number of viewing directions N_{dir} • Viewing/illumination geometry • Quality indices, etc.
Reflectances at 443, 670, 865 nm and SW estimate	• N_{dir} spatially averaged values
Albedoes at 443, 670, 865 nm and SW estimate	• Mean and standard deviation of N_{dir} N_{pixels} values • Standard deviation of the N_{dir} spatially averaged values • Standard deviation of the N_{pixels} angularly averaged values • Mean of the clear-sky estimates
Cloud cover	• Fraction derived from the N_{dir} N_{pixels} values and accuracy • N_{dir} fractions derived from the N_{pixels} values
Water vapour content (only for clear-sky conditions)	• Mean and quality index
Cloud optical thickness (simple linear average and energy-weighted average) O_2-apparent pressure O_2-cloud pressure Rayleigh-cloud pressure	• Mean and standard deviation • N_{dir} spatially averaged values (means and standard deviations) • Distribution in 42 optical thickness/pressure classes
Cloud phase	• Index (Liquid, Ice, Mix, Undeterminated, Not calculated)
Auxiliary atmospheric data	• Ozone amount • Meteorological profiles (7 levels + surface)

The description of the first algorithm, which concerns correction for gaseous absorption and stratospheric aerosol effect, is reported in the appendix. The algorithms for cloud detection and the derivation of cloud properties are described in the next sections. The algorithm for precipitable water content is described in Leroy *et al.* (1996).

3. Cloud detection scheme

3.1. *POLDER data*

As ADEOS was launched in August 1996, we did not have any satellite data at our disposal during the preliminary phase of the POLDER mission. However, our algorithms have been made from the experience acquired by analysing a large number of measurements performed by the airborne simulator of POLDER during several international field experiments (for instance, ASTEX/SOFIA, Weill *et al.* 1996, EUCREX'94, Descloitres *et al.* 1995). The greater part of POLDER measurements related to the study of clouds has been performed using spectral filters that are very similar to those mounted in the spaceborne version of the instrument but have been

Table 3. POLDER level 3 ERB & clouds product provided for each month.
(*a*) At the global scale

Parameter	Description
Bidirectional reflectance distribution functions	● Number of observations, mean reflectance and standard deviation, mean bidirectional function (reflectance/albedo) and standard deviation, for 12 scene types and 800 angular bins
Bidirectional polarization distribution functions (only for ice clouds)	● Number of observations, mean polarized reflectance and standard deviation, in 36 angular bins

(*b*) At the super-pixel scale

Parameter	Description
General information	● Number of days N_{days}, number of orbits N_{orb}, etc.
Albedoes at 443, 670, 865 nm and SW estimate	● Monthly mean and standard deviation ● Mean of the clear-sky estimates
Cloud cover	● Monthly mean and standard deviation ● Monthly mean uncertainty ● Occurence (number of days) in 10 classes
Water vapour content (only for clear-sky conditions)	● Monthly mean and standard deviation ● Occurrence (number of days) in 10 classes
Cloud optical thickness (simple linear average and energy-weighted average) O_2-apparent pressure O_2-cloud pressure Rayleigh-cloud pressure	● Monthly mean and standard deviation ● Distribution (percentage of pixels) in 42 optical thickness/pressure classes ● Occurrence (number of days) in 42 optical thickness/pressure classes
Cloud phase	● Distribution (percentage of pixels) in 5 classes ● Occurrence (number of days) in 5 classes

acquired mainly over the ocean (for instance, off the coast of Brittany in the case of the EUCREX'94 campaign). In our operational processing line, the treatment of POLDER data is divided into two classes of geographical pixels labelled namely, 'ocean' and 'land'. While the body of the overall algorithm is the same, the different thresholds used either in the cloud detection scheme or in the derivation of cloud properties are adapted depending on the scene type, i.e., depending on the geographical location of the POLDER pixel.

In this paper, in order to illustrate the working and/or the results of the different algorithms running in the 'ERB & clouds' line, we mainly utilize, some sets of POLDER images acquired during the EUCREX'94 campaign. Figure 2 shows typical features of bidirectional measurements performed by the POLDER instrument aboard the German FALCON aircraft during this campaign. The three sets of images correspond to acquisitions over clear ocean, stratocumulus and cirrus, respectively (table 4). From lidar measurements made in the vicinity of the FALCON, the

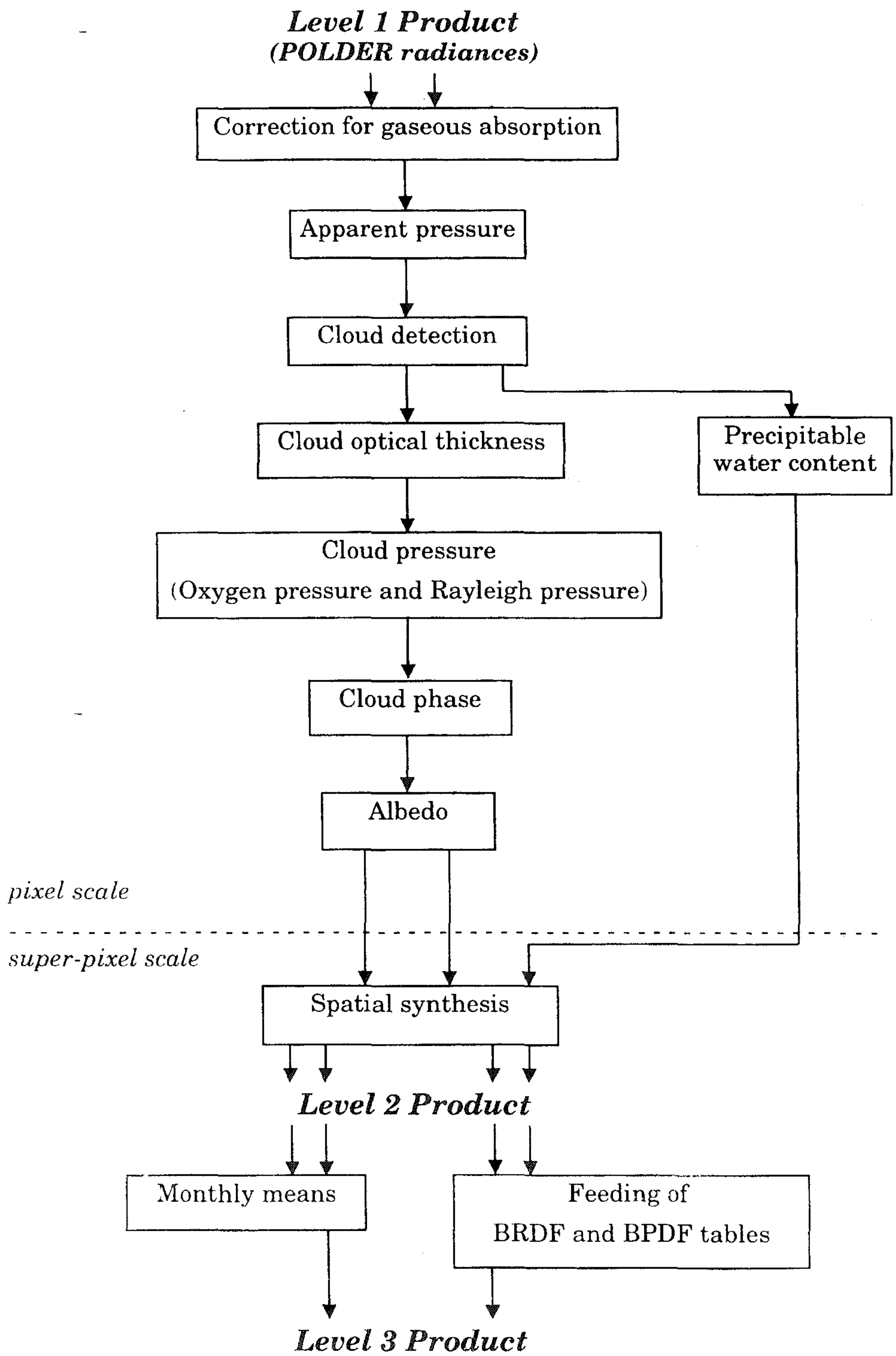

Figure 1. Flow chart of POLDER data processing in the 'ERB & clouds' line.

stratocumulus cloud top was at $(1{\cdot}0 \pm 0{\cdot}1)$ km and the cirrus cloud top varied from 6 to 10 km.

For each scene type, figure 2 displays instantaneous images that represent (*a*) the ratio of reflectances measured in the narrow and the wide channels centred at 763 and 765 nm, R_{763}/R_{765}, (*b*) the reflectance measured at 865 nm, R_{865}, (*c*, and *d*) the polarized reflectances measured at 443 and 865 nm, PR_{443} and PR_{865}, respectively. Useful information about viewing directions is reported in (*e*): the expected region of the solar specular reflection (within a cone of half-angle of 30°), the expected

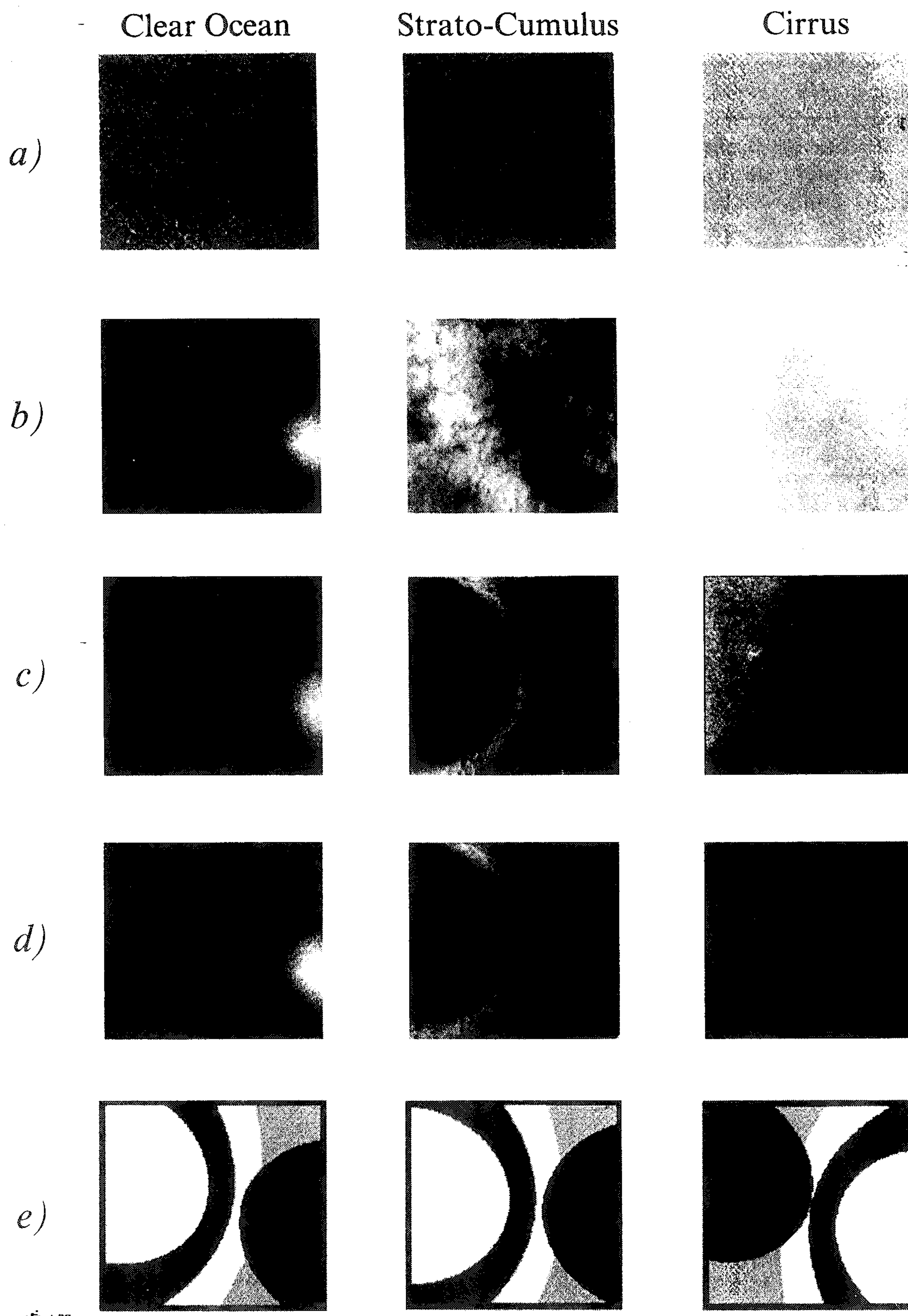

Figure 2. Typical airborne POLDER measurements acquired during EUCREX'94 over clear ocean, stratocumulus and cirrus respectively. From top to bottom, are reported: (*a*) the ratio of reflectances measured in the narrow and the wide channels centered at 763 and 765 nm, (*b*) the reflectance measured at 865 nm, (*c*) the polarized reflectance measured at 443 mm, (*d*) the polarized reflectance measured at 865 nm, and (*e*) some information about viewing directions, that is the expected region of the solar specular reflection (black), the expected cloud-bow region (dark grey) and the expected region of maximum molecular polarization (light grey).

Table 4. Some characteristics of the observations reported in figure 2.

EUCREX Flight number/ POLDER Scene number	Day	Aircraft altitude (m)	Observed cloudiness	Sea-surface wind speed ($m\ s^{-1}$)	Solar zenith angle
206/955	18 April 1994	6090	Clear-sky	7	40°
206/820	18 April 1994	6090	Stratocumulus	7	40°
205/713	17 April 1994	10670	Cirrus	8·5	38°

cloud-bow region (scattering angle γ between 135° and 150°) and the expected region of maximum molecular polarization ($80° < \gamma < 120°$). Note that the Sun zenith angle was close to 40° for the three pictures but the aircraft direction relative to the Sun was different from one another. All this information is used either for detecting cloudy pixels or for inferring cloud properties over ocean as illustrated in the following.

Airborne POLDER images presented in figure 2 correspond to an area of about $(5\,km)^2$ and are composed of pixels with footprint of about $(20\,m)^2$. As mentioned above the main difference between POLDER and a usual scanning radiometer is its capability to provide instantaneously the BRDF of an observed scene as long as it is homogeneous (at the scale of $(5\,km)^2$ in the present case). This is clearly highlighted on the 'clear-ocean' pictures where the glitter phenomenon is quite recognizable. For the stratocumulus cloud, the rainbow phenomenon which is characteristic of liquid water droplets markedly appears in the polarization images whilst it is not discernible in the unpolarized reflectance image because of cloud heterogeneity. Single and low-order scattering occurs near the cloud top results in polarized reflectance, but the effects of this polarization are washed out by multiple scattering deeper in the cloud. Consequently, the fraction of polarized light scattered by the cloud does not depend on the cloud optical thickness as soon as it is larger than about 2 (Goloub *et al.* 1994). Therefore the polarized signal, unlike the unpolarized one, is hardly sensitive to the spatial variability of the cloud optical thickness, i.e. to cloud heterogeneity. On the third set of pictures, the cirrus cloud appears rather flat, which indicates both a weak heterogeneity of the cloud structure and a weak anisotropy of the reflected light.

3.2. *Overview of the algorithm*

Most cloud detection algorithms use both visible reflectance and brightness temperature (e.g., the review in Rossow *et al.* 1989). Indeed, these two quantities are mainly sensitive to the visible cloud optical thickness and to the cloud altitude, which are the most important cloud parameters with respect to cloud-radiation interactions. Here the spectral range of the POLDER instrument is restricted to visible and near-infrared wavelengths. However, the two spectral channels centred on the oxygen A band allow the derivation of an apparent pressure which represents roughly the cloud pressure as the brightness temperature represents roughly the cloud top temperature. Moreover, additional information about cloud location within the atmosphere can be obtained from polarization measurements.

The POLDER cloud detection algorithm is based on a series of sequential tests applied to each individual pixel. The first step concerns every viewing direction (figure 3). Four tests aim at detecting clouds while two additional ones are used to

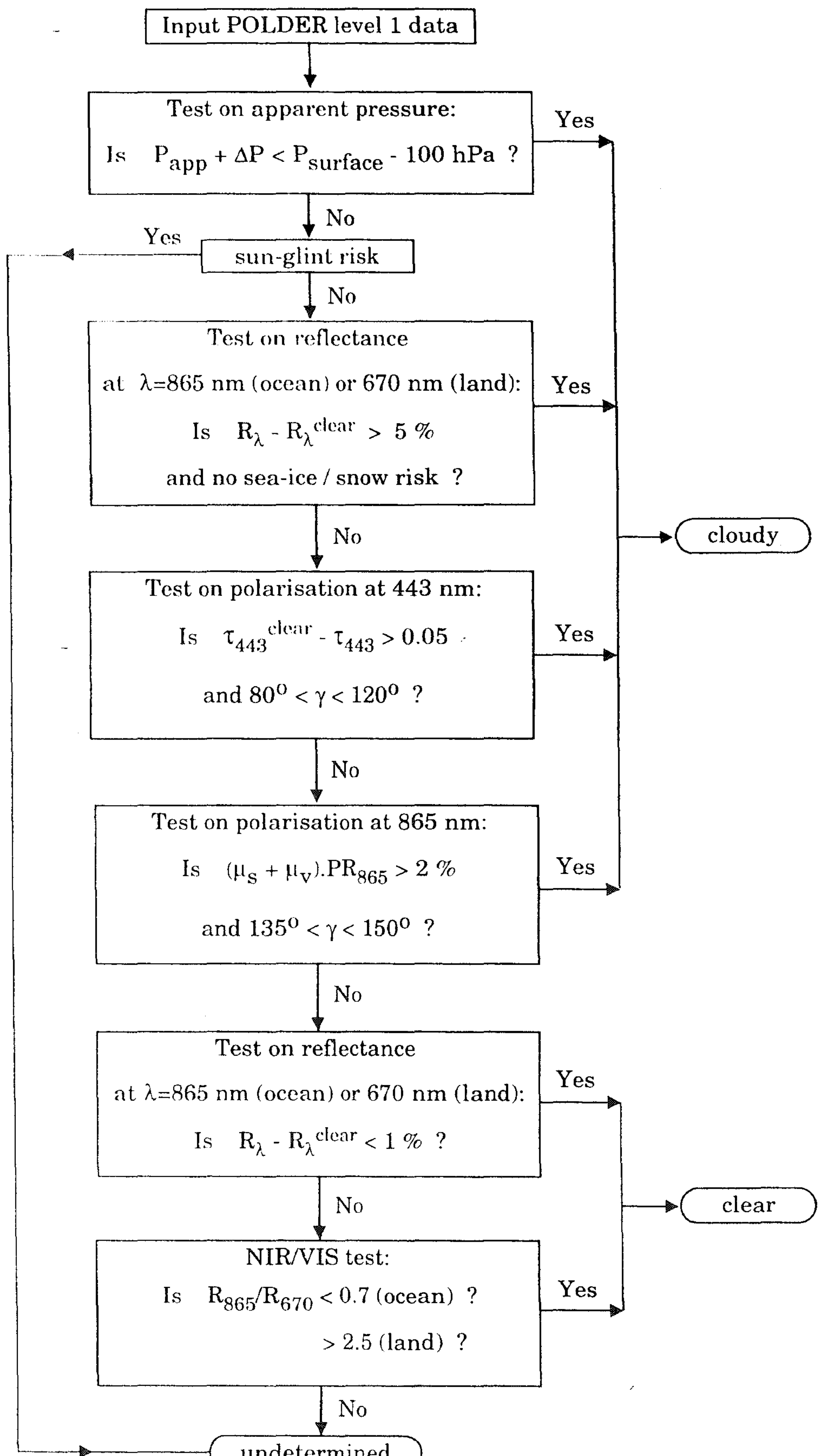

Figure 3. Outline of the part of the cloud detection algorithm applied to each pixel and for every direction. The threshold values are only indicative.

identify cloud-free pixels. Pixels that do not satisfy any of these six tests are labelled undetermined. After this series of tests, each individual pixel is thus labelled as clear, cloudy or undetermined for a given viewing direction. Note that, particularly for cloud edges, a pixel may appear as cloudy in a direction and clear in another one. A second series of tests is performed by using the multi-directional and the spatial information to re-examine the undetermined pixels.

The tests are detailed in the following and discussed with the help of the data acquired with the airborne version of the instrument. The threshold values used in these tests are only indicative. They will be adjusted after the launch of ADEOS.

3.3. *Apparent pressure test*

The first test is a pressure threshold one, using mainly the R_{763}/R_{765} ratio as indicative of the cloud contamination. The use of atmospheric absorption in the oxygen A band to infer cloud pressure has been suggested by several authors (e.g., Yamamoto and Yark 1961, Chapman 1962). Since then some theoretical efforts (Fisher and Grassl 1991, O'Brien and Mitchell 1992) and aircraft measurements (Fisher *et al.* 1991, Parol *et al.* 1994 b) have been carried out. All these studies have shown that the oxygen A band is potentially efficient for determining the cloud-top pressure. They also showed that the main difficulty lies in the photon penetration problem and the influence of ground reflectivity. However, in this first step, all scattering effects are neglected and the atmosphere is assumed to behave as a pure absorbing medium overlying a perfect reflector located at pressure P_{app}. This apparent pressure is related to the oxygen transmission T_{O_2} that is derived from the R_{763}/R_{765} ratio (see appendix). Practically, P_{app} is calculated from a polynomial function of T_{O_2} and the air-mass factor m. The coefficients of the polynomial are fitted from line-by-line simulations.

Figure 4 shows the histograms of P_{app} for the three selected scenes of figure 2. The apparent pressure is close to 350 hPa and 900 hPa for the cirrus and the stratocumulus cloud, respectively. These values agree with the cloud pressure values expected from lidar measurements. On the contrary, for the clear-ocean case, P_{app}

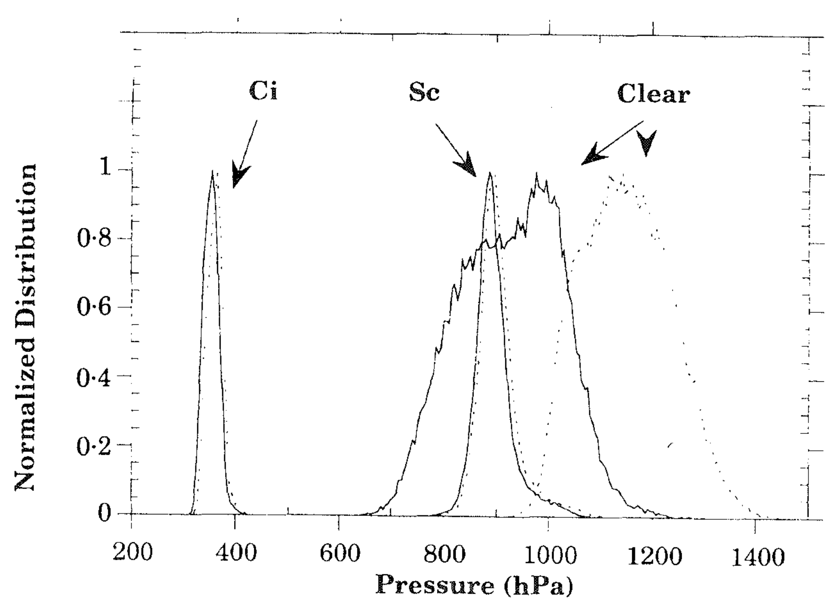

Figure 4. Histogram of the apparent pressure P_{app} for the three scenes of figure 2 (solid lines). Are also reported the histograms of $P_{app} + \Delta P$ (dashed). See text for explanations.

ranges from 650 to 1200 hPa while the sea-surface pressure was 1008 hPa. This large scatter of values of P_{app} is due to the low value of the sea-surface reflectance outside of the sunglint region. Indeed, when the measured reflectance values are very low, the radiometric noise induces a very large error on P_{app}. In addition, the part of the reflected light due to molecules and aerosols cannot be ignored since it can induce a slight bias on the apparent pressure. When only the highest values of reflectance are preserved for the clear-ocean case, the values of P_{app} tend towards the sea-surface pressure.

Using a crude threshold on P_{app} would allow only the pixels for which the apparent pressure is lower than about 600 hPa to be identified as cloudy (see figure 4). Consequently, a simple correction is made by adding to P_{app} a term ΔP which is inversely proportional to the reflectance. Practically, from simulations, we established:

$$\Delta P = \frac{\sum_{i=0}^{2} a_i \cos^i \gamma}{\mu_s \mu_v R^*} \tag{1}$$

where R^* is the reflectance at 763 nm which would be measured if there were no absorption (see appendix), γ is the scattering angle, μ_s and μ_v are the cosine of the solar and the satellite zenith angles respectively. The a_i ($i=0$, 2) coefficients are determined from simulations of radiative transfer through a clear atmosphere above various surfaces.

The sum $P_{app} + \Delta P$ is reported in figure 4. For the stratocumulus and cirrus cases, ΔP is only about 7–8 hPa. For the clear-ocean case, ΔP is about 13 hPa near the sunglint direction but as large as 300 hPa far from that direction. Now, using a threshold on $P_{app} + \Delta P$ allows the pixels of which the pressure appears lower than 900 hPa to be identified as cloudy. Generally speaking, a pixel is assumed to be cloud-contaminated when the pressure $P_{app} + \Delta P$ is significantly weaker than the surface pressure derived from the nearest ECMWF (European Centre for Medium range Weather Forecasts) analysis. In this way, the use of the apparent pressure allows unambiguously thick and high/middle-level clouds to be detected. However, pixels remain unclassified in the case of clear-sky, very low level clouds, very thin cirrus clouds and broken clouds.

3.4. *Reflectance tests*

In many daytime cloud detection algorithms, a pixel is declared cloudy if the measured reflectance is above some reference value that represents clear-sky conditions. Over the ocean, in the absence of glitter effects, the surface is easily distinguished from clouds by its low reflectance, particularly in the near-infrared portion of the spectrum where the signal is less sensitive to molecular and aerosol scattering effects. Figure 5 shows the histograms of the difference R_{865}–R_{865}^{clear} between the measured reflectance at 865 nm and its clear-sky estimate for the POLDER measurements reported in figure 2. Practically, over the ocean, the clear-sky reflectance is estimated from radiative transfer simulations using the sea-surface reflectance model of Cox and Munk (1956); the sea-surface wind velocity used in this model is derived from the ECMWF analysis. This comparison only concerns the viewing directions outside of the expected region of the solar specular reflection. Note that the difference R_{865}–R_{865}^{clear} can be slightly negative because our clear-sky model does not correspond to perfectly clean conditions but to a typical aerosol optical thickness of 0·1. Pixels that present a negative or hardly positive difference (say, weaker than 0·01)

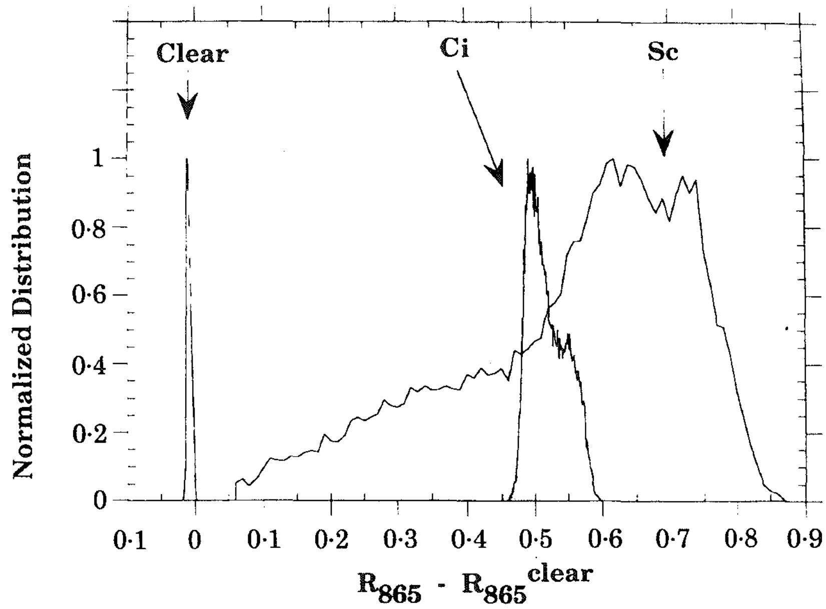

Figure 5. Histogram of the difference between the measured reflectance at 865 nm and its clear-sky estimate (outside the sunglint zone), for the three scenes of figure 2.

can be classified as clear while pixels that present a noticeable difference (say, larger than 0·05) can be classified as cloudy. For intermediate values of R_{865}–$R_{865}{}^{clear}$ or inside the expected region of the specular reflection, the pixels remain unclassified.

Over land, the test makes use of the reflectance at 670 nm instead of 865 nm because of the high reflectivity of vegetation in the near-infrared. The use of the 670 nm reflectance increases the contrast between land and cloud. The clear-sky reflectance will be derived from a time series of POLDER observations previously analysed by the POLDER 'Land surfaces' processing line (Leroy *et al.* 1996). On account of the possible presence of lakes and rivers, this test does not work when the radiometer is pointing to the expected region of the solar specular reflection; however, this region is then restricted to a cone of half-angle of 2° instead of 30°. Neither is this test used when there is any risk of sea-ice or snow according to ECMWF analysis, because snow and ice are highly reflecting.

In most cases, the two threshold tests on apparent pressure and on reflectance are sufficient to classify a pixel as clear or cloudy. This is the case for the three situations of figure 2 with the exception of the clear-sky pixels in the sunglint region. However, these pixels will be labelled as clear by using a multi-directional test (see § 3.8). Nevertheless, these two tests are insufficient when $P_{app}+\Delta P$ is high and $R_{865}-R_{865}^{clear}$ (or $R_{670}-R_{670}^{clear}$) is rather low (say, between 0·01 and 0·05), which is the case of thin clouds or broken clouds over highly reflecting surfaces. Therefore, the following tests based on polarization are added. The polarized reflectance is known to be less sensitive to multiple scattering effects than the total reflectance (Hansen and Travis 1974). So, the polarized reflectance is expected to be much less contaminated by surface contribution.

3.5. *Test on polarization at 443 nm*

The polarized reflectance at 443 nm is mainly related to the atmospheric molecular optical thickness above the observed surface (cloud, land or ocean), assuming that the radiance originating from this surface is negligibly polarized. This assumption may be wrong for particular directions such as that corresponding to the cloud

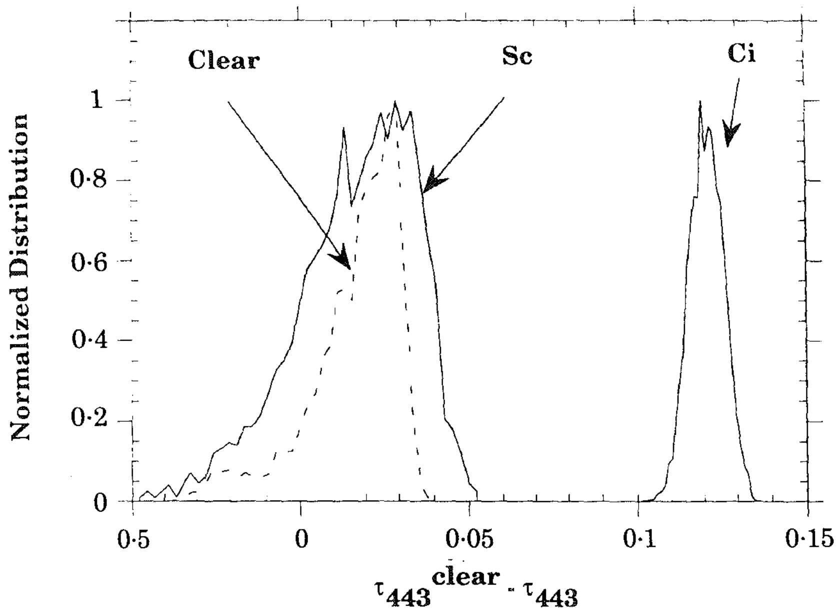

Figure 6. Histogram of the difference between the molecular optical thickness of the atmosphere above the sea-surface and the estimate of the molecular optical thickness above the observed surface (ocean or cloud) from polarization at 443 nm, for the three scenes of figure 2. It is restricted to the region of maximum molecular scattering polarization ($80° < \gamma < 120°$) and outside the sunglint area.

rainbow ($\gamma \sim 140°$) or to the ocean glitter. Therefore the use of the polarized reflectance PR_{443} is restricted to the region of maximum molecular scattering polarization ($80° < \gamma < 120°$) and outside the sunglint area. According to single scattering approximation, one can estimate the molecular optical thickness:

$$\tau_{443} = (16/3)\mu_s\mu_v PR_{443}/(1-\cos^2\gamma). \tag{2}$$

Figure 6 presents the difference $\tau_{443}^{clear} - \tau_{443}$, where τ_{443}^{clear} is the total molecular optical thickness of the atmosphere between the aircraft and the sea-surface for the three situations shown on figure 2. The histograms present a large dispersion of which a part can be explained by the measurement of polarization from three successive polarized images and the associated difficulty of co-registration. This defect ought to be reduced with the satellite version of POLDER of which filters are equipped by prisms for better superposition of the images.

Another effect that can bias the measurements comes from the polarization of the observed surface (cloud, land or ocean) which can be slightly different from 0. Nevertheless, in figure 6, the cirrus cloud histogram noticeably differs from the clear-sky one and it clearly appears that a threshold on the $\tau_{443}^{clear} - \tau_{443}$ difference permits cirrus-free pixels to be discriminated from others. With the spaceborne version of the instrument, this test is expected to help to detect not only high-level clouds but also middle-level clouds.

3.6. *Test on polarization at 865 nm*

The typical feature of polarization by liquid water clouds in the rainbow direction (near 140°) clearly appears in figure 2 for the stratocumulus clouds. Such high values of polarized signal in the 865 nm channel, that is, hardly affected by the molecular scattering, are not observed for clear-sky conditions, except in the sunglint region. Therefore, when the scattering angle is within the range 135°–150° and outside the

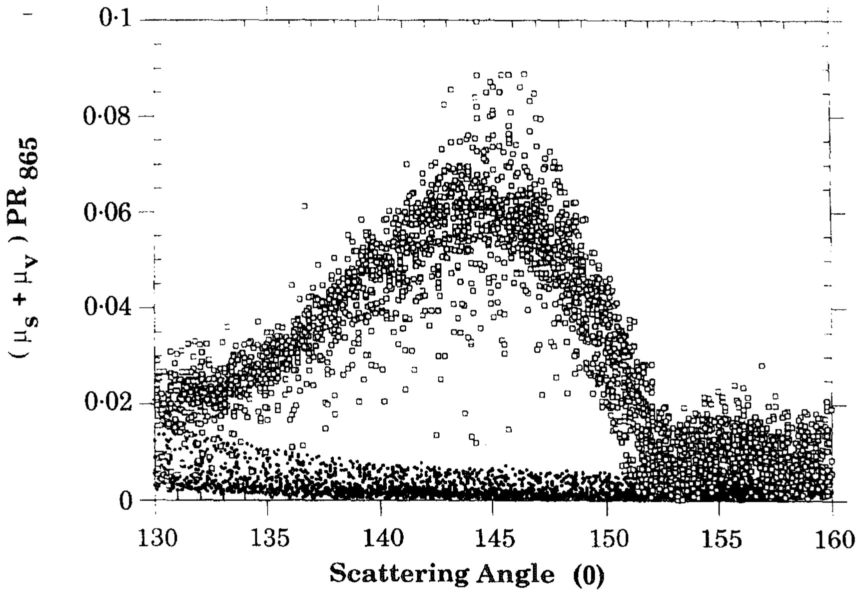

Figure 7. Polarized reflectance at 865 nm weighted by $(\mu_s + \mu_v)$ versus scattering angle for the stratocumulus cloud (open squares) and for the clear ocean (solid circles). μ_s and μ_v are the cosine of the solar and the satellite zenith angle respectively.

sunglint region, low/middle-level clouds can be detected when the polarized reflectance at 865 nm is large enough (figure 7). As written in § 3.4 the polarized reflectance is less sensitive to multiple scattering effects than the total reflectance, i.e., the polarized light is formed mainly by the single scattering process. According to this approximation and for a large enough cloud optical thickness, one can show that the corrected polarized reflectance term, $(\mu_s + \mu_v)\ PR_{865}$, is less sensitive to μ_v and μ_s than PR_{865} and is mainly governed by the scattering angle. Consequently, a pixel will be labelled as cloudy when the $(\mu_s + \mu_v)\ PR_{865}$ value is large enough.

Note that the threshold value on corrected polarized reflectance has to be higher over land than over ocean. Clear-sky observations over the *La Crau* site in southern France have been reported by Deuze *et al.* (1993): for scattering angles within 135°–150°, the $(\mu_s + \mu_v)\ PR_{865}$ values were in the range 0·002–0·02, that is, significantly higher than over clear ocean.

3.7. *Near-infrared/visible test*

The four previous tests should allow the detection of a lot of cloud-filled POLDER pixels. On the other hand, when all the tests of cloud detection prove negative, two additional tests are carried out in order to identify pixels that are definitely clear. The first of these tests has already been presented in § 3.4. It is a reflectance threshold test applied to the 865 nm or to the 670 nm bidirectional reflectance over sea or land respectively. Pixels that present a negative or hardly positive difference between the measured reflectance and its clear-sky estimate are classified as clear.

The last of the tests that are applied pixel by pixel and direction by direction uses the spectral variability of the reflectance. As the reflectance hardly varies from 670 nm to 865 nm over clouds and the anisotropy effects are similar in both channels, the ratio of near-infrared reflectance to visible reflectance is always close to unity over clouds. By contrast, the ocean colour or the presence of vegetation over land can induce difference between 670 and 865 nm reflectances. Then, a pixel can be

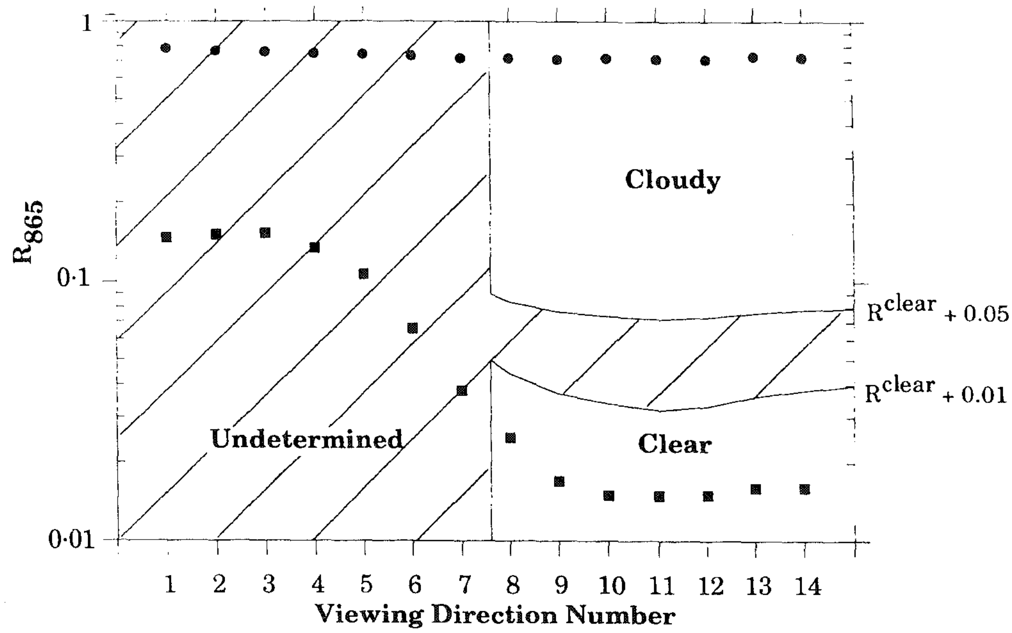

Figure 8. Example of the 865 nm reflectance versus the viewing direction number, for a pixel of the stratocumulus scene (dots) and for a pixel of the clear-ocean scene (squares). The reflectance tests described in § 3.4 do not work in the expected sunglint region (here, direction numbers 1 to 7) nor when the difference between the measured reflectance and its clear sky estimate is between 0·01 and 0·05. In the multi-directional test, a pixel that is labelled undetermined in some direction is re-labelled cloudy (or clear) for this direction if it has been declared cloudy (or clear) in the others directions.

labelled as clear when the reflectance at 865 nm is significantly different from the one at 670 nm, i.e., when the ratio is different from 1. This additional test is similar to the one used in operational AVHRR algorithms (e.g., Saunders and Kriebel 1988, Stowe *et al.* 1991).

3.8. *Multi-directional and spatial tests*

When applying the different threshold tests to the POLDER pixels, in some cases, the pixel remains unclassified for a given direction. For instance, when some of the viewing directions correspond to the sunglint area, the pixel is labelled undetermined for those directions, whereas it has been declared as cloud-filled or cloud-free in the other ones (figure 8). Therefore, if the pixel is labelled as cloudy (or clear) in some directions and undetermined in all the other ones, then it is labelled as cloudy (or clear) for all the directions. Clearly, that multi-directional test chiefly concerns the cases with possible sunglint but can be useful for broken cloud or thin cirrus situation.

At this stage, a pixel can remain undetermined in a given direction if the pixel appears cloudy from one direction and clear from another or if the pixel is undetermined in whatever the direction. For that direction, the pixel is classified as clear or cloudy by utilizing the spatial information at the scale of a 'super-pixel' (see § 2) composed of 81 pixels. If the super-pixel contains some clear and cloudy pixels in the direction, the undetermined ones are relabelled as clear or cloudy according to whether $(R_{670} - \langle R_{670}^{clear} \rangle)/\sigma_{670}^{clear}$ is lower or higher than $(R_{670} - \langle R_{670}^{cloudy} \rangle)/\sigma_{670}^{cloudy}$, where $\langle R_{670}^{clear} \rangle$ and $\langle R_{670}^{cloudy} \rangle$ are the mean reflectances of the clear and cloudy pixels respectively, and σ_{670}^{clear} and σ_{670}^{cloudy} are their associated standard deviations. In the few cases where all the pixels are undetermined, they are all relabelled as clear or cloudy depending on the spatial variability of the reflectance at 865 nm (over ocean) or 670 nm (over land). Indeed, aerosols are expected to present a lower spatial variability of the reflectance than clouds. However, that test cannot be used when there is sea-ice or snow risk; in that case, the cloudiness diagnosed by ECMWF will be used to allow the continuation of the data processing. Of course, these doubtful cases will be flagged.

Classification in cloud-filled and cloud-free pixels is then followed by the derivation of the cloud cover of each super-pixel. First, the cloud amount is determined direction by direction and then the averaged cloudiness is computed. The percentage of pixels undetermined at the end of the first series of tests as well as the variation of the cloud cover from direction to direction will indicate the reliability of the averaged cloud cover.

Cloud parameters (i.e. optical thickness, pressure, phase) can then be inferred from the cloud-filled radiances as explained in the following sections. For pixels labelled as clear for *all* viewing directions, the water vapour content is determined as in the POLDER 'Land surfaces' processing line (Leroy *et al.* 1996). Over ocean, this determination will be restricted to the case of high surface reflectivity, that is, for sunglint conditions.

4. Retrieval of cloud properties

4.1. *Cloud optical thickness*

Cloud optical thickness is directly related to the total condensed water content and is thus a crucial parameter in cloud modelling. Despite POLDER multi-directional capabilities the derivation of cloud optical thickness remains very close to that of the first ISCCP cloud analysis (Rossow and Schiffer 1991) and assumes a homogeneous plane-parallel cloud layer composed of water drops with an effective radius of $10\,\mu$m and an effective variance of 0·15 (Hansen and Travis 1974); the difference is that this retrieval is carried out for up to 14 viewing directions. This choice is supported by two reasons: (*i*) the objective of these algorithms, which are called of class 1, is to provide a series of products that are robust and that can be validated rapidly, (*ii*) the comparison of the optical thicknesses retrieved for ~ 14 viewing directions will allow a test of the validity of the model. It is our opinion that a considerable step forward would be made if, for example, one would be able to evaluate at global scale to what extent and under what conditions the plane parallel hypothesis fails to represent the radiative properties of liquid water clouds. It should be possible to make some progress in this direction by simply testing the consistency of the retrieved optical thickness according to the direction of observation. Cloud optical thickness is thus determined for each viewing direction and each pixel. However, as mentioned in § 2, cloud optical thicknesses as well as all the other products are finally averaged at the *super-pixel* scale, i.e., on a 9 pixel by 9 pixel area.

The relation between the reflectance at top of the atmosphere $R_\lambda(\lambda = 443$, 670 and 865 nm) and the cloud optical thickness is dependent on the surface reflectivity. For land scenes, the surface reflectance is obtained from surface parameters previously retrieved from POLDER observations under clear-sky conditions by the POLDER 'Land surfaces' processing line (Leroy *et al.* 1996). For ocean scenes, the surface reflectance is calculated using the Cox and Munk (1956) model depending on the surface wind velocity derived from ECMWF analysis. The surface anisotropy can have an important effect on the light directly reflected by the surface without any scattering in the atmosphere; but it is assumed to have a negligible effect on the diffuse light scattered by the atmosphere. Consequently, the reflectance R_λ is decomposed into a direct part calculated using the bidirectional surface reflectance $\rho_\lambda^{surface}(\mu_s, \mu_v, \phi)$ and a diffuse part calculated using the hemispherical surface reflectance (or albedo) $\alpha_\lambda^{surface}(\mu_s)$:

$$R_\lambda = R_\lambda^{direct} + R_\lambda^{diffuse}$$
$$= \rho_\lambda^{surface}(\mu_s, \mu_v, \phi) e^{-(1/\mu_s + 1/\mu_v)\delta_\lambda} + R_\lambda^{diffuse}(\mu_s, \mu_v, \phi, \alpha_\lambda^{surface}, \delta_\lambda) \quad (3)$$

where δ_λ is the scaled total optical thickness taking into account the sharp diffraction peak near 0° scattering angle (Potter 1970). Practically, off-line calculations of reflectance are performed for various conditions of viewing/illumination geometry, surface albedo and cloud optical thickness by using the discrete ordinate method (Stamnes *et al.* 1988). The value of $R_\lambda^{diffuse}$ is then interpolated for the observation conditions. Then, R_λ values are obtained from (3) for various values of δ_λ. It results in a table of reflectances from which the optical thickness is interpolated.

Finally only the optical thickness at 670 nm is preserved in the products; the values at 443 and 865 nm are used as indicators of the reliability of the 670 nm optical thickness. Individual optical thicknesses are averaged on the cloudy pixels of a super-pixel. Variation of the cloud optical thickness from pixel to pixel will give key information on the horizontal cloud heterogeneity. On the other hand, comparisons of the optical thickness from direction to direction will provide information on the validity of our model.

Using the POLDER images acquired just before and after those presented on figure 2, 14 values of cloud optical thickness were determined for each target of 9 pixels by 9 pixels from the 865 nm reflectance values measured in 14 different viewing directions. The mean and the standard deviation of the 14 optical thicknesses of each cloudy target were computed; the histograms are reported on figure 9. Figure 9 (*a*) shows that the spatial variability of the optical thicknesses is notably higher for the stratocumulus than for the cirrus, as expected from the reflectance pictures (see figure 2 (*b*)). The non-zero standard deviation of the optical thickness (figure 9 (*b*)) is chiefly related to the weakness of the plane-parallel approximation for the stratocumulus and to the wrong hypothesis of spherical water drops in the case of the cirrus. Due to the non-linear relations between optical thickness and reflected flux, the effect of the angular dispersion of the optical thickness is rather difficult to interpret. The hemispherical reflectance (or albedo) which is independent of the direction of observation is easily calculated from the optical thickness (see § 4.4). It is interesting to check the angular dependence of the albedo retrieved from POLDER measurements. Histograms of standard deviation of the 865 nm albedo are reported in figure 10. The two clouds under study are compared to a stratocumulus deck selected for its homogeneous aspect in Descloitres *et al.* (1995). For this almost ideal case, the angular dispersion of the retrieved albedo is close to 0·01, a large part of which is certainly due to the instrument and algorithm noises. This dispersion varies from 0·01 up to more than 0·05 for the heterogeneous stratocumulus cloud and is close to 0·035 for the cirrus cloud. An albedo error of 0·035 typically corresponds to a SW flux error of 30 W m^{-2}, that is quite significant for ERB studies. This clearly emphasizes the importance of departure from the model for the more heterogeneous parts of the stratocumulus layer and for the ice cloud. Note that these results have been performed from 20 m-size pixels; they might be different for satellite observations at the 6 km-resolution since the effects of cloud inhomogeneities can depend strongly on the scale of the observations.

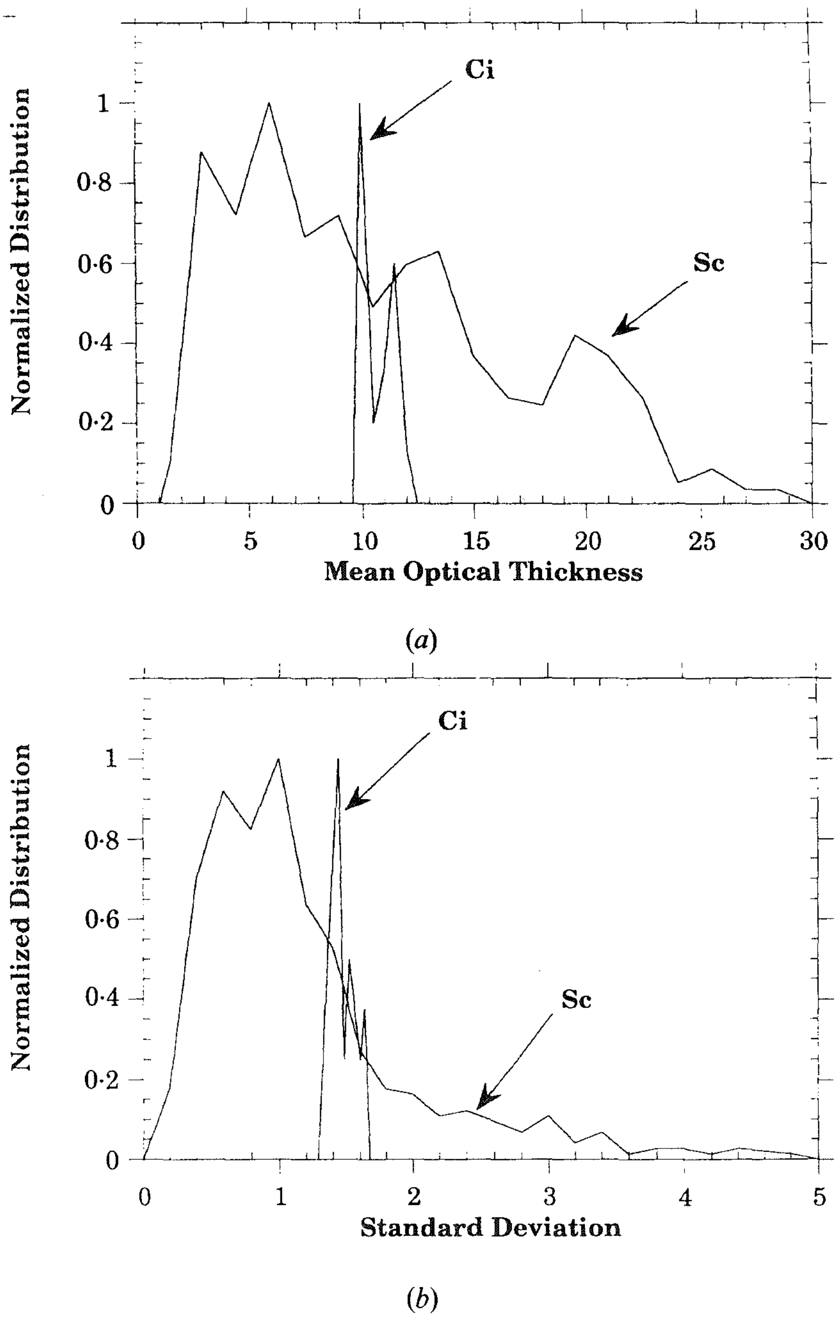

Figure 9. Histogram of the mean of the 14 retrieved cloud optical thickness values (*a*) and of the standard deviation (*b*), for the stratocumulus and the cirrus pixels of figure 2.

4.2. *Cloud pressure*

Together with the cloud optical thickness which regulates the influence of clouds on the terrestrial albedo, one of the most important cloud properties, with respect to global climate changes, is cloud height—or cloud pressure. For instance, Ohring and Adler (1978) found that an increase of 1 km in cloud height would result in a 1·2 K increase in surface temperature. Several techniques for deriving cloud altitude from satellites have already been developed, including the well-known brightness temperature technique (Stowe *et al.* 1988), the CO_2 slicing technique introduced by Smith and Platt (1979) or the analysis of backscattered radiances within the oxygen A band introduced by Yamamoto and Wark (1961). In the present scheme, two methods are used. The first one makes use of the ratio of the two POLDER radiances

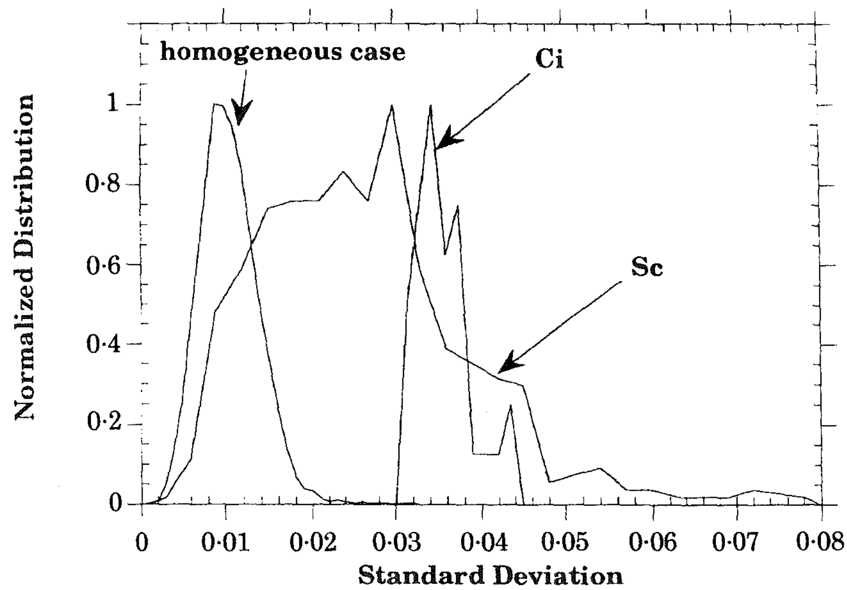

Figure 10. Histogram of the standard deviation of the 14 retrieved albedo values for the stratocumulus and the cirrus pixels of figure 2. Also is reported the histogram corresponding to a homogeneous stratocumulus deck.

measured in the oxygen A band. The second one is based on the analysis of polarized reflected sunlight at 443 nm.

4.2.1. *Cloud pressure derived from O_2 absorption*

As already stated in § 3.3, the apparent pressure differs from the cloud top pressure because of the effect of surface reflection and multiple scattering inside the cloud. For a cloud layer thick enough for the surface influence to be negligible, the apparent pressure P_{app} becomes mainly dependent on the vertical distribution of liquid water and is practically always situated between the cloud top level and the cloud base one, so that we can call it the cloud pressure. In case of a thin cloud layer, a considerable if not preponderant, amount of photons can reach the ground surface and be reflected back to space. In this case, the apparent pressure can be outside of the cloud layer limits. Here, we remove the surface effect from the apparent pressure and the cloud pressure P_{cloud} is thus defined as the apparent pressure that would be observed if the surface reflectivity were equal to zero.

In first approximation, the transmission of the oxygen A band can be treated by means of a random band model composed of strong lines (Goody 1964) so that:

$$T_{O_2} = \exp(-C\sqrt{m}\,P_{app}), \tag{4}$$

where m is the air-mass factor and C is a constant depending on spectroscopic data. Schematically, T_{O_2} can be decomposed into a term corresponding to the light directly reflected by the cloud and a term corresponding to the light reflected after reaching the surface (figure 11). Let $r = R^{**}/R^{*}$, where R^{*} is the reflectance measured near 763 nm without gaseous absorption and R^{**} is the reflectance that would be measured if in addition the surface was black. Then,

$$\begin{aligned}\exp(-C\sqrt{m}\,P_{app}) &= r\exp(-C\sqrt{m}\,P_{cloud})\\ &\quad + (1-r)\exp(-C\sqrt{\{mP_{cloud}^2 + M(P_{surface}^2 - P_{cloud}^2)\}})\end{aligned} \tag{5}$$

where $P_{surface}$ is the surface pressure and M is an effective air-mass factor corresponding

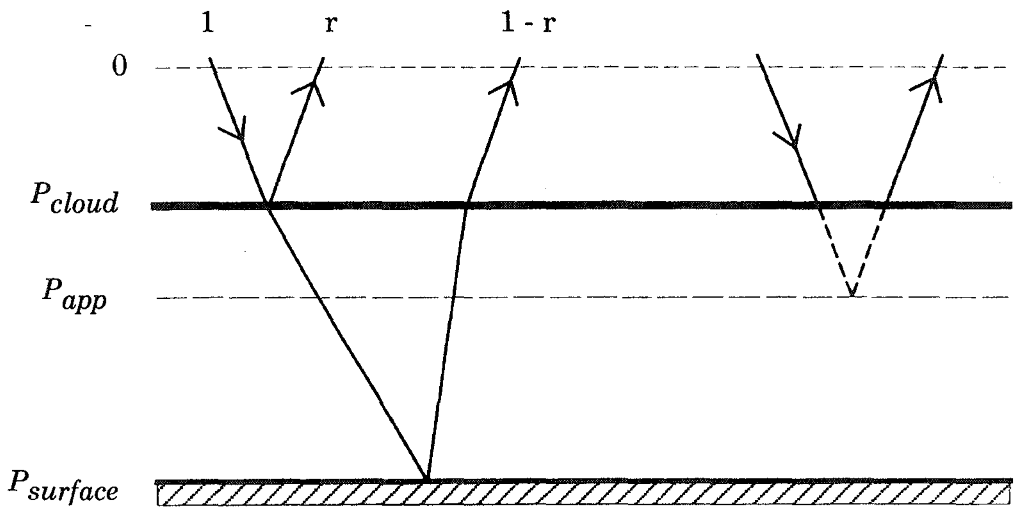

Figure 11. Schematic representation of radiation transfer through a cloudy atmosphere. *r* is the percentage of photons directly reflected by the cloud.

to the mean photon path between the cloud and the surface. Practically, M is approximated by a bilinear function of m and r from numerical simulations of the photon path calculated for various surface reflectances and various cloud optical thicknesses (figure 12).

In practice, R^* results from the correction algorithm (see appendix), R^{**} is computed by using the previously derived cloud optical thickness and $P_{surface}$ is obtained from ECMWF analysis. Thus, P_{cloud} is derived from P_{app} by inverting (5).

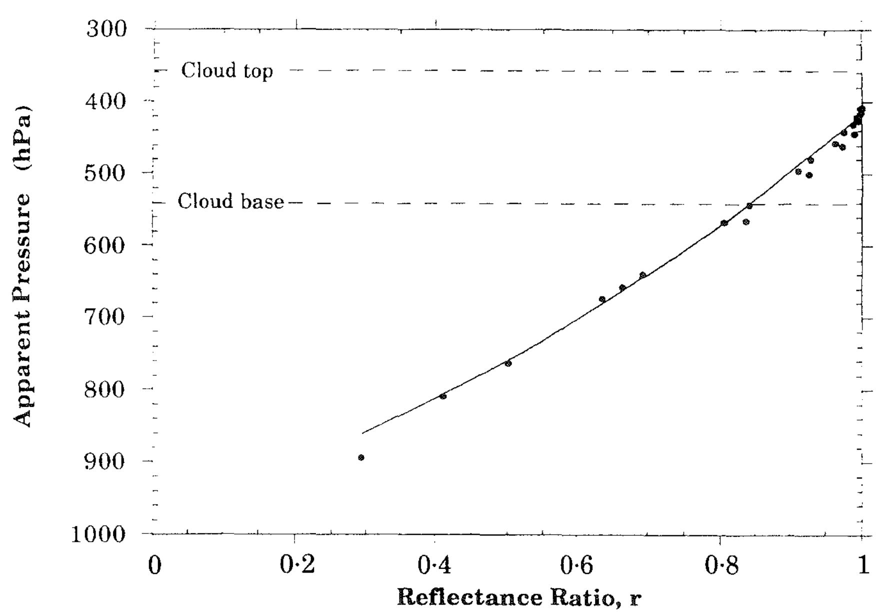

Figure 12. Apparent pressure as a function of the ratio between the 763 nm reflectances calculated without and with the surface influence. The symbols correspond to values calculated by solving the radiative transfer equation for various surface reflectances and various cloud optical thicknesses. The simulation looks like the cirrus case shown on figure 2. The cloud top and cloud base pressure are 360 hPa and 540 hPa respectively. The air-mass factor m is equal to 3·3. The solid line corresponds to our approximation; it was obtained from equation (5), by using for P_{cloud} the value calculated for a black surface. This value of P_{cloud} varies from 410 to 510 hPa depending on the cloud optical thickness.

Note that the random band model is only used to derive the cloud pressure from the apparent pressure. The derivation of the apparent pressure is based on a line-by-line model (see § 3.3).

However, in the case of thin cloud layer over surface with high reflectivity near 763 nm, P_{cloud} may remain undetermined because of the impossibility of solving (5) due to radiometric and algorithmic noises. Moreover, as P_{cloud} is more reliable when a variation of P_{app} induces a smaller variation of P_{cloud}, the values of P_{cloud} are weighted by the derivative $\partial P_{app}/\partial P_{cloud}$ when averaged at the super-pixel scale.

4.2.2. *Cloud pressure derived from polarization at 443 nm*

In this approach, the cloud pressure is retrieved from the polarization measurements at 443 nm. As already outlined in § 3.5, for scattering angles γ ranging from 80° to 120° and outside the sunglint direction, it corresponds chiefly to the light scattered by the molecular layer above the cloud. There is, however, a small contamination by the cloud layer itself. This effect is removed from the polarization measurement at 443 nm by using that at 865 nm where molecular scattering is negligible. Thus, we first calculate the optical thickness $\tau_R^{(0)}$ by using this corrected polarized reflectance instead of PR_{443} in equation (2). Then we derive a better estimate of the molecular optical thickness τ_R by taking into account multiple scattering within molecular layers. Based on off-line calculations, τ_R is obtained by using a polynomial function of $\tau_R^{(0)}$, m, $\cos\gamma$ and $\sin\phi$, where ϕ is the relative azimuth angle. The Rayleigh cloud pressure is then directly proportional to τ_R.

Figure 13 compares the Rayleigh cloud pressure to that derived from O_2 absorption for the two cloudy cases of figure 2. The root mean square difference is 50 hPa and 100 hPa for the cirrus and the stratocumulus cloud respectively. Considering the calibration and co-registration uncertainties of the airborne simulator, the agreement is satisfactory. However, in case of cloud layers much thinner than those presented in figure 12, it is to be feared that the retrieved Rayleigh pressure—and even more the retrieved O_2 pressure—differ significantly from the actual cloud pressure. Therefore, the pressure value will be preserved only when the cloud optical thickness will be large enough (say 1 or 2).

4.3. *Cloud thermodynamic phase*

Cloud phase recognition is important for cloud studies. Ice crystals correspond to physical process and present optical properties that differ from those of liquid water drops. The angular polarization signature of clouds will, in some cases, help in discriminating between liquid and solid phases of cloud particles. Liquid cloud droplets exhibit the very specific polarization feature of the rainbow for scattering angles near 140°. Conversely, theoretical studies of scattering by various crystalline particles (prisms, hexagonal crystals) all show that the rainbow characteristic disappears as soon as the particles depart from spherical geometry (Cai and Liou 1982, de Haan 1987, Brogniez 1992). Thus, the presence or absence of this characteristic feature in cloud polarized reflectance should indicate the presence or absence of liquid water and conversely that of crystals. This is clearly supported by figure 2. Nonetheless, the angular dependence of cloud polarized reflectances may be influenced by other factors such as cloud heterogeneity. In these conditions, it is likely that cloud phase will not always be determined unambiguously: since the rainbow is typical of liquid drops, from its presence we can conclude the presence of liquid

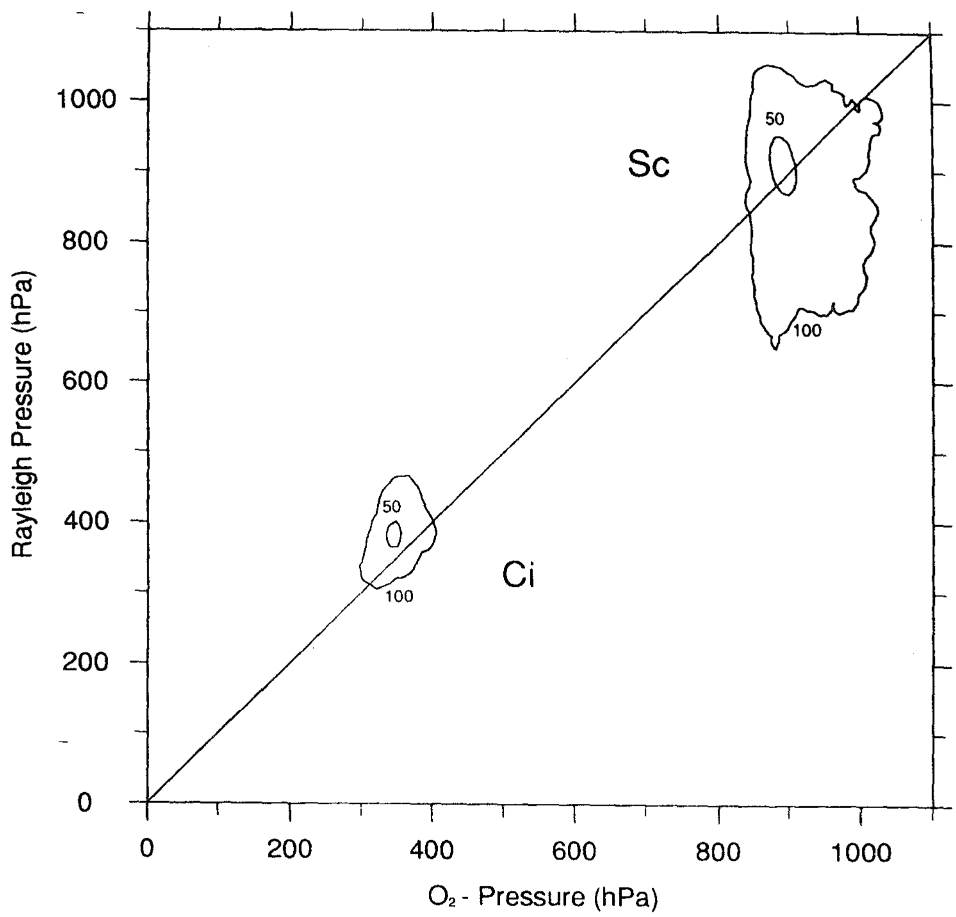

Figure 13. Cloud pressure derived from polarization at 443 nm versus O_2-derived cloud pressure for the stratocumulus and the cirrus cloud (scattering angle between 80° and 120°, outside the sunglint zone). For each case, 50 per cent of the pixels are situated within the isoline 50.

water, but the reverse is not true. Consequently, the phase cannot be determined for all the cloudy pixels.

For scattering angles in the range 135°–150° outside the sunglint region, $(\mu_s + \mu_v)$ PR_{865} is compared to two values F_{max} and F_{min} (figure 14). When $(\mu_s + \mu_v)$ PR_{865} is larger than F_{max}, the phase is assumed to be liquid. When $(\mu_s + \mu_v)$ PR_{865} is weaker than F_{min}, the phase is expected to be ice. In the other cases, both ice and liquid water clouds may occur and the phase will remain undetermined. As a precaution, the phase will not be determined either in case of a very tenuous cloud layer with optical thickness lower than ~ 1.

4.4. *Cloud albedo*

Unlike the bidirectional reflectance, the directional reflectance (or albedo) is independent of the direction of observation. As already noted in §4.1, it is interesting to check the angular dependence of the albedo retrieved from POLDER measurements under the assumption of a plane-parallel cloud layer composed of spherical droplets. So, cloud albedo is determined for each viewing direction.

Moreover, the estimate of cloud forcing is of prime importance for climate study. The SW cloud forcing is directly related to the difference between the observed SW albedo and its clear-sky estimate. Thus, we attempt to determine the narrow-band

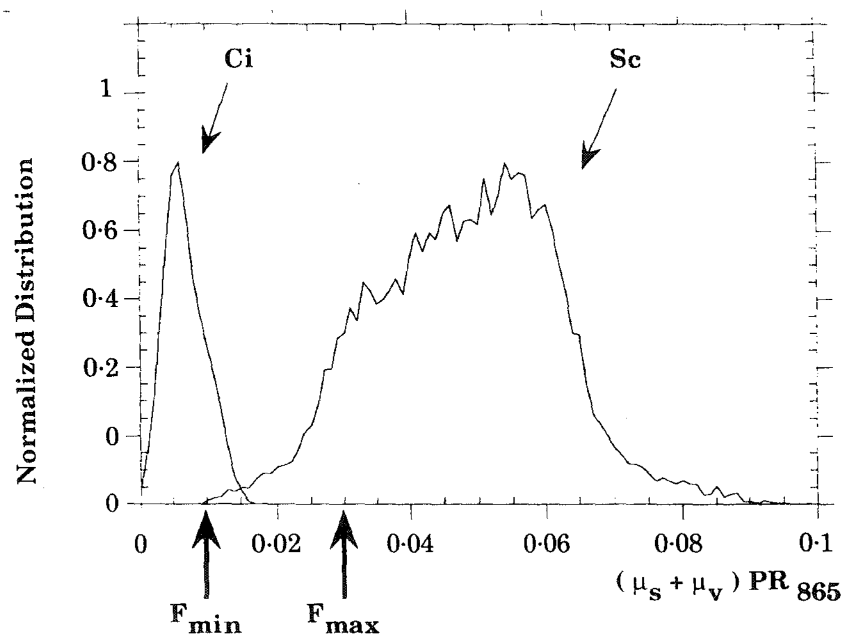

Figure 14. Histogram of the weighted polarized reflectance $(\mu_s + \mu_v)$ PR_{865} for the stratocumulus and the cirrus cloud. It is restricted to the cloud-bow region (scattering angle between 135° and 150°), outside the sunglint zone. Cloud phase is assumed to be liquid or ice when $(\mu_s + \mu_v)$ PR_{865} is respectively larger than F_{max} or weaker than F_{min}.

albedo in several channels of POLDER and then to estimate the albedo integrated over the whole range of the solar spectrum.

The albedo at 443, 670 and 865 nm, without gaseous absorption is calculated off-line as a function of solar elevation, surface reflectance and cloud optical thickness. For each channel noted j, it results in a table from which the albedo A_j is interpolated by using the previously derived cloud optical thickness.

Then the SW albedo is estimated from these narrow-band albedoes as

$$A_{SW} = f_{443} A_{443} + f_{670} A_{670} + f_{865} A_{865} \tag{6}$$

where f_{443} and f_{670} are functions of the total ozone amount measured from TOMS (Total Ozone Mapping Spectrometer) onboard ADEOS and f_{865} depends on the water-vapour content and is approximated by a linear function of the R_{910}/R_{865} ratio. These weighting functions f_j are fitted from simulations using a radiative transfer code with 4750 spectral intervals between 0·2 and 4 μm; the radiative transfer equation was solved using the discrete ordinate method and the interactions between scattering and molecular absorption were accounted for by exponential sums fitting the molecular absorption. Various atmospheres and ground surfaces were considered. The major uncertainty concerns the cloud optical properties; for consistency with the optical thickness derivation, clouds were assumed to be composed of spherical droplets with an effective radius of 10 μm.

In order to evaluate the SW cloud forcing, the clear-sky values A_j^{clear} of the cloudy areas need to be estimated. This is done by assuming a cloud optical thickness equal to zero. The corresponding SW clear-sky albedo A_{SW}^{clear} is calculated as in (6) by replacing f_{865} by a function of the water vapour content derived from ECMWF analysis.

In a similar way, the SW bidirectional reflectances are estimated from the measured narrow-band bidirectional reflectances. That should be useful for ERB studies.

However, these integrations over the whole spectrum will remain speculative as long as they are not validated from ERB scanner measurements.

5. Conclusion

POLDER presents some specific capabilities that make it a powerful tool to investigate cloud properties and to improve the accuracy of Earth Radiation Budget measurements: namely, its multi-spectral, angular and polarization capabilities. The 'ERB & clouds' algorithms have been designed so as to take advantage of these new possibilities. The objective when designing the present algorithms has been to reduce the validation time; the consequence is that a full exploitation of POLDER capabilities has not been completely possible. This will be the case of a second class of algorithms which will be developed after the validation of this first class. However, it should already be possible to make significant progress, for example, by testing the consistency of the retrieved optical thickness according to the viewing direction. Thus, one would be able to evaluate at global scale to what extent and under what conditions the plane parallel hypothesis fails at representing radiative properties of liquid water clouds.

The present algorithms for the cloud detection and the derivation of cloud properties have been developed from the experience acquired by analysing POLDER airborne measurements made during several campaigns, such as EUCREX'94. However, the various thresholds introduced in these algorithms have to be adjusted and afterwards controlled.

A series of validation plans have been designed. They are based on (1) the checking of consistency between the different output data, such as the cloud covers determined from different viewings of a given super-pixel, the two cloud pressures derived from O_2 absorption and from polarization respectively, etc., and (2) the comparison with quantities derived from fully independent data.

The cloud detection algorithm has to be severely monitored since it plays a crucial role in the cloud properties determination. The dynamic cluster analysis method developed by Desbois *et al.* (1982) and improved by Raffaelli and Seze (1995) has been selected mainly because it is a robust and very different method which does not make use of thresholds. Full resolution visible and thermal infrared data from geostationary satellites at the ADEOS crossing time will be used and, as soon as available, those from OCTS (Ocean Colour and Temperature Scanner) on ADEOS. The cloud classification results will be averaged at the POLDER super-pixel resolution and the cloud cover derived from POLDER can thus be tested. In the same way, the Rayleigh and the O_2 cloud pressure can be compared to that derived from the radiative temperature by using ECMWF atmospheric profiles.

The cloud pressure and optical thickness derived from POLDER will be also compared to the ISCCP data. The BRDFs will be compared with the ERBE ones and the short-wave albedo with coincident Meteor/ScaRaB measurements (Kandel *et al.* 1994), if possible.

These validations will be conducted under the control of the International POLDER Scientific Team.

Acknowledgments

This work was supported by the French Centre National d'Etudes Spatiales. The authors wish to thank F. Lemire for data processing, J. Descloitres for derivation of cloud optical thickness, P. Flamant and J. Pelon for lidar data, F. M. Breon,

P. Dubuisson and J. P. Duvel for helpful discussions and A. Lifermann for her comments on the manuscript.

Currently updated information about POLDER project is available from http://earth-sciences.cnes.fr:8060/

Appendix: Correction for gaseous absorption and stratospheric aerosol effect

Measured radiances are first corrected for primary scattering by stratospheric aerosol. Stratospheric aerosol optical thickness will be regularly updated from SAGE (Stratospheric Aerosol and Gas Experiment) measurements. This correction, which remains insufficient in case of a major volcanic event, scarcely affects the unpolarized radiance values but is necessary for the polarized ones, which correspond chiefly to the first order of scattering.

Typical values of gaseous absorption in the different channels used in the 'ERB & clouds' processing line are reported in table A1. Radiances in channels centred at 443, 670, 765 and 865 nm are weakly affected by absorption while radiances at 763

Table A1. Typical values of gaseous absorption in the POLDER channels used in the ERB & clouds line. These values correspond to a twofold path through the U.S. standard atmosphere (COESA 1976), with an air-mass factor of 3.

Channel (nm)	Ozone absorption (%)	Oxygen absorption (%)	Water vapour absorption (%)
443	0·3	0	0·0
670	4·5	0	1·5
763 (narrow)	0·6	41·6	1·4
765 (wide)	0·6	12·4	2·2
865	0·0	0	2·7
910	0·0	0	31·1

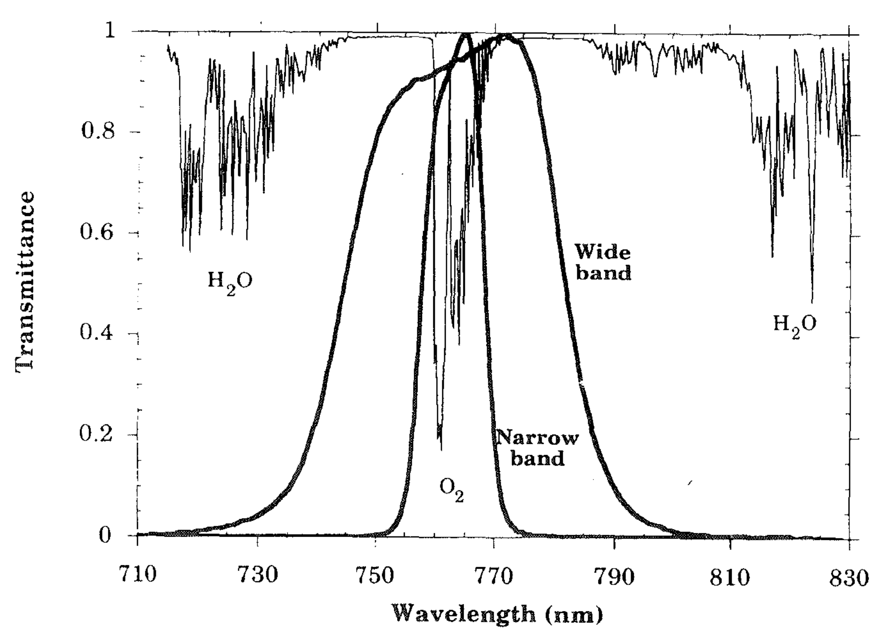

Figure A1. Atmospheric transmission in the oxygen A-band region and filter transmissions in the narrow and wide bands centered at 763 nm and 765 nm respectively.

and 910 nm are selected for their strong absorption by oxygen and water vapour lines, respectively.

Ozone absorption is removed by calculating the transmissions as functions of mU_{O_3} where m is the air-mass factor and U_{O_3} is the column abundance of ozone measured from TOMS. The water vapour absorption of the 865 nm channel is corrected according to a function of the ratio of the 910 and 865 nm reflectances R_{910}/R_{865}. The parameterizations of ozone and water vapour transmissions are derived from simulations using a line-by-line model (Scott 1974).

A particular treatment concerns the 763 nm and 765 nm channels. The reflectance R^* that would be measured if there was no absorption is assumed to be the same in both channels. The R_{763} and R_{765} measured reflectances can be written respectively as:

$$R_{763} = R^* T_{O_2} T'_{H_2O} T'_{O_3} \tag{A1}$$

$$R_{765} = AR_{763} + (1 - A)R^* T''_{H_2O} T''_{O_3} \tag{A2}$$

where the constant A may be considered as the percentage of the wide spectral band where oxygen lines are located (figure A1); its value derived from line-by-line simulations is close to 0·3. The ozone transmittances T'_{O_3} and T''_{O_3} are parameterized as functions of $m\ U_{O_3}$. The water vapour transmittances T'_{H_2O} and T''_{H_2O} are approximated by a function of the R_{910}/R_{865} ratio. Finally, the oxygen transmittance T_{O_2} and the reflectance R^* which is assumed to be the same in both channels, can be derived by combining (A1) and (A2).

References

BALDWIN, D. G., and COAKLEY JR., J. A., 1991, Consistency of Earth radiation budget experiment bidirectional models and the observed anisotropy of reflected sunlight. *Journal of Geophysical Research*, **96**, 5195–5207.

BARKSTROM, B. R., HARRISON, E. F., and LEE, R. B., 1990, Earth Radiation Budget Experiment. Preliminary seasonal results. *EOS*, **71**, 297–305.

BROGNIEZ, G., 1992, Contribution à l'étude des propriétés optiques et radiatives des cirrus, Thèse d'Etat, Université des Sciences et Technologies de Lille, France.

BROGNIEZ, G., PAROL, F., BURIEZ, J. C., and FOUQUART, Y., 1992, Bidirectional reflectances of cirrus clouds modelized from observations during the International Cirrus Experiment 89. *Proceedings of International Radiation Symposium, Tallin*, pp. 133–136.

CAI, Q., and LIOU, K. N., 1982, Polarized light scattering by hexagonal ice cristals: theory. *Applied Optics*, **21**, 3569–3580.

CESS, R. D., POTTER, G. L., BLANCHET, J. P., BOER, G. J., DEL GENIO, A. D., DEQUE, M., DYMNIKOV, V., GALIN, V., GATES, W. L., GHAN, S. J., KIEHL, J. T., LACIS, A. A., LE TREUT, H., LI, Z. X., LIANG, X. Z., MCAVANEY, B. J., MELESHKO, V. P., MITCHEL, J. F. B., MORCRETTE, J.-J., RANDALL, D. A., RIKUS, L., ROECKNER, E., ROYER, J. F., SCHLESE, U., SHEININ, D. A., SLINGO, A., SOKOLOV, A. P., TAYLOR, K. E., WASHINGTON, W. M., WETHERALD, R. T., YAGAI, I., and ZHANG, M. H., 1990, Intercomparison and interpretation of climate feedback processes in 19 atmospheric general circulation models. *Journal of Geophysical Research*, **95**, 16601–16616.

CHAPMAN, R. M., 1962, Cloud distributions and altitude profiles from satellite. *Planetary Space Science*, **9**, 70–71.

COESA, 1976, *U.S. Standard Atmosphere, 1976*, U.S. Government Printing Office, Washington, D.C.

COX, C., and MUNK, W., 1956, Slopes of the sea surface deduced from photographs of the sun glitter. *Bulletin of the Scripps Institute of Oceanography*, **6**, 401–488.

DE HAAN, J., 1987, Effects of aerosols on the brightness and polarization of cloudless planetary atmospheres, M.S. Thesis, Free University of Amsterdam, Netherlands.

Desbois, M., Seze, G., and Szejwach, G., 1982, Automatic classification of clouds on Meteosat imagery: Application to high-level clouds. *Journal of Applied Meteorology*, **21**, 401–412.

Deschamps, P. Y., Breon, F. M., Leroy, M., Podaire, A., Bricaud, A., Buriez, J.-C., and Seze, G., 1994, The POLDER mission: Instrument characteristics and scientific objectives. *I.E.E.E. Transactions on Geoscience and Remote Sensing*, **32**, 598–615.

Descloitres, J., Parol, F., and Buriez, J.-C., 1994, On the validity of the plane-parallel approximation for cloud reflectances as measured from POLDER during ASTEX. *Annales Geophysicae*, **13**, 108–110.

Descloitres, J., Buriez, J.-C., Parol, F., and Vanbauce, C., 1995, About cloud reflectances as measured from POLDER during CLEOPATRA, ASTEX and EUCREX. In *Atmospheric Sensing and Modeling II*, edited by Richard P. Santer, *Proceedings of SPIE*, **2582**, 253–263.

Deuze, J.-L., Breon, F. M., Deschamps, P.-Y., Devaux, C., and Herman, M., 1993, Analysis of the POLDER (POLarization and Directionality of Earth's Reflectances) airborne instrument observations over land surfaces. *Remote Sensing of Environment*, **45**, 137–154.

Fisher, J., and Grassl, H., 1991, Detection of cloud-top height from backscattered radiances within the Oxygen A band. Part 1: Theoretical study. *Journal of Applied Meteorology*, **30**, 1245–1259.

Fisher, J., Cordes, W., Schmitz-Peiffer, A., Renger, W., and Mörl, P., 1991, Detection of cloud-top height from backscattered radiances within the Oxygen A band. Part 2: Measurements. *Journal of Applied Meteorology*, **30**, 1260–1267.

Goloub, P., Deuze, J. L., Herman, M., and Fouquart, Y., 1994, Analysis of the POLDER polarization measurements performed over cloud covers. *I.E.E.E. Transactions on Geoscience and Remote Sensing*, **32**, 78–88.

Goody, R. M., 1964, *Atmospheric Radiation I. Theoretical Basis*, Oxford: Clarendon Press.

Han, Q., Rossow, W. B., and Lacis, A. A., 1994, Near-global survey of effective droplet radii in liquid water clouds using ISCCP data. *Journal of Climate*, **7**, 465–497.

Hansen, J. E., and Travis, L. D., 1974, Light scattering in planetary atmospheres. *Space Science Review*, **16**, 527–610.

Kandel, R. S., Monge, J. L., Viollier, M., Pakhomov, L. A., Adasko, V. I., Reitenbach, R. G., Rasckhe, E., and Stuhlmann, R., 1994, The ScaRaB project: Earth radiation budget observations from the Meteor satellites, *Advances in Space Research*, **14**, 147–154.

Leroy, M., Deuze, J.-L., Breon, F.-M., Hautecoeur, O., Herman, M., Buriez, J.-C., Tanré, D., Bouffies, S., Chazette, P., and Roujean, J.-L., 1996, Retrieval of atmospheric properties and surface bidirectional reflectances over the land from POLDER/ADEOS. *Journal of Geophysical Research*, forthcoming.

O'Brien, D. M., and Mitchell, R. M., 1992, Error estimates for retrieval of cloud-top pressure using absorption in the A band of Oxygen. *Journal of Applied Meteorology*, **31**, 1179–1192.

Ohring, G., and Adler, S., 1978, Some experiments with a zonally averaged climate model. *Journal of Atmospheric Sciences*, **35**, 186–205.

Parol, F., Buriez, J.-C., Crétel, D., and Fouquart, Y., 1994a, The impact of cloud inhomogeneities on the Earth radiation budget: The 14 October 1989 I.C.E. convective cloud case study. *Annales Geophysicae*, **12**, 240–253.

Parol, F., Goloub, P., Herman, M., and Buriez, J.-C., 1994b, Cloud altimetry and water phase retrieval from POLDER instrument during EUCREX'94. In *Atmospheric Sensing and Modelling*, edited by Richard P. Santer, *Proceedings of SPIE*, **2311**, 171–181.

Potter, J. F., 1970, The Delta function approximation in radiative transfer theory, *Journal of Atmospheric Sciences*, **27**, 943–949.

Raffaelli, J. L., and Seze, G., 1995, Clouds type separation using local correlation between visible and infrared satellite images. *Proceedings of the 7th EUCREX Workshop, Villeneuve d'Ascq, France*, edited by G. Brogniez, pp. 123–133.

Rossow, W. B., and Schiffer, R. A., 1991, ISCCP cloud data products. *Bulletin of the American Meteorological Society*, **6**, 2394–2418.

Rossow, W. B., Garder, L. C., and Lacis, A. A., 1989, Global, seasonal clouds variations from satellite radiance measurements. Part I: sensitivity of analysis. *Journal of Climate*, **2**, 419–458.

SAUNDERS, R. W., and KRIEBEL, K. T., 1988, An improved method for detecting clear sky and cloudy radiances from AVHRR data. *International Journal of Remote Sensing*, **9**, 123–150.

SCOTT, N. A., 1974, A direct method of computation of the transmission function of an inhomogeneous gaseous medium. I: description of the method. *Journal of Quantitative Spectroscopy and Radiative Transfer*, **14**, 691–704.

SENIOR, C. A., and MITCHELL, J. F. B., 1993, Carbon dioxide and climate: The impact of cloud parameterization. *Journal of Climate*, **6**, 393–418.

SMITH, W. L., and PLATT, C. M. R., 1979, Comparison of satellite-deduced clouds heights with indications from radiosonde and ground-based laser measurements. *Journal of Applied Meteorology*, **17**, 1796–1802.

STAMNES, K., TSAY, S. C., WISCOMBE, W. J., and JAYAWEERA, K., 1988, Numerically stable algorithm for discrete-ordinate-method radiative transfer in multiple scattering and emitting layered media. *Applied Optics*, **27**, 2502–2509.

STOWE, L. L., WELLWMEYER, C. G., ECK, T. F., YEH, H. Y. M., and the NIMBUS-7 CLOUD DATA PROCESSING TEAM, 1988, Nimbus-7 global cloud climatology. Part I: algorithms and validation. *Journal of Climate*, **1**, 445–470.

STOWE, L. L., MCCLAIN, E. P., CAREY, R., PELLEGRINO, P., GUTMAN, G. G., DAVIS, P., LONG, C., and HART, S., 1991, Global distribution of cloud cover derived from NOAA/AVHRR operational satellite data. *Advances in Space Research*, **11**, 351–354.

SUTTLES, J. T., GREEN, R. N., MINNIS, P., SMITH, G. L., STAYLOR, W. F., WIELICKI, B. A., WALKER, I. J., YOUNG, D. F., TAYLOR, V. R., and STOWE, L. L., 1988, Angular radiation models for Earth-atmosphere system, volume I-Shortwave radiation, NASA RP-1184.

WEILL, A., BAUDIN, F., DUPUIS, H., EYMARD, L., FRANGI, J.-P., GERARD, E., DURAND, P., BENECH, B., DESSENS, J., DRUIHET, A., RECHOU, A., FLAMANT, P., ELOURAGINI, S., VALENTIN, R., SEZE, G., PELON, J., FLAMANT, C., BRENGUIER, J.-L., PLANTON, S., ROLLAND, J., BRISSON, A., LE BORGNE, P., MARSOUIN, A., MOREAU, T., KATSAROS, K., MONIS, R., QUEFFEULOU, P., TOURNADRE, J., TAYLOR, P. K., KENT, E., PASCAL, R., SCHIBLER, P., PAROL, F., DESCLOITRES, J., BALOIS, J.-Y., ANDRE, M., and CHARPENTIER, M., 1995, SOFIA 1992 experiment during ASTEX, *The Global Atmosphere and Ocean System*, **3**, 355–395.

WIELICKI, B. A., CESS, R. D., KING, M. D., RANDALL, D. A., and HARRISON, E. F., 1995, Mission to Planet Earth: role of clouds and radiation in climate. *Bulletin of the American Meteorological Society*, **76**, 2125–2153.

YAMAMOTO, G., and WARK, D. Q., 1961, Discussion of the letter by R. A. Hanel: Determination of cloud altitude from a satellite. *Journal of Geophysical Research*, **66**, 3596.

GEOPHYSICAL RESEARCH LETTERS, VOL. 25, NO.16, PAGES 3159-3162, AUGUST 15, 1998

Apparent pressure derived from ADEOS-POLDER observations in the oxygen A-band over ocean

C. Vanbauce, J.C. Buriez, F. Parol, B. Bonnel
LOA, Université des Sciences et Technologies de Lille, 59655 Villeneuve d'Ascq, France

G. Sèze
LMD, Université de Jussieu, 75252 Paris, France

P. Couvert
LSCE, Centre d'Etudes de Saclay, 91191 Gif-sur-Yvette, France

Abstract. The POLDER radiometer was on board the ADEOS satellite from August 1996 to June 1997. This instrument measures radiances in eight narrow spectral bands of the visible and near infrared spectrum. Two of them are centered on the O_2 A-band in order to infer cloud pressure. By assuming the atmosphere behaves as a pure absorbing medium overlying a perfect reflector, an "apparent" pressure P_{app} is derived from POLDER data. For validation purposes, P_{app} is first compared to the sea-surface pressure P_s for clear-sky conditions; P_{app} is found to be close to P_s (within ~30 hPa) for measurements in the sunglint region. For overcast conditions, P_{app} differs from the cloud-top pressure mainly because of multiple scattering inside the cloud. When P_{app} is compared to the cloud pressure determined from brightness temperature measurements, large differences are observed (typically 180 hPa).

Introduction

Yamamoto and Wark [1961] have suggested the use of oxygen A-band absorption to infer cloud pressure. Recently, some theoretical efforts [*Fisher and Grassl*, 1991; *O'Brien and Mitchell*, 1992; *Kuze and Chance*, 1994] and aircraft measurements [*Fisher et al.*, 1991] have been carried out. All these studies have shown that the oxygen A-band is potentially efficient for determining the cloud-top pressure. They have also shown that the main difficulty lies in the photon penetration problem and the influence of ground reflectivity.

The POLDER (POLarization and Directionality of the Earth's Reflectances) [*Deschamps et al.*, 1994] radiometer has two spectral bands centered on the oxygen A-band. It was launched on ADEOS (Advanced Earth Observing Satellite) in August 1996.

This paper presents first results of the apparent pressure derived from ADEOS-POLDER data by using a non-scattering model. This pressure is compared to the meteorological sea-surface pressure for clear-sky conditions and to the cloud pressure deduced from brightness temperature measurements for overcast conditions.

Paper number 98GL02324.
0094-8534/98/98GL-02324$05.00

Data

The POLDER instrument on ADEOS is described in *Deschamps et al.* [1994]. It consists of a CCD matrix detector, a rotating filter wheel and a wide field of view lens. When the satellite passes over a target, up to 14 different images are acquired in eight narrow spectral bands of the visible and near infrared spectrum.

The POLDER level 1 products processed by the French Space Center (CNES) consist of calibrated radiances at 6.2 km resolution. The level 2 and 3 products are split in three processing lines: "Earth Radiation Budget (ERB) and clouds", "Ocean color and aerosols over the ocean", "Land surfaces and aerosols over land".

The apparent pressure P_{app} is one of the outputs of the "ERB and clouds" processing line. It is inferred from the differential absorption between the reflectances measured in the narrowband and wideband channels centered at 763 and 765 nm respectively. Practically, P_{app} is calculated as a function of the oxygen transmission derived from these two reflectances after removing ozone and water vapor absorption (see *Buriez et al.* [1997] for further details). The gaseous transmissions are based on line by line simulations using HITRAN'96 spectroscopic data bank [*Rothman et al.*, 1998]. All scattering effects are neglected and the atmosphere is assumed to behave as a pure absorbing medium overlying a perfect reflector located at pressure P_{app}. In addition, the reflectance R^* that would be measured if there was no absorption is derived by assuming it is the same in both channels. These calculations are made for every geographic pixel but the POLDER products correspond to means over super-pixels composed of 9 by 9 pixels (0.5° by 0.5° at the equator).

The interband calibration between the 763 nm and 765 nm channels is expected to be accurate within 1 % [*Hagolle et al.*, 1997]; it corresponds to an absolute accuracy of about 20 hPa on the retrieved pressure. The radiometric noise induces a rms error varying from less than 7 hPa for very bright scenes ($R^* > 50$ %) to more than 60 hPa for very dark scenes ($R^* < 2$ %) ; these values are divided at most by 9 when averaging over a super-pixel. There are however additional uncertainties, mainly due to residual defaults in the stray light correction and in the multi-directional co-registration. The stray light strongly affects the dark scenes while co-registration errors concern scenes with high spatial or angular variability such as heterogeneous clouds and ocean in the sunglint direction. From these considerations and comparison of values of the super-pixel apparent pressure retrieved for slightly different viewing directions, the overall rms error due to all error sources is estimated to vary from $\leq$ 30 hPa for very bright scenes up to $\sim$ 40 - 60 hPa for very dark scenes.

POLDER data presented here were acquired during the 14 daily overpasses of ADEOS over ocean on November 10, 1996. These data are complemented by brightness temperature measurements from Meteosat and by the sea-surface pressure and meteorological profiles derived from the ECMWF (European Centre for Medium range Weather Forecasts) analysis.

Comparison to sea-surface pressure

First we are interested in the behavior of the apparent pressure derived from POLDER measurements in clear-sky conditions. We select the fully clear-sky super-pixels by using a simple reflectance test. For each pixel and for each viewing direction, the clear-sky reflectance at 865 nm R_{865}^{clear} is estimated from radiative transfer simulations. A super-pixel is declared clear if the measured reflectance R_{865} is weaker than $R_{865}^{clear} + 0.02$ for all the 81 pixels of the super-pixel and for each viewing direction outside the expected region of the solar specular reflection delimited by a cone of half-angle of 30°. A more severe threshold (0 instead of 0.02) reduces the number of selected clear cases but does not change significantly the following results.

For these clear-sky conditions, the POLDER apparent pressure P_{app} is compared to the sea-surface pressure P_s (Figure 1). For the 78,364 selected cases, the mean difference is - 412 hPa with a standard deviation of 144 hPa. Not surprisingly, P_{app} is generally smaller than P_s. Indeed, P_{app} must be equal to P_s only when all of the reflected radiation directly comes from the sea-surface. In the other cases, we would have to take into account the atmospheric effects. In order to illustrate these effects, we consider a simple model where R^* is the sum of the reflectances directly generated by molecular scattering, aerosol scattering and surface reflectance :

$$R^* = R_m + R_a + R_s\, t_{atm} \, , \tag{1}$$

where t_{atm} stands for the atmospheric transmittance.

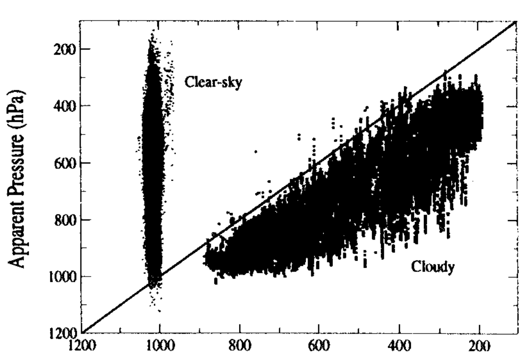

Figure 1. Comparison between the apparent pressure P_{app} derived from POLDER and respectively (i) the meteorological sea-surface pressure P_s for clear-sky pixels and (ii) the cloud pressure P_c derived from Meteosat brightness temperature for cloudy pixels.

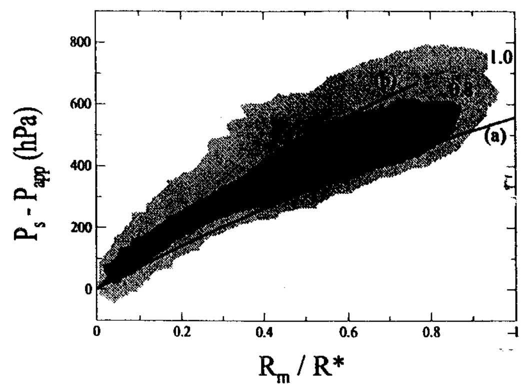

Figure 2. Difference between the apparent pressure and the sea-surface pressure versus the ratio between the calculated molecular reflectance and the measured total reflectance. 100%, 80% and 50% of the cases are situated within the isoline 1.0, 0.8 and 0.5 respectively. The theoretical curves correspond to an air-mass factor m = 3. Curve a corresponds to a clean atmosphere. Curve b corresponds to a ratio between the aerosol reflectance and the molecular reflectance equal to 0.3 and a formation pressure equal to 50 hPa.

The reflectance affected by O_2-absorption is formally

$$R^*\, t(P_{app}) = R_m\, t(P_m) + R_a\, t(P_a) + R_s\, t_{atm}\, t(P_s) \tag{2}$$

where $t(P)$ is the two-path oxygen transmission between the top-of-atmosphere and the pressure P. Writing $\alpha = R_a/R_m$, (1) and (2) give

$$t(P_{app}) = t(P_s) + \{t(P_m) - t(P_s) + \alpha[t(P_a) - t(P_s)]\}\, \frac{R_m}{R^*}. \tag{3}$$

The molecular reflectance R_m is easily calculable, based on single-scattering approximation ; it is typically $\sim$ 1 %. From line-by-line simulations for standard atmospheres, the pressure P_m is found to hardly decrease (from 470 to 440 hPa) when the air-mass factor increases from 2 to 5. The aerosol reflectance R_a and above all its associated pressure P_a are a lot more uncertain. The aerosol pressure values extend from about 50 hPa for stratospheric aerosol to more than 900 hPa for tropospheric aerosol.

Figure 2 reports the difference P_s - P_{app} versus the ratio between the calculated molecular reflectance R_m and the total reflectance R^* inferred from POLDER measurements. Two theoretical curves are also reported for a typical air-mass factor $m = 3$. Curve a corresponds to a clean atmosphere ($\alpha = 0$). Curve b corresponds to an aerosol layer with a reflectance ratio $\alpha = 0.3$ and a formation pressure $P_a = 50$ hPa. This curve b can also be obtained for other conditions: for example $P_a = 200$ hPa but $\alpha = 0.38$, or Pa = 900 hPa but $\alpha = 4.3$. However, R_m/R^* is strictly limited by $1/(1+\alpha)$ that is 0.77 for $\alpha = 0.3$ but only 0.19 for $\alpha = 4.3$.

Of course, a fixed value of α whatever the solar and viewing directions is unrealistic. Nevertheless, the comparison between the measurements and these theoretical curves leads to some remarks: the general trend of the observations is rather well represented by the theoretical curves. As expected, the measured difference P_s - P_{app} tends toward 0 when the contribution of the photons reflected by the atmosphere becomes negligible. Deviations from the "mean" curve (not drawn) are mainly random, with a standard deviation increasing from ~ 30 hPa to 70 hPa when R_m/R^* increases.

On the average, the observations significantly depart from the theoretical clean atmosphere case (curve a). Tropospheric aerosol typically located between 800 and 1000 hPa cannot explain this bias which is observed for large values of R_m/R^*. It could be due to a stratospheric aerosol layer and/or a very tenuous cirrus cloud layer. The stratospheric aerosol contents derived from SAGE (Stratospheric Aerosol and Gas Experiment) measurements are found to be nearly ten times too small to explain such a bias. The frequent occurrence of thin cirrus with reflectance on the order of 1-2 % cannot be excluded but is questionable.

Besides an unlikely failure in the retrieval of the apparent pressure, another explanation could be in part a slight bias in the stray light correction [*Hagolle*, private communication]. Fortunately, such a bias would have a negligible effect in the case of bright clouds as considered in the following.

Comparison to Meteosat data

Now we are interested in the behavior of the apparent pressure in cloudy conditions. A super-pixel is declared overcast if the condition $R_{865} > 0.50$ is satisfied for all the 81 pixels of the super-pixel and for each viewing direction. A large threshold is chosen in order to privilege the clouds that are opaque in the Meteosat infrared channel and to avoid as far as possible the presence of partly cloud-filled pixels.

In this section, are only considered the cloudy pixels observed both from POLDER and from Meteosat within ±1/4 hour (some trials using GOES instead of Meteosat observations gives similar results). Three ADEOS orbits are concerned on November 10, 1996. For each selected super-pixel, a pressure P_c is derived from the brightness temperature measured in the 11 μm channel of the geostationary satellite by using meteorological profile. Disregarding errors chiefly caused by uncertainties in temperature profile, the pressure P_c is close to the cloud-top pressure when the cloud is opaque. Note however that the auxiliary atmospheric data archived with the POLDER products are given for only eight pressure levels, namely 180, 310, 440, 560, 680, 800, 1000 hPa and the surface level. Therefore the well-known inversion observed near the top of the stratocumulus clouds may be missed in these data ; it can result in a large error in the derivation of the cloud pressure from the observed temperature. In the following, results are thus to be considered cautiously in the case of low-level clouds.

The comparison between the Meteosat cloud pressure P_c and the POLDER apparent pressure P_{app} is reported in Fig. 1. For the 32,471 selected cases, the mean difference is 184 hPa with a standard deviation of 87 hPa. As the reflectance threshold is large enough, no significant variation of the difference as a function of the reflectance is observed. A slight variation of P_{app} with the air-mass factor m is noted. Each super-pixel is observed under several directions to which correspond different values of m; on average, $\partial P_{app}/\partial m \approx$ - 65 hPa.

As expected from theoretical considerations [e.g., *Wu*, 1985], P_{app} is now larger than P_c. Simulations using the Discrete Ordinate Method [*Stammes et al.*, 1988] were performed for various cloudy situations and various solar illumination and viewing conditions. Some examples are reported in Figure 3. Clouds are assumed to be homogeneous plane-parallel layers. The microphysical model for low-level clouds is a distribution of liquid water drops with an effective radius of 10 μm [*Hansen and Travis*, 1974]. High-level clouds are assumed to be composed of hexagonal ice plates with dimensions L/2R = 15 μm/300 μm [*Brogniez et al.*, 1995]. In Fig. 3, the cloud optical thickness δ varies from 0 to 500. As noted previously, P_{app} differs notably from P_s when $\delta = 0$.

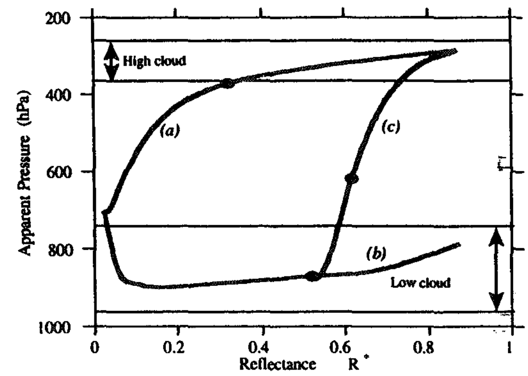

Figure 3. Theoretical curves of the apparent pressure as a function of the reflectance for mono-layered clouds (curves a and b) and for a multi-layered cloud system (curve c) above the ocean. All the clouds are 2 km thick. In cases a and b, the cloud optical thickness varies from 0 to 500. In case c, the high-level cloud optical thickness varies from 0 to 500 while the low-level cloud optical thickness is fixed to 16. The dots correspond to an optical thickness of 16 for both the low and the high cloud. The viewing and the solar angles are 0° and 60° respectively.

The apparent pressure does not correspond to the cloud top because of multiple scattering inside the cloud. This photon penetration effect remains significant even for cloud optical thickness larger than 100. From many simulations such as those reported in Fig. 3, it appears that for single cloud layers with a typical reflectance value of 50 %, the apparent pressure is generally slightly larger than the mean cloud pressure (i.e. rather toward the cloud bottom than toward the cloud top).

In the case of multi-layered cloud systems, the difference between the apparent and the cloud top pressure is amplified (curve c in Fig.3). Indeed, a large part of the reflected radiation can come from the lower cloud layer. That can explain very large differences between the POLDER apparent pressure and the pressure P_c derived from thermal infrared channels. Note that the brightness temperature technique also can overestimate the cloud-top pressure in case of multiple cloud layers ; if so, the difference between the apparent and the true cloud-top pressure would be still larger than P_{app} - P_c.

Note that our simulations agree with the observed variation of the photon penetration with the air-mass factor. Typically, we found $\partial P_{app}/\partial m \approx$ - 30 hPa and - 80 hPa for single and two-layered clouds respectively, to be compared to the observed - 65 hPa.

Conclusion

The first results of the apparent pressure P_{app} derived from ADEOS-POLDER data have been presented. They only concern oceanic situations. Over land, the interpretation of the apparent pressure is even more complicated because the surface reflectivity can present a large spectral variability [*Bréon and Bouffiès*, 1996].

Under clear-sky conditions, the apparent pressure tends toward the sea-surface pressure (within ~30 hPa) when the contribution of the photons reflected by the atmosphere becomes negligible. Outside the sunglint region, the sea-surface reflectivity is very weak and the apparent pressure is thus highly dependent on the atmosphere composition; the presence of a high-level scattering layer, even very tenuous, can have a significant impact on the measure of the apparent pressure.

Under cloudy conditions, the apparent pressure is greater than the cloud top pressure because of the effect of surface reflectivity and multiple scattering inside the cloud. The measured difference between the POLDER apparent pressure and the cloud top pressure derived from infrared measurements is on the average 180 hPa. Such a difference appears rather large for single cloud layers. However, there is often occurrence of both low and high clouds [*Warren et al.*, 1988]. In this case, very large differences can arise even when the high cloud appears opaque in the thermal infrared window.

Some doubt remains concerning the spectroscopic data and the modeling of the apparent pressure based on line-by-line calculations [*Kuze and Chance*, 1994; *Chance*, 1997]. However, forcing the adjustment between the average of the clear-sky observations and the clean-sky simulations (curve a in Fig. 2) would increase the observed differences between the cloud top and the apparent pressure.

The POLDER apparent pressure is thought to be useful for discriminating clear and cloudy pixels and for deriving the cloud pressure. These first results outline that the use of the apparent pressure in the cloud detection has to be made with precautions. For cloudy scenes, even when the sea-surface reflectivity effect is negligible, the apparent pressure is not the cloud top pressure. Its comparison with the actual cloud top pressure (or at least the cloud top derived from thermal infrared measurements) is expected to contain information about the cloud vertical structure. More studies are needed in order to extract this information that could be very useful particularly for the derivation of surface thermal fluxes from satellite observations.

Acknowledgments. This work was supported by CNES, Région Nord-PdC, EEC and Préfecture du Nord through EFRO. Meteorological and Meteosat data were provided by Météo-France. The authors thank C. Brogniez for processing the SAGE data provided by NASA LaRC and F.M. Bréon and O. Hagolle for helpful discussions.

References

Bréon, F. M., and S. Bouffiès, Land surface pressure estimate from measurements in the oxygen A absorption band, *J. Appl. Meteor.*, *35*, 69-77, 1996.

Brogniez, G., J.C. Buriez, V. Giraud, F. Parol, and C. Vanbauce, Determination of effective emittance and radiatively equivalent microphysical model of cirrus from ground-based and satellite observations during the International Cirrus Experiment: The 18 October 1989 case study, *Mon. Wea. Rev.*, *123*, 1025-1036, 1995.

Buriez, J.C., C. Vanbauce, F. Parol, P. Goloub, M. Herman, B. Bonnel, Y. Fouquart, P. Couvert, and G. Sèze, Cloud detection and derivation of cloud properties from POLDER, *Int. J. Remote Sensing*, *18*, 2785-2813, 1997.

Chance, K.V., Improvement of the O_2 A-band spectroscopic database for satellite-based cloud detection, *J. Quant. Spectrosc. Radiat. Transfer*, *58 no. 3*, 375-378, 1997.

Deschamps, P.Y., F. M. Bréon, M. Leroy, A. Podaire, A. Bricaud, J.C. Buriez, and G. Sèze, The POLDER mission: Instrument characteristics and scientific objectives, *IEEE Trans. Geosci. Rem. Sens.*, *32*, 598-615, 1994.

Fisher, J., and H. Grassl, Detection of cloud-top height from backscattered radiances within the O_2 A-band. Part 1: Theoretical study, *J. Appl. Meteor.*, *30*, 1245-1259, 1991.

Fisher, J., W. Cordes, A. Schmitz-Peiffer, W. Renger, and P. Mörl, Detection of cloud-top height from backscattered radiances within the O_2 A-band. Part 2: Measurements, *J. Appl. Meteor.*, *30*, 1260-1267, 1991.

Hagolle, O., P. Goloub, P.Y. Deschamps, T. Bailleul, J.M. Nicolas, Y. Fouquart, A. Meygret, J.L. Deuzé, M. Herman, F. Parol, and F.-M. Bréon, Results of POLDER in-flight calibration. In Sensors Systems and Next Generation Satellite III, Proc. SPIE 3221, 1997.

Hansen, J.E., and L. D. Travis, Light scattering in planetary atmospheres, *Space Sci. Rev.*, *16*, 527-610, 1974.

Kuze, A., and K.V. Chance, Analysis of cloud top height and cloud coverage from satellites using the O_2 A and B bands, *J. Geophys. Res.*, *99*, 14481-14492, 1994.

O'Brien, D.M., and R. M. Mitchell, Error estimates for retrieval of cloud-top pressure using absorption in the A band of Oxygen, *J. Appl. Meteor.*, *31*, 1179-1192, 1992.

Rothman, L.S., C.P. Rinsland, A. Goldman, S.T. Massie, D.P. Edwards, J.-M. Flaud, A. Perrin, C. Camy-Peyret, V. Dana, J.-.Y. Mandin, J. Schroeder, A. McCann, R.R. Gamache, R.B. Wattson, K. Yoshino, K. Chance, K. Jucks, L.R. Brown, V. Nemtchinov, and P. Varanasi, The HITRAN Molecular Spectroscopic Database and HAWKS: 1996 Edition, to be submitted to *J. Quant. Spectrosc. Radiat. Transfer*, 1998.

Stamnes, K., S.C. Tsay, W. Wiscombe, and K. Jayaweera, Numerically stable algorithm for discrete-ordinate-method radiative transfer in multiple scattering and emitting layered media, *Appl. Opt.*, *27*, 2502-2509, 1988.

Warren, S.G., C.J. Hahn, J. London, R.M. Chervin, and R.L. Jenne, Global distribution of total cloud cover and cloud type amounts over the ocean, *NCAR Tech. Note TN-317+STR/DOE Tech. Rep. ER-0406*, 212 pp., 1988.

Wu, M.C., Remote sensing of cloud-top pressure using reflected solar radiation in the Oxygen A-band, *J. Clim.Appl. Meteor.*, *24*, 539-546, 1985.

Yamamoto, G., and D. Q. Wark, Discussion of the letter by R.A. Hanel: "Determination of cloud altitude from a satellite", *J. Geophys. Res.*, *66*, 3596, 1961.

(Received March 26, 1998; revised June 12, 1998; accepted June 26, 1998.)

First Results of the POLDER "Earth Radiation Budget and Clouds" Operational Algorithm

Frédéric Parol, Jean-Claude Buriez, Claudine Vanbauce, Pierre Couvert, Geneviève Sèze, Philippe Goloub, and Sylvain Cheinet

***Abstract*— The POLDER instrument is devoted to global observations of the solar radiation reflected by the earth-atmosphere system. Algorithms of the "Earth Radiation Budget and Clouds" processing line implemented at the French Space Center are applied to ADEOS-POLDER data. First results on derived cloud properties are presented from POLDER level 2 data of 10 November 1996 and level 3 products of June 1997.**

A good correlation is observed between the POLDER cloud detection algorithm and the Dynamical Clustering Method applied to METEOSAT data. The multidirectional capability of POLDER appears useful to check schemes of cloud optical thickness retrieval. As expected, a water droplet model is suitable for liquid water clouds and inadequate for ice clouds. That indirectly validates our algorithm of cloud phase recognition. An apparent pressure is derived from O_2-absorption measurements and a Rayleigh cloud pressure from polarization observations. For overcast conditions, the apparent pressure is larger (by more than 100 hPa) than the Rayleigh pressure chiefly due to the photon penetration effect. For partly cloudy conditions, it can be larger or weaker depending on the surface reflectivity.

Preliminary comparisons between POLDER and ISCCP monthly mean products outline some differences resulting in part from the original characteristics of POLDER.

***Index Terms*—Clouds, polarization, remote sensing.**

I. Introduction

HUMAN activities are increasing the atmospheric concentrations of both greenhouse gases and anthropogenic aerosols, which tend, respectively, to warm and to cool the earth-atmosphere system [22], [11]. Global climate models (GCM's) endeavor to project what the future has in store for the earth, but the large range of possible scenarios mainly comes from the little understood in the climate sensitivity to such perturbations [22]. A major uncertainty in the determination of this sensitivity is the misunderstanding in the feedbacks associated with cloudiness changes and the difficulty of GCM's to correctly account for cloud-radiation-climate interactions [8], [9], [36]. Indeed, cloud-radiation interactions are really complex and depend on numerous physical parameters such as the cloud macrophysical and microphysical characteristics but also the atmospheric and terrestrial environment. Consequently, GCM's need realistic representation of clouds and their effects on radiation balance at global scale as well as at regional scale. It is essential to correctly simulate the present forcing of clouds on radiation but especially to model what the future forcing of clouds will be. Global observations of cloud properties and global measurements of the effects of clouds on radiation are essential to achieve this objective.

The most comprehensive way to obtain global cloud observations is by means of satellite-based measurements, even if field experiments and ground-based measurements remain essential to support the satellite observations. Satellites can directly observe not only the spatial and temporal variabilities of clouds [33] but also their effects on earth's radiation budget (ERB) at the top of the atmosphere [30], [20]. Since the first satellite images were used [1], satellite observations of clouds and satellite derivation of cloud properties have been widely developed and investigated (see [32] for an almost exhaustive historical summary of cloud algorithms).

POLDER (POLarization and Directionality of the Earth's Reflectances) is a component of a series of new sensors that may provide key information for improving our knowledge of clouds, radiation, and climate interactions. POLDER is a CNES (the French Space Agency) instrument which was on board the Japanese ADEOS (ADvanced Earth Observing Satellite) polar orbiting platform, successfully launched in August 1996. In November 1996, POLDER entered into its nominal acquisition phase and functioned perfectly until ADEOS early end of service in June 1997. POLDER is a multispectral imaging radiometer-polarimeter designed to provide global and repetitive observations of the solar radiation reflected by the earth-atmosphere system [13]. The instrument concept is based on a wide field of view (~2200 km) telecentric optics, a rotating wheel carrying spectral filters and polarizers, and a charged coupled device (CCD) array of (242 × 274) detectors that induces a moderate spatial resolution of 6.2 km. As the ADEOS satellite passes over a scene, up to 14 successive measurements are acquired in eight narrow spectral bands located between 443 and 910 nm. The POLDER level 1 products routinely processed by CNES consist of calibrated radiances and Stokes parameters at full spatial resolution. The

Manuscript received April 2, 1998; revised November 18, 1998. This work was supported by CNES, European Economic Community, Région Nord-Pas De Calais, and Préfecture du Nord through EFRO. Meteorological data have been provided by Météo-France. METEOSAT data have been provided by the Centre de Météorologie Spatiale in Lannion. Currently updated information about POLDER project is available from http://polder@www-projet.cnes.fr:8060.

F. Parol, J.-C. Buriez, C. Vanbauce, P. Goloub, and S. Cheinet are with the Laboratoire d'Optique Atmosphérique, URA CNRS 713, Université des Sciences et Technologies de Lille, UFR de Physique, 59655 Villeneuve d'Ascq Cedex, France (e-mail: fred@loa.univ-lille1.fr).

P. Couvert is with the Laboratoire des Sciences du Climat et de l'Environnement, Centre d'Etudes de Saclay, 91191 Gif-sur-Yvette, France.

G. Sèze is with the Laboratoire de Météorologie Dynamique, CNRS, Université P. et M. Curie, Jussieu, 75252 Paris Cedex 05, France.

Publisher Item Identifier S 0196-2892(99)03575-5.

level 2 and 3 products are split into three processing lines which are the "ERB, water vapor, and clouds" (hereafter noted as "ERB & clouds"), the "Ocean color and aerosols over the ocean," and the "Land surfaces and aerosols over land" lines. For different reasons put forward in [7], all of the results of the "ERB & clouds" processing line are averaged at the "super-pixel" scale that typically corresponds to (9 × 9) pixels. The spatial resolution of the super-pixel (0.5° × 0.5° at the equator, i.e., ~50 km × 50 km) appears suitable both for comparison with ISCCP (International Satellite Cloud Climatology Project, [33]) products and for use in connection with ERB instruments like ScaRaB (Scanner for the Earth Radiation Budget) [23] and CERES (Cloud and the Earth's Radiant Energy System) [45].

The "ERB & clouds" thematic interest takes advantage of the multispectral, multidirectional, and multipolarization capabilities of POLDER to derive useful information on clouds and their effects on short-wave radiation [7]. This paper deals with one of the main goals of the "ERB & clouds" line which is the derivation of cloud properties, such as cloud amount, cloud optical thickness, cloud pressure, and cloud thermodynamic phase at global scale. The atmospheric water vapor content is presented in a companion paper in this issue [43]. Similarly to many "cloud algorithms" [32], the "ERB & clouds" processing line uses two basic steps: the cloud detection phase and the cloud properties derivation phase. The first step is crucial since it controls further processing and it has a major impact on determining other products. Particular attention is therefore given to the cloud detection algorithm of the "ERB & clouds" line; it is a threshold method employing several sequential tests for the presence of clouds. The adjustments of the different tests involved in the algorithm are presented in the next section. The so-derived POLDER pixel identification is compared to a cloud classification applied to METEOSAT data and based on the Dynamical Clustering Method [37]. The following sections present the others cloud properties, cloud optical thickness, cloud pressure, and cloud phase, respectively. The original contribution of POLDER regarding these products is emphasized. The discussions are supported by the analysis of POLDER data acquired on November 10, 1996, especially along three ADEOS orbits over the Atlantic Ocean (orbit numbers 3107–3109), i.e., in the METEOSAT field of view (see Fig. 1). At the end of a validation period foreseen in July 1998, the complete set of POLDER data will be processed by CNES and level 2 and 3 products will be made available to the scientific community. For the moment, the only available monthly synthesis of the "ERB & clouds" line is for June 1997. Section VI presents the global monthly means of POLDER-derived cloud properties and compares them to the ISCCP products. Finally, Section VII summarizes the results and concludes.

II. Cloud Amount: The Cloud Detection Algorithm

The physical principles of the POLDER cloud detection algorithm are extensively developed in [7]. They were based on the analysis of measurements performed by the airborne simulator of POLDER. Since then, POLDER has flown aboard ADEOS, and some adjustments and improvements have been brought to the algorithm. First, this section briefly covers the different threshold tests used in the algorithm and presents the methodology used to adjust the different threshold values. This consists mainly in analyzing the coherence of results from the various tests involved in the algorithm. The validation of the cloud identification is emphasized through comparison with the results of the Dynamical Clustering Method applied to METEOSAT satellite observation [37].

Fig. 1. Image constructed from 670 nm reflectance measured by POLDER on November 10, 1996 along three ADEOS paths (orbit numbers 3107–3109) over the Atlantic Ocean. Clouds appear as light shades against a darker ocean or land background.

The cloud detection algorithm of the "ERB & clouds" line is mainly based on a series of sequential threshold tests applied to each individual pixel (6.2 km) and for every viewing direction. Some of these tests use the spectral reflectance defined as $R_\lambda = \pi L_\lambda/(\cos\theta_s E_\lambda)$, where L_λ is the measured spectral radiance, θ_s is the solar zenith angle, and E_λ is the spectrally averaged solar irradiance at the top of the atmosphere. Four tests aim at detecting clouds, and a pixel is declared cloudy when one of these tests proves positive.

1) An "apparent" pressure P_{app} is derived from the ratio of reflectance measured in the channels centered at 763 and 765 nm (see Section IV). The pixel is labeled

cloudy if P_{app} is markedly lower than the sea-surface pressure $P_{surface}$. The threshold applied to $P_{surface} - P_{app}$ depends on the ratio between the molecular and the total reflectance at 765 nm, R_{mol}/R^* [42].

2) A pixel is declared cloudy if the measured reflectance at wavelength λ, R_λ ($\lambda = 865$ nm over ocean and $\lambda = 443$ nm over land) is significantly larger than its clear-sky estimate R_λ^{clear}. Over ocean, a large threshold value (15%) is chosen in order to avoid classifying aerosols as clouds. The same value is chosen over land, but the spatial variability is taken into account.

3) For scattering angles less than 140°, the molecular optical thickness τ_{443} of the atmospheric layer above the observed surface (cloud or sea-surface) is directly derived from the polarized reflectance at 443 nm. It is compared to the total molecular optical thickness of the atmosphere τ_{443}^{clear}. If the $\tau_{443}^{clear} - \tau_{443}$ difference is above threshold, the pixel is rejected as cloud contaminated. In [7] the threshold was set to a constant value. In the new version of the algorithm, it varies as a linear function of the air-mass factor.

4) The polarized radiance at 865 nm presents different features for clear-sky and for cloud conditions specifically in the rainbow direction (see Section V). A pixel is identified as cloud-contaminated if the actual polarized radiance is outside the expected range for clear-sky conditions. This range is now defined as a function of the scattering angle.

If all of the previous tests prove negative, two more tests are added in order to identify the clear pixels.

5) A pixel that has not been declared cloudy is labeled as clear if $R_\lambda - R_\lambda^{clear}$ ($\lambda = 865$ nm over ocean and $\lambda = 443$ nm over land) is small enough (<2%).

6) Finally, a pixel is expected to be clear if its reflectance exhibits a large spectral variability. Practically, following [5] the R_{865}/R_{443} ratio was found to be a better indicator than the R_{865}/R_{670} ratio initially considered in [7]. Over ocean, a pixel is declared as cloud-free if the R_{865}/R_{443} ratio is less than 0.4. Over land surface, this ratio has to be more than 1.2.

The different thresholds presented above have been adjusted according to the following philosophy. When adjusting the four first tests, the reflectance threshold test, $R_\lambda - R_\lambda^{clear} < 2\%$ is considered as a reference test. Indeed, all the pixels that satisfy this test for all the viewing directions are expected to be clear. Consequently, the reflectance threshold test is used as an indicator of the relevance of the different "cloud" thresholds. At this stage, the philosophy of the cloud detection algorithm is to adjust the "cloud" thresholds in order to make sure that all the four tests prove negative when the pixel is clear. When detecting the cloud-free pixels, a similar approach is adopted. Pixels are expected to be "cloudy" if the reflectance threshold test, $R_\lambda - R_\lambda^{clear} > 15\%$, is satisfied whatever the direction of view. The spectral variability thresholds are thus adjusted in such a way that practically no cloudy pixel is declared as clear. Illustration of this methodology can be found in [38].

If a POLDER pixel does not satisfy at least one of the six tests described above, it remains unclassified for a given viewing direction. However, if this pixel is labeled as clear (or cloudy) in some viewing directions and undetermined in all the other ones, then it is labeled as clear (or cloudy) for all the directions. If the pixel remains undetermined, it is then relabeled as clear or cloudy depending on the classification of the neighboring pixels and the spatial variability of R_{670}. Afterwards, when all of the elementary pixels are identified as cloud-free or cloudy, the cloud cover is computed at the super-pixel scale (~9 × 9 pixels), direction by direction. An example of so-derived global distribution of the monthly mean cloud cover retrieved from ADEOS/POLDER data is presented in Section VI.

A first validation of the POLDER cloud identification algorithm goes through a comparison with the results of the Dynamical Clustering Method [37] applied to METEOSAT data acquired every 30 min between 7 and 14 UTC from October 30 to November 10, 1996. The spatial resolution of the METEOSAT data is 5 km at nadir. The Dynamical Clustering Method uses two spectral parameters, the infrared and visible radiances and two structural parameters, the local spatial standard deviation of the visible and infrared radiances (computed for 3 × 3 neighboring pixels). These data are processed following [29] for five latitudinal regions over ocean and six regions over land. The result is a set of cloud type classifications valid between 7 and 14 UTC for the October 30–November 10, 1996 period. From this set, any ADEOS-POLDER path in the METEOSAT field of view can be simulated with a time lag of ±15 min.

The POLDER and METEOSAT cloud covers are compared for the three ADEOS paths (orbit numbers 3107–3109) on November 10 (Fig. 1). The proportion of clear (overcast) pixels is 28% (49%) in the METEOSAT classification and 34% (53%) in the POLDER one. The smaller clear pixel percentage in the METEOSAT classification is compensated by a larger percentage of partially covered pixels (small cumulus, cloud edges, very thin cirrus) than in the POLDER cloud classification. Note that "partly" does not have the same meaning for METEOSAT and POLDER pixels. In the former, it is used for METEOSAT pixels that are expected to be partly covered by clouds. In the latter, it is used for POLDER pixels that are labeled as cloudy for some viewing directions and clear for the others. The co-occurrence matrix obtained from the pixel-to-pixel comparison of the two classifications (Table I) shows that 76% of the pixels belong to the same class and only 1.7% belong to opposite classes (clear/overcast or overcast/clear). The percentage of pixels declared clear by POLDER but declared cloud-contaminated by METEOSAT (9%) is larger than the opposite case (3%). Only 13% of these anomalous pixels are overcast in the first case, and 17% in the second case. Tables II and III, respectively, give the distribution of the METEOSAT cloud types for each of the three POLDER classes and the distribution of the three POLDER classes for each of the METEOSAT cloud types. The overcast cloud types (low, middle, multilayer, cirrus, high thick clouds) have at least 85% of their pixels belonging to the overcast class in the POLDER classification and less than

TABLE I
CO-OCCURRENCE MATRIX OBTAINED FROM THE PIXEL-TO-PIXEL COMPARISON OF METEOSAT AND POLDER IDENTIFICATION FOR THE 3 POLDER-ADEOS PATHS OF FIG. 1

METEOSAT	POLDER Clear	POLDER Partly	POLDER Overcast
Clear	25.1%	2.5%	0.5%
Partly	7.9%	6.6%	8.0%
Overcast	1.2%	3.9%	44.3%

TABLE II
DISTRIBUTION OF THE METEOSAT CLOUD TYPES IN EACH OF THE THREE POLDER CLASSES FOR THE THREE POLDER-ADEOS PATHS OF FIG. 1

METEOSAT Cloud types	POLDER classes		
	Clear	Partly	Overcast
28.1% clear	89%	9%	2%
9.6% nearly clear	46%	28%	26%
7.0% thin edges	40%	38%	22%
5.9% partly cloudy	12%	21%	68%
9.2% low clouds	2%	3%	96%
7.4% middle clouds	3%	6%	91%
5.8% multi-layers	3%	13%	85%
4.2% thin cirrus clouds	11%	32%	57%
11.5% cirrus clouds	2%	10%	89%
11.3% high thick clouds	0%	0%	100%

3% of them are classified as clear. An exception is the thin cirrus class. For the partly cloudy types, the percentage of clear POLDER pixels decreases as the subpixel cloud cover is expected to increase. Study of the spatial neighboring of these partially covered METEOSAT pixels shows that when they are declared clear by POLDER, the percentage of clear METEOSAT pixels in the neighboring is larger than in the other cases.

The cloud cover derived from POLDER compares well with the METEOSAT cloud classification on an instantaneous basis and at the pixel scale. The percentage of full agreement between POLDER and METEOSAT (76%) is close to the 81% which is found by comparing the METEOSAT classification with itself by introducing a shift of one pixel. However, in this last case, only 0.2% of the pixels are classified in opposite categories against 1.7% in the POLDER-METEOSAT comparison. This discrepancy between POLDER and METEOSAT classifications comes from the differences both in the observations and the algorithms. The METEOSAT algorithm is very sensitive to a very small spatial variability of radiance values close to surface ones. In the POLDER scheme, thresholds have been set up to avoid the inclusion of "false clouds" such as Saharan dust. When the apparent pressure threshold and/or the reflectance threshold is decreased, the percentage of clear POLDER pixels declared clear by METEOSAT increases, but the percentage of clear METEOSAT pixels declared cloudy by POLDER increases, too. This comparison appears encouraging though there are some discrepancies especially for the partly cloudy and the thin cloud cases.

One has to keep in mind that the aim of the "ERB & clouds" processing line is to derive cloud properties and not to detect surface parameters. Consequently, the cloud detection algorithm is very different from a cloud-clearing algorithm. The previous discussion highlights that broken cloudiness as well as thin cloud cover are sometimes classified as clear by the POLDER pixel identification scheme. In fact, one verifies that the different thresholds of the POLDER algorithm have been adjusted in such a manner that questionable cloud cases as well as thick aerosol layers are rejected as clear. Generally speaking, it seemed to the authors that it was preferable not to allocate to an entire POLDER pixel some mean cloud properties corresponding only to a small fraction of the pixel. However, this philosophy may have some impact on the final results, as illustrated in Section VI.

III. CLOUD OPTICAL THICKNESS

Cloud optical thickness is directly related to the ice/water content and is thus a key parameter in cloud modeling. It can be derived from bidirectional reflectance measurements. However, this needs some assumptions both on cloud microphysics and on cloud morphology and spatial distribution. Cloud fields are commonly viewed as a single and homogeneous plane-parallel layer composed of prescribed particles despite possibly large effects due to both cloud heterogeneities (e.g., [25], [10]) and different particles [28]. Unlike the usual scanner radiometers, POLDER provides up to 14 quasi-simultaneous reflectance measurements of a geographical target. While it is always possible to find a cloud model that satisfies one single bidirectional observation of a given target, it is not so easy to fulfill the complete set of 14 observations. Consequently, POLDER not only allows the determination of cloud optical thickness under some hypotheses, but it also enables us to test the validity of these hypotheses.

A cloud water droplet model is used in our algorithm that operationally derives cloud optical thickness from ADEOS-POLDER data [7]. The cloudy pixels are assumed fully covered by a plane-parallel layer composed of liquid water droplets with an effective radius of 10 μm and an effective variance of 0.15 [18]. In these conditions, the optical thickness is the only cloud property that is allowed to vary. This model is similar to the one used in the first ISCCP analysis [33]. The uncertainties due to the use of this model have been discussed in [32].

An example of global distribution of the monthly mean cloud optical thickness retrieved from ADEOS-POLDER data is presented in Section VI. The purpose here is to illustrate the ability to test the cloud model used. To do that, for the cloudy situations observed over ocean during three ADEOS

TABLE III
DISTRIBUTION OF THE THREE POLDER CLASSES IN EACH OF THE METEOSAT CLOUD TYPES FOR THE THREE POLDER-ADEOS PATHS OF FIG. 1

	METEOSAT cloud types									
POLDER classes	Clear	Nearly clear	Thin edges	Partly cloudy	Low clouds	Middle clouds	Multi-layers	Thin cirrus	Cirrus clouds	High Thick
34.2% Clear	73%	13%	8%	2%	0%	1%	0%	1%	1%	0%
13.0% Partly	19%	21%	20%	9%	2%	4%	6%	10%	8%	0%
52.8% Overcast	1%	5%	3%	8%	17%	13%	9%	5%	19%	21%

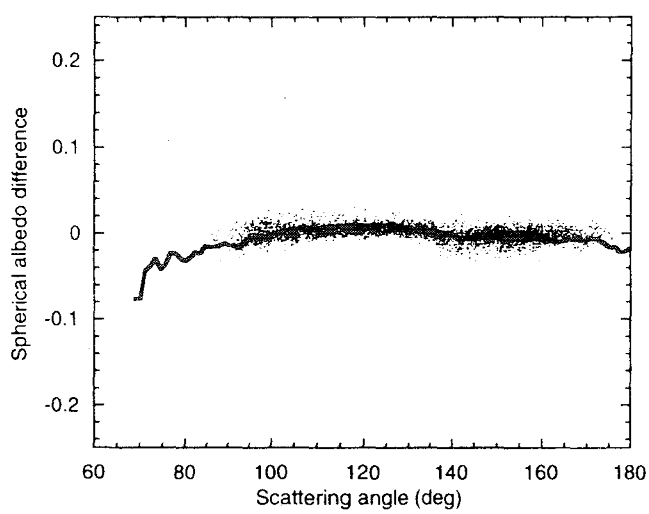

(a)

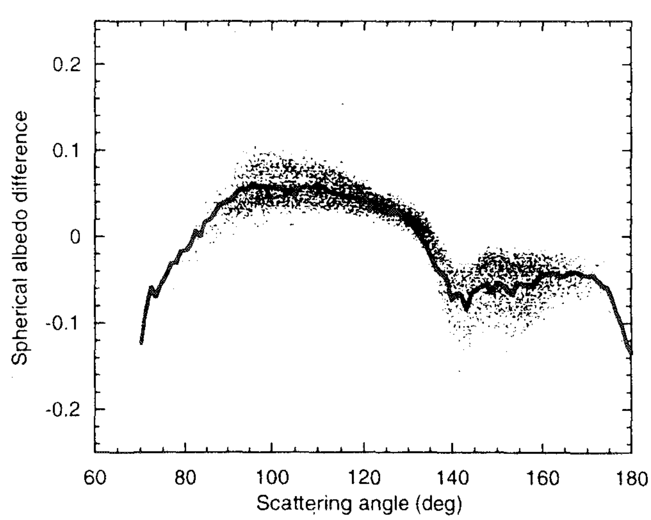

(b)

Fig. 2. Differences between the "directional" values of cloud spherical albedo and their mean value as a function of scattering angle for (a) liquid water clouds and (b) ice clouds. The wavelength is 670 nm. The line corresponds to the average difference. POLDER data corresponds to ADEOS orbits 3107–3109.

overpasses (orbit numbers 3107–3109), we make use of the $N(\leq 14)$ "directional" values of cloud optical thickness, given in the "ERB & clouds" products. Since the retrieval is based on the standard cloud droplet model, these N values are expected to be close to one another in the case of liquid water clouds and dispersed in the case of ice clouds. By another way, for each cloudy pixel the thermodynamic phase is identified following the method described in Section V. We thus select the super-pixels only composed of pixels for which the phase is found liquid and the super-pixels for which the phase is ice whatever the pixel. For every superpixel observed under at least seven directions, we calculate the difference between each of the "directional" values of optical thickness and their mean value. More precisely, we make use of a representation, introduced in the ISCCP scheme, that is equivalent in radiative energy amount. Indeed, the variability of the cloud properties we are interested in is important according to their contribution to the earth radiation budget. Additionally, as the basic measurements are radiances, the precision of the calculated differences is more easily interpretable in energy rather than in optical thickness. Practically, the calculated parameter is the cloud spherical albedo (over a black surface) which is a one-to-one function of the optical thickness (see [34, Fig. 3.13]).

These cloud spherical albedo differences are reported as a function of scattering angle for the selected liquid water clouds in Fig. 2(a). On average, the liquid water clouds appear well represented by the standard droplet model. The absolute difference of retrieved spherical albedo is typically 0.01. Only about ten superpixels, located near a depression off Iceland, notably depart from this good behavior; the large spherical albedo differences are certainly due to shortcomings in the cloud phase detection for these ambiguous multilayered cloud systems. The spherical albedo difference averaged over the 2278 superpixels classified as liquid water clouds remains very close to zero for all the scattering angles larger than 90°. The values of scattering angle around 80° correspond to large values of the solar and/or the viewing zenith angle, which may induce a serious weakness of the plane-parallel approximation [25]. However, note that the abrupt decrease of the spherical albedo difference near 70° corresponds to the ambiguous cases mentioned above and must not be considered as representative of the liquid water clouds.

The spherical albedo differences calculated for the superpixels classified as ice clouds are reported in Fig. 2(b). As expected, it clearly appears that the liquid water droplet model is not suitable for ice clouds. The difference of retrieved spherical albedo often reaches values as large as ±0.1. The value of the spherical albedo difference averaged over the 1197 superpixels varies by 0.12 when the scattering angle varies from 100° to about 140°. The minimum observed near 140° is related to the peak of the phase function of the water droplet model in the rainbow direction. A smoother phase function would give a better agreement in the treatment of ice clouds.

However, the standard water droplet model which is used in the POLDER operational algorithm—a cloud droplet radius of 10 μm—is in good agreement with mean values retrieved from near-infrared radiance observations over low-level clouds: about 11–12 μm in maritime clouds and 8–9 μm in continentals clouds [17]. On the opposite, many studies have shown that the single-scattering properties of ice cloud particles differ substantially from those of liquid water spheres (see [28] and references therein). For that reason, an ice fractal polycrystal model, which is expected to be representative of irregularly shaped and randomly oriented ice particles, was introduced in the treatment of cold clouds in the recent ISCCP re-analysis [34]. On the other hand, the analysis of airborne POLDER data acquired during the EUCREX'94 (European Cloud and Radiation Experiment) campaign confirmed that the standard water droplet model is suitable for stratocumulus and the ice polycrystal model is more adequate for cirrus clouds [14].

Thus, the POLDER bidirectional reflectance measurements appear useful to check the schemes of cloud optical thickness retrieval. In the near future, different cloud particle models will be investigated in order to minimize the angular variability of the cloud spherical albedo.

IV. Cloud Pressure

Together with cloud optical thickness, one of the most important cloud properties with respect to global climate changes is cloud height. Several techniques for deriving cloud altitude from satellite have already been developed, generally using radiances in the 15 μm CO_2 band (e.g., [40], [27]) or in the atmospheric windows (e.g., [31], [26]). Two different methods were developed to retrieve cloud pressure from ADEOS-POLDER data [7]. Here we present the first comparison between these two cloud pressures, respectively, derived from absorption measurements in the oxygen A-band and from spectral polarization measurements.

The algorithm of derivation of the "apparent pressure" P_{app} is extensively described in [7]. It is based on a differential absorption technique using the radiances measured in the POLDER narrow-band and wide-band channels centered on the oxygen A-band. In this algorithm, P_{app} is calculated both for clear and for cloudy conditions (cf., Section II; see also [42]). Here we consider only the cloudy conditions. The atmosphere is assumed to behave as a pure absorbing medium overlying a perfect reflector located at pressure P_{app}. Because all scattering effects are neglected, P_{app} is not the cloud top pressure; it is somewhat of a mean pressure, between the bottom and the top of a single cloud or of a multilayered cloud system. This difference between P_{app} and the cloud top pressure can be amplified when the ground influence is not negligible. A correction for this effect, proposed in [7], is yet to be validated and is not considered here.

Another retrieved cloud pressure is the so-called "Rayleigh cloud pressure," P_{Ray}, derived from polarization measurements at 443 nm. At this wavelength, the polarized reflectance is mainly related to the atmospheric molecular optical thickness above the observed cloud, at least for scattering angles ranging from 80° and 120° and outside the sunglint direction. A correction is introduced to remove the small contamination by the cloud layer itself as explained in [7]. The pressure P_{Ray} is then directly proportional to the retrieved molecular optical thickness. That pressure is thus expected to be close to the cloud top pressure, at least when the whole signal comes from the molecules situated above the cloud, that needs overcast conditions.

Fig. 3 compares the Rayleigh cloud pressure to that derived from O_2 absorption for the clouds observed during the three selected ADEOS overpasses. As expected, P_{app} is almost always larger than P_{Ray} for overcast conditions [Fig. 3(a), (b)]. The mean difference is 140 hPa for the 2776 oceanic superpixels and 209 hPa for the 219 continental ones. A comparable difference was observed for optically thick clouds between P_{app} and the cloud top pressure derived from the brightness temperature measured in the 11-μm channel of METEOSAT [42]. These differences are thought to be chiefly due to the photon penetration effect that strongly affects the retrieval of the pressure from O_2 absorption measurements. This effect is known to be more negligible as the volume scattering coefficient is larger [46]. That is the case of maritime stratocumulus clouds for which P_{app} is much closer to P_{Ray} [see the range 900–1000 hPa in Fig. 3(a)].

The comparison between P_{app} and P_{Ray} appears more complex for the partly cloudy superpixels [Fig. 3(c) and (d)]. The difference $P_{app} - P_{Ray}$ remains positive over land but is very often negative over ocean. The mean difference is 225 hPa for the 711 continental superpixels but −32 hPa for the 3462 oceanic ones. When the cloud cover tends toward zero, the retrieved pressures do not tend necessarily to the surface pressure $P_{surface}$. The Rayleigh pressure tends to $P_{surface}$ only if there is no additional polarization by the surface. The apparent pressure tends to $P_{surface}$ only if all of the reflected light comes from the surface. Practically, P_{app} is close to $P_{surface}$ for highly reflecting surfaces but can be as weak as 500 hPa for dark surfaces such as the ocean outside the region of the solar specular reflection [42]. Therefore, for partly cloudy pixels, P_{Ray} is generally larger than the actual cloud top pressure and P_{app} is weaker or larger than the cloud mean pressure depending on whether the surface is dark or bright. That explains that $P_{app} - P_{Ray}$ is generally positive for partly cloudy superpixels over land [Fig. 3(d)] but is now negative now positive over ocean depending on the relative contribution of the cloud in the observed reflectance [Fig. 3(c)].

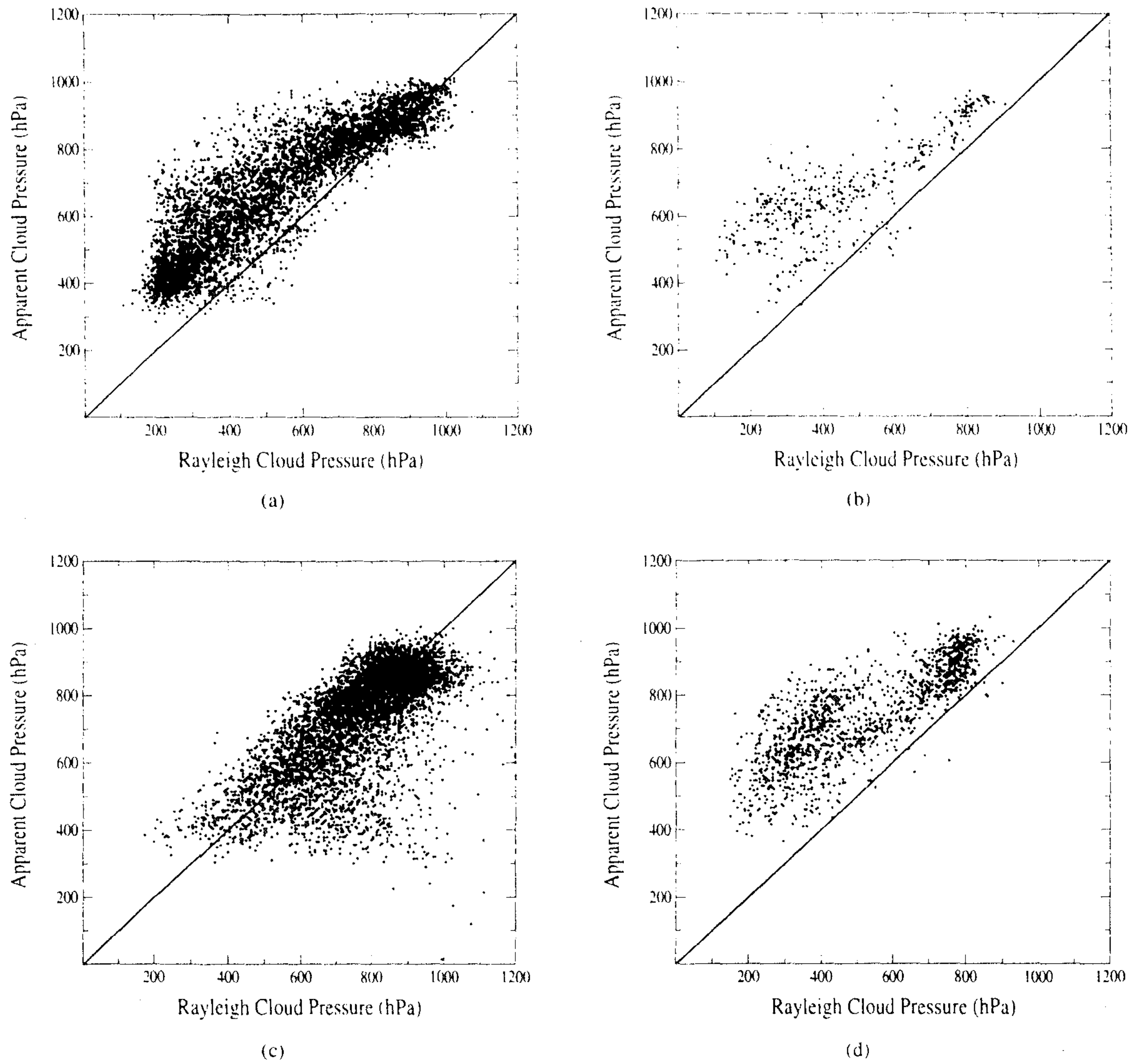

Fig. 3. Apparent cloud pressure derived from O_2 absorption versus Rayleigh cloud pressure derived from polarization at 443 nm, for overcast conditi over (a) ocean and (b) land and for partly cloudy conditions over (c) ocean and (d) land. POLDER data correspond to ADEOS orbits 3107–3109.

V. Cloud Thermodynamic Phase

An improved algorithm for remotely determining the cloud-top thermodynamic phase is described hereafter. The algorithm utilizes near-infrared polarized reflectance over a large range of scattering angles in order to discriminate between ice and liquid water phases. Indeed, theoretical as well as experimental studies have shown that polarized signatures of water droplets and ice particles are quite different [15], [16], [6], [35], [12].

Considering a cloudy system observed from satellite, the polarized component of the upward radiance is mainly formed in the upper cloud layer [15]. Around 80% of the single-scattered radiation reflected by the cloud arises from the upper hundred meters of the layer. In studying cloud polarization, the physical interesting quantity is the polarized reflectance PR_λ, which is less sensitive to multiple scattering effects than the total reflectance [19]. Thus, the polarization features, mainly governed by single scattering, are preserved in PR_λ.

For a large enough optical thickness ($\tau > 1$), the polarized reflectance PR_λ roughly varies as the cloud polarized phase function, which depends on cloud microphysics propert (shape/size) and refractive index.

In most cases, cloud water droplets are expected to h a particle effective radius ranging between 5 μm and 15 Fig. 4(a) and (b) presents, respectively, theoretical simulati and observations of the main polarization features for sc tering angles that can be observed by POLDER. The li scattering by cloud water droplets exhibits a strong maxim about 140° from the incoming direction. This peak, the called primary rainbow, is highly polarized which make easily detectable. The maximum and the width of the p are dependent on the droplet size distribution [15]. Ano noticeable property is the neutral point, which is loc between 75° and 120° according to droplet size. For nar size distributions, several supernumary bows appear [16]. the contrary, if the size distribution is relatively broad, supernumary bow appears. In some cases these properties used to retrieve the effective radius of liquid water drop [4]. The last polarization feature that can be observed is glory, which is centered on the backscattering peak (scatte

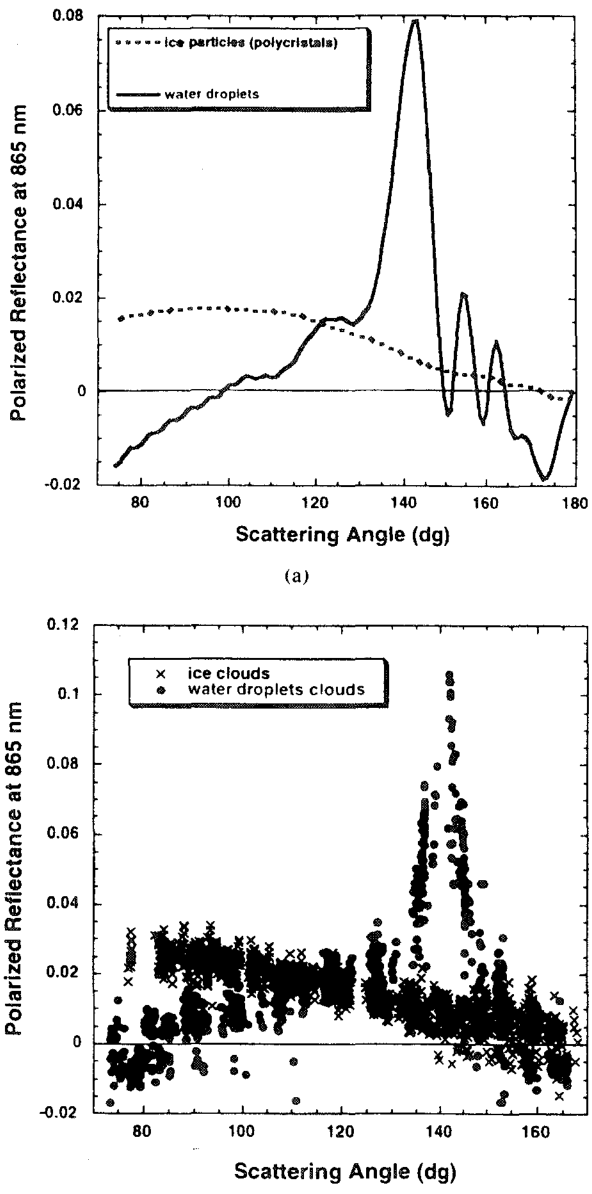

Fig. 4. Polarized reflectance at 865 nm as a function of scattering angle. (a) corresponds to simulation in the solar principal plane for polycrystals randomly oriented in space (dashed line) and water spheres of effective radius of 10 μm (solid line). In both cases cloud optical thickness is two. The sun zenithal angle is 55°. (b) is an example of polarized reflectance measured by POLDER over cirrus cloud (crosses) and over liquid water cloud (full circle) on November 10, 1996.

angle equal to 180°). This is a typical characteristic of water spheres [41].

Unlike water clouds, cirrus clouds are mainly composed of ice crystals with extremely large variabilities in shape and size [21]. Diversity and complexity of ice crystal shape and size depend on temperature and humidity in cloud. For scattering angles that can be observed from space, radiative transfer computations [6], [12] performed for randomly oriented hexagonal particles [Fig. 4(a)] and observations [Fig. 4(b)] show different important features: i) a generally positive polarization (vibration perpendicular to the scattering plane), ii) a decreasing of the polarization for increasing scattering angles (i.e. negative slope), and iii) a neutral point around 160°.

Since [7], preliminary analysis of polarized reflectances acquired by ADEOS-POLDER has highlighted a possible new way to recognize the cloud thermodynamic phase. The present operational algorithm is described hereafter. Two specific angular ranges are considered. For scattering angles smaller than 110°, the direction of the polarization plane with respect to the scattering plane is predominately 90° (positive polarized component and negative slope) for ice clouds and 0° (negative polarization and positive slope) for liquid water clouds. For larger scattering angles (around 140°) the two cloud types positively polarize the radiation, but the polarized reflectance is ten times higher for liquid water clouds than for ice clouds. The POLDER angular coverage in term of available scattering angles depends on the latitude and the season. The most complete POLDER angular sampling can give access to these two angular ranges. In some cases, one or both angular domains can be not sampled. The phase detection is based on tests performed in the two scattering angle domains at 865 nm. At this wavelength, the molecular contribution is rather weak and is corrected for by using the Rayleigh cloud top pressure (see Section IV).

The algorithmic principle and results are illustrated in Fig. 5. First, examine the 670-nm reflectance image [Fig. 5(a)] acquired over France on November 10, 1996. The size of the selected area is about 1000 km × 1000 km. Clouds cover a large part of the scene. Now, examine the corresponding polarized reflectance images at 865 nm for scattering angles around 100° [Fig. 5(b)] and for scattering angles around 140° [Fig. 5(c)]. In Fig. 5(b) black pixels correspond to negative polarization near 100°. This characterizes the "liquid" phase. The same pixels exhibit large polarized reflectance around 140° [Fig. 5(c)]. A combination of the polarization information in these two scattering angle domains leads to label these pixels as "liquid" [Fig. 5(d)]. On the other hand, gray pixels [Fig. 5(b)] correspond to relatively high positive polarization around 100° and to very small (<0.01) polarization around 140° [dark pixels in Fig. 5(c)]. The corresponding pixels are labeled "ice" [Fig. 5(d)]. The processing of the POLDER level 1 data thus allows the determination of cloud phase at global scale. Each cloudy "superpixel" of the level 2 POLDER product is finally identified as "liquid," "ice," "mixed" or else "undetermined."

VI. Monthly Mean Cloud Properties

The level 2 POLDER "ERB & clouds" products contain for each orbit the retrieved cloud property parameters (cloud cover, cloud pressures, optical thickness, . . .) with their full directional properties and their angular averaging as nondirectional parameters [7]. In level 3 processing, most of the latter, coming from up to 420 orbits, are averaged on a global coverage scale to provide monthly mean climatologies and associated temporal dispersions. For each pixel, the number of daily POLDER observations extend from at most one between 30° N and 30° S to up to 14 close to the poles. For the June 1997 POLDER data presented here, the number of averaged

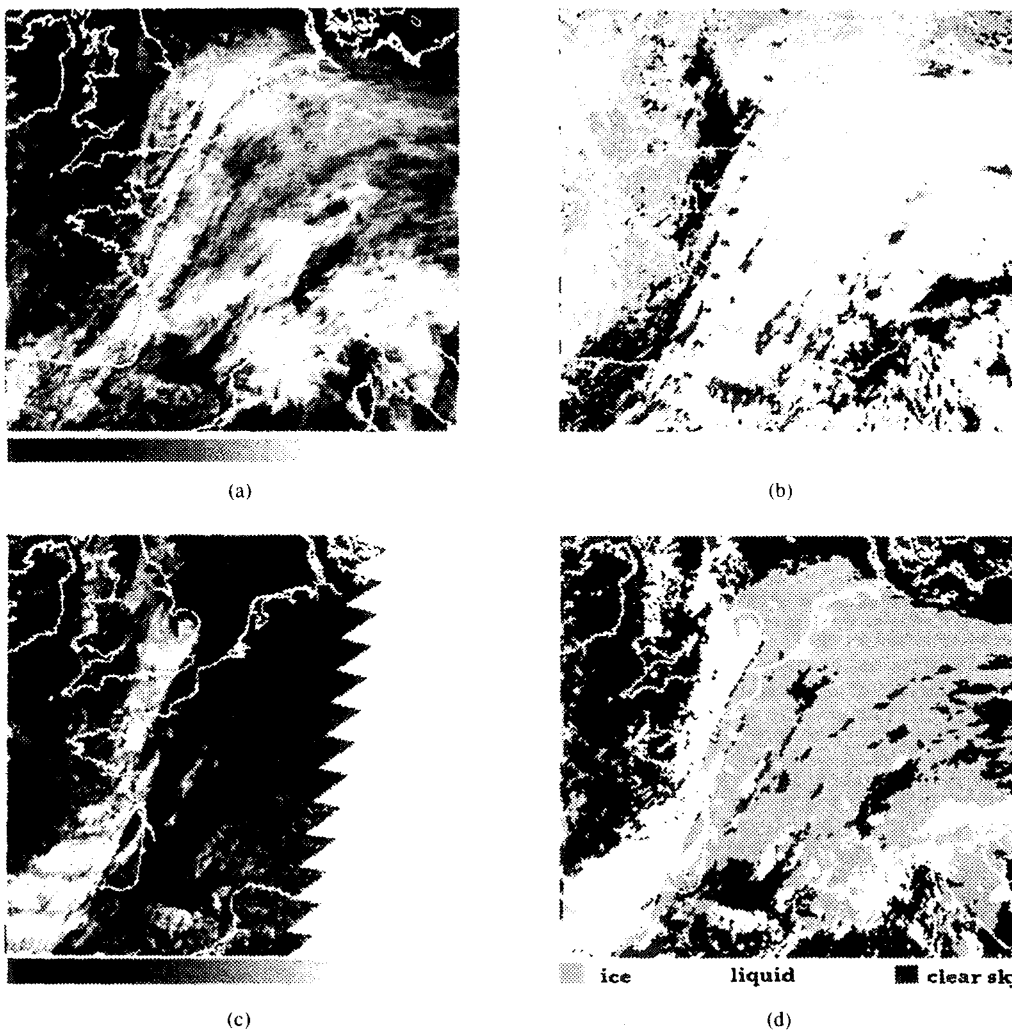

Fig. 5. Illustration of the cloud thermodynamic phase recognition. (a) Reflectance image in the 670-nm band acquired over France on November 1(1996. Reflectance dynamic ranges from 0–0.9. (b) Polarized reflectance at 865 nm for scattering angles close to 100°. Black pixels indicate negati(polarization ($-0.04 < \mathrm{PR} < 0$). Gray levels are for positive polarization up to 0.02. (c) Same as (b), but for scattering angles near 140°. Polariz(reflectance ranges from 0–0.07. (d) Thermodynamic phase index (black is for clear sky, light gray for liquid, and dark gray for ice). This resultir image is a combination of information contained in (b) and (c).

observations used to construct these climatologies lies, in most cases and depending on cloud cover and latitude, from 15 up to more than 150 observations.

As quoted in Section I, "ERB & clouds" products are averaged at a $\sim 50 \times 50$ km^2 scale which corresponds, except very near the poles, to 9×9 aggregates of elementary POLDER equal area pixels. This low-resolution grid has been constructed in direct relationship with the equal area ISCCP grid, in such a way that each ISCCP cell contains an integer number of these "superpixels" (namely 5×5, between 80° N and 80° S).

As an example of the first available "ERB & clouds" level 3 monthly synthesis, we present here the June 1997 climatology of four selected parameters (cloud cover, optical thickness, O_2 apparent cloud pressure, and Rayleigh cloud pressure) and make a first comparison to interannual means of ISCCP monthly mean data. For this, we have used both C2 (1983–1991) [33] and D2 (1987, 1989–1993) [34] data interpolated at 10:30 a.m. local time, but we will concentrate on the latter, as the most recent reprocessing of the archives. More exactly, we reprocess the D2-level data from ISCCI D1 data by weighting the cloud optical thickness and clou pressures by the cloud cover to obtain monthly means cohere with POLDER processing.

In the following, all comparisons of POLDER and ISCC data are restricted to the 60° N–60° S latitude band becau of the large snow and sea-ice occurrence near the pole. Fu thermore, for all statistical studies, the POLDER observatio have been averaged at the ISCCP cell resolution.

A. Cloud Cover

The POLDER cloud cover for June 1997 is presented Fig. 6. All the large cloud structures associated with the ma climate processes are easily identified and their location coherent with what we would expect for the month of Ju the intertropical convergence zone (ITCZ) along the 10° parallel, large clear-sky area over the deserts of Sahara, Sou West Africa, and Australia, subtropical zones of heavy clo cover west of Peru, Angola, California, and over the northe Pacific. We note, however, an abnormal overcast area arou

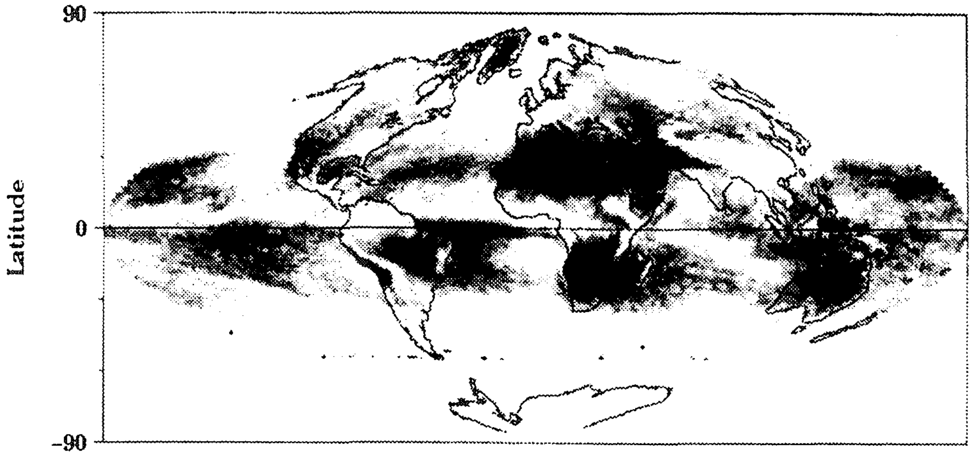

Fig. 6. POLDER level 3 monthly synthesis of cloud cover for June 1997. Coverage ranges from zero (black) to one (white) over a light gray background.

TABLE IV
GLOBAL MEANS OF ISCCP C&D AND POLDER CLOUD COVERS. FOR THE D DATA SET, MIN AND MAX GIVE THE INTERANNUAL DISPERSION AMONG THE SIX PROCESSED YEARS

	C	D			POLDER
	Mean	Min	Mean	Max	Mean
All cells	0.63	0.65	0.66	0.68	0.58
Over ocean	0.68	0.68	0.70	0.72	0.63
Over land	0.50	0.56	0.58	0.61	0.48

the North Pole corresponding, as it will be confirmed later, to a faulty cloud detection over sea ice.

Crude statistics of this cloud cover (Table IV) show that POLDER data underestimate the global cloud amount by 8% (5%) when compared with ISCCP D2 (C2) interannual mean data sets. When comparing these cloud covers at pixel scale, we see that POLDER is always weaker over ocean, but close to the C2 data set over land.

A more detailed view of these statistics in terms of cloud cover distribution (Fig. 7) shows that, for POLDER and ISCCP D2 data sets, 20% of the cells have a cloud cover higher than 0.8. However, 34% of POLDER cells have a cloud cover lower than 0.5, whereas this percentage drops to 20% for ISCCP-D2 climatology. A closer look at the POLDER (respectively, ISCCP-D2) cloud covers shows that, over ocean, 22% (respectively, 30%) of the cells have a coverage higher than 0.8, while 28% (15%) of cells have a coverage less than 0.5. Over land, these percentages become 8% (10%) for POLDER (ISCCP) cells with a coverage higher than 0.8 and 48% (32%) for cells with a coverage lower than 0.5.

Over land, in the 60° N–60° S latitude range, the increase of cloud coverage observed between the C2 data set and the D2 reprocessing is mainly due to the lower brightness temperature threshold used to separate clear and cloudy cells [34]. We may thus presume that the POLDER underestimation of cloud cover over land comes from a weaker detection of thin cirrus, as it is typically observed over the Saharan desert. This can be extended for ocean observations and is coherent with the precautions included in the cloud detection algorithms to avoid aerosol contamination (see Section II).

Finally, we have checked the coherence between POLDER cloud cover and ISCCP reprocessed climatologies at the pixel scale by looking at the cloud cover differences (δCC) with POLDER. Over ocean, δCC is weaker than 0.1 for 62% of the pixels while over land, this is observed for only 49% of the pixels. When the tolerance threshold is set to $\delta CC < 0.2$, these percentages reach 86% over ocean and 79% over land. That shows a good coherence at a global coverage scale despite the fact that i) we compare June 1997 to a six-year interannual mean and ii) POLDER has a daily global coverage, while ISCCP climatologies use multisensor data.

B. Cloud Optical Thickness

In both level 2 (with full directional properties) and level 3 processings, spatial and angular, then temporal averagings of optical thickness have been performed separately in terms of linear means and energy equivalent means (see Section III). Both sets of information are given in "ERB & clouds" POLDER products as in ISCCP products; but we will concentrate here on the latter.

The POLDER energy averaged optical thickness for June 1997 is presented in Fig. 8. Besides the values much larger than 15 at high latitudes which are obviously due to the large reflectivity of sea-ice areas detected as overcast pixels, the

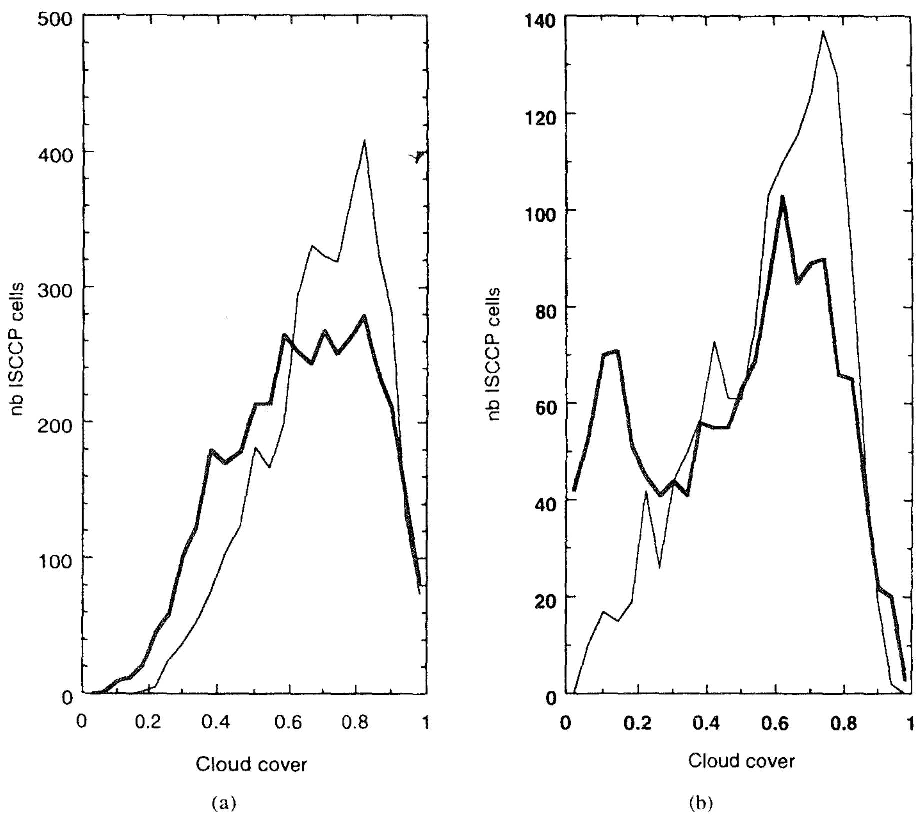

Fig. 7. Comparison of POLDER (thick solid line) and ISCCP D2 (thin solid line) cloud cover distributions (a) over ocean and (b) over land. The cc axis corresponds to the number of ISCCP equal area grid cells in 4% bins.

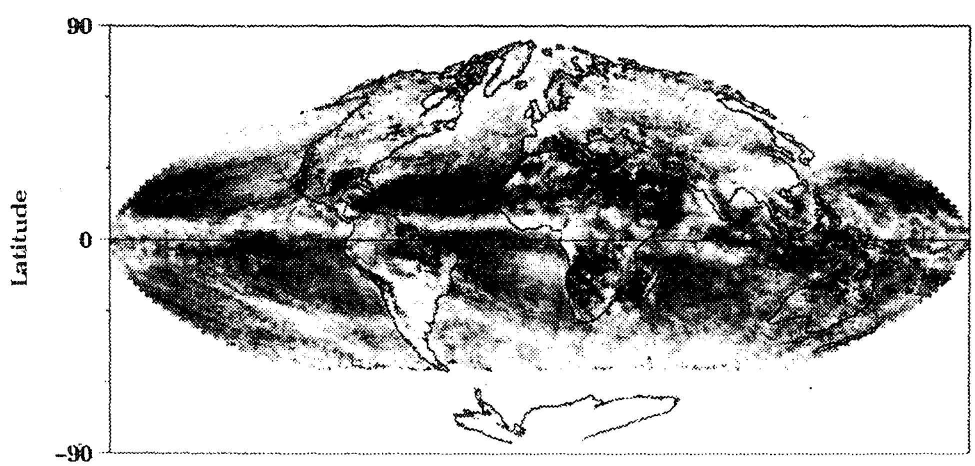

Fig. 8. POLDER level 3 monthly synthesis of cloud optical thickness (energy means) for June 1997. The scale ranges from zero (black) to 15 (wh over a light gray background.

observed optical thickness is coherent with the above-observed cloud structures and their expected regional reflectivity characteristics: high mean values all along the ITCZ, over midlatitude depression areas and for frequent thick enough cirrus banks as seen over the Sahara.

The statistical distribution of all the retrieved optical thicknesses between 60° N and 60° S is presented in Fig. 9 along with the corresponding ISCCP data. The pixel values (coded in equivalent energy amount) have been averaged, with cloud cover weighting, at the ISCCP cell scale and then converted to corresponding optical thickness for presentation. We observe a noticeable spreading of the POLDER distribution (4.66 0.64) toward higher optical thickness values, compared ISCCP (3.91 $\pm$ 0.58). At this stage of a first comparison, may think of different grounds for this discrepancy. First, CCP and POLDER present differences in the optical thickn retrieval methods as well as in the measurements. Anot would be the effect of the POLDER cloud detection algorit thresholds on thin cirrus and small or broken clouds at subpixel scale, compared to the ISCCP rate of detection. Si optical depth averaging is only done for nonzero cloud co the statistical effect may be far from negligible, even

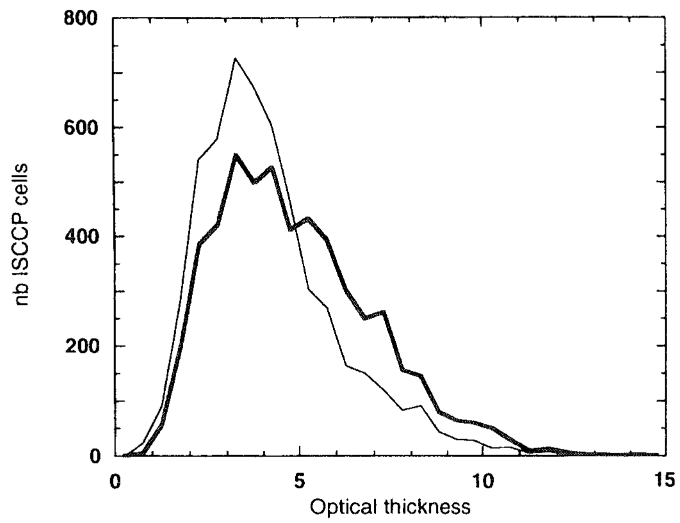

Fig. 9. Comparison of POLDER (thick solid line) and ISCCP (thin solid line) optical thickness distributions. The count axis corresponds to the number of ISCCP equal area grid cells in 0.5 bins.

energy means, and would lead toward the observed spreading over higher optical thickness values. Given the importance of optical thickness as a cloud characteristic, more precise studies are clearly needed, in particular with June 1997 ISCCP data when available.

C. Cloud Pressure

As explained in Section IV, two different POLDER cloud pressures ($P_{\rm app}$ and $P_{\rm Ray}$) have been defined, using two different physical principles. We may thus expect to attain different characteristics of the usually complex cloud structures.

The POLDER mean "apparent" cloud pressure $P_{\rm app}$ for June 1997 is presented in Fig. 10. The abnormally high values around the pole are in fact surface pressures of snow and sea-ice, as mentioned above. The main climatic trends of cloud top heights are easily recognizable: large areas of dense low cloud structures on subtropical west sides of main continents and the southern Indian Ocean, high cloud accumulation all along the ITCZ and over high altitude continental zones. However, but not surprisingly (see Section IV), $P_{\rm app}$ appears systematically lower than the expected cloud "top" pressure.

This is clearly confirmed by a global statistical comparison of this retrieved pressure against ISCCP pressures (Table V). For the latter, we have chosen to confront POLDER pressures to both "adjusted cloud top pressure" (noted P78, following ISCCP D2 notation [34]) and "nonadjusted cloud top pressure" (P79). When averaged, $P_{\rm app}$ appears very close to the uncorrected P79 pressure but significantly higher than P78.

Pressure distributions over all ICCP cells (Fig. 11) furnish further hints. First, $P_{\rm app}$ and P78 present a very similar shape of distribution which shows, more or less clearly, three expected structures: the concentration of large strato-cumulus decks with high pressure values, thick high-level clouds on the other end of the histogram, and a majority of middle/multilayered cloud structures in between. Second, there is an overall shift of 139 hPa between $P_{\rm app}$ and P78, the latter being expected to be close to the top cloud pressure. This overall value is probably a complex statistical mixing of two main radiative processes: photon penetration inside cloud layers and transparency of thin upper layer to lower cloud layers or surface reflectivity (see Section IV and [42]).

The POLDER mean "Rayleigh pressure" $P_{\rm Ray}$ for June 1997, presented in Fig. 12, is expected to be closer to the top cloud pressure (Section IV). Indeed, all the main climatic trends of known cloud top heights are enhanced when compared to $P_{\rm app}$: geographic extension of the high-level clouds, particularly over land, and clear higher mean values of the cloud pressure. We note, however, an abnormal amount of large (>900 hPa) pressure values which are currently under investigation.

When $P_{\rm Ray}$ is compared to ISCCP cloud top pressure P78 (Table V and Fig. 13) we observe a shift of 78 hPa toward high pressure values, whereas the general trends of the pressure distribution are comparable. Given the very different radiative physics involved in the retrieval of these two cloud pressures (brightness temperature in one case and polarized visible reflectivity in the other), a detailed comparison is far beyond the scope of this paper. However, when exploring the lower pressure end of the distribution (Fig. 3) at the pixel scale, we observe that (22%) (16%) (36%) of (all)(ocean)(land) ISCCP P78 pixels have a cloud top pressure weaker than 450 hPa, while the corresponding percentages drop to (5%) (4%) (7%) for $P_{\rm Ray}$. As observed for $P_{\rm app}$, one part of this lack of high pressures is due to the POLDER misdetection of thin cirrus, particularly over land; another part may be interpreted as a transparency effect of the polarization due to molecules underneath high rather thin cloud layers; further studies are nonetheless needed to confirm such a statement.

At the present state of the validation, the comparisons presented above for three of the main cloud properties are encouraging and lead to rather coherent hints regarding the observed discrepancies. However, this preliminary study is limited to a single month and any conclusive statement should wait until the whole eight months of level 3 POLDER data are processed.

VII. Summary and Conclusion

First results on the derivation of cloud properties from ADEOS-POLDER have been presented in this paper. The original contribution of POLDER has been emphasized for each cloud property investigated. Particular attention was given to POLDER level 2 data of November 10, 1996 and level 3 products of June 1997.

A first key result is a good correlation between the POLDER cloud detection algorithm and the Dynamical Clustering Method [37] applied to METEOSAT data. Some discrepancies appear for broken cloudiness and very thin cirrus cloud cases. However, we think that it is preferable to not allocate to an entire POLDER pixel (6.2 km × 6.2 km) cloud properties that correspond only to a small fraction of the pixel. This choice can explain why our cloud cover appears to be weaker (typically by 0.08) than the ISCCP climatological values.

Cloud optical thickness was derived from bidirectional reflectances by using the standard water droplet model with

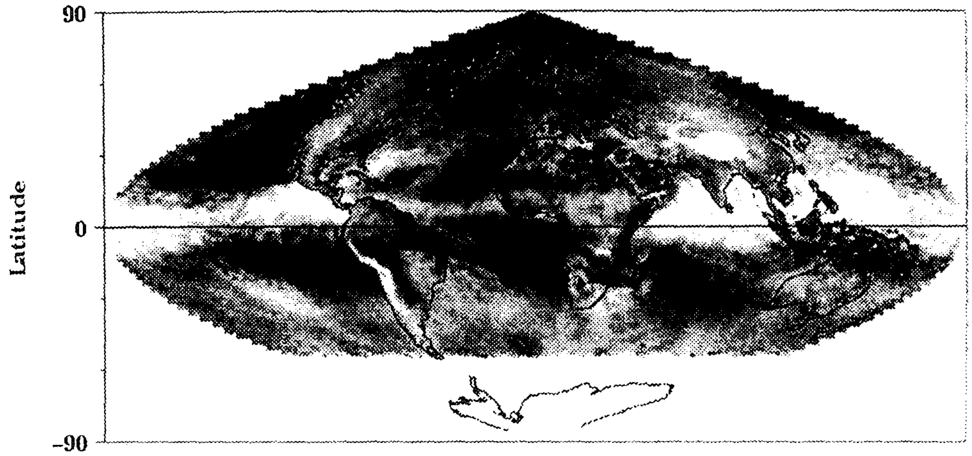

Fig. 10. POLDER level 3 monthly synthesis of apparent O2 pressure (P_{app}) for June 1997. Pressure ranges from 200 hPa (white) to 1000 hPa (black).

TABLE V
GLOBAL MEANS AND STANDARD DEVIATIONS (hPa) OF ISCCP P78 AND P79 (SEE TEXT) AND POLDER P_{app} AND P_{Ray} PRESSURE DISTRIBUTIONS

	P78	P79	P_{app}	P_{Ray}
All cells	565 ± 131	670 ± 103	704 ± 108	643 ± 135
Over ocean	545 ± 132	660 ± 105	700 ± 116	668± 137
Over land	605 ± 117	685 ± 94	717 ± 87	585 ± 136

an effective radius of 10 μm. The multidirectional capability of POLDER is demonstrated to be useful to check schemes of cloud optical thickness retrieval. As expected, the standard water droplet model is suitable for liquid water clouds and inadequate for ice clouds. This statement indirectly validates our algorithm of cloud thermodynamic phase recognition, since it was used to select these two types of clouds. The next "ERB & clouds" algorithm planned for POLDER2 on ADEOS2 (end of 2000) should begin with the cloud phase detection; then the more adequate particle models should be used to derive the cloud optical thickness. For this purpose, different ice crystal models will be analyzed and validated in the very near future.

Two POLDER cloud pressures are derived by two different ways: the O_2-apparent pressure is derived from absorption measurements in the oxygen-A band, while the Rayleigh cloud pressure makes use of spectral polarization observations. On average, the apparent pressure is weaker (typically by 60 hPa) than the Rayleigh pressure. For overcast conditions, the Rayleigh pressure is expected to be close to the cloud top pressure; the O_2-apparent pressure is larger by more than 100 hPa chiefly due to the photon penetration effect inside the cloud layers. For partly cloudy conditions, the difference between the two retrieved pressures can be now negative now positive depending on the importance of the surface reflectivity.

Comparisons between POLDER and ISCCP monthly mean products were performed for the month of June. However, they are still only preliminary since the ISCCP data are not yet

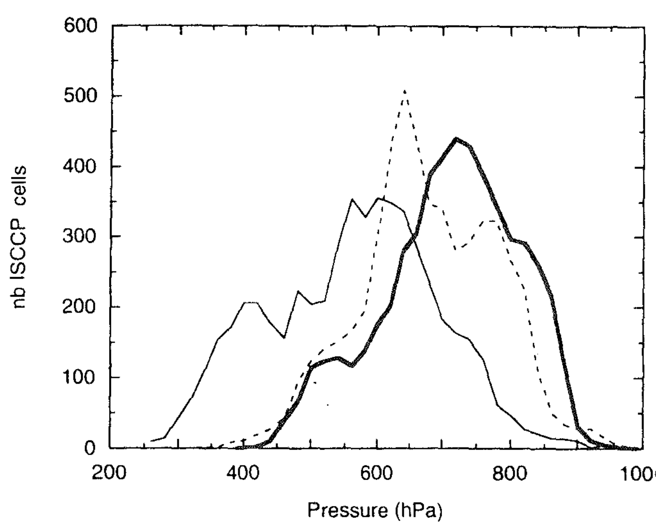

Fig. 11. Comparison of P_{app} (thick solid line), ISCCP P78 pressure (th solid line) and P79 pressure (dotted line) distributions. The count ax corresponds to the number of ISCCP equal area grid cells in 20 hPa bins.

available for the period of the ADEOS-POLDER acquisitic (November 1996–June 1997). Overall, the agreement is rath good. Differences between POLDER and ISCCP cloud optic thickness and cloud pressure certainly result for a large pa from differences in the cloud detection schemes. They al result from the original characteristics of the POLDER instr ment, which is complementary to usual satellite radiometer

The multispectral multipolarization and multidirectional c pabilities of POLDER thus appear useful for cloud studie

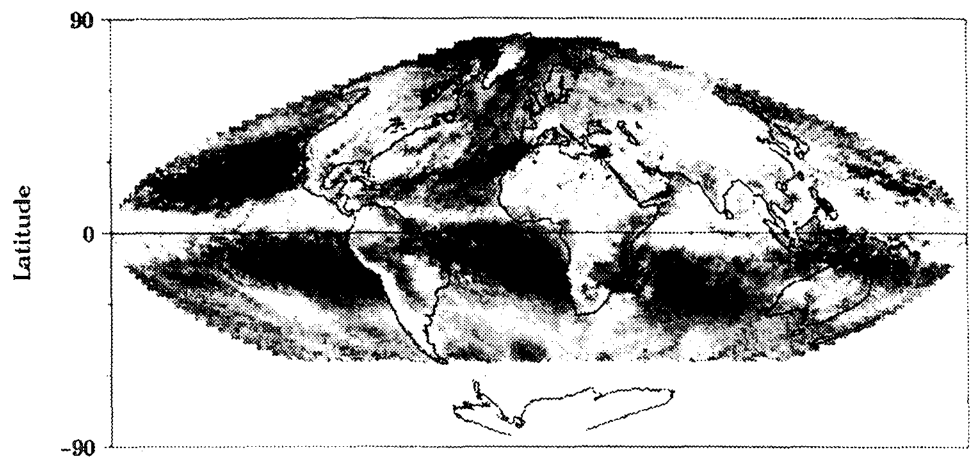

Fig. 12. As in Fig. 10 for POLDER "Rayleigh" pressure (P_{Ray}).

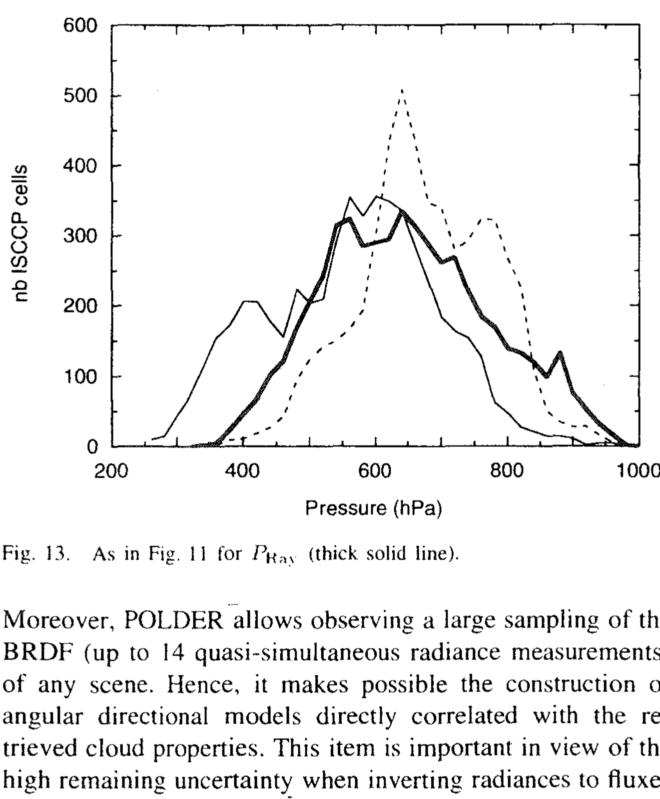

Fig. 13. As in Fig. 11 for P_{Ray} (thick solid line).

Moreover, POLDER allows observing a large sampling of the BRDF (up to 14 quasi-simultaneous radiance measurements) of any scene. Hence, it makes possible the construction of angular directional models directly correlated with the retrieved cloud properties. This item is important in view of the high remaining uncertainty when inverting radiances to fluxes in the Earth Radiation Budget Experiment (ERBE) project, which is simply due to the use of limited and sometimes incorrect angular directional models [3], [2]. In the recent Tropical Rainfall Measuring Mission (TRMM) [39] and near-future Earth Observing System (EOS) projects [44], this fundamental problem is expected to be improved by combining broadband CERES measurements [45] with the use of narrow-band moderate spatial resolution cloud imagers like Moderate Resolution Imaging Spectrometer (MODIS) [24] and Visible and Infrared Scanner (VIRS).

ACKNOWLEDGMENT

The authors wish to thank A. Lifermann for her comments on the manuscript. They also gratefully acknowledge Dr. I. Melnikova and two anonymous referees for their very helpful comments and suggestions.

REFERENCES

[1] A. Arking, "Latitudinal distribution of cloud cover from TIROS III photographs," *Science*, vol. 143, pp. 569–572, 1964.
[2] D. G. Baldwin and J. A. Coakley, Jr, "Consistency of Earth radiation budget experiment bidirectional models and the observed anisotropy of reflected sunlight," *J. Geophys. Res.*, vol. 96, pp. 5195–5207, 1991.
[3] B. R. Barkstrom, E. F. Harrison, and R. B. Lee, "Earth radiation budget experiment. Preliminary seasonal results," *EOS*, vol. 71, pp. 297–305, 1990.
[4] F. M. Bréon and P. Goloub, "Cloud droplet effective radius from spaceborne polarization measurements," *Geophys. Res. Lett.*, vol. 25, pp. 1879–1992, 1998.
[5] F. M. Bréon and S. Colzy, "Cloud detection from the spaceborne POLDER Instrument and validation against synoptic observations," *J. Appl. Meteorol.*, to be published.
[6] G. Brogniez, "Light scattering by finite hexagonal crystals arbitrarily oriented in space," in *Proc. IRS'88*, J. L Lenoble, J. F. Geleyn, and A. Deepak, Eds., Hampton, VA, 1988, p. 64.
[7] J.-C. Buriez, C. Vanbauce, F. Parol, P. Goloub, M. Herman, B. Bonnel, Y. Fouquart, P. Couvert, and G. Sèze, "Cloud detection and derivation of cloud properties from POLDER," *Int. J. Remote Sens.*, vol. 18, pp. 2785–2813, 1997.
[8] R. D. Cess *et al.*, "Intercomparison and interpretation of climate feedback processes in 19 atmospheric general circulation models," *J. Geophys. Res.*, vol. 95, pp. 16601–16610, 1990.
[9] ——, "Cloud feedback in atmospheric general circulation models: An update," *J. Geophys. Res.*, vol. 101, pp. 12791–12794, 1996.
[10] L. H. Chambers and B. A. Wielicki, "Accuracy of independent pixel approximation for satellite estimates of oceanic boundary layer cloud optical depth," *J. Geophys. Res.*, vol. 102, pp. 1779–1794, 1997.
[11] R. J. Charlson, S. E. Schwartz, J. M. Hales, R. D. Cess, J. A. Coackley, Jr., J. E. Hansen, and D. J. Hofmann, "Climate forcing by anthropogenic aerosols," *Science*, vol. 255, pp. 423–430, 1992.
[12] H. Chepfer, G. Brogniez, L. Sauvage, P. H. Flamant, V. Trouillet, and J. Pelon, "Remote sensing of cirrus radiative parameters during EUCREX'94. Case study of Apr. 17, 1994. Part 1: Microphysical modelization," *Mon. Wea. Rev.*, vol. 127, pp. 504–519, 1999.
[13] P. Y. Deschamps, F. M. Breon, M. Leroy, A. Podaire, A. Bricaud, J. C. Buriez, and G. Sèze, "The POLDER mission: Instrument characteristics and scientific objectives," *IEEE Trans. Geosci. Remote Sensing*, vol. 32, pp. 598–615, 1994.
[14] J. Descloitres, J.-C. Buriez, F. Parol, and Y. Fouquart, "POLDER observations of cloud bidirectional reflectances compared to a plane-parallel model using the ISCCP cloud phase functions," *J. Geophys. Res.*, vol. 103, pp. 11411–11418, 1998.
[15] P. Goloub, J.-L. Deuzé, M. Herman, and Y. Fouquart, "Analysis of the POLDER polarization measurements performed over cloud covers," *IEEE Trans. Geosci. Remote Sensing*, vol. 32, pp. 78–88, 1994.
[16] P. Goloub, H. Chepfer, M. Herman, G. Brogniez, and F. Parol: "Use of polarization for clouds study," in *Proc. SPIE*, 1997, vol. 3121, pp. 330–341.
[17] Q. Han, W. B. Rossow, and A. A. Lacis, "Near-global survey of effective droplet radii in liquid water clouds using ISCCP data," *J. Climate*, vol. 7, pp. 465–497, 1994.

[18] J. E. Hansen and L. D. Travis, "Light scattering in planetary atmospheres," *Space Sci. Rev.*, vol. 16, pp. 527–610, 1974.

[19] J. E. Hansen, "Multiple scattering of polarized light in planetary atmospheres. Part II. Sunlight reflected by terrestrial water clouds," *J. Atmos. Sci.*, vol. 28, pp. 1400–1426, 1971.

[20] E. F. Harrison, P. Minnis, B. R. Barkstrom, V. Ramanathan, R. D. Cess, and G. G. Gibson, "Seasonal variations of cloud radiative forcing derived from the Earth radiation budget experiment," *J. Geophys. Res.*, vol. 95, pp. 18687–18703, 1990.

[21] A. J. Heymsfield, "Cirrus unicinus generating celles and evolution of cirriform clouds. Part I: Aircraft observations of the growth of the ice phase," *J. Atmos. Sci.*, vol. 32, pp. 799–807, 1975.

[22] J. T. Houghton, G. J. Jenkins, and J. J. Ephraums, Eds., "Climate change: The IPCC scientific assessment," in *World Meteorological Organization/United Nations Environment Programme*. Cambridge, U.K.: : Cambridge Univ. Press, 1990, p. 364.

[23] R. S. Kandel, J. L. Monge, M. Viollier, L. A. Pakhomov, V. I. Adasko, R. G. Reitenbach, E. Raschke, and R. Stuhlmann, "The ScaRaB project: Earth radiation budget observations from the Meteor satellites," World Space Congress (Washington)-COSPAR Symp. A.2-S, *Adv. Space Res.*, vol. 14, no. 1, pp. 47–54, 1994.

[24] M. D. King, Y. J. Kaufman, W. P. Menzel, and D. Tanré, "Remote sensing of cloud, aerosol, and water vapor properties from the moderate resolution imaging spectrometer (MODIS)," *IEEE Trans. Geosci. Remote Sensing*, vol. 30, pp. 2–27, Jan. 1992.

[25] T. Kobayashi, "Effects due to cloud geometry on biases in the albedo derived from radiance measurements," *J. Climate*, vol. 6, pp. 120–128, 1993.

[26] X. Lin and J. A. Coaklley, "Retrieval of properties for semitransparent clouds from multispectral infrared imagery data," *J. Geophys. Res.*, vol. 98, pp. 18501–18514, 1993.

[27] W. P. Menzel, D. P. Wylie, and K. L. Strabala, "Seasonal and diurnal changes in cirrus clouds in four years of observations with the VAS," *J. Appl. Meteorol.*, vol. 31, pp. 370–385, 1992.

[28] M. I. Mishchenko, W. B. Rossow, A. Macke, and A. A. Lacis, "Sensitivity of cirrus cloud albedo, bidirectional reflectance and optical thickness retrieval accuracy to ice particle shape," *J. Geophys. Res.*, vol. 101, pp. 16973–16985, 1996.

[29] J. L. Raffaelli and G. Sèze, "Cloud type separation using local correlation between visible and infrared satellite images," in Passive Infrared Remote sensing of clouds and the atmosphere III, *Proc. SPIE*, vol. 2578, pp. 61–67, 1995.

[30] V. Ramanathan, R. D. Cess, E. F. Harrison, P. Minnis, B. R. Barkstrom, E. Ahmad, and D. Hartmann, "Cloud radiative forcing and climate: Results from the Earth radiation budget experiment," *Science*, vol. 243, pp. 57–63, 1989.

[31] D. W. Reynolds and T. H. Vonder Harr, "A bi-spectral method for cloud parameter determination," *Mon. Wea. Rev.*, vol. 105, pp. 446–457, 1977.

[32] W. B. Rossow, L. C. Garder, and A. A. Lacis, "Global, seasonal cloud variations from satellite radiance measurements. Part I: Sensitivity of analysis," *J. Climate*, vol. 2, pp. 419–458, 1989.

[33] W. B. Rossow and R. A. Schiffer, "ISCCP cloud data products," *Bull. Amer. Meteorol. Soc.*, vol. 6, pp. 2394–2418, 1991.

[34] W. B. Rossow, A. W. Walker, D. E. Beuschel, and M. D. Roiter, "International satellite cloud climatology project (ISCCP). Documentation of new cloud datasets," WMO/TD 737, World Meteorolog. Org., 1996, p. 115.

[35] L. Sauvage, H. Chepfer, V. Trouillet, P. H. Flamant, G. Brogniez, J. Pelon, and F. Albers, "Remote sensing of cirrus radiative parameters during EUCREX'94. Case study of Apr. 17, 1994. Part 1: Observations," *Mon. Wea. Rev.*, vol. 127, pp. 486–503, 1999.

[36] C. A. Senior and J. F. B. Mitchell, "Carbon dioxide and climate: The impact of cloud parameterization," *J. Climate*, vol. 6, pp. 393–418, 1993.

[37] G. Sèze and M. Desbois, "Cloud cover analysis in satellite imagery using spatial and temporal characteristics of the data," *J. Climate Appl. Meteorol.*, vol. 26, pp. 287–303, 1987.

[38] G. Sèze, C. Vanbauce, J.-C. Buriez, F. Parol, and P. Couvert, "Comparison of the POLDER cloud detection over ocean with a METEOSAT cloud classification," in *Proc. AMS'98*, Paris, France, May 25–29, 1998, pp. 500–503.

[39] J. Simpson, R. F. Adler, and G. R. North, "A proposed tropical rainfall measuring mission (TRMM) satellite," *Bull. Amer. Meteorol. Soc.*, vol. 69, pp. 278–295, 1988.

[40] W. L. Smith and C. M. R. Platt, "Comparison of satellite-deduced cloud heights with indications from radiosonde and ground-based measurements," *J. Appl. Meteor.*, vol. 17, pp. 1796–1802, 1978.

[41] J. D. Spinhirne and T. Nakajima, "Glory of clouds in the near-infrared," *Appl. Opt.*, vol. 33, pp. 4652–4662, 1994.

[42] C. Vanbauce, J. C. Buriez, F. Parol, B. Bonnel, G. Sèze, and P. Couvert "Apparent pressure derived from ADEOS-POLDER observations i the oxygen A-band over ocean," *Geophys. Res. Lett.*, vol. 25, pp 3159–3162, 1998.

[43] M. Vespérini, F. M. Bréon, and D. Tanré, "Atmospheric water va por content from POLDER spaceborne measurements," this issue, pp 1613–1619.

[44] B. A Wielicki, R. D. Cess, M. D. King, D. A. Randall, and E. F Harrison, "Mission to Planet Earth: Role of clouds and radiation i climate," *Bull. Amer. Meteorol. Soc.*, vol. 76, pp. 2125–2152, 1995.

[45] B. A Wielicki and B. R. Barkstrom, "Cloud and the Earth's radiar energy system (CERES): An Earth observing system experiment," i *2nd Symp. Global Change Studies*, New Orleans, LA, Amer. Meteo Soc., 1991, pp. 11–16.

[46] M. C. Wu, "Remote sensing of cloud-top pressure using reflected sola radiation in the oxygen-A band," *J. Clim. Appl. Meteorol.*, vol. 24, pp 539–546, 1985.

Frédéric Parol, for a photograph and biography, see this issue, p. 1566.

Jean-Claude Buriez received the M.S. degree i physics in 1968 and the "Doctorat d'Etat" in physic in 1981, both from the University of Lille, France

He is currently a Professor of physics at th University of Lille and a Researcher at the Labc ratoire d'Optique Atmosphérique. Before 1981, h worked on radiative transfer theory of inhomoge neous scattering atmospheres to analyze planetar spactra. Since then his research has focused on th remote sensing of cloud properties using space- an ground-based instruments. His scientific interes include the influence of clouds on radiation in climate modeling. He is i charge of the inversion of POLDER measurements for cloud and radiativ budget analysis.

Claudine Vanbauce received the M.Sc. degree i physics in 1988 and the Ph.D. degree in atmospheri physics from the University of Lille, France, in 199 for studies about remote sensing of fog.

During 1993, she worked on a Centre Nation d'Etudes Spatiales (CNES) Post-Doctoral subje devoted to the possibility of detection and classific tion of clouds from multispectral and multiangul POLDER data. She is currently an Assistant Pr fessor of physic and a Researcher employed the Laboratoire d'Optique Atmospherique, Lill France. She participated in the POLDER "ERB & Clouds" line algorithn development and in the validation of associated products.

Pierre Couvert received the "Doctorat de 3ièn cycle" in nuclear physics in 1974 and the "Doctor d'Etat" in 1982.

From 1974 to 1993, he worked mainly at t Laboratoire National Saturen, Saclay, France, as member of the Nuclear Physics Department of t Commissariat à l'Energie Atomique. From 1982 1984, he spent two sabbatical years at TRIUM Vancouver, B.C., Canada. His domain of resear was mainly devoted to nucleon scattering and mes production in nuclei. In 1994, he turned to earth s ences by joining the Laboratoire des Sciences du Climat et de l'Environneme of Saclay as a Researcher and Member of the POLDER project. In charge the technical aspects of the "Earth Radiation Budget and Clouds" POLDI data processing line with the Centre National d'Etude Spatiale, Toulouse, participates in the validation of the first POLDER data with the scientific te of the Laboratoire d'Optique Atmosphérique, Lille.

Geneviève Sèze received the Ph.D. degree in computer science from the University of Paris VI, France, in 1977.

In 1978, she joined the Laboratoire de Météorologie Dynamique (LMD) of the Centre National de la Recherche Scientifique. In 1985 and 1986, she was a Visiting Scientist at the Goddard Institute for Space Studies, New York, where she also collaborated with the International Satellite Cloud Climatology Program (ISCCP) team. In November 1989, she was selected as a member of the First ISCCP Regional Experiment (FIRE) Science Team. At LMD, she conducts research on cloud cover analyses from satellite observation and the validation of Global Circulation Model cloud cover. She participates in the definition and development of future space missions dedicated to cloud cover analyses. For the POLDER project, she is in charge of the analysis and the validation of the cloud cover.

Philippe Goloub, for photograph and biography, see p. 525 of the January 1999 issue of this TRANSACTIONS.

Sylvain Cheinet graduated from Ecole Polytechnique, Palaiseau, France, in 1994. In 1998, he received the M.S. degree in atmospheric physics from the University of Lille, France, where he participated in the exploitation of POLDER products with the working group "Earth Radiation Budget & Clouds" of the Laboratoire d'Optique Atmosphérique. He is currently pursuing the Ph.D. degree in the Laboratoire de Météorologie Dynamique (working group: Modélisation Du Climat), whose topic is to determine the influence of cloud parameterization in the General Circulation Model of the LMD.

Top-of-Atmosphere Albedo Estimation from Angular Distribution Models Using Scene Identification from Satellite Cloud Property Retrievals

NORMAN G. LOEB

Center for Atmospheric Sciences, Hampton University, Hampton, Virginia

FRÉDÉRIC PAROL, JEAN-CLAUDE BURIEZ, AND CLAUDINE VANBAUCE

Laboratoire d'Optique Atmosphérique, Université des Sciences et Technologies de Lille, Lille, France

(Manuscript received 5 March 1999, in final form 3 June 1999)

ABSTRACT

The next generation of earth radiation budget satellite instruments will routinely merge estimates of global top-of-atmosphere radiative fluxes with cloud properties. This information will offer many new opportunities for validating radiative transfer models and cloud parameterizations in climate models. In this study, five months of Polarization and Directionality of the Earth's Reflectances 670-nm radiance measurements are considered in order to examine how satellite cloud property retrievals can be used to define empirical angular distribution models (ADMs) for estimating top-of-atmosphere albedo. ADMs are defined for 19 scene types defined by satellite retrievals of cloud fraction and cloud optical depth. Two approaches are used to define the ADM scene types. The first assumes there are no biases in the retrieved cloud properties and defines ADMs for fixed discrete intervals of cloud fraction and cloud optical depth (fixed-τ approach). The second approach involves the same cloud fraction intervals, but uses *percentile* intervals of cloud optical depth instead (percentile-τ approach). Albedos generated using these methods are compared with albedos inferred directly from the mean observed reflectance field.

Albedos based on ADMs that assume cloud properties are unbiased (fixed-τ approach) show a strong systematic dependence on viewing geometry. This dependence becomes more pronounced with increasing solar zenith angle, reaching $\approx$12% (relative) between near-nadir and oblique viewing zenith angles for solar zenith angles between 60° and 70°. The cause for this bias is shown to be due to biases in the cloud optical depth retrievals. In contrast, albedos based on ADMs built using *percentile* intervals of cloud optical depth (percentile-τ approach) show very little viewing zenith angle dependence and are in good agreement with albedos obtained by direct integration of the mean observed reflectance field (<1% relative error). When the ADMs are applied separately to populations consisting of only liquid water and ice clouds, significant biases in albedo with viewing geometry are observed (particularly at low sun elevations), highlighting the need to account for cloud phase both in cloud optical depth retrievals and in defining ADM scene types. ADM-derived monthly mean albedos determined for all 5° × 5° lat–long regions over ocean are in good agreement (regional rms relative errors <2%) with those obtained by direct integration when ADM albedos inferred from specific angular bins are averaged together. Albedos inferred from near-nadir and oblique viewing zenith angles are the least accurate, with regional rms errors reaching ~5%–10% (relative). Compared to an earlier study involving Earth Radiation Budget Experiment ADMs, regional mean albedos based on the 19 scene types considered here show a factor-of-4 reduction in bias error and a factor-of-3 reduction in rms error.

1. Introduction

One of the major weaknesses in current climate models is the manner in which clouds are represented (Cess et al. 1990). Current models have difficulty simulating even the gross zonal mean seasonal changes in cloud radiative forcing, and uncertainties on a regional scale are even larger (Hartmann et al. 1986; Kiehl et al. 1994; Chen and Roeckner 1996). Since clouds have a dominant influence on the geographic and temporal distribution of the earth radiation budget, global observations of top-of-atmosphere fluxes coincident with cloud properties are needed to provide the information necessary to improve climate models. The Earth Radiation Budget Experiment (ERBE) (Barkstrom 1984) and the Scanner for Radiation Budget (Kandel et al. 1998) provided the most accurate top-of-atmosphere radiation budget measurements to date but did not provide details on the physical cloud properties. The International Satellite Cloud Climatology Project (ISCCP) (Rossow and Schiffer 1991) and First ISCCP Regional Experiment (Cox

Corresponding author address: Dr. Norman G. Loeb, Mail Stop 420, NASA Langley Research Center, Hampton, VA 23681-0001. E-mail: n.g.loeb@larc.nasa.gov

et al. 1987) provided valuable new datasets of cloud properties over different temporal and spatial scales but did not provide routine top-of-atmosphere radiation budget measurements. The next generation of satellite instruments such as Clouds and the Earth's Radiant Energy System (CERES), Polarization and Directionality of the Earth's Reflectances (POLDER), Multi-angle Imaging Spectroradiometer, and Geostationary Earth Radiation Budget will routinely merge top-of-atmosphere radiative fluxes with cloud properties, thereby providing comprehensive global datasets for climate model studies. Improved estimates of albedo, together with coincident cloud retrievals, will provide critical information needed to validate climate models and improve cloud parameterizations.

One of the largest sources of uncertainty in estimating planetary radiation budget from narrow field-of-view satellite instruments is the conversion of measured radiances to fluxes (Wielicki et al. 1995). The problem dates back to some of the earliest satellite measurements (House et al. 1986) and continues to be a major area of concern. Because satellite radiometers can only instantaneously measure radiances in a limited number of viewing directions—while albedo or flux requires radiances from all angles—assumptions are needed to account for the anisotropy (or angular variation) in the radiance field. ERBE used a set of 12 angular distribution models (ADMs) to convert the ERBE measured radiances to top-of-atmosphere (TOA) fluxes (Smith et al. 1986; Suttles et al. 1988). The ERBE ADMs were constructed using *Nimbus-7* earth radiation budget (ERB) scanner data and were applied to ERBE radiance measurements on *NOAA-9, -10,* and the *Earth Radiation Budget Satellite* (*ERBS*) using scene identification based on the maximum likelihood estimation method (Wielicki and Green 1989). To construct the ERBE ADMs, the sorting into angular bins (SAB) method was used (Taylor and Stowe 1984). Postflight analyses have revealed some problems with ERBE radiative fluxes. Payette (1989) and Suttles et al. (1992) have shown that estimated shortwave fluxes increase systematically with viewing zenith angle and estimated longwave fluxes decrease with viewing zenith angle. The cause for such biases is believed to be due either to the methodology used in deriving ERBE ADMs (Suttles et al. 1992; Green and Hinton 1996) and/or to errors in scene identification (Ye and Coakley 1996; Smith and Manalo-Smith 1995).

Large errors in ADM derived albedos can also occur if the scene category an ADM is defined for is too general or encompasses too wide a range of surface types (i.e., if the ADM variance is large) (Green and Hinton 1996). One method of reducing such errors is to increase the number of scene types or classes the ADMs are defined for (Wielicki et al. 1996). Since the anisotropy of earth scenes depends on their physical and optical properties (e.g., cloud fraction, cloud optical depth, etc.), a logical approach is to define ADM scene types from satellite-derived cloud retrievals. However, as pointed out by Loeb and Davies (1996) and Loeb and Coakley (1998), satellite retrievals (particularly cloud optical depths based on 1D theory) can suffer from large systematic biases that depend on viewing geometry. Such biases are shown here to be of major importance for TOA albedo estimation based on the ADM approach.

In the following, three months of POLDER measurements are used to construct ADMs at a wavelength of 670 nm for scene types defined by satellite retrievals of cloud fraction and cloud optical depth. Two approaches are considered in building the ADMs. The first assumes there are no biases in the cloud property retrievals and defines ADMs for 19 scene types stratified by fixed discrete intervals of cloud fraction and cloud optical depth. The second, more general, approach uses the same cloud fraction intervals but allows for potential biases in the cloud optical depth retrievals by defining ADM scene types for *percentile* intervals of cloud optical depth in each angular bin rather than fixed intervals of cloud optical depth. Albedos estimated from the two sets of ADMs are compared with mean albedos inferred by direct integration of mean reflectances using two independent months of POLDER data.

2. Observations

The POLDER instrument flew on the *Advanced Earth Observation Satellite* (*ADEOS*) between August 1996 and June 1997. POLDER is a camera composed of a two-dimensional charged coupled device detector array, wide field-of-view telecentric optics, and a rotating wheel carrying spectral and polarized filters. POLDER is in a sun-synchronous orbit with an equatorial crossing time of 1030 LT, has a swath width of approximately 2200 km, and a pixel size of about 6×7 km^2 at nadir. As the satellite moves over a region, up to 14 different images are acquired in each spectral band from various geometric configurations. Figure 1 provides an example of the angular sampling typical of POLDER. It shows the viewing zenith and relative azimuth angle coverage within the region defined by a latitude of $0° \pm 0.5°$ and a longitude of $0° \pm 0.5°$ for seven days in November 1996. Each day, the region is sampled from a different set of viewing directions, so that full azimuth and viewing zenith (up to $\approx 60°$) angle coverage is obtained by compositing measurements over time. POLDER spectral bands are shown in Table 1. Note that only channels with the wider dynamic range are used in the POLDER level-2 ERB and clouds product (Buriez et al. 1997) considered in this study. POLDER calibration uncertainty is estimated to be $<3\%–4\%$ (Hagolle et al. 1999). A more detailed description of the POLDER instrument is provided by Deschamps et al. (1994).

In this study, five months (November 1996; January, April, May, and June 1997) of POLDER level-2 ERB and clouds product data (Buriez et al. 1997) over ocean

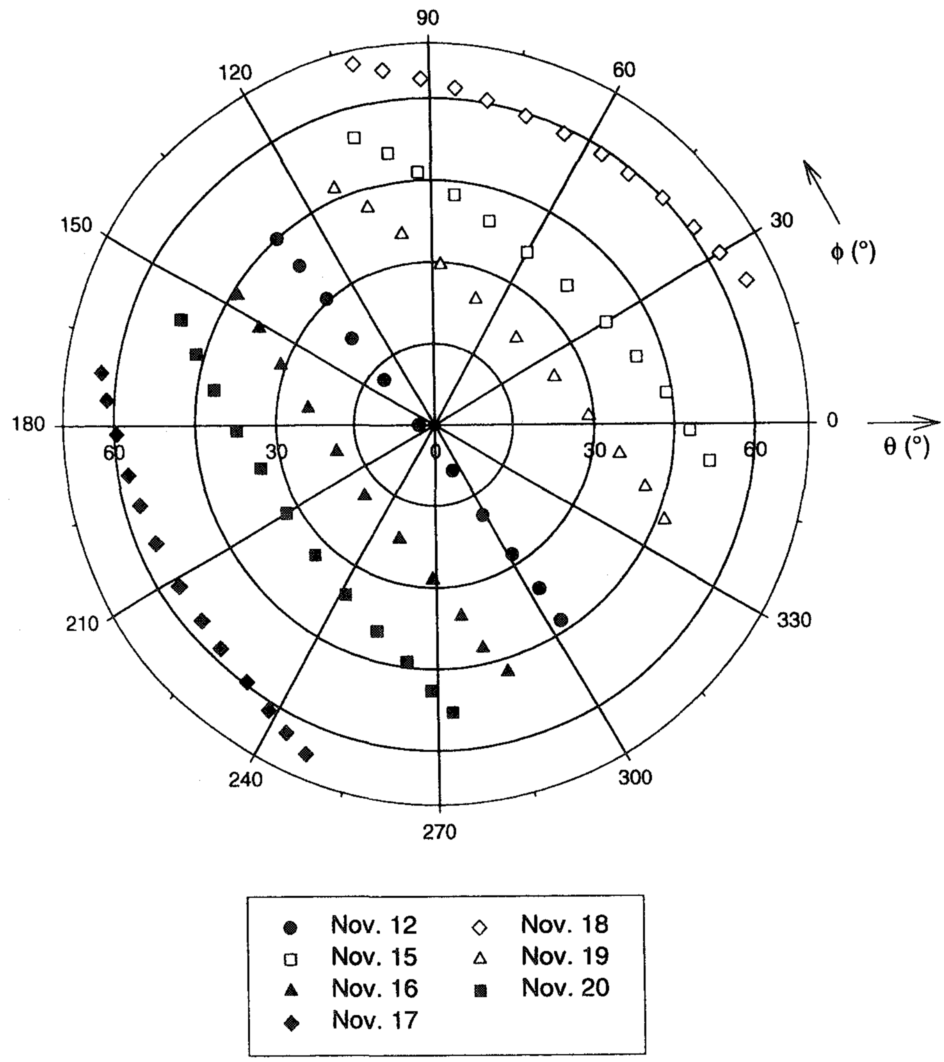

FIG. 1. Angular sampling typical of POLDER. Each set of points (i.e., on a given day) corresponds to viewing zenith and azimuthal angles for near-simultaneous measurements over a region defined by a lat of 0° ± 0.5° and a long of 0° ± 0.5° (Nov 1996). Each day, the region is sampled from a different set of viewing directions, so that full azimuth and viewing zenith (up to ≈60°) angle coverage is obtained by compositing measurements over time.

TABLE 1. Characteristics of the spectral bands of the POLDER instrument. Dynamic range is the range in equivalent reflectance [$=\pi^* I/F$; I = radiance (W m^{-2} sr^{-1} μm^{-1}); F = solar irradiance (W m^{-2} μm^{-1})] that POLDER channels are sensitive to.

Central wavelength (nm)	Bandwidth (nm)	Polarization	Dynamic range
443	20	No	0–0.22
443	20	Yes	0–1.10
490	20	No	0–0.17
565	20	No	0–0.11
670	20	Yes	0–1.10
763	10	No	0–1.10
765	40	No	0–1.10
865	40	Yes	0–1.10
910	20	No	0–1.10

between 60°S and 60°N are considered. Briefly, the level-2 ERB and clouds product provides cloud properties (cloud fraction, cloud phase, cloud optical depth, apparent pressure, etc.) and radiances in all viewing directions over ≈56 × 56 km² "super-pixel" regions (≈9 × 9 full-resolution 6 × 7 km² POLDER pixels). Cloud fractions are determined by applying a cloud detection algorithm to each full-resolution POLDER pixel and direction. The cloud detection scheme consists of a sequence of threshold tests on a pixel's apparent pressure, reflectance (865 nm over ocean, 443 nm over land), 443- and 865-nm polarized radiance, and the ratio of 865- and 443-nm channel reflectances (Parol et al. 1999). Cloud phase is determined using polarized reflectance at 865 nm (Parol et al. 1999). The algorithm takes advantage of the differences in polarized reflectance between liquid water and ice clouds in different scattering angle ranges. For example, (i) polarized reflectance from liquid water clouds increases with scattering angle (Θ) for $60° < \Theta < 140°$, while the opposite is true for ice clouds; (ii) for $135° < \Theta < 145°$, the polarized reflectance from liquid water clouds shows a distinct peak (primary rainbow) that is not apparent for ice clouds; and (iii) for $140° < \Theta < 180°$, the magnitude of polarized reflectance is typically larger for liquid water clouds than for ice clouds. Cloud optical depth is estimated for each full-resolution POLDER pixel and direction flagged as cloud-contaminated using a look-up table approach based on plane-parallel theory. In the current version of the POLDER level-2 product, the cloud layer is assumed to be composed of liquid water droplets with an effective radius of 10 μm and an effective variance of 0.15 (Hansen and Travis 1974). Future versions of the POLDER algorithm will improve the treatment of ice clouds by using more realistic phase functions based on representative ice particle shapes (Parol et al. 1999). The full-resolution cloud optical depth retrievals in each viewing direction are converted into equivalent 1D spherical albedos, which are averaged spatially over the super-pixel. An energy-equivalent cloud optical depth in each viewing direction is inferred from the super-pixel cloud spherical albedos following the approach of Rossow et al. (1996) (Parol et al. 1999).

3. Methodology

a. Albedo estimation from POLDER reflectances

The fact that POLDER measurements are restricted to viewing zenith angles less than ≈60° requires a slightly different approach for defining ADMs than the conventional approach of Taylor and Stowe (1984). Here, an empirical "partial" ADM ($R_{p,j}$) is first defined for a given scene type from the following:

$$R_{p,j}(\theta_o, \theta, \phi) = \frac{\overline{r}_j(\theta_o, \theta, \phi)}{\overline{A}_{p,j}(\theta_o)}, \tag{1}$$

where $\overline{r}_j$ and $\overline{A}_{p,j}$ are the mean reflectance and partial albedo for scene type "j" given by

$$\overline{r}_j(\theta_o, \theta, \phi) = \left\langle \frac{\pi I_j(\theta_o, \theta, \phi)}{\cos(\theta_o) E_o} \right\rangle \tag{2}$$

$$\overline{A}_{p,j}(\theta_o) = \int_0^{2\pi} \int_{\mu_m}^{1} \overline{r}_j \mu \, d\mu \, d\phi \tag{3}$$

- I_j instantaneous radiance (W m^{-2} sr^{-1} μm^{-1}),
- E_o solar irradiance (W m^{-2} μm^{-1}) corrected for Earth–Sun distance,
- θ viewing zenith angle,
- θ_o solar zenith angle,
- ϕ azimuth angle relative to the solar plane defined between 0° and 180° (ϕ = 0° corresponds to forward scattering),
- μ cosine of viewing zenith angle.

In Eq. (3), $\mu_m = \cos\theta_m$, where θ_m is the maximum viewing zenith angle where observations are consistently obtained. A value of 55° for θ_m is used since this corresponds to the midpoint of the most oblique angular bin. Bin mean reflectances are determined over 10° solar and viewing zenith angle bins, and over relative azimuth angle bins of width 20° between ϕ = 10° and ϕ = 170°, and 10° elsewhere (see Table 2). The integral in Eq. (3) is evaluated using Gaussian quadrature by interpolating $\overline{r}_j$ to Gauss–Legendre abscissas (200 quadrature points are considered).

TABLE 2. Angular bin definitions (°).

Solar zenith angle (θ_o)	Viewing zenith angle (θ)	Relative azimuth (ϕ)
0–10	0–10	0–10
10–20	10–20	10–30
20–30	20–30	30–50
30–40	30–40	50–70
40–50	40–50	70–90
50–60	50–60	90–110
60–70		110–130
70–80		130–150
80–90		150–170
		170–180

An instantaneous reflectance measurement [$r_j(\theta_o, \theta, \phi)$] is converted to a partial albedo [$\hat{A}_p(\theta_o, \theta, \phi)$] by first identifying the appropriate ADM scene type and applying the partial ADM as follows:

$$\hat{A}_p(\theta_o, \theta, \phi) = \frac{r_j(\theta_o, \theta, \phi)}{R_{p,j}(\theta_o, \theta, \phi)}. \tag{4}$$

Next, the albedo over the entire upward hemisphere or "full" albedo [$\hat{A}(\theta_o, \theta, \phi)$] is estimated from $\hat{A}_p(\theta_o, \theta, \phi)$ using a theoretical conversion. Figures 2a–c show theoretical full against partial albedos for three solar zenith angles at a wavelength of 670 nm. The curves were inferred from three sources: (i) clear-sky values were based on MODTRAN (Kneizys et al. 1996) calculations modified to account for ocean bidirectional reflectance according to the Cox and Munk (1954) formulation; (ii) 1D liquid and ice cloud [using the measured ice phase function of Sassen and Liou (1979)] values are based on DISORT (Stamnes et al. 1988) calculations for cloud optical depths ranging between 0.5 and 200; and (iii) 3D cloud values are based on Monte Carlo simulations (no atmospheric scattering) for 16 broken and overcast stochastic cloud fields with bumpy tops (Várnai 1996; Loeb et al. 1998). Cloud fractions ranged from 0.25 to 1.0, and averaged cloud optical depths were between 5 and 160 (see Table 3). As shown in Figs. 2a–c, a very simple relationship between partial and full albedo is obtained, even for horizontally inhomogeneous cloud fields. To infer $\hat{A}$ from $\hat{A}_p$, fits to the curves in Figs. 2a–c are applied. These have the form:

$$\hat{A}(\theta_o, \theta, \phi) = \sum_{i=0}^{3} a_i(\theta_o) \hat{A}_p^i(\theta_o, \theta, \phi), \tag{5}$$

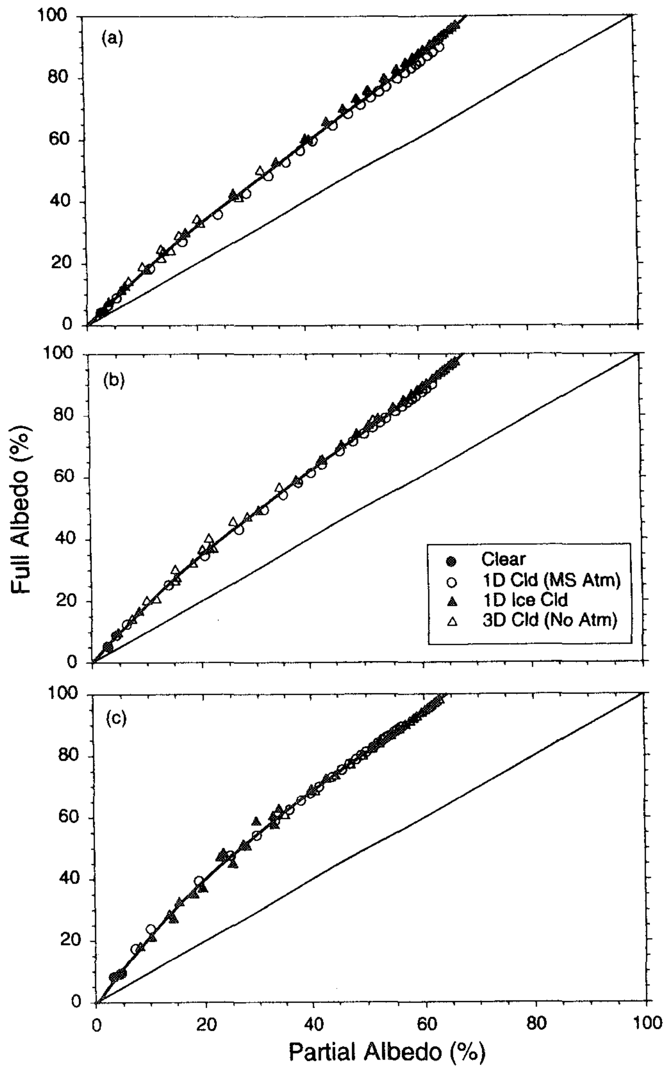

FIG. 2. Full and partial albedos (%) from theory for clear and cloudy conditions at (a) $\theta_o = 25°$; (b) $\theta_o = 45°$, and (c) $\theta_o = 65°$. Curve is a third-order polynomial fit to all points.

where a_i's are coefficients of a third-order polynomial. For the cloud fields considered in Figs. 2a–c, root-mean-square (rms) errors based on these fits are less than ~1%.

b. ADM scene types

The purpose of defining ADMs by scene type is to better account for the variability in the anisotropy of earth scenes. Since earth scenes have distinct anisotropic characteristics that depend on their physical and optical properties (e.g., thin vs thick clouds, cloud-free, broken, overcast, etc.), it seems reasonable to define ADM scene types from scene parameters that have the greatest influence on anisotropy. To illustrate, Figs. 3a–b show ADMs constructed from POLDER measurements for overcast scenes with cloud optical depth (τ) < 2.5 (Fig. 3a) and τ = 18–40 (Fig. 3b). The ADMs were determined by replacing the denominator in Eq. (1) with mean albedos obtained by averaging instantaneous full

TABLE 3. Cloud fractions and cloud optical depths of cloud fields used in Monte Carlo model simulations considered in Figs. 2a–c.

Cloud fraction	Cloud optical depth			
0.25	20	40	80	160
0.50	10	20	40	80
0.75	6.7	13.3	26.7	53.3
1.00	5	10	20	40

albedos inferred from Eqs. (4)–(5). Differences between the two ADMs are as large as a factor of 2 close to nadir but decrease with increasing viewing zenith angle.

In order to define ADM scene types based on cloud optical properties, an obvious approach is to use satellite retrievals of these parameters (e.g., cloud fraction, cloud optical depth, etc.). However, since ADMs are constructed by compositing radiances from many scenes measured in different satellite viewing geometries, this approach assumes that scene identification is consistent with angle. That is, it assumes that a given scene type (e.g., defined for a given cloud property interval) identified from one satellite viewing geometry can be consistently identified from all other directions. Since satellite-based retrievals often rely on simplified radiative transfer models (e.g., plane-parallel theory) that use idealized cloud microphysics (e.g., particle shape and phase), this poses a potential problem. Loeb and Davies (1996) and Loeb and Coakley (1998) showed that cloud optical depth retrievals based on 1D theory show a systematic dependence on solar zenith and viewing zenith angle, even for overcast marine stratiform clouds—arguably the closest to plane-parallel in nature. Mishchenko et al. (1996) demonstrated theoretically how incorrect assumptions on cloud particle shape and phase can result in large angle-dependent errors in retrieved cloud optical depths. Figures 4a–b show mean cloud optical depth retrievals against solar zenith and viewing zenith angle (azimuthally averaged) from two months (January and May 1997) of POLDER measurements for all overcast clouds (Fig. 4a) and for overcast clouds composed only of liquid water droplets as determined by the POLDER cloud phase algorithm (Fig. 4b). As shown, a systematic dependence in retrieved cloud optical depth on viewing zenith angle is observed in both cases for solar zenith angles >50°, in a manner consistent with the earlier studies.

The question arises as to whether such biases in cloud optical depth retrievals introduce similar biases in ADM derived albedos. To answer this question, two approaches (described below) are considered in constructing partial ADMs for 19 scene classes based on POLDER angle-dependent cloud fraction and cloud optical depth retrievals. Both sets of ADMs assume the same six cloud fraction intervals (Table 4) but employ a different cloud optical depth stratification. To construct the partial ADMs, three months of POLDER observations (November 1996, April and June 1997) are considered.

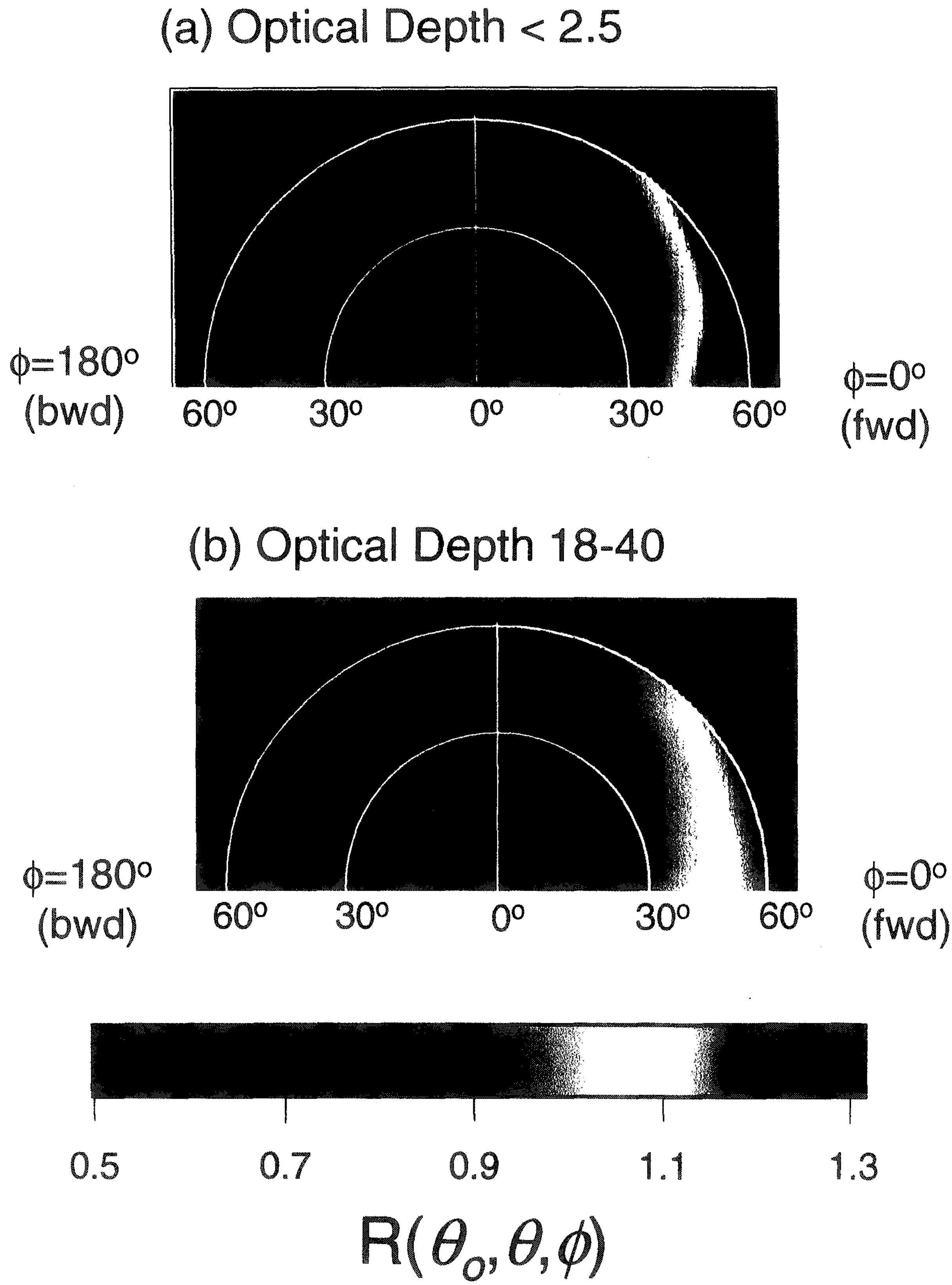

FIG. 3. Overcast ADMs [$R(\theta_o, \theta, \phi)$] from POLDER 670-nm reflectance measurements for θ_o = 60°–70°. (a) $\tau < 2.5$ and (b) τ = 18–40.

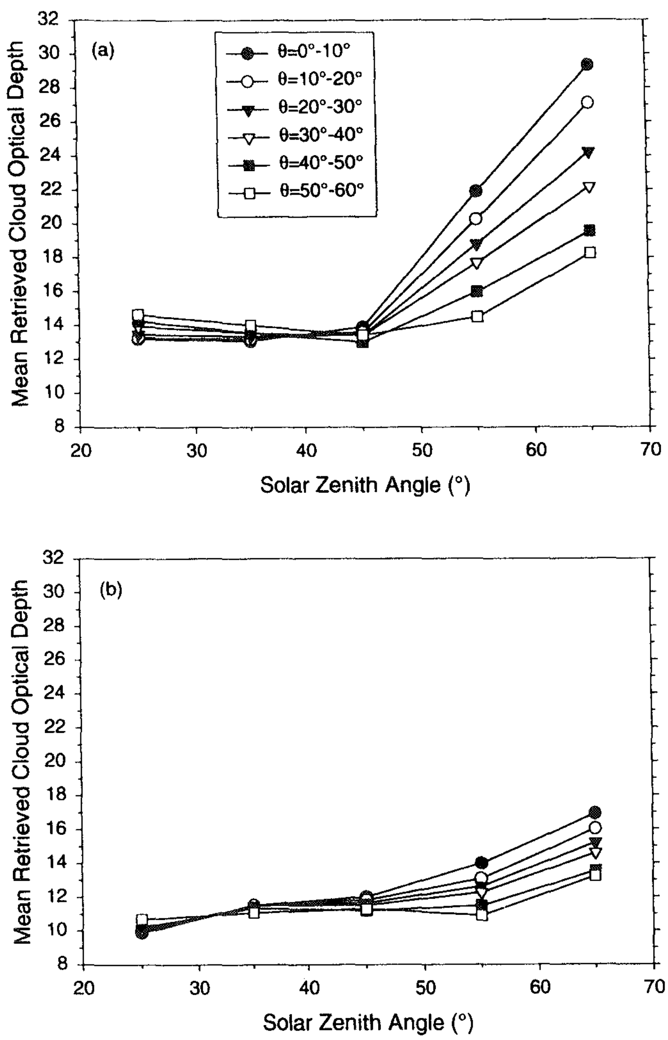

FIG. 4. Mean retrieved cloud optical depth inferred from two months (Jan and May 1997) of POLDER measurements for overcast scenes against solar zenith and viewing zenith angle (azimuthally averaged) for (a) all clouds and (b) clouds composed only of liquid water droplets as determined by the POLDER cloud phase algorithm.

1) PARTIAL ADMs BASED ON FIXED ABSOLUTE INTERVALS OF CLOUD OPTICAL DEPTH

Assuming cloud optical depth retrievals are perfect in all viewing geometries, each of the six cloud fraction intervals in Table 4 can be stratified into fixed discrete intervals of cloud optical depth. Note that the number of cloud optical depth intervals in Table 4 increases with cloud fraction. The reason is because cloud optical depth distributions have a tendency to broaden with increasing cloud cover, so that more intervals are needed to cover the full range of cloud optical depth at larger cloud fractions. A similar broadening in cloud optical depth distributions with cloud cover was also observed by Barker et al. (1996). For each cloud fraction–cloud optical depth interval, a partial ADM is determined by compositing the POLDER 670-nm reflectances in each angular bin and calculating the partial ADM using the approach described in section 3a. In order to reduce sampling bias errors due to temporal and spatial autocorrelation between pixel measurements, the month mean reflectance values in each angular bin are calculated from daily mean reflectances, which are assumed independent. Hereafter, this approach is referred to as the fixed-τ approach.

TABLE 4. Cloud fraction and cloud optical depth intervals defining ADM scene types.

Cloud fraction interval (%)	Cloud optical depth fixed interval	Cloud optical depth percentile interval	Total
0–1	All	0–100	1
1–25	0–1.5	0–50	2
	>1.5	50–100	
25–50	0–1.5	0–50	2
	>1.5	50–100	
50–75	0–1	0.0–33.3	3
	1–2.5	33.3–66.6	
	>2.5	66.6–100	
75–99	0–1	0.0–20	5
	1–2	20–40	
	2–3	40–60	
	3–5	60–80	
	>5	80–100	
99–100	0–2.5	0–5	6
	2.5–6	5–25	
	6–10	25–50	
	10–18	50–75	
	18–40	75–95	
	>40	95–100	

2) PARTIAL ADMs BASED ON FIXED PERCENTILE INTERVALS OF CLOUD OPTICAL DEPTH

An alternate, more general, approach is to define ADM scene types using *percentile* intervals of cloud optical depth rather than fixed discrete intervals of cloud optical depth [as in section 3b(1)]. The aim is to define ADM scene types that can be identified consistently from all angles, regardless of whether cloud optical depth retrievals show biases with viewing geometry. As an example, an ADM scene type for the thinnest 5% of all overcast scenes can be defined by compositing scenes in each angular bin with a retrieved cloud optical depth that lies below a predetermined (angle-dependent) threshold that corresponds to the 5th percentile of cloud optical depth. Predetermined cloud optical depth thresholds (corresponding to a given cloud optical depth percentile) are inferred from frequency distributions of cloud optical depth from a large ensemble of measurements. Separate cloud optical depth thresholds are defined for each angular bin. Consequently, scenes corresponding to a given cloud optical depth percentile interval range (e.g., thinnest 5% of the population) are grouped consistently in all angles. It is worth noting that while the percentile-τ approach attempts to reduce the effect of scene identification errors on albedo, it does not reduce biases in the cloud property retrievals themselves. Such a correction would require a reassessment of the cloud retrieval scheme. Hereafter, this approach is referred to as the percentile-τ approach.

Scene types for partial ADMs based on the percentile-τ approach are provided in Table 4. Note that the same cloud fraction intervals used in defining fixed-τ ADMs are also used for the percentile-τ ADMs.

c. *Mean ADM albedo validation using direct integration method*

ADMs provide instantaneous fluxes or albedos at the time of the satellite overpass. Instantaneous fluxes are needed together with narrowband measurements from geostationary satellites to estimate diurnal means, which are used to estimate monthly mean fluxes (Young et al. 1998). One method of validating ADMs is to separate ADM errors from diurnal modeling errors by ignoring diurnal effects. ADM albedo averages determined from a large ensemble of measurements (e.g., one or several months) are compared with mean albedos determined by direct integration of the mean reflectances. The mean ADM albedos are inferred from instantaneous ADM albedo estimates and are stratified by solar zenith, viewing zenith, and relative azimuth angle bins. A direct integration mean albedo (for a given solar zenith angle bin) is computed by compositing all reflectances (regardless of scene type) into angular bins and directly integrating the mean reflectances [$\overline{r}(\theta_o, \theta, \phi)$]. Since the same data are used in both cases, and since no diurnal effects are involved, differences between the ADM and direct integration mean albedos are due to ADM errors.

Unfortunately, since viewing zenith angles >60° are not consistently available from POLDER, it is only possible to use direct integration to determine mean *partial* albedos ($\overline{A}_p^D(\theta_o)$). Since $\overline{A}_p^D(\theta_o)$ is determined using all scenes (so that no scene identification errors are introduced), comparison between $\overline{A}_p^D(\theta_o)$ and the mean partial albedo based on partial ADMs [$\overline{\hat{A}}_p(\theta_o, \theta, \phi)$] provides an estimate of the error in $\overline{\hat{A}}_p(\theta_o, \theta, \phi)$. To estimate the uncertainty in the full ADM albedo [$\overline{\hat{A}}(\theta_o, \theta, \phi)$], an estimate of the full direct integration albedo [$\overline{A}^D(\theta_o)$] is needed. We estimate $\overline{A}^D(\theta_o)$ using the assumption that the relative error in the full *angle-average* ADM albedo is the same as that for the partial *angle-average* ADM albedo. That is, we assume

$$\frac{\overline{\hat{A}}(\theta_o) - \overline{A}^D(\theta_o)}{\overline{A}^D(\theta_o)} = \frac{\overline{\hat{A}}_p(\theta_o) - \overline{A}_p^D(\theta_o)}{\overline{A}_p^D(\theta_o)}, \tag{6}$$

where $\overline{\hat{A}}_p(\theta_o)$ and $\overline{\hat{A}}(\theta_o)$ are the partial and full angle-average ADM albedos obtained by averaging mean albedos from all available viewing zenith and relative azimuth angular bins (Table 2). An estimate of $\overline{A}^D(\theta_o)$ is obtained by rearranging the terms in Eq. (6) as follows:

$$\overline{A}^D(\theta_o) = \overline{A}_p^D(\theta_o)\frac{\overline{\hat{A}}(\theta_o)}{\overline{\hat{A}}_p(\theta_o)}. \tag{7}$$

The error in $\overline{\hat{A}}(\theta_o, \theta, \phi)$ is thus determined by comparison with $\overline{A}^D(\theta_o)$, assuming that $\overline{A}^D(\theta_o)$ represents the "true" mean albedo. Since $\overline{A}^D(\theta_o)$ is based on an assumption [Eq. (6)] that depends on a ratio between ADM derived albedos, there is some uncertainty in $\overline{A}^D(\theta_o)$. Sensitivity in $\overline{A}^D(\theta_o)$ to the ADM albedo ratio in Eq. (7) is estimated to be <0.25% (relative) based on comparisons between percentile-τ, fixed-τ, and Lambertian (i.e., no angular correction) ADMs. If the direct integration technique is applied using a subset of scenes (e.g., specific cloud fraction range), errors in scene identification can also occur since the true scene identification is not available.

4. Results

In some applications, such as the use of TOA albedos in conjunction with surface measurements, it is not always feasible to collect albedos for all scene types in all satellite-viewing geometries. Instead, it may be necessary to restrict the sampling to a small range of angles (e.g., near-nadir views). Therefore, a powerful check on the quality of the ADMs is to statistically test whether they provide consistent albedo estimates in all viewing geometries. Here, this criterion is used extensively to evaluate the performance of the fixed-τ and percentile-τ approaches.

In the following, mean albedos inferred using fixed-τ and percentile-τ ADMs are compared with albedos obtained by direct integration of mean reflectances. As noted earlier, the ADMs were constructed from three months of POLDER measurements (November 1996, April and June 1997). The ADMs are now applied to produce albedo estimates from two independent months (January and May 1997).

a. *Albedo and cloud property retrieval viewing zenith angle dependence*

To compare albedos obtained from fixed-τ and percentile-τ ADMs, it is useful to first restrict the analysis to overcast (cloud fraction > 0.99) scenes. Figures 5a–f show overcast mean albedos and mean cloud optical depth retrievals against viewing zenith angle for solar zenith angles between 20° and 30° (Figs. 5a,b), 40° and 50° (Figs. 5c,d), and 60° and 70° (Figs. 5e,f). Each mean ADM derived albedo in a given viewing zenith angle bin was determined by averaging mean albedos from 10 relative azimuth bins (Table 2), so that each relative azimuth bin contributes an equal weight to the overall mean.

As shown in Figs. 5a, 5c, and 5e, albedos obtained using the fixed-τ ADMs show a large dependence on viewing zenith angle. The viewing zenith angle dependence closely follows that in the mean cloud optical

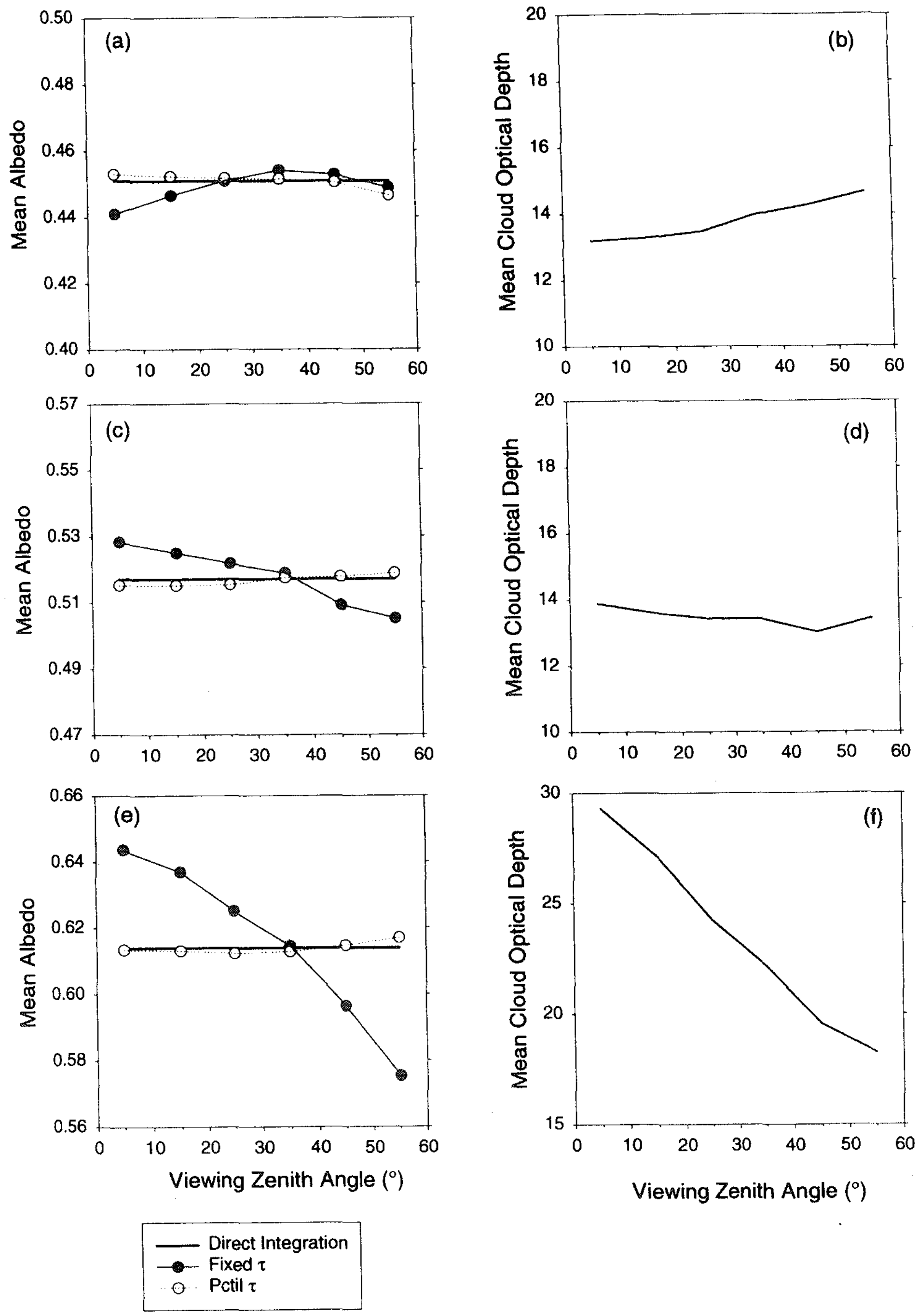

FIG. 5. (left) Mean albedos and (right) mean retrieved cloud optical depths against viewing zenith angle for θ_o between (a), (b) 20° and 30°; (c), (d) 40° and 50°; and (e), (f) 60° and 70°.

depth retrievals (Figs. 5b, 5d, and 5f) and becomes more pronounced with increasing solar zenith angle—fixed-τ albedos decrease by as much as $\approx$12% between near-nadir and oblique viewing zenith angles for θ_o = 60°–70°. In contrast, albedos based on the percentile-τ ADMs show very little dependence on viewing zenith angle and are in good agreement with albedos obtained by direct integration.

Figures 6a–f show similar results to those in Figs. 5a–f, but for all scenes. Also, mean cloud fraction retrievals are provided in Figs. 6b, 6d, and 6f instead of mean cloud optical depth. As shown, the viewing zenith angle dependence in mean cloud fraction retrievals is much smaller than that in mean cloud optical depth (Figs. 5b, 5d, and 5f). Because fixed absolute intervals of cloud fraction were used to define the ADM scene types, any viewing zenith angle dependence in albedo from the percentile-τ ADMs closely follows that in mean cloud fraction. In contrast, mean albedos based on the fixed-τ approach are influenced by viewing zenith angle biases in both cloud fraction and cloud optical depth (the latter being more pronounced in this case).

Since climate research requires an understanding of how albedo responds to changes in cloud properties,

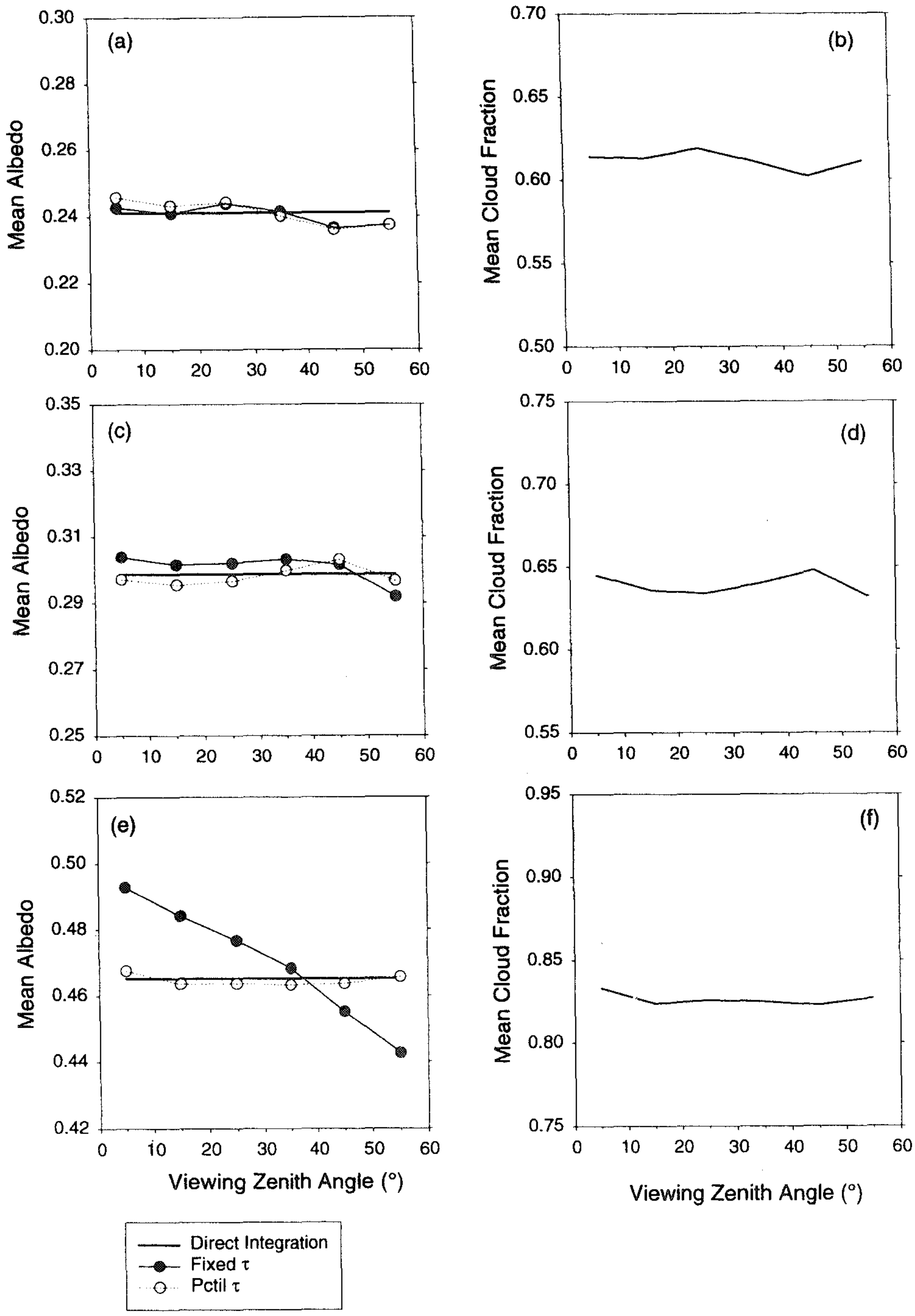

FIG. 6. (left) Mean albedos and (right) mean cloud fractions against viewing zenith angle for θ_o between (a), (b) 20° and 30°; (c), (d) 40° and 50°; and (e), (f) 60° and 70°.

satellite-based estimates of these parameters need to be consistently identified under a wide range of cloud and viewing conditions. Figures 7a–i compare the relationship between albedo and cloud fraction for different viewing zenith and solar zenith angle bins for the fixed-τ and percentile-τ approaches. Figures 7a–c show the direct integration albedo, which is assumed to represent the true albedo (i.e., errors in cloud fraction are assumed to be negligible), while the remaining curves provide relative errors in ADM derived albedos for different solar zenith angle ranges (relative error = $[(A_e - A)/A] \times 100\%$, where A_e is the estimate and A is "truth"). For the fixed-τ approach, relative errors in albedo are generally <2% for θ_o = 20°–30° (Fig. 7d) and show a weak dependence on cloud fraction. As solar zenith angle increases, the relative errors increase and show a stronger dependence on cloud fraction. For θ_o = 40°–50° (Fig. 7e), relative errors are generally negative at all viewing zenith angles for cloud fractions <0.25 (reaching −6%) and positive for cloud fractions >0.50 (reaching 5%). At lower sun (θ_o = 60°–70°), relative errors increase further (reaching ±6%–7% for cloud

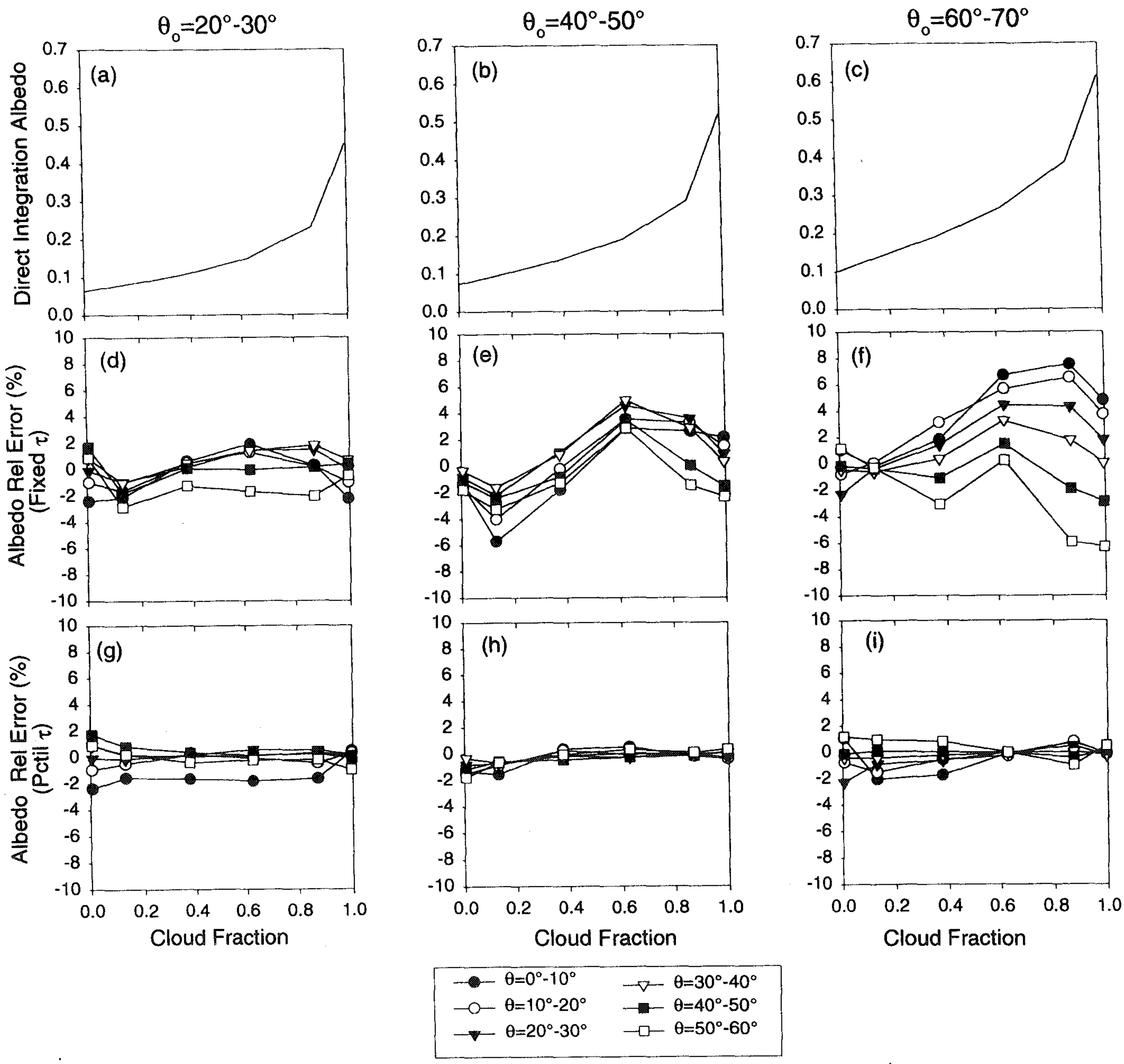

FIG. 7. (a)–(c) Direct integration mean albedo against cloud fraction; relative error in (d)–(f) fixed-τ and (g)–(i) percentile-τ ADM albedos against cloud fraction for various solar zenith and viewing zenith angle ranges.

fractions between 75% and 99%) and show a larger dependence on viewing zenith angle (Fig. 7f). Results are much more encouraging for the percentile-τ approach—relative errors are generally <2% for all solar zenith angles observed by POLDER over the full cloud fraction range.

b. *Albedo errors due to neglect of cloud phase*

Given that the ADMs in this study are defined only in terms of cloud fraction and cloud optical depth, the question arises as to whether other cloud parameters are likely to have a significant influence on cloud anisotropy and albedo. Based on several studies (Minnis et al. 1993; Mishchenko et al. 1996; Descloitres et al. 1998), an obvious candidate is cloud phase. To examine the importance of cloud phase on albedo estimation, the ADMs defined in section 3 were applied separately to overcast scenes for all conditions, clouds composed only of liquid water droplets, clouds containing both liquid droplets and ice particles ("mixed-phase" clouds), and clouds containing only ice particles. Figures 8a–p show the viewing zenith angle and relative azimuth angle dependence in cloud optical depth and albedo for each of these cases in two solar zenith angle bins (θ_o = 30°–40° and θ_o = 60°–70°) for the percentile-τ approach, and Tables 5–7 provide the overall means and standard deviations determined from individual angular bin means (i.e., 6

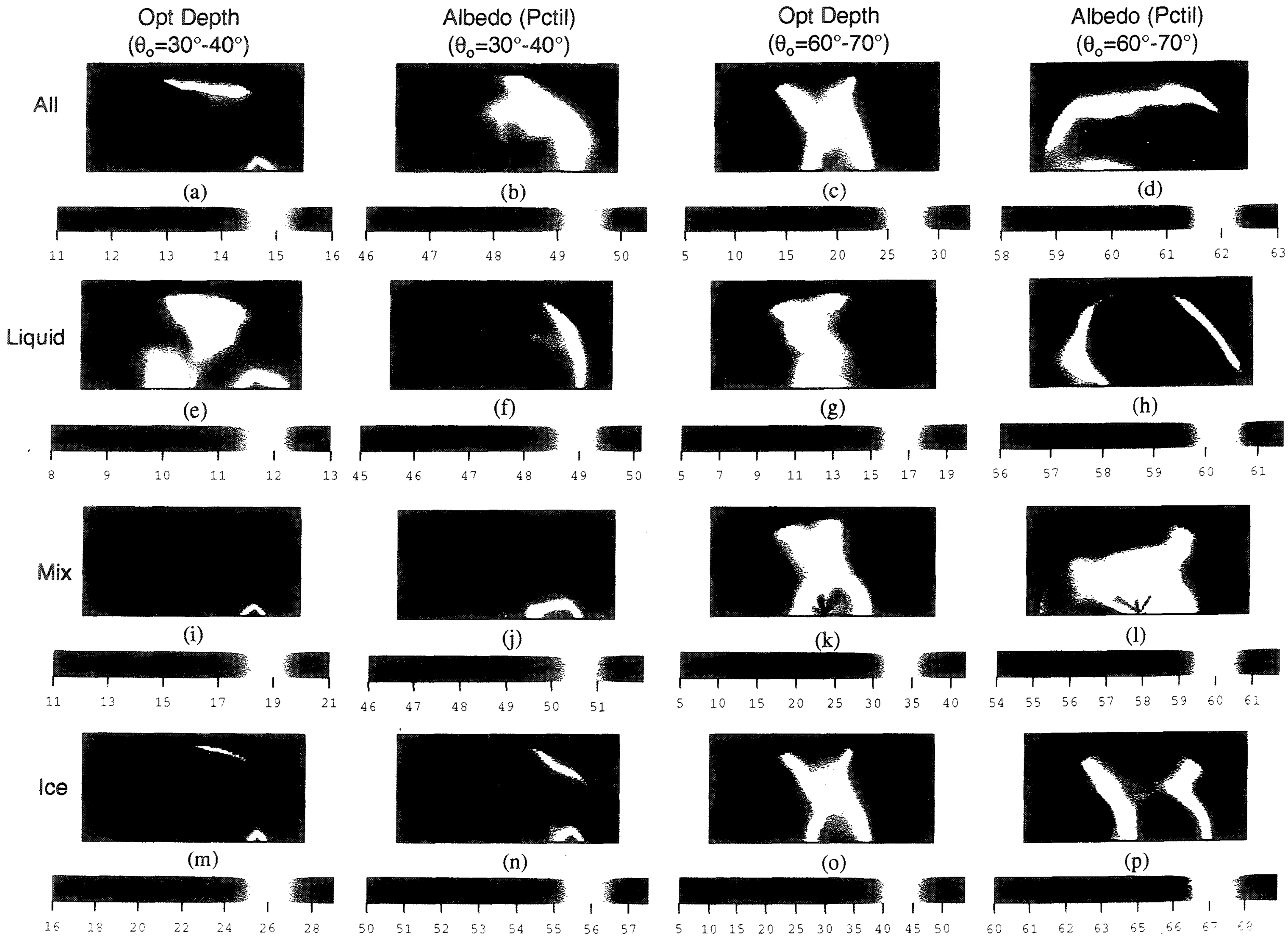

FIG. 8. (a)–(p) Mean cloud optical depth and mean albedo (%) based on the percentile-τ ADMs for overcast scenes consisting of all cloud conditions, liquid, mixed-phase, and ice-phase, for θ_o = 30°–40° and θ_o = 60°–70°. The bidirectional plots use the same angle convention as that shown in Figs. 3a,b.

TABLE 5. Cloud optical depth mean and std dev (in parentheses) inferred from means in individual viewing zenith and relative azimuth angle bins.

θ_o	All	Water	Mix	Ice
20°–30°	13.8 (1.5)	10.1 (0.9)	13.7 (1.2)	21.6 (3.7)
30°–40°	13.5 (0.8)	11.4 (0.5)	14.7 (1.2)	20.2 (2.6)
40°–50°	13.5 (1.0)	11.6 (0.6)	15.6 (1.7)	19.9 (3.3)
50°–60°	18.2 (3.5)	12.4 (1.5)	20.7 (4.1)	26.3 (6.8)
60°–70°	23.4 (6.1)	14.9 (2.3)	29.5 (7.9)	35.1 (12.4)

viewing zenith angle × 10 relative azimuth angle bins). For θ_o = 30°–40°, the most persistent feature in both the cloud optical depth and albedo results is the peak between θ = 30° and θ = 40° in the forward scattering direction. This feature likely corresponds to sun glint, perhaps due to ambiguities in ocean surface correction in the presence of thin clouds, or possibly due to clear-sky breaks in the POLDER full-resolution pixels. At other angles, the percentile-τ albedo estimates appear reasonable (the overall albedo standard deviation in Table 6 is ≤0.01). There does appear to be a slight dependence on relative azimuth angle; however, slightly lower albedos occur in the backscattering direction, a trend that is more pronounced (relative difference between forward and backscattering albedos of ≈5%) when only ice clouds are considered (Fig. 8m).

For θ_o = 60°–70°, the influence of cloud phase is much stronger. In all cases, a significant decrease in mean cloud optical depth with viewing zenith angle occurs in the forward scattering direction. For liquid water clouds, this decrease is more than a factor of 2 (from 17 close to nadir to 8 between θ = 50° and θ = 60°). In the backscattering direction, optical depths show a much smaller change (≈10%). These results are consistent with those reported by Loeb and Coakley (1998). In that study, cloud optical depths for moderate solar zenith angles decreased from 14 to 8 in the forward scattering direction, while there was very little variation with viewing zenith angle in the backscattering direction. Loeb et al. (1998) were able to reproduce this behavior in Monte Carlo simulations when variations in cloud-top structure ("cloud bumps") were included.

For mixed-phase and ice clouds, a sharp decrease in cloud optical depth with viewing zenith angle occurs in the forward and backscattering directions. Mean cloud optical depths are 3 times larger than those from liquid water clouds at nadir and at relative azimuth angles between ≈70° and 110°, whereas optical depths in the forward scattering direction (ϕ = 0°–30°) are similar for liquid water and ice clouds. These findings are qualitatively consistent with simulations by Mishchenko et al. (1996), who showed that reflectances from liquid water clouds tend to be lower than those from ice clouds close to nadir and at side-scattering angles, while the opposite is true at oblique viewing zenith angles in the forward and backscattering directions. Such differences would cause retrieved cloud optical depths (i.e., using a liquid water cloud model) to show a pattern similar to that in Fig. 8p.

For θ_o = 60°–70°, albedos inferred from the percentile-τ ADMs show little dependence on viewing geometry when applied to all overcast clouds (Fig. 8d). In contrast, significant biases occur when albedos are stratified by cloud phase. Interestingly, while the overall bidirectional patterns in mean albedo for liquid water (Fig. 8h) and ice clouds (Fig. 8e) are qualitatively similar, the relative position of albedo minima and maxima for these two cases is interchanged. This suggests that significant cancellation of error must occur when all cloud types are combined (Fig. 8d). Standard deviations in albedo are largest for ice clouds (~0.019) and smallest when the ADMs are applied to all clouds (0.006; Table 6). By comparison, when the fixed-τ ADMs are used (Table 7), standard deviations are ≈0.044 for ice clouds and ≈0.032 for all clouds.

It is clear from these results that there is a need to account for cloud phase both in cloud optical depth retrievals and in defining ADM scene types. Stratifying by cloud phase and defining ADMs using the percentile-τ approach appear to be the most promising means of reducing albedo errors.

c. *Regional monthly mean albedos*

Monthly mean albedos were determined for all 5° × 5° lat–long regions over ocean between 60°S and 60°N for different solar zenith and viewing zenith angle ranges. The regional monthly albedos are not true monthly averages because no diurnal effects have been considered. Instead, the averages were determined from all monthly samples falling in each angular bin at the time of observation. For each region, ADM derived albedos were compared with albedos determined by direct integration. Figures 9a–d provide bias and rms errors for fixed-τ and percentile-τ ADMs. For comparison, Figs.

TABLE 6. Percentile-τ albedo mean and std dev (in parentheses) inferred from means in individual viewing zenith and relative azimuth angle bins.

θ_o	All	Water	Mix	Ice
20°–30°	0.451 (0.008)	0.426 (0.006)	0.446 (0.014)	0.514 (0.012)
30°–40°	0.489 (0.006)	0.478 (0.008)	0.490 (0.011)	0.538 (0.011)
40°–50°	0.517 (0.003)	0.507 (0.006)	0.521 (0.016)	0.560 (0.011)
50°–60°	0.560 (0.004)	0.540 (0.007)	0.547 (0.009)	0.600 (0.017)
60°–70°	0.614 (0.006)	0.591 (0.011)	0.601 (0.011)	0.666 (0.019)

TABLE 7. Fixed-τ albedo mean and std dev (in parentheses) inferred from means in individual viewing zenith and relative azimuth angle bins.

θ_o	All	Water	Mix	Ice
20°–30°	0.449 (0.018)	0.424 (0.018)	0.444 (0.018)	0.513 (0.021)
30°–40°	0.489 (0.011)	0.478 (0.011)	0.490 (0.015)	0.538 (0.015)
40°–50°	0.518 (0.013)	0.509 (0.012)	0.522 (0.026)	0.562 (0.020)
50°–60°	0.563 (0.026)	0.543 (0.023)	0.549 (0.029)	0.602 (0.030)
60°–70°	0.615 (0.032)	0.593 (0.025)	0.602 (0.036)	0.667 (0.044)

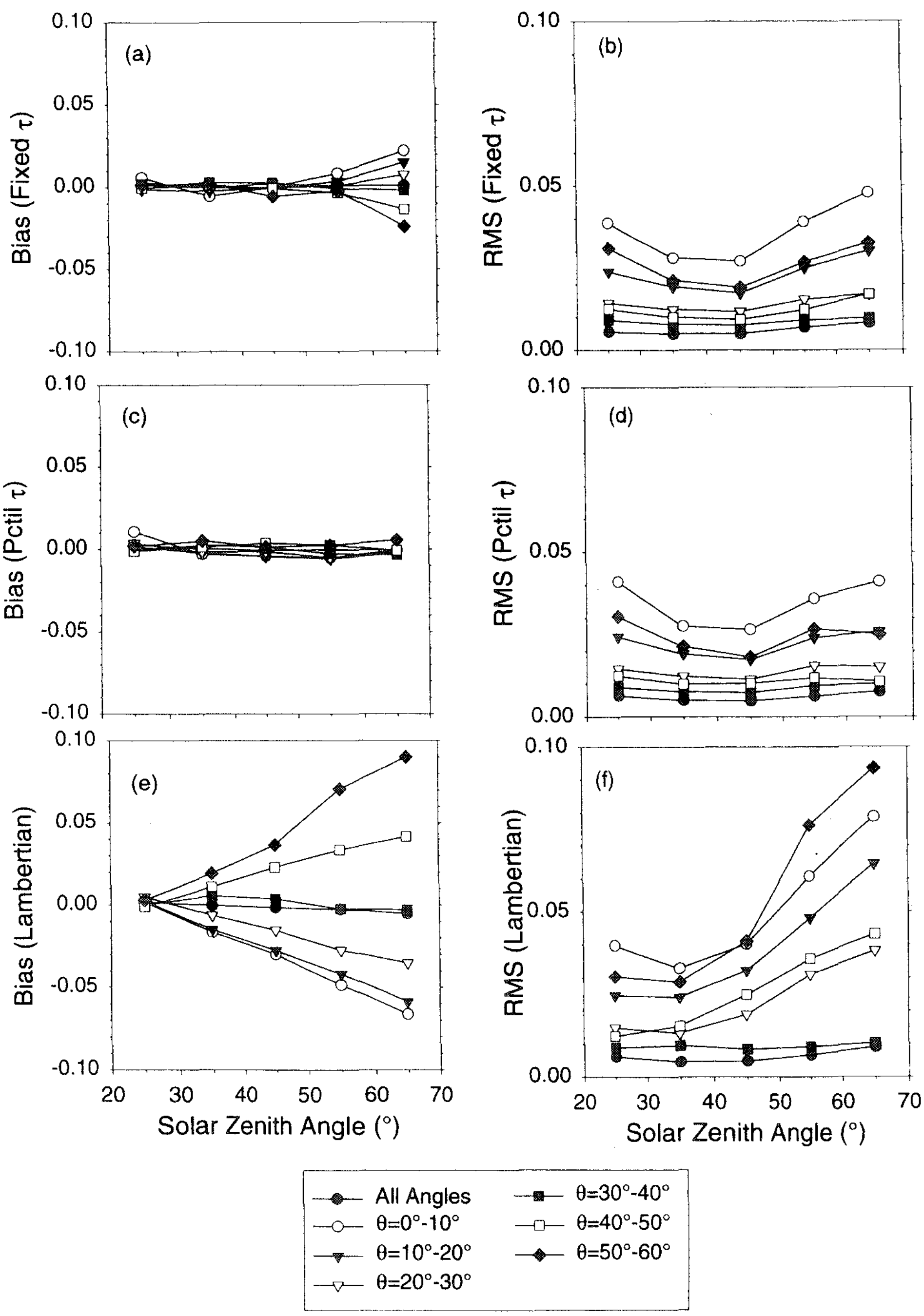

FIG. 9. Bias and rms errors in monthly mean albedos determined for all 5° × 5° lat–long regions over ocean between 60°S and 60°N for different solar zenith and viewing zenith angle ranges. (a)–(d) provide bias and rms differences for fixed-τ and percentile-τ ADMs. For comparison, (e), (f) show results obtained when no angular correction (i.e., "Lambertian") is assumed.

9e–f show results when no angular correction (i.e., "Lambertian") is used. If no angular correction is used, bias and rms errors increase sharply with solar zenith angle for oblique and near-nadir viewing zenith angles, reaching ≈0.1 for θ_o = 60°–70°. In contrast, when monthly mean albedos are inferred by averaging albedos from all viewing zenith angles, errors are drastically reduced (≲0.005), even for the Lambertian case. Albedo biases for the fixed-τ approach are most pronounced for θ_o = 60°–70°, reaching ≈0.02, while bias errors for the percentile-τ approach generally remain <0.01 at all angles. Rms errors show a clear trend with both solar and viewing zenith angle, with larger values close to nadir and oblique viewing zenith angles.

Suttles et al. (1992) compared global ERBE ADM albedos over 500 km × 500 km regions with albedos inferred by direct integration (which they refer to as the SAB method). ERBE ADM albedos showed a bias of 1.2% (relative) and a regional rms difference of 6% (relative). The corresponding values from the present study based on the percentile-τ approach are 0.3% and 1.9%, a reduction by a factor 4 in bias error and a factor of 3 in rms error. The likely reason for this reduction in error is the number of scene types considered: ERBE considered only four classes of cloud cover (clear, partly cloudy, mostly cloudy, and overcast) compared to 19 in the present study. The larger number of scene types improves albedo estimates by increasing ADM sensitivity to scene parameters that have the greatest influence on anisotropy (cf. Figs. 3a,b). Interestingly, the reduction in error based on the current set of 19 ADMs (compared to ERBE) is consistent with the expected reduction in error for CERES albedos based on a new set of CERES ADMs defined for a larger set of scene types (Wielicki et al. 1995). Further improvements in regional mean albedo accuracy are expected by further stratifying scene types by cloud phase (section 4b).

5. Summary and conclusions

Three months of POLDER 670-nm reflectance measurements were used to construct ADMs for scene types defined by satellite retrievals of cloud fraction and cloud optical depth. Two approaches were considered in building the ADMs. The first assumes there are no biases in cloud property retrievals and defines ADMs for 19 scene types stratified by fixed discrete intervals of cloud fraction and cloud optical depth (fixed-τ ADMs). The second, more general, approach allows for potential biases in cloud optical depth retrievals by defining ADM scene types based on cloud fraction and *percentile* intervals of cloud optical depth in each angular bin (percentile-τ ADMs). Albedos based on these ADMs were compared with albedos obtained by direct integration of mean reflectances for two independent months.

Albedos estimated based on the assumption that cloud properties are unbiased (i.e., fixed-τ ADMs) show a strong systematic dependence on viewing geometry. This dependence becomes more pronounced with increasing solar zenith angle, reaching ≈12% (relative) between near-nadir and oblique viewing zenith angles for θ_o = 60°–70°. The cause for this bias is shown to be directly linked with a viewing zenith angle dependence in the cloud optical depth retrievals. In contrast, albedos inferred using percentile intervals of cloud optical depth (percentile-τ ADMs) show very little viewing zenith angle dependence and are in good agreement with direct integration albedos at all angles. A consistent albedo estimate in all viewing configurations is highly desirable, particularly in studies that relate top-of-atmosphere albedos with surface measurements.

When ADM albedos are stratified by cloud fraction and compared with albedos obtained by direct integration, errors in albedo are less sensitive to cloud fraction for percentile-τ ADMs than for fixed-τ ADMs. Relative errors in mean albedo based on percentile-τ ADMs generally remain <2% for all solar zenith angles observed by POLDER over the full cloud fraction range.

The ADMs considered in this study do not account for changes in anisotropy due to cloud phase. While this approach provides reasonable estimates of mean albedo for the ensemble of all cloud scenes, significant albedo biases occur when liquid water and ice cloud populations are considered separately. Mean albedos for these cases depend strongly on viewing zenith angle and relative azimuth angle, particularly at low sun elevations. These results highlight the importance of including cloud phase in defining ADM scene types.

ADM derived monthly mean albedos determined for all 5° × 5° lat–long regions over ocean between 60°S and 60°N are in good agreement with those obtained by direct integration when ADM albedos inferred from specific angular bins are averaged together. This is true even when no angular correction is applied (i.e., Lambertian). Albedos inferred from near-nadir and oblique viewing zenith angles are the least accurate, with regional rms errors reaching 0.03–0.04 (relative rms error of ~5%–10%) when ADMs are used, and 0.09–0.10 (relative rms error of ~15%–20%) when clouds are assumed Lambertian. Relative bias and rms errors in regional mean albedos are 0.3% and 1.9%, respectively, when all angles are considered, while ERBE ADM albedos show a bias of 1.2% (relative) and a regional rms difference of 6% (relative). The reason for this improvement in albedo accuracy is likely associated with the larger number of ADM scene types considered in the present study (19 cloud classes and only 4 for ERBE).

The results in this study demonstrate the benefits of defining many ADM scene types according to parameters that have a large influence on anisotropy. One of the limitations of using ADMs defined for broad scene classes (e.g., ERBE's clear, partly cloudy, mostly cloudy, and overcast scene types) is that large ADM related albedo biases can occur for a specific subset of scenes (e.g., thick or thin overcast). By increasing the number of ADM scene types according to parameters that influence anisotropy, improved estimates of albedo are obtained for a range of cloud conditions, making it possible to examine how albedo changes as a function of a given cloud property (e.g., cloud fraction), cloud type (e.g., stratiform, cumuliform, or cirrus), or as a function of cloud transmission (in studies of atmospheric absorption). Other areas that benefit from improved albedo estimates include radiative transfer model (e.g., plane-parallel theory) validation, surface and atmospheric flux estimation by constraining a model to the TOA albedo estimate, validation of climate model monthly mean fluxes and cloud radiative forcing estimates, and development of subgrid cloud parameterizations.

Further work in ADM development is needed to examine how other parameters (in addition to cloud fraction and cloud optical depth) improve albedo estimates. For example, the accuracy in regional albedos over areas of frequent cirrus cloud cover would likely be improved by incorporating cloud phase as an additional scene classifier. Such a strategy is a major component of ongoing research in both the CERES (Wielicki et al. 1996) and POLDER (Buriez et al. 1997) projects.

Acknowledgments. The authors would like to thank Dr. Bruce Wielicki, Mr. Richard Green, and Dr. Seiji Kato for their insightful comments. This research was supported by NASA Grant NAG-1-1963, CNES, European Economic Community, Région Nord-Pas De Calais, and Préfecture du Nord through EFRO.

REFERENCES

Barker, H. W., B. A. Wielicki, and L. Parker, 1996: A parameterization for computing grid-averaged solar fluxes for inhomogeneous marine boundary layer clouds. Part II: Validation using satellite data. *J. Atmos. Sci.*, **53**, 2304–2316.

Barkstrom, B. R., 1984: The Earth Radiation Budget Experiment (ERBE). *Bull. Amer. Meteor. Soc.*, **65**, 1170–1186.

Buriez, J. C., and Coauthors, 1997: Cloud detection and derivation of cloud properties from POLDER. *Int. J. Remote Sens.*, **18**, 2785–2813.

Cess, R. D., and Coauthors, 1990: Intercomparison and interpretation of climate feedback processes in 19 general circulation models. *J. Geophys. Res.*, **95**, 16 601–16 615.

Chen, C.-T., and E. Roeckner, 1996: Validation of the Earth radiation budget as simulated by the Max Planck Institute for Meteorology general circulation models ECHAM4 using satellite observations of the Earth Radiation Budget Experiment. *J. Geophys. Res.*, **101**, 4269–4287.

Cox, C., and W. Munk, 1954: Some problems in optical oceanography. *J. Mar. Res.*, **14**, 63–78.

Cox, S. K., D. S. McDougal, D. A. Randall, and R. A. Schiffer, 1987: FIRE—The First ISCCP Regional Experiment. *Bull. Amer. Meteor. Soc.*, **68**, 114–118.

Deschamps, P. Y., F.-M. Bréon, M. Leroy, A. Podaire, A. Bricaud, J.-C. Buriez, and G. Sèze, 1994: The POLDER mission: Instrument characteristics and scientific objectives. *IEEE Trans. Geosci. Remote Sens.*, **32**, 598–615.

Descloitres, J. C., J. C. Buriez, F. Parol, and Y. Fouquart, 1998: POLDER observations of cloud bidirectional reflectances compared to a plane-parallel model using the International Satellite Cloud Climatology Project cloud phase functions. *J. Geophys. Res.*, **103**, 11 411–11 418.

Green, R. N., and P. O. Hinton, 1996: Estimation of angular distribution models from radiance pairs. *J. Geophys. Res.*, **101**, 16 951–16 959.

Hagolle, O., and Coauthors, 1999: Results of POLDER in-flight calibration. *IEEE Trans. Geosci. Remote Sens.*, in press.

Hansen, J. E., and L. D. Travis, 1974: Light scattering in planetary atmospheres. *Space Sci. Rev.*, **16**, 527–610.

Hartmann, D. L., V. Ramanathan, A. Berroir, and G. E. Hunt, 1986: Earth radiation budget data and climate research. *Rev. Geophys.*, **24**, 439–468.

House, F. B., A. Gruber, G. E. Hunt, and A. T. Mecherikunnel, 1986: History of missions and measurements of the Earth Radiation Budget (1957–1984). *Rev. Geophys.*, **24**, 357–377.

Kandel, R., and Coauthors, 1998: The ScaRaB earth radiation budget dataset. *Bull. Amer. Meteor. Soc.*, **79**, 765–783.

Kiehl, J. T., J. J. Hack, and B. P. Briegleb, 1994: The simulated Earth radiation budget of the National Center for Atmospheric Research community climate model CCM2 and comparisons with the Earth Radiation Budget Experiment (ERBE). *J. Geophys. Res.*, **99**, 20 815–20 827.

Kneizys, F. X. and Coauthors, 1996: The MODTRAN 2/3 Report and LOWTRAN 7 Model. Contract F19628-91-C-0132, 261 pp. [Available from Phillips Laboratory, Geophysics Directorate, Hanscom AFB, MA 01731.]

Loeb, N. G., and R. Davies, 1996: Observational evidence of plane parallel model biases: Apparent dependence of cloud optical depth on solar zenith angle. *J. Geophys. Res.*, **101**, 1621–1634.

——, and J. A. Coakley Jr., 1998: Inference of marine stratus cloud optical depths from satellite measurements: Does 1D theory apply? *J. Climate*, **11**, 215–233.

——, T. Várnai, and D. M. Winker, 1998: Influence of sub-pixel scale cloud-top structure on reflectances from overcast stratiform cloud layers. *J. Atmos. Sci.*, **55**, 2960–2973.

Minnis, P., P. W. Heck, and D. F. Young, 1993: Inference of cirrus cloud properties using satellite-observed visible and infrared radiances. Part II: Verification of theoretical cirrus radiative properties. *J. Atmos. Sci.*, **50**, 1305–1322.

Mishchenko, M. I., W. B. Rossow, A. Macke, and A. A. Lacis, 1996: Sensitivity of cirrus cloud albedo, bidirectional reflectance and optical thickness retrieval accuracy to ice particle shape. *J. Geophys. Res.*, **101**, 16 973–16 985.

Parol, F., J.-C. Buriez, C. Vanbauce, P. Couvert, G. Sèze, P. Goloub, and S. Cheinet, 1999: First results of the POLDER "Earth Radiation Budget and Clouds" operational algorithm. *IEEE Trans. Geosci. Remote Sens.*, in press.

Payette, F., 1989: Applications of a sampling strategy for the ERBE scanner data. M. S. thesis, Dept. of Atmospheric and Oceanic Sciences, McGill University, 100 pp. [Available from McGill University, 805 Sherbrooke Street West, Montreal, PQ H3A 2K6, Canada.]

Rossow, W. B., and R. A. Schiffer, 1991: ISCCP cloud data products. *Bull. Amer. Meteor. Soc.*, **72**, 2–20.

——, A. W. Walker, D. E. Beuschel, and M. D. Roiter, 1996: International Satellite Cloud Climatology Project (ISCCP). Documentation of the New Cloud Datasets. World Meteorological Organization Tech. Document WMO/TD-No. 737, 115 pp.

Sassen, K., and K.-N. Liou, 1979: Scattering of polarized laser light by water droplet, mixed-phase and ice-crystal clouds. Part I: Angular scattering patterns. *J. Atmos. Sci.*, **36**, 838–851.

Smith, G. L., and N. Manalo-Smith, 1995: Scene-identification error probabilities for evaluating Earth radiation measurements. *J. Geophys. Res.*, **100**, 16 377–16 385.

——, R. N. Green, E. Raschke, L. M. Avis, J. T. Suttles, B. A. Wielicki, and R. Davies, 1986: Inversion methods for satellite studies of the Earth's radiation budget: Development of algorithms for the ERBE mission. *Rev. Geophys.*, **24**, 407–421.

Stamnes, K., S.-C. Tsay, W. Wiscombe, and K. Jayaweera, 1988: Numerically stable algorithm for discrete-ordinate-method radiative transfer in multiple scattering and emitting layered media. *Appl. Opt.*, **24,** 2502–2509.

Suttles, J. T., and Coauthors, 1988: Angular radiation models for Earth–atmosphere systems. Vol. I, shortwave models. NASA Report NASA RP-1184.

——, B. A. Wielicki, and S. Vemury, 1992: Top-of-atmosphere radiative fluxes: Validation of ERBE scanner inversion algorithm using *Nimbus-7* ERB data. *J. Appl. Meteor.*, **31,** 784–796.

Taylor, V. R., and L. L. Stowe, 1984: Reflectance characteristics of uniform Earth and cloud surfaced derived from Nimbus 7 ERB. *J. Geophys. Res.*, **89,** 4987–4996.

Várnai, T., 1996: Reflection of solar radiation by inhomogeneous clouds. Ph.D. thesis, McGill University, 146 pp. [Available from McGill University, 805 Sherbrooke Street West, Montreal, PQ H3A 2K6, Canada.]

Wielicki, B. A., and R. N. Green, 1989: Cloud identification for ERBE radiation flux retrieval. *J. Appl. Meteor.*, **28,** 1133–1146.

——, R. D. Cess, M. D. King, D. A. Randall, and E. F. Harrison, 1995: Mission to planet Earth: Role of clouds and radiation in climate. *Bull. Amer. Meteor. Soc.*, **76,** 2125–2153.

——, B. R. Barkstrom, E. F. Harrison, R. B. Lee III, G. L. Smith, and J. E. Cooper, 1996: Clouds and the Earth's Radiant Energy System (CERES): An Earth Observing System experiment. *Bull. Amer. Meteor. Soc.*, **77,** 853–868.

Ye, Q., and J. A. Coakley Jr., 1996: Biases in Earth radiation budget observations, Part 2: Consistent scene identification and anisotropic factors. *J. Geophys. Res.*, **101,** 21 253–21 263.

Young, D. F., P. Minnis, D. R. Doelling, G. G. Gibson, and T. Wong, 1998: Temporal interpolation methods for the Clouds and the Earth's Radiant Energy System (CERES) Experiment. *J. Appl. Meteor.*, **37,** 572–590.

CONCLUSION ET PERSPECTIVES

Si l'on veut, dans un avenir proche, mieux comprendre quelle est la sensibilité du Climat à l'activité humaine, il est impératif de prendre correctement en compte les interactions nuages rayonnement et la réponse des nuages à une éventuelle perturbation climatique. Cela nécessite une bonne connaissance de leurs propriétés microphysiques (distribution en taille, phase et forme des particules) et de leur morphologie (la distribution spatiale de l'eau liquide). Compte tenu de leurs effets importants sur le bilan radiatif terrestre, deux types de couverture nuageuse sont au centre de ce sujet : les nuages de glace, les Cirrus, qui sont composés de particules de formes variées et complexes et les nuages de couche limite, Stratocumulus, Cumulus et autres.

Bien que les Cirrus couvrent en permanence 20% de la surface du globe (environ 10% pour les cirrus semi-transparents), leur influence réelle sur le bilan radiatif est encore mal connue. De nombreuses études concluent cependant à une influence importante, tout au moins à l'échelle régionale (*Raval et Ramanathan*, 1989 ; *Ramanathan et Collins*, 1991). Les difficultés expérimentales auxquelles sont confrontés les scientifiques expliquent cette large méconnaissance : les mesures *in situ* sont rendues difficiles par l'altitude de ces nuages et par les conditions de pression et de température rencontrées. Par ailleurs, si les cirrus constituent a priori d'excellentes cibles pour l'observation satellitale puisqu'ils ne sont masqués par aucun autre type de système nuageux, ils sont difficiles à observer du fait de leur semi-transparence. Ils sont, en outre, extrêmement variable dans le temps et l'espace. Ceci implique, en premier lieu, de disposer de cas bien documentés. C'est ce qui a été entrepris ces dix dernières années dans le cadre d'expériences internationales comme FIRE, ICE, EUCREX, mais aussi CEPEX, qui ont fourni des données permettant de développer les premiers modèles de cirrus. Les cirrus tropicaux restent cependant pratiquement inconnus.

Compte-tenu de la grande variabilité spatiale des cirrus et de la difficulté de leur observation *in situ*, des expériences aéroportées seules ne pouvaient suffire à valider les modèles de processus ; l'observation satellitale a donc occupé ces dernières années une position centrale dans cette stratégie. La semi-transparence des cirrus et les caractéristiques de la diffusion par les cristaux non sphériques ont impliqué le développement d'algorithmes spécifiques, qui, à leur tour, ont du être validés ou complétés par des expériences in situ. Ma contribution personnelle à ce travail a démarré fin des années 1980 avec l'utilisation de l'instrument spatial AVHRR pour déterminer les propriétés radiatives, optiques et microphysiques de cirrus. Ce travail, initié dans le cadre de ICE, s'est poursuivi ensuite dans le contexte de la préparation à la campagne EUCREX. Aujourd'hui la méthodologie est appliquée à des données GOES et ATSR2 dans le cadre de la thèse d'Odile Thouron que je co-encadre depuis fin 1999.

La seconde limite évidente dans la modélisation des propriétés radiatives des nuages vient du fait que ceux-ci sont communément traités dans les modèles de transfert radiatif comme des couches dites "planes parallèles", horizontalement homogènes, dont la composition microphysique est fixée. Cette limite intervient d'ailleurs aussi bien pour l'estimation de l'influence des nuages sur le rayonnement dans les modèles de circulation générale que pour la détermination des propriétés des nuages (albédo, épaisseur optique, contenu en eau ou en glace) à partir des luminances mesurées depuis satellite. Même dans le cas de nuages relativement "plans-parallèles" comme les stratocumulus, *Cahalan et al.* (1994) ont montré que la répartition de l'eau liquide à l'intérieur des nuages pouvait engendrer de graves différences sur la détermination de l'épaisseur optique du nuage depuis satellite. Si la forme des nuages s'éloigne fortement d'un plan-parallèle les conséquences sont encore plus significatives. De nombreux travaux ont montré que la forme des nuages avait une influence considérable tant sur le flux (par exemple, *Welch et Wielicki*, 1984; **Parol et al, 1994**) que sur les réflectances bidirectionnelles (par exemple, *Bréon*, 1992; *Kobayashi*, 1993).

A partir du début des années 1990, la version aéroportée de l'instrument POLDER construite au Laboratoire d'Optique Atmosphérique avec le support du CNES a permis d'engager des travaux originaux sur ces deux thèmes essentiels. Les études menées sur de nouveaux types de mesures (entre autre sur la directionalité du rayonnement solaire) nous ont guidé dans la conception des algorithmes opérationnels qui ont été par la suite utilisés pour exploiter les données de la version spatiale de POLDER. En premier lieu, la mise en œuvre de l'instrument au cours de campagnes internationales de mesures nous a permis de montrer la faisabilité de certaines méthodes de dérivation de propriétés géophysiques des nuages. Elle a permis ensuite de finaliser les algorithmes d'extraction de ces grandeurs géophysiques et parfois de mettre en évidence la ou les limitations de ces algorithmes d'inversion des mesures de POLDER.

L'étude qui a été menée a fourni de nombreux résultats intéressants et souvent originaux. POLDER est aujourd'hui le premier capteur capable de mesurer la polarisation de la lumière et de fournir en même temps des informations sur la répartition angulaire de la lumière solaire réfléchie par le système Terre-atmosphère. Comme cela a été souligné dans le chapitre 3 de ce document, la polarisation permet par exemple de construire un indicateur de la présence de glace dans les nuages. La mesure de la répartition angulaire de la lumière solaire réfléchi a permis de vérifier que le modèle de nuage plan-parallèle homogène utilisé dans les programmes comme ISCCP ou les modèles de climatologie ou de prévision du temps n'était pas totalement irréaliste, mais qu'il pouvait être avantageusement "aménagé" (c.f. chapitres 2 et 3). Les mesures de réflectance bidirectionnelle effectuées à l'aide de la version aéroportée de POLDER (**Descloitres et al., 1995 ; 1998**) puis à partir de POLDER sur ADEOS (**Parol et al., 1999** ; *Doutriaux-Boucher et al.*, 2000) ont mis clairement en évidence les faiblesses du modèle de nuage plan-parallèle.

Quoiqu'il en soit, des progrès significatifs sont déjà bien en vue pour la modélisation des propriétés optiques et radiatives des nuages (*Doutriaux-Boucher et al.*, 2000). Toutefois, comme cela a été souligné plusieurs fois dans ce document, une limitation importante vient du fait que l'écart entre les mesures bidirectionnelles et leur simulation avec un modèle de nuage donné peut être dû à une mauvaise prise en compte (i) de la microphysique du nuage observé, (ii) de la répartition horizontale du contenu (intégré verticalement) de l'eau condensée, ou encore (iii) de la forme du nuage (essentiellement la variation de l'altitude du sommet du nuage).

Si on a bien une information sur la microphysique des nuages à partir des mesures de polarisation de POLDER, celle-ci reste encore insuffisante. De même il est difficile de relier de façon univoque la structure spatiale des champs nuageux au diagramme de rayonnement solaire réfléchi observé par POLDER. Ces informations devraient être améliorées de façon évidente par une combinaison entre divers types d'instruments présentant des résolutions spatiales, spectrales et angulaires variables.

C'est le but d'une récente proposition de recherche dont je suis le Principal Investigateur et qui a été acceptée par le CNES et la NASDA sur l'utilisation conjointe des instruments POLDER-2 et GLI qui seront à bord de la station japonaise ADEOS-2 à partir de fin 2001. L'objectif de cette proposition est d'utiliser les possibilités instrumentales originales de POLDER (multi-directionalité, polarisation, et mesures spectrales) et des comparaisons entre POLDER et GLI pour mieux comprendre et améliorer la détermination des propriétés des nuages depuis l'espace. L'utilisation de données GLI à haute résolution spatiale, avec des caractéristiques spectrales élevées, et une parfaite coïncidence dans le temps avec les données POLDER permettra de mieux comprendre les résultats des algorithmes d'analyse des nuages appliqués à POLDER. Par ailleurs, les capacités originales de POLDER (multi-directionalité et polarisation) devraient être complémentaires pour interpréter les résultats dérivés de GLI.

Nos connaissances sur les nuages et leurs effets sur le rayonnement devraient être nettement améliorées également par la combinaison entre les instruments PARASOL (POLDER sur micro-satellite), PICASSO-CENA, CLOUDSAT et Aqua (EOS-PM) qui seront dans l'espace durant une période commune en 2003-2004. Par exemple, la complémentarité la plus importante entre PARASOL, PICASSO-CENA et EOS pour le problème des hétérogénéités de nuages est attendue de la combinaison entre le champ de rayonnement mesuré par PARASOL, la forme du sommet du nuage mesurée par le lidar à bord de PICASSO-CENA et les variabilités horizontales du contenu en eau et de la taille des gouttes dérivées de l'instrument MODIS à bord d'EOS. Il existe très peu d'observations sur les variations spatiales couplées de l'altitude du sommet et de la base des nuages et le contenu en eau condensée. Même pour le type de nuages dont la structure semble la moins complexe, les stratocumulus, le lien entre ces variations spatiales est encore mal connu. Des relations simples basées sur quelques observations spatiales ou *in situ* ont déjà été proposées (*Minnis et al*, 1992 ; **Pawlowska et al, 2000; Annexe B**), mais elles ne peuvent être généralisées à l'échelle globale.

L'intérêt du couplage PICASSO-CENA/EOS réside d'abord dans le fait que le profil d'altitude des nuages dérivé du lidar pourra être comparé à la variabilité spatiale de la température radiative déduite des canaux thermiques de MODIS. Cela devrait permettre ensuite d'étendre la détermination de l'altitude des nuages au champ de vue complet de MODIS. L'association de ce champ d'altitude aux champs d'épaisseur optique (de rayon des gouttes / de la dimension des cristaux) dérivés par ce même MODIS, fournit alors un jeu de données privilégié pour envisager des modélisations de nuage. L'étape naturelle suivante sera de comparer le champ de rayonnement simulé par le modèle de nuage considéré avec l'observation multidirectionnelle effectué par PARASOL. Ici encore les mesures bidirectionnelles de POLDER apparaissent comme une manière de contraindre le modèle.

Un autre aspect qui peut être abordé est d'avantage lié à la distribution verticale des nuages. En effet, bien que POLDER permette la mesure de l'altitude du nuage (à partir de l'absorption par l'oxygène et à partir de la polarisation due à la diffusion moléculaire), il ne fournit aucune information sur la structure de sous-échelle (c'est à dire en dessous de 6 x 6 km^2 à l'heure actuelle).

Toutefois les premiers résultats obtenus avec la version spatiale de POLDER semblent indiquer qu'une information sur l'extension verticale du nuage est contenue dans les mesures de l'absorption par l'oxygène (**Vanbauce et al, 1998**). Ainsi, il devient intéressant de coupler les informations fournies par le lidar et par MODIS, via les canaux thermiques, avec les mesures d'altitudes effectuées par POLDER pour essayer d'appréhender la variabilité verticale des nuages. Dans ce contexte, on peut citer également l'intérêt du spectromètre à bord de PICASSO-CENA, puisqu'il effectuera des mesures à haute résolution spectrale dans la bande d'absorption de l'oxygène.

Comme cela a été illustré par exemple par *Wielicki et al.* (1996), trouver des solutions aux problèmes difficiles de la modélisation des nuages requiert aussi des observations simultanées du bilan radiatif terrestre et des propriétés des nuages. Lorsque l'on utilise l'imagerie satellitale pour appréhender les effets des nuages sur le bilan radiatif, la procédure appliquée communément consiste à dériver les paramètres nuageux - l'épaisseur optique par exemple - à partir de mesures effectuées dans des bandes spectrales étroites et ensuite de les utiliser pour estimer le flux solaire réfléchi. Un autre type de méthode fait appel à des modèles angulaires (ADMs) pour estimer le flux réfléchi à partir de mesures de luminances dans des bandes larges. Cette seconde procédure a été appliquée aux données ERBE, et ensuite à celles de ScaRaB (*Kandel et al*, 1994) et plus récemment à celles de CERES (*Wielicki et Barkstrom*, 1991).

L'algorithme de la chaîne de traitement "ERB&Clouds" de POLDER suit la première procédure (l'approche physique) pour estimer le flux réfléchi et le forçage radiatif des nuages aux courtes longueurs d'onde (**Buriez et al, 1997**). Par ailleurs, après une estimation des luminances ondes courtes à partir des mesures de luminances effectuées dans les bandes spectrales étroites de POLDER, il est possible d'établir de nouveaux ADMs (l'approche statistique). Toutefois, un point faible de la chaîne de traitement POLDER concerne actuellement cette intégration spectrale qui n'a pas pu être validée. De ce fait, la construction d'ADMs à partir des données POLDER ne peut pratiquement être réalisée avec confiance que pour un canal étroit (**Loeb et al., 2000**). Ce manque dans le plan de validation a été provoqué par l'absence de mesures simultanées de POLDER et de ScaRaB qui étaient initialement prévues. La simultanéité spatio-temporelle de mesures POLDER et CERES pourrait permettre de résoudre enfin ce problème. Cela devrait se réaliser avec le lancement de POLDER-2 fin 2001 et la combinaison avec les données de CERES à bord de Terra (EOS-AM). Il est également prévu de faire coïncider au mieux l'orbite de PARASOL avec celle d'Aqua (EOS-PM).

Une fois ce problème résolu, il est possible d'appliquer aux données POLDER les deux approches (physique et statistique) et de comparer les flux radiatifs estimés entre eux et de les comparer également aux flux radiatifs dérivés de CERES. Il est important de souligner que même les deux approches statistiques (celle appliquée à POLDER et celle appliquée à CERES) peuvent conduire à des résultats très différents, car ils utiliseront inévitablement des identifications de scène différentes (basées sur les canaux POLDER dans un cas et sur les canaux MODIS dans l'autre).La comparaison de ces trois déterminations de flux [1- statistique CERES (utilisant des ADMs CERES basés sur une identification de scène MODIS), 2- statistique POLDER (utilisant des ADMs et une identification de scène POLDER) et 3- physique POLDER (via la détermination de l'épaisseur optique du nuage)] mettront certainement en évidence des écarts très importants pour certaines situations. Ces différences pourront être analysées soigneusement en les reliant aux propriétés physiques de la scène à différentes échelles (POLDER, MODIS, et PICASSO-CENA). La combinaison des deux puis trois (voire quatre) satellites "synchrones" est une occasion exceptionnelle pour analyser et valider des mesures de flux radiatifs "instantanés" et non plus seulement en moyenne mensuelle.

Il apparaît évident à la lecture des précédents paragraphes que des modifications du champ angulaire, du domaine spectral et éventuellement de la résolution spatiale de l'instrument POLDER actuel, amélioreraient la dérivation des propriétés de nuage et indirectement l'estimation du flux ondes courtes réfléchi via une détermination plus complète des ADMs. Puisque le domaine spectral actuel de POLDER est limité à des longueurs d'onde inférieures à $1\,\mu m$, un instrument additionnel basé sur le même concept que POLDER serait requis pour le domaine du moyen infrarouge (MIR : $1\,\mu m$ à $3\,\mu m$). Depuis fin 1998, la continuité des projets POLDER et PARASOL est déjà amorcée et a donné naissance à un nouveau concept instrumental nommé GC-NG (Grand Champ - Nouvelle génération). Je suis le Principal Investigateur de la composante "Nuage" de ce projet CNES. Ma proposition de sujet de thèse Technologique a été retenue par le CNES et c'est dans ce cadre qu'Odile Thouron a débuté une thèse d'Université depuis septembre 1999.

Pour l'étude des nuages, l'intérêt de l'extension spectrale est triple :
(i) On espère une amélioration de la détection nuageuse au dessus de la glace et la neige puisque la réflectivité de la neige/glace diminue fortement dans le MIR comparée à celle des nuages d'eau liquide. L'apport d'un canal à $1.37\,\mu m$ devrait permettre également une meilleure détection des cirrus fins (*Gao et al.*, 1992).

(ii) En associant des mesures à 1.6µm et/ou 2.2µm à des mesures dans le visible (670nm - 865nm) on peut séparer les effets de la macrophysique (variation du contenu en eau) et de la microphysique (taille et peut-être forme des particules) des nuages sur le rayonnement (*Nakajima et King*, 1990 ; *Han et al*, 1994). Il est clair que des mesures à 1.6µm et/ou 2.2µm permettent de discriminer certain types de particules nuageuses. L'apport devrait être encore plus net si les mesures sont effectuées en polarisation, puisque dans le MIR, la contribution des molécules est négligeable et les luminances polarisées sont sensibles aux premières diffusions, donc certainement à la forme des particules.

(iii) L'estimation des flux ondes courtes réfléchis pourrait être améliorée puisqu'on pourrait alors explicitement tenir compte de l'absorption par l'eau liquide (au delà de 1µm) dans le calcul de l'intégration spectrale du flux à partir des bandes étroites.

POLDER permet actuellement de comparer 13 à 14 mesures de réflectances bidirectionnelles d'une scène nuageuse à celle d'un modèle de nuage (dans le cas présent plan-parallèle et gouttes de 10 microns). Les différences entre un champ de nuage réel et le modèle plan-parallèle apparaissent nettement aux grands angles de vue, au-delà de 60° (voir **Parol et al, 1999 ; Loeb et al, 2000**). Cet effet est illustré également sur la figure ci-dessous.

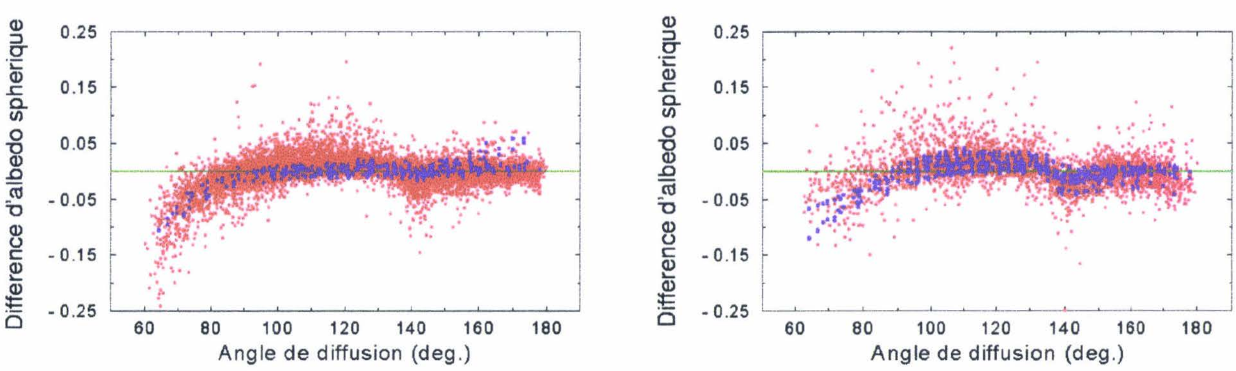

Fig. 2. Différences obtenues pour les nuages d'eau liquide entre les valeurs "directionnelles" de l'albédo sphérique et leur valeur moyenne en fonction de l'angle de diffusion. (a) correspond aux cas de couverture nuageuse totale et (b) aux cas de couverture partielle (inférieure à 0.8). En rouge les résultats actuels obtenus avec des données du POLDER spatial acquises au cours d'une journée, et en bleu des simulations effectuées en utilisant un modèle de nuages hétérogènes, mais le même type de gouttes que dans le modèle plan-parallèle utilisé actuellement (d'après *Jolivet et al*, 1999).

La figure 2 présente les résultats obtenus avec POLDER en séparant les cas de couverture nuageuse totale (Fig. 2.a) des cas de couverture nuageuse partielle, inférieure à 0.8 (Fig. 2.b).

Seuls les nuages d'eau liquide sont retenus dans ce traitement. Après inversion des données de POLDER avec le modèle de nuage actuellement implanté dans la chaîne "ERB&Clouds" les résultats (points rouges) montrent une nette déficience du modèle aux angles rasants, c'est à dire ici aux angles de diffusion inférieurs à 70°, et ce quelle que soit la nébulosité. Par contre, des simulations effectuées avec un modèle de nuage hétérogène (en bleu) montrent un relativement bon accord avec les mesures (d'après *Jolivet et al*, 1999). Ce type de modèle basé sur la méthode de Monté Carlo reste toutefois trop complexe pour être intégré dans la chaîne de traitement opérationnelle des mesures acquises par POLDER. Par contre, ces résultats nous confortent dans l'idée que des mesures effectuées à des angles de vue rasants permettraient d'ajuster et/ou de sélectionner parmi plusieurs modèles de nuage pour améliorer l'inversion des mesures radiatives. Dans la version actuelle de POLDER, l'angle de visée est très rarement supérieur à 60°. C'est pourquoi une extension du champ angulaire fournirait une information plus précise sur les effets des hétérogénéités des nuages sur le rayonnement réfléchi, ainsi qu'une meilleure "qualification" des ADMs qui sont produits par la chaîne de traitement des données POLDER.

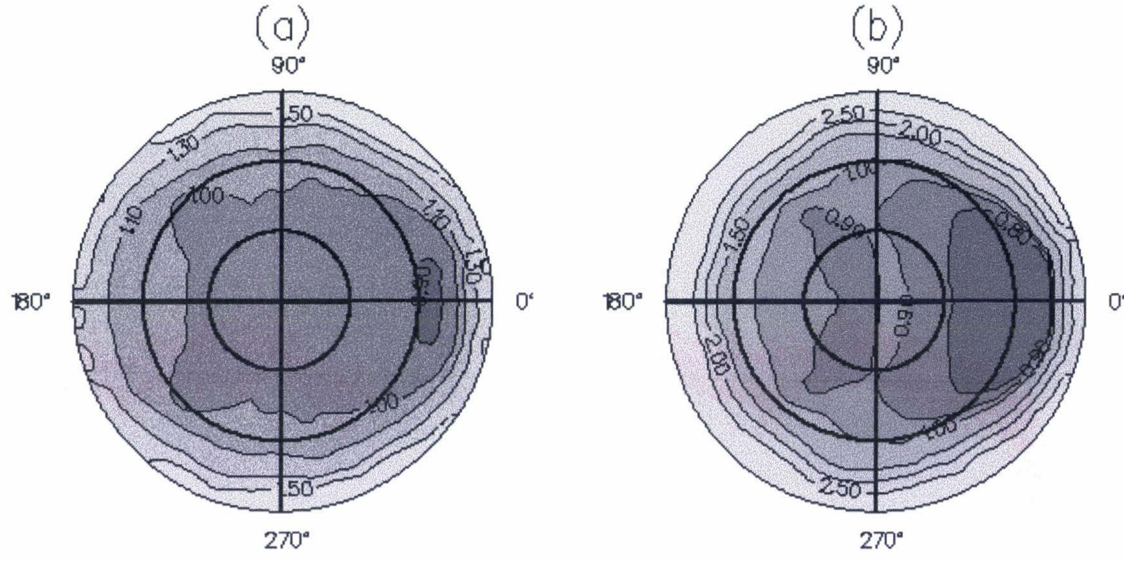

Fig.3. Diagramme polaire du rapport entre le flux ondes courtes estimé à partir de l'approximation plan-parallèle et le flux "vrai". Les cas (a) et (b) correspondent à des nébulosités de 100% et 50% respectivement. L'angle solaire est de 45° et l'épaisseur optique de la scène nuageuse est fixée et égale à 10 dans tous les cas. Le rayon des différents cercles varie comme l'angle zénithal de visée (petit cercle, 30°, puis 60° et enfin 80°). L'angle de rotation correspond à l'angle azimutal de visée. L'angle azimutal du soleil est égal à 180°.

Cette extension en angle de visée permettrait également une meilleure estimation du flux onde courtes réfléchi qui correspond à l'intégration angulaire des luminances réfléchies sur le demi-espace - environ 30% de l'énergie totale se trouve dans l'angle solide qui n'est actuellement pas échantillonné par POLDER. La figure 3 présente des diagrammes polaires du rapport entre le flux ondes courtes estimé à partir de l'approximation plan-parallèle et le flux "vrai". Ici le flux "vrai" est en fait un flux également simulé, mais à partir de situations nuageuses hétérogènes (*Jolivet et al*, 1999). Cette figure montre que, suivant le type de situation nuageuse observée, le modèle plan-parallèle peut très nettement surestimer le flux ondes courtes réfléchi au sommet de l'atmosphère.

Tout comme cela s'était engagé dans le cadre du projet POLDER, nous avons entrepris des cette année de mettre en œuvre des versions aéroportées simplifiées de ces nouveaux concepts instrumentaux pour pouvoir appréhender rapidement les difficultés à la fois techniques et scientifiques associées à ces projets d'extension spectrale et angulaire. Une version inclinée de l'instrument POLDER aéroporté a été réalisée et devrait effectuer des premiers vols scientifiques cette année. La version aéroportée d'un instrument effectuant des mesures dans le moyen-infrarouge et en polarisation est en cours de conception au laboratoire. Elle devrait effectuer ces premiers vols technologiques au printemps 2001.

Annexe A

SOFIA 1992 Experiment during ASTEX

The Global Atmosphere and Ocean System, 3, 355-395, 1995

The Global Atmosphere and Ocean System, 1995, Vol.3, pp. 355–395
Reprints available directly from the publisher
Photocopying permitted by license only

SOFIA 1992 EXPERIMENT DURING ASTEX

A. WEILL[1], F. BAUDIN[1], H. DUPUIS[1], L. EYMARD[1], J.P. FRANGI[1], E. GÉRARD[1], P. DURAND[2], B. BENECH[2], J. DESSENS[2], A. DRUILHET[2], A. RÉCHOU[2], P. FLAMANT[3], S. ELOURAGINI[3], R. VALENTIN[3], G. SÉZE[3], J. PELON[4], C. FLAMANT[4], J.L. BRENGUIER[5], S. PLANTON[5], J. ROLLAND[6], A. BRISSON[7], J. LE BORGNE[7], A. MARSOUIN[7], T. MOREAU[7], K. KATSAROS[8,13], R. MONIS[13], P. QUEFFEULOU[8], J. TOURNADRE[8], P.K. TAYLOR[9], E. KENT[9], R. PASCAL[9], P. SCHIBLER[10], F. PAROL[11], J. DESCLOITRES[11], J.Y. BALLOIS[11], M. ANDRÉ[12], M. CHARPENTIER[12]

[1]CETP (CNRS) 10-12 Av. de L'Europe 78140 Velizy (France); [2]L.A. UMR CNRS/UPS5560 Université Paul Sabatier, 31000 Toulouse (France); [3]LMD (CNRS), Ecole Polytechnique, 91 Palaiseau (France); [4]SA (CNRS) Université P. et M. Curie, tour 15, 5 place Jussieu 75005 Paris (France); [5]CNRM (METEO FRANCE) Avenue Coriolis 31000 Toulouse (France); [6]CMM (METEO FRANCE) BP 70, 29280, Plouzané (France); [7]CMS (METEO FRANCE) Avenue Lorraine, Lannion, (France); [8]IFREMER, BP 70, 29280, Plouzané (France); [9]RENNELL CENTRE, Southampton and IOS (Wormley) U.K.; [10]INSU (Division Mesures) Av. de Neptune, 94 St Maur les Fossées (France); [11]LOA, Université de Lille 1, 59655 Villeneuve d'Ascq Cedex (France); [12]METEO FRANCE/CAM, Bretigny (France); [13]University of Washington (USA)

The SOFIA experiment which took place in the Azores region during ASTEX, in June 1992 was devoted to surface flux and marine atmospheric boundary layer investigations at the mesoscale.

The different instrumented platforms used are described: shipborne instruments, drifting buoys, airborne instruments, satellites. After a description of the main characteristics of the whole experiment which corresponded to perturbed cloudy meteorological situations with a latent heat flux close to 100 W/m^2, a sensible heat flux smaller than 30 W/m^2 and moderate wind speeds < 10m/s, an analysis of two observing periods of June 8 and 17 is undertaken. For these two days we illustrate the use of several kinds of equipment such as the airborne Lidar LEANDRE, the radiometer POLDER, the acoustic system OCARINA and the microwave radiometer DRAKKAR. In particular, the wake effect due to Santa-Maria island is documented with the constant level balloons and the instrumented aircraft ARAT.

KEY WORDS: Ocean-atmosphere interactions, marine atmospheric boundary layer, energy budget

1. INTRODUCTION

In global models of general circulation (GCM) fluxes inside meshes of the order of 100 km × 100 km to 500 km × 500 km are estimated by very simple bulk parameterization as described by Delsol et al. 1971, based on Monin-Obukhov (1954) similarity theory such as presented by Businger et al. (1971).

These parameterizations are probably valid over homogeneous surfaces (Francey and Garratt, 1978) but need to be validated over large surfaces where inhomogeneities exist. These parameterizations often employ drag coefficients and need the knowledge of humidity, wind speed, temperature near the surface and the sea surface temperature (SST) (Businger, 1975; Garratt and Hyson, 1975, Garratt, 1977). Hence, during the past an intensive effort has been made to build and validate parameterizations of fluxes using different methods (eddy correlations, boundary layer parameterizations): see Francey and Garrat (1978), Liu et al. (1979), Large and Pond (1982), Champagne-Phillipe (1989), Wu (1974), Smith (1988), Brown and Liu (1982), Saïd and Druilhet (1991) or the excellent book edited by Geernaert and Plant (1990) to quote a few.

Fleagle et al. (1967), in an attempt to extend flux measurements up to the 500 km scale, showed the inconsistency of the method in the presence of inhomogeneitieis by comparisons to local measurements. Since inhomogeneity is often substantial over the ocean, another strategy is needed to find the "integrated fluxes". Moreover, this problem of flux extension had become more and more in evidence with the use of satellite information from which global information can be obtained, which is very important for a climatic survey. It requires development of a strategy of validation of the satellite products such as wind fields, sea state, sea surface temperature (SST), fluxes and humidity content.

For these reasons, several field campaigns for measuring sea surface energy exchange have been undertaken such as BOMEX Barbados Oceanographic and Meteorologic Experiment during which attempts were made to estimate fluxes (Holland and Rasmusson (1973), Nitta and Esbensen (1974)), GATE Global Atlantic Tropical Experiment (Nicholls and Le Mone, 1980), AMTEX Air Mass Transformation Experiment (Garatt and Hyson (1975)), ATEX Atlantic Experiment (Augstein et al. (1974)), JASIN Joint Air Sea Interaction programme (Nicholls (1985)), FASINEX Frontal Air Sea Interaction Experiment (Friehe et al. (1991), Weller et al. (1991)) in attempts to analyze the marine atmospheric boundary layer (MABL) and the sea surface exchange in presence of oceanic or atmospheric mesoscale forcing such as fronts. These experiments have shown the importance of having accurate measurements of SST (Sea Surface Temperature) for good estimates of fluxes using exchange coefficients. Moreover, these field experiments have illustrated that atmospheric inhomogeneities exist related to oceanic structures such as sea surface temperature fronts and observed by Atlas et al. (1986) with an airborne lidar.

However, flux measurements near the sea surface remain a difficult task and although drag coefficients are relatively very well established for strong or moderate wind speeds, more work is needed on exchange coefficients for low wind speeds. Sea state influence on the drag coefficient has been analyzed by Geernaert et al. (1986). New studies are required to take into account a wide spectrum of sea states. Concerning methods of flux measurement using second order statistic of momentum, Fairall et al., 1990 have shown the suitability of the inertial-dissipation method to obtain surface flux. However, there remain some questions about the universality of the empirical constants employed and the necessity to explain some discrepancies between heat flux obtained using eddy correlation techniques and inertial dissipation techniques (Fairall et al., 1990).

Modelling of the coupling between the ocean and the atmosphere involves also an "integrated" analysis of the whole system: the ocean surface and the subsurface, the oceanic mixed layer, the MABL, in which cloud and radiative processes have to be taken into account; see Betts, 1975; Betts and Albrecht, 1987; Albrecht, 1981; Albrecht et al. 1988, 1990.

To that end, a research program SOFIA (Surface of the Ocean, Fluxes and Interactions with the Atmosphere), was carried out by French groups from CRPE Centre de Recherche En Physiaue de l'Environment, Laboratoire d'Aérologie (Toulouse), CMM Centre de Météorologie Spatiale (Brest), IFREMER Institut Français de Recherche sur la Mer (Brest), SA Service d'Aéronomie (Paris), LMD Laboratorie de Météorologid Dynamique (Palaiseau), LOA Laboratoire d'Optique Atmosphérique (Lille) with a cooperation from CNRM Centre National de Recherches Météorologiques (Météo-France), Toulouse and CMS Centre de Météorologie Spatiale (Météo-France, Lannion). The scientific objective of SOFIA was the study of energy transfer (heat, humidity and momentum fluxes) between the sea surface and the MABL at scales ranging from local (10's of meters) to mesoscale (100's of kilometers). The general idea of the program was to develop a strategy of measurement based on nested boxes in which we intend to estimate fluxes. The instruments from which fluxes at different scales will be estimated have to be associated with satellite measurements to validate the "satellite" estimates of flux, particularly in presence of mesoscale oceanic and atmospheric structures responsible for spatial inhomogeneity of these fluxes. Indeed, considering the potential of satellites for estimating wind, fluxes and sea surface properties, an important task is to validate satellite estimates and therefore to have a relevant data base of good quality to be compared to these data from space. In particular, during the SOFIA/ASTEX experiment, the data from METEOSAT, LANDSAT, ERS1 (European Research Satellite), SPOT were used. It was also an opportunity to test and validate algorithms and techniques for the retrieval of some atmospheric and air-sea interface parameters from operational meteorological satellite data.

The SOFIA experiment took place from June 1 to June 28 in the Azores region (Figure 1) and was a cooperative experiment with ASTEX (Atlantic Stratocumulus Transition Experiment). In this paper we present in the first part the equipment used during SOFIA and in a second part how they are used. In a third part we illustrate the essential features of the experiment. Then, in part 4 and 5 we give an overview of highlights of SOFIA, presenting preliminary results from two intensive operating periods about which was initiated a cooperative work: June 8 was devoted to cloud structure and air-sea interaction, and June 17 to the analysis of cloud structure.

2. DATA SOURCES AND EQUIPMENT

Rather than describe all the instruments, we prefer to present them in synoptic tables and to comment instrument characteristics.

2.1. *Data sources*

2.1.1. *The Surface Measurements*

Instruments on board the research vessel *Le Suroit* are indicated in Table 1. We note here that we have on board at the same time:

- different instruments to estimate turbulent surface flux using inertial dissipative and bulk methods

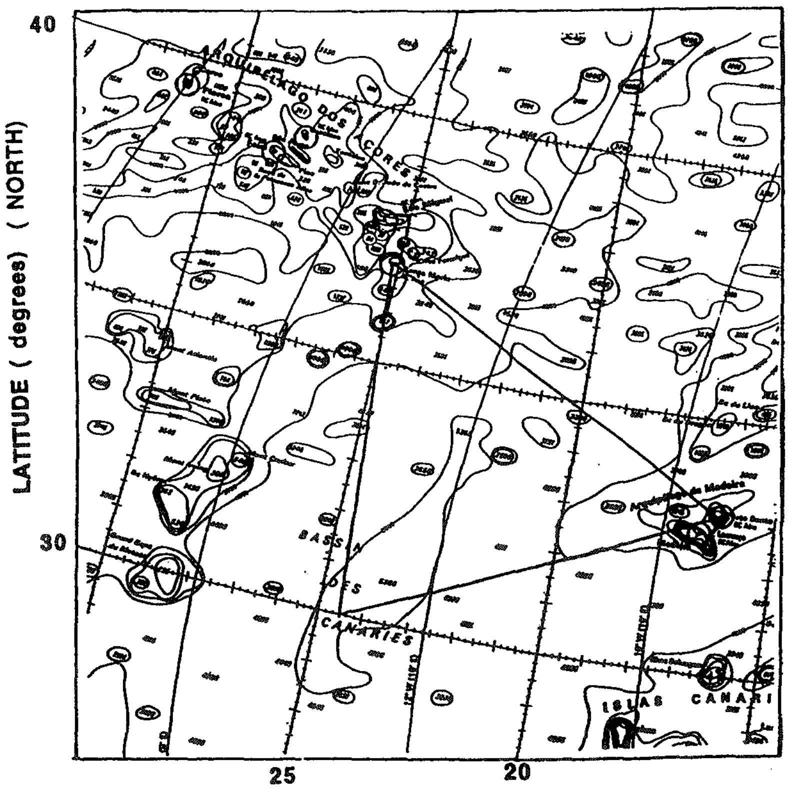

FIGURE 1 Map of the Azores region and the triangle in which ASTEX took place. SOFIA took place in the corner at the North of the triangle.

and radiative flux with redundant systems; (Note the systems deployed by the Rennel Centre and IOS (Wormley) U.K. and University of Washington; Yelland et al., 1994; Dupuis et al. 1994).

- surface observations with digital pictures of the surface.
- description of the lower atmosphere using in particular the tethered balloon and the OCARINA system (acoustic sounders system on a stabilised platform)
- microwave radiometer to obtain atmosphere vapor content (to be compared with radiosonde measurement) and liquid water content using experimental algorithms.

It is important to notice here as explained by Weill (1993) that acoustic sounder measurements are representative of horizontal scales larger than local in-situ measurements.

Table 2 indicates the different types of buoys used. Note that the hydrophone is an instrument which can give estimates of wind speed representative of different horizontal scales using the different acoustic frequencies and providing the sea state data to be compared to video pictures on board Le Suroit (Dupuis and Weill, 1993; Dupuis et al., 1993). Measurements from the oceanic drifting buoys provide a description of the ocean surface layer structure and the wave buoy gives a rough estimate of the non-directional wave spectrum.

TABLE 1

Instrumentation on board the ship Le Suroit. The ship position and heading are recorded on board and transmitted to the different recording systems which allows in particular to compute the true wind speed and direction and to know the location of the ship. IOS uses also a independent Magnavox GPS system.

In charge of IOS	Instrument	parameter estimated	characteristics
	Solent Sonic anemometer	wind fluctuations U V W	sampling 11 cps and 21 cps 16.5 metres height above sea level
	barometer	pressure	2m above sea level, sampling 15 mn
	(Young A Q)	Wind speed	10 meters mast, sampling 15 mn
	anemometer	and direction	10 meters mast, sampling 15 mn
	2 dry bulb	temperature	10 meters mast, sampling 15 mn
	2 wet bulb	humidity	
	IR radiometer	SST	for comparison
	bucket	SST	sampling 15 minutes
	trailing thermistor	SST	sampling 15 mintues
University of Washington	Lyman -α	humidity fluctuations	at 7 m upon sea level on a 5m boom in front of the ship sampling 20 cps
	two thermocouples (wet and dry bulb)	humidity and temperature fluctuations	in the lower section of the 10 meters mast carriage sampling 20 Hz
	incoming long wave and short wave infra red radiation	3–50 microns .28–2.8 microns 0.7–2.8 microns	one minute averages on the roof of the winch control cabin one minute average
French system stabilized systems	incoming short wave	.28–2.8 microns	ten minutes average located on the
	long wave	3.0–50 microns	top of the walkway
	net radiation	net radiation budget	ten minutes average on a boom in front of the ship
	Drakkar microwave radiometer	brightness temperature 23 and 27 Ghz	one minute average on the wheelhouse top
	OCARINA Sodar	vertical velocity backscattering intensity	pulse repetition period 4s range 20–400 m height (stabilized by a gyroscopic system roll and pitch <1 degree)
	minisodar	wind speed and backscattering intensity profile	pulse repetition period is range 14–100 m (located on a stabilized platform) roll, pitch $<.3$ degrees
	accelerometer	vertical acceleration	on each platform (Sodar and minisodar)
	tethered ballon	pressure, humidity temperature, wind and temperature structure function profiles	sampling 10 s
	sea surface photographs (ION canon system)	sea state (% breaking)	one picture every minute one observation lasts 50 minutes recording on magnetic diskette
	radiosondes	pressure, temperature humidity, wind profiles	launch every six hours from 23:00 hour U.T.C.
	Pommar	pressure, temperature humidity, true wind speed and direction, clouds	at 19.5 meters height upon the level, every three hours

TABLE 2
Description of the different buoys used.

In Charge of characteristics	type of buoy	estimated parameter	
CETP	drifting hydrophone	wind speed, percent of breakers	spectrum of noise and noise variance computed and recorded on board
METEO FRANCE	5 drifting buoys	a 100 m depth bathytermic chain	wind estimated at ≃3m height. data transmitted via Argos system
	three with surface wind wind swell drifting buoy "spear"	wave spectrum	H1/3 is estimated and data transmitted via Argos system

2.1.2. Balloon and Aircraft Measurements

Constant Volume Balloons. The constant volume balloons (CVB) are spherical balloons, 1.6m in diameter, composed of a polyester sheet of 75 micrometer thickness. They are filled with helium, and pressurized in such a way that the balloon internal pressure exceeds by 70 hPa the environmental pressure at the mean flight level (Benech et al., 1987). The balloons describe the vertical currents in the atmospheric boundary layer, and are equipped with radiosondes to estimate wind, temperature and pressure. During SOFIA CVB were launched from Santa-Maria island (36.96 N, 26.15 W) and tracked along trajectories of about 50–70 km to document the island wake. The data analysis requires as a first step a physical interpretation of the balloons behaviour, mainly in order to deduce the true vertical air velocity. The MABL can then be described through its "lagrangian" and "eulerian" properties, by combining ballon and aircraft measurements.

Aircraft. Two instrumented aircraft were flown during the SOFIA experiment: a Merlin IV of the French Meteorological Office (Meteo-France), and a Fokker 27 "ARAT" (Avion de Recherche Atmospherique et de Télédétection) of INSU (Institut National des Sciences de l'Univers). Concerning the "in situ" measurements of dynamical and thermodynamical variables, both aircraft have the same capabilities, but with different measurement systems. The airbone data used in this paper were gathered by the Fokker 27. Its main characteristic was a boom, 6m long, on the nose of the aircraft, on which were installed the fast response sensors for turbulence measurement: the dynamic pressure, as well as the attack and sideslip angles were measured by a Rosemount 858 probe. Moisture fluctuations were deduced from a Lyman alpha hygrometer, calibrated against a dew-point hygrometer. Temperature was measured by a "classical" Rosemount 102–E2 AL probe. The aircraft speeds, attitude angles and angular velocities were provided by an Inertial Navigation System (INS) (mechanized platform SAGEM, Société Applications Générales Electricité Mécanique). After filtering, most of the turbulence signals were obtained at a rate of $16 s^{-1}$, which, considering the typical airspeed of the aircraft (about 80m/s in the boundary layer), corresponds to a spatial resolution of 5m. Aircraft measurements gave then access to the horizontal mean wind, and to the mean temperature and moisture along the aircraft track and also to the fluctuations of the three components of the wind, temperature and moisture, from which the turbulent fluxes of momentum, sensible heat, and latent heat can be computed using the eddy-correlation technique.

CNRM Meteo-France has also tested its new FSSP to document the drop dimensions of non precipitating clouds.

Airbone remote Sensing Systems. To analyze cloud structure the LOA has used the POLDER (Polarization and Directionality of the Earth's Reflectances) system, which is a new instrument designed for the global observation of the polarization and directionality of solar radiation reflected by the earth surface-atmosphere system. This instrument concept will be launched on the Japanese ADEOS platform scheduled in early 1996. This concept is evaluated using an airborne version of POLDER. The advantage of POLDER compared to previous current radiometers are: 1) its polarized reflectance in the visible and near-infrared part of the solar spectrum and 2) a surface target reflectance from about 10 directions during a single pass.

The POLDER radiometer is based on the simple concept of the association of a CCD (Charge Coupled Device) matrix detector, a rotating filter wheel and a wide of view optics, with a maximum of 114°.

During the SOFIA/ASTEX campaign the airborne version of POLDER (on board the ARAT Fokker F-27) has worked in "cloud Study" configuration. The rotating wheel supported 3 unpolarized and 2 polarized filters (3 polarization directions for each of them) with spectral band selected to meet the mission requirement: 4,43 μm and 8,65 μm for polarized filters and 7,63 μm, 7,65 μm and 9,10 μm for unpolarized ones.

The airbone backscatter lidar instrument LEANDRE, has flown on board the ARAT to document the vertical structure of the marine boundary layer and clouds. The lidar measurements are taken either at nadir or zenith. Switching from one configuration to the other requires less than one minute. Cross-track scanning is available at nadir (maximum scan angle of $\pm 15°$), according to the measurement objectives.

The two working Nd-YAG laser wavelengths are in visible and near infrared (0.53 and 1.06 mm respectively), allowing to use both molecules and particles as targets, to fulfill the scientific objectives underlined in the following sections. Two detection channels are used simultaneously, one for each wavelength, and an additional channel is for depolarization measurement at 0.53 mm. A depolarization factor gives information on particle shape and cloud thermodynamics (water droplets versus ice crystals). The lidar vertical resolution is 15 m for the three channels (s and p polarization at 0.53 mm and 1.06mm). In addition, a 1.8m resolution channel over a 1000 m-window is available on the 0.53mm s-polarization channel. The lidar pulse repetition rate is 9.5 Hz. Usually, the measurements are made of an average of 4 pulses, which corresponds to an horizontal sampling of about 35 m (it depends on the aircraft velocity which is around 85 ms^{-1}). Taking into account the transceiver characteristics and a flight altitude around 4.6 km, the lidar footprint at ground, averaged over 4 shots, is about 50 m along track and 20 m cross track. The two pulses at the lidar wavelengths are slightly attenuated by scattering from clear air and aerosol particles in the free troposphere, and slightly to moderately in the boundary layer. The lidar radiation can penetrate cirrus and thin clouds while the penetration depth is restricted to several tens to a few hundred meters only in clouds like stratus or stratocumulus.

Constant level balloons, airborne systems are used to give a spatial description of the ABL and aircraft passages upon the ship have been made for comparison between local and spatial measurement.

The satellite observation is then used.

2.1.3. Satellite Measurements

Meteorological satellites. During SOFIA/ASTEX, the following air-sea interface parameters were calculated at CMS from NOAA/AVHRR and Meteosat data: SST, surface solar irradiance, cloud types and downward longwave irradiance. In addition, a daily structure analysis was performed on nighttime AVHRR data (Brisson et al., 1993). Table 3 describes the main characteristics of the retrievial of these parameters during the campaign. These parameters were calculated on a fixed latitude-longitude grid bounded by 26.99 N, 40.3 N, 14.97 W, −30.01 W (external limits). A real time calculation at the finest space resolution was performed on the CMS main computer as oftenas possible. All further processing including the interactive ones, have been made on a dedicated workstation

Sea Surface Temperature. SST was derived from AVHRR data using a split window expression completed by a satellite zenith angle dependent correction term. Details about this algorithm and its validation are described by Antoine et al., 1992. During ASTEX, the same algorithm was used for both day and night for NOAA11 and NOAA12. An example of a composite SST field (from June 5 to 11, 1992) is given in Figure 2.

Nightime AVHRR data were analyzed on a dedicated workstation, the two main tasks of this analysis were to correct the automatic cloud mask and to interpret and draw the sea surface frontal systems. Real time SST analysis of the Azores front was indeed requested for comparison, however particular meteorological and ocean surface conditions during SOFIA/ASTEX: cloudiness, weak thermal signature of the Azores front, made this task particularly difficult to achieve.

Surface solar Irradiance. Surface solar irradiance fields have been derived from METEOSAT visible radiometer data using a physical method similar to that presented by Gautier et al., 1980. The downward longwave irradiance was calculated with an algorithm based on combined use of satellite data (for cloud types) and numerical weather forecast models (surface air temperature and humidity; Le Borgne and Marsouin 1988). The methods used to calculate the surface irradiances during SOFIA/ASTEX are described by Brisson et al.; 1993.

Cloud Classification. The CMS algorithm uses a clustering technique (Desbois et al. 1982, sèze and Desbois 1987) to partition the data into classes representative of

TABLE 3

Characterisitics of the air-sea interface parameter retrieval at CMS zone: 40.03 N, 26.99 N, – 30.01 W, – 14.97 W, June 1992.

Parameter	space resolution (in degree)	field size (pixels* lines)	status (at CMS)	time sampling	satellite	delay between satellite data acquisition and product availability	non satellite data used
sea surface temperature (TSM)	0.02	752*652	operational since 1989	4 times/day	NOAA 11 and 12	12h to 24h	none
surface solar irradiance (ES)	0.04	376*326	operational since 1989	hourly	METEOSAT	1h	integrated water vapour content (climatology)
downward longwave flux (RA)	0.08	188*163	under development	hourly	METEOSAT	6h	predicted air temperature and humidity (EMERAUDE)
cloud types (CL)	0.08	188*163	under development	hourly	METEOSAT	1h	none

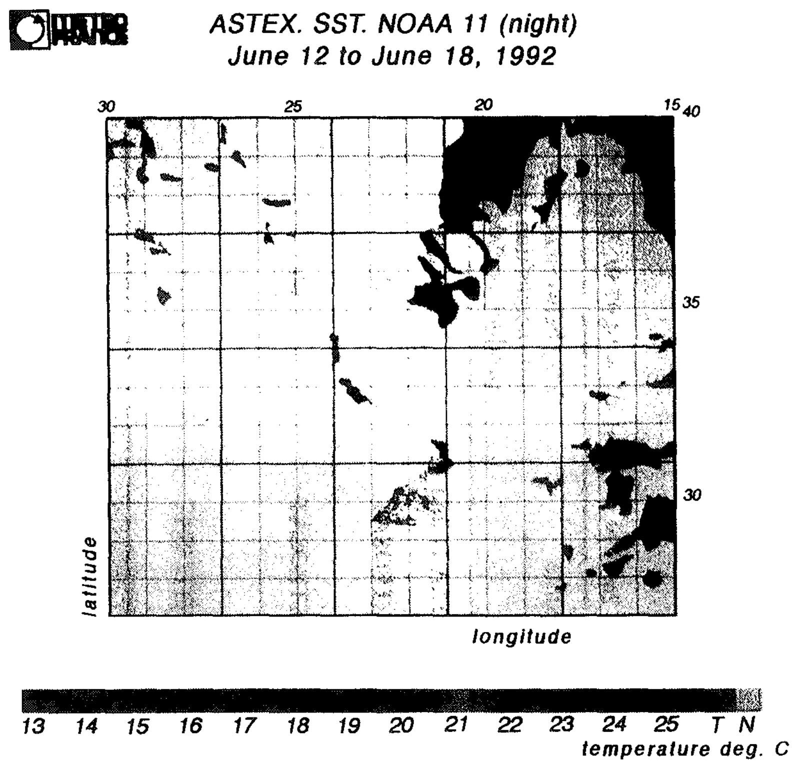

FIGURE 2 SST obtained by CMS (METEO FRANCE) Lannion from NOAA12 (nocturnal orbits). (see color plate XII at the end of this issue)

the surface or cloud types: surface, cloud edges, thin cirrus, high thick clouds, low stratiform clouds, low cumuliform clouds and medium clouds (Bellec et al. 1992). This cloud classification was performed hourly in real time at the 0.08 degree resolution; see Table 4.

Experimental Satellites. Data from satellites ERS1 and SPOT were collected during the experiment. ERS1 was used for surface wind estimates, SST to be compared with in situ measurements and for atmospheric water vapor content or liquid water content to be compared with Drakkar.

Six SPOT scenes were acquired during the SOFIA/ASTEX Intensive Field period of observations for analysis of cloud structure to be compared with the airborne systems (Polder and Leandre): two scenes on June 1 and four scenes on June 17 were all centered near (36.2°N, 23.5°W).

TABLE 4

Contribution coefficients as a function of the cloud type.

cloud type	clear sky	cloud edges	thin cirrus	thick cirrus	high thick cloud	low cumulus	low stratiform
contribution coefficients	0	0.26	0.41	0.53	0.69	0.58	0.70

2.2. Strategy of Use of the Different Intrument of the Central Cell of SOFIA

we briefly describe here how each group of instruments is used.

Shipboard Instruments: ship (Le Suroit) From several different platforms different flux estimates were obtained. To test the validity of the different estimates and to explain the probable reasons for discrepancies, a surface and in the boundary layer structure descriptions are needed: the tethered balloon was used to the latter end, but data at heights lower than 30 meters height are contaminated by the ship.

Fluxes are dependent on the surface roughness. To investigate this dependency a video camera recorded pictures from which the surface properties were determined (breaking occurence, distance between breakers, etc.). Thus, very locally we have obtained observations to help the understanding of parameterization and measurement of fluxes.

Measurements of SST and oceanic temperature profiles obtained from the drifting buoys will be used to retrieve heat flux in the ocean and we hope to validate budget measurement of fluxes.

The lower part of the MABL below approximatively 100 m height was only documented with the minisodar (Weill et al., 1986). During SOFIA/ASTEX the 2000 Hz Sodar range was limited due to the low level of thermal turbulence above 100 m. Nevertheless, tethered balloon profiles and radiosondes were used for complete acoustic sounder data and to document the vertical structure of the boundary layer.

Radiosonde data were transmitted to the GTS network, and 0.5 Hz sampled data were also used as a complement to the tethered balloon vertical profiles in the lower part of the MABL.

Measurements from the microwave radiometer Drakkar correspond to brightness temperature mainly related to the water vapor content of the atmosphere in the absence of clouds. This water vapor content will be compared to integrated humidity from radiosondes and satellite data (ERS-1, SSMI). With Drakkar data, cloud liquid water content is also estimated. This estimate needs comparisons with POLDER and satellite-deduced liquid water contents. The time evolution of water vapor and cloud water contents is also a domain of interest in the analysis of the relations between the atmospheric water content and surface evaporation.

Hydrophone Noise: Acoustic noise estimates provide wind speed at different spatial scales and the sea state and has already been examined in relation to sea surface pictures, (Dupuis et al., 1993).

Aircraft Measurements: ARAT from INSU (with Leandre (the airborne lidar) and the meteorological and micrometeorological package) and MERLIN IV from METEO FRANCE (during two days) provided boundary layer information at different horizontal scales and hence help in the analysis of the spatial variation of MABL parameters documenting the MABL inhomogeneity.

Cloud structure and boundary layer characteristics determined with Leandre correspond to different scales of observations, but document mainly the mesoscale; they are complemented by smaller scales informations determined with POLDER which used during ASTEX the following working characteristics.

Cloud top temperature is a major parameter of the cloud radiative forcing. So, this parameter is needed for the characterization of the cloud cover and for climate studies. A method based on a differential absorption technique has been used to retrieve the cloud top pressure during SOFIA/ASTEX. It makes use of the ratio of two radiances measured in the A-band absorption of the oxygen. The first one is a narrow band of 0.10 μm width centered at 7.65 μm. This ratio is sensitive to the oxygen amount along the optical path, which is related to the cloud top pressure. With this method, an accuracy of a few tens of hPa is expected for the estimate of cloud top pressure, provided that the cloud layer has an extent significantly larger than the pixel size.

Another parameter of the cloud radiative forcing is the cloud optical thickness, which is directly related to the vertically integrated liquid water content and to the size of the cloud particles. Using the capability of POLDER to measure the radiances reflected by cloudy surfaces from several directions, it is possible to retrieve both the cloud bidirectional reflectance distribution function (BRDF) and the cloud optical thickness (from 4.43 mm and/or 8.65 mm bands).

The Wave Buoy. It is considered as fundamental to document the form drag at the sea surface and the wave spectra. In the analysis of friction velocity from the minisodar data (if it is possible) and also from other instruments (sonic anemometer) a relationship to the observed wave spectra is an analysis objective.

The Drifting Buoys. Drifting buoys are used to provide oceanic mixed layer vertical profiles and to document the mixed layer depth evolution. SST obtained from these buoys is very important and needs comparisons with ship SST estimate, aircraft and satellite estimates.

Satellite Data. The different satellite observations collected during SOFIA/ASTEX are now analyzed in relation with the observations collected during SOFIA from the ship, the buoy and the aircraft for the different analyzed variables such as wind, waves, SST, fluxes and cloud structure. We are mainly concerned with METEOSAT, SPOT and ERS1, but also with SSM/I, LANDSAT and NOAA. The problem of cloud structure involves the analysis of LANDSAT and SPOT scenes observed also from airborne systems as POLDER and LEANDRE.

SOFIA/ASTEX has given an opportunity to test and validate algorithms and techniques for the retrieval of some air-sea interface parameters from operational meteorological satellite data. Preliminary validation results have been obtained by comparing satellite sensor estimates with pyrgeometric or pyranometric measurements made simultaneously aboard the IFREMER ship *Le Suroit*. In situ measurements integrated over 1 hour have been compared to the calculations spatially integrated on a 0.3 degree × 0.3 degree box centred on the ship position. The results of this comparison are given on Figure 3a) and b). Figure 4 shows also wind speed and wave height estimates from IFREMER CERSAT in the region during SOFIA obtained from ERS1 altimetry.

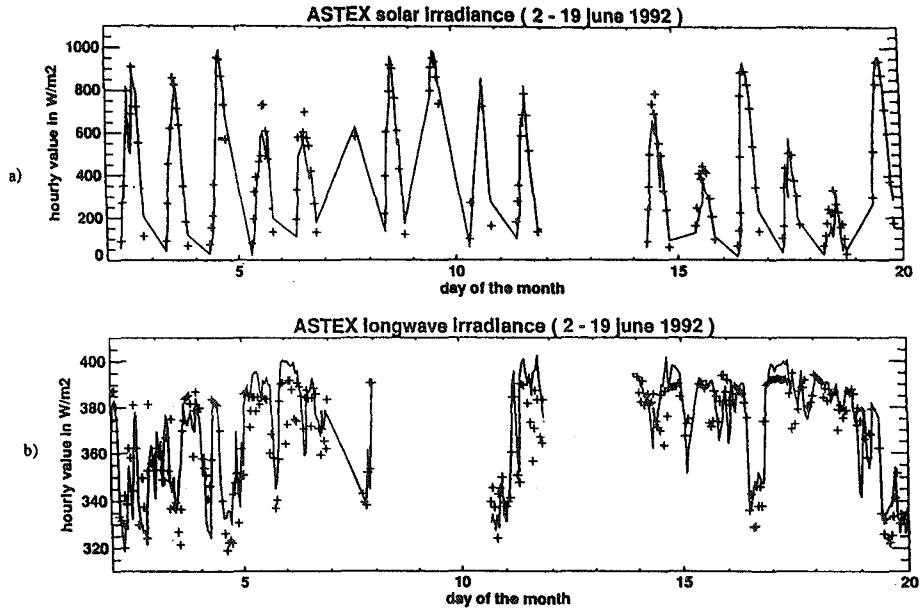

FIGURE 3 a) ASTEX solar irradiance estimated in a 0.3 degree × 0.3 degree domain centered around *Le Suroit* (satellite estimate) compared to *Le Suroit* measurement. b) the same for long wave solar irradiance. Data from CMS (METEO FRANCE). Solid line and crosses represent the ship measurements and the satellite sensor estimates, respectively.

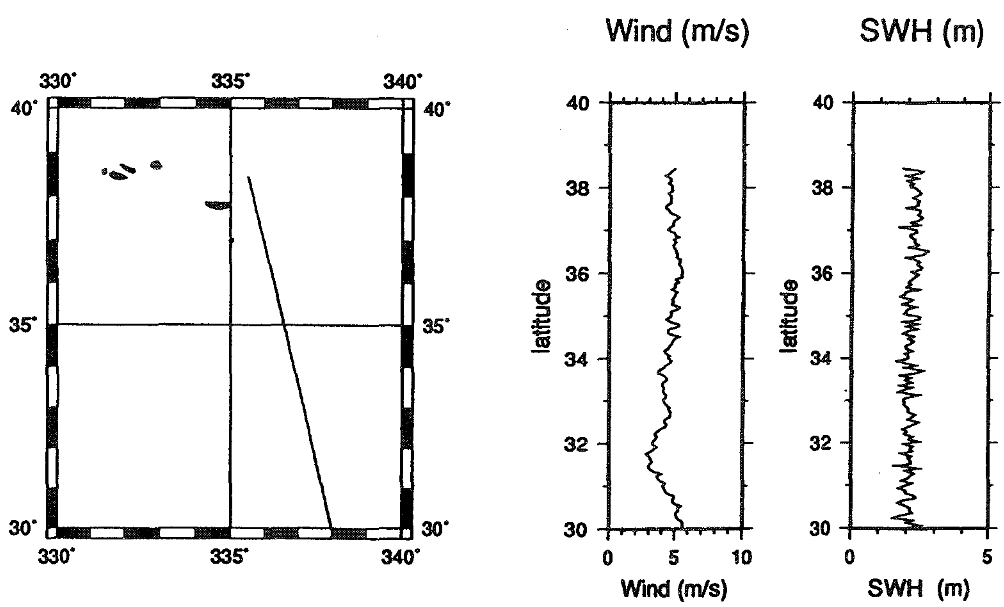

FIGURE 4 Example of ERSI estimate of sea significant wave height (SWH) and wind speed from altimetry on June 19 in the ASTEX region (data from IFREMER). The swath is indicated on the left.

3. OVERVIEW OF THE WHOLE EXPERIMENT

From May 31 to June 10 high pressure was centered over or to the west of the work area resulting in a northeasterly to northerly wind varying between 4 to 8 m/s. Until June 4 the air was relatively dry with 3 to 4/10 cumulus and stratocumulus, increasing to 9/10 in the afternoon of June 2 and 3. Moister air followed a weak front on June 4 with 6 to 10/10 cloud cover and light rain and showers (drizzle) on June 6.

After a cold front passage on June 8, a dry airflow from the west or northeast and small cloud amounts continued until a warm front passage on June 10. Hence the high pressure region on the south became centered over the work area. Wind speeds were below 5m/s and became northerly on June 11, then turned from northeast on June 12 and 13. The anticyclone continued to move north from June 15 to June 21. It was located at the north of the work area resulting in a 5 to 10 m/s wind from east or north east. The airflow was generally warm and moist, and there was extensive cloud cover. From June 22 to June 27 different meteorological situations were observed with generally extensive cloud cover. On June 27 small cumulus occurred in the lee of Santa-Maria but it was relatively clear air in the open sea region.

We notice indeed, that during ASTEX the Azores anticyclone was not stationary.

Rather than presenting all the meteorological charts, we show only synoptic charts of two days characteristic of the perturbed situations that we have met and which will be discussed further, (Figure 5). June 8 was a cloudy day with a small

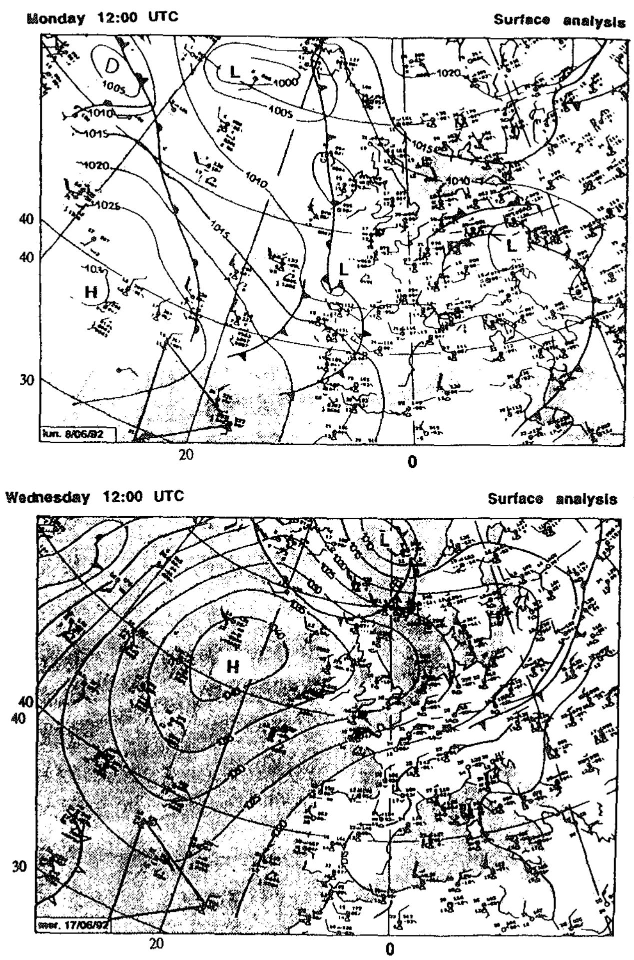

FIGURE 5 Meteorological chart of June 2 and June 14 representative of the different situations met during ASTEX: an anticyclonic situation (the Azores anticyclone and frontal passages): a relatively uncommon situation relative to climatology.

amount of clouds during which the Astex triangle was close to the anticyclone centre; on the contrary June 17 was associated with deeper clouds and the Astex triangle was at the edge of the Azores anticyclone.

Figure 6 (a and b) gives the trajectory of Le Suroit during the experiment and the surface meteorological conditions. Figure 7 illustrates radiation variations during SOFIA which shows that besides clouds the visible solar energy input is relatively large and Figure 8 shows that the SST variation is relatively low. Note on Figure 8 that the SST difference between two methods used on board *Le Suroit* do not exceed 0.4 °C. During the experiment, the wind speed was low and the sea was not expected to be very rough, though whitecapping was often observed, except around June 15–16 when the wind speed was stronger. Figure 9 gives the percent of breaking determined with the video camera (see table 1) using automatic software. Sea state is in fact determined with a set of fifty pictures taken at a rate of once per minute, concurrent with the hydrophone measurements.

Trajectories of the drifting buoys during the experiment (Figure 10) indicate the presence of an oceanic vortex which is probably a part of a meander. Figure 11, obtained from one of these buoys on June 10 characterizes temperature profile as function of depth and time. Note the SST variation across the meander at the .50 m depth level. SST was also computed from METEOSAT data by CMS (see Figure 2)

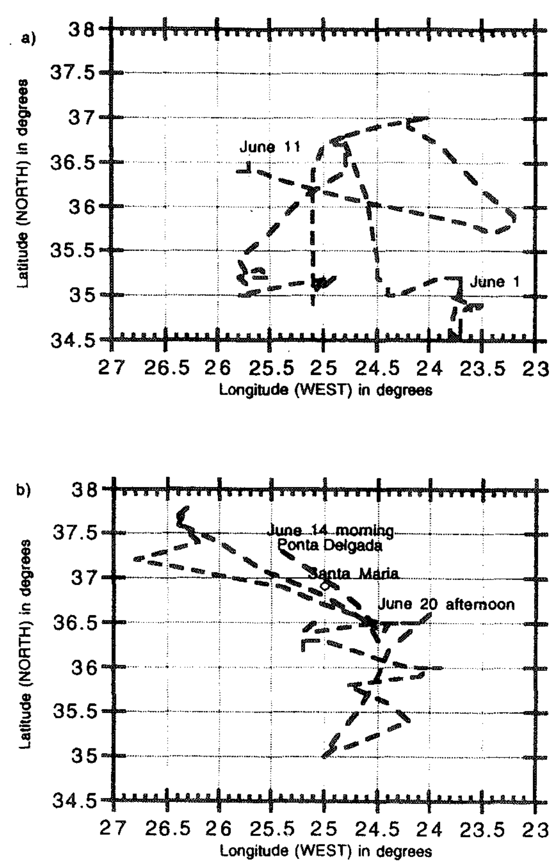

FIGURE 6 a) Le Suroit trajectory from June 1 to June 11. b) Le Suroit trajectory from June 14 to June 20. Notice that the day time trajectory are generally in front of wind.

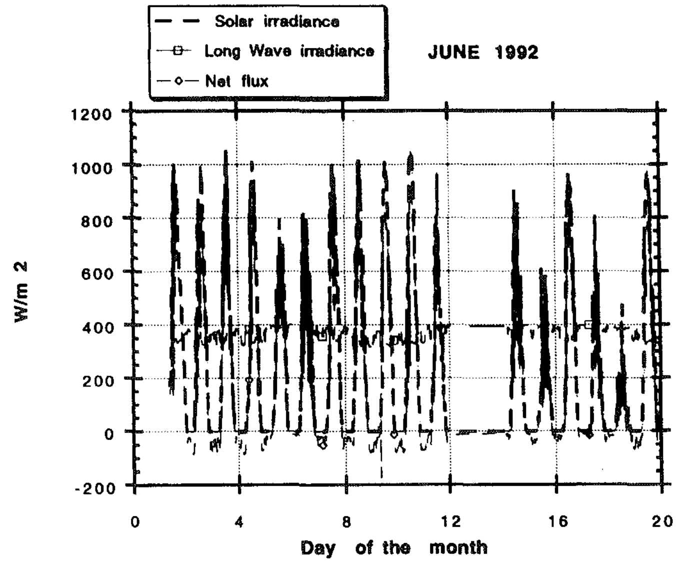

FIGURE 7 Incident solar flux, incident long wave flux and net radiation flux measured on board during SOFIA/ASTEX.

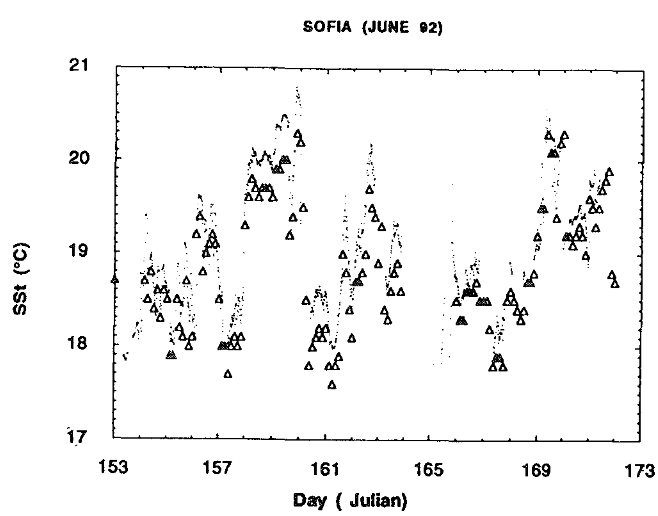

FIGURE 8 SST estimates during SOFIA on board Le Suroit: triangles Rennell Centre estimates, knots POMMAR system observations every three hours.

and validation was performed on a routine basis over the whole acquisition zone but the validation also involves specific comparisons with other SST estimates from ASTEX data.

Fluxes are estimated during the experiment on Le Suroit using bulk parametrization (Large and Pond, 1982) and compared to measurements using the inertial-dissipation method are presented on Figure 12. The latent heat flux is near 100 W/m^2 and the sensible heat flux is very small, close to a few ten of W/m^2. Hence a consideration of the net daily radiation radiation budget implies an input to the ocean of a around 9MJm^{-2} per day. The bulk formulae have been applied to the different instruments measuring mean meteorological parameters on board Le Suroit, (see Table 1) to get

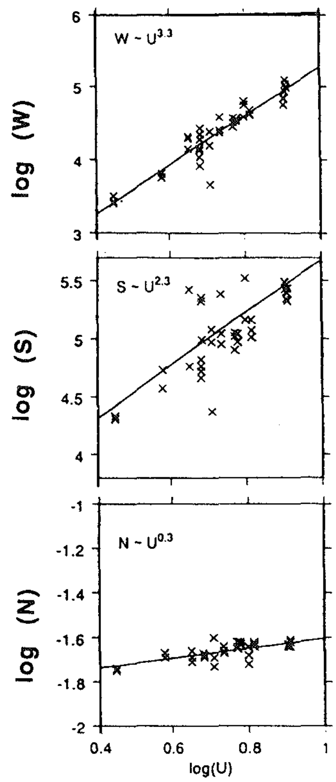

FIGURE 9 Estimate of (a) foam coverage (W%), (b) mean surface covered by foam S and (c) the number of breakers N: the estimate has been validated using video camera observations.

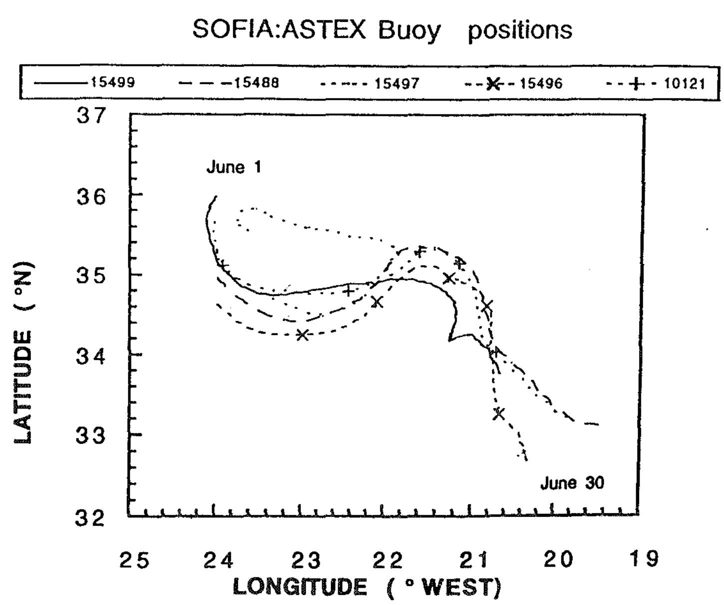

FIGURE 10 Position of drifting buoys during SOFIA/ASTEX showing a meander. Data from CMM (METEO FRANCE).

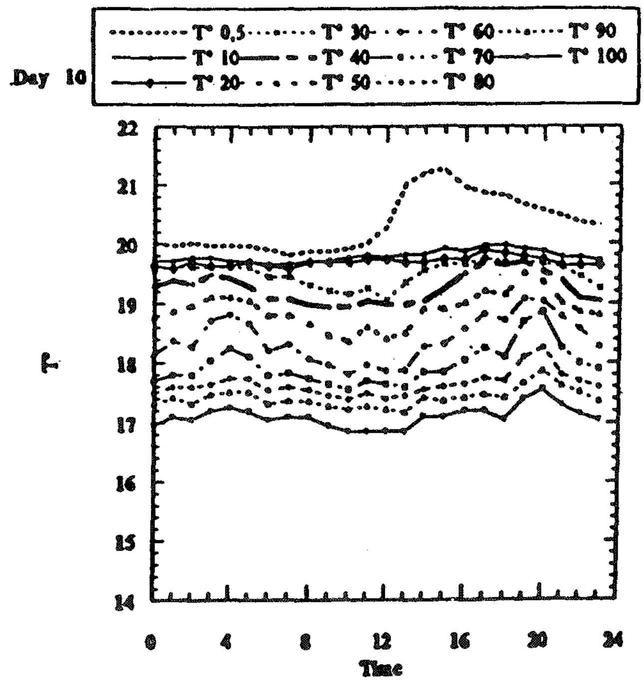

FIGURE 11 SST and depth of the oceanic mixed layer change accross a meander (from CMM (METEO-FRANCE)).

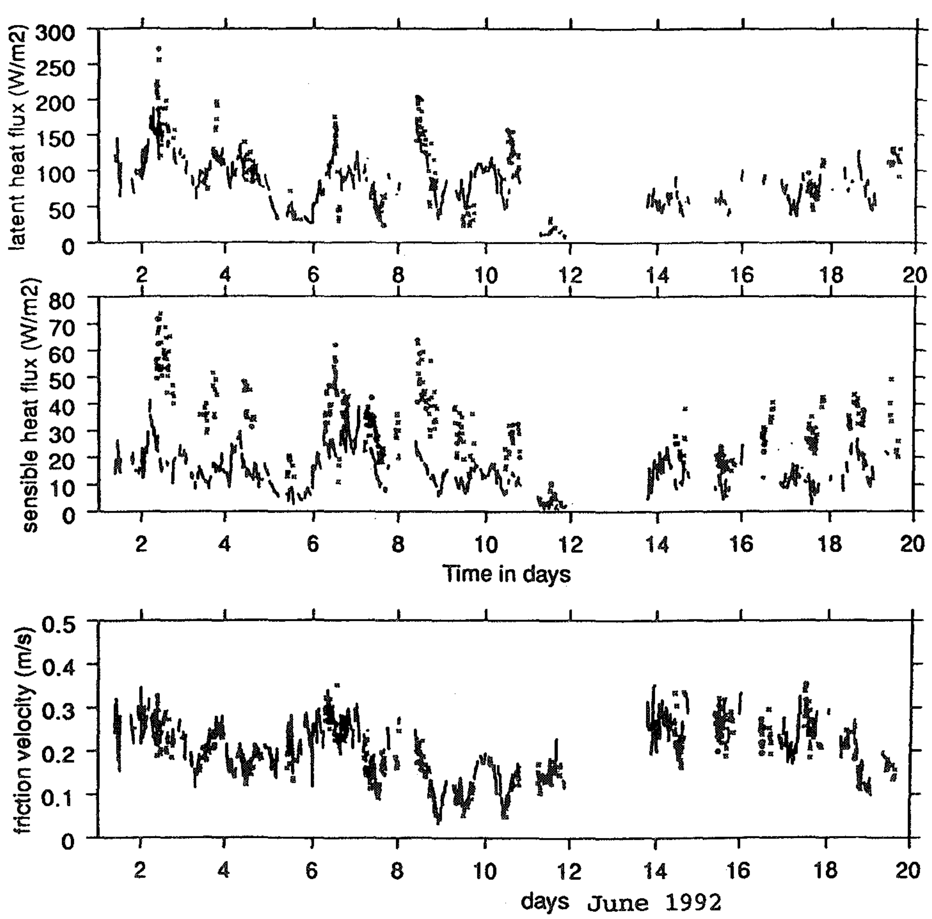

FIGURE 12 Fluxes estimated during SOFIA/ASTEX on board Le Suroit: crosses are inertial-dissipative estimate and continuous line are bulk estimates. The large difference between the two methods for the sensible heat flux has been found to be related to salt contamination to the inertial-dissipative method.

flux. Taking into account on the SST uncertainty, the uncertainties in the flux estimation are less than 20%. The largest discrepancy between bulk and inertial – dissipative method has been found for sensible heat flux. It seems to be related to salt contamination in the inertial – dissipation measurement, the bulk estimate being probably correct when compared with aircraft estimates.

4. JUNE 8 AND 17 OBSERVATIONS

These days have been choosen as priority days since they correspond at first to different aspects of the MABL and intensive observations have been undertaken; secondly because some particular phenomenae have been identified and analyzed. Some observations corresponding to these days are preliminary but they give the outlines of research undertaken.

June 8 Observations. The typical meteorological situation was characterized by a frontal disturbance accompanied by mesoscale forcing (Figure 5a.). This mesoscale situation is characterized by a wind blowing from north to north-east in the boundary layer, variable in strength, but always below 10m/s. The profiles of potential temperature and wind speed estimated from radiosoundings on board *Le Suroit* for the hours of 00,12 and 18 UTC (Figure 13) show advection in the boundary layer both in temperature, humidity and wind during the day. The mixed layer was rather deep for this day compared to the others during the experiment. The surface layer extent was determined from the radiosonde on the measurements of temperature and humidity and not from the wind, which is observed from the tethered balloon and minisodar observations (Figure 14). Indeed, at 12:00 UT the lapse rate in the lowest 50 m is unstable, whereas above m up to 90 m the temperature profile is quite neutral, and hence this layer is well mixed. At 900 m, the wind increases significantly, the temperature profile above is slightly stably stratified, and the wind increases slowly with height up to 1500m where a strong inversion occurs. This inversion marks the top of the clouds, whereas 900 m height can be considered as the top of the mixed layer which develops from the sea surface. Latent heat flux reached 140 W/m^2 in the morning and sensible heat flux was lower than 30 W/m^2 (Figure 15). A possible contamination of the temperature probe is suggested by this figure likewise Figure 36.

On June 8th there were two flights: one devoted to boundary layer clouds, the other dedicated to MABL observations.

1. Flight one: cloud structure and MABL observations

The flight trajectory and the ship location are indicated on Figure 16.

Lidar backscatter ratio at 0.53 mm computed as function of altitude is presented on Figure 17. These data were recorded by the backscatter lidar Leandre on board the Fokker 27 on this day at flight altitude of 4.6 km. On Figure 17 backscattering intensity value slightly above 1 indicate a low aerosol burden, as it is observed in the free troposphere (above 1700m). Two distinct layers are clearly observed: a first layer between the ocean surface and 900 m corresponding to the mixed layer, and an other layer from 900m up to 1700m. A remarkable coherence between radiosounding

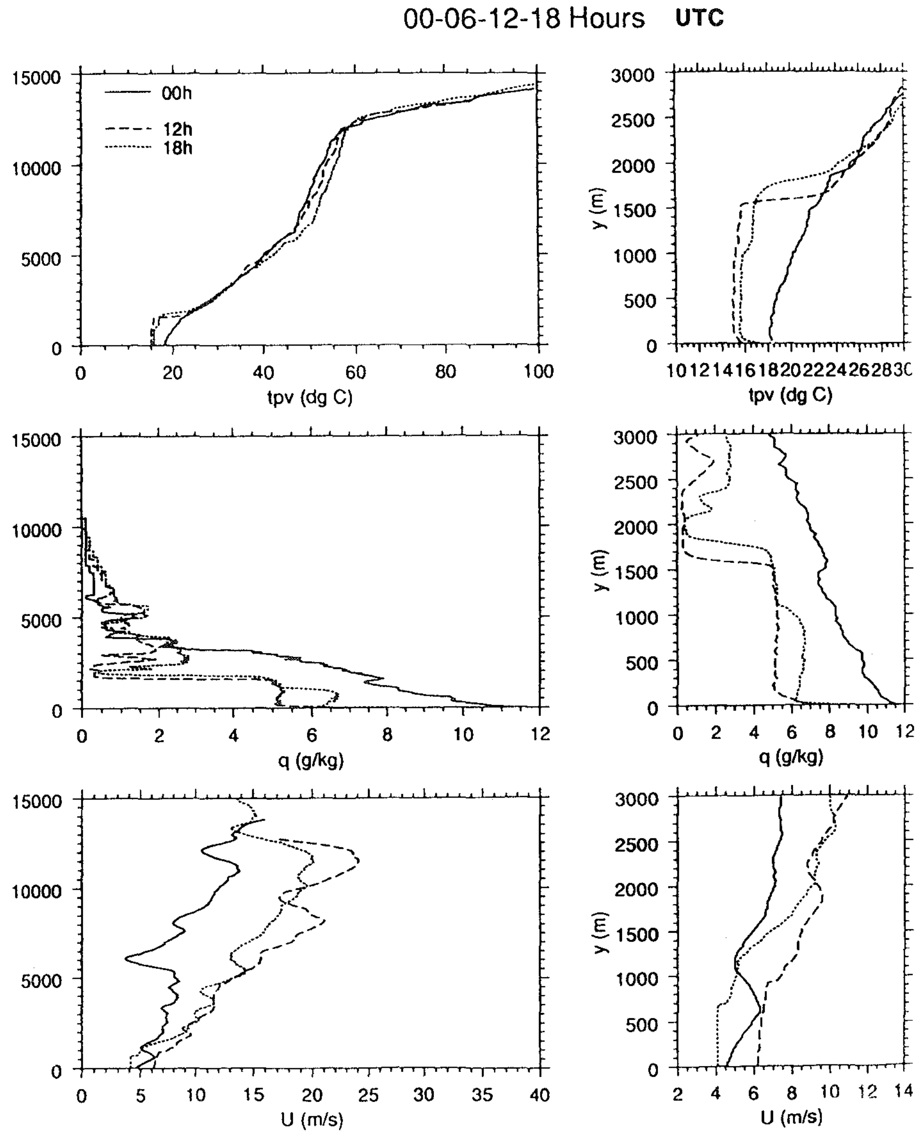

FIGURE 13 Le Suroit radiosounding data for virtual potential temperature (top), specific humidity (middle) and wind wind speed (bottom) on June 8th. Vertical profiles up to 2000 m are shown inside every figure. Solid line 00:00 UT, dashed 12:00 UT and dotted line 18:00 UT.

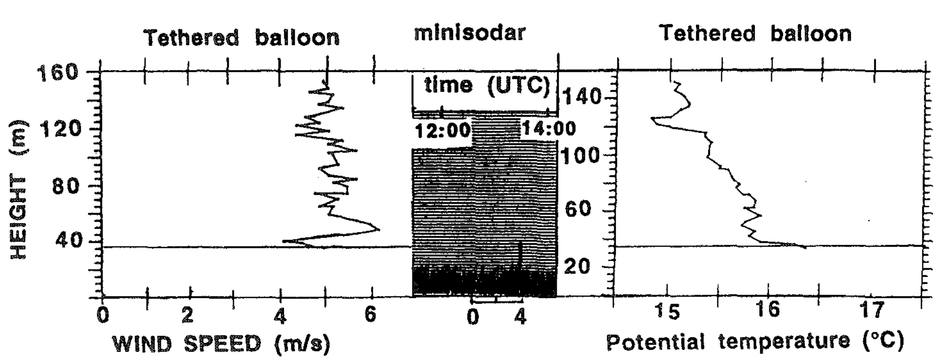

FIGURE 14 Vertical profiles of wind speed (left) and potential temperature from tetheredsonde. Between these profiles, the minisodar backscattering intensity profile is given to show the most turbulent part of the surface layer (maximum backscattering intensity proportional to CT^2). The top of the minisodar turbulent layer is lower than the surface layer as determined by the wind shear.

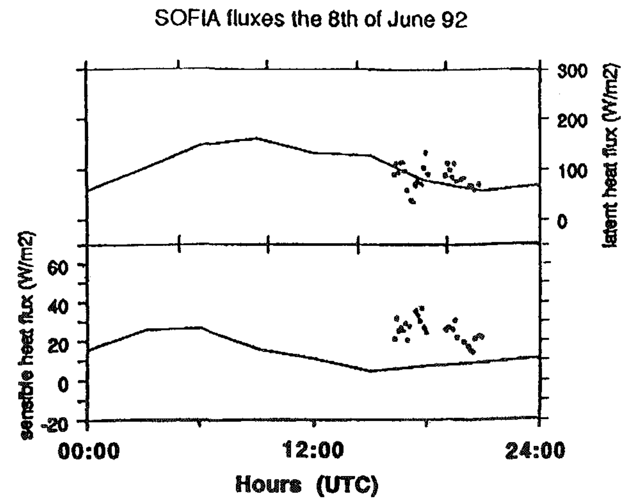

FIGURE 15 Latent heat flux (upper) and sensible heat flux (lower), on June 8th. The continuous line is the bulk estimate (following Large and Pond (1982)). The points denote values by the inertial-dissipative method.

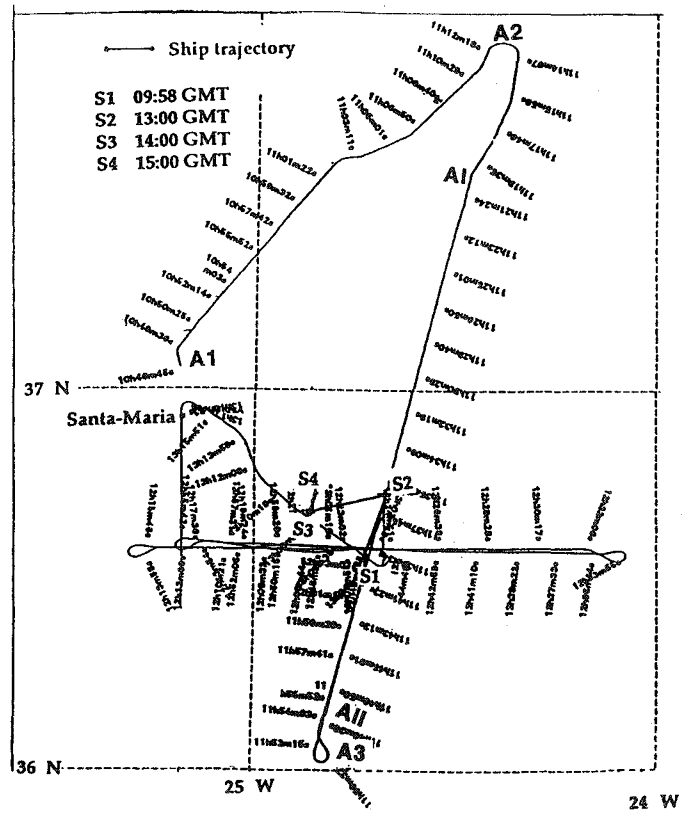

FIGURE 16 Flight trajectory and Le Suroit location on June 8th morning.

information is noticed. The peak value around 1000 m as observed during the flight marks the occurence of a cumulus condensation layer, while a maximum in backscatter ratio at 1600 m marks the synoptic inversion and formation of a stratocumulus layer as recorded before or latter on, during the leg.

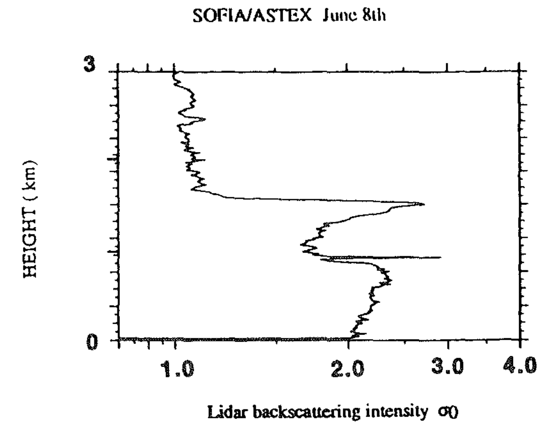

FIGURE 17 Lidar Backscatter ratio profile (at .53mm) on June 8th between 11:15 UT and 11:49 UT.

Indeed during the leg a two dimensional display (Intensity versus time) of a stratocumulus layer and marine boundary layer was observed (Figure 18). The aircraft ground velocity was about 90 m/s. Accordingly a flight time of 100 s corresponds to a 9 km horizontal range. Each profile is an average of sixty lidar shots (6 s horizontal resolution). The stratocumulus top occurs at an altitude of 1700 m at the beginning of the leg, and ends at 1550 m after a 140 km trac. Three large holes occur in the stratocumulus deck during the leg; but the optical porosity of the cloud cover is illus-

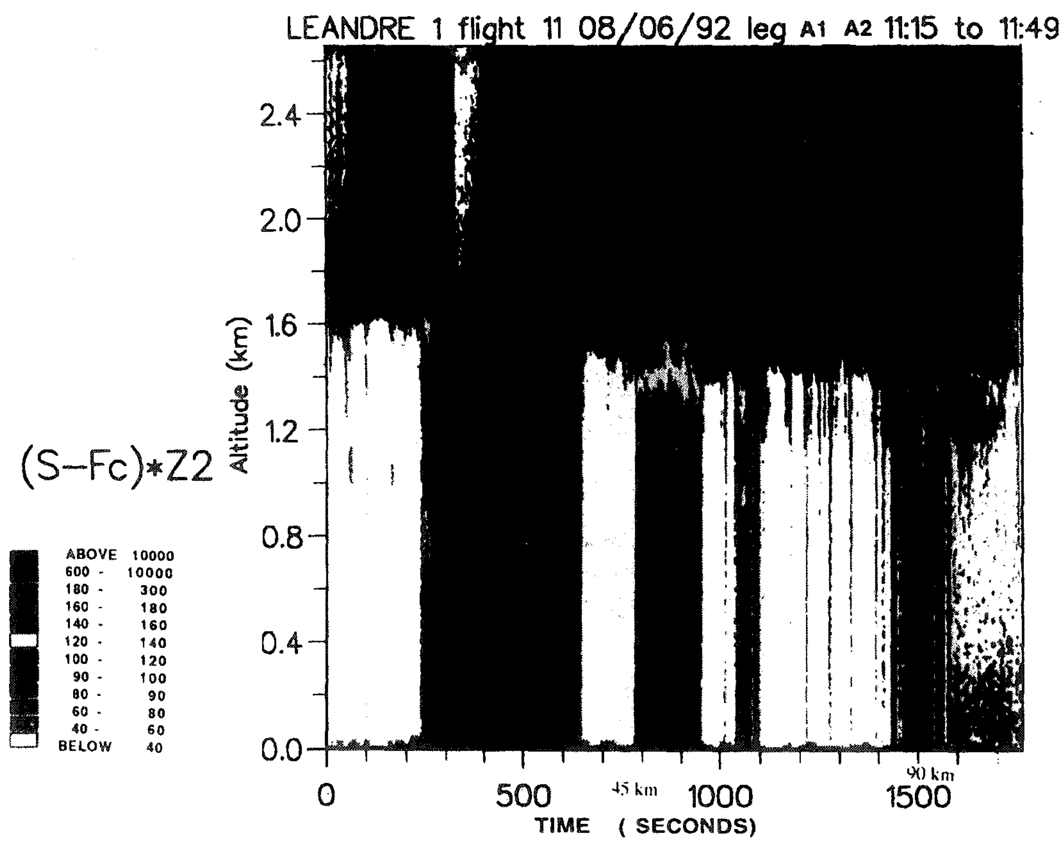

FIGURE 18 Lidar cross-section as function of height during the same period as Figure 6. (see color plate XIII at the end of this issue)

trated by the surface lidar echoes all along the flight track. At the edges of the holes, it is observed that the top of the marine atmospheric boundary layer reaches the bottom of the Sc layer. An analysis of the boundary layer structure in holes, shows two distinct features. During the first cloud free section, between 250 and 600 s, two distinct layers are observed; a layer connected to the surface, the top of which ranging from 900 m to 700 m, and a decoupled layer up to the Sc layer. On the contrary, in the two following cloud free areas; 900–950 s and 1550–1750 s (not presented), the mixed layer extends from the surface to the Sc condensation level without any remarkable feature. The color code represents the range corrected lidar signal at 0.53 mm (in arbitrary units). Hence one obtains units proportional to the total optical power backscattered by molecules, particles and cloud droplets. Therefore the lidar information gives an idea of spatial variability on the trajectory between Santa-Maria and *Le Suroit*.

Considering now the microwave radiometer Drakkar on board *Le Suroit*, it shows a constant level water content along the day (Figure 19) since the brightness temperature is around 28°C, except near 17:00–18:00 where there is a weak increase (not shown here): this increase corresponds to a reduction in latent and sensible heat flux as observed on Figure 15. However, during morning until 14:00 periodic fluctuations are observed with a period of about 20–25 min, corresponding to a wavelength of about 10 km. These fluctuations seem to be associated with thin clouds and were indeed present on the Lidar observations. Of course these observations will an objective of a careful analysis to determine what kind of phenomenae are associated with these observations: oscillations of the whole MABL layer corresponding to waves related to the frontal system passage or forced convection related to wind rotation. NOAA (AVHRR data) from ASTEX are also awaited to document these oscillations.

2. After Flight, Island Wake Flight

Another aspect of the spatial and temporal variability is documented using constant level balloons CVB and low level flights of the F27. Six balloons were launched this

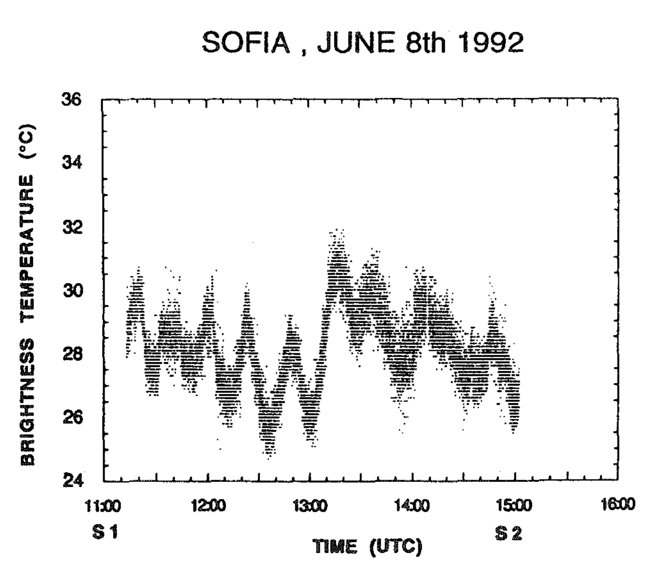

FIGURE 19 Brightness temperature at 36 GHz from the microwave radiometer Drakkar on June 8th. Before 15:00 UT oscillations are observed.

day, two at 10:00UT, two at 14:00UT and two at 17:00UT. Their flight altitude were between 200 and 800m. Figure 20 presents, in a vertical N-S plane, the trajectories of 3 balloons whose equilibrium level was between 200 and 300 m. These three CVB made 2 or 3 vertical oscillations whose amplitude reaches 500 to 600m. These oscillations are localized in the first tens of kilometers from the island, and are damped beyond. These motions are probably due to organized vertical currents which develop in the wake of the island through the whole thickness of the ABL. These features are present from the morning to the afternoon, although they appear to be attenuated when the last balloon was launched. The balloons flown in the upper part of the ABL (not shown here) do not thave similar oscillations: their trajectories are flatter, with vertical range never exceeding 100m. This difference in behaviour can be explained by the structure of the ABL: at 200–3200m (approximately one third of the ABL thickness), the upward vertical velocities were probably strong enough to transport the balloon (against its buoyancy) up to the upper levels. Furthermore, the upward deviations are much greater than the downward, which translates a positive skewness of the vertical air velocity. Then the return to the equilibrium level is due to the balloon buoyancy and, possibly, to downdrafts. In the upper part of the ABL, however, the air vertical velocities are too weak to work against the buoyancy of a balloon and the vertical deviations of the trajectory are small. The vertical structures tracked by the balloons in the wake of the island appear to be persistent through the daytime. Their horizontal length scale is of the order of 10 km, and the vertical velocities of the balloons reach 1 to 2m/s.

The Fokker 27 described 3 horizontal rectangles at about 60m, 400m and 800m altitude, 60 km × 30 km, elongated in the E-W direction. The western half of these

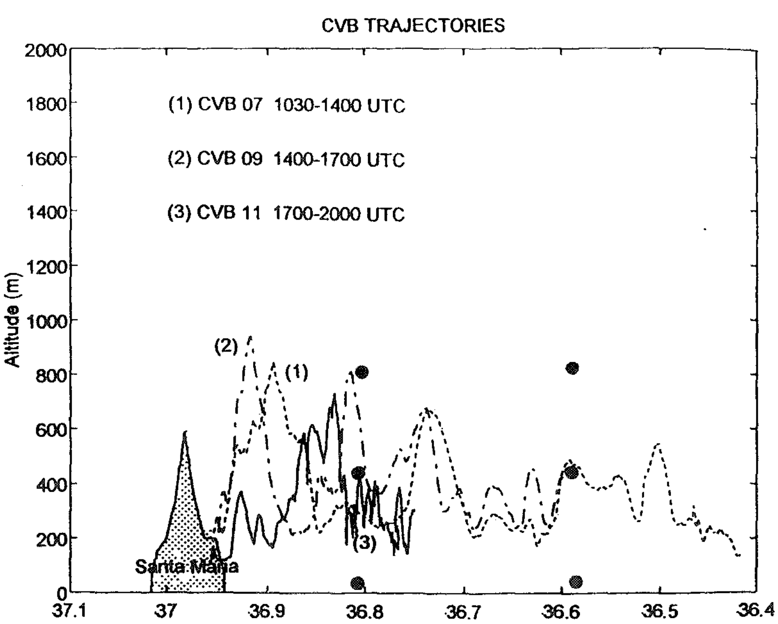

FIGURE 20 Vertical trajectories of the CVB Nr 07, 09 and 11, launched from Santa Maria at 1030, 1400 and 1700UT respectively, in a vertical N-S plane crossing Santa Maria. The relief of the island corresponds to 25.09° longitude (maximum relief). The circles indicate the locations where the aircraft W-E legs cross the plane.

rectangles was on the south of the island, and then in the wake area for a northern wind, as it is was the case that day. On the contrary, the eastern half can be considered as free of the island effects. The ship "Le Suroit" was located in this eastern half during the flight. The aircraft flew during 15:00 to 17:00 UT. Over the flight area, there was a cloud cover by cumulus (Cu) and broken strato-cumulus SC (about 5/10) as previously observed from high level LEANDRE flight. The upper rectangle (800m) was flown under the base of the clouds whose top was no higher than 1600m (inversion level).

Figure 21 presents the horizontal wind calculated along the aircraft track at 60m, 400m and 800m altitude. Each vector is a 10 s average, which corresponds approximately to an horizontal distance of 800 m. In the lowest panel the momentum flux calculated on the E-W axes are noted. In the two upper panels are drawn

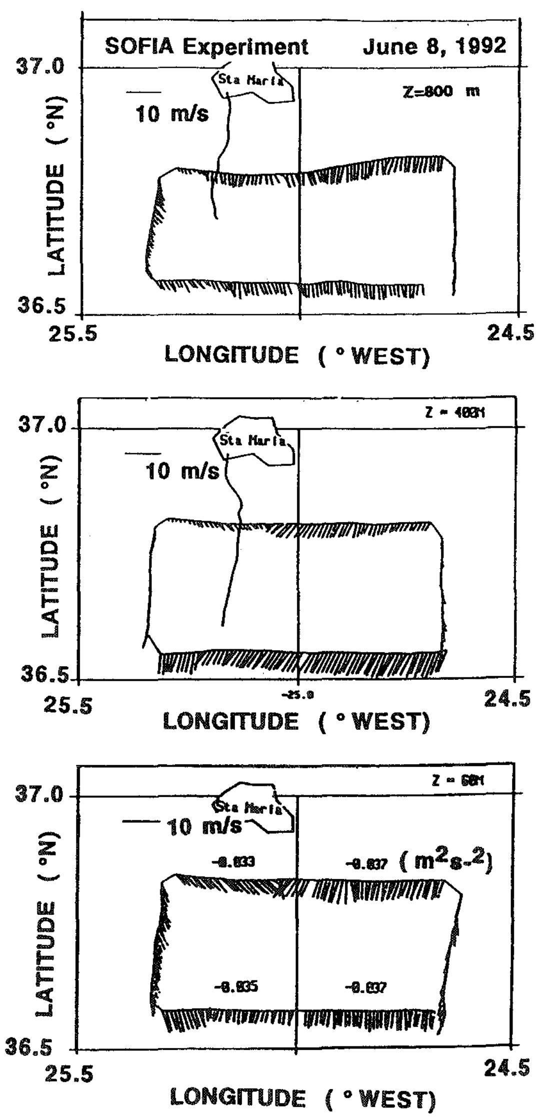

FIGURE 21 Horizontal wind measured along the aircraft track for the three horizontal rectangles; from bottom to top: 60m, 400m and 800m altitude. In the lowest panel the momentum values are typed. The horizontal track of the CVB 09 and that of the CVB 10 are drawn in the middle and upper panel respectively. These two balloons were simultaneously launched at 1400 UT.

the horizontal trajectories of the two balloons which flew during the aircraft measurements: they were launched at 14:00 UT, and their mean flight level was 350m (for the trajectory drawn in the middle panel) and 680m (for the balloon drawn in the upper panel. In spite of being averaged over long periods (300s), these trajectories are meandering, and track the singularities of the flow. The two balloons were simultaneously launched, but followed very different tracks: the lower presents oscillations, whereas the upper is more straight. This behaviour is quite similar to that of the vertical trajectories (Figure 20): those of the upper balloons are much flatter than those of the lowest. So, the structures evidenced by the vertical oscillations appear also on the horizontal tracks.

The horizontal wind plotted along the aircraft track presents two major discontinuities on the W-E axes: the first is located at about 36.8 N-25.07 W and the second 36.6 N-25.2 W. There are large variation in wind direction and/or velocity. These features appear on the 3 planes at approximately the same location but have different characteristics depending on the altitude: at 60 m, there is a strong but localized, horizontal shear, whereas at 400 m the wind vanishes in the whole downstream area of the island. They are accompanied by an increase in turbulence, restricted to the horizontal shear areas. These perturbations in the wind field are closely related to the wake effect of the island, which is confirmed by the much more homogeneous fields in the eastern half of the area. The momentum flux do not present important variations. In fact, as mentioned above, the influence of the wind shears on the turbulence is localized in the restricted area of the shear. So, when calculated by the eddy-correlation method over a 30km leg, the turbulent fluxes are little modified by these disturbances.

The thermodynamic fields are illustrated on Figure 22 and 23 by the potential temperature and the humidity mixing ratio plotted along the aircraft track. On the lowest panel the sensible heat flux (on the potential temperature field) and the latent heat flux (on the moisture field) are also indicated. The sensible heat flux is small but homogeneous except in the wake of the island where the air is warmer. The latent heat flux is larger (75 to 110W/m^2) and is not different from *Le Suroit* fluxes measured at the same moment near 80 W/m^2, and its contribution to buoyancy is of 5 to 7 W/m^2, that is to say approximately the same amount as the sensible heat flux (3–7 W/m^2). Ten W/m^2 is also what is found for the ship with the bulk method. It can also be noted that the highest latent heat flux corresponds to the lowest mixing ratio, whereas the lowest latent heat flux corresponds to high values of moisture. Taking into account that the wind velocity varies little on the lowest plane (when averaged over 30km, which corresponds to the length at which the flux were calculated), this agrees with a bulk parameterization of the latent heat flux. Potential temperature and humidity mixing ratio are negatively correlated at mesoscale: on the two lower planes, the southern edge is warm and dry, whereas the northern one is colder and moister. Furthermore, mesoscale variations are well reproduced from one plane to the other. In particular, the wind horizontal shear on the northern edge is co-localized with the temperature variation. These inhomogeneities could be related to the structures tracked by the balloons in the wake of the island. The upper plane is quite different, where variations in temperature and moisture are larger, and cannot be correlated to the other planes. This is due to the influence of clouds, which act

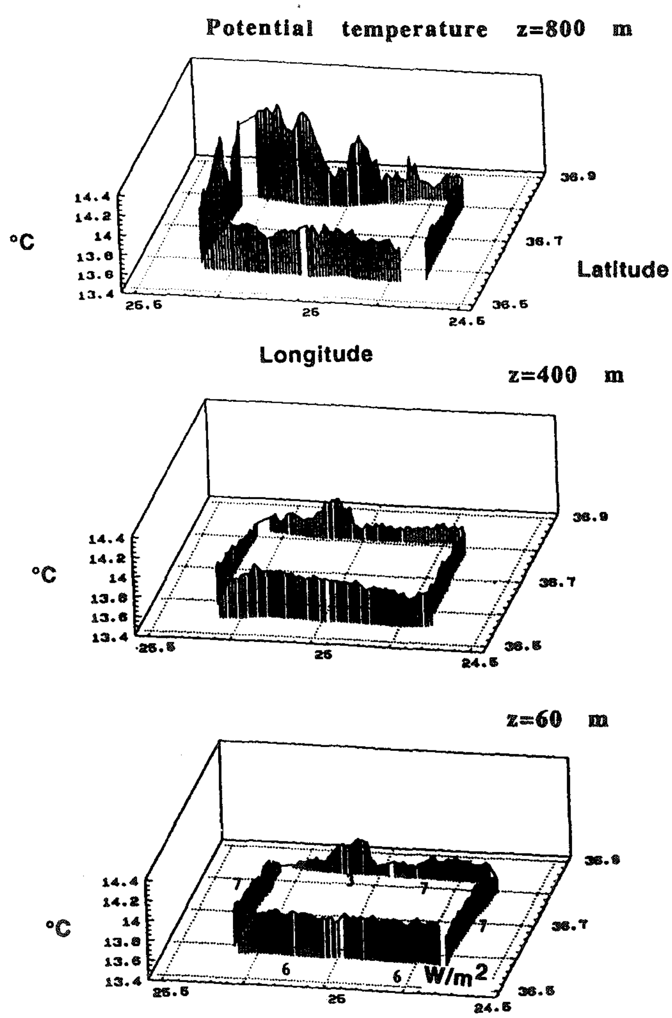

FIGURE 22 Potential temperature field along the aircraft track. Same levels as in Fig. 21. On the lowest level are typed the sensible heat flux values in W/m^2.

on the boundary layer structure. In particular, the warm and dry parcels encountered in the NW corner are probably due to parcels related to entrainment.

The turbulent structure of the MABL is illustrated in Figure 24 which presents the profile of the latent heat flux, as well as the respective contribution of the various components to this flux: moist updrafts ($W^1 > 0$ and $q^1 > 0$), dry downdrafts ($w^1 < 0$ and $q^1 > 0$) and dry updrafts ($w^1 > 0$ and $q^1 < 0$). The first two have a positive contribution to the flux, whereas the latter a negative. In the simple scheme of a convective boundary layer, the first corresponds to buoyancy updrafts which originate from the lowest altitudes, the second to entrained parcels coming from the top of the boundary layer, and the two latter are generally called "environment". For a modeling of the boundary layer dymamics, in simple models (see for instance Randall et al., 1992), or in large eddy simulation models, the knowledge of the relative importance of these various events is of crucial importance. The data presented on Figure 24 are averaged at each altitude over the four legs of the rectangle track of the aircraft. The lower part of the figure represents the fractional area covered by each of the four events (it is assumed that these fractions, computed along the aircraft track, can be

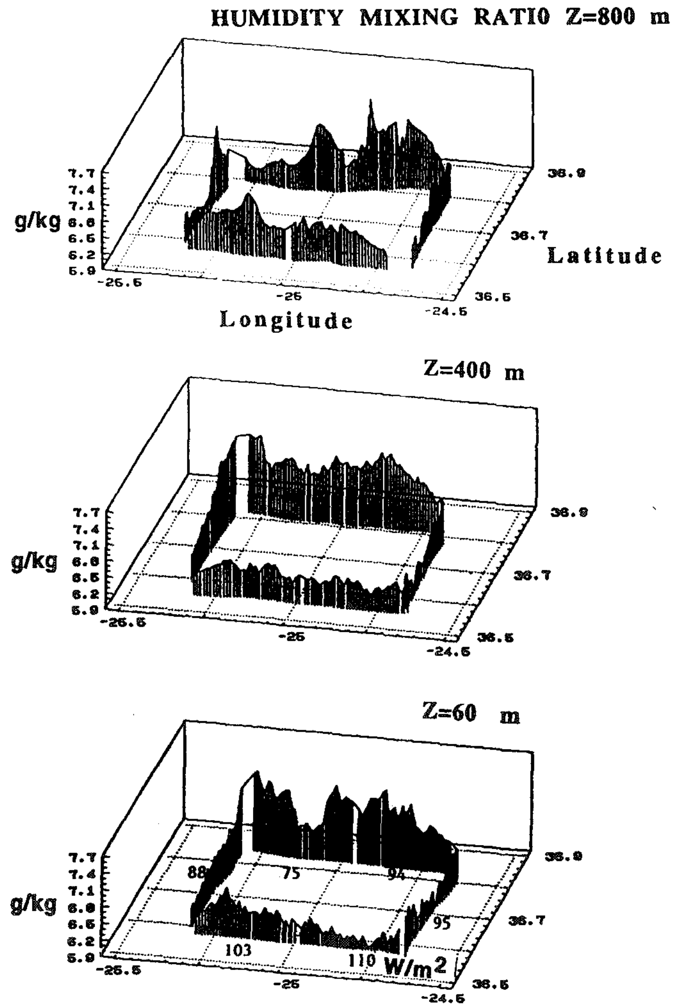

FIGURE 23 Same as Fig. 22, but for humidity mixing ratio (g/kg) and latent heat flux (W/m^2).

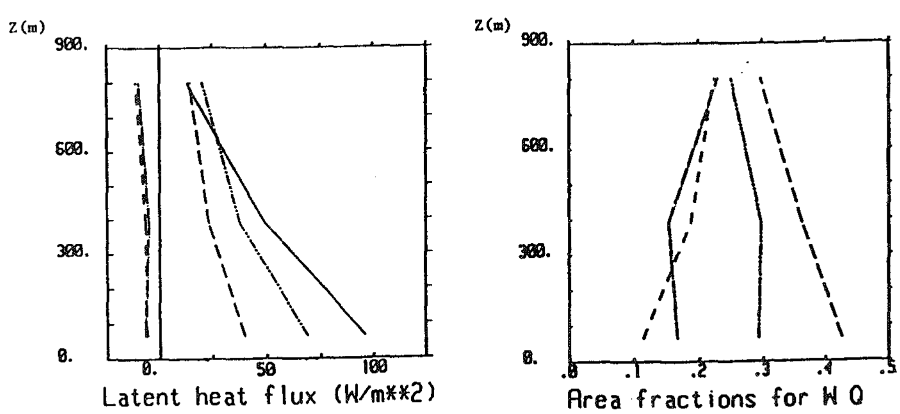

FIGURE 24 Left: Latent heat flux profile (solid line), and respective contribution of the various events: moist updrafts (dash-double dotted line); dry downdrafts (long dashed line); dry updrafts (short dashed line) and moist downdrafts (dash-dotted line). Right: fractional area covered by each of the four events. Same definition as for the left part of the picture.

interpreted in terms of "area"). The main results are the following: it appears that, the greatest contribution to the transfer is from the moist upward plumes or parcels, whereas these parcels cover only 25 to 30% of the total area. The greatest area is covered by dry downdrafts (between 30 and 43%, according to the altitude), which contribute less than half of the net flux. The other "environmental" contributions to the flux are low (about -5 top $-10\mathrm{W/m^2}$), and the corresponding areas covered vary from 11 to 23%. Areas covered by moist and dry updrafts give a total area of the positive velocities, which is 41% at the lowest altitude, and about 48% at the two upper levels. The skewness behaviour with altitude represents the turbulent kinetic energy transported by these vertical motions is positive at low altitudes, and becomes weak in the middle and the upper part of the ABL confirming the previous assumption. However, considering the mixing ratio, the values are quite constant throughout the ABL: 45 to 48% of positive values, corresponding to a slightly positive skewness.

It is early to synthetize all the features of the boundary layer observed June 8. Are just pointed out a few studies undertaken with first highlights; the response to the question of flux estimate at the mesoscale cannot indeed be done before a coordination and synthesis of all the studies undertaken.

From the measurement on June 8, different levels of MABL variability to be studied are:

1) mesoscale cloud structure variability, to look more deeply into radiation, SST, humidity, cloud variability from the different data of ASTEX

2) mesoscale variability in the wake of the islands, as documented by F27 and constant level balloons

3) oceanic variability observed from SST and drifting buoy information.

However comparisons of fluxes between Le Suroit and F27 do not show strong spatial variability which is probably due to the small values of the fluxes. But anyway it remains to confirm with ASTEX data from the other ships and aircraft operated on this day.

5. OBSERVATIONS OF JUNE 17

June 17 was a more cloudy day and was choosen since there were a priority on cloud analysis. During this day we have several different kinds of cloud data, which justifies an approach by different scales:

a) meteorological and satellite observation, b) an aircraft "mesoscale" description and c) a "microscopic" or local approach.

Figure 25 gives a map with the ship location represented on a small square and the Fokker 27 flight on this day.

The meteorological chart (Figure 5b) shows that on June 27 the ASTEX region is at the edge of the Azores anticyclone. A complete cloud cover was observed all the day though in the afternoon and evening altostratus was observed through the low level stratocumulus. The air progressively dried out during the day after being quite humid up to 06:00UT. The radiosounding (Figure 26) shows, in the lowest part of

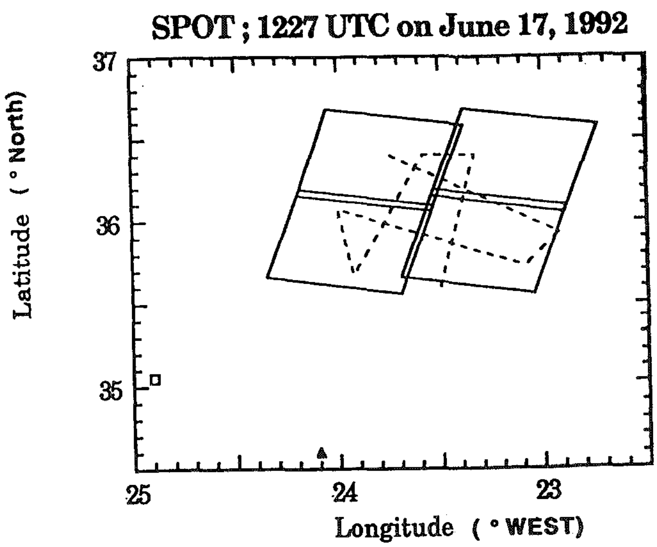

FIGURE 25 Ship location (small rectangle) and F27 flight pattern – on June 17th morning. Centre of the landsat scene, solid triangle.

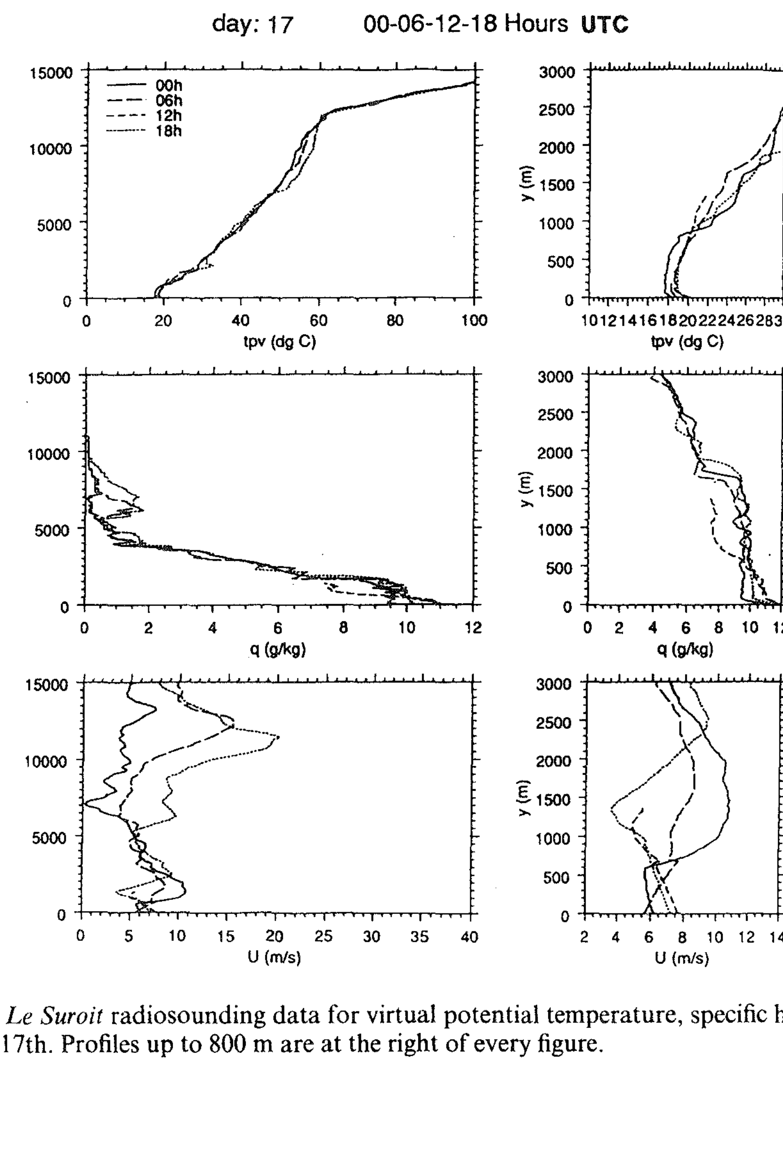

FIGURE 26 *Le Suroit* radiosounding data for virtual potential temperature, specific humidity and wind speed on June 17th. Profiles up to 800 m are at the right of every figure.

the boundary layer, a very thin mixed layer deepening with time and reaching a depth of 400 meters at 12:00 UTC. Beyond 400 m height no time variation of virtual potential temperature is observed, but for humidity time variation is noticed between 400 m and 2000 m while wind speed variation is observed during the day at all levels. The wind speed on the ship increased from 6m/s to 8-9m/s with a wind direction shifting from north-east to east at about 09:00 UT.

Spatial information from CMS (Figure 27) shows the solar irradiance fields over the SOFIA/ASTEX zone this day: we note the relatively large variability in the region. Indeed, looking at slot 31 corresponding to 12:40 UT (that is at the same period as the F27 flight) one observes in the flight region a solar irradiance roughly between 600 and 700 W/m^2, while the atmospheric radiation on Figure 28 does not present such a large horizontal variation.

The cloud classification on Figure 29 shows in the Azores area an homogeneous zone corresponding to a stratocumulus mass and a cirrus cloud or a thick cloud which is progressing slowly northeasterly.

The LEANDRE system also observes along its track a solid stratocumulus deck with no broken features. A vertical lidar backscattering intensity index as a function of altitude is displayed on Figure 30 (the flight altitude is around 4.6 km). This backscattering intensity indicates if there are clouds and for example a backscatter intensity much larger than 100 indicates a dense stratocumulus on this day, which is

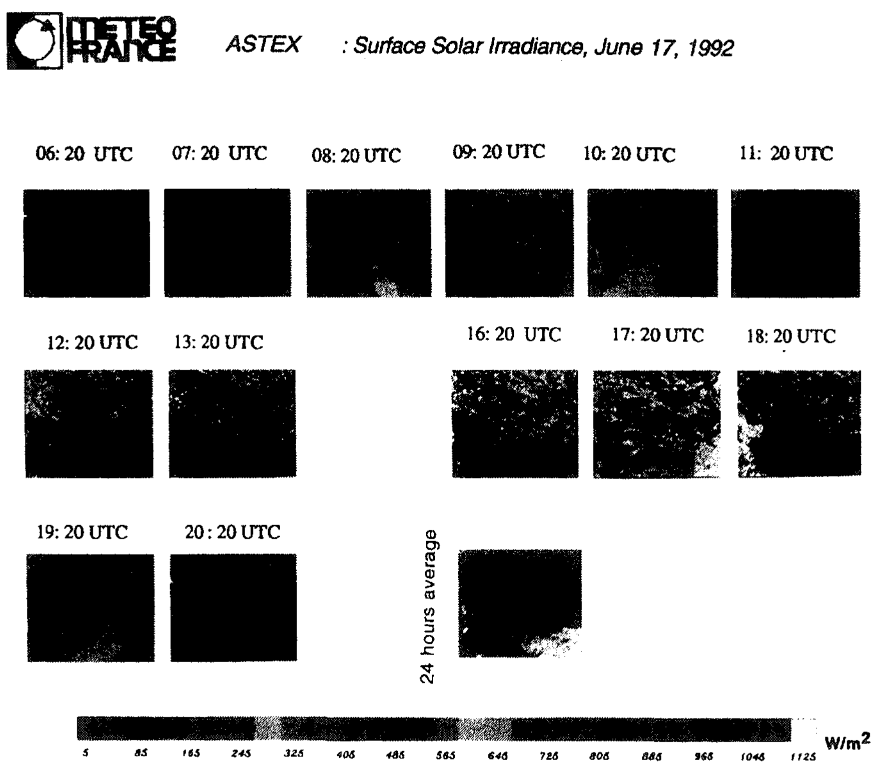

FIGURE 27 Surface solar irradiance fields on June 17th. These images represent the hourly solar irradiance fields calculated over the SOFIA/ASTEX zone (29.99 N, 40.03 N, 14.97 W, 30.01 W) at a .04 degree resolution. The daily mean (calculated over 24 hours) is also presented. They are expressed in W/m^2, according to the color scale displayed below the images. (see color plate XIV at the end of this issue)

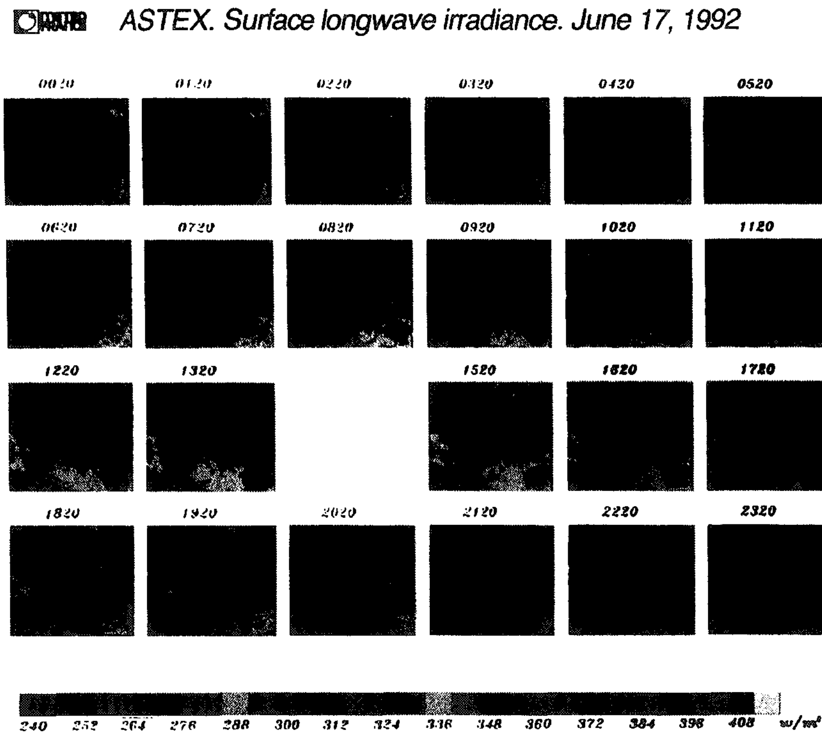

FIGURE 28 Surface longwave irradiance fields on June 17th. Same as Figure 27, except that the spatial resolution is .08 degree and the daily average has not been computed in that case. (see color plate XV at the end of this issue)

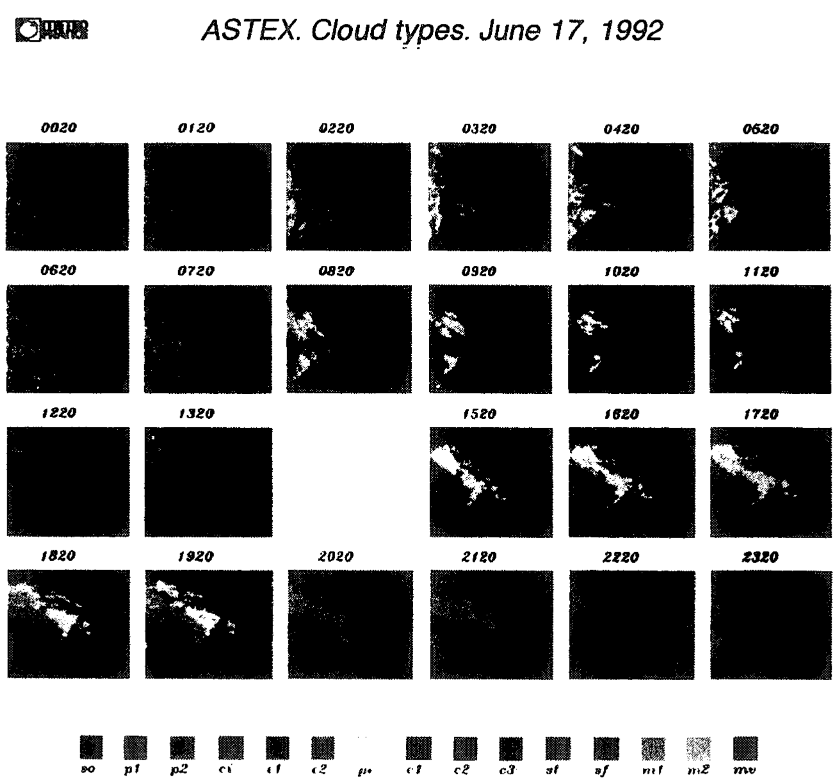

FIGURE 29 Cloud classification on June 17th The spatial resolution is 0.08 degree. The colour code is the following: surface: green; cloud edges 1 and 2: dark and pale violet Thin cirrus, thick cirrus land 2: dark to pale blue; high thick clouds: white cumulus 1 to 3: light to dark red; stratus and stratiform clouds: dark and light orange medium cloud 1 and 2: yellow and pale yellow; medium C13: borwnish grey. (see color plate XVI at the end of this issue)

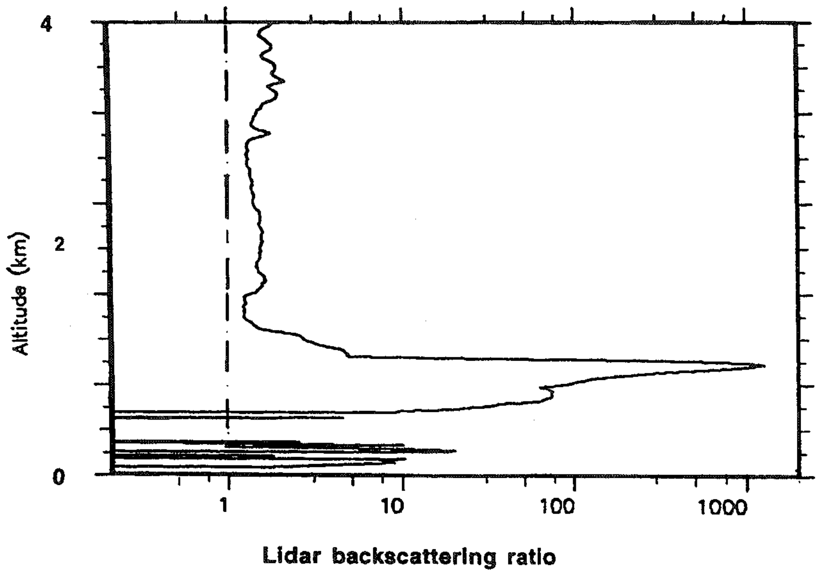

FIGURE 30 Lidar backscatter ratio at 0.53 mm as a function of altitude. The data were recorded by the backscatter lidar LEANDRE on board the Fokker F-27 on June 17th, 1992.

confirmed by the absence of surface echo; i.e. small scale optical porosity. Calculated backscatter values are however only significant near the cloud base, due to poor signal to noise ratio in the lower boundary layer. Refering to clear air return and signal to noise ratio, the cloud optical thickness is estimated to be larger than 3. The backscatter ratio is maximum at 1000 m and rapidly decreases above as cloud top occurs at 1050 m, in agreement with synoptic temperature inversion on radiosounding. The lidar signal is negligible below 500 m, where only noise is present. It indicates a minimum cloud thickness of about 550 m and a maximum cloud base height of 500 m, in agreement with the mixed layer top height measured by radiosonde. During this flight backscatter ratios around 2 are observed in the free troposphere (above 1200 m). These values are larger than those observed on June 8th. It is due to a large scale advection of aerosols layers over the Azores are during this period.

Figure 31 shows a satellite picture taken by the HRV (Haute Résolution Visible) instrument on board of SPOT 2 on 17 June at 12:26UT. This SPOT picture location can be also observed by the small parallelograms on figure 25 the picture is centered on (35.9°N, 23.3°W). The size of the SPOT-HRV image is about 60 km × 60 km and its spatial resolution (20m) shows the small-scale cloud structure which might affect the large scale radiation field. Figure 32 is channel 3 (0.79–0.89 mm) reflectance image. The grey scale represents a change in reflectivity from 0 to 0.7.

A large low-level cloud system covers nearly all the area but two different cloud structures are clearly identified. The southern part of the picture contains stratocumulus rolls whose both cloud radiative and optical properties. These cloud streets display a uniformity in size over a wide area, i.e. over several streets, as seen on the lower left part of the figure. It may be noted that there is in the lower right part of the picture a tendency to form cloud streets in a perpendicular direction. This could be due to the wind shear at cloud top level.

FIGURE 31 Reflectance image constructed from channel 3 (0.79–0.89 mm) of HRV (Haute Résolution Visible) instrument on board off SPOT 2, for a 60 km × 60 km region of the Atlantic Ocean centered at (35.9° N, 23.3° W) on 17 June 1992 at 1226UT. The pixel size is around 20 m. The HRV digital count values are given a grey level from black to 0 count to Atlantic Ocean centered at (35.9° N, 23.3° W) on 17 June 1992 at 1226UT. The pixel size is around 20 m. The HRV digital count values are given a grey level from black to 0 count to white at 255 counts. The grey scale represents a change in reflectance from 0 to 0.7.

The northern part of the image shows a totally different cloud pattern with large stratocumulus closed cells about 15–20 km in size. This second cloud system covers a large area and additional information from surrounding SPOT 2 images show the same characteristics. The average reflectance of the cells is slightly higher than that of rolls (about 0.6 instead of 0.5).

Small scale observations were also made with POLDER and LEANDRE on the same flight. Figure 32 shows the 865nm reflectance image and Figure 33 shows the cloud optical thickness derived from POLDER measurements collected from 1103 to 1113UT for a 50km × 6km region centered at (35.9° N, 23.4° W). About 55 POLDER scenes are used to construct these maps. Since the plane and cloud top altitudes were around 4600m and 1000m respectively, the POLDER pixel size is about 20m, that is similar to SPOT-HRV one. The shape of these pictures is simply due to the change of course of the plane during the data acquisition. A cross section of LEANDRE data from 11:03 to 11:18 UT (Figure 34), shows the cloud top altitude as a function of time. The lidar data are displayed at two horizontal resolutions: an aver-

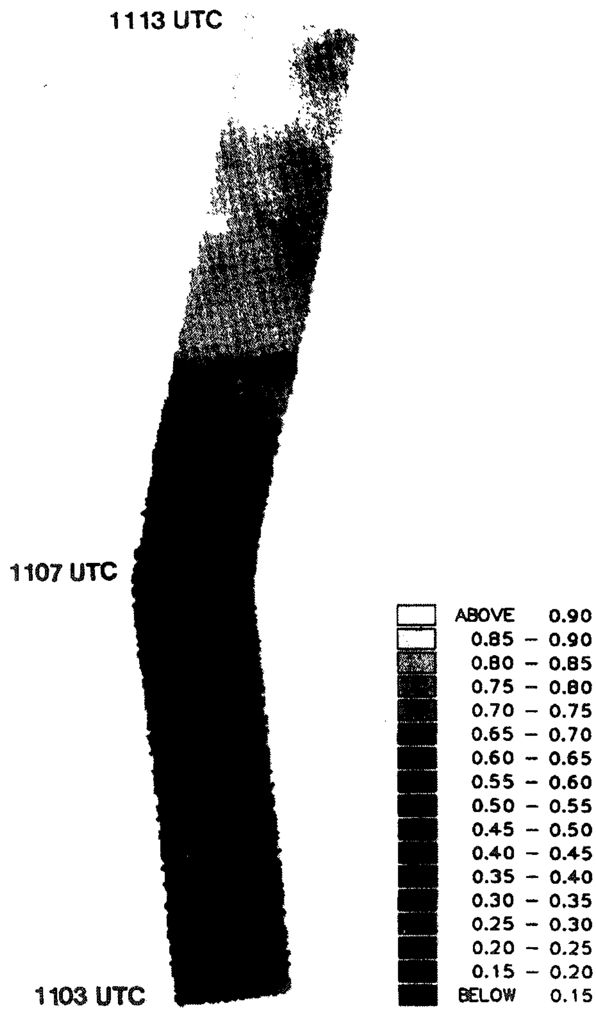

FIGURE 32 Image constructed from near-infrared reflectance at 865nm measured by POLDER for 50km × 6 km region centered at (35.9° N, 23.4° W) on 17 June 1992 from 1103 to 11:13 UTC. The pixel size is around 20 m. The grey scale represents a change in reflectance from 0 to 1.

age of 4 shots corresponding to 0.42 s or 35 m (dashed line), and a sliding average over 164 shots or 172 s and 1450 m (solid line). The horizontal distances are computed for an aircraft speed of 85 ms-1.

Unfortunately, the Fokker F-27 overpass is not exactly coincident with the SPOT overpass, but the POLDER reflectance image and the LEANDRE data clearly show the same features. From south to north (i.e. from bottom to top of the POLDER images) the Fokker has flown over a transition between very thin clouds, stratocumulus rolls and then very large cloud cells (only small part of these cells is seen by the POLDER instrument). The cloud reflectance variations (Figure 34) are also very similar to those observed with SPOT-HRV, i.e reflectance values lower for stratocumulus rolls than for closed-cells. Consequently the derived mean cloud optical thickness (Figure 33) also varies from about 10 to 30 (from bottom to top of the picture respectively), corresponding to different cloud structures with a sharp limit between rolls and cells. The lidar data (Figure 34) also make clear two distinct regions for stratocumulus, displaying different spatial features corresponding to cloud streets

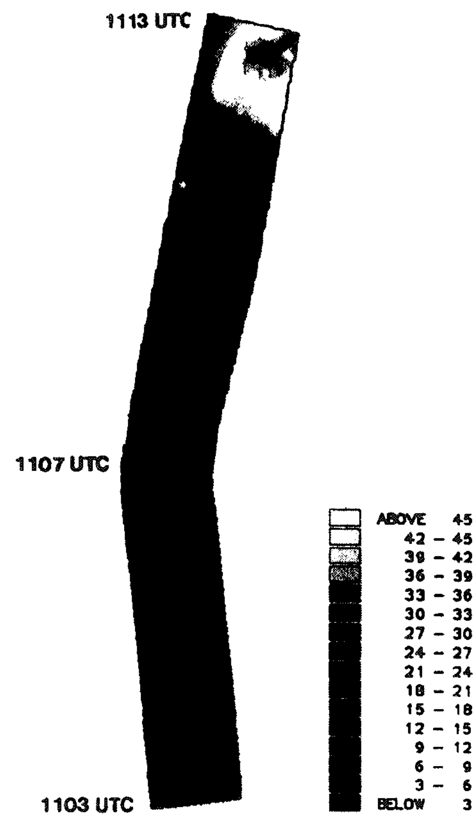

FIGURE 33 Cloud optical thickness derived from POLDER measurements at 865 nm, for the same area as in figure 32. the color scale represents a change in optical thickness from 0 to 50. (see color plate XVII at the end of this issue)

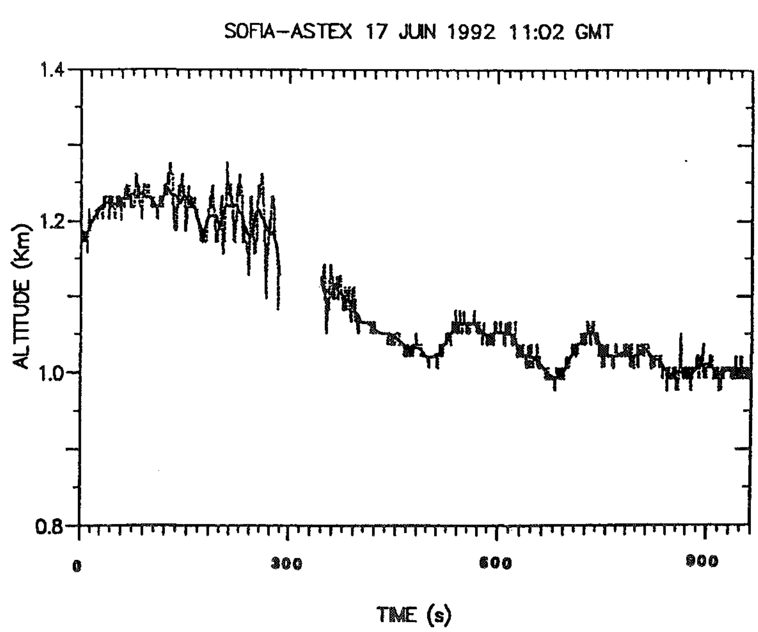

FIGURE 34 Cross section of LEANDRE data recorded on June 17, 1992, from 1103 to 11:18 UTC, on a stratocumulus deck. The cloud top height is displayed as a function of time. Two horizontal resolutions of 35 m (4 lidar shots ---) and 1450 m (164 shots —) are used (same flight as figures 32 and 33).

and closed cells. The average cloud top heights are 1.2 km and 1.0 km respectively. During the first part of the flight a deep modulation of cloud top altitude with characteristic length of 1.4 km is observed; this is well filtered out with the 4 shot average. Such a 1.4 km characteristic length is to be compared to a 0.9 km transverse dimension for cloud streets as retrieved from SPOT 2 (Figure 31, lower part) and POLDER (Figure 32, lower part). It would represent a 1D lidar sampling at an average angle of about 43° with respect to the orientation of the rolls. This is in agreement with POLDER observations (Figure 34, lower section) which shows, towards the transition between the two airmasses, a rotation from a 35° to a 50° orientation of the cloud streets with respect to the flight track. The small scale structure seems to vanish progressively during a transition zone of about 5 km (from 11::08:30 UTC to 11:10:30 UTC). This is however not clearly evidenced as lidar measurements are not available at the beginning of the transition. Then after 11:10:30 UTC, the mesoscale features dominate. The lidar data do agree with the striking transition and change in cloud organization represented on the SPOT 2 (Figure 31) and POLDER images (Figures 32 and 33). The mesoscale structure observed from 11: 10: 00 to 11: 19: 00 shows two distinct characteristics lengths; one ranging from 3 to 7 km, while the other is around 15 km. These features would correspond to a random 1D sampling by LEANDRE of cloud cells pictured on Figure 34. A 15 km length compares well to the cell diameter retrieved from SPOT 2.

We notice at this point the advantage we have to be able to describe the cloud structure at different scales and to be able to make the link with the radiation (via the microphysics, the dynamic and thermodynamic). Drakkar observations on this day are characterized by constant water vapor content of 3g/cm2 and clouds of varying liquid water content (Figure 35): two larger clouds are observed corresponding to the zone of thick clouds on the satellite map.

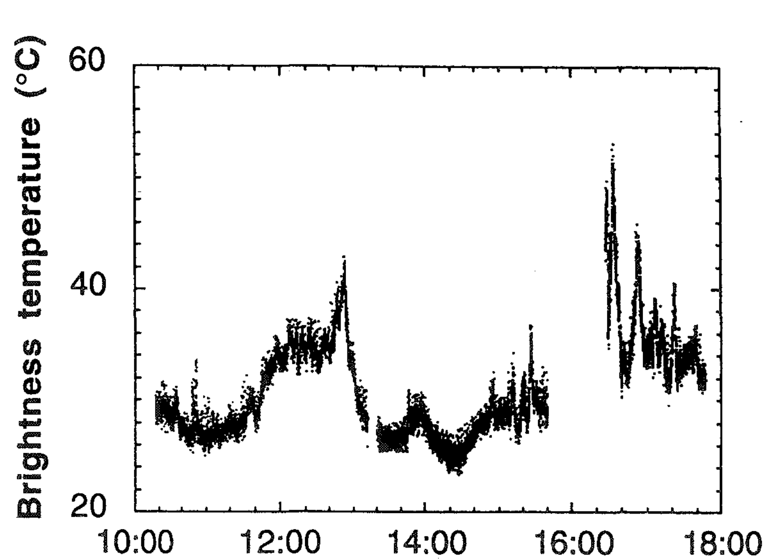

FIGURE 35 Drakkar 36 Ghz brightness temperature on June 17th. Near 16:40 a thick cloud influence is observed.

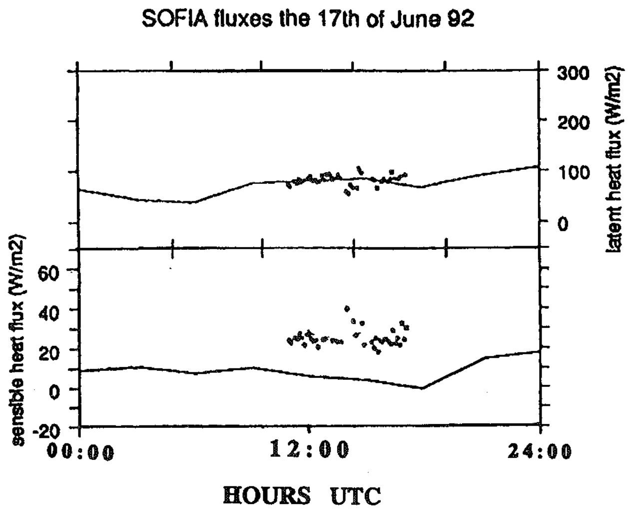

FIGURE 36 Sofia heat fluxes on June 17th.. The continuous line is the bulk estimate (following Large and Pond (1982)). The dots correspond to inertial-dissipative method use.

Sensible heat flux during this day shown in Figure 36 was always very small (below 30 W/m2) and a salt contamination problem on the temperature probe is noticed as in Figure 12, while latent heat flux was below 100 W/m2. We notice an increase of the heat flux (sensible and latent) at the end of the day corresponding probably to cloud "holes" implying an increase in the incoming radiation, but the heat flux variation remains relatively flat during June 17th.

6. CONCLUSIONS

This paper shows the instruments which have been used during SOFIA (the french component of ASTEX) and how these instruments are used to document the MABL and fluxes. A synoptic description of the campaign has shown that the meteorological situation was generally perturbed. The wind speed was was slow, between 1 to 1 m/s; the latent heat flux close to 100 W/m^2 and the sensible heat flux below 30 W/m^2.

Using early results obtained during June 8 and June 17, we have given examples of the MABL structure as observed by shipborne instruments as a microwave radiometer Drakkar, an acoustic sounder system OCARINA and a tethered balloon. Spatial variability of the boundary layer has been described using airborne instruments as POLDER and LEANDRE and also with in situ airborne measurements. In particular, a wake effect due to Santa – Maria Island has been documented with constant-level balloons and aircraft: the wake effect in case of North wind extends horizontally up to 80 km in the lee of Santa-Maria and vertically up to 400 m height.

During June 17, a very cloud day, cloud structure has been described using a multi-scale analysis with first a cloud analysis from satellite then from aircraft with LEANDRE and POLDER observing the same SPOT scene. The changing cloud structure identified both on the SPOT picture and on the POLDER image demonstrate the importance of being able to differentiate cloud scales corresponding probably to different boundary layer characteristics. All the Sofia data are now in a data bank available for future users and several studies have already been undertaken on various subjects.

Acknowledgements

We wish to acknowledge the support of DRET, INSU (CNRS), METEO-FRANCE, IFREMER and the US National Science Foundation in the SOFIA program. We wish to thank all the technical staff of CNET, CRPE, LA, Meteo-France and University of Washington for their contributions in the SOFIA experiment.

Special thanks are due to J. Bilbille, B. Piron, P. Celin, R. Riguet, A. Lecornec, D. Borié, R. Monis and F. Weller, without whom the experiment would not have been possible. We are grateful to S. Prieur of L.A. (Laboratoire d'Aérologie) for the radiation recording system deployed on board *Le Suroit*, Special thanks are due to INSU (Division technique), IGN and METEO-FRANCE for aircraft facilities.

The captain and crew of *Le Suroit* provided invaluable assistance.

The spatial data from Lannion were computed on a GREOS (Group de Recherche et d'Etude d'Océanographie Spatiale) funded workstation.

References

Antoine, J.Y., Derrien, M., Harang L., Leborgne P., Le Gleau, H. and Le Goas C. (1992). Errors at large satellite zenith angles on AVHRR derived sea surface temperatures, International Journal of Remote Sensing, 1797–1804.

Albrecht, B.A. (1981). Parameterization of trade-cumulus cloud amounts. *J. Atmos. Sci.*, **38**, 97–105.

Albrecht, B.A., Randall, D.A. and Nicholls, S. (1988). Observations of marine stratocumulus clouds during FIRE. Bull. *Amer. Meteor. Soc.*, **69**,618–626.

Albrecht, B.A., Fairall, C.W., Thomson, D.W., White, A.B., Snider, J.B., and Schubert, W.H. (1990). Surface-based remote sensing of the observed and adiabatic liquid water content of stratocumulus clouds. Geophysical Research Letters, **17**, 89–92.

Atlas, D., Walter, B., Chou, S.H. and Sheu, P.J. (1986). The structure of the unstable marine boundary layer viewed by lidar and aircraft observations. *J. Atmos. Sci.* **43**, 1301–1318.

Augstein, E., Schmidt, H. and Ostapoff, F. (1974). The vertical structure of the atmospheric planetary boundary layer in undisturbed trade winds over the atlantic ocean. *Bound, Layer Metor.*, **6**, 129–150.

Bellec, B., Brisson, A., Le Borgne, P., Marsouin, A. (1992). Operational cloud classification with METEOSAT data. Proceedings of the Central Symposium of the International Space Year Conference, Munich (Germany), Mars 30-April 4, ESA SP- 341, pp 283–288.

Benech, B., Druilhet, A., Cordesse, R., Dartigues-Longues, B., Fournier-Fayard, J., Mesnager, J.C., Durand, P. and Malaterre, A. (1987). Un dispositif expérimental utilisant les ballons plafonnants pour l'étude de la couche limite atmosphérique. *Adv. Space Res.*, **7**, pp. 78–83.

Betts, A.K. (1975). Parametric interpretation of trade-wind cumulus budget studies, *J. Atmos. Sci.*, **32**, 1934–1945.

Betts, A.K. and Albrecht, B.A. (1987). Conserved variable analysis of the convective boundary layer thermodynamic structure over the tropical oceans. *J.Atmos. Sci.*, **44**, 83–99.

Brisson, A., Le Borgne, P., Marsouin, A., and Moreau, T. (1994). Surface irradiances calculated from METEOSAT sensor during SOFIA/ASTEX, *Int. J. of Remote Sensing*, **15**, 197–203.

Brown, R.A. and Liu, W.T. (1982). An operational large scale marine planetary boundary layer model. *J. Applied Meteorology*, **21**, 261–269.

Businger, J.A. (1975). Interactions of sea and atmosphere. *Rev. Geophys. Space Phys.*, **13**, 720–822.

Businger, J.A., Wyngaard, J.C., Izumi, T. and Bradley, E.F. (1971). Flux-profile relationships in the atmospheric surface layer, *J.Atmos. Sc.*, **28**, 181–189.

Champagne-Phillipe, M. (1989). Coastal wind in the transition from turbulence to Mesoscale, *J. Geoph. Re.*, **94**, C6, 8055–8074.

Delsol, F., Miyakoda, K. and Clarke, R.H. (1971). Parameterized processes in the surface boundary layer of an atmospheric circulation model. Quart. *J. Roy. Meteorol. Soc.* **97**, 181–208.

Desbois, M., Sèze, G. and Szejwach, G. (1982). Automatic classification of clouds on METEOSAT imagery. Application to high level clouds. *Journal of Climate and applied Meteorology*, **21**, 401–42.

Dupuis, H., Frangi, J.P., Weill, A. (1993). Comparison of wave breaing statistics using underwater noise and sea surface photographic analysis conducted under moderate wind speed conditions during the SOFIA/ASTEX experiment, *Ann. Geophysicae*, **11**, 960–969.

Dupuis, H., Katsaros, K.B., Taylor, P.K. and Weill, A. (1994). Turbulent momentum and latent heat fluxes by spectral methods during the SOFIA/ASTEX experiment in the Azores region, submitted.

Dupuis, H. and Weill, A. (1993). A model to estimate the density, characteristic suurface, and coverage of whitecaps using underwater sound, **98**, C10, 18213–18219.

Fairall, C.W., Edson, J.B. and Miller, A. (1990). In heat fluxes, whitecaps, and Sea Spray, editors Geernaert and W. plant, Kluwer Academic Publishers, Vol.1, 173–208.

Fleagle, R.G., Badgley, F.I. and Hsueh, Y. (1967). Calculation of turbulent fluxes by integral methods. *J. Atmos. Sci.*, **24**, 356–373.

Francey, R.J. and Garratt, J.R. (1978). Eddy flux measurements over the ocean and related transfer coefficients. *Bound. Layer Meteor.*, **14**, 153–166.

Friehe, C.A., Shaw, W.J., Rogers, D.P., Davidson, K.L., Large, W.G., Stage, S.A., Crescenti, G.H., Khalsa, S.J.S., Greenhut, G.K., and Li, F. (1991). Air-Sea fluxes and surface layer turbulence around a sea surface temperature front, J.G.R., **96**, C5, 8593–8609.

Garratt, J.R. (1977). Review of drag coefficients over oceans and continents. *Mon. Wea. Rev.*, **105**, 915–926.

Garratt, J.R. and Hyson, P. (1975). Vertical fluxes of momentum, sensible heat and water vapor during the Air-Mass Transformation Experiment (AMTEX) 1974, *J. Meteor, Soc.*, Japan **53**, 149–160.

Gautier, C., Diak, G. and Masse, S. (1980). A simple physical model to estimate incident solar radiation at the surface from GOES satellite data. *Journal of applied Meteor.*, **19**, 1005–1012.

Geernaert, G.L., Plant Editors, W.J. (1990). Surface Waves and Fluxes, Vol. 1-Current theory and Plant, Kluwer Academic Publishers, 336pp.

Geernaert, G.L., Katsaros, K.B. and Richter, K. (1986). Variation of the drag coefficients and its dependence on sea state. *J. Geophys. Res.*, **91**, C6, 7667–7679.

Holland, J.Z. and Rasmusson, E.M. (1973). Measurements of the atmospheric mass, energy, and momentum budgets over a 500 kilometer square of tropical ocean. *Mon. Wea. Rev.*, **101**, 44–55.

Large, W.G. and Pond, S. (1982). Sensible and latent heat flux measurements over the ocean *J. Phys. Oceanogr.*, **12**, 464–482.

Le Borgne, P. et Marsouin, A. (1988). Determination du flux ondes courtes incident à la surface. Mise au point d'une méthode opérationnelle à partir de données du canal visible de Météosat. *La Météorologie*, **20**, 9–19.

Liu, W.T., Katsaros, K.B. and Businger, J.A. (1979). Bulk parameterization of air-sea exchanges of heat and water vapor including the molecular constraints at the interface. *J. Atmos. Sci.*, **36**, 1722–1735.

Monin, A.S. and Obukhov, A.M. (1954). Basic laws of the turbulent mixing in the atmosphere near the ground. *Tr. Akad. Nauk SSSR Geofiz. Inst.* **24**, 163–187.

Nicholls, S. and LeMone, M.A. (1980): the fair weather boundary layer in GATE: The relationship of subcloud fluxes and structure to the distribution and enhancement of cumulus clouds, *J. Atmos. Sci.*, **37**, 2051–2067.

Nicholls, S. (1985). Aircraft observations of the Ekman layer during the Joint Air-Sea Interaction Experiment, *Q.J.R.Meteor. Soc.*, **111**, 391–426.

Nitta, T. and Esbensen, S. (1974). Heat and moisture budget analyses using BOMEX data. *Mon. Wea. Rev.*, 102, 17–28.

Randall, D.A., Sho, Q.S. and Moeng, C.H. (1992). A second-order bulk boundary-layer model, J. Atmos. *Sci.*, **49**, 1903–1923.

Said, F. and Druilhet, A. (1991). Experimental study of the atmospheric marine boundary layer from in-situ aircraft measurements (Toscane-T campaign): variability of boundary conditions and eddy flux parameterizations, Boundary Layer Meteor., **57**, 219–249.

Séze, G. and Desbois, M. (1987). Cloud cover analysis from satellite imagery using spatial and temporal characteristics of the data. *Journal of Climate and Applied Meteor.*, **26**, 287–303.

Smith, S.D. (1988). Coefficients for sea surface wind stress, heat flux, and wind profiles as a function of wind speed and temperature. *J. Geophys. Res.*, **93**, 15467–15472.

Weill, A., Eymard, L., Durand, P., Druilhet, A., Ezraty, R., Le programme SOFIA (La Surface Océanique: Flux et Interactions avec l'Atmosphére) Internal report, 17 pp.

Weill, A., Klapisz, C., Baudin, F. (1986). The CRPE minisodar: applications in micrometeorology and physics of precipitations, *Atmos. Res.*, **20**, 317–333.

Weill, A. (1993). Indirect measurements of fluxes using Doppler Sodar, In land surface evaporation: measurement and parameterization, T.J. Schmugge and J.C. André Editors, *Springer Verlag*, 301–311.
Weller, R.A., Rudnick, D.L., Eriksen, G.C., Polzin, K.L., Oakley, N.S., Toole, J.W., Schmitt, R.W. and Pollard, R.T. (1991). Forced ocean response during Frontal Air-Sea Interaction Experiment, *J.G.R*, **96**, C5, 8611–8638.
Wu, J. (1974). Viscous sublayer below a wind-disturbed water surface. *J.Phys. Oceano.*, **14**, 138–144.
Yelland, M.J. and Taylor, P.K., Consterdine, I.E. and Smith, M.H. (1994). The use of the inertial dissipation technique for shipboard wind stress determination, *J.Atmos. Ocean Tech.* ;in press.

Annexe B

Microphysical and Radiative Properties of Stratocumulus Clouds: The EUCREX Mission 206 Case Study

Accepted in *Atmospheric Research*

MICROPHYSICAL AND RADIATIVE PROPERTIES OF STRATOCUMULUS CLOUDS: THE EUCREX MISSION 206 CASE STUDY

Hanna Pawlowska[1*], J. L. Brenguier[1], Yves Fouquart[2]
Wolfgang Armbruster[3], Jacques Descloitres[2], Jürgen Fischer[3], C. Flamant[6], Anne Fouilloux[4]
Jean-Francois Gayet[4], Sat Ghosh[5], Peter Jonas[5],
Frederic Parol[2], Jacques Pelon[6], Lothar Schüller[3]

[1] Météo-France (CNRM/GAME), Toulouse, France
* on leave from Institute of Geophysics, University of Warsaw, Poland
[2] Laboratoire d'Optique Atmosphérique, Université des Sciences et Techniques de Lille, France
[3] Institut für Weltraumwissenschaften, Freie Universität Berlin, Germany
[4] Laboratoire de Météorologie Physique, Clermont-Ferrand, France
[5] Dept. of Physics, UMIST, Manchester, England
[6] Service d'Aéronomie, Paris, France

Accepted in Atmospheric Research

Corresponding author: J. L. Brenguier,
Centre National de Recherches Meteorologiques
GMEI, 42 av. Coriolis, 31057 Toulouse Cedex 01, France.
Tel: 5 61 07 93 21; Fax: 33 5 61 07 96 27; e-mail: jlb@meteo.fr

ABSTRACT

In this conclusion paper, remote sensing retrievals of cloud optical thickness performed during the EUCREX mission 206 are analyzed. The comparison with estimates derived from in situ measurements demonstrates that the adiabatic model of cloud microphysics is more realistic than the vertically uniform plane parallel model for parameterization of optical thickness. The analysis of the frequency distributions of optical thickness in the cloud layer then shows that the adiabatic model provides a good prediction when the cloud layer is thick and homogeneous, while it overestimates significantly the optical thickness when the layer is thin and broken. Finally, it is shown that the effective optical thickness over the whole sampled cloud is smaller than the adiabatic prediction based on the mean geometrical thickness of the cloud layer. The high sensitivity of the optical thickness on cloud geometrical thickness suggests that the effect of aerosol and droplet concentration on precipitation efficiency and therefore on cloud extent and life time is likely to be more significant than the Twomey effect.

Keywords: cloud-radiation interaction, stratocumulus, aerosol indirect effect, climate change.

1. Introduction

Part of the EUCREX-94 experiment was dedicated to the study of the indirect effect of aerosols on boundary layer stratocumulus clouds. In order to document and parameterize the relationships between cloud microphysics and cloud radiative properties, a strategy based on simultaneous measurements of both cloud properties has been designed (Brenguier and Fouquart, 2000) The various papers in this special issue have described the instruments and the data processing techniques. This conclusion paper aims at combining all these approaches in order to test parameterization schemes of cloud optical thickness, document the natural variability of this parameter, and evaluate its effects on the mean cloud radiative properties.

Figure 1 in Fouilloux et al. (2000), hereafter referred to as FG reveals that the stratocumulus layer sampled by the instrumented aircraft along the leg **M-A** is not homogeneous horizontally. The cloud layer is thick and continuous at the southern end (**M**), while it is thin and broken at the northern end (**A**). This trend in the direction perpendicular to the mean flow (from the North-East) has been documented in more details by in situ measurements. At the beginning of the M-IV flight, from 09:30 to 10:30, i.e. 1 to 2 hours after the AVHRR image shown in FG, clouds as thick as 400 m were observed close to **M** and the layer was continuous as shown by the statistics of LWC in Fig. 7 of Pawlowska et al (2000), hereafter referred to as PBB (only 10 % of the samples were in clear air). Towards **A**, the layer was thinner (less than 200 m) and broken (35 % of the samples were in clear air). This geographical trend evolved with time and at the end of the flight (12:30 UTC), the thickest (300 m) cells were observed at the middle of the leg while at both ends the cloud layer was thinner (Fig. 4 in PBB). In this conclusion paper the first step will be to document spatial and time variations of the cloud radiative properties as measured remotely. The second step will be to compare the remotely measured optical thickness to the one derived from in situ measurements of droplet concentration and cloud geometrical thickness, in order to test the adiabatic model discussed in PBB versus the parameterization based on a vertically uniform plane parallel model (VUPPM). Independent estimates of cloud geometrical thickness with POLDER and the lidar LEANDRE will be used to strengthen the validation. The third step will be to provide detailed information about the statistics of optical thickness, which are particularly needed for the parameterization of the effects of horizontal cloud inhomogeneities on mean cloud albedo.

2. Spatial and time variations of optical thickness

Four measurements of optical thickness are available in mission 206: POLDER and OVID (Schüller et al, 2000) on the DLR-F20, and POLDER and LEANDRE (Pelon et al, 2000) on the ARAT. The field of view of the POLDER instrument across the flight direction depends on the altitude of the aircraft above cloud top. During mission 206 the field of view was about 7.3 km for the ARAT flying at 4500 m, and 4.4, 9.2, and 11.2 km for the DLR-F20 flying at 3000 m (10:06 to 10:41 UTC), 4600 m (10:46 to 11:00 UTC), and 6000 m (11:04 to 11:42 UTC) respectively. OVID measurements on board the DLR-F20 were made towards the nadir, that is the instrument was pointing at the middle of the F20 POLDER field of view. The spatial resolution after processing is of the order of 220 m (2 seconds of flight). On board the ARAT the lidar LEANDRE was performing measurements of the profiles of in cloud extinction. Its beam was pointing at the middle of the ARAT POLDER field of view. A novel technique has been developed by Pelon et al (2000) for the retrieval of optical thickness at a spatial resolution of 100 m.

Fig. 1 shows the contours of optical thickness derived from measurements performed by POLDER on the ARAT (a) and on the DLR-F20 (b) and by OVID on the DLR-F20 (c). The space coordinate (y-axis) is the distance from point **M** along the leg towards **A**. The flight tracks are overplotted in the figures. The ARAT started at 09:58 UTC, about 40 km from point **M**, flying southward towards this point. From **M**, the ARAT performed 5 additional complete legs between M and **A**, and ended its seventh leg at 12:18 UTC, about 70 km from point **A**. Both aircraft were flying along a fixed geographical track, while the cloud layer was flowing from the North-East, perpendicularly to the track at a wind speed of about $10\,ms^{-1}$ (Fig. 3 in PBB). The time scale (x axis) is such that 1 hr is equivalent to 36 km. Therefore, if the cloud layer was stationary, at least for the large scale features, the space/time representation in the figures can be viewed as an instantaneous image of a cloud section of length 120 km, oriented along the direction **M-A**, and of width 84 km (2 hr 20 min) for the ARAT and 60 km (1 hr 40 min) for the DLR-F20 in the North-East direction .

The similarities between Fig. 1a and Fig. 4 in PBB are noticeable. At the beginning of the flight large optical thicknesses are observed towards the southern end with a continuous trend towards low values at the northern end. This corresponds to the trend in the altitude of the inversion layer, from 1100 m, down to 850 m, in Fig. 4 of PBB, between 10:00 and 10:40. At the end of the flight, maximum optical thicknesses are observed at the middle of the leg, with decreasing values on both sides. This corresponds to the bowl shape of the inversion layer altitude, from 1000 m at the middle of the leg, down to less than 900 m on both sides, in Fig. 4 of PBB, between 11:30 and 12:00. Fig. 1b and 1c for the DLR-F20 POLDER and OVID measurements confirm the observations made with the ARAT POLDER for the spatial and time variations of the cloud layer. This significant variability of the cloud structures is interesting for the case study because it provides a large range of optical thicknesses for comparison with in situ the measurements. However in situ and remote sensing measurements were not precisely synchronized during EUCREX. Because of the horizontal variability, comparison between the two is thus possible only after interpolation in space and time.

3. Test of the optical thickness parameterization

3.1 with in situ measurements of cloud geometrical thickness

An important objective in EUCREX is to test the parameterization of optical thickness at the scale of a cloud cell. In PBB in situ measurements have been analyzed to show that the vertical profiles of the microphysical parameters are close to adiabatic profiles. In such a case the optical thickness can be parameterized as:

$$\tau = \bar{Q}_{ext} \left(\frac{c_w}{\frac{4}{3}\pi\rho_w} \right)^{2/3} (kN)^{1/3} H^{5/3}, \tag{1}$$

where $\bar{Q}_{ext}$ is the mean Mie extinction factor, c_w is the adiabatic condensation rate, ρ_w is the liquid water density, N is the droplet concentration, H is the cloud geometrical thickness, and $k^{1/3}$ is defined as the ratio of the droplet mean volume diameter to the mean effective diameter $k = (r_v/r_e)^3$. For the EUCREX mission 206 case, $\bar{Q}_{ext} = 2.2$, $c_w = 1.5 \cdot 10^{-3}\, g\, m^{-4}$, and $k = 0.8$.

In the adiabatic parametrisation (1) optical thickness increases as $H^{5/3}$ while it is simply proportional to H in the VUPPM (Twomey, 1977; Baker, 1997). Even though in situ measurements were not synchronized with remote sensing measurements, a comparison will be made possible via interpolation in space and time. In a first step, each of the ascents or descents made during legs 2, 5 and 6 of the M-IV (except the 4 first cloud traverses in leg 2 that are too early) has been located in space and time with respect to the coordinates used in Fig. 1. For each cloud traverse the measured cloud geometrical thickness is used in (1) to derive an estimate of the optical thickness, with $N = 400\, cm^{-3}$ (Fig. 9 in PBB). In Fig. 2 these estimates are compared to the values shown in Fig. 1a after space and time interpolation between the three nearest ARAT POLDER mean values. The agreement between these two estimates is remarkable, especially when considering that POLDER measurements have been averaged over areas of $7.3 \times 5\, km$, while an ascent or descent through the cloud layer with the M-IV provides information along a line of 5 to 8 km length.

3.2. with POLDER measurements of cloud top altitude

Cloud top altitude has been derived from stereo measurements of cloud radiances with POLDER. Two dimensional fields of cloud top altitude have thus been provided along with the fields of optical thickness, for legs 2 and 3 of the ARAT (10:11 to 10:54 UTC). The analysis here consists in the selection of peak values of optical thickness that are assumed to correspond to the top of the convective cores. An automatic procedure has been developed to select maximum values of optical thickness within boxes of 20×20 pixels. Fig. 3 shows the horizontal map of optical thickness derived from the second ARAT POLDER leg, with the pixels selected as cloud tops marked by black dots. In Fig. 4 each point represents a peak value of optical thickness (y axis) with the corresponding cloud depth (x axis) derived from the POLDER estimate of cloud top altitude by assuming the cloud base is at 650 m (i.e. the mean value of the cloud base height, as shown in Fig. 3 in PBB). The solid line is the 5/3 slope; the dotted line is the 1/1 slope. This figure confirms that the optical thickness is proportional to $H^{5/3}$ rather than to H.

3.3 with LEANDRE measurements of cloud top altitude

Measurements of in cloud extinction have been performed on board the ARAT with the lidar LEANDRE looking at nadir. The lidar beam is aligned with the middle of the POLDER field of view. The cloud top altitude is derived from the lidar profiles as the altitude of maximum gradient of extinction above the extinction maximum value (Pelon et al., 2000). Fig. 5 shows the comparison with POLDER. Fig. 5a is the horizontal map of optical thickness derived from the ARAT POLDER. Fig.5b shows the variation of the POLDER optical thickness at the middle of the field of view (solid line) compared to the estimate of optical thickness (dotted line) calculated with (1) and the cloud depth H derived from the lidar cloud top altitude, by assuming the cloud base is at 650 m. Fig. 5c compares both estimates.

3.4 Discussion

The estimates of optical thickness derived from multidirectional measurements of cloud radiances with POLDER on board the ARAT have been used to test the adiabatic parameterization of optical thickness (1). The droplet concentration measured in situ was about $400\,cm^{-3}$. The cloud geometrical thickness has been estimated by three different ways. (1) from in situ measurements during ascents or descents of the M-IV through the cloud layer, (2) from estimates of the cloud top altitude with the ARAT POLDER, and (3) from estimates of the cloud top altitude with the lidar LEANDRE, which was aligned with POLDER on the ARAT. The three comparisons converge in demonstrating that the cloud optical thickness is rather proportional to $H^{5/3}$ than to H.

4. Statistics of cloud optical thickness

The parameterization of optical thickness based on the adiabatic profile of microphysical parameters is valid only in the core of a convective cloud cells. However, a stratocumulus is made of a patchwork of convective cells separated by regions of lower optical thickness related to downdrafts and even patches of clear air. In the downdraft regions, the profile of the microphysics deviates significantly from adiabaticity. The radiative parameter of interest in climate studies is the mean cloud albedo and several authors have shown that this mean value is quite sensitive to the horizontal distribution of optical thickness in a non linear way (Cahalan et al, 1995). A parameterization of the mean cloud albedo thus requires a relationship between cloud microphysics and cloud geometrical thickness such as that given by (1), but also a relationship between the spatial inhomogeneity of the cloud properties and its mean albedo. In this section the cloud layer observed during mission 206 will be divided into samples of different morphological characteristics and the statistics of optical thickness will be documented. They are fitted to lognormal distributions (as was done by Barker et al., 1996) because of the non linear relationship between optical thickness and cloud albedo. The optical thickness corresponding to the logarithmic mean is referred to hereafter as the effective optical thickness: $\tau_e = e^{\overline{ln \tau}}$.

4.1 Frequency distributions of optical thickness

From the observations shown in Fig. 1, the leg **M-A** has been arbitrarily divided into three sections (0-40 km), (40-80 km) and (80-120 km). Such samples are sufficiently large for providing significant statistics and short enough for discriminating the different cloud morphologies. Fig. 6 shows the time evolution of the frequency distributions of optical thickness for the three sections and for each of the ARAT legs. For each distribution τ_e and the log standard deviation σ have been reported. This figure reflects the space/time variations discussed in Sec. 2. The figure also confirms that the optical thickness distributions are correctly represented by lognormal distributions. The most interesting feature, however, in this figure is the fact that the regions of deep clouds, such as in the southern part of the leg and at the beginning of the flight, are characterized by narrow distributions compared to regions of thinner clouds, such as in the northern part.

Fig. 7 summarizes the above analysis with τ_e versus σ, as derived from the distributions measured with the ARAT POLDER, DLR-F20 POLDER, and DLR-F20 OVID. It illustrates clearly the inverse relationship between the mean and the width of the distributions.

4.2 Comparison with the adiabatic estimate

The feature discussed above has significant consequences for the parameterization of optical thickness in stratocumulus. A scheme based on droplet concentration and cloud geometrical thickness provides an estimate of the optical thickness at the top of the convective cores. However, the mean cloud albedo is dependent upon the frequency distribution of optical thickness in the cloud layer, that includes regions of downdraft and clear air regions. More precisely it depends upon the effective optical thickness. The adiabatic estimate thus overestimates τ_e. Depending on how the cloud geometrical thickness is defined, either corresponding to the maximum cloud top altitude or the mean cloud top altitude, the adiabatic estimate will correspond to the maximum optical thickness or a value slightly below the maximum. If the frequency distribution of optical thickness gets broader, it is likely that the difference between the adiabatic estimate and the effective optical thickness increases.

The determination of an adiabatic reference of optical thickness for each of the samples analyzed in the previous section is a difficult task. In situ measurements provide accurate estimates of the droplet concentration and of the cloud base and top, for deriving cloud geometrical thickness. However, they are local estimates that do not represent correctly the actual distribution of cloud geometrical thickness within each sample of 7×40 km. In addition, in situ measurements during EUCREX mission 206 were not synchronized with remote sensing measurements so that the comparison between the two is possible only after space/time interpolation (Sec. 3.1). Remote sensing measurements provide two independent estimates of the cloud top altitude (from POLDER stereo analysis and from LEANDRE), but the altitude of the cloud base is not documented with these instruments and it must be derived from in situ measurements.

Fig. 8 combines these various estimates. It shows the ratio of the effective optical thickness within each sample to the adiabatic reference τ_{ad}, as a function of the corresponding standard deviation within the sample. As in Sec. 3 the adiabatic reference is calculated by three different ways: with in situ measurements of H and N (vertical bars), and with measurements of cloud top altitude derived from POLDER and LEANDRE. Only seven of the samples defined in Sec. 4.1 can be documented with in situ measurements. For each of those seven samples however more than one ascent or descent through the cloud layer are available, providing various values of the adiabatic reference. The vertical bar in Fig. 8 reflects the range of variability of the adiabatic estimates in each of the seven samples. The values of cloud top altitude derived from POLDER stereo analysis (Sec. 3.2) and from LEANDRE (Sec. 3.3) have been averaged over each sample. Values of the adiabatic reference of optical thickness have been derived from the values of mean cloud top altitude by assuming the cloud base is at 650 m and the droplet concentration is $400\,cm^{-3}$. The corresponding values of the ratio τ_e/τ_{ad} are represented by white (POLDER) and black (LEANDRE) dots.

Fig. 8 confirms that the adiabatic estimate provides a good diagnostic of the effective optical thickness when the frequency distribution of optical thickness is narrow. When the distribution is broad the ratio depends significantly upon the value selected for the cloud geometrical thickness in the estimate of the adiabatic reference. There is a significant scatter in the relationship between τ_e/τ_{ad} and the width of the optical thickness distribution because the sampling strategy was not optimum for the estimate of the cloud geometrical thickness. However, this analysis demonstrates that the effective optical thickness can be as small as 40 % of the value derived from the adiabatic model when the width of the optical thickness distribution is larger than 0.8.

4.3 Comparison with satellite measurements

At the scale of a GCM grid, that is at a scale of about 100 km, the question is to what extent the mean radiative properties of the cloud system can be predicted from its mean dynamical and microphysical properties, and how the inhomogeneity of the cloud structure affects the prediction.

OVID and LEANDRE measurements characterize a thin line along the DLR-F20 and ARAT flight tracks respectively. POLDER measurements on board the ARAT (7 legs) and the DLR-F20 (5 legs) provide a better statistics of the horizontal field of optical thickness with their larger field of view of about 7 km width (Sec. 2). Finally, satellite measurements with AVHRR, described in FB cover the whole area, but the image was taken 1.5 hour before the beginning of the ARAT flight. The frequency distributions of optical thickness derived from these instruments are compared in Fig. 9a. OVID and LEANDRE measurements have a spatial resolution of 220 m and 100 m respectively. POLDER measurements on board the ARAT have been processed at a resolution of 230 m. The spatial resolution of POLDER on board the DLR-F20 depends on the aircraft altitude but it is comparable to the resolution of the ARAT POLDER. AVHRR measurements however have been processed with a coarser spatial resolution of 1.1 km and then averaged over 5×5 pixels. The image has been taken at 08:30 UTC. For the comparison it is assumed that the cloud system is stationary in time and that it moves uniformly at a wind speed of $10\,ms^{-1}$ from a direction of 50° (Fig. 3 in PBB). The leg **M-A** in the satellite image is thus translated by 54 km, in the direction of 50°, corresponding to the delay between the image and the beginning of the flight (1.5 hours). It is then translated by an additional 84 km distance corresponding to 2:20 h of flight duration. The area between these two boundaries is assumed to represent the part of the cloud system that crosses the leg **M-A** between 10:00 and 12:20 UTC. The frequency distribution of the optical thickness derived from the AVHRR measurements is then calculated within this area for comparison with aircraft measurements.

The five distributions are reported in Fig. 9a. While OVID and POLDER data are available for the whole flight, the LEANDRE data have been processed for optical thickness on only a part of the ARAT third leg (Pelon et al, 2000). Their statistical significance is thus slightly lower. The values of effective optical thickness and standard deviation σ measured by the various instruments are summarized in Table 1. Both POLDER measurements have similar distributions, but OVID estimates show almost no values larger than 35, while the maximum values with POLDER are larger than 70. The AVHRR distribution is narrower with no values larger than 15. Three reasons can be explored for explaining such a discrepancy:

(i) The difference in spatial resolution: The pixels of AVHRR are 4 to 5 times larger than POLDER pixels. Smoothing of the optical thickness field obviously reduces the proportion of large values if they are restricted to single pixels. This hypothesis has been tested by averaging the POLDER values over 25 pixels areas before the calculation of the frequency distribution. The difference with the initial distribution is not significant and it can be concluded that spatial resolution is not sufficient to account for the discrepancy. In addition, OVID data show the same feature while their spatial resolution is even smaller than the POLDER one.

(ii) Stationarity of the cloud system: The AVHRR image analyzed here was taken at 08:30 UTC while aircraft measurements were performed between 10:00 and 12:20 UTC. Numerical mesoscale simulations (Fouilloux and Iaquinta, 1998) have shown that the horizontal inhomogeneity of the cloud system increases during the morning, with a maximum at 12:00 UTC. In addition, the translation used to compensate for the cloud advection between 08:30 and 10:00 to 12:20 UTC is such that part of the analyzed cloud layer is over land while the aircraft measurements were performed over sea. It is also likely that the surface could influence cloud homogeneity, even if the main structures are stationary.

(iii) The retrieval scheme: Both OVID and AVHRR optical thicknesses are derived from monodirectional radiance measurements at two wavelengths. POLDER estimates are derived from measurements of the multidirectional radiances. It is likely that the difference between the distributions reflects the difference in the retrieval methods. In particular, the use of directional radiances with POLDER provides a better description of the variability of the cloud optical thickness and possibly a better estimate of the large values.

Fig. 9b shows additional information from AVHRR and OVID with the retrieved values of droplet effective radius. Both instruments, despite their very different spatial resolutions, show similar distributions of droplet radii. However, the comparison with in situ measurements (Fig. 5 in PBB) reveals that the droplet radii are overestimated, with values up to 11 to 14 μm while the maximum values in PBB are smaller than 8 μm. This is confirmed by the comparison with the values of effective radius at the top of an adiabatic cloud that are reported in Fig. 9b, for various values of the cloud geometrical thickness, from 100 m to 400 m. The overestimation of the droplet effective radius seems to be inherent to the multiwavelength retrieval methods. It has been reported by many authors (Platnick and Twomey, 1994) and it has been attributed to anomalous absorption (Stephens and Tsay, 1990). This additional similarity between OVID and AVHRR measurements supports our above conclusion that the difference in the distributions of optical thickness are related to the retrieval techniques rather than to the spatial resolution of the instruments.

The effective optical thickness derived from POLDER (10.6) corresponds to the adiabatic estimate over the smallest observed cloud cells, such as in the northern end of the leg at the beginning of the flight and well below the adiabatic estimate derived with the mean geometrical thickness observed with the M-IV during the cloud traverses, namely 280 m. At 280 m and a droplet concentration of $400\,cm^{-3}$ the adiabatic estimate of optical thickness would be 14.9. In other words, to obtain an adiabatic estimate of optical thickness of 10.6, with a geometrical thickness of 280 m, a droplet concentration of $150\,cm^{-3}$ is required, well below the value of $400\,cm^{-3}$ measured in situ with the M-IV. The comparison is worst with the effective value derived from AVHRR (8.8). These various calculations illustrate the difficulty in assessing experimentally the indirect effect because of the low sensitivity to droplet concentration ($N^{1/3}$) compared to the high sensitivity to cloud geometrical thickness ($H^{5/3}$). They also reveal that the effect of cloud inhomogeneities on the prediction of optical thickness is significant compared to the accuracy needed in a GCM for the simulation of the indirect effect.

5. Conclusions

The stratocumulus sampled during mission 206 of the EUCREX experiment was inhomogeneous, with regions of thick and continuous cloud layer and regions of thin and broken cloud layer. Therefore this case study is particularly suited for tests of parameterization schemes of optical thickness. The primary objective is to test a parameterization based on the adiabatic vertical profile of the microphysics described in PBB as opposed to the VUPPM currently used in climate models. Both schemes predict a dependence of optical thickness as $N^{1/3}$, but the key difference between the two is the dependence on the cloud geometrical thickness H: the optical thickness is proportional to H in the VUPPM, while it is proportional to $H^{5/3}$ in the adiabatic model.

The adiabatic model strictly applies within the core of the convective cells. Therefore the first step has been to select peak values of optical thickness, measured at the top of the convective cells with the POLDER multidirectional radiometer. They have been compared to estimates derived from the adiabatic model, with the droplet concentration and the cloud geometrical thickness measured in situ with the M-IV. Independent tests have been performed with the cloud geometrical thickness derived from measurements of cloud top altitude with the POLDER stereo analysis and with the lidar LEANDRE. The three methods confirm that the optical thickness is proportional to $H^{5/3}$ rather than to H, at the scale of the convective cells.

The second step extends the comparison to the whole cloud system. The horizontal maps of optical thickness derived from POLDER measurements along the ARAT legs cover a domain of 7×120 km for each leg. They have been divided into three samples of 7×40 km each. The frequency distribution of optical thickness within each sample has been fitted to a lognormal distribution characterized by its mean, referred to as the effective optical thickness and its standard deviation. The regions of thick and continuous cloud layer show narrow distributions with a standard deviation smaller than 0.4, while regions of broken clouds are characterized by values of σ greater than 0.9. Similar analysis has been performed with the DLR-F20 POLDER and OVID measurements. The composite of these three data sets shows that the effective optical thickness is inversely proportional to the standard deviation.

In the third step, the effective optical thickness of the ARAT samples has been compared to the adiabatic prediction with the geometrical thickness directly measured in situ, and from POLDER and LEANDRE estimates of cloud top altitude. In regions of narrow optical thickness distributions the adiabatic prediction is close to the effective value. In regions of broad distributions, there is a significant scatter in the comparison and the effective value can be as small as 40 % of the adiabatic prediction.

For the study of the aerosol indirect effect, parameterizations are needed that capture the physics of the interaction between droplet concentration N and cloud radiative properties. It is known for long time that the cloud optical thickness should be proportional to $N^{1/3}$, though such a relationship has never been demonstrated experimentally. The dependence of cloud optical thickness upon cloud geometrical thickness H is still uncertain, either H in the VUPPM or $H^{5/3}$ in the adiabatic model. The difference is crucial for the prediction of the aerosol indirect effect. A high sensitivity to H implies that second order effects of aerosols on precipitation efficiency and cloud life time (Albrecht, 1989) could significantly reinforce the Twomey effect. The EUCREX mission 206 suggests that the adiabatic parameterization ($H^{5/3}$) is more realistic at the scale of the convective cells. However in GCMs, the radiative properties are meaningful only at the scale of a cloud system. It is thus essential to validate experimentally the relationship between the effective optical thickness and the mean cloud geometrical thickness at such a scale. Scaling up of the observations in mission 206 reveals that the effective optical thickness is correctly diagnosed with the adiabatic model in homogeneous regions but significantly overestimated by this model in inhomogeneous regions.

Finally the frequency distributions have been calculated at the scale of the whole system with the POLDER and OVID measurements and the values derived from AVHRR satellite measurements. They show that estimates based on monodirectionnal measurements of radiances at two wavelength (OVID and AVHRR) tend to underestimate the proportion of large values of optical thickness compared to measurements of the directional radiances with POLDER. The effective value of the POLDER optical thickness distribution (10.6) corresponds to a cloud geometrical thickness of 230 m with the adiabatic model. Such a value is close to the smallest values measured in situ and smaller than the mean cloud geometrical thickness derived from in situ measurements. Further field campaigns are then required to document precisely the microphysics/radiation interaction, from the scale of the cloud cells to the scale of the cloud system. The EUCREX mission 206 suggests that special attention must be given to the synchronization of in situ measurements of cloud microphysics with the remote sensing measurements of the cloud radiative properties.

However, the natural variability of the microphysical fields in stratocumulus is too diverse for establishing empirical parameterizations of their effects on the mean cloud radiative properties.

Stochastically generated cloud fields can be used for the numerical simulation of the radiative transfer but they miss the vertical organization of the turbulent structures which play a significant role in the horizontal distribution of optical thickness within a stratocumulus layer. Our strategy will thus be to perform simulations with cloud resolving models. The data collected in situ can then been used for constraining the statistical properties of the simulated fields of microphysics and optical thickness at the cloud scale. Such simulations will be more suited than incomplete data sets or stochastically generated fields for studying the sensitivity of the mean cloud albedo to cloud inhomogeneities.

Acknowledgments:

The authors are grateful to the Meteo-France Merlin-IV, ARAT, and DLR-F20 teams for their efficient contribution to the data collection. This work has been supported by INSU-PATOM under grant 94/08 and by the European Union, Environment and Climate Division, under grant ENV4-CT95-0117.

FIGURE CAPTIONS

Figure 1: Contours of optical thickness derived from the ARAT POLDER, (a), the DLR-F20 POLDER (b), and the DLR-F20 OVID (c) measurements. Solid lines indicate the flight track. The space coordinate (y) is the distance from point **M** along the leg **M-A**. The time unit is such that 1 hour corresponds to 36 km, a value equal to the wind speed across the direction **M-A**.

Figure 2: Comparison of the optical thickness derived from the ARAT POLDER, τ_{polder}, with the adiabatic value derived from in situ measurements, τ_{ffssp}, with the M-IV.

Figure 3: Horizontal map of the ARAT POLDER optical thickness during leg 2, with the selected peak values indicated by black dots.

Figure 4: Peak values of optical thickness during legs 2 (black dots) and 3 (white dots) of the ARAT, versus the cloud geometrical thickness derived from the POLDER stereo analysis at the same location. The solid line is the 5/3 slope; the dotted line is the 1/1 slope.

Figure 5: Comparison of the optical thickness derived from the ARAT POLDER with the adiabatic model prediction.

(a) Horizontal map of the ARAT POLDER optical thickness

(b) Variations along the second ARAT leg of the POLDER optical thickness at the middle of the POLDER field of view (solid line: τ_{polder}) and of the value calculated with the adiabatic model and the cloud geometrical thickness derived from LEANDRE cloud top altitude measurements (dotted line: $\tau_{leandre}$). The values of droplet concentration ($400\,cm^{-3}$) and cloud base altitude (650 m) for the adiabatic prediction are selected from the M-IV in situ data.

(c) Comparison of the estimates defined in (b): τ_{polder} versus $\tau_{leandre}$.

Figure 6: Frequency distributions of the POLDER optical thickness for the 7 ARAT legs. The leg **M-A** has been divided into three sections from 0 to 40 km, from 40 to 80 km and from 80 to 120 km. The values indicated in each distribution are the log of the effective optical thickness $Log(\tau_e)$ and its standard deviation σ. The corresponding lognormal distributions are plotted with dashed lines.

Figure 7: Effective optical thickness τ_e versus the standard deviation of the distributions σ, for the ARAT POLDER, DLR-F20 POLDER and OVID measurements. The frequency distributions have been calculated over the same sections as in Fig. 6.

Figure 8: Ratio of the effective optical thickness τ_e to the adiabatic prediction versus the standard deviation of the optical thickness frequency log distribution σ. The vertical bars correspond to the range of variability of the adiabatic predictions derived from in situ measurements of cloud geometrical thickness. The white dots correspond to values derived from the POLDER stereo analysis and the black dots correspond to the estimates derived from the LEANDRE measurements of cloud top altitude.

Figure 9: (a) Frequency distributions of optical thickness over the whole cloud system sampled by the aircraft, derived from the ARAT POLDER, DLR-F20 POLDER, OVID, AVHRR, and LEANDRE measurements. (b) Frequency distributions of effective radius derived from the DLR-F20 OVID and AVHRR measurements. The adiabatic predictions of effective radius at cloud top, for 4 values of cloud geometrical thickness, from 100 to 400 m, are indicated by vertical bars on top of the graph.

Table 1: Values of effective optical thickness (τ_e) and standard deviation (σ) for different instruments.

Table 1: Values of effective optical thickness (τ_e) and standard deviations (σ) for different instruments.

instrument	$\overline{\tau}_{ln}$	$\sigma_{ln(\tau)}$
POLDER ARAT	9.27	0.91
DLR-F20 POLDER	10.48	0.90
OVID	7.39	0.73
LEANDRE	6.46	0.75
AVHRR	8.21	0.44

References

Baker, M. B., 1997. Cloud microphysics and climate. Science, 276, 1072-1078.

Barker H. W., B. A. Wielicki, and L. Parker, 1996. A parameterization for computing grid-averaged solar fluxes for inhomogeneous boundary layer clouds. Part II: Validation using satellite data. J. Atmos. Sci, 53, 2304-2316.

Brenguier, J. L., and Y. Fouquart, 2000. Introduction to the EUCREX-94 mission 206. Atmos. Res. This issue.

Cahalan, R. F., D. Silberstein and J. B. Snider, 1995. Liquid water path and plane-parallel albedo bias during ASTEX, J. Atmos. Sci, 52, 3002-3012.

Fouilloux, A., and J. Iaquinta, 1997. Comparison of stratocumulus cloud modeling with satellite observations and in-situ measurements. Journal of Geophysical Research, 102, 13595-13602.

Fouilloux, A., J. F. Gayet, and K. T. Kriebel, 2000. Determination of cloud microphysical properties from AVHRR images: comparisons of three approaches. Atmos. Res. This issue.

Pawlowska, H., J. L. Brenguier, and F. Burnet 2000. Microphysical properties of stratocumulus clouds. Atmos. Res. This issue.

Pelon, J., C. Flamant, V. Trouillet, and P. H. Flamant, 2000. Optical and microphysical parameters of dense stratocumulus clouds during mission 206 of EUCREX'94 as retrieved from measurements made with the airborne lidar LEANDRE1. Atmos. Res. This issue.

Platnick, S., and S. Twomey, 1994. Determining the susceptibility of cloud albedo to changes in droplet concentration with the advanced very high resolution radiometer. J. Appl. Meteor., 33, 334-347.

Schüller, L., W. Armbruster, and J. Fischer, 2000. Retrieval of cloud optical and microphysical properties from multispectral radiances. Atmos. Res. This issue.

Stephens, G. L., and S. Tsay, 1990. On the cloud absorption anomaly. Quart. J. Roy. Meteor. Soc., 116, 671-704.

Twomey S., 1977. The influence of pollution on the shortwave albedo of clouds. J. Atmos. Sci., 34, 1149-1152.

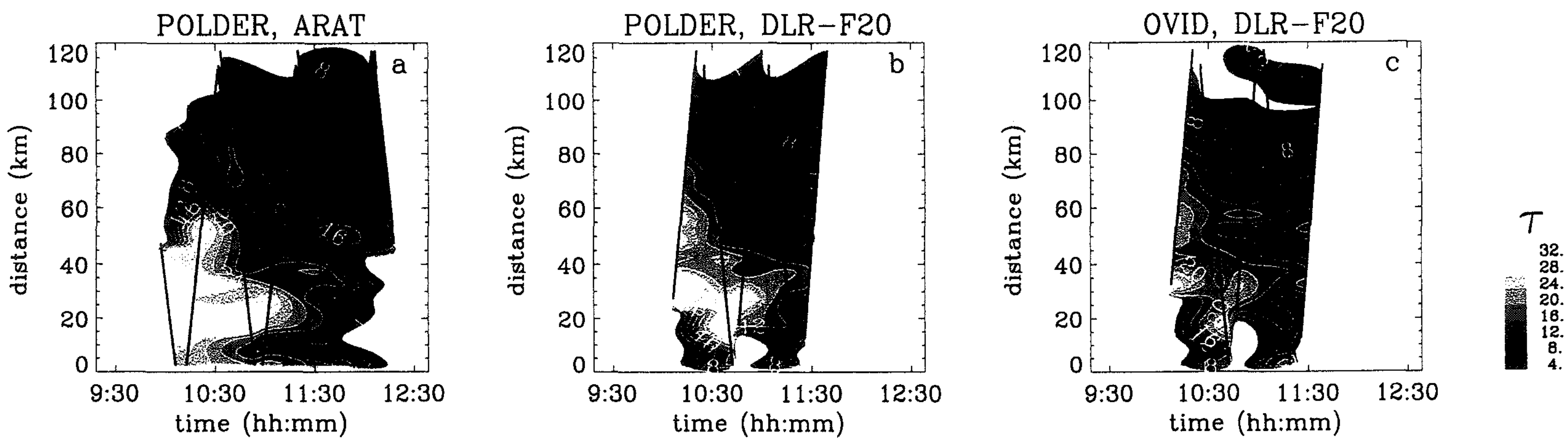
POLDER, ARAT
a
POLDER, DLR-F20
b
OVID, DLR-F20
c
distance (km)
0
20
40
60
80
100
120
time (hh:mm)
9:30
10:30
11:30
12:30
τ
32.
28.
24.
20.
16.
12.
8.
4.

Fig.1

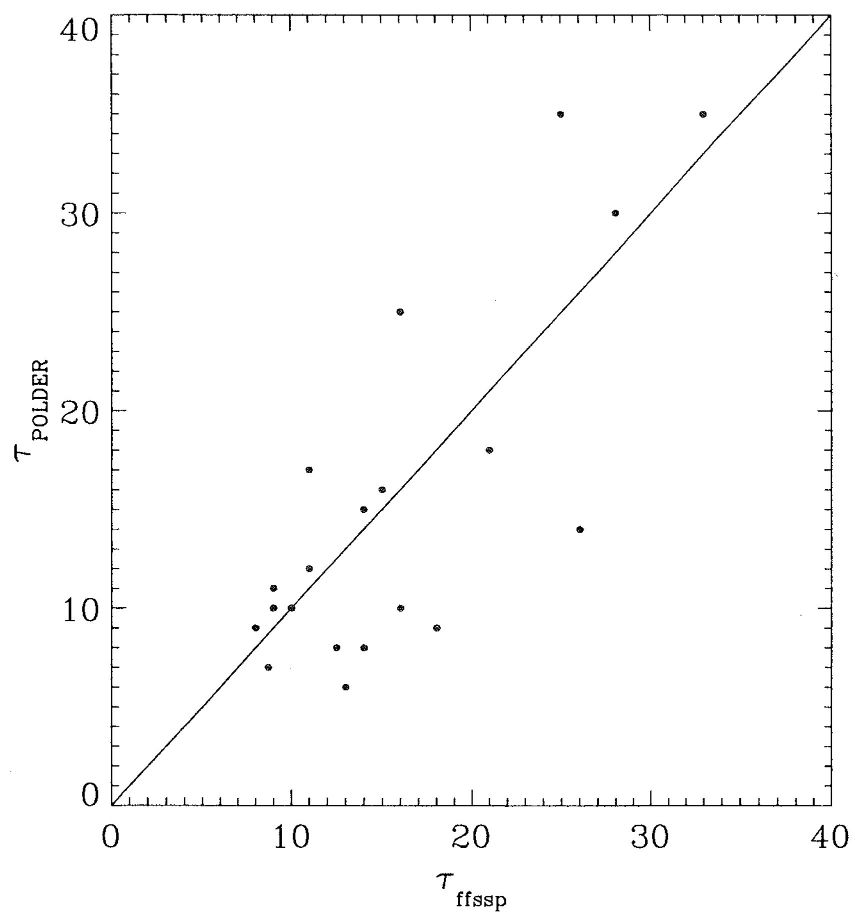

Fig.2

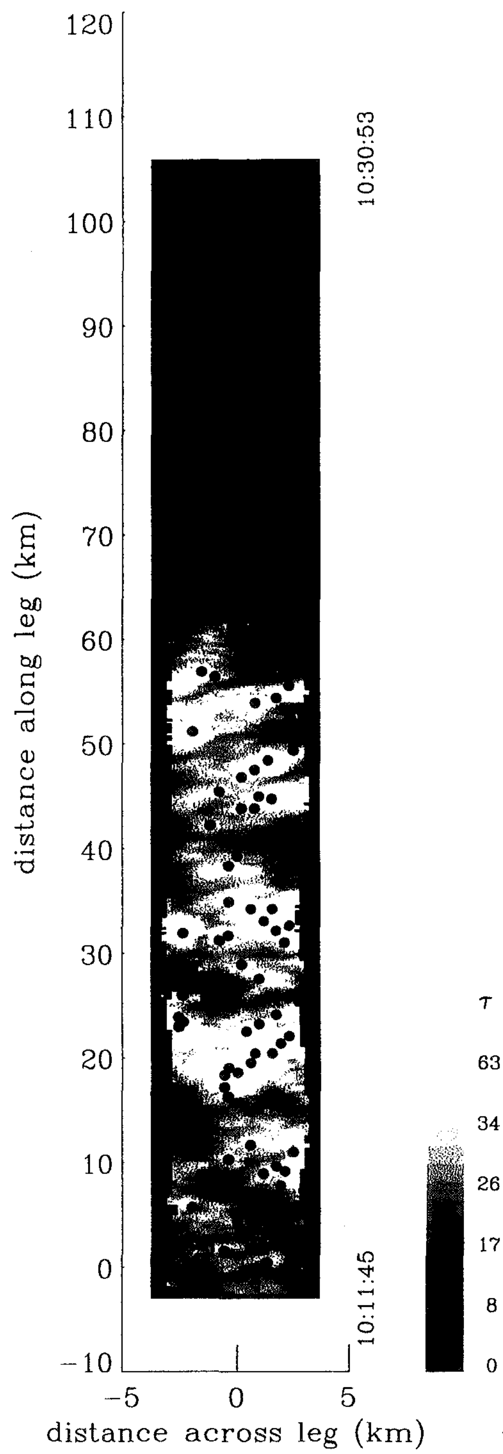
120
110
100
90
80
70
60
50
40
30
20
10
0
−10
distance along leg (km)
−5
0
5
distance across leg (km)
10:30:53
10:11:45
τ
63
34
26
17
8
0

Fig.3

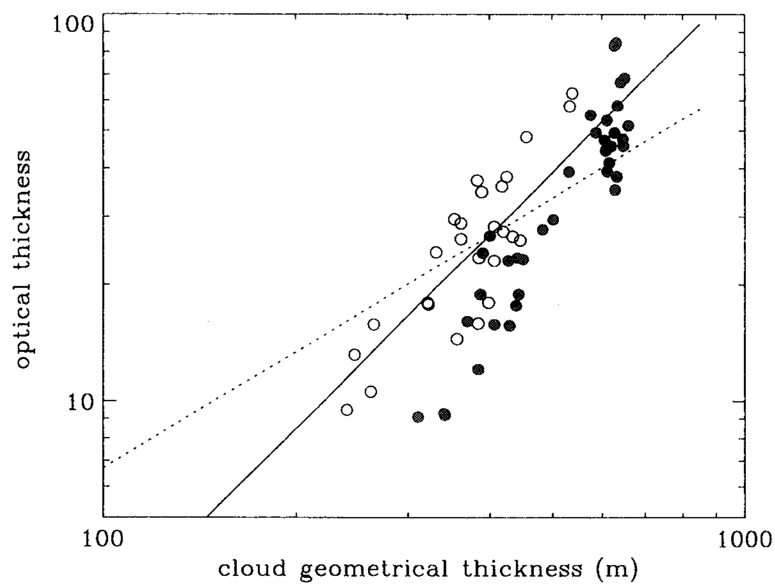
100
10
optical thickness
100
1000
cloud geometrical thickness (m)

Fig.4

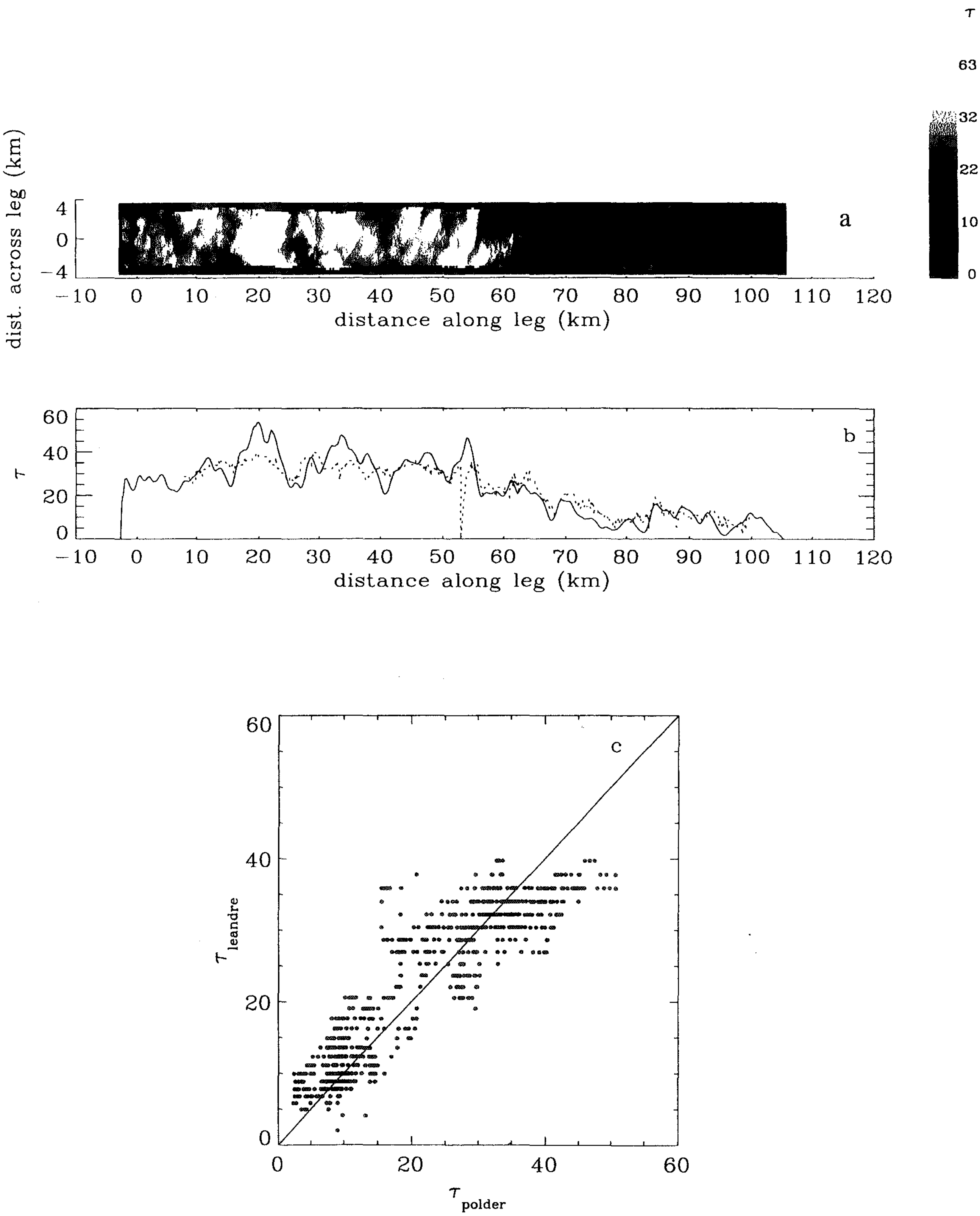
τ
63
32
22
10
0
a
dist. across leg (km)
distance along leg (km)
b
τ
distance along leg (km)
c
τ leandre
τ polder

Fig.5

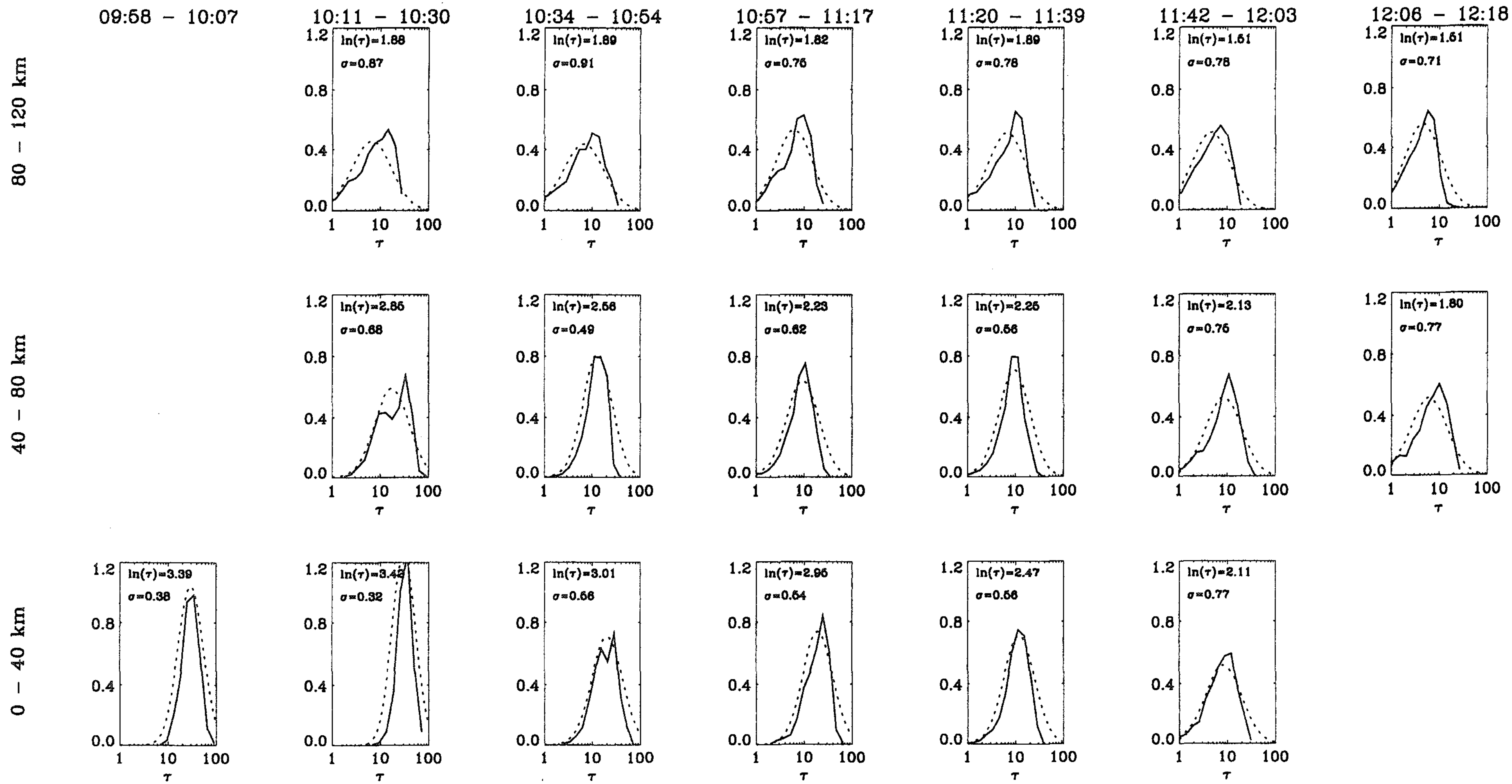
09:58 – 10:07
10:11 – 10:30
10:34 – 10:54
10:57 – 11:17
11:20 – 11:39
11:42 – 12:03
12:06 – 12:18
80 – 120 km
40 – 80 km
0 – 40 km
ln(τ)=1.88 σ=0.87
ln(τ)=1.89 σ=0.91
ln(τ)=1.82 σ=0.76
ln(τ)=1.89 σ=0.78
ln(τ)=1.61 σ=0.78
ln(τ)=1.61 σ=0.71
ln(τ)=2.85 σ=0.68
ln(τ)=2.56 σ=0.49
ln(τ)=2.23 σ=0.62
ln(τ)=2.25 σ=0.56
ln(τ)=2.13 σ=0.76
ln(τ)=1.80 σ=0.77
ln(τ)=3.39 σ=0.38
ln(τ)=3.42 σ=0.32
ln(τ)=3.01 σ=0.66
ln(τ)=2.96 σ=0.64
ln(τ)=2.47 σ=0.58
ln(τ)=2.11 σ=0.77
τ

Fig.6

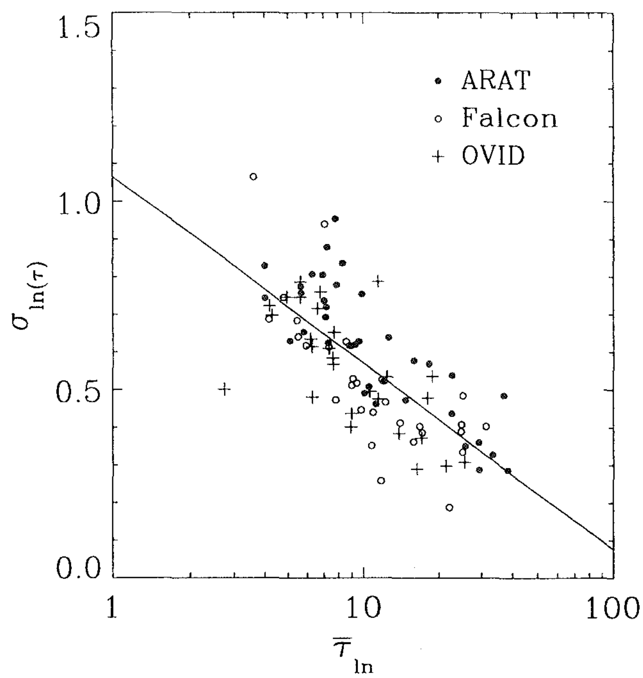
1.5
1.0
0.5
0.0
1
10
100
ARAT
Falcon
OVID
$\sigma_{\ln(\tau)}$
$\overline{\tau}_{\ln}$

Fig.7

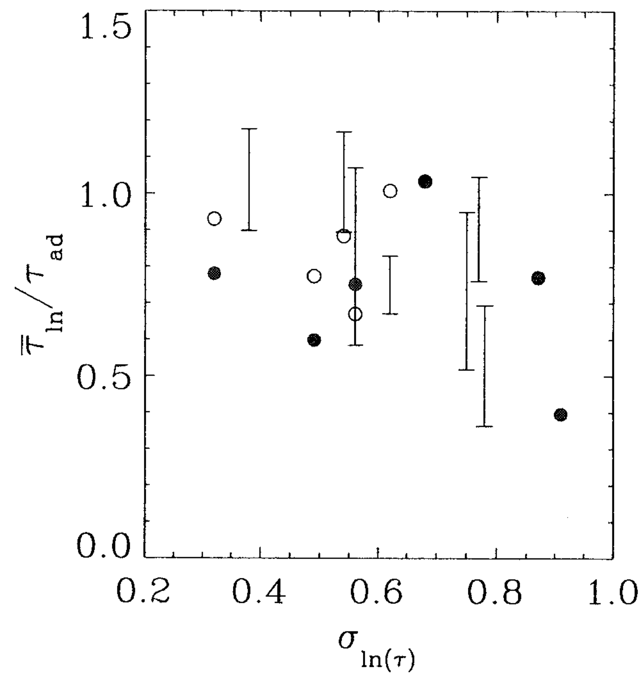

Fig.8

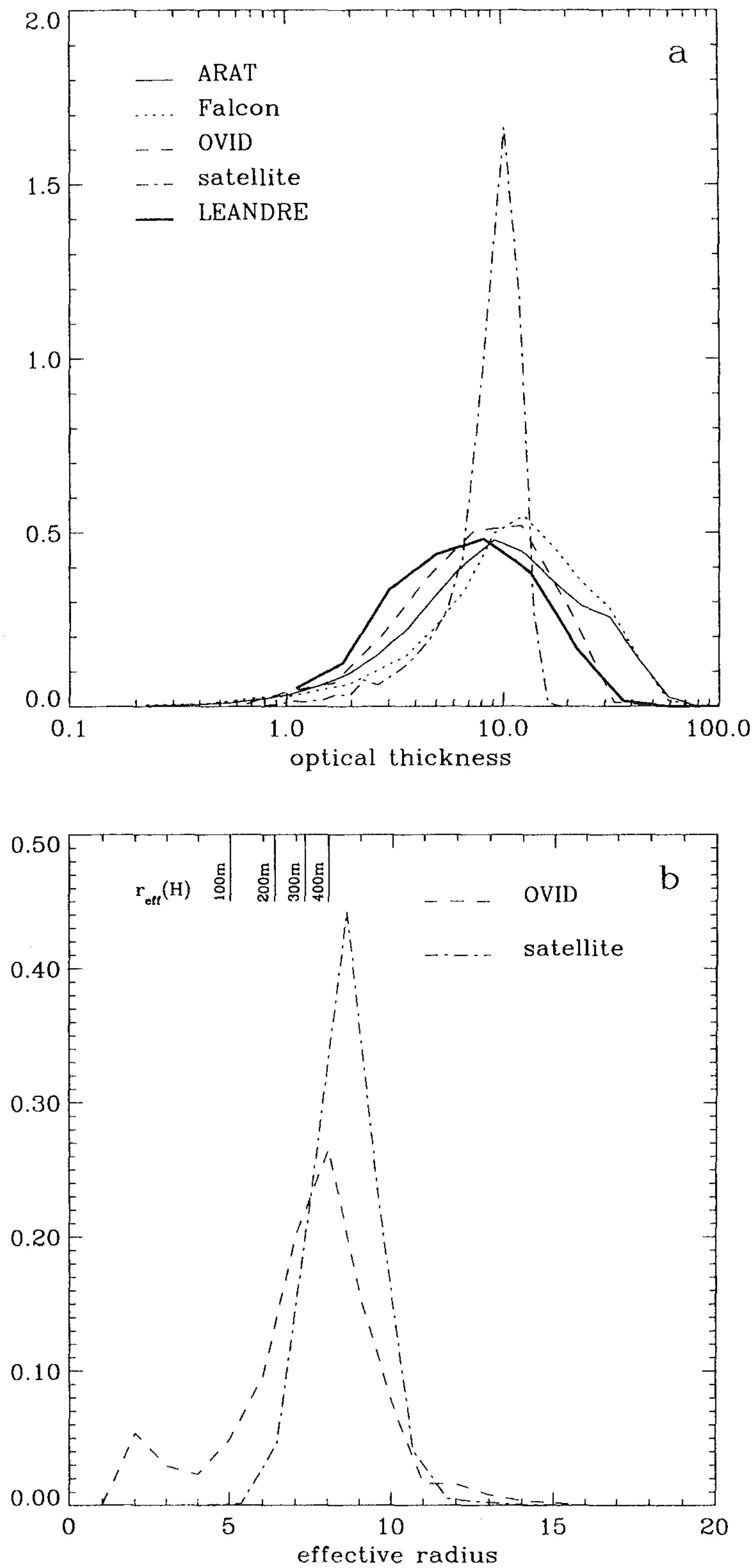
a
ARAT
Falcon
OVID
satellite
LEANDRE
2.0
1.5
1.0
0.5
0.0
0.1
1.0
10.0
100.0
optical thickness
b
r_{eff}(H)
100m
200m
300m
400m
OVID
satellite
0.50
0.40
0.30
0.20
0.10
0.00
0
5
10
15
20
effective radius

Fig.9

Annexe C

An Overview of the ACE-2 CLOUDYCOLUMN Closure Experiment

Tellus, 52B, 815-827, Avril 2000

Tellus (2000), 52B, 815 827
Printed in UK. All rights reserved

TELLUS
ISSN 0280 6509

An overview of the ACE-2 CLOUDYCOLUMN closure experiment

By J. L. BRENGUIER[1]*, P. Y. CHUANG[2], Y. FOUQUART[3], D. W. JOHNSON[4] F. PAROL[3], HANNA PAWLOWSKA[5]**, JACQUES PELON[6], LOTHAR SCHÜLLER[7], F. SCHRÖDER[8] and J. SNIDER[9] [1]*Météo-France (CNRM/GAME), Toulouse, France,* [2]*California Institute of Technology, Pasadena, California, USA,* [3]*Laboratoire d'Optique Atmosphérique, Université des Sciences et Techniques de Lille, France,* [4]*Met. Research Flight, DERA, Farnborough, UK,* [5]*Laboratoire de Météorologie Dynamique, Paris, France,* [6]*Service d'Aéronomie, Paris, France,* [7]*Institut für Weltraumwissenschaften, Freie Universität Berlin, Germany,* [8]*Deutsches Forschungszentrum für Luft- und Raumfahrt e.V., Wessling, Germany,* [9]*Dept of Atmos. Sciences, University of Wyoming, USA*

(Manuscript received 2 February 1999; in final form 15 October 1999)

ABSTRACT

CLOUDYCOLUMN is one of the 6 ACE-2 projects which took place in June-July 1997, between Portugal and the Canary Islands. It was specifically dedicated to the study of changes of cloud radiative properties resulting from changes in the properties of those aerosols which act as cloud condensation nuclei. This process is also refered to as the aerosol indirect effect on climate. CLOUDYCOLUMN is focused on the contribution of stratocumulus clouds to that process. In addition to the basic aerosol measurements performed at the ground stations of the ACE-2 project, 5 instrumented aircraft carried out in situ characterization of aerosol physical, chemical and nucleation properties and cloud dynamical and microphysical properties. Cloud radiative properties were also measured remotely with radiometers and a lidar. 11 case studies have been documented, from pure marine to significantly polluted air masses. The simultaneity of the measurements with the multi-aircraft approach provides a unique data set for closure experiments on the aerosol indirect effect. In particular CLOUDYCOLUMN provided the 1st experimental evidence of the existence of the indirect effect in boundary layer clouds forming in polluted continental outbreacks. This paper describes the objectives of the project, the instrumental setup and the sampling strategy. Preliminary results published in additional papers are briefly summarized.

1. Introduction and scientific background

CLOUDYCOLUMN was one of the 6 field projects in ACE-2 (Raes et al., 2000). It was specifically dedicated to the study of the indirect effect of aerosols on climate. "Indirect effect" refers here to changes of cloud radiative properties resulting from changes in the properties of those aerosols which act as cloud condensation nuclei (CCN). Changes in chemical composition or physical properties of CCN has the potential to induce changes in cloud droplet number concentration. 2 effects are recognised. For a given liquid water content (LWC) a cloud made of numerous small droplets is brighter (higher albedo) than a cloud made of a few big droplets. This 1st effect is also known as the Twomey effect (Twomey, 1977).

* Corresponding author
METEO-FRANCE, CNRM, GMEI/MNP, 42 av. Coriolis, 31057 Toulouse Cedex 01, France.
e-mail: jlb@meteo.fr
** On leave from Institute of Geophysics, University of Warsaw, Poland.

Polluted clouds are also less efficient at producing precipitation, resulting in an increase of cloud lifetime and horizontal extent (Albrecht, 1989).

The 1995 IPCC report (Houghton et al., 1995) draws together recent study results which show that the current estimate of the global mean radiative forcing due to anthropogenic aerosols, although highly uncertain, is of a comparable magnitude but opposite in sign to the forcing due to anthropogenic greenhouse gases. For the direct effect the IPCC report gives a best estimate of -0.5 W/m^2 (range -0.2 to -1.5 W/m^2) for the effect of aerosol on the global radiation balance. No best estimate is given for the indirect effect, only an uncertainty range of 0 to -1.5 W/m^2. Thus the authors of the IPCC report consider the net effect is a cooling of the climate system, with the main contribution coming from marine boundary layer clouds. The high albedos (30–40%) of these clouds compared with the ocean background (10%) give rise to large deficits in the absorbed solar radiative flux at the top of the atmosphere, while their low altitude prevents significant compensation in thermal emission (Randall et al., 1984).

Although "indirect effects" have been implicitly accepted in the difference between marine and continental clouds for some decades, few experiments have been able to qualify these effects in individual cloud systems. Examples are the ship track studies off the west coast of the USA (King et al., 1993) and, at a larger scale, the difference in radiative properties between summer and winter clouds off the coast of Australia, that are attributed to changes in the natural CCN concentration (Boers et al., 1998).

One difficulty with in situ studies arises from the dependence of the radiative properties of a cloud on its morphological properties (particularly geometrical thickness), whereas the effect of anthropogenic aerosols through changes in droplet concentration is a second order effect. In the Twomey approximation (plane parallel cloud vertically uniform), the optical thickness varies with cloud geometrical thickness H and the cube root of droplet concentration $N^{1/3}$ (Twomey, 1977):

$$\tau \propto N^{1/3} H. \tag{1}$$

For a cloud with an adiabatic vertical profile of LWC, a more realistic description, the optical thickness is proportional to the power 5/3 of the geometrical thickness (Boers and Mitchell, 1994, Brenguier et al., 2000):

$$\tau \propto N^{1/3} H^{5/3}. \tag{2}$$

The 2nd indirect effect is related to changes in cloud precipitation efficiency. At a fixed LWC value, an increase of the droplet concentration results in a decrease of the droplet sizes and a reduced probability of collision-coalescence between droplets to form precipitation (Albrecht, 1989). It is thus likely that an increase of the droplet concentration will result in a decrease of the precipitation efficiency and therefore in an increase of the cloud spatial extent and lifetime, hence an increase of mean cloud albedo. The higher dependence of optical thickness on geometrical thickness ($H^{5/3}$ instead of H) is important because it suggests that the second indirect effect could be more significant than the first.

The experimental assessment of the indirect effect is challenging because of the high variability of the cloud morphological characteristics whereas changes in the droplet concentration that are related to changes of the CCN population are rather limited. Radiative properties observed in a cloud system are also highly variable with a standard deviation of the same order of magnitude as the change expected between a pure marine cloud and a polluted one. Droplet number concentration is also highly variable (Pawlowska and Brenguier, 2000). Although values observed near cloud base in convective updrafts closely reflect the CCN population, these conditions represent a limited fraction of the cloud systems. In other regions the droplet concentration is affected by entrainment and mixing with sub-saturated air and by the formation of precipitation.

A careful experimental design is essential to establish a direct link between CCN properties, droplet number concentration and cloud radiative properties. The methodology used in CLOUDYCOLUMN to examine both aspects of the indirect effect was designed to overcome these difficulties. In situ measurements of the cloud microphysics were synchronized with simultaneous measurements of the cloud radiative properties made by a second aircraft flying above the cloud layer. Data obtained in this manner have been particularly useful for the validation of the anticipated relationship between optical and cloud geometrical thickness (Brenguier et al., 2000).

Furthermore, cloud systems with similar morphologies but which were fed by air with different aerosol properties were studied, with emphasis on thin stratocumulus cloud systems. This is because the radiative properties of thin clouds are the most sensitive to a change in the droplet concentration. In addition, to avoid sampling artifacts, identical sampling strategies were used in the various cases studied. Finally, the flight track used for most missions (60 km square) allowed retrieval of turbulent fluxes in the boundary layer.

2. The instrumental setup

The instrumental setup during the CLOUDYCOLUMN field experiment included 5 instrumented aircraft (Fig. 1).

- The MRF C-130 was equipped for measurements of the physical, chemical and nucleation properties of the aerosols, and for measurements of the turbulent fluxes and cloud microphysics. The complete description of the C-130 equipment is given in Johnson et al. (2000).
- The Pelican is operated by the Center for Interdisciplinary Remotely Piloted Aircraft Studies (CIRPAS). The Pelican, a highly modified Cessna Skymaster, although significantly smaller than the C-130, was also equipped for measurement of aerosol properties and turbulent fluxes. A complete description of the CIRPAS Pelican equipment is given in Raes et al. (2000). Chemical composition measurements were conducted for some CLOUDYCOLUMN flights and provide a single measurement of average boundary layer sulfate, nitrate, chloride, organic carbon and trace metal concentrations (Schmeling et al., 2000).

These 2 aircraft were dedicated to boundary layer measurements.

- The Météo-France M-IV was equipped for microphysical measurements of aerosols, cloud droplets, precipitation, aerosol physical and nucleation properties, and turbulent fluxes.
- The DLR Do-228 carried a multiwavelength radiometer (FUB-OVID), a multidirectional radiometer (LOA-POLDER) and a scanning radiometer (FUB-CASI).
- The ARAT F-27 participated in the field experiment for a short period with its airborne lidar (SA-LEANDRE).

These latter 2 aircraft carried out remote measurements of the cloud radiative properties. In addition to these aircraft measurements, information on the properties of aerosols was obtained at the ACE-2 ground stations in Portugal, Madeiras, Canaries and Azores (see Heintzenberg and Russell, 2000).

Details on the instrumentation of the M-IV,

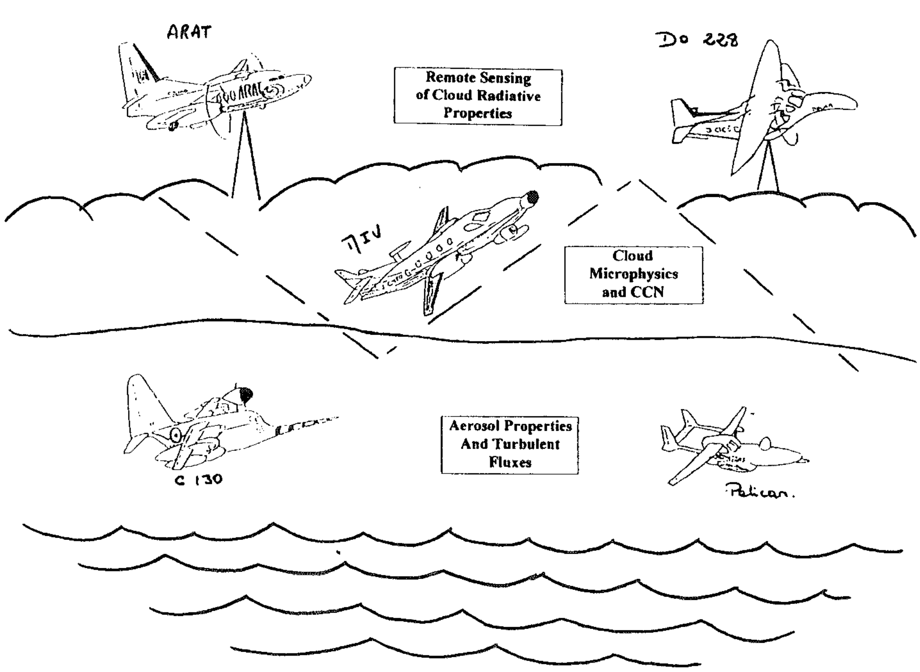

Fig. 1. Illustration of the CLOUDYCOLUMN experiment.

Do-228 and ARAT aircraft are given in the following sections.

2.1. *Instrumentation on board the M-IV*

Sampling characteristics of the aerosol instrumentation flown on the M-IV during ACE-2 are summarized in Figs. 2 and 3. Four instruments, 2 condensation nuclei (CN) counters (TSI 3760A; Schröder and Ström, 1997), the PCASP-100X (Petzold et al., 1997), and the University of Wyoming cloud condensation nucleus counter (WYO-CCN; Snider and Brenguier, 2000) were located inside the M-IV and sampled aerosol via 2 separate inlets. The CCN were sampled via a quasi-isokinetic inlet which was located within a velocity diffuser. The 3 other aerosol instruments sampled via a reverse-flow inlet similar to the device characterized by Schröder and Ström (1997). The upper cut-off diameters were estimated to be 8 µm and 1 µm, respectively (Snider and Brenguier, 2000). The former is a semi-quantitative assessment and because of non-ideal effects discussed by Huebert et al. (1990) it probably overestimates the actual size cut.

In addition, the M-IV instrumentation included three optical spectrometers for the characterization of larger aerosol (FSSP-300; Baumgardner et al., 1992), droplets (Fast-FSSP; Brenguier et al., 1998), and precipitation (OAP 200-X, PMS Inc. Boulder, Colorado, USA). These devices were mounted on the fuselage below the cockpit. The M-IV was also equipped for the measurements of wind, thermodynamics, broad-band radiation, and turbulent fluxes.

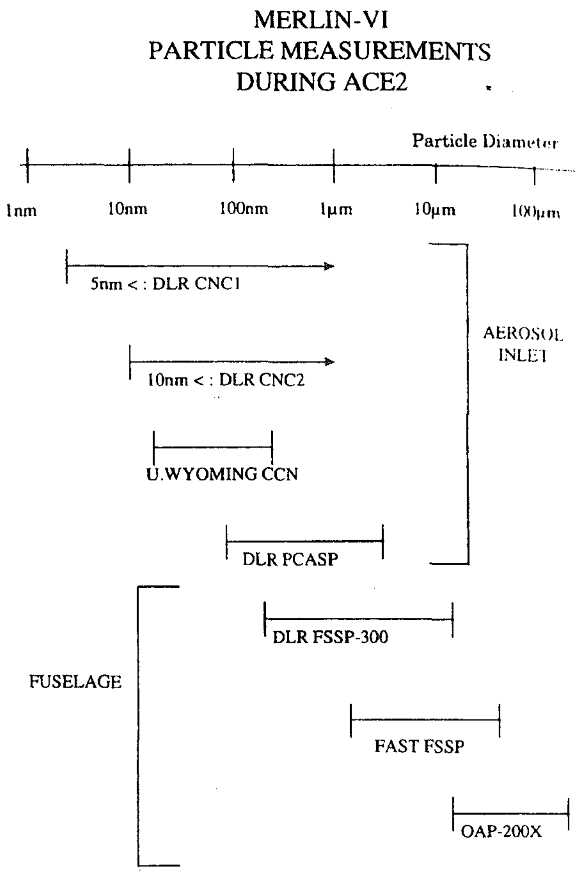

Fig. 3. Summary of the particle measurement capability on board the M-IV. *Aerosol inlet* refers to instruments installed inside the aircraft and connected to the aerosol inlet, thus measuring dry aerosols. *Fuselage* refers to instruments mounted on the aircraft nose, thus measuring the aerosols and cloud particles at ambient humidity.

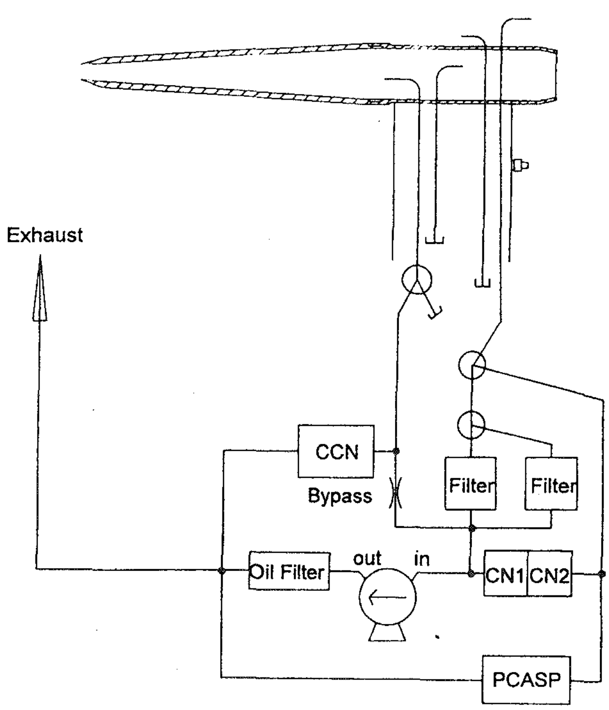

Fig. 2. Aerosol sampling system implemented on the MERLIN aircraft.

2.2. *Radiative measurements on board the Do-228*

The Do-228 was equipped with three radiometers. POLDER is a multidirectional radiometer in the visible, operated by the Laboratoire d'Optique Atmospherique (Lille, France). The instrument and preliminary results are described in Parol et al. (2000). A similar instrument was installed on the ADEOS satellite and provided measurements for the first week of the experiment.

The Optical Visible and Near Infrared Detector (OVID) is a high resolution multichannel analyzer for airborne remote sensing of atmospheric properties in the spectral range of 500 nm to 1700 nm (Schüller et al., 1997). The instrument consists of two separate, but nearly identical detection systems. During the ACE 2 field campaign, the OVID performed radiance measurements of the reflected solar radiation in a nadir viewing configuration, with a spectral resolution of 0.8 nm between 700 nm and 1000 nm (OVID-VIS) and 6 nm between 1000 nm and 1700 nm (OVID-NIR). The sampling time of both systems was about 100 ms during the ACE 2 flights above clouds. The combination of non-absorbing shortwave channels and near infrared channel within absorbtion bands of liquid water (1500 nm) enables the remote sensing of cloud optical and microphysical properties. Channels within absorption bands can be used to determine cloud top heights (O_2-A band at 760 nm) and atmospheric water vapour content ($\rho\sigma\tau$ band at 900 nm).

The Compact Airborne Spectrographic Imager (CASI) (Babey and Soffer, 1992) is a "pushbroom" imaging spectrometer with a 34° field of view (across track). The spectral range from 430 nm to 870 nm can be covered with 512 pixels in the spatial axis and 288 spectral channels. During the ACE 2 campaign, CASI was operated onboard the Do-228 aircraft to measure reflected solar radiation. The programmable channels were chosen to allow derivation of cloud albedo and optical thickness (with maximum spatial resolution) as well as cloud top height, using measurements within the O_2-A band over 39 directions.

2.3. Lidar measurements on board the ARAT

The French Atmospheric and Remote sensing Aircraft (ARAT) took part in the Cloudy Column experiment after the first continental aerosol outbreak was observed from the south of Portugal. It was flown with the airborne lidar LEANDRE2 (Flamant et al., 1998), which was operating at 730 nm. The lidar measurements allowed retrieval of the cloud top height and the in-cloud extinction near cloud top. Updrafts and downdrafts were identified from cloud-top height variations. The altitude of the cloud base has been obtained in some of the downdrafts, where the optical thickness was less than 3, allowing the lidar beam to penetrate the cloud down to the surface. Lidar data were taken simultaneously with upward and downward shortwave and longwave flux measurements from Eppley pyranometers and pyrgeometers.

3. Summary of the field campaign

The meteorological conditions during the ACE-2 experiment are presented in Raes et al. (2000). CLOUDYCOLUMN performed experiments during the 1st and 2nd ACE-2 pollution events (7–9 July and 17–19 July, respectively) and in the clean periods before these events. The list of the flights is reported in Table 1. With the exception of problems with the PCASP (17 June–16 July) and POLDER (8 July), all instrumentation functioned throughout the campaign. The ARAT aircraft with the LEANDRE lidar only participated in the experiment on 8, 9 July.

4. Sampling strategy

As indicated in Table 1, most flights were performed along a square flight-track; the typical horizontal dimension was 60 km. The M-IV was flown either at constant altitude (in cloud or below cloud), or along a zig-zag track that extended from above to below the cloud layer. The Do-228 was flown about 1 km above cloud top. These two aircraft were synchronized by maintaining the M-IV within the field of view of the Do-228 radiometers, with an accuracy of 100 m.

Data acquired from the constant-altitude legs were used to characterize the CCN activation and aerosol spectra (below cloud), droplet and drizzle distributions (in cloud), and turbulent fluxes (all legs). The zig-zag legs provide a rapid characterization of cloud base and top altitudes and of the vertical profile of the microphysics. The distance flown by the M-IV for a complete traverse of the layer ranges between 5 and 10 km depending on the cloud geometrical thickness.

The third aircraft, either the C-130 or the Pelican, was flown in the boundary layer below cloud base (except for flights on 25 June and 8 and 17 July). For flight safety reasons the third aircraft was positioned across the square from the

Table 1. *CLOUDYCOLUMN flights summary*

Date	Boundary layer	In situ	Remote sensing	Air mass	Flight description
17 Jun		M-IV			spectrometer tests
19 Jun		M-IV			spectrometer tests
21 Jun		M-IV			spectrometer tests
24 Jun		M-IV			spectrometer tests
25 Jun		M-IV	Do-228	marine	square*
26 Jun	C-130	M-IV	Do-228	marine	square
01 Jul		M-IV			intercalibration
04 Jul	Pelican	M-IV	Do-228	marine	square
05 Jul	Pelican	M-IV		marine	square
07 Jul	Pelican	M-IV	Do-228	polluted	long legs
08 Jul		M-IV	Do-228		transit to Porto-Santo
08 Jul		M-IV	Do-228/ARAT	polluted	long legs
08 Jul		M-IV	Do-228		transit to Tenerife
09 Jul	Pelican	M-IV	Do-228/ARAT	polluted	square
16 Jul	C-130/Pelican	M-IV	Do-228	marine	square
16 Jul		M-IV	Do-228		transit to Tenerife
17 Jul		M-IV	Do-228	polluted	square
18 Jul	Pelican	M-IV	Do-228	polluted	square
19 Jul	C-130/Pelican	M-IV	Do-228	polluted	square
21 Jul		M-IV	Do-228		intercalibration
07/22		M-IV	Do-228		intercalibration

* "Square" refers to 60 km side square figures flown by the aircraft below, inside, and above the cloud layer, as shown in Fig. 4.

M-IV. The delay between the two aircraft was less than 30 min. Close synchronization between the M-IV and the C-130/Pelican was not as important as between the M-IV and the Do-228 because the aerosol was distributed homogeneously within the boundary layer. But on 19 July, a significant trend in aerosol concentrations was observed between the southern and the northern extent of the square. On this day, both the Pelican and the C-130 conducted boundary layer measurements, with the Pelican flying an octogonal pattern ≈ 100 km upwind of the 60 km square. The spatial inhomogeneity of the aerosol distributions is thus well described in this case.

Fig. 4 shows AVHRR derived cloud images from both a clean and a polluted CLOUDYCOLUMN experiments. The bottom figures represent a large view of the Eastern-Atlantic area and the top figures show the local region of the Canary Islands, with the aircraft trajectory superimposed. The cloud systems in these two days look similar morphologically, although microphysical and radiative measurements demonstrate that their properties are quite different. Fig. 5 shows a typical M-IV trajectory, with horizontal sampling below and inside cloud, and a series of ascents and descents throughout the layer. Each of these ascents or descents provides an estimation of the typical droplet concentration N and of the cloud geometrical thickness H at the location of the traverse. The whole campaign is summarized in Fig. 6 where each point corresponds to one of the vertical profiles. Eight flights are reported in the figure. The two most marine cases are characterized by droplet number concentrations lower than 100 cm^{-3} and cloud geometrical thickness up to 350 m. The other flights show more or less polluted conditions with droplet number concentration up to 400 cm^{-3} on 9 July. The geometrical thickness is slightly lower for the polluted cases. This could be related to the observation that polluted air was also dryer than marine air. CLOUDYCOLUMN experiments generally were conducted at the end of pollution outbreaks over the region, when the influence of continental air was declining. Isolines in Fig. 6 illustrate how various cases could be classified in term of optical thickness and effective radius. For example, it can be seen that an effective radius of about 9 μm is representative of either a

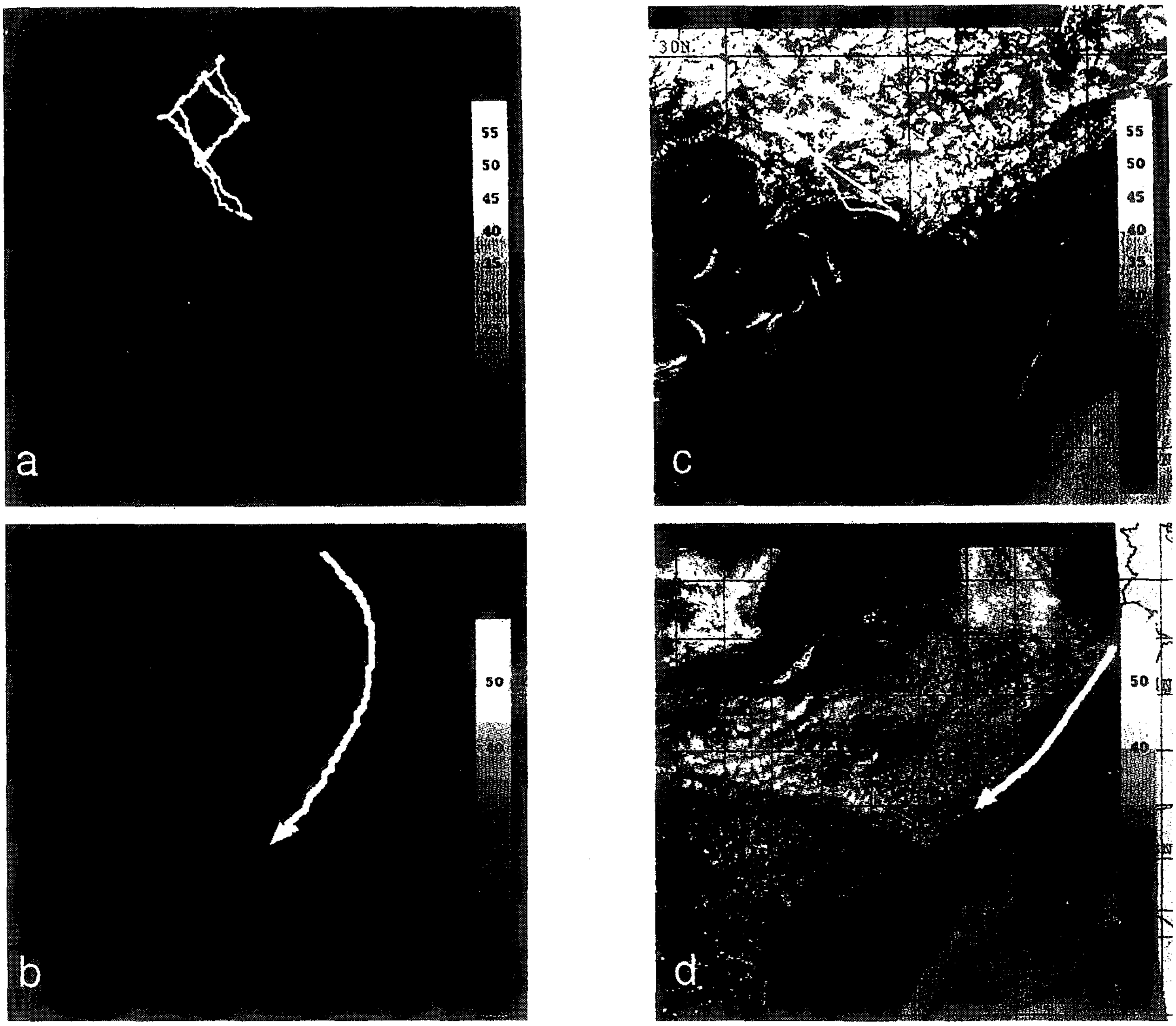

Fig. 4. AVHRR visible channel images for the 26 June (a) and (b), and the 9 July (c) and (d) cases; detailed view of the sampling area (Canary Islands, 13–19W, 25.5–30.5N) in (a) and (c), with the aircraft track superimposed; large view of the North-East Atlantic region (6–26W, 22–40N) in (b) and (d), with the trajectory of the air mass in the boundary layer superimposed.

thin marine cloud or a thick polluted one. Hence, the droplet effective radius is not a particularly good parameter for detecting the anthropogenic aerosol effects on clouds, if cloud geometrical thickness or the liquid water path are not measured concomitantly. On the other hand, droplet concentration is a good parameter for characterizing the air mass type.

5. Scientific analysis

The ultimate objective of the CLOUDY-COLUMN project is to develop a reliable parameterization of the indirect effect in marine boundary layer clouds. The primary steps have been designed as partial closure experiments. They are briefly described in this section.

5.1. Cloud base

The 1st step in a climate model, for the simulation of the indirect effect, is to predict the physical and chemical properties of the aerosols in the atmosphere, their sources, transport, transformations and sinks. The 2nd step is to derive from these properties the probability distribution of the droplet number concentration in clouds, as a

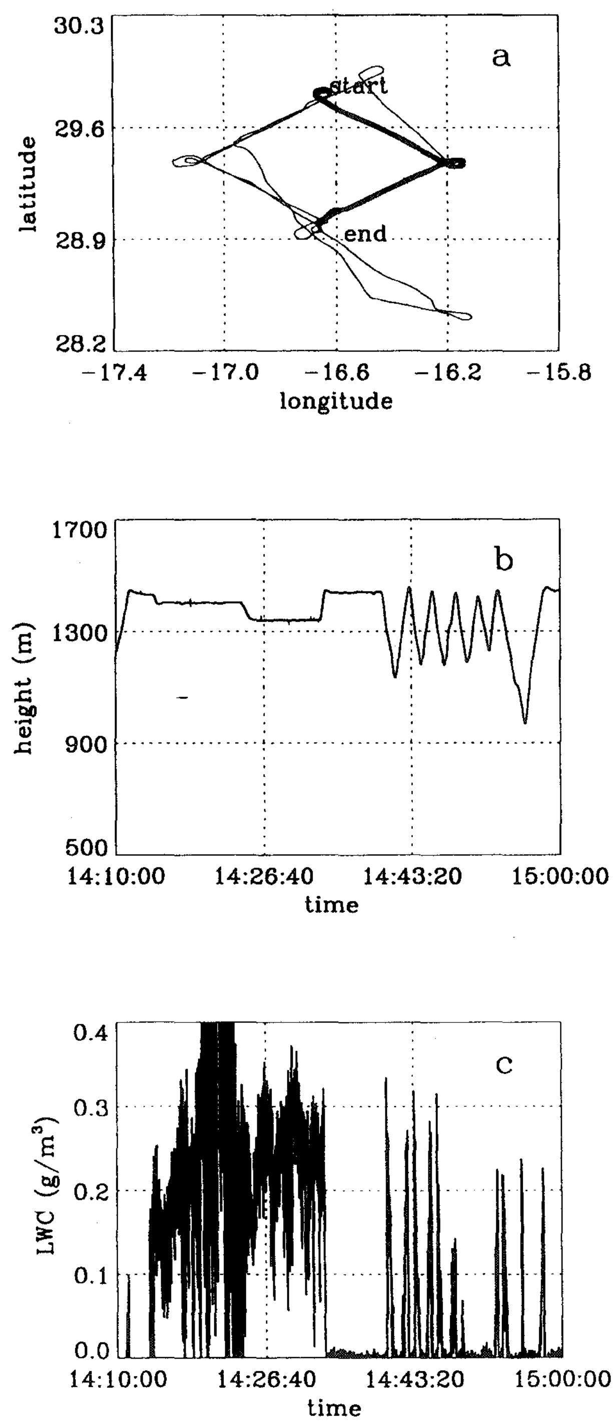

Fig. 5. M-IV flight on 26 June 1997: (a) horizontal trajectory; (b) altitude versus time for the flight section indicated by a thick line in (a); (c) same as (b) for LWC.

function of the probability distribution of vertical speed at the cloud base. Cloud base closure in CLOUDYCOLUMN consists in the comparison between values of droplet number concentration measured in cloud with the values derived from the activation model initialized with the measured aerosol distributions and vertical velocity. With measurements of CCN activation spectra it is also possible to proceed in 2 steps. The first closure involves the comparison of the measured CCN activation spectra with those derived from the measured aerosol properties and the Köhler theory. The work of Chuang et al. and Wood et al (2000) shows that predicted CCN concentrations are substantially larger than the direct observations. Further analysis and intercomparisons using laboratory aerosols will be needed to identify the source of this discrepancy.

Closure was also evaluated between the measured droplet concentration and the value derived from measured CCN activation spectra and vertical velocity. Two approaches can be tested:

(i) *Single updraft closure.* It is possible from aircraft measurements to characterize the vertical velocity and the droplet number concentration within convective updrafts. Closure is evaluated between the measured concentration and the one predicted with the models or parameterizations initialized with the measured CCN activation spectrum and the measured vertical velocity.

(ii) *Statistical updraft closure.* There is a serious limitation in the approach described above because it must be assumed that the vertical velocity measured inside the cloud, at a level where droplets are detectable, that is about 100 m above the activation level, correctly characterizes the velocity the parcel has experienced from below cloud base up to the observation level. Alternatively, the frequency distribution of the vertical velocity can be derived from horizontal legs at the cloud base. The frequency distribution of the predicted concentration is then derived from the CCN properties measured below cloud base and from the frequency distribution of vertical velocity. For closure it is compared to the frequency distribution of the droplet number concentration measured higher in the cloud.

This is the approach tested by Snider and Brenguier (2000). These authors show that the degree of consistency between measured and predicted values of droplet concentration is within a factor of two over a broad range extending from 20 to 400 cm^{-3}. This result is encouraging but does not provide the link between aerosol physico-chemical properties and droplet concentration needed for GCM simulations. Continued analysis

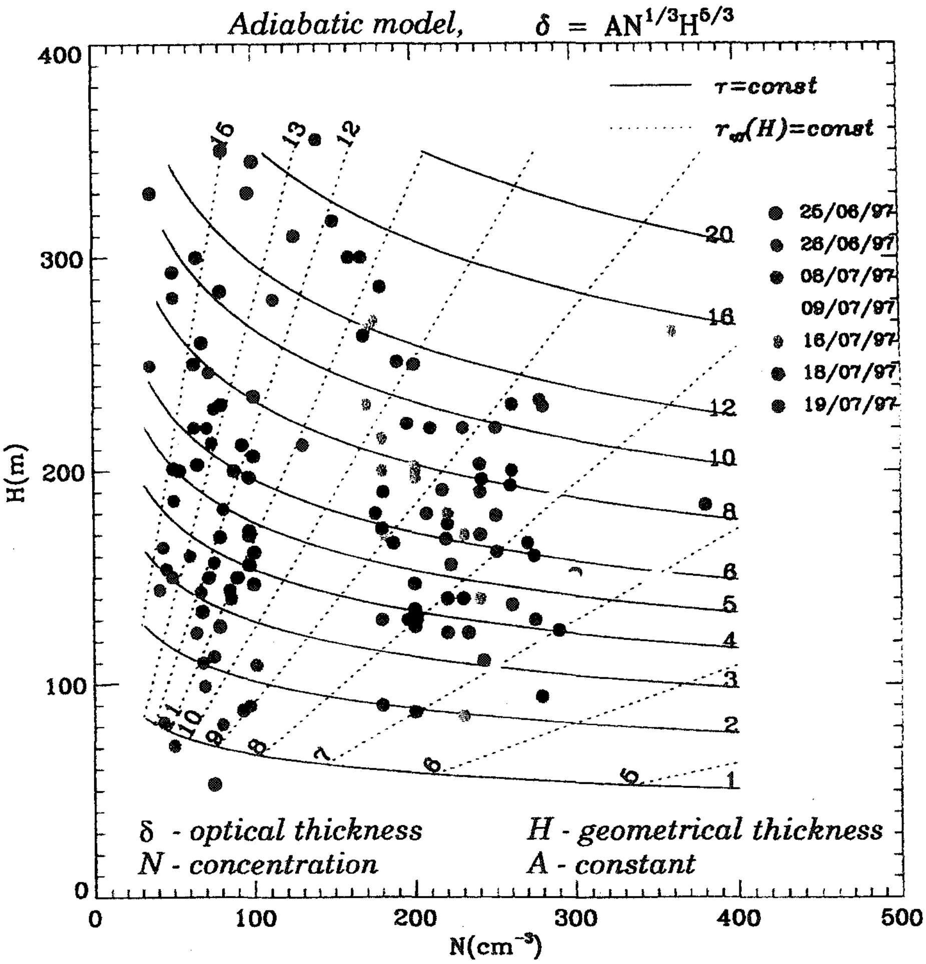

Fig. 6. Summary of cloud droplet number concentrations and cloud geometrical thicknesses measured by the M-IV during eight flights of the ACE-2 campaign. Each dot corresponds to values measured during either an ascent or a descent throughout the cloud layer. The superimposed isolines are the effective radius at the top of the cloud layer and the optical thickness, as derived from the adiabatic model with the corresponding geometrical thickness and droplet number concentration.

is needed to identify the most important aerosol and meteorological properties that are necessary for describing the indirect effect in climate models.

5.2. *Cloud depth*

An actual cloud is far from the idealized plane parallel model that has been used extensively for radiation calculations (Slingo and Schrecker, 1982). In such a model the cloud microphysical properties are assumed to be uniform horizontally and vertically. Vertical uniformity implies that the cloud optical thickness τ is proportional to the geometrical thickness H (Twomey, 1977). But, for convective updraft, the broad structure observed is that the liquid water content increases linearly with altitude above cloud base, droplet number concentration is constant and the droplet mean volume diameter increases as $H^{1/3}$. Although values of the microphysical parameters are always smaller than the adiabatic prediction, the adiabatic model provides a more realistic description of the vertical profiles of microphysics than the vertically uniform model. The resulting higher sensitivity to H implies that changes in the cloud morphology due to the effects of aerosols on precipitation efficiency might induce cloud albedo modifications exceeding the first indirect effect.

The partial closure here is concerned with the characterization of the vertical profiles of microphysics compared to the profile predicted with an adiabatic parcel model. The zig-zag legs are particularly suited for such an analysis. The observations presented in Brenguier et al. (2000) and in

Pawlowska and Brenguier (2000) show that most of the observed profiles are close to the adiabatic model, thus validating this model for radiative transfer calculations.

5.3. *Single cloud albedo*

The next step consists in the validation of the radiative transfer calculation throughout a vertically stratified cloud at the scale of a stratocumulus cell. Such a local closure experiment was possible in CLOUDYCOLUMN because of the close synchronization between in-cloud measurements of the vertical profile of the microphysics and the remote sensing measurements of the cloud radiative properties. Comparisons between the values of optical thickness derived from OVID measurements and the values calculated with the adiabatic parameterization initialized with the measured H and N are presented in Brenguier et al. (2000). They clearly demonstrate proportionality between optical thickness and $H^{5/3}$ rather than H. The adiabatic parameterization provides a way of deriving H and N from the measured reflectances in the visible and near infra-red (Fig. 7), with a method similar to the ones developed by Twomey and Cocks (1989) or Nakajima and King (1990) for the retrieval of τ and the effective droplet diameter, using the plane-parallel model. The analysis of the ACE-2 cases shows that the derived values of the droplet number concentration ($100\ \mathrm{cm}^{-3}$ in polluted and $25\ \mathrm{cm}^{-3}$ in clean) are always underestimated with respect to the measured values ($244\ \mathrm{cm}^{-3}$ in polluted and $55\ \mathrm{cm}^{-3}$ in clean). Such a discrepancy, similar to the overestimation of the values of droplet effective diameter retrieved with the plane-parallel model, has been often attributed to anomalous absorption (Twomey and Cocks, 1989; Stephens and Tsay, 1990).

The single cloud albedo closure experiment thus demonstrates that the adiabatic model is more realistic than the plane-parallel model for the parameterization of the cloud radiative properties, but also that the main discrepancy between measured and predicted values of cloud reflectances still remains unexplained.

5.4. *Cloud system albedo*

The last step is to provide parameterization at the scale of a climate model grid, that is at a scale of 100 km. In the plane-parallel model it has also been assumed that cloud properties are uniform horizontally. In fact actual clouds are inhomogeneous with regions of stratocumulus convection, where the adiabatic model is appropriate, and regions affected by mixing with the dry overlying air and by drizzle formation, where the microphysical properties are sub-adiabatic. Various numerical studies have been performed to evaluate the sensitivity of radiative transfer calculations to cloud inhomogeneities (Barker, 1992; Cahalan et al., 1994a, b; Cahalan et al., 1995; Davis et al., 1996; Duda et al., 1996; Barker, 1996). In particular, it has been demonstrated that the horizontal distribution of the cloud microphysical properties is important to account for the radiative effect of real stratocumulus systems. These effects are commonly referred to as the inhomogeneous cloud bias.

Closure at the scale of a cloud system thus consists in the characterization of the turbulent structure of the boundary-layer, of the related statistics of cloud microphysical parameters and of its influence on the mean cloud albedo. This step also includes a study of the consistency between close radiative measurements on board the Do-228 and radiative measurements performed with POLDER on the ADEOS satellite. The M-IV horizontal legs are particularly suited for this approach. Preliminary results are presented in Pawlowska and Brenguier (2000), for the frequency distribution of the microphysical parameters. Further analysis is required to document the scale distribution of the inhomogeneities which is important for the calculation of the inhomogeneous cloud bias. The parameterization of the radiative properties of inhomogeneous cloud systems is a challenge. However, measurements of the cloud reflectances in the visible and near infrared performed during the CLOUDYCOLUMN experiment show clearly that the difference between clean and polluted clouds is quite significant. Fig. 7 shows the comparison of the distributions of measured reflectances for the 26 June and the 9 July case studies. The contour plots of all the values measured with a horizontal resolution of 100 m over each complete flight are clearly distinct. The isolines represent the values of droplet number concentration and cloud geometrical thickness of an adiabatic cloud with the corresponding values of reflectances at the two wavelengths (Brenguier et al., 2000). The measured reflectances are distributed along the 100 cm^{-3} N isoline for the polluted case, and along the 25 cm^{-3} N isoline for the marine case. In situ measurements (Pawlowska and Brenguier, 2000) show distributions of the droplet number concentration centered at 244 cm^{-3} and 55 cm^{-3} for the polluted and marine cases respectively. This illustrates the underestimation of the retrieved droplet concentration mentioned in the previous section, but the ratio between the droplet concentrations of the polluted and the clean cases, which is of the order of 4, is correctly reproduced. This observation can be considered as an experimental evidence of the indirect effect at the scale of a cloud system.

6. Conclusion

CLOUDYCOLUMN is the most recent field experiment where it has been possible to perform simultaneous measurements of aerosol properties, cloud microphysics and cloud radiative properties, in marine stratocumulus. Up to 4 instrumented aircraft were used to sample the same cloud system, with special emphasis on the synchronization between microphysical and radiative measurements. Eleven cases have been documented, with two particularly clean conditions (25, 26 June) and one case of heavy pollution (9 July). The redundancy of the measurements for critical parameters, such as aerosol physical and chemical properties, and CCN activation spectrum, or cloud reflectances measured with multidirectional radiometers, and multiwavelength radiometers, provides a robust data set. Aerosol/microphysics and microphysics/radiation interactions at the scale of the convective cells have been analyzed and important results have already been obtained.

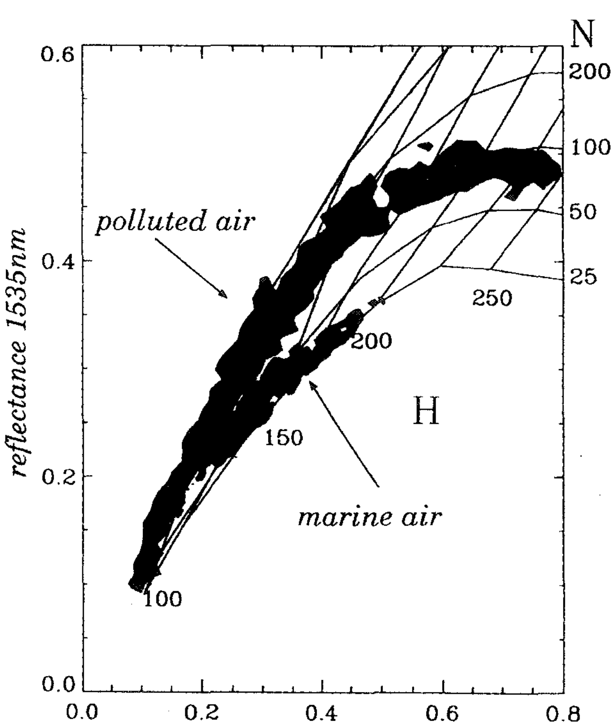

Fig. 7. Isocontour of measured cloud reflectances in the visible (754 nm) and near infra-red (1535 hm) with OVID, on 26 June (blue) and 9 July (green). Isolines represent cloud geometrical thickness and droplet number concentration, producing the corresponding cloud reflectances with radiative transfer calculations in an adiabatic cloud model.

Consistency has been tested between aerosol properties and CCN activation spectrum (Chuang et al.; Wood et al., 2000), and between CCN activation spectrum and the droplet concentration by way of the measured vertical velocity (Snider and Brenguier, 2000). These tests have revealed a discordant comparison between predicted and observed CCN number densities. Also documented is an acceptable closure between measurements of CCN, updraft, and cloud droplets. The former result is disapointing since closure between aerosols and CCN is needed to better constrain GCM predictions of the indirect effect. The disparity should inspire future intercomparisons of CCN and aerosol measurement systems. Modeling work is also needed to improve methodologies used to incorporate bulk chemistry, hygroscopicity, and surface tension data into Köhler theory.

The comparison between values of optical thickness derived from in situ measurements of cloud geometrical thickness and droplet concentration, and values derived from remote sensing measurements of cloud reflectances have demonstrated that the optical thickness is proportional to $H^{5/3}$ instead of H, thus validating the adiabatic model of cloud vertical profile for parameterizations of the optical thickness (Brenguier et al., 2000). This result is important because it suggests that the second indirect effect (precipitation efficiency) could be more significant than the first indirect effect (Twomey effect). With the simultaneity of in situ and remote sensing measurements, it has also been possible to check that the significant difference between the distributions of the measured reflectances in the visible and near infra-red, between a clean and a polluted case, is not due to differences in the cloud morphology, but only due to changes in droplet concentration. This provides clear evidence of the indirect effect of aerosols at the scale of a cloud system. The analysis is now being extended to larger scales and reliable parameterizations of the indirect effect for climate models are anticipated.

7. Acknowledgements

The authors acknowledge the contributions of the ACE-2 participants. This work has been supported by the European Union under grant ENV4-CT95-0117 and by the affiliation laboratories and administrations of the authors.

REFERENCES

Albrecht, B. A. 1989. Aerosols, cloud microphysics, and fractional cloudiness. *Science* **245**, 1227–1230.

Babey, S. K. and Soffer, R. J. 1992. Radiometric calibration of the compact airborne spectrographic imager (CASI). *Canadian Journal of Remote Sensing* **18**, 233–242.

Barker, H. W. 1992. Solar radiative transfer through clouds possessing isotropic variable extinction coefficient. *Quart. J. Roy. Meteor. Soc.* **118**, 1145–1162.

Barker, H. W. 1996. Estimating cloud field albedo using one-dimensional series of optical depth. *J. Atmos. Sci.* **53**, 2826–2837.

Baumgardner, D., Dye, J. E., Gandrud, B. W. and Knollenberg, R. G. 1992. Interpretation of measurements made by the forward scattering spectrometer probe (FSSP-300) during the Airborne Arctic Stratospheric Expedition. *J. Geoph. Rev.* **97**, 8035–8046.

Boers, R. and Mitchell, R. M. 1994. Absorption feedback in stratocumulus clouds: influence on cloud top albedo. *Tellus* **46A**, 229–241.

Boers, R., Jensen, J. B. and Krummel, P. B. 1998. Microphysical and short-wave radiative structure of stratocumulus clouds over the Southern Ocean: Summer results and seasonal differences. *Quart. J. Roy. Meteor. Soc.* **124**, 151–168.

Brenguier, J. L., Bourrianne, T., Coelho, A., Isbert, J., Peytavi, R., Trevarin, D. and Wechsler, P. 1998. Improvements of droplet size distribution measurements with the Fast-FSSP. *J. Atmos. Oceanic. Technol* **15**, 1077–1090.

Brenguier, J. L., Pawlowska, H., Schüller, L., Preusker, R., Fischer, J. and Fouquart, Y. 2000. Radiative properties of boundary layer clouds: droplet effective radius versus number concentration. *J. Atmos. Sci.* in press.

Cahalan, R. F., Ridgway, W., Wiscombe, J. W. and Bell, T. L. 1994a. The albedo of fractal stratocumulus clouds. *J. Atmos. Sci.* **51**, 2434–2455.

Cahalan, R. F., Ridgway, W. and Wiscombe, J. W. 1994b. Independent pixel and Monte Carlo estimates of stratocumulus albedo. *J. Atmos. Sci.* **51**, 3776–3790.

Cahalan, R. F., Silberstein, D. and Snider, J. B. 1995. Liquid water path and plane-parallel albedo bias during ASTEX. *J. Atmos. Sci.* **52**, 3002–3012.

Chuang, P. Y., Collins, D. R., Pawlowska, H., Snider, J. R., Jonsson, H. H., Brenguier, J. L., Flagan, R. C. and Seinfeld, J. H. 2000. CCN measurements during ACE-2 and their relationship to cloud microphysical properties. *Tellus* **52B**, 843–867.

Davis, A., Marshak, A., Wiscombe, J. W. and Cahalan, R. 1996. Scale invariance of liquid water distributions in marine stratocumulus. Part I: spectral properties and stationarity issues. *J. Atmos. Sci.* **53**, 1538–1558.

Duda, D. P., Stephens, G. L., Stevens, B. and Cotton, W. R. 1996. Effects of aerosols and horizontal inhomogeneity on the broadband albedo of marine stratus numerical simulations. *J. Atmos. Sci.* **53**, 3757–3769.

Flamant, C., Trouillet, V., Chazette, P. and Pelon, J. 1998. Wind speed dependence of atmospheric boundary layer optical properties and ocean surface reflectance as observed by airborne backscatter lidar. *J. Geophys. Res.* **103**, 25 137–25 258.

Russell, P. B. and Heintzenberg, J. 2000. An overview of the ACE-2 Clear Sky Column Closure Experiment (CLEARCOLUMN). *Tellus* **52B**, 463–483.

Houghton, J. T., Meira Filho, L. G., Callander, B. A., Harris, N., Kattenberg, A. and Maskell, K. 1995. IPCC 95: Climate change 1995: The science of climate change. Contribution of WG1 to the 2nd Assessment Report of the Intergovernmental Panel on Climate Change, Cambridge Univ. Press.

Huebert, B. J., Lee, G. L. and Warren, W. L. 1990. Airborne aerosol inlet passing efficiency measurements. *J. Geophys. Res.* **95**, 16 369–16 381.

Johnson, D. W., Osborne, S., Wood, R., Suhre, K., Johnson, R., Businger, S., Quinn, P. K., Durkee, P. A., Russell, L. M., Andreae, M. O., O'Dowd, C., Noone, K., Bandy, B., Rudolph, J. and Rapsomanikis, S. 2000. An overview of the Lagrangian Experiments undertaken during the North Atlantic Regional Aerosol Characterisation Experiment (ACE-2). *Tellus* **52B**, 290–320.

King, M. D., Radke, L. F. and Hobbs, P. V. 1993. Optical properties of marine stratocumulus clouds modified by ships. *J. Geoph. Res.* **98**, 2729–2739.

Nakajima, T. and King, M. D. 1990. Determination of the optical thickness and effective particle radius of clouds from reflected solar radiation measurements. Part I: theory. *J. Atmos. Sci.* **47**, 1878–1893.

Parol, F., Descloitres, J. and Fouquart, Y. 2000. Cloud optical thickness and albedo retrievals from bidirectional reflectance measurements of POLDER instruments during ACE-2. *Tellus* **52B**, 888–908.

Pawlowska, H. and Brenguier, J. L. 2000. Microphysical properties of stratocumulus clouds during ACE-2. *Tellus* **B**, this issue.

Petzold A., Busen, R., Schröder, F., Baumann, R., Kuhn, M., Ström, J., Hagen, D. E., Whitefield, P. D., Baumgardner, D., Arnold, F., Borrmann, S. and Schumann, U. 1997. Near field measurements on contrail properties from fuels with different sulfur content. *J. Geophys. Res.* **102**, 29 867–29 880.

Raes, F., Bates, T., McGovern, F. and van Liedekerke, M. 2000. The second aerosol characterization experiment (ACE-2): General context, and main results. *Tellus* **52B**, 111–126.

Randall, D. A., Coakley, J. A. Jr., Fairall, C. W., Kropfli R. A. and Lenschow, D. H. 1984. Outlook for research on subtropical marine stratiform clouds. *Bull. Am. Met. Soc.* **65**, 1290–1301.

Schmeling, M., Russel, L. M., Erlick, C., Collins, D. R., Jonsson, H., Wang, Q., Kregsamer, P. and Streli, C. Aerosol particle chemical characteristics measured from aircraft in the lower troposphere during ACE-2. *Tellus* **52B**, 185–200.

Schröder, F. and Ström, J. 1997. Aircraft measurements of sub micrometer aerosol particles (>7 nm) in the midlatitude free troposphere and tropopause region. *Atmos. Research* **44**, 333–356.

Schüller, L., Fischer, J., Armbruster, W. and Bartsch, B. 1997. Calibration of high resolution remote sensing instruments in the visible and near infrared. *Adv. Space. Res.* **19**, 1325–1334.

Snider, J. R. and Brenguier, J. L. 2000. Cloud condensation nuclei and cloud droplet measurements obtained during ACE-2. *Tellus* **52B**, 828–842.

Slingo, A. and Schrecker, H. M. 1982. On the shortwave radiative properties of stratiform water clouds. *Quart. J. Roy. Meteor. Soc.* **108**, 407–426.

Stephens, G. L. and Tsay, S. 1990. On the cloud absorption anomaly. *Quart. J. Roy. Meteor. Soc.* **116**, 671–704.

Twomey, S. 1977. The influence of pollution on the shortwave albedo of clouds. *J. Atmos. Sci.* **34**, 1149–1152.

Twomey, S. and Cocks, T. 1989. Remote sensing of cloud parameters from spectral reflectance measurements in the near-infrared. *Beitr. Phys. Atmos.* **62**, 172–179.

Wood, R., Johnson, D., Osborne, S., Andreae, M. O., Bandy, B., Bates, T., O'Dowd, C., Glantz, P., Noone, K., Quinn, P., Rudolph, J. and Suhre, K. 2000. Boundary layer and aerosol evolution during the third Lagrangian experiment of ACE-2. *Tellus* **52B**, 401–422.

Annexe D

Results of POLDER In-Flight Calibration

IEEE Trans. Geosci. Remote Sensing, 37, 1550-1566, May 1999

Results of POLDER In-Flight Calibration

Olivier Hagolle, Philippe Goloub, Pierre-Yves Deschamps, Hélène Cosnefroy, Xavier Briottet, Thierry Bailleul, Jean-Marc Nicolas, Frédéric Parol, Bruno Lafrance, and Maurice Herman

Abstract—**POLDER is a CNES instrument on board NASDA's ADEOS polar orbiting satellite, which was successfully launched in August 1996. On October 30, 1996, POLDER entered its nominal acquisition phase and worked perfectly until ADEOS's early end of service on June 30, 1997. POLDER is a multispectral imaging radiometer/polarimeter designed to collect global and repetitive observations of the solar radiation reflected by the earth/atmosphere system, with a wide field of view (2400 km) and a moderate geometric resolution (6 km). The instrument concept is based on telecentric optics, on a rotating wheel carrying 15 spectral filters and polarizers, and on a bidimensional charge coupled device (CCD) detector array. In addition to the classical measurement and mapping characteristics of a narrow-band imaging radiometer, POLDER has a unique ability to measure polarized reflectances using three polarizers (for three of its eight spectral bands, 443 to 910 nm) and to observe target reflectances from 13 different viewing directions during a single satellite pass.**

One of POLDER's original features is that its in-flight radiometric calibration does not rely on any on-board device. Many calibration methods using well-characterized calibration targets have been developed to achieve a very high calibration accuracy. This paper presents the various methods implemented in the in-flight calibration plan and the results obtained during the instrument calibration phase: absolute calibration over molecular scattering, interband calibration over sunglint and clouds, multiangular calibration over deserts and clouds, intercalibration with Ocean Color and Temperature Scanner (OCTS), and water vapor channels calibration over sunglint using meteorological analysis. A brief description of the algorithm and of the performances of each method is given.

Index Terms—**Atmosphere, calibration, in-flight, optical remote sensing, vicarious.**

Acronyms

ADEOS	Advanced Earth Observing Satellite.
ATSR2	Along Track Scanning Radiometer-2.
BRDF	Bidirectional reflectance distribution function.
ECMWF	European Center for Mean-Range Weather Forecast.
ERS2	European Remote-Sensing Satellite 2.
LUT	Look-up table.
MISR	Multiangle Imaging Spectro-Radiometer.
MODIS	Moderate-Resolution Imaging Radiometer.
OCTS	Ocean Color and Temperature Scanner.
POLDER	Polarization and directionality of earth reflectances.
SeaWIFS	Sea-Viewing Wide Field-of-View Sensor.
SPOT	Satellite pour l'Observation de la Terre (earth observing satellite).
SOS	Successive orders of scattering.
TOA	Top of atmosphere.

Manuscript received April 16, 1998; revised January 25, 1999. The results presented in this paper were obtained using data from CNES's POLDER on board NASDA's ADEOS. The ECMWF meteorological data was provided by Meteo France.

O. Hagolle and B. Lafrance are with the Centre National d'Etudes Spatiales (CNES), 31055 Toulouse Cedex France (e-mail: Olivier.Hagolle@cnes.fr).

P. Goloub, P.-Y. Deschamps, T. Bailleul, J.-M. Nicolas, F. Parol, and M. Herman are with the Université des Sciences et Technologies de Lille, Laboratoire d'Optique Atmosphérique, Lille, France.

H. Cosnefroy and X. Briottet are with the Office National d'Etudes et Recherches Aerospatiales, Département d'Optique Théorique et Appliquée, Toulouse, France.

Publisher Item Identifier S 0196-2892(99)03569-X.

I. Introduction

RADIOMETRIC calibration accuracy is one of the major elements contributing to the quality of the measurements obtained with optical remote sensing instruments. This radiometric calibration can be obtained through preflight measurements in optical laboratories, but the accuracy of these measurements is not perfect (precise radiance calibration is a difficult subject, and extraterrestrial solar irradiance is not perfectly known). Moreover, the instruments are subject to degradation after launch because of the aging of the optics or of the outgassing which occurs when the instrument leaves the atmosphere. To cope with this problem, many spaceborne instruments are equipped with on-board calibration devices. SPOT satellites [22] have an inner lamp and an optical fiber system to observe the sun. Actually, the inner lamp is used only for multitemporal monitoring of the instrument sensitivity and for detector normalization. The solar observations are affected by a difficult preflight calibration of the system itself and by a slow degradation of the optical fibers. SPOT calibration relies now mainly on natural targets. OCTS on board ADEOS is also equipped with inner lamps and a solar observation system: but the OCTS calibration provided by these devices is not very accurate because of degradation of the lamps after the launch and of nonuniformity in the mirror which allows observation of the sun. These problems lead to the decision of using natural targets for OCTS calibration [26]. ATSR2 on board ERS2 is also equipped with a visible sun-observing calibration device which is operationally used but needs to be completed by multitemporal calibration over desert sites to correct a drift of the solar calibration signal [34]. Many future instruments have also based their calibration mainly on on-board devices, such as SeaWIFS, MODIS, and MISR on-board EOS AM-1, but are also developing vicarious methods in order to verify the on-board device [33].

The POLDER project team has decided to avoid the development of an on-board calibration system. Past experiences of on-board calibration devices in CNES with SPOT satellites have failed to provide accurate results, and vicarious

TABLE I
SPECTRAL BAND CHARACTERISTICS FOR THE POLDER INSTRUMENT ABOARD THE ADEOS-1 SATELLITE. THIS TABLE DIFFERS FROM THE FIGURES PREVIOUSLY PUBLISHED IN [9], WHICH WERE BASED ON EARLY BUDGETS

POLDER band	443	443	490	565	670	763	765	865	910
Central Wavelength (nm)	444.5	444,9	492.2	564.5	670.2	763.3	763.1	860.8	907.7
Band Width (nm)	20	20	20	20	20	10	40	40	20
Polarization	Yes	No	No	No	Yes	No	No	Yes	No
Saturation level (normalized radiance)	1.1	0.97	0.75	0.48	1.1	1.1	1.1	1.1	1.1

methods using natural targets were necessary to obtain the required absolute calibration. Moreover, the implementation of a calibration system in POLDER compact design would have been expensive and hazardous in case of failure, and it was difficult to build a device that could have covered the entire POLDER bidimensional field of view. To compensate for the lack of an on-board calibrating source, lots of effort has been invested in the development of a very stable instrument [1], in an exhaustive and accurate preflight calibration [3], and in the adaptation and enhancement of calibration methods over natural targets.

Such methods have been intensively used to calibrate AVHRR/NOAA or METEOSAT and have achieved good results [24], [36], [38] using natural targets such as molecular scattering over ocean for absolute calibration, high altitude clouds, or ocean sunglint for interband calibration and desert sites. The POLDER calibration plan adapts all these methods to make use of the multidirectional and polarization measurements of the instrument. New calibration methods have also been introduced to characterize the POLDER sensitivity to polarization [43].

II. THE POLDER INSTRUMENT ON ADEOS

The POLDER radiometer design consists of three principal components: a charge coupled device (CCD) matrix detector, a rotating wheel carrying the polarizers and spectral filters, and a wide field of view (FOV) telecentric optics [9], [21]. The optics has a focal length of 3.57 mm, opening to f/4.5 with a maximum FOV of 114°.

The CCD sensor array is composed of 242 × 274 independent sensitive areas. The total array detection unit size is 6.5 × 8.8 mm^2, which corresponds to along-track and cross-track field-of-view of ±43° and ±51°, respectively, and to a diagonal FOV of ±57°. The spectral sensitivity of the CCD array extends between 400 and 1050 nm.

The rotating wheel, which rotates steadily with a period of 4.9 s, carries the interference filters and polarizers that select the spectral band and polarization direction. It carries 16 slots, including an opaque filter to estimate the CCD detector dark current. The remaining 15 slots carry six unpolarized and nine polarized filters (three polarization directions for three different wavelengths). Thus, POLDER acquires measurements in nine bands, three of which are polarized. POLDER filters have been designed to avoid any spectral variation of the filters when passing from air to vacuum (filters are made with an ion-assisted deposition technology). This characteristic is the key for an accurate in-flight calibration, since the spectral sensitivity of the bands measured before launch is still reliable after launch.

A. Spectral Bands

POLDER has nine spectral bands ranging from 443 to 910 nm. Two of these spectral bands are centered on molecular absorption bands: 763 (O_2) and 910 (H_2O). The nine bands are defined by their central wavelength, spectral width, and polarization capability. The saturation levels are given in unit of normalized radiance, i.e., the maximum spectral radiance divided by the solar spectral irradiance at nadir and multiplied by π. The saturation level in reflectance is subsequently obtained by dividing the value given in Table I by $\cos(\theta_s)$, where θ_s is the solar zenith angle. Owing to the signal-to-noise requirements for ocean color measurements, the 443-nm channel had to be split into a polarized band (three filters: 443P) and an unpolarized band (one filter: 443NP).

B. Polarization Measurements

For three of the nine spectral bands (443, 670, and 865 nm), a polarizer is added to the filters in order to assess the degree of linear polarization and the polarization direction. These parameters are derived by combining measurements in three channels with the same spectral filters but with the polarizer axes turned by steps of 60°. The three polarization measurements in a spectral band are successive and have a total time lag of 0.6 s between the first and the third (last) measurement. In order to compensate for spacecraft motion during the lag and to register the three measurements, a small-angle wedge prism is used in each polarizing assembly. As a consequence, the matrix image is translated in the focal plane to offset the satellite motion, and the three polarization measurements are collocated.

C. Spatial Resolution

The ground size or resolution of a POLDER-measured pixel from ADEOS is 6 × 7 km^2 at nadir. Due to the earth curvature, the pixel size depends slightly on the viewing angle, leading to an increase of 21% for an incidence angle of 60°.

D. Data Acquisition

The POLDER instrument is in imaging mode on the sunlit part of the ADEOS orbit only. Data acquisition starts when the solar zenith angle on the earth surface at the satellite

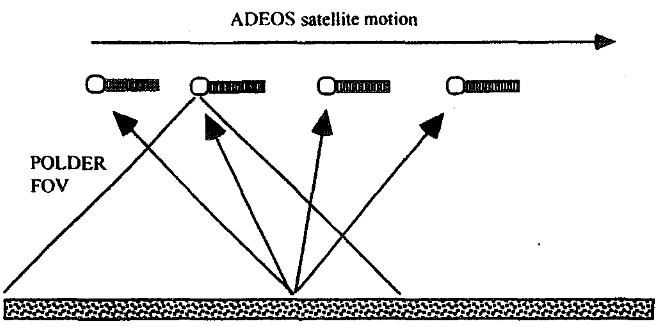

Fig. 1. POLDER multidirectional viewing principle. Owing to its bidimensional wide field of view, POLDER has the ability of looking at the same point on the ground from different viewing angles during a single orbit.

nadir is smaller than 75° and stops, in the south, when it is larger than 75°. The 16-filter sequence is repeated every 19.6 s. During this interval, a given point on the surface, initially at nadir viewing, moves by about 9° relative to the satellite (Fig. 1). The point remains within the POLDER field of view. As the satellite passes over a target, about 12 (up to 14) directional radiance measurements (for each spectral band) are performed aiming at the point. Therefore, POLDER successive observations allow the measurement of the bidirectional reflectance properties of any target within the instrument swath.

ADEOS is on a sun synchronous orbit at an altitude of 797 km. Thanks to POLDER's very wide field of view, each point on the earth is observed by POLDER every day, except near the equator where one point is only observed four days out of five. Combining all the viewing directions obtained during a one-week period, a very complete sampling of any target's BRDF can be obtained.

III. Preflight Calibration

A. Radiometric Model

The aim of the radiometric model of the instrument is to give a synthetic but totally representative description of the physics of the instrument. It characterizes completely the response to the incoming polarized light for each pixel of the CCD matrix, in each spectral band. This model has been described in Hagolle *et al.* [15], as well as the inversion of the Stokes parameters. Since polarization is not the purpose of this paper, we present here the simplified POLDER radiometric model, which can be used to retrieve the first Stokes parameter, once all the polarization effects have been removed. Let I, the normalized total radiance, be defined as

$$I = \pi \cdot \text{radiance/solar irradiance.}$$

The Stokes parameters are expressed in normalized radiance units, because accurate calibration of normalized radiances is easier than direct calibration of radiances. A unique solar spectral irradiance profile has been adopted by POLDER project (the solar spectrum recommended by the World Meteorological Organization [41]), and POLDER in-flight absolute calibration is, in fact, a relative calibration to this solar irradiance profile.

The radiometric model can be written

$$DN_{lp}^k = A^k \cdot R_{lp}^k I_{lp}^k \qquad (1)$$

where

- l, p line and column numbers of the CCD array;
- k spectral band number;
- DN_{lp}^k digital number measured by the elementary detector (l, p) with a quantization over 12 bits;
- I_{lp}^k normalized radiance observed by (l, p);
- A^k absolute calibration coefficient, which accounts for the conversion of normalized radiance units into digital numbers;
- R_{lp}^k multiangular calibration coefficient: it corresponds to sensitivity variations within the instrument field of view, coming either from the elementary detectors or from the optics.

7)

This parameter is not easy to measure in-flight and has been split into three terms, and a different in-flight calibration method is used for each term. This is explained in Section IV-B.

B. Preflight Calibration

POLDER preflight calibration [3] gives rise to two main difficulties: 1) the calibration of a bidimensional very wide field of view and 2) the characterization of the polarization sensitivity in the whole field of view. The accuracy of preflight calibrations relies on the following important hardware.

- *Two Integrating Spheres:* A large integrating sphere for the calibration measurements and a transfer integrating sphere in order to check the air/vacuum stability of the absolute calibration, to control the stability of the reference radiometer and to determine the large integrating sphere nonuniformity.
- A polarizing system which enables the generation of different polarization rates and directions. It is made up of two parallel glass plates which can be oriented around two axes.
- A reference radiometer fitted with filters identical to POLDER ones. The radiometer is used for absolute calibration and has been calibrated with each of the filters in L.C.I.E. (Laboratoire Central des Industries Electriques). This calibration has been operated against a spectrally calibrated source: a standard incandescent lamp and a $BaSO_4$ plate with a good uniformity, and a standard radiometer. The estimated accuracy of this calibration is ±3.5%.
- A monochromator to measure the spectral response of the instrument; the rotation of the grating is synchronous with the instrument imaging cycle, and the emission stability of the lamp is checked all along the measurement. The stability of the response over several measurements is better than 1% and the variation of the center of the spectral profile is less than 0.3 nm.

The evaluated accuracy of the preflight absolute calibration is 5%. The relative calibration performances are divided in two parts: the high spatial frequency is determined with an

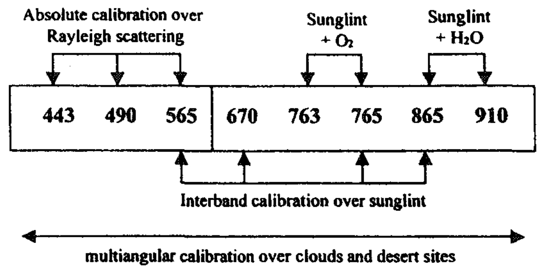

Fig. 2. Schematic view of the nominal calibration methods.

uncertainty of 0.1%, while the low spatial frequencies are obtained with an uncertainty of 1% (because of residual errors in integrating sphere nonuniformity correction). Absolute calibration and thus spectral responses of the filters did not vary when measurements were made in a vacuum chamber. Preflight calibration was also successfully compared to OCTS calibration through a round robin of both projects' calibrating radiometers [29]. However, it was foreseen that because of the ultraviolet irradiation of the external lenses, a slight decrease in the sensitivity of POLDER blue spectral bands could occur (10% maximum for 443 nm band after three years, but less than 1% for 670). From all these arguments, it appears that POLDER calibration should only vary slightly after launch but needs to be monitored in-flight to comply with its strict calibration requirements.

IV. Inflight Radiometrical Calibration: Nominal Methods

In order to ensure good in-flight radiometric performances, each calibration parameter of the radiometric model can be measured and monitored using various in-flight calibration methods. Absolute calibration methods (Section IV-A) aim to measure the A^k parameter, while multiangular calibration methods (Section IV-B) measure the $p^k(\theta)$ and $g^k lp$ parameters. Polarization calibration methods are presented in Goloub *et al.* [13] and Toubbé *et al.* [43].

Among the various calibration methods that were considered in the preliminary studies for POLDER in-flight calibration, one method for each parameter was chosen as the nominal method (the one having the best error budget). The other methods are used as validation methods to control the results of the nominal methods. This chapter details the procedure, the error budget computed before launch, and the in-flight results for each nominal method. A schematic view of the nominal calibration methods is given in Fig. 2.

A. Absolute Calibration

POLDER absolute calibration is achieved through an absolute calibration of the "blue" spectral bands (443P, 443, 490, 565) using the well-characterized Rayleigh scattering signal over ocean. This absolute calibration is then transferred to the other wavelengths through interband calibration using the specular reflection of the sun over the ocean.

1) Absolute Calibration over Rayleigh Scattering:

a) Method: The scattering of light by the air molecules (Rayleigh scattering) over ocean is a bright and well-characterized target in the lower POLDER spectral bands (443P to 565 spectral bands). For given viewing and solar angles, the Rayleigh scattering can be accurately predicted by radiative transfer codes, and the radiance observed over ocean depends mainly on water-leaving radiance, foam presence, and aerosol amount. The uncertainty that comes from these parameters can be reduced through a strict selection of the pixels used for calibration. The calibration points are selected among POLDER data according to criteria defined to minimize the nonmolecular contribution to the measured signal. They are chosen inside oligotrophic geographic areas having an *a priori* well-known weak and stable chlorophyll content (oligotrophic waters), with no clouds, a low wind speed, and a low aerosol optical thickness. (Fig. 3 shows the geographical zones.)

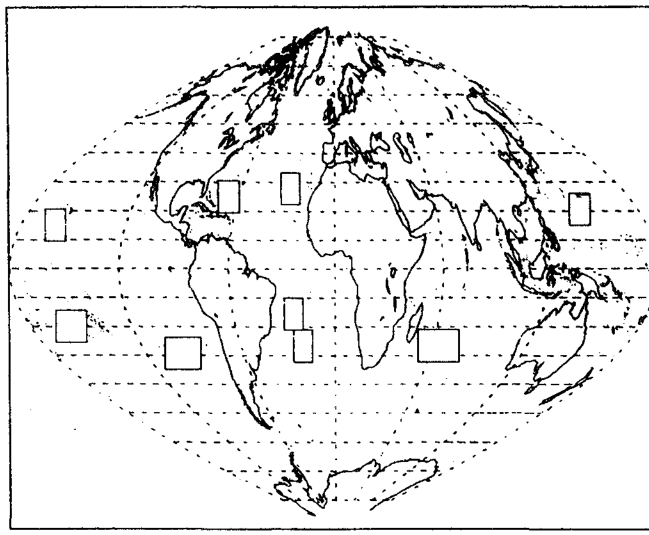

Fig. 3. The boxes on the map are the zones with low chlorophyll concentration where the calibration points for the Rayleigh method are chosen.

Cloudy pixels are eliminated using a cloud screening based on the 865-nm radiance, and meteorological data (ECMWF) are used to select zones with a low wind speed (<5 ms^{-1}). The aerosol content is estimated using the channel 865 nm: only the observations with a normalized radiance under 0.002 (after subtraction of Rayleigh scattering contribution) are selected for calibration.

Our calibration method is derived from Vermote *et al.* [39]. The preflight/in-flight variation of the calibration coefficient is obtained through the formula

$$\Delta A^k = \frac{A^k_{\text{in-flight}}}{A^k_{\text{preflight}}} = \frac{MI^{k,oz}}{I^k(v_w) + T^{k,865} \cdot (MI^{865} - I^{865}(v_w))} \quad (2)$$

where

- $MI^{k,oz}$ is the normalized radiance measured by POLDER (level 1 product with preflight calibration) in a band k among $\{443\,490\,565\}$. This radiance has been corrected for ozone absorption as described in the Appendix;
- $I^k(v_w)$ is the radiance that would be observed above a pure molecular atmosphere. It is a function of geometrical conditions, chlorophyll concentration, and wind speed v_w. The LUT's are obtained with the SOS code [10].

TABLE II
MARINE REFLECTANCES USED FOR RAYLEIGH CALIBRATION

Spectral Band	Chlorophyll concentration : 0.17 mg/m³	Chlorophyll concentration : 0.035 mg/m³
443	0.0212	0.0344
490	0.0174	0.0193
565	0.0052	0.0037

Two "extreme" chlorophyll contents (0.035 mg·m^{-3} and 0.17 mg·m^{-3}) are systematically considered for these areas, and the associated water reflectance (Table II) is estimated using the Morel model [23] updated by using new pure water absorption coefficients [27];

- $T^{k,865}$ is a unitless LUT, function of the viewing geometry, which expresses the ratio between the aerosol contribution in spectral band k and aerosol contribution at 865 nm. This LUT is computed with SOS for two aerosol models [32]: a coastal model with 70% humidity (C70) and a marine model with 98% humidity (M98). These models consist of a mixture of sea-salt component and continental component with a log-normal distribution. M98 is an open-sea aerosol model with more sea-salt components than C70, and with a flatter spectral dependence.

b) Error budget: The main error sources for the theoretical error budget are listed below.

- TOMS measures the ozone amount with an accuracy of 10 Dobson units. The resulting uncertainty on the calibration coefficient is of 0.5% on 565-nm channel, and far less for 490- and 443-nm channels.
- The wind speed modifies the sunglint geometry and the contribution of the photons scattered by the atmosphere after their reflection over the sea-surface. The uncertainty on wind speed (ECMWF meteorological data) is 2 m/s and induces a 0.5 to 1.5% calibration error on the three channels.
- The surface pressure (meteorological data) is accurately known. (Its bias is estimated under 1 hPa.) This leads to a 0.1% uncertainty on the three channels.
- Aerosol amounts and properties cannot be obtained from external data, but 865 channel is used to discard turbid atmospheres or to estimate aerosol contribution on clear ones. For this error budget, simulations were performed with an aerosol model different from the one used as reference for computing the LUT. These simulations show that the impact of the aerosol model on calibration coefficients is always under 1%. Calibration errors in the 865-nm band also result in some errors in the aerosol correction: a 5% error for 865-nm calibration induces a 1% error on 565 and less for 443 and 490.
- The water-leaving radiance is the main uncertainty for the channel 443. According to bio-optical models and if assumptions on phytoplankton concentrations are globally verified, an error of 50% on the chlorophyll concentration leads to an uncertainty on calibration coefficient up to 2% for 443 nm channel.

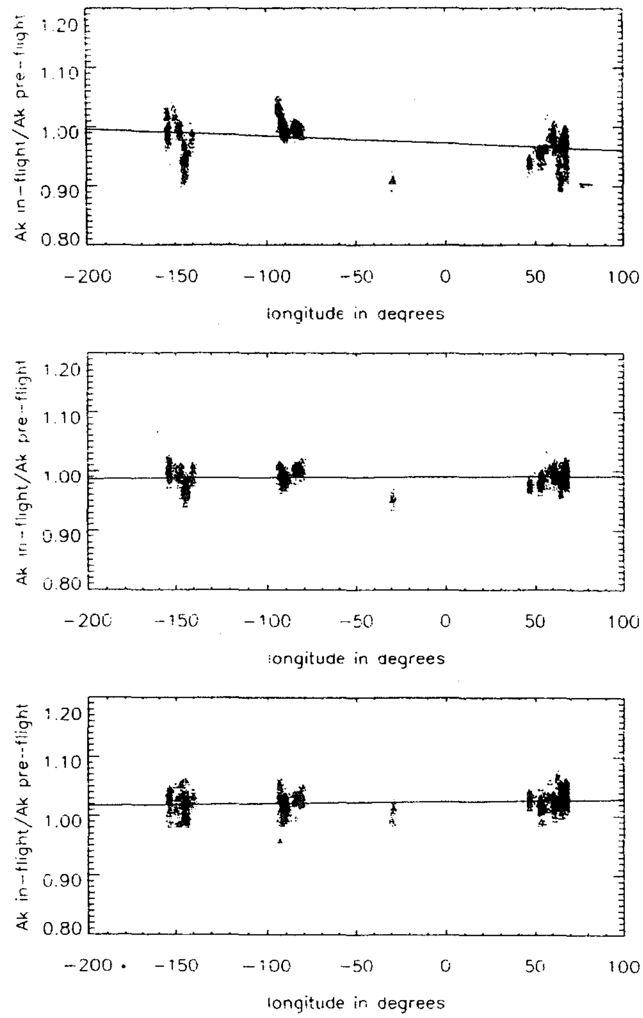

Fig. 4. Absolute calibration elementary results for Rayleigh scattering method as a function of the longitude (with C70 aerosol model and a chlorophyll concentration of 0.035 mg·m^{-3}). Each grey level corresponds to a different location or date of acquisition of the calibration points. All dates are within the first week of November. For 443 nm, the dispersion of the results inside a given site is lower than the dispersion from one site to another. This fact is related to the high variability of water-leaving radiances as a function of chlorophyll concentration. From top to bottom, Rayleigh scattering is 443 nm, 490 nm, 565 nm.

All these uncertainties lead to a 4% maximal error for 443 and 3% for 490 and 565 channels.

c) Results: For each selected calibration point, an elementary calibration result ΔA^k is computed for channels 443, 490, and 565: using all the POLDER level 1 products obtained during one week (100 orbits), more than 200 000 elementary results are collected. It is interesting to analyze how the individual measurements vary with the various parameters of the algorithm. Fig. 4 shows that channel 443 is far more sensitive to the variations of chlorophyll concentration with the calibration sites (4% standard deviation for 443) than channels 490 and 565, because water reflectance variation as a function of the chlorophyll content is high at 443 nm and lower around 500 nm. Fig. 5 shows that the estimated calibration coefficients do not depend on the aerosol amount determined with POLDER 865 nm measurements, when the proper aerosol model is used. According to the aerosol model

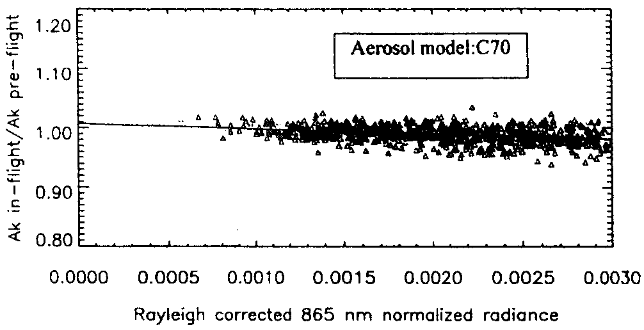

(a)

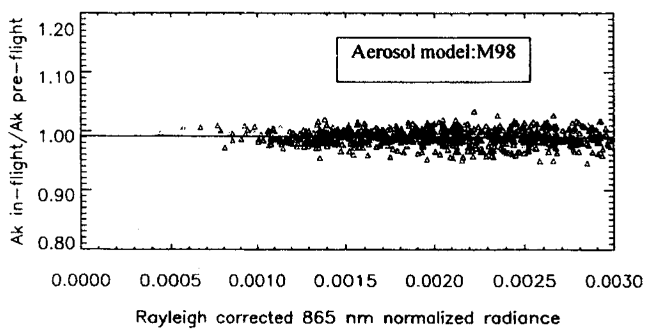

(b)

Fig. 5. Absolute calibration elementary results for Rayleigh scattering method, as a function of the Rayleigh corrected 865 nm radiance, for two different aerosol models (a) C70 and (b) M98 (modeled radiances simulated with a chlorophyll concentration of 0.035 mg·m^{-3}). The 865-nm radiance is used to determine the effect of the aerosols in the calibrated band. Calibration coefficient and 865-nm radiance are correlated in (a) but not in (b): M98 is likely the most frequent aerosol model in this data set. The Rayleigh method for both plots is 490 nm.

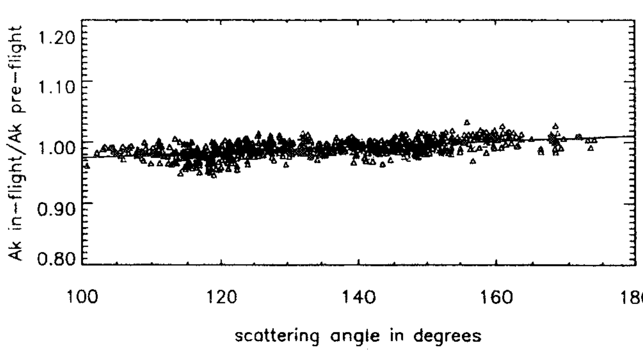

Fig. 6. Absolute calibration elementary results for Rayleigh scattering method as a function of the scattering angle (with C70 aerosol model and a chlorophyll concentration of 0.035 mg·m^{-3}). Here, a correlation exists between the calibration elementary results and the scattering angle. This correlation appears also for the 443-nm spectral band and could be related to directional effects in water-leaving radiances (considered as Lambertian in the algorithm). The Rayleigh scattering is 490 nm.

used in the simulations, the A^k values differ by 1.5% for 565 and by less than 1% for 490 and 443. Finally, calibration coefficients almost linearly depend on the scattering angle (Fig. 6): some effects might not be perfectly modeled, such as directional variations of water-leaving radiance (assumed to be Lambertian). Many more parameters have been studied, such as wind speed, ozone amount, or geometric conditions, but the estimated absolute calibration is not correlated to any of them.

To determine the in-flight calibration coefficients, the elementary results collected during one week are averaged. Four simulations are performed using each "extreme" chlorophyll content and both aerosol models, and this is done for three sets of one week of data, leading to 12 calibration results. The A^k(in-flight)/A^k(preflight) ratio is the mean value of these 12 results (Table III). The zero-peak dispersion of the averaged results is 4% for 443, 2% for 490, and 3% for 565. The higher dispersion for 443 is related to the impact of water-leaving radiance: the thresholds imposed both on the contribution of aerosols at 865 nm and on the wind speed (smaller than 5 m/s) prevent the effect of these parameters on calibration coefficients from being greater than 2%. The uncertainty on oceanic water reflectance seems to be greater than expected in this band.

However, the Rayleigh scattering method is an efficient method for the absolute calibration of optical instruments without using *in-situ* measurements. This method provides calibration coefficients with a 3–4% uncertainty for spectral bands 490 and 565, but a better knowledge of the cartography of water-leaving radiance at 443 nm is required to obtain the same results for 443. Of course, the use of oligotrophic waters is not the ideal case for the calibration of 443 channel since the water-leaving radiance is high. But it is not easy to find ocean zones away from the coasts with high and stable chlorophyll concentrations. Another way of enhancing the results is to use *in-situ* measurements: Fougnie *et al.* [11] have acquired *in-situ* data of water-leaving radiances, using SIMBAD instruments quasi-simultaneously with POLDER acquisitions.

2) *Interband Calibration over Sunglint:* This method uses the specular reflection of the sun (sunglint) on the sea-surface to transfer the calibration of 565 to the spectral bands 670, 763, 765, 865, and 910 (Fig. 2). The sunglint is spectrally flat and has a high radiance that limits the influence of other parameters such as water leaving radiance or aerosols. The sunglint radiance depends mainly on the sea-surface roughness, which is related to the wind speed. For a mirror-like sea-surface, the sunglint radiance would be very high in the exact sunglint direction and very low outside of it, whereas an agitated sea-surface scatters a lower radiance in a wider cone. The 565-nm radiance is used to estimate the sea-surface roughness (via a radiative transfer code). The surface roughness is then used to estimate the radiance for 670, 765, and 865 spectral bands. The calibration of 763- and 910-nm channels requires ancillary information to evaluate the high atmospheric absorption: surface pressure (for 763) and atmospheric water vapor content (for 910) derived from ECMWF analysis. The sunglint method can also be used to calibrate 443 and 490 spectral bands with of a reduced accuracy, just to verify that the results are consistent with the Rayleigh scattering results.

a) Calibration of 670-, 765-, and 865-nm spectral bands:

i) Method: The radiance measured in 565, 670, 765, and 865 spectral bands is first corrected for molecular absorption as described in the Appendix. Then, the sunglint radiance observed by POLDER in each spectral band k within 670, 765, and 865 is estimated at the top of atmosphere (TOA) and is compared to the real POLDER measurement.

TABLE III
ABSOLUTE CALIBRATION RESULTS ΔA^k OBTAINED WITH THE NOMINAL IN-FLIGHT CALIBRATION METHODS. SUNGLINT CALIBRATION IS AN INTERBAND CALIBRATION METHOD AND THUS NEEDS A REFERENCE (565) TO BECOME AN ABSOLUTE CALIBRATION METHOD. THE ΔA^k OBTAINED WITH RAYLEIGH SCATTERING FOR 565 IS COPIED IN ITALIC IN THE SUNGLINT COLUMN. RESULTS REPORTED IN "IN-FLIGHT" COLUMN ARE OPERATIONALLY USED IN POLDER LEVEL 1 PRODUCTS

Spectral band	Pre-Flight	Rayleigh Scattering	Sunglint	In-Flight V2.0
443	1.00	0.95		0.97
490	1.00	0.99		0.99
565	1.00	1.035	*1.035*	1.035
670	1.00		1.03	1.03
763	1.00		1.025	1.025
765	1.00		1.035	1.035
865	1.00		1.05	1.05
910	1.00		1.025	1.05

Equation (3) shows the different parameters that control the TOA normalized radiance $I_{\rm spe}^k$ in the specular direction

$$I_{\rm spe}^k = I_m^k + I_a^k + (I_g + I_w^k + I_f)T_m^k \cdot T_a^k. \quad (3)$$

I_g is the normalized radiance of the sunglint with no atmosphere, I_m^k is the radiance of the light scattered by the molecules, I_a^k corresponds to aerosols scattering, T_m^k and T_a^k are the scattering transmission of the molecules and aerosols, and the water-leaving radiance I_w^k and the foam radiance I_f are modeled by Lambertian contributions [19]. (Actually, the scattering transmission factors are not exactly the same when applied to sunglint highly directional target, or to a quite Lambertian target like foam, but the equation has been simplified for better clarity).

I_g depends on the viewing geometry and on the surface roughness (related to wind speed), but not on the spectral band [8]. However, because I_m^k is not negligible in comparison to I_g, the TOA reflectances depend on the spectral bands and this dependence varies with the sea-surface roughness. An estimate of surface roughness is thus necessary to perform the interband calibration.

Equation (3) is just an approximation limited to single scattering. To accurately compute the sunglint radiance $I_{\rm spe}^k$ observed by POLDER, (4) is used, for which all the terms are obtained using LUT's obtained through radiative transfer simulations.

A first LUT is used to estimate the wind speed from the 565-nm radiance. The LUT is computed assuming the atmosphere is purely molecular, and using the SOS method [10], which takes into account multiple scattering in the atmosphere and multiple reflections on the sea-surface. The sea-surface is represented by a Lambertian contribution (the water-leaving radiance), and by the Cox and Munk model which relates the wind speed to the sea-surface roughness. The simulations are made for a dense grid of geometrical conditions, and for 15 different wind speeds (from 1 to 15 m/s). The first step of the methods seeks the wind speed v_w that corresponds to a radiance equal to the one measured at 565 nm. The obtained wind speed may be not very accurate and is just an indicator of the sea-surface roughness.

Then the radiance for the bands 670, 765, and 865 is estimated using (4)

$$I_{\rm spe}^k = I_{\rm PMA}^k(v_w) + \Delta I^k\left(I_{\rm PMA}^k(v_w), MI_{\rm atm}^{670}, MI_{\rm atm}^{865}\right). \quad (4)$$

The first term of (4) is the sunglint radiance $I_{\rm PMA}^k(v_w)$ that would be observed with a pure molecular atmosphere (PMA) with no aerosol and a surface wind-speed v_w. A second LUT is used to derive the PMA radiance in spectral band k from the wind speed.

The second term of (4) is an empirical correction of the first term. ΔI^k accounts for the effect of atmospheric aerosols on the sunglint radiance, through the use of an empirical model obtained by mean squares minimization. This model depends on the POLDER measurements $MI_{\rm atm}^{670}$ and $MI_{\rm atm}^{865}$ in a viewing direction outside the sunglint, and on the sunglint radiance $I_{\rm PMA}^k(v_w)$. $MI_{\rm atm}^{865}$ gives information on the optical depth of aerosols, and combined with $MI_{\rm atm}^{670}$, on the Angstrom coefficient α which accounts for the spectral variation of aerosol optical depth.

The coefficients of the model of the aerosol effect are derived statistically through a mean square minimization of the difference between the two parts of (4). A regression is performed for each node of a very dense grid of viewing geometry (sunglint and off-sunglint viewing and solar angles), and each regression is obtained from simulations with the SOS method, performed for a large set of aerosol models [six Shettle and Fenn models [32]: C70, C90, C98 (coastal models) and M70, M90, M98 (maritime models)] [14], [32], optical thickness (four values: 0.025, 0.05, 0.075, 0.1) and wind speeds (2, 5, 10, 15). These simulations apply not only to the exact specular direction, but also to a small cone around this direction.

ii) Error Budget: Various error sources limit the accuracy of the interband calibration method. The error budget presented below is computed with simulated data for $k = 865$ nm (budget for 670 would be even better); the reported errors are averaged over 96 cases (six aerosol models, four aerosol optical thickness, and four wind speeds) for solar zenith angles between 20 and 40°. This error budget has been computed for the exact specular direction, but other simulations have shown that the accuracy remains stable for an angular distance to the specular point lower than 3°. The residual rms error after regression over 96 simulation cases is about 0.1%.

Instrumental Errors:

Noise: The effect of instrumental noise is completely negligible, since more than 1000 calibration points are averaged to compute each absolute calibration coefficient.

Calibration errors: An error in the absolute calibration of the 565 channel introduces an error on the estimated surface roughness and therefore on the PMA estimation of the sunglint radiance. If we have an absolute calibration bias of 3% for 565, simulations show that the bias for 865 is also 3%, leading to no error on the interband calibration (this is not true if 443 is used as a reference). Errors on the initial calibration of 670 and 865 impact on the estimation of the aerosol influence. Given an error $(\Delta A^{670}, \Delta A^{865})_1$, applying the interband calibration method gives a smaller new error $(\Delta A^{670}, \Delta A^{865})_2$ and the process needs to be iterated. Final errors are below 0.5%.

Geophysical Errors:

Foam Contribution: To evaluate the influence of foam radiance, the coefficients are applied on two different data sets, one with foam scattering and one without. The error budget was made assuming that foam scattering is spectrally flat, and the impact on the budget is negligible. Some new studies have shown that the foam might not be spectrally flat, so we discarded calibration points having a wind speed higher than 5 m/s.

Chlorophyll Concentration: To estimate the impact of a realistic error on the chlorophyll concentration, the coefficients calculated with the radiance of sea water with a chlorophyll concentration of 0.05 mg/m^3 (water-leaving normalized radiance of 0.0042 for 565), were applied to a simulation with a water leaving radiance associated to a chlorophyll concentration of 0.10 mg/m^3. The resulting error is 0.3%.

Atmospheric Pressure: The coefficients are calculated for the standard atmospheric pressure at sea level. They were applied on simulations calculated with a higher pressure (10 hPa, more than the expected rms error on the ECMWF meteorological data). Impact of this error is about 0.1%.

Gaseous Absorption: An uncertainty of 20% on water vapor amount has no impact on the method, but an uncertainty of 5% on ozone amount induces an error on the gaseous transmission, which leads to an error on I^{565}_{spe} of less than 0.1%.

Aerosol Model: The coefficients a^k_m obtained by fitting various aerosol models were applied to simulations performed with a unique coastal aerosol model. The resulting error is about 0.1%.

The total error budget gives an interband calibration accuracy better than 1%, and an absolute calibration error of 3.5% for 865 assuming 565 nm absolute calibration is accurate to 3%.

b) Calibration of 763- and 910-nm spectral bands: 763 and 910 channels are centered on gaseous absorption bands: oxygen A-Band and 910-nm water vapor absorption band, respectively. The absolute calibration of the 763-nm (respectively, 910-nm) band can be derived from the absolute calibration of the 765-nm (respectively, 865-nm) band over the sunglint, provided the atmospheric gaseous absorption is known.

i) Calibration of 763-nm band: Owing to the fact that O_2 proportion is constant within the atmosphere, the O_2 absorption can be related to the atmospheric pressure at sea level in clear sky conditions. Based on line-by-line simulations (using the spectroscopic data from HITRAN96 database [28]) a polynomial model is derived that links the O_2 transmission at 765 nm to the sea-surface pressure and to the air-mass factor. The atmospheric pressure is obtained with ECMWF analysis, and the O_2 transmission derived through this method, T^{ECMWF}_{O2}, is compared to that derived from the POLDER measurements, T^{763}_{O2}. From the two equations in the Appendix, T^{763}_{O2} can be written as

$$T^{763}_{O_2} = \frac{(1-A)\dfrac{MI^{763}}{MI^{765}}}{1-A\dfrac{MI^{763}}{MI^{765}}} \frac{T^{765}_{O_3}\cdot T^{765}_{H_2O}}{T^{763}_{O_3}\cdot T^{763}_{H_2O}} \tag{5}$$

where MI^{763} and MI^{765} are the POLDER radiances and where the other parameters are described in the Appendix. Finally, the variation of the absolute calibration coefficient at 763 nm is expressed as

$$\Delta A^{763} = \frac{A^{763}_{\text{in-flight}}}{A^{763}_{\text{preflight}}} = \frac{T^{763}_{O_2}}{T^{\text{ECMWF}}_{O_2}}. \tag{6}$$

Since the 765-nm band is involved in the computation of T^{763}_{O2}, it may be necessary to iterate the method in case of a large variation of the calibration coefficient of this band.

The error sources of this interband calibration are quite small: they mainly come from the aerosol scattering, (but we still select only low aerosol contents using an off-sunglint measurement at 865 nm), from the accuracy of the surface pressure (less than 1 hPa of bias), and from the quality of absorption corrections. However, the main error for 763 absolute calibration results from the 765-nm absolute calibration error. But, as 763 nm is never used alone but always with 765-nm band to determine apparent pressure [37], POLDER data users are only interested by 763/765 interband calibration that should be better than 1%.

ii) Calibration of 910-nm band: This band is calibrated in a similar way as 763-nm band, replacing surface pressure by vertical profiles of atmospheric water vapor content, since it has been shown that total water vapor absorption does not depend only on the total water vapor amount but also on its vertical distribution. Derivation of water vapor absorption from the vertical profile is described in Bouffies *et al.* [2].

These vertical profiles are obtained from ECMWF analysis every 6 h and interpolated to the date of acquisition. Although the data are known to be inaccurate over the oceans where radiosoundings are very sparse, some studies [25] have shown they are globally unbiased. The corresponding error should therefore be reduced to 1.5% by accumulating a large number of calibration points. The 910 and 865 spectral bands are not as close as 763 and 765, but effects of spectral variations of the target between both wavelengths are very low thanks to the use of sunglint.

Because of their high altitude (above water vapor), stratospheric aerosols could induce some errors in the estimation of the total water vapor absorption, but POLDER was calibrated in a period of very low stratospheric aerosol content. The amount of tropospheric aerosols is limited by using only the pixels which have a 865-nm radiance in an off-sunglint viewing direction under 0.005 (after correction of the molecular scattering contribution). As shown in [40], 6S simulations show that the total impact of aerosols on the error budget is less than 0.3%.

The choice of this sunglint method is arguable because of radiosoundings scarcity in the open ocean, but it combines two advantages: spectral variation of surface reflectance is far better known than that of any land surface, and the effects of aerosols are lower because selecting clear atmospheres is easier. Total error budget for this calibration method is estimated to 1.6%. Vesperini *et al.* [40] have carried out a validation of the calibration of band 910 by comparing water vapor content derived from POLDER to water vapor measured by radiosoundings.

c) Results: The sunglint interband calibration uses the same kind of target as the molecular scattering method: very clear ocean scenes with a very low aerosol optical thickness. Of course, a third selection criterion has been added: the viewing direction of the calibration point must be within a cone of 3° of radius, centered on the specular direction [$\theta_s = \theta_v$, $j = 180°$ (Fig. 14)]. For higher values, the dispersion of the results increases quickly, indicating that the geometrical modeling of the sunglint is less accurate. The off-sunglint 865-nm maximal radiance threshold (0.005 in normalized radiance units) is a little higher than for calibration over molecular scattering.

The dispersion of the elementary results (Fig. 7) is very low, except for 910 nm because of the dispersion of meteorological data. A complete analysis of the elementary measurements does not show any significant dependency of the elementary results on any of the algorithm parameters. For example, the correlation between the measured calibration coefficient and the aerosol normalized radiance (Fig. 8) is very low, indicating that the aerosol scattering has been properly corrected. Some correlation was found, however, between A865 and the atmospheric water vapor amount. The correlation disappeared when we decided not to correct for the absorption by water vapor continuum (the existence of this continuum of absorption in the near infrared is questionable). To prevent any impact of this parameter on calibration accuracy, only low water vapor contents have been selected.

To determine the in-flight calibration coefficients, the elementary results collected during one week are averaged. Averaged results have been obtained for the five channels over five periods of one week distributed during the whole life of the instrument. The results given in Table III are obtained after having calibrated the 565 reference band over Rayleigh scattering. Fig. 8 shows that the dispersion of the averaged results is small and Fig. 9 shows that interband calibration does not evolve with time.

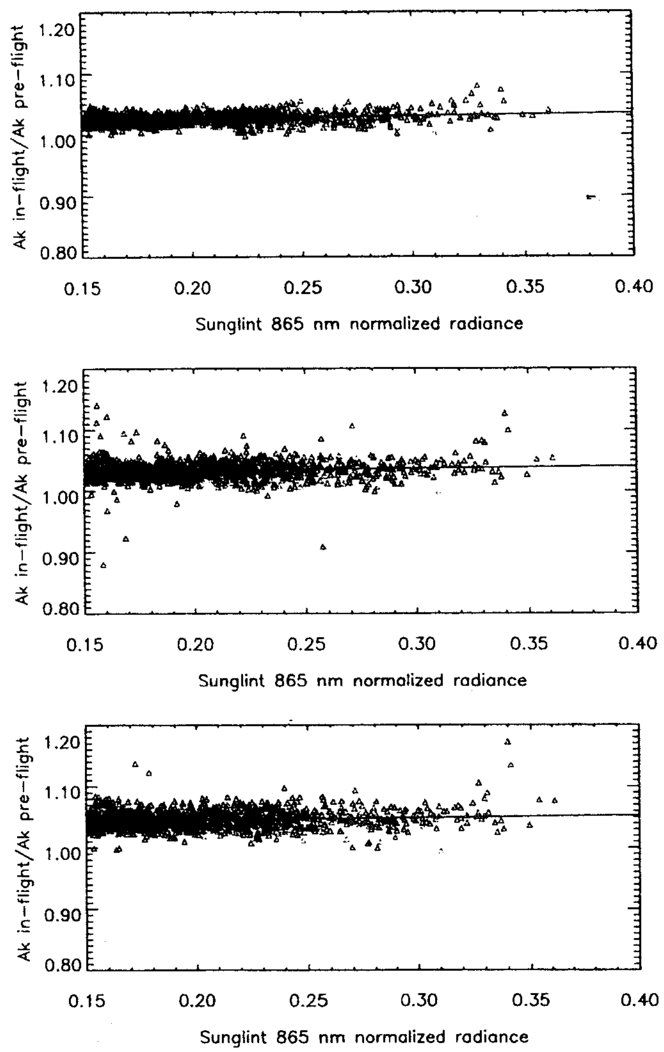

Fig. 7. Absolute calibration elementary results for sunglint interband method as a function of sunglint 865-nm radiance (for all the calibration points selected during the first week of November 1996). Standard deviation is very low for 670-nm calibration (0.8%) and increases slightly when spectral distance to 565 reference band increases (1.5% for 865 nm). The curves show no correlation between calibration results and sunglint radiance at 865 nm. From top to bottom, the Sunglint method is 670 nm, 765 nm, and 865 nm.

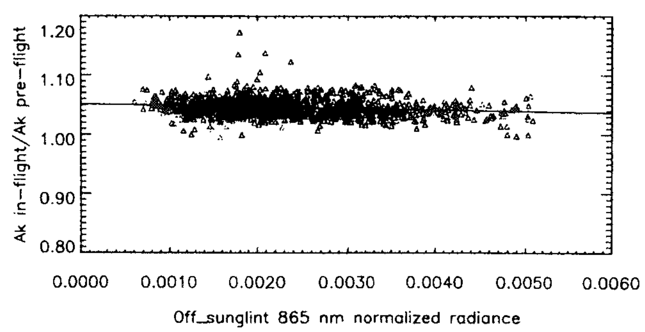

Fig. 8. Absolute calibration elementary results for sunglint interband method as a function of the Rayleigh corrected 865-nm radiance in an off-sunglint direction (for all the calibration points selected during the first week of November 1996). Correlation with the aerosol content is very small: this validates the aerosol effect correction. The Sunglint method is 865 nm.

The results obtained for the 910-nm spectral band show a rather high dispersion (4%) which comes from the limited accuracy of the water vapor information from ECMWF data.

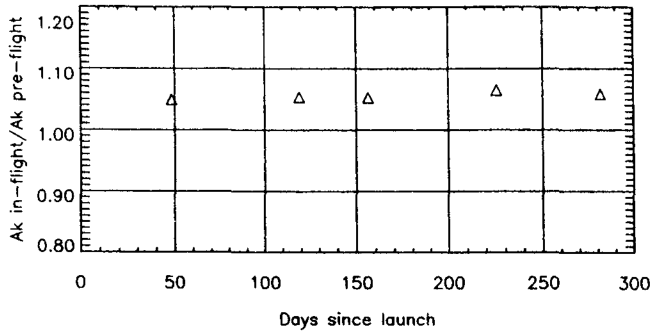

Fig. 9. Absolute calibration averaged results for sunglint interband method as a function of time: each point is the average of all the elementary results obtained with one week of POLDER data (100 orbits). The dispersion of the results is very low and the curve shows no drift during the whole life of POLDER instrument. The Sunglint method (averaged results) is 865 nm.

Fig. 10. Typical response on a radial section of the CCD ($p^k \cdot gmf_{lp}^k \cdot ghf_{lp}^k$). The smooth line represents the low-frequency variation of multiangular calibration p^k.

The results obtained in the other spectral bands are excellent and a great confidence can be given to this calibration method.

The same calibration method can be applied using 443P instead of 565 as the reference band. This leads to a degraded calibration performance because of water-leaving radiance uncertainty and because of the higher spectral distance between 443P and the near infrared spectral bands. However, this method enabled us to check 443P/565 interband calibration with an independent method. Assuming $\Delta A^k(565) = 1.035$ (as obtained with Rayleigh scattering method), the interband calibration gives 0.96 for 443P, very close to 0.95 obtained with Rayleigh scattering method (Table V).

B. Multiangular Calibration

Multiangular calibration is defined as the process of estimating the sensitivity variations at different points of POLDER wide field of view. Usually, the multiangular calibration methods consist in having the instrument look at a spatially uniform landscape, which can be an internal source (VGT/SPOT4, SPOT) or natural targets such as snow fields (SPOT). For a wide field-of-view instrument (2400 km * 1800 km), a continuous uniform landscape does not exist. As POLDER is not equipped with an on-board calibration device, new methods have been defined to simulate a spatially uniform landscape.

However, no method was found able to completely calibrate the sensitivity differences for all POLDER detectors. Different methods are used to calibrate the low spatial frequencies and the high spatial frequencies of the multiangular calibration coefficients. This explains why multiangular calibration coefficients R_{lp}^k in the radiometric model have been split into three terms:

$$R_{lp}^k = p^k(\theta) \cdot gmf_{lp}^k \cdot ghf_{lp}^k. \tag{7}$$

- $p^k(\theta)$ expresses the low-frequency variations of the optic transmission which decreases slightly when the viewing angle θ increases (Fig. 10). Its measurement is performed over desert sites as described below and the targeted accuracy is 1%. Desert sites are neither uniform enough nor frequent enough to be used for high frequency.

TABLE IV
CENTER LOCATIONS OF THE DESERT SITES (LONGITUDE > 0 FOR EAST LOCATION)

Site Name	Latitude (°)	Longitude (°)
Arabia1	18.88	46.76
Arabia2	20.13	50.96
Arabia3	28.92	43.73
Sudan1	21.74	28.22
Niger1	19.67	9.81
Niger2	21.37	10.59
Niger3	21.57	7.96
Egypt1	27.12	26.10
Libya1	24.42	13.35
Libya2	25.05	20.48
Libya3	23.15	23.10
Libya4	28.55	23.39
Algeria1	23.80	-0.40
Algeria2	26.09	-1.38
Algeria3	30.32	7.66
Algeria4	30.04	5.59
Algeria5	31.02	2.23
Mali1	19.12	-4.85
Mauritania1	19.40	-9.30
Mauritania2	20.85	-8.78

- ghf_{lp}^k refers to high-frequency variations of the sensitivity of the elementary detectors. It is measured over clouds. Its targeted accuracy is 0.1%. Of course clouds are not Lambertian targets, and their BRDF depends on the type of cloud: the low-frequency variation of the multiangular calibration cannot be estimated by this method.
- gmf_{lp}^k refers to low-frequency variations in the sensitivity of the elementary detectors that cannot be modeled by a polynomial function of the viewing angle. The targeted accuracy is 1%. Since this parameter is mainly linked to heterogeneity in the CCD matrix, it is expected not to vary after launch, and preflight calibration is used for this parameter. However, calibration over desert sites could be used to detect an unlikely large variation.

TABLE V
COMPARISON OF THE NOMINAL IN-FLIGHT ABSOLUTE CALIBRATION RESULTS ΔA^k WITH THE VALIDATION METHOD RESULTS. VALUES IN ITALIC INDICATE THAT THE CORRESPONDING BAND IS USED AS A REFERENCE FOR AN INTERBAND METHOD. ITALIC VALUE IS COPIED FROM "IN-FLIGHT" COLUMN

Spectral band	OCTS (pre-flight)	OCTS (in-flight)	Sunglint	Clouds	ATSR-2	In-Flight (Used in level 1)
443	0.96	0.955	0.96	1.01		0.97
490	0.92	0.975	0.98	1.02		0.99
565	1.045	1.01	*1.035*		1.06	1.035
670	1.01	1.09		*1.03*	1.035	1.03
765	1.01	1.12				1.035
865	0.98	1.28			1.00	1.05

1) Low-Frequency Multiangular Calibration over Desert Sites: Stable desert areas of the Sahara and Saudi Arabia can potentially be used as calibration test sites in the solar reflected spectrum. Such sites have already been used to monitor the calibration temporal drifts of the AVHRR [18], [30], [36], ATSR-2 [34], Meteosat [5], [24], and HRV/SPOT sensors [17]. They can also be used to estimate the multiangular calibration of wide field of view sensors equipped with CCD arrays such as POLDER. This requires a good characterization of the directional variations of their top-of-atmosphere reflectances, to account for the variations of the solar or viewing configurations between measurements.

a) Method: A procedure has been defined to select 100 $\times$ 100 km^2 desert areas in North Africa and Saudi Arabia [6] using a spatial uniformity criterion in Meteosat-4 visible data. Twenty such sites (Table IV) meet this criterion within 3%. The temporal stability of the spatially averaged reflectance of each selected site has been investigated at seasonal and hourly time scales with multitemporal series of Meteosat-4 data. It was found that the temporal variations of an 8–15% typical peak-to-peak amplitude (in relative value) were mostly controlled by directional effects. Once the directional effects are removed, the residual root mean square variations, representative of random temporal variability, are in the order of 1–2% in relative values.

Second, a field experiment [7] took place in February–March 1993 to characterize the BRDF of four desert sites (Algeria 2, Algeria 3, Algeria 4, and Algeria 5). The purpose of this experiment was to measure the BRDF of the sites to use them as a reference for multiangular calibration of optical sensors. Bidirectional measurements of the surface reflectance (and also polarization) were collected in three different planes (principal, perpendicular, and 45°) at four wavelengths: 450, 650, 850, and 1650 nm. Then, the surface reflectance measurements have been adjusted against an empirical model of BRDF defined as

$$\rho_{TOA}^k(\theta_s, \theta_v, \varphi) = a^k + \theta_s\theta_v \frac{\cos\theta_s \cos\theta_v}{\cos\theta_s + \cos\theta_v} \cdot \left(b^k \cos\varphi + \theta_s\theta_v\left(c^k + d^k \cos^4\varphi\right)\right) \quad (8)$$

where $(\theta_s, \theta_v, \varphi)$ are, respectively, the solar zenith angle, the viewing zenith angle, and the difference of solar and viewing azimuth angles, and where the coefficients a^k, b^k, c^k, and d^k are determined by a least square regression (more details about this model are included in [7]). A spectral linear interpolation is then performed to adapt the model to POLDER spectral bands.

The TOA surface reflectance ρ^* in each spectral band is then estimated by decoupling the absorption and scattering effects

$$\rho_{TOA}^k(\theta_s, \theta_v, \varphi) = T_g(\theta_s, \theta_v)\rho_{\text{surf+atm}}^k(\theta_s, \theta_v, \varphi). \quad (9)$$

$\rho_{\text{surf+atm}}^k(\theta_s, \theta_v, \varphi)$ is computed with the SOS code [10] with as inputs i) the atmospheric optical thickness in the POLDER bands (derived from the barometric pressure for the Rayleigh scattering and, for the aerosols, from the extinction measurements during the field campaign), ii) an aerosol model (a Junge size distribution associated with the Angstrom coefficient derived from the extinction measurements, and a standard refractive index of the aerosols chosen to be that of silica) and iii) the BRDF measured during the field campaign. The gaseous absorption T_g is derived from a climatology of absorbing gas concentrations for ozone, and oxygen and water vapor absorption are estimated using POLDER 763 and 910 spectral bands as explained in the Appendix.

To obtain an experimental error budget, the retrieved BRDF has been compared to the reflectance measurements made by AVHRR in channel 1 for the four desert sites (Algeria 2, Algeria 3, Algeria 4, and Algeria 5) [7]. The AVHRR instrument is used as a reference, since its only detector does not introduce calibration variation within the field of view. Using the revolution symmetry of the polynomial function $p(\theta)$, this comparison gives a zero-peak error of 1% for high sun zenith angles (50–60°) that correspond to the range observed during the field campaign. Unfortunately, this budget does not apply to 443-nm band, which is not covered by AVHRR channel 1.

Once the BRDF of each site is obtained for POLDER spectral bands, it is possible to perform POLDER multiangular calibration. After discarding cloudy acquisitions, selected POLDER data are averaged over the site surface (15 $\times$ 15 POLDER pixels), and an estimation of the evolution of calibration coefficients is performed for each viewing direction using the following formula:

$$\Delta(Ap(\theta))^k = \frac{A_{\text{in-flight}}^k \cdot p_{\text{in-flight}}^k(\theta)}{A_{\text{preflight}}^k \cdot p_{\text{preflight}}^k(\theta)} = \frac{M\rho^k}{\rho_{TOA}^k(\theta_s, \theta_v, \varphi)} \quad (10)$$

where $M\rho^k$ is the reflectance measured by POLDER and comes from the level 1 product obtained with preflight calibration, $p^k_{\text{preflight}}(\theta)$ is low frequency preflight calibration, and $p^k_{\text{in-flight}}(\theta)$ is the in-flight calibration. Of course, during a clear day, up to 12 different satellite viewing angles θ (Fig. 14) are obtained for a given desert site. $\Delta(Ap(\theta))^k$ is computed for each reference site as a function of the viewing angle and a polynomial fit is performed to estimate the low-frequency polynomial $p^k(\theta)$. Even if absolute calibration coefficients are present in the above equation, it is not possible to derive an accurate absolute calibration from this method, since absolute calibration was not the aim of the *in-situ* campaign. However, if EOS had worked longer, this method could have been used to verify multitemporal calibration, i.e., variations of absolute calibration with time.

b) Results: The data have been acquired during four weeks in November 1996, and a second set during the two first weeks in January 1997. More than 650 images have been used on the 20 desert sites to perform the multiangular calibration. For each image, the areas corresponding to the reference sites are extracted and then automatic tests are used to discard clouds. Six tests were used but the most efficient are:

- a spectral index computed between bands 865P and 443P (desert TOA reflectance increases with the wavelength whereas clouds are whiter);
- statistics on the spatial uniformity of the measurements inside each desert site.

Since only four of the 20 selected desert sites have been characterized with *in-situ* measurements, the nominal method was to use the four Algerian sites for calibration and those having a similar behavior among the others. In Fig. 11(a), the results obtained on one of the Algerian sites (Algeria 2) are plotted. These sites have been affected by bad weather during November, 1996, and only a small amount of cloud-free data has been collected, but moreover, the results have a great standard deviation. Multiangular calibration seems to be correct (except for 443), but the forecast accuracy of 1.5% cannot be achieved with this data set. For 443 spectral band, multiangular calibration seems to be correct up to 45°. For higher viewing angles, the calibration seems to decrease, but it is difficult to prove that the error comes from POLDER multiangular calibration: the data in this zone were only collected with two cloud-free acquisitions (one clear day gives 12 different viewing directions).

In Fig. 11(b), the multiangular calibration results obtained for site Niger 2 are plotted. Even if this site was not among the sites characterized with *in-situ* data, the standard deviation of multiangular calibration results is lower than for Algeria, ranging from 2.3% in band 443 to 0.8% for 865. The errors decrease when the wavelength increases, as do the directional effects of the desert site. Once again, the results indicate a good multiangular calibration for all spectral bands except 443, but it is still difficult to conclude if it comes from the inaccuracy of the BRDF model in this band or from multiangular calibration.

As a conclusion, this multiangular calibration method confirms the quality of the preflight multiangular calibration and the temporal stability of the instrument, except for spectral band 443: in this case, multiangular calibration may have evolved after launch. But since confidence in 443 nm result is low, preflight calibration of this parameter is still used in the level 1 product. The BRDF's of the 20 desert sites are now being characterized using POLDER data in order to use it to cross calibrate POLDER with over optical sensors (Section V-C).

2) High-Frequency Multiangular Calibration over Clouds: Changes after launch in the high-frequency multiangular calibration of POLDER might occur for two reasons: i) if the elementary sensitivities of the detectors in the CCD array change because of temperature variation or because of air-vacuum transition or ii) if particles of dust are deposited on the optics after the last preflight calibration, or if they move in the field-of view (POLDER pupil dimension is around 0.4 mm^2 in the center of the external lens). However, the POLDER CCD array is thermally controlled and air vacuum transition was tested before launch without showing any significant variation: the first cause of variation is unlikely.

In order to determine this high-frequency multiangular in-flight calibration with an accuracy around 0.1%, a new method has been developed using cloud observations. For each elementary detector of the CCD array, and for each channel, the method consists in averaging all the cloud observations performed by the detector. The procedure assumes that if a very high number of cloud observations is collected for each elementary detector, the high-frequency variations of the average of all the measurements will characterize the sensitivity variations within the array, and only the low frequencies will be affected by artifacts of cloud anisotropy.

This calibration method has been experimented with NOAA/AVHRR band 1 raw data using the fact that one line in an AVHRR product is obtained with a single detector. 30 000 lines of AVHRR data have been used. The data have been processed as if each line was acquired with 2048 different detectors having exactly the same sensitivity. The observed high frequencies variations would then be only artifacts. AVHRR cloud detection is performed by a simple threshold on the normalized radiance ($I > 0.25$), since the procedure does not require a precise cloud mask. For each column number of AVHRR data, all the cloud measurements are averaged, and the standard deviation of the averages is computed: the obtained accuracy is under 0.3%.

The same method has been used for POLDER. In this case, the only difficulty is related to the amount of data necessary for the calibration: the required number of cloud measurements is 15(channels) $\times$ 66 308(detectors) $\times$ 15 000(measurements). This requires the use of three entire weeks of POLDER data (there are only 120 measurements per orbit for a given POLDER detector in one spectral band and only one half of them are clouds). In order to estimate the accuracy of the results, two sets of three weeks have been used to obtain two results with independent data sets. The difference between the results of the two data sets has a standard deviation around 0.2%, which indicates that the results obtained from the whole six weeks of data have a precision better than 0.2%. The difference between preflight and in-flight data is between 0.3% and 0.1%, depending on the spectral bands. A few dust particle

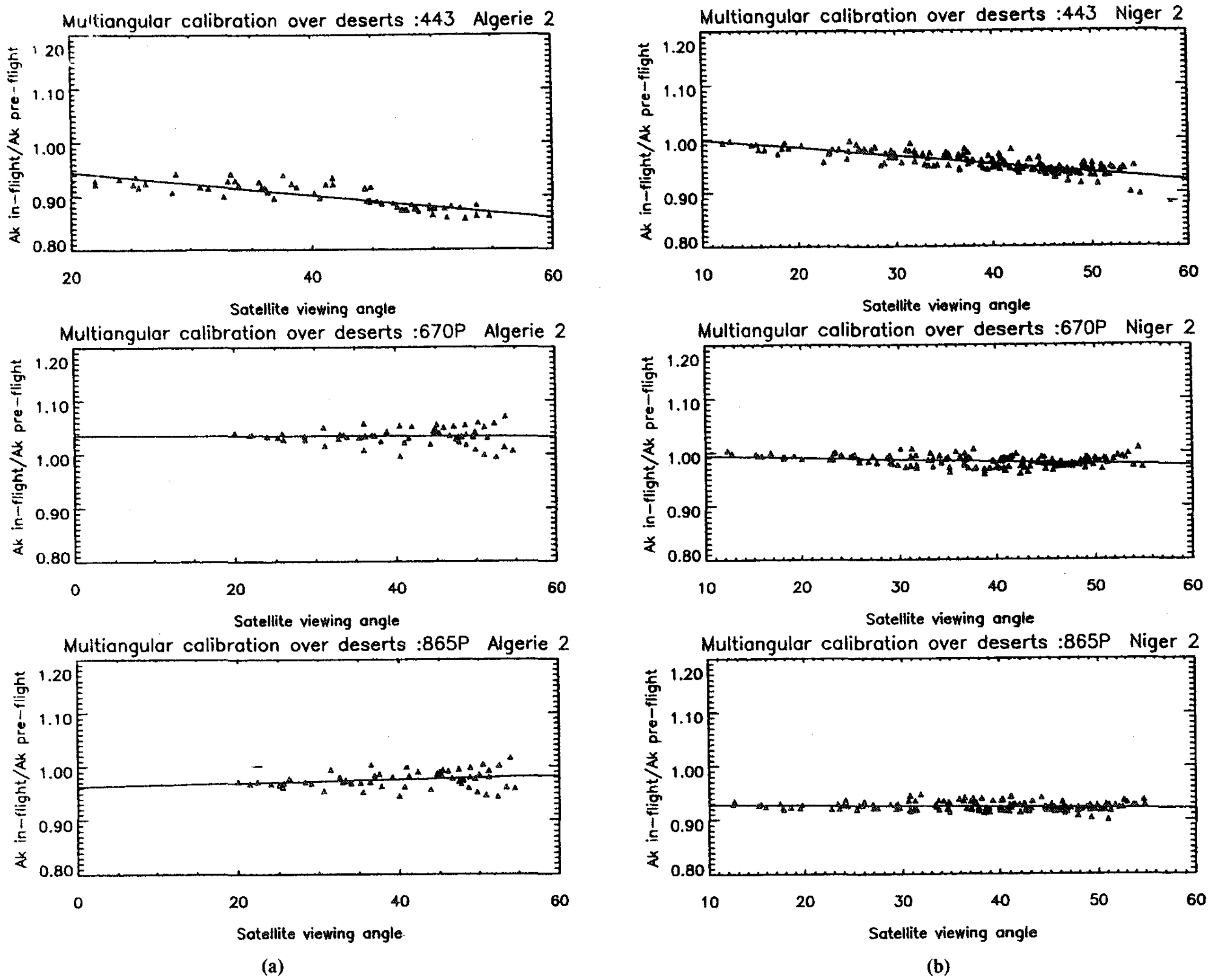

Fig. 11. Multiangular calibration of POLDER over desert sites as a function of satellite viewing angle θ: (a) Algeria 2 site: the number of cloud-free acquisitions during November, 1996, was low over this site, and dispersion of the results is rather high for the remaining points. A variation of POLDER multiangular calibration may be possible for 443 nm band. (b) Niger 2 site: the number of cloud-free acquisitions during November, 1996, was much higher than for Algeria 2, and the dispersion of the results is also lower, but the BRDF model was not measured on this site. A variation of POLDER multiangular calibration might be possible for 443-nm band, whereas the two other bands seem to be correctly calibrated.

effects have been noticed with differences of about 1%, and some differences are linked to the disappearing of artifacts in the preflight calibration.

The coefficients determined by this method are now implemented in POLDER level 1 processing.

V. In-Flight Radiometrical Calibration: Validation

In this chapter are presented three additional calibration methods that were used to validate the results of POLDER in-flight calibration nominal methods. These independent calibration methods are based on different atmospheric models or different calibration sources (including on-board sources for POLDER/ATSR2 cross calibration) in order to verify that the nominal methods are not biased.

A. Interband Calibration Using Clouds

Starting from level 1 data calibrated with the nominal methods, we use the 670-nm radiance measurements as a reference for the estimation of 443-nm and 490-nm absolute calibration coefficients (565 is usually saturated over high reflective clouds). The calibration pixels are selected when their reflectance is over 0.8, when the cloud top apparent pressure deduced from the band ratio 763/765 [4] is under 250 hPa, and when the clouds are uniform enough. Data are corrected for ozone absorption using TOMS data.

Simulations of TOA radiances above convective clouds have been performed using a discrete ordinate method: they are arranged in look-up tables calculated for 443-, 490-, and 670-nm channels. They correspond to three different ice particles (hexagonal plates or columns with a radius 20–60 μm, assumed to be dominant in the highest layers of cumulonimbus), to a cloud top altitude of 10 or 15 km, to a dense grid of observation angles, and to scattering cloud optical thickness between 20 and 200.

For a given altitude and ice particle model, the first step of the procedure finds the scattering optical thickness δ_{est} that corresponds to the observed radiance at 670 nm. Then the

LUT at 443 and 490 are used to estimate the radiances in these bands, assuming the cloud optical thickness does not vary between 443 and 670 nm.

The new estimated calibration coefficient is obtained from the initial coefficient A^k and from measured MI^k and estimated radiance $CI^k(\delta_{\text{est}})$ by

$$A^k_{\text{in-flight}} = A^k_{\text{preflight}} \times \frac{MI^k}{CI^k(\delta_{\text{est}})}. \tag{11}$$

The average results derived from 12 POLDER orbits in November 1996, are reported in Table V. The standard deviation is below 0.8% for the 443 and 490 channels. Changing the cloud top altitude from 15 to 10 km results in an increase of 1% in the calibration coefficient, and the choice of the particle model does not introduce more than 0.5% of variation. The results do not depend on the cloud reflectance, meaning that the selected clouds are thick enough so that the radiance of the surface and of the atmospheric layer below the cloud does not impact on the calibration. The interband calibration results over clouds do not agree perfectly with the results obtained with the nominal methods: the discrepancy at 443 nm is about 6% (only 3% at 490) and has still not been explained in spite of comprehensive verifications.

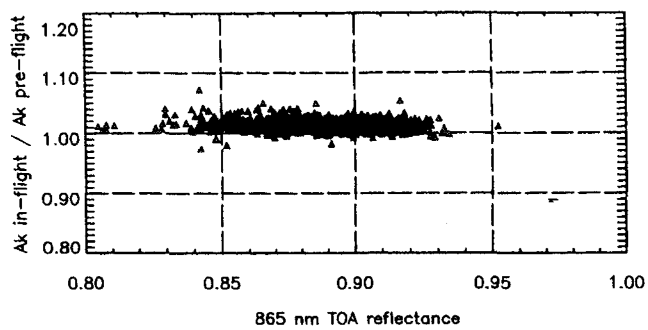

Fig. 12. Absolute calibration elementary results for clouds interband method as a function of the cloud 865-nm reflectance. The interband calibration over clouds is 443 nm.

B. Cross Calibration Between POLDER and OCTS

OCTS is a NASDA radiometer which flew on board ADEOS. Its nadir resolution is around 800 m, the swath is 1400 km wide, and acquisitions are made with eight visible and near infrared bands and four thermal infrared bands. OCTS scanning mechanism is based on a rotating mirror with a maximum scanning angle of 40°, and ten detectors per spectral band are used to collect simultaneously ten lines across-track. Since POLDER and OCTS are on the same platform and share six spectral bands (443, 490, 565, 670, 765, and 865), it is possible to compare the radiance of targets observed at the same instant with the same viewing and solar angles and in nearly identical spectral bands. Simultaneous acquisitions of POLDER and OCTS data have been used in order to cross calibrate both sensors.

In order to enhance the accuracy of the cross calibration, the targets are chosen so that they have a quite high normalized radiance (more than 0.2), a very low polarization rate (polarization sensitivity is not corrected for OCTS), and a good spatial uniformity to avoid possible registration errors between the two sensors: a POLDER pixel is used for cross calibration if the standard deviation of the OCTS measurements inside it is less than 1% of the radiance. The targets corresponding to these criteria are mostly clouds, which also have the advantage of being quite spectrally flat.

Table V gives the absolute calibration derived considering OCTS preflight calibration as a reference (this preflight calibration was still used in the OCTS level 1B products with software ID 3 7). Agreement with the POLDER in-flight method stays within a 7% margin. The same computation has been made using the in-flight calibration of OCTS that is used to produce the version 3.0 ocean color products. This calibration is in fact called "algorithm tuning parameters" by the OCTS calibration team: it was obtained for all spectral bands by comparing *in-situ* chlorophyll-a data with OCTS data [26], and its aim was not to perfectly calibrate OCTS data but to obtain the best ocean color products. One can note that the agreement is good for 443 and 490 and gets worse as the wavelength increases (22% for 865 nm band). This can probably be explained by OCTS in-flight calibration of 865-nm band with a Rayleigh method that uses very low radiances in the near-infrared bands over ocean.

C. Cross Calibration Between POLDER and ATSR2

ATSR-2 is a multispectral scanner on board the ERS-2 satellite launched in 1995. It is based on a conical scanning mechanism which allows the acquisition of the same scenes from two viewing angles during a single pass: a forward along track view (viewing zenith angle around 60°) and a nadir view. ATSR-2 has four infrared channels and three visible/near-infrared channels very close to POLDER spectral bands: 560, 660, and 870 nm. ATSR-2 is calibrated using an on-board diffuser monitored by a photodiode, and using desert sites to measure the drift of the on-board calibration system [34]. A successful cross-calibration between both instruments would be a good validation of both sensor's absolute calibration and also a partial validation of POLDER multiangular calibration.

Since POLDER and ATSR-2 acquisitions of the same scenes are not simultaneous, the cross calibration target must be stable with time, uniform to avoid geometrical registration problems, and its BRDF has to be known: the desert site Sudan 1 has been used for this cross calibration. Thanks to its bidirectional capabilities, POLDER is able to obtain a dense sampling of the viewing conditions over one site. Each month, a BRDF model of the desert site is derived from all the cloud-free measurements obtained by POLDER. Each available cloud-free ATSR2 measurement is then compared to the interpolation of the BRDF model of the same month for ATSR2 viewing conditions. Cloud detection for POLDER data is described in Section IV-B, and for ATSR-2 in Smith *et al.* [32]. POLDER data are corrected for gaseous absorption as described in the Appendix and ATSR-2 data are corrected for ozone absorption using TOMS data. Of course, aerosols above the desert site can cause some variability in the results, but by accumulating enough data, the results should not be biased.

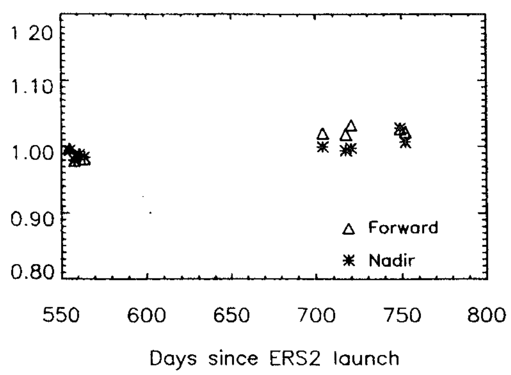

Fig. 13. Ratio of the reflectances at 670 nm measured by ATSR2 and POLDER over a desert site (Sudan 1) from November 1996 to May 1997 with the same viewing angles. Stars indicate that the data have been acquired with nadir viewing, whereas triangles correspond to a forward viewing. In most of the cases, triangles and stars overlap when acquired the same day, and this provides a validation of POLDER multiangular calibration.

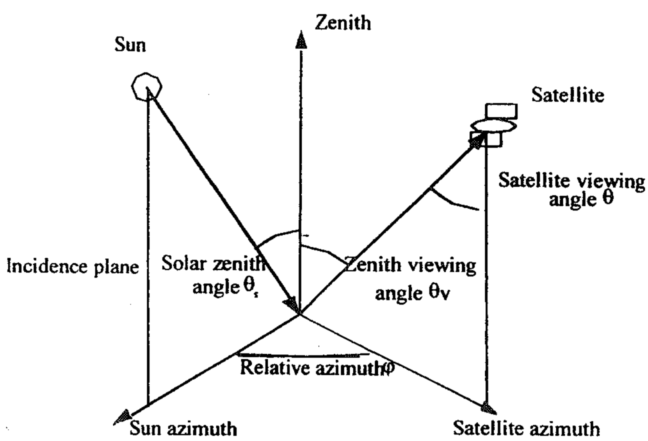

Fig. 14. Definition of the various angles used to characterize the geometry of satellite acquisitions.

The results are quite good (Table V): the agreement between the radiance measured by ATSR-2 and the BRDF derived from POLDER is better than 6% for 565, 1% for 670, but degrades to 5% for 865. The agreement between the directional variations of POLDER BRDF and ATSR-2 reflectances is also very satisfactory and validates partially POLDER multiangular calibration in these spectral bands (Fig. 13).

VI. Conclusion

A new calibration approach has been developed for POLDER based on the design of a very stable instrument, on an exhaustive preflight calibration of the instrument, and on the development of many in-flight operational calibration methods using natural targets. The result is very satisfactory since the in-flight absolute calibration has shown that:

- *POLDER Instrument is Stable:* All in-flight absolute calibration coefficients differ from preflight coefficients by less than 5%, and multiangular calibration did not evolve after launch (except maybe for 443);
- in-flight calibration methods (except POLDER/OCTS cross calibration) agree within a margin of 4% for all the spectral bands but 443.

This calibration process is efficient to provide a correct absolute calibration within a few months (five months were necessary for POLDER 1, but this delay will be reduced with POLDER 2). It is less expensive than developing an on-board calibration device, and more reliable than using *in-situ* measurement campaigns which are subject to weather conditions and provide very few calibration points; maximizing the impact of random error sources. However, all these methods are perfectly suited to POLDER measurements and could not be easily applied to other instruments that do not provide multidirectional measurements (for aerosol detection in sunglint calibration method) or O_2 pressure (for cloud altitude determination in interband calibration using clouds). Such accuracy also could not be achieved without a good characterization and correction of POLDER polarization sensitivity, since our calibration targets (Rayleigh scattering and sunglint) have a high polarization rate.

Still, some uncertainty exists in the calibration of the 443-nm channels, with a discrepancy of 6% between the Rayleigh and the cloud methods that has not yet been explained in spite of intensive verifications.

Appendix
Corrections for Gaseous Absorption

Ozone absorption is removed by computing the transmissions $T^k_{O_3}$ as functions of $m \cdot U_{O_3}$, where m is the air mass factor and U_{O_3} is the column amount of ozone measured by TOMS. The water vapor transmission $T^k_{H_2O}$ is modeled as a function of the ratio of 910- and 865-nm normalized radiances (MI^{910}/MI^{865}). The parameterizations of ozone and water vapor transmissions are derived from simulations using a line-by-line model.

For the oxygen absorption in the 763 and 765 spectral bands, the normalized radiance MI^* that would be measured if there was no absorption is assumed to be the same in both channels (which is really true for sunglint targets). The normalized radiances measured by POLDER (MI^{763} and MI^{765}) can be expressed as a function of MI^* as follows:

$$MI^{763} = MI^* \cdot T^{763}_{O_2} \cdot T^{763}_{H_2O} \cdot T^{763}_{O_3} \tag{A1}$$

$$\boxed{MI^{765} = A \cdot MI^{763} + (1 - A) \cdot MI^* \cdot T^{765}_{H_2O} \cdot T^{765}_{O_3}} \tag{A2}$$

In this formula, the constant A may be considered as the percentage of the 765 spectral band where oxygen lines are located. Its value is derived from line-by-line simulations and is close to 0.3. The oxygen transmittance $T^{763}_{O_2}$ and the normalized radiance without absorption MI* can be derived by combining (A1) and (A2).

Acknowledgment

The authors are grateful to H. Oaku (NASDA/EORC) for supplying OCTS data, to D. L. Smith in the Rutherford Appleton Laboratory, U.K. for providing ATSR-2 extractions over site Sudan1, and to all the persons in CNES who helped the authors exploiting the huge amount of POLDER data used to provide the above results: C. Gélis, P. Théron, A. Meygret, P. Soulé, J. M. Laherrére, A. Guerry, and S. Lafont.

References

[1] Y. Andre, J. M. Laherrere, T. Bret-Dibat, M. Jouret, J. M. Martinuzzi, and J. Perbos, "Instrumental concept and performances of the POLDER instrument," in *SPIE Proc. Infrared Spaceborne Remote Sensing III*, San Diego, CA, July 1995, vol. 2553.

[2] S. Bouffiès, D. Tanré, F. M. Bréon, and P. Dubuisson, "Atmospheric water vapor estimate by a differential absorption technique with the POLDER instrument," *J. Geophys. Res.*, vol. 102, pp. 3831–3841, 1997.

[3] T. Bret-Dibat, Y. André, and J. M. Laherrere, "Preflight calibration of the POLDER instrument," in *SPIE Proc. Remote Sensing and Reconstruction for Three Dimensional Objects and Scenes*, San Diego, CA, July 1995, vol. 2572.

[4] J. C. Buriez, C. Vanbauce, F. Parol, P. Goloub, M. Herman, B. Bonnel, Y. Fouquart, P. Couvert, and G. Sèze, "Cloud detection and derivation of cloud properties from POLDER," *Int. J. Remote Sens.*, vol. 18, no. 13, pp. 2785–2813, 1997.

[5] F. Cabot, G. Dedieu, and P. Maisongrande, "Monitoring NOAA/AVHRR and Meteosat shortwave bands and calibration over stable areas," in *Proc. 6th ISPRS Int. Symp. Physics*, "Measurements and signatures in remote sensing," Val d'Isére, France, Jan. 17–21, 1994, pp. 41–46.

[6] H. Cosnefroy, M. Leroy, and X. Briottet, "Selection and characterization of Saharan and Arabian desert sites for the calibration of optical satellite sensors," *Remote Sens. Environ.*, vol. 58, no. 1, pp. 101–114, 1996.

[7] H. Cosnefroy, X. Briottet, M. Leroy, P. Lecomte, and R. Santer, "A field experiment in Sahara for the calibration of optical satellite sensors," *Int. J. Remote Sens.*, vol. 18, no. 16, pp. 3337–3359, 1997.

[8] C. Cox and W. Munk, "Slopes of the sea surface deduced from photographs of sun glitter," *Bull. Scripps Inst. Ocean.*, vol. 6, pp. 401–488, 1985.

[9] P.-Y. Deschamps, F. M. Bréon, M. Leroy, A. Podaire, A. Bricaud, J. C. Buriez, and G. Sèze, "The POLDER mission: Instrument characteristics and scientific objectives," *IEEE Trans. Geosci. Remote Sensing*, vol. 32, pp. 598–615, 1994.

[10] J.-L. Deuzé, M. Herman, and R. Santer, "Fourier series expansion of the transfer equation in the atmosphere ocean system," *J. Quant. Spectrosc. Radiat. Transfer*, vol. 41, pp. 483–494, 1989.

[11] B. Fougnie, P.-Y. Deschamps, and R. Frouin, "Vicarious calibration of the POLDER ocean color spectral bands using *in situ* measurements," *IEEE Trans. Geosci. Remote Sensing*, this issue, pp. 1567–1574.

[12] B. Fougnie and P. Y. Deschamps, "Observation et modélization de la signature spectrale de l'écume de mer," in *Proc. 7th Int. Colloq. Physical Measurements and Signatures in Remote Sensing*, Apr. 7 and 11, 1997, pp. 227–234.

[13] P. Goloub, B. Toubbe, M. Herman, T. Bailleul, O. Hagolle, J. M. Martinuzzi, and B. Rougé, "In-flight polarization calibration of POLDER," in *Proc. EUROPTO Advanced and Next-Generation Satellites*, 1996, vol. 2957, pp. 299–310.

[14] H.-R. Gordon and M. Wang, "Retrieval of water leaving radiance and aerosol optical thickness over the oceans with Seawifs: A preliminary algorithm," *Appl. Opt.*, vol. 33, pp. 443–452, 1994.

[15] O. Hagolle, A. Guerry, L. Cunin, B. Millet, J. Perbos, J.-M. Laherrere, T. Bret-Dibat, and L. Poutier, "POLDER Level 1 processing algorithms," in *SPIE Aerosense Proc. Algorithms for Multispectral and Hyperspectral Imagery II*, Orlando, FL, 1996, pp. 308–319.

[16] O. Hagolle, A. Guerry, L. Cunin, B. Millet, J. Perbos, J.-M. Laherrere, and T. Bret-Dibat, "POLDER level 1 processing algorithms," *SPIE Proc.*, vol. 2758, pp. 308–319, 1996.

[17] P. Henry, M. Dinguirard, and M. Bodilis, "Spot multitemporal calibration over stable desert areas," in *SPIE Int. Symp. Aerospace and Remote Sensing, Tech. Conf. 1938*, Orlando, FL, Apr. 12–16, 1993, pp. 67–76.

[18] B.-N. Holben, Y.-J. Kaufman, and J.-D. Kendall, "NOAA_11 AVHRR visible and near-infrared in-flight calibration," *Int. J. Remote Sens.*, vol. 11, pp. 1511–1519, 1990.

[19] P. Koepke, "Effective reflectance of oceanic white caps," *Appl. Opt.*, vol. 20, p. 34, 1984.

[20] J. M. Laherrere, L. Poutier, T. Bret-Dibat, O. Hagolle, C. Baqué, P. Moyer, and E. Verges, "POLDER on-ground stray light analysis, calibration and correction," *EUROPTO SPIE Proc.*, vol. 3221, pp. 132–140.

[21] A. Lifermann, J.-L. Counil, J.-M. Martinuzzi, and J. Perbos, "General outlines of the POLDER experiment," in *SPIE Proc. Symp. Satellite Remote Sensing II*, Paris, France, Sept. 1995, pp. 245–252.

[22] A. Meygret, O. Hagolle, P. Henry, M. Dinguirard, P. Hazane, R. Santer, and J.-L. Deuzé, "SPOT 3: First in-flight calibration results," in *Proc. IGARSS'94*, Pasadena, CA, 1994.

[23] A. Morel, "Optical modeling of the upper ocean in relation to its biogenous matter content (case I waters)," *J. Geophys. Res.*, vol. 93, no. C9, pp. 10 749–10 768, Sept. 15, 1988.

[24] C. Moulin, C. E. Lambert, J. Poitou, and F. Dulac, "Long term (1983–1994) calibration of the Meteosat solar (VIS) channel using desert and ocean targets," *Int. J. Remote Sens.*, vol. 17, no. 6, pp. 1183–1200, 1996.

[25] A.-P. McNally and M. Vesperini, "Variational analysis of humidity information from TOVS radiances," EUMETSAT/ECMWF Res. Rep. 1.

[26] OCTS Team: M. Shimada *et al.*, "A CAL/VAL report on the OCTS Version 3 products," Feb. 98, NASDA Intern. Rep.

[27] R. M. Pope and E. S. Fry, "Absorption spectrum (380–700nm) of pure water—II: Integrating cavity measurements," *Appl. Opt.*, vol. 36, no. 33, p. 8710, 1997.

[28] L.-S. Rothman, C.-P. Rinsland, A. Goldman, S.-T. Massie, D.-P. Edwards, J.-M. Flaud, A. Perrin, C. Camy-Peyret, V. Dana, J.-Y. Mandin, J. Schroeder, A. McCann, R.-R. Gamache, R.-B. Wattson, K. Yoshino, K. Chance, K. Jucks, L.-R. Brown, V. Nemtchinov, and P. Varanasi, "The HITRAN molecular spectroscopic database and HAWKS (HITRAN Atmospheric Workstation): 1996 Edition," *J. Quant. Sprectrosc. Radiat. Transfer*, 1998.

[29] F. Sakuma, T. Bret-Dibat, H. Sakate, A. Ono, J. Perbos, J. M. Martinuzzi, K. Imaoka, H. Oaku, T. Moriyama, Y. Miyachi, and Y. Tange, "POLDER-OCTS preflight cross calibration using round robin radiometers," in *SPIE Proc. Infrared Spaceborne Remote Sensing III*, San Diego, CA, July 1995, vol. 2553.

[30] R. Santer, M. Asmani, E. Vermote, and M. Sharman, "In-flight calibration of channels 1 and 2 of AVHRR using desertic sites and clouds," in *Proc. 5th ISPRS Int. Symp. Physics on Measurements and Signatures in Remote Sensing*, Courchevel, France, 1991, pp. 65–68.

[31] M. Schwindling, P.-Y. Deschamps, and R. Frouin, "Verification of aerosol models for satellite ocean color remote sensing," *J. Geophys. Res.*, pp. 24 919–24 935, 1998.

[32] E. Shettle and R. Fenn, "Models for the aerosols of the lower atmosphere and the effects of humidity variations on their optical properties," AGFL-TR-79-0214, Sept. 20, 1979.

[33] P.-N. Slater, S.-F. Biggar, K.-J. Thome, D.-I. Gellman, and P.-R. Spyak, "Vicarious radiometric calibrations of EOS sensors," *Amer. Meteorol. Soc. J.*, 1996.

[34] D.-L. Smith, P.-D. Read, and C.-T. Mutlow, "The calibration of the visible/near infra-red channels of the along-track-scanning-radiometer-2 (ATSR2)," in *EUROPTO Proc. Sensors, Systems, and Next Generation Satellites*, London, Brittany, Sept. 97, vol. 3221, pp. 53–62.

[35] K. Stamnes, S. C. Tsay, W. Wiscombe, and K. Jayaweera, "Numerically stable algorithm for discrete ordinate method radiative transfer in multiple scattering and emitting layered media," *Appl. Opt.*, vol. 12, pp. 2502–2509, 1998.

[36] W. F. Staylor, "Degradation rates of the AVHRR visible channel for the 6, 7 and 9 spacecraft," *J. Atmos. Ocean. Technol.*, vol. 7, pp. 411–423, 1990.

[37] C. Vanbauce, J.-C. Buriez, F. Parol, B. Bonnel, G. Sèze, and P. Couvert, "Apparent pressure derived from ADEOS-POLDER observations in the oxygen A-band over ocean," *Geophys. Res. Lett.*, 1998.

[38] E. Vermote and Y.-J. Kaufman, "Absolute calibration of AVHRR visible and near infrared using ocean and cloud views," *Int. J. Remote Sensing*, vol. 16, no. 13, pp. 2317–2340, 1995.

[39] E. Vermote, R. Santer, P. Y. Deschamps, and M. Herman, "In-flight calibration of large field of view sensors at short wavelengths using Rayleigh scattering," *Int. J. Remote Sensing*, vol. 13, no. 18, pp. 3409–3429.

[40] E. Vermote, D. Tanré, J. L. Deuzé, M. Herman, and J. J. Morcrette, "Second simulation of the satellite signal in the solar spectrum, 6S: An overview," *IEEE Trans. Geosci. Remote Sensing*, vol. 35, pp. 675–685, May 1997.

[41] M. Vesperini, F. M. Breon, and D. Tanré, "Atmospheric water vapor content from POLDER spaceborne measurements," this issue, pp. 1613–1619.

[42] C. Wehrli, "Extraterrestrial solar spectrum," Publ. no. 615 Physikalisch-Meteorologishes Observatorium, World Radiation Center, Davosdorf, Switzerland, 1985.

[43] B. Toubbé, T. Bailleul, J. L. Deuzé, Ph. Goloub, O. Hagolle, and M. Herman, "In flight calibration of the POLDER instrument using the sun's glitter," *IEEE Trans. Geosci. Remote Sensing*, vol. 37, pp. 513–525, Jan. 1999.

Olivier Hagolle, for a photograph and biography, see p. 525 of the January 1999 issue of this TRANSACTIONS.

Philippe Goloub, for a photograph and biography, see p. 525 of the January 1999 issue of this TRANSACTIONS.

Pierre-Yves Deschamps received the Ph.D. degree in 1977 in atmospheric physics from the Université de Lille, France.

Since then, he has been a Researcher at the Centre National de la Recherche Scientfique, working at the Laboratoire d'Etudes et de Recherches en Télédétection Spatiale and at the Laboratoire d'Optique Atmosphérique. He conducts research in atmospheric satellite remote techniques to retrieve various biophysical parameters for use in climate change studies.

Hélène Cosnefroy, photograph and biography not available at the time of publication.

Xavier Briottet received the Ph.D. degree in electronics from Ecole National Supérieure de l'Aéronautique et de l'Espace, Toulouse, France, in 1986.

Since 1986, his primary research interest in the remote sensing domain are in vicarious calibration using Rayleigh scattering and desert sites and in multiresolution problems.

Thierry Bailleul, for a photograph and biography, see p. 525 of the January 1999 issue of this TRANSACTIONS.

Jean-Marc Nicolas graduated from the Institut National des Telecommunications in 1992.

He has been working at the Laboratoire d'Optique Atmospherique, Lille, France, since 1994, where he began to participate in the POLDER experiment as a Computer Scientist. He is interested in both atmospheric correction over ocean and calibration/validation activities for POLDER.

Frédéric Parol was born in 1963. He studied at the University of Lille, France, and received the M.S. degree in physics in 1986 and the Ph.D. degree in atmospheric physics in 1990.

He is currently an Assistant Professor of physics at the University of Lille and a Researcher employed at the Laboratoire d'Optique Atmosphérique, Lille, France. He participated in the development of the first POLDER "Earth Radiation Budget and Clouds" processing line and he was especially in charge of the "Molecular absorption correction" and "Cloud pressure" algorithms. He has been a member of the International POLDER Science Working Team (IPSWT) since 1994. His work covers theoretical and experimental research in atmospheric science, radiative transfer, and remote sensing. His major areas of activity concern remote sensing of cloud properties, interaction between clouds and radiation, and the influence of clouds on climate.

Bruno Lafrance received the Ph.D. degree in atmospheric physics from the Université des Sciences et Technologies de Lille, Laboratoire d'Optique Atmosphérique, Lille, France, in 1997. His dissertation focused on the stratospheric aerosol correction for the POLDER data processing and the formation of polarized light in the atmosphere.

He is currently with the Center National d'Etudes Spatiales, Toulouse, France. He works on the interband calibration of POLDER and vegetation over thick clouds.

Maurice Herman, for a photograph and biography, see p. 525 of the January 1999 issue of this TRANSACTIONS.

REFERENCES BIBLIOGRAPHIQUES

Brenguier, J.L., H. Pawlowska, L. Schüller, R. preusker, J. Fischer, and Y. Fouquart, 2000: Radiative properties of boundary layer clouds : optical thickness and effective radius versus geometrical thickness and droplet concentration. Accepted in *J. Atmos. Sci.*

Bréon, F.-M., 1992: Reflectance of broken clouds fields: simulation and parameterization, *J. Atmos. Sci.*, **49**, 1221-1232.

Cahalan, R.F., W. Ridgway, W.J. Wiscombe, S. Gollmer, and Harshvardhan, 1994: Independent pixel approximation and Monte Carlo estimates of stratocumulus albedo, *J. Atmos. Sci.*, **51**, 3776-3790.

Cess, R.D., et *al.*, 1990: Intercomparison and interpretation of climate feedback processes in 19 atmospheric general circulation models, *J. Geophys. Res.*, **95**, 16601-1661.

Cess, R.D., et *al.*, 1996: Cloud feedback in atmospheric general circulation models: An update, *J. Geophys. Res.*, **101**, 12791-12794.

Cox, S.K., D. MacDougal, D. Randall, and R. Schiffer, 1987: The First ISCCP Regional Experiment. *Bull. Amer. Meteor. Soc.*, **67**, 14-118.

Deschamps, P.Y., F. M. Breon, M. Leroy, A. Podaire, A. Bricaud, J. C. Buriez, and G. Sèze, 1994: The POLDER mission: Instrument characteristics and scientific objectives, *IEEE Trans. Geosci. Rem. Sens,* **32**, 598-615.

Descloitres, J., H. Pawlowska, J. Pelon, J.-L. Brenguier, F. Parol, J.-C. Buriez and P. Flamant, 1996: Experimental retrieval of cloud optical thickness during EUCREX : Comparison of three approaches. *12th International Conference on Clouds and Precipitation,* Zurich, Suisses, 20-24 Août 1996.

Doutriaux-Boucher, M., J.C. Buriez, F. Parol and A.J. Baran, 1999: Angular Dependence of POLDER Cloud Optical Thickness According to Various Cloud Particle Models, *Proc. of the ALPS99 Meeting*, Meribel, France, 18-22 January 1999.

Doutriaux-Boucher, M., J.C. Buriez, G. Brogniez, L. C.-Labonnote, and A.J. Baran, 2000: Sensitivity of retrieved POLDER directional cloud optical thickness to various ice particle models, *Geophys. Res. Letters*, **27**, 109-112.

Gao, B. C., A. F. H. Goetz, and W. J. Wiscombe, 1992: Cirrus cloud detection from airborne imaging spectrometer data using the 1.375 µm water vapor band, *Geophys. Res. Lett.*, **260**, 523-526.

Han, Q., W.B. Rossow, and A.A. Lacis, 1994 : Near-global survey of effective droplet radii in liquid water clouds using ISCCP data. *J. Climate*, **7**, 465-497.

Houghton, J.T., G.J. Jenkins, and J.J. Ephraums, (eds.), 1990: *Climate Change: The IPCC Scientific Assessment*, World Meteorological Organization/United Nations Environment Programme, Cambridge University Press, 364 pp.

Houghton, J.T., L.G. Meira Filho, J. Bruce, Hoesung Lee, B.A. Callander, E. Haites, N. Harris, and K. Maskell, (eds.), 1994: *Climate Change 94: Radiative Forcing of Climate Change and An Evaluation of the IPCC IS92 Emission Scenarios,* World Meteorological Organization/United Nations Environment Programme, Cambridge University Press, 340 pp.

Jolivet, D., J.C. Buriez, F. Parol and Y. Fouquart, 1999 : Simulations of the Anisotropy of the Radiation Reflected by Heterogeneous Clouds. Application to POLDER, *Proc. of the ALPS99 Meeting*, Meribel, France, 18-22 January 1999.

Kandel, R.S., J.L. Monge, M. Viollier, L.A. Pakhomov, V.I. Adasko, R.G. Reitenbach, E. Raschke, and R. Stuhlmann, 1994: The ScaRaB project : Earth radiation budget observations from the Meteor satellites, World Space Congress (Washington) -COSPAR symp. A.2-S, *Adv. Space Research*, **14(1)**, 47-54.

Kobayashi, T., 1988: Parameterization of reflectivity for broken cloud fields; *J. Atmos. Sci.*, **45**, 3034-3045.

Kobayashi, T., 1993: Effects due to cloud geometry on biases in the albedo derived from radiance measurements, *J. Climate*, **6**, 120-128.

Loeb, N. G., T. Várnai, and D. M. Winker, 1998: Influence of sub-pixel scale cloud-top structure on reflectances from overcast stratiform cloud layers, *J. Atmos. Sci.*, **55** , 2960-2973.

Loeb, N.G., F. Parol, J.-C. Buriez, and C. Vanbauce, 1999: Influence of biases in 1D cloud optical depth retrievals on albedo estimation from Angular Distribution Models, *Proc. of the ALPS99 Meeting*, Meribel, France, 18-22 January 1999.

Minnis, P., P.W. Heck, D.F. Young, C.W. Fairall, and J.B. Snider, 1992: Stratocumulus cloud properties derived from simultaneous satellite and island-based instrumentation during FIRE, *J. Appl. Meteor.*, **31**, 317-339.

Nakajima, T., and M.D. King, 1990 : Determination of the optical thickness and effective particle radius of clouds from reflected solar radiation measurements. Part I : Theory, *J. Atmos. Sci.*, **47**, 1878-1893.

Parol, F., 1999: The Contribution of POLDER for Cloud Study: An Overview, sollicited paper, *Proc. of the ALPS99 Meeting*, Meribel, France, 18-22 January 1999.

Ramanathan, V., and W. Collins, 1991: Thermodynamic regulation of ocean warming by cirrus clouds deduced from observations of the 1987 El Nino, *Nature*, **351**, 27-32.

Raschke, E., J. Schmetz, J. Heintzenberg, R. Kandel, and R. Saunders, 1990: The International Cirrus Experiment (ICE) - A joint European effort, *ESA Journal*, **14**, 193-199.

Raschke, E., P. Flamant, Y. Fouquart, P. Hignett, H. Isaka, P. Jonas, and H. Sundqvist, 1998: Cloud-radiation studies during the European Cloud and Radiation Experiment (EUCREX), *Surv. Geophys.*, **19**, 89-138.

Raval, A., and V. Ramanathan, 1989: Observational determination of the greenhouse effect, *Nature*, **342**, 758-761.

Sèze, G, and M. Desbois, 1987: Cloud cover analysis in satellite imagery using spatial and temporal characteristics of the data, *J. Climate Appl. Meteor.*, **26**, 287-303.

Starr, D.O'C., 1987: A cirrus-cloud experiment: Intensive field observations planned for FIRE. *Bull. Amer. Meteor. Soc.*, **67**, 119-124.

Welch, R.M., and B.A. Wielicki, 1984: Stratocumulus cloud field reflected fluxes: The effect of cloud shape, *J. Atmos, Sci.*, **41**, 3085-3103.

Wielicki, B. A, and B.R. Barkstrom, 1991: Cloud and the Earth's Radiant Energy System (CERES): An Earth observing system experiment, *Second Symp. On Global Change Studies*, New Orleans, LA, *Amer. Meteor. Soc.*, 11-16.

Wielicki B.A., B.R. Barkstrom, E.G. Harrison, R.B Lee III, G.L Smith, and J.E. Cooper, 1996: Clouds and the Earth's Radiant Energy System (CERS): An Earth observing system experiment, *Bull. Amer. Meteor. Soc.*, **77**, 853-868.

LISTE DES ACRONYMES ET ABREVIATIONS

ADEOS	ADvanced Earth Observing System
ADM	Angular Distribution Model
ASTEX	Atlantic Stratocumulus Transition Experiment
ATSR	Along Track Scanning Radiometer
AVHRR	Advanced Very High resolution Radiometer
CENA	Climatologie Etendue des Nuages et des Aérosols
CEPEX	Cloud Equatorial Pacific Ocean EXperiment
CERES	Clouds and the Earth's Radiant Energy System
CLOUDSAT	Cloud Satellite
CNES	Centre National d'Etudes Spatiales
CNRM	Centre National de Recherches Météorologiques
EOS	Earth Observing System
ERBE	Earth Radiation Budget Experiment
EUCREX	EUropean Cloud Radiation EXperiment
FIRE	First ISCCP Regional Experiment
FSSP	Forward Scattering Spectrometer Probe
GCM	Global Climate Model
GLI	Global Imager
GOES	Geostationary Operational Environmental Satellite
ICE	International Cirrus Experiment
IPA	Independent Pixel Approximation
IPCC	Intergovernmental Panel on Climate Change
IPSWT	International POLDER Science Working Team
ISCCP	International Satellite Cloud Climatology Project
LaRC	Langley Research Center
LEANDRE	Lidar Embarqué pour l'étude des Aérosols, Nuages, Dynamique, Rayonnement et Espèces minoritaires
LMD	Laboratoire de Météorologique Dynamique
LSCE	Laboratoire des Sciences du Climat et de l'Environnement
MIR	Moyen Infrarouge
MODIS	Moderate Resolution Imaging Spectroradiometer
NASA	National Aeronautics & Space Administration
NASDA	NAtional Space Development Agency of Japan
NOAA	National Oceanic and Atmospheric Adiministration
OCTS	Ocean Color and Temperature Scanner

PARASOL	Polarisation et Anisotropie des Réflectances au sommet de l'Atmosphère, couplées avec un Satellite d'Observation emportant un Lidar
PICASSO	Pathfinder Instrument for Cloud and Aerosol Spaceborne Observations
POLDER	POLarization and Directionality of the Earth's Reflectances
ScaRaB	Scanner for Radiation Budget
SOFIA	Surface of the Ocean, Fluxes and Interactions with the Atmosphere